STIMULI-RESPONSIVE POLYMERIC BIOMATERIALS FOR THERAPEUTIC APPLICATIONS

by

Aysun Değirmenci

B.Sc. Chemistry, Canakkale Onsekiz Mart University, 2013

M.Sc. Chemistry, Canakkale Onsekiz Mart University, 2014

Submitted to the Institute for Graduate Studies in
Science and Engineering in partial fulfillment of
the requirement for the degree of
Doctor of Philosophy

Graduate Program in Chemistry

Boğaziçi University

2023

STIMULI-RESPONSIVE POLYMERIC BIOMATERIALS FOR THERAPEUTIC APPLICATIONS

Pr[illegible]na Sa[illegible] .....
(Thesis S[illegible]isor)

[illegible] Amit [illegible]nyal .....
[illegible]

DATE OF APPROVAL: 10.01.2023

To memory of Memduh Bilmez

ACKNOWLEDGEMENTS

I would like to express my sincere gratitude to my thesis supervisor Prof. Rana Sanyal for being a great advisor. I am thankful for her motivation and endless support during my graduate studies. She is the strongest woman in my life I know. She is a role model for me. I have always felt very happy and lucky to be a member of 'Sanyal Lab," and I am very proud to have graduated from this group.

I would like to express my sincere gratitude to my thesis co-advisor Prof. Amitav Sanyal. I am so lucky because I met him at a chemistry conference. If I did not participate in this conference, now I would not be where I am. He has always motivated me, and he gave me different projects to improve my scientific skills. I have felt lucky due to these different projects because they enabled me to achieve my current level. I am grateful for his motivation, enthusiasm, and endless support during my graduate studies.

I would like to extend my thanks to my thesis jury, Prof. Fatih Algı, Prof İlknur Doğan, Assoc. Prof. Oktay Demircan and Assoc. Prof. Mehmet Arslan for taking the time to review and evaluate my work. I am also thankful to Assoc. Prof. Mehmet Arslan for providing me with the monomer and copolymer for my project.

A great piece of gratitude is due to my MSc. thesis advisor Prof. Fatih Algı who encouraged me to apply to this university. I am also thankful to Melek Pamuk Algı for everything she has taught me. Thanks to them, I did not have any difficulty during my graduate studies. I always felt their support. I believe that we will keep strong ties for much longer.

I would like to thank Burcu Sümer Bolu, Hatice Damla Kayhan and Seda Tarhan Şahin due to their help with *in vitro* cell experiments. I am grateful to Sedef Kutlu Özkaya and Ali Rıza Ülker for *in vitro* release data collection.

I would like to thank Tuğçe Nihal Gevrek Civan for her friendship, support and valuable guidance throughout my surface-related projects. Also, I would like to thank her due to help with XPS analysis and data interpretation. We were coauthors in two publications, and I am so happy about this.

I would like to thank all my fellow labmates of the Sanyal group (present and past members).

I would like to thank Enfâl Çivril for her intimate friendship and the unforgettable memories we shared. She is my sister, and I believe that we will sustain the strong friendship for much longer. I am also thankful to Kamil Çöllü for his valuable friendship.

I would like to thank undergraduate students for their valuable contributions to my research projects. I appreciate Ceyda Erden, Ata Girit and Hüseyin Kuruoğlu for enjoyable days.

I would like to thank the Scientific and Technological Research Council of Turkey (TÜBİTAK, Project No. 115S997 and 221Z223) and RS Research for financial assistance for the work reported in this thesis.

Finally, I would like to thank my dear family for their enduring love, support and encouragement. I am also thankful to my mother her patience with my student dorm-like lifestyle while I was writing my PhD thesis.

ABSTRACT

STIMULI-RESPONSIVE POLYMERIC BIOMATERIALS FOR THERAPEUTIC APPLICATIONS

This thesis explores the development of novel polymeric materials to address challenges in disease diagnosis and drug delivery. This thesis's first and second studies are related to developing novel polymer-based drug delivery systems. The first study synthesized different polymer-drug conjugates to find the best candidate for *in vitro* performance towards pancreas adenocarcinoma. Drugs were conjugated to the polymer backbone via pH and/or redox-responsive linkers, and drug release profiles and cytotoxic activities against different cancer cells were evaluated for each copolymer. In the second study, biodegradable nanogels for targeted drug delivery were fabricated using self-assembly, and the drug was physically loaded into nanogels to achieve efficient drug delivery vehicles. In the third part, biodegradable and injectable hydrogels were fabricated using a metal-free click reaction. Azide and gemcitabine-containing copolymers containing carbamate and disulfide linkers between the drug and polymer backbone were synthesized and crosslinked using cyclooctyne-terminated telechelic poly(ethylene glycol) polymer. Hydrogels were evaluated for drug release and cytotoxic activity. The other projects reported in this thesis focus on the fabrication of novel polymeric coatings for biomedical applications such as biomolecular immobilization, cellular attachment, and release. In the fourth study, hydrophilic polymer brushes were prepared and functionalized using a radical-exchange cross-coupling reaction to develop sensing and protein immobilization platforms. In the fifth project, thiol-reactive redox-responsive polymer brushes containing pyridyl disulfide units were fabricated, and functionalization with thiol-containing dyes, drugs, and biomolecules was shown. In the sixth study, thiol-reactive benzothiazole-disulfide-containing polymeric thin films were prepared and investigated for cellular attachment and cell release studies. In the final study, adamantane-containing polymeric thin films were fabricated, which could undergo supramolecular interaction with functional ligands bearing beta-cyclodextrin, and modified surfaces were used for protein and cell attachment.

ÖZET

TERAPÖTİK UYGULAMALAR İÇİN UYARICI-DUYARLI POLİMERİK BİYOMATERYALLER

Bu tez, hastalık teşhisi ve ilaç salımındaki zorlukları ele almak için yeni polimerik malzemelerin geliştirilmesini araştırmaktadır. Bu tezin birinci ve ikinci çalışması yeni polimer bazlı ilaç taşıyıcı sistemlerin geliştirilmesi ile ilgilidir. İlk çalışmada, pankreatik adenokarsinomaya karşı hücre içi değerlendirmelerdeki en iyi adayı belirlemek için farklı polimer-ilaç konjugatları sentezlenmiştir. İlaçlar polimer iskeletlerine pH ve/veya redoks duyarlı bağlayıcılar ile bağlanmıştır ve her bir polimerin ilaç salım profili ve sitotoksik aktiviteleri değerlendirilmiştir. İkinci çalışmada, hedefli ilaç salımı için biyobozunur nanojel kendiliğinden kurulma yoluyla tasarlanmıştır ve etkili ilaç taşıma aracı elde etmek için ilaç nanojele fiziksel olarak yüklenmiştir. Üçüncü bölümde, biyobozunur ve enjekte edilebilir hidrojel metal kullanılmaksızın gerçekleşen klik tepkimesi ile sentezlenmiştir. Polimer iskeleti ile ilaç arasında karbamat ve disülfid bağlayıcıları içeren ve azid ve gemsitabin içeren kopolimerler sentezlenmiştir ve bu polimerler siklooktin-sonlu telekelik poli(etilen glikol) polimeri ile çapraz bağlanmıştır. Hidrojellerin ilaç salımı ve sitotoksisitesi incelenmiştir. Tezde raporlanan diğer projeler, biyomolekül sabitleme, hücre kültürü ve salım gibi biyomedikal alanlar için yeni polimerik kaplamaların dizaynı üzerine odaklanmaktadır. Dördüncü çalışmada, hidrofilik polimer fırçalar hazırlanmıştır ve bu fırçalar sensör ve protein sabitleme platformları geliştirmek için radikal-değişim çapraz-çiftleme tepkimesi ile fonksiyonelleştirilmiştir. Beşinci çalışmada, piridil disulfid içeren tiyol-reaktif redoks-duyarlı polimer fırçalar hazırlanmıştır ve fırçaların modifikasyonları tiyol içeren boya, ilaç ve biyomoleküllerle gösterilmiştir. Altıncı çalışmada, benzotiyazol-disülfid içeren tiyol-reaktif polimerik ince filmler hazırlanmıştır ve filmler hücre sabitleme ve hücre salım çalışmaları için incelenmiştir. Son çalışmada, beta siklodekstrin taşıyan fonksiyonel ligandlar ile supramoleküler etkileşime girebilen adamantan içeren polimerik ince filmler tasarlanmıştır ve modifiye edilmiş yüzeyler protein ve hücre bağlanması için kullanılmıştır.

TABLE OF CONTENTS

ACKNOWLEDGEMENTS....iv
ABSTRACT....vi
ÖZET....vii
TABLE OF CONTENTS....viii
LIST OF FIGURES....xx
LIST OF TABLES....xli
LIST OF ACRONYMS/ABBREVIATIONS....xliv
1. INTRODUCTION....1
1.1. Polymer Drug Conjugates for Delivery of Anticancer Drugs....1
1.1.1. Cancer....1
1.1.2. Chemotherapy....4
1.1.3. Polymer Therapeutics....5
1.1.4. Polymer Drug Conjugates (PDCs) as Polymer Therapeutics....6
1.1.5. Importance of Polymer in Polymer Drug Conjugates....7
1.1.6. The Choice of Linker in Polymer Drug Conjugates....8
1.1.7. Molecular Weight, Size, and Enhanced Permeation and Retention (EPR) Effect....10
1.1.8. Active Targeting....11
1.1.9. Polymeric Nanomedicine....12
1.2. Nanogels and Hydrogels for Delivery of Anticancer Drugs....13
1.2.1. Nanogels....13
1.2.2. Hydrogels....16
1.2.3. Chemically Crosslinked Hydrogels....18
1.2.4. Stimuli-Responsive Hydrogels....20
1.2.5. Injectable Hydrogels....21
1.3. Fabrication of Polymer Coatings on Solid Substrates....21
1.3.1. Polymeric Thin Films....22
1.3.2. Polymer Brushes....24
1.3.3. Surface-Initiated RAFT (SI-RAFT) Polymerization....25

1.3.4. Post-Polymerization Modification and Biomedical Applications of Polymer Brushes 27
1.3.5. Functionalization and Biomedical Applications of Reactive Polymeric Coatings.....29
2. RESEARCH OVERVIEW 32
3. FABRICATION OF POLYMER GEMCITABINE AND HYDROXY-CHLOROQUINE CONJUGATES FOR PANCREATIC ADENOCARCINOMA ..34
3.1. Introduction.....34
3.2. Experimental.....36
3.2.1. Materials.....36
3.2.2. Methods.....37
3.2.3. Synthesis and Characterization of Ester-Containing Hydroxychloroquine Methacrylate Monomer (HCQ-E-MA).....38
3.2.4. Synthesis and Characterization of Carbamate-Containing Hydroxychloroquine Methacrylate Monomer (HCQ-C-MA).....38
3.2.5. Synthesis and Characterization of Carbonate-Including Hydroxychloroquine Methacrylate Monomer (HCQ-CB-MA).....39
3.2.6. Synthesis and Characterization of Carbamate-Containing Gemcitabine Methacrylate Monomer (GEM-C-MA).....40
3.2.7. Synthesis and Characterization of Disulfide-Carbamate-Containing Gemcitabine Methacrylate Monomer (GEM-SSC-MA).....40
3.2.8. Synthesis and Characterization of BODIPY-Methacrylate Monomer.....41
3.2.9. Synthesis and Characterization of Copolymer P(OEG/HCQ-E).....42
3.2.10. Synthesis and Characterization of Copolymer P(OEG/HCQ-C) 42
3.2.11. Synthesis and Characterization of Copolymer P(OEG/HCQ-CB).....43
3.2.12. Synthesis and Characterization of Copolymer P(OEG/GEM-C).....43
3.2.13. Synthesis and Characterization of Copolymer P(OEG/GEM-SSC) 44
3.2.14. Synthesis and Characterization of Copolymer P(OEG/HCQ-E/GEM-C)..44
3.2.15. Synthesis and Characterization of Copolymer P(OEG/HCQ-C/GEM-C) 45
3.2.16. Synthesis and Characterization of Copolymer P(OEG/HCQ-C/GEM-SSC) 45

3.2.17. Synthesis and Characterization of Copolymer P(OEG/HCQ-CB/GEM-SSC) 46
3.2.18. Synthesis and Characterization of Copolymer P(OEG/HCQ-CB/GEM-SSC/BODIPY) 46
3.2.19. Evaluation of Drug Stability 47
3.2.20. *In Vitro* Drug Release Study 47
3.2.21. Cell Culture 47
3.2.22. *In Vitro* Cytotoxicity Experiments 48
3.2.23. *In Vitro* Cellular Uptake of P(OEG/HCQ-CB/GEM-SSC/BODIPY) in BxPC-3 Monolayer 48
3.2.24. *In Vitro* 3D Spheroid Formation and Inhibition Ability of Free Drugs and Copolymer 49
3.2.25. Penetration of P(OEG/HCQ-CB/GEM-SS-C/BODIPY) into BxPC-3 Spheroids 49
3.3. Results and Discussion 50
3.3.1. Synthesis of HCQ-E-MA Monomer 50
3.3.2. Synthesis of P(OEG/HCQ-E) Copolymer via RAFT Polymerization 51
3.3.3. *In Vitro* Drug Release Study and Cytotoxicity of P(OEG/HCQ-E) Copolymer 52
3.3.4. Synthesis of HCQ-C-MA Monomer 54
3.3.5. Synthesis of P(OEG/HCQ-C) Copolymer via RAFT Polymerization 55
3.3.6. *In Vitro* Drug Release Study and Cytotoxicity of P(OEG/HCQ-C) Copolymer 57
3.3.7. Synthesis of GEM-C-MA Monomer 59
3.3.8. Synthesis of P(OEG/GEM-C) Copolymer via RAFT Polymerization 60
3.3.9. *In Vitro* Drug Release Study and Cytotoxicity of P(OEG/GEM-C) Copolymer 62
3.3.10. Synthesis of P(OEG/HCQ-E/GEM-C) Copolymer via RAFT Polymerization 64
3.3.11. *In Vitro* Drug Release Study and Cytotoxicity of P(OEG/HCQ-E/GEM-C) Copolymer 65
3.3.12. Synthesis of P(OEG/HCQ-C/GEM-C) Copolymer via RAFT Polymerization 67

3.3.13. *In Vitro* Drug Release Study and Cytotoxicity of P(OEG/HCQ-C/GEM-C) Copolymer 68
3.3.14. Synthesis of Disulfide-Carbamate Containing Gemcitabine Monomer 70
3.3.15. Synthesis of Disulfide-Carbamate Containing Gemcitabine Monomer 72
3.3.16. Synthesis of P(OEG/GEM-SSC) Copolymer via RAFT Polymerization 73
3.3.17. *In Vitro* Drug Release Study and Cytotoxicity of P(OEG/GEM-SSC) Copolymer 74
3.3.18. Synthesis of P(OEG/HCQ-C/GEM-SSC) Copolymer via RAFT Polymerization 77
3.3.19. *In Vitro* Drug Release Study and Cytotoxicity of P(OEG/HCQ-C/GEM-SSC) Copolymer 78
3.3.20. Synthesis of HCQ-CB-MA Monomer 81
3.3.21. Synthesis of P(OEG/HCQ-CB) Copolymer via RAFT Polymerization 82
3.3.22. *In Vitro* Drug Release Study and Cytotoxicity of P(OEG/HCQ-CB) Copolymer 84
3.3.23. Synthesis of P(OEG/HCQ-CB/GEM-SSC) Copolymer via RAFT Polymerization 86
3.3.24. *In Vitro* Drug Release Study and Cytotoxicity of P(OEG/HCQ-CB/GEM-SSC) Copolymer 88
3.3.25. *In Vitro* Cytotoxicity of P(OEG/HCQ-CB/GEM-SSC) Copolymer on PSC and PDAC Cells 90
3.3.26. Synthesis of BODIPY-MA Monomer 92
3.3.27. Synthesis of P(OEG/HCQ-CB/GEM-SSC/BODIPY) Copolymer 93
3.3.28. Inhibition of Tumor Spheroid Growth 94
3.3.29. Cellular Uptake of P(OEG/HCQ-CB/GEM-SSC) on BxPC-3 Monolayer 95
3.3.30. Penetration of BODIPY-Conjugated Copolymer into 3D Tumor Spheroids 96
3.4. Conclusion 97
4. FABRICATION OF CYCLODEXTRIN-BASED REDOX-RESPONSIVE NANOGELS FOR TARGETED DRUG DELIVERY 99
4.1. Introduction 99
4.2. Experimental 102

4.2.1. Materials....102
4.2.2. Methods....102
4.2.3. Synthesis of βCD-Dex Polymer and Bis-Ada-TEG-SS Linker....103
4.2.4. Synthesis of Empty- and DOX-loaded Nanogels (NGs)....103
4.2.5. Encapsulation and *In Vitro* Drug Release....103
4.2.6. Synthesis of NHS-activated Adamantane (NHS-Ada) and RGD-conjugated Adamantane (RGD-Ada)....104
4.2.7. *In Vitro* Cytotoxicity....104
4.2.8. *In Vitro* Cell Internalization....105
4.3. Result and Discussion....106
4.3.1. Synthesis and Characterization of Nanogel Precursors: βCD-Functionalized Dextran and Disulfide-Containing Bis-Ada Crosslinker....106
4.3.2. Preparation and Characterization of Self-assembled Empty and Drug-loaded Nanogels....106
4.3.3. Nanogel Disassembly in Reducing Environment....108
4.3.4. Synthesis of RGD-conjugated Adamantane (RGD-Ada)....110
4.3.5. *In Vitro* Studies of Peptide-targeted Drug-loaded βCD Nanogels....111
4.4. Conclusion....115
5. FABRICATION OF REDOX-RESPONSIVE HYDROGEL VIA STRAIN-PROMOTED AZIDE-ALKYNE CYCLOADDITION (SPAAC) REACTION FOR DRUG DELIVERY....116
5.1. Introduction....116
5.2. Experimental....119
5.2.1. Materials....119
5.2.2. Methods....119
5.2.3. Synthesis of Disulfide-Containing Poly(ethylene glycol)-diol....120
5.2.4. Synthesis of Dibenzocyclooctyne-Containing PEG Crosslinker....120
5.2.5. Synthesis of P(OEG/N_3) Copolymer via RAFT Polymerization....121
5.2.6. Synthesis of P(OEG/GEM-C/N_3) Copolymer via RAFT Polymerization....121
5.2.7. Synthesis of P(OEG/GEM-SSC/N_3) Copolymer via RAFT Polymerization....122
5.2.8. Synthesis of P(OEG/GEM-SS-C/N_3/BODIPY) Copolymer via RAFT...122

5.2.9. Preparation of Hydrogels via SPAAC Reaction 123
5.2.10. Swelling Study 123
5.2.11. Rheological Study 123
5.2.12. Degradation, Injectability, and Self-Healing Properties of Hydrogel 124
5.2.13. Gemcitabine Release Study 124
5.2.14. Biocompatibility of Hydrogels on L-929 Mouse Fibroblast Cells 125
5.2.15. Cytotoxicity Experiment on BxPC-3 Pancreatic Adenocarcinoma Cells 125
5.2.16. Cellular Internalization 126
5.3. Results and Discussion 127
5.3.1. Synthesis of Azide (N_3)-containing PEG-based Copolymer P(OEG/N_3) 127
5.3.2. Synthesis of Azide (N_3) and Carbamate-containing Gemcitabine-including PEG-based Copolymer P(OEG/N_3/GEM-C) 128
5.3.3. Synthesis of Azide (N_3) and Disulfide-carbamate-containing Gemcitabine-including PEG-based Copolymer P(OEG/N_3/GEM-SSC) . 130
5.3.4. Synthesis of Azide (N_3) and GEM and BODIPY-containing PEG-based Copolymer P(OEG/N_3/GEM-SSC/BODIPY) 131
5.3.5. Synthesis of Disulfide-Containing DBCO-PEG Crosslinker 133
5.3.6. Preparation and Characterization of SPAAC Hydrogels 135
5.3.7. Hydrogel Swelling 139
5.3.8. Degradation of Redox-Responsive Hydrogels 141
5.3.9. Injectability and Self-Healing Behaviour of Hydrogel 142
5.3.10. GEM Release from Hydrogels 146
5.3.11. Biocompatibility of Hydrogels *In Vitro* Cytotoxicity towards Healthy and Cancer Cells 147
5.3.12. *In Vitro* Cytotoxicity towards Cancer Cells 148
5.3.13. *In Vitro* Cellular Internalization 150
5.4. Conclusions 152
6. MULTIVALENT POLYMER BRUSHES FOR BIOMOLECULAR IMMOBILIZATION 154
6.1. Introduction 154
6.2. Experimental 156
6.2.1. Materials 156
6.2.2. Methods 157

6.2.3. Synthesis and Characterization of Double Bond End Group Functionalized G0 Dendron (Azobis-G0-ene) 158
6.2.4. Synthesis and Characterization of Double Bond End Group Functionalized G1[alkyne] Dendron (G1- alkyne-diene) 158
6.2.5. Synthesis and Characterization of Azobis-G1-diene 159
6.2.6. Synthesis and Characterization of Double Bond End Group Functionalized G2[alkyne] Dendron (G2- alkyne-tetraene) 159
6.2.7. Synthesis and Characterization of Azobis-G2-tetraene 160
6.2.8. Synthesis and Immobilization of Surface Anchoring RAFT Reagent 160
6.2.9. Surface Initiated RAFT Polymerization (SI-RAFT) of DEGMA 161
6.2.10. Typical Radical Cross-Coupling End Group Modification of DEGMA Brush with Azobis-p-maleimide 161
6.2.11. Activation of Maleimide Group via Retro Diels-Alder Reaction 161
6.2.12. Post-polymerization Modification of Maleimide-containing DEGMA Brush with BODIPY-Thiol via Michael Addition 161
6.2.13. Maleimide-containing Brush Modification with Biotin-thiol and Immobilization Streptavidin-Coated Quantum Dot Nanoparticles 162
6.2.14. Post-polymerization Modification of DEGMA Brush with Azobis-G0-ene 162
6.2.15. Post-polymerization Modification of DEGMA Brush with Azobis-G1-diene 162
6.2.16. Post-polymerization Modification of DEGMA Brush with Azobis-G1-diene and AIBN 163
6.2.17. Post-polymerization Modification of DEGMA Brush with Azobis-G2-tetraene and AIBN 163
6.2.18. Modification of Reactive Dendron Grafted Surfaces with Fluorescent Dye 163
6.2.19. Post-polymerization Modification of Alkene Grafted Dendrons with Mannose-SH 164
6.2.20. Immobilization of ConA onto Mannose Functionalized Brushes 164
6.2.21. Preparation of Mannose Conjugated Polymer Brush on SiO_2-Coated Gold SPR Surface 164
6.2.22. Surface Plasmon Resonance and Immobilization of ConA 165

6.3. Results and Discussion 165
6.3.1. Synthesis and Characterization of Azobis-G0-ene 165
6.3.2. Synthesis and Characterization of Alkyne-bearing G1-diene 166
6.3.3. Synthesis and Characterization of Azobis-G1-diene "*Click*" Reaction ... 168
6.3.4. Synthesis and Characterization of Alkyne-bearing G2-tetraene 169
6.3.5. Synthesis and Characterization of Azobis-G2-tetraene 170
6.3.6. Fabrication of DEGMA Polymer Brush via SI-RAFT Polymerization ... 172
6.3.7. Installation of 'Clickable' Maleimide Functional Group at the Interface 176
6.3.8. Installation of 'Clickable' Alkene Functional Group at the Interface 179
6.3.9. Functionalization of Maleimide-containing Brushes 181
6.3.10. Functionalization of Alkene-containing Brushes 183
6.3.11. Preparation and Characterization of Multivalent Dendron-based Brushes 184
6.3.12. Functionalization of Dendron Conjugated Brushes with Mannose-SH via Thiol-Ene "*Click"* Chemistry 189
6.3.13. Immobilization of Concanavalin A on Dendron Functionalized Polymer Brushes 191
6.4. Conclusions 194
7. PYRIDYL-DISULFIDE CONTAINING REDOX-RESPONSIVE THIOL-REACTIVE POLYMER BRUSHES 195
7.1. Introduction 195
7.2. Experimental 198
7.2.1. Materials 198
7.2.2. Methods 198
7.2.3. Fabrication of Polymer Brush P1 (100/0) (Homopolymer Brush) 199
7.2.4. Fabrication of Copolymer Brush P2 (90/10) (DEGMA/PDSMA) 199
7.2.5. Preparation of Copolymer Brush P3 (80/20) (DEGMA/PDSMA) 199
7.2.6. Preparation of Copolymer Brush P4 (70/30) (DEGMA/PDSMA) 200
7.2.7. Preparation of Copolymer Brush P5 (0/100) (DEGMA/PDSMA) 200
7.2.8. Functionalization of the Polymer Brush with BODIPY-SH 200
7.2.9. Cleavage of BODIPY from Polymer Brush 200
7.2.10. Functionalization of the Polymer Brush with TFBM 201

7.2.11. Functionalization of the Polymer Brush with Mannose-SH for Protein Immobilization 201
7.2.12. Functionalization of the Polymer Brush with Thiol-containing Peptide..201
7.2.13. FITC Conjugation on Peptide Functionalized Polymer Brush.....201
7.2.14. Cell Attachment on Peptide Functionalized Polymer Brush and Actin Filament Staining 202
7.2.15. Cell Detachment from Peptide Functionalized Brush and Live-Dead Assay 202
7.2.16. Functionalization of the Polymer Brush with Thiol-containing Doxorubicin.....203
7.2.17. Orthogonal Functionalization with Aminopropanol and Maleimide-containing Molecules and Cell Adhesive Peptide.....203
7.2.18. Fabrication of Both DOX and cRGD-containing Polymer Brush.....203
7.2.19. Cell Culture on the cRGD End Group Functionalized Polymer Brushes 204
7.3. Results and Discussion 205
7.3.1. Fabrication of PDS-Containing Polymer Brushes 205
7.3.2. Functionalization of the Copolymer Brush P2 with BODIPY-SH 210
7.3.3. Functionalization of the Copolymer Brush P2 with 4-Trifluoromethylbenzyl mercaptan (TFBM) 211
7.3.4. Functionalization of Polymer Brush with Mannose-Thiol and Evaluation of Lectin Binding Efficiency 213
7.3.5. Conjugation of Polymer Brushes with Thiol-containing Peptide and Cell Attachment and Release 214
7.3.6. Cell Attachment and Release from RGD-Conjugated Brush.....215
7.3.7. The Fabrication of DOX Conjugated Polymer Brush for Delivery into Cells.....218
7.3.8. The End Group Functionalization Using Orthogonal Reaction.....219
7.3.9. Cell Adhesive Peptide Functionalization Using Orthogonal Reaction 220
7.3.10. DOX Release from Polymer Brush and Cellular Internalization.....221
7.4. Conclusion 224
8. FABRICATION OF BENZOTHIAZOLE-DISULFIDE-BASED REDOX-RESPONSIVE POLYMER COATINGS.....226
8.1. Introduction.....226

8.2. Experimental 229
8.2.1. Materials 229
8.2.2. Methods 229
8.2.3. Synthesis of Benzothiazole-Disulfide Methacrylate Monomer (BDSMA) 230
8.2.4. Synthesis of PEGMA-BDSMA Copolymer ($P(P_x\text{-}B_y)$) 230
8.2.5. Synthesis of PEGMA-BDSMA-TMSPMA Copolymer ($P(P_x\text{-}B_y\text{-}T_z)$) 231
8.2.6. Release of Benzothiazolethione Moiety under Reducing Conditions 231
8.2.7. Post-Polymerization Modification of $P(P_{80}\text{-}B_{20})$ using Thiol-containing Molecule 231
8.2.8. Fabrication of Polymeric Coatings on Glass Surfaces 232
8.2.9. Functionalization of Polymer Coatings with 4-Trifluoromethylbenzyl Mercaptan (TFBM) 232
8.2.10. Functionalization of Polymer Coatings with Thiol-containing Dye 232
8.2.11. Cleavage of Dye from Surface 233
8.2.12. Functionalization of Thiol-containing Polymer Film with Maleimide-conjugated Fluorescein 233
8.2.13. Functionalization of Polymer Coatings with Thiol-containing Peptide 233
8.2.14. Cell Attachment on Peptide Functionalized Films 233
8.2.15. Cell Detachment from Peptide Functionalized Films and Live-Dead Assay 234
8.3. Results and Discussion 234
8.3.1. Synthesis and Characterization of BDSMA Monomer 234
8.3.2. Synthesis and Characterization of BDSMA-containing Copolymers 236
8.3.3. Release of Benzothiazolethione from Copolymers 238
8.3.4. Post-Polymerization Modification of $P(P_{80}\text{-}B_{20})$ Copolymer 239
8.3.5. Synthesis and Characterization of Surface Reactive Copolymers 240
8.3.6. Fabrication and Characterization of Polymer Coating on Glass Surface 244
8.3.7. Surface Modification with TFBM via Thiol-Disulfide Exchange Reaction 246
8.3.8. Reversible Attachment of Thiol-containing Dye on Polymer Coated Surfaces 247
8.3.9. Cell Attachment and Release from Peptide-conjugated Surface 249

8.4. Conclusion 252
9. PLUG-AND-PLAY BIOINTERFACES: HARNESSING HOST-GUEST INTERACTIONS FOR FABRICATION OF FUNCTIONAL POLYMERIC COATINGS 253
9.1. Introduction 253
9.2. Experimental 256
9.2.1. Materials 256
9.2.2. Methods 256
9.2.3. RAFT Synthesis of Copolymers Carrying DEGMA-AdaMA-TMSPMA monomers ($P(D_x\text{-}A_y\text{-}T_z)$) 257
9.2.4. Cleaning Procedure for Silicon Surfaces 258
9.2.5. Fabrication of Polymeric Coatings on Silicon Surfaces 258
9.2.6. Stability Experiment of Polymeric Coatings 258
9.2.7. Synthesis of β-CD and Lissamine-Rhodamine B conjugate 258
9.2.8. Synthesis of Mono-mannose Conjugated β-Cyclodextrin 259
9.2.9. Synthesis of β-Cyclodextrin Conjugated RGD Peptide 259
9.2.10. β-CD-Lissamine B Conjugation to Polymer Coating via Microcontact Printing 260
9.2.11. βCD grafted-Biotin Functionalization for Qdot-Streptavidin Immobilization 260
9.2.12. Surface Functionalization with βCD grafted-Mannose and Immobilization of Dye-labeled ConA and PNA Conjugates 260
9.2.13. Surface Functionalization with βCD grafted-RGD Peptide 261
9.2.14. Cell Culture on Peptide Functionalized Films: Actin Filament Staining 261
9.3. Results and Discussion 262
9.3.1. Synthesis and Characterization of Adamantane-Containing Copolymer 262
9.3.2. Fabrication and Characterization of Polymer Coatings on Silicon Surfaces 264
9.3.3. Synthesis of βCD-Lissamine Rhodamine B Conjugate 266
9.3.4. Surface Functionalization with βCD-Lissamine-Rhodamine-B Dye 267
9.3.5. Surface Functionalization with βCD-Biotin for Protein Immobilization 269
9.3.6. Synthesis of Mono-Mannose Containing βCD Conjugate 272
9.3.7. Lectin Binding to Mannose-Containing Polymer Coatings 274

9.3.8. The Synthesis of Cyclic-RGD-containing βCD Conjugate.....276
9.3.9. cRGD-βCD Immobilization and Evaluation of Cell Attachment 277
9.4. Conclusion 279
10. CONCLUSION.....281
REFERENCES 286
APPENDIX A: ADDITIONAL SPECTRA 336
APPENDIX B: COPYRIGHT NOTICES 345

LIST OF FIGURES

Figure 1.1. Schematic illustration of normal cell division. 1

Figure 1.2. Schematic illustration of uncontrolled cell growth. 2

Figure 1.3. (a) Schematic illustration of angiogenesis process, (b) tumor growth via angiogenesis. 3

Figure 1.4. Timeline of development polymeric nanomedicine. Reprinted with permission from [22]. 6

Figure 1.5. Components of a polymer-drug conjugate according to Ringsdorf's model. 7

Figure 1.6. Commonly used linkers between drug and polymer backbone. 9

Figure 1.7. Schematic representation of the EPR effect. 10

Figure 1.8. Preparation methods of nanogels. 14

Figure 1.9. The fabrication of nanogels via self-assembly and subsequent chemical crosslinking strategy. Reprinted with permission from [58]. 15

Figure 1.10. Fabrication of biodegradable nanogels via self-assembly and further chemical crosslinking via thiol-pyridyl disulfide exchange reaction. Reprinted with permission from [59]. 16

Figure 1.11. Schematic illustration for fabrication of hydrogels. 17

Figure 1.12. Illustration of SPAAC reaction between an azide and DBCO-based cyclooctyne. 19

Figure 1.13. Polymeric surface coatings are studied in this thesis. 22

Figure 1.14. Types of the polymeric thin film in terms of the position of surface attachable groups on the polymer backbone. 23

Figure 1.15. Fabrication of polymer brush via grafting from and grafting to method. 25

Figure 1.16. Proposed mechanism of RAFT polymerization. 26

Figure 1.17. Functionalization and fabrication of succinimidyl-carbonate-containing amine reactive polymer brushes. Reprinted with permission from [160]. 29

Figure 1.18. Fabrication of antibacterial thin film coating. Reprinted with permission from [162]. 30

Figure 1.19. Schematic illustration of fabrication and functionalization of reactive polymeric surface. Reprinted with permission from [166]. 31

Figure 3.1. Fabrication of HCQ and GEM-containing polymer-drug conjugate, the influence of linkers on drug release. 36

Figure 3.2. Synthesis of hydroxychloroquine monomer via ester linkers (HCQ-E-MA).... 50

Figure 3.3. ^{1}H NMR spectrum of HCQ-E-MA monomer ($CDCl_3$). 50

Figure 3.4. Synthesis of P(OEG/HCQ-E) via RAFT polymerization..... 51

Figure 3.5. ^{1}H NMR spectrum of POEGMA-HCQ-E in $CDCl_3$. 52

Figure 3.6. HCQ release profiles from P(OEG/HCQ-E) copolymer in pH = 5.4, pH = 7.4, PLE, and plasma at 37 ^{o}C for 72 h. 53

Figure 3.7. Cell viabilities of (a) BxPC-3 cells, (b) Capan-1 cells treated with free HCQ and P(OEG/HCQ-E) copolymer. 54

Figure 3.8. Synthesis of HCQ-C-MA monomer via carbamate linker. 55

Figure 3.9. ^{1}H NMR spectrum of HCQ-C-MA monomer ($CDCl_3$). 55

Figure 3.10. Synthesis of P(OEG/HCQ-C) via RAFT polymerization. 56

Figure 3.11. ^{1}H NMR spectrum of P(OEG/HCQ-C) copolymer ($CDCl_3$) 57

Figure 3.12. HCQ release profiles from P(OEG/HCQ-C) in pH = 5.4, pH = 7.4, PLE, and plasma at 37 ^{o}C for 72 h. 58

Figure 3.13. Cell viabilities of (a) BxPC-3 cells, (b) Capan-1 cells treated with free HCQ and P(OEG/HCQ-C) copolymer. 59

Figure 3.14. Synthetic pathway of GEM-MA-C monomer. 59

Figure 3.15. ^{1}H NMR spectrum of GEM-C-MA monomer (DMSO d6). 60

Figure 3.16. Synthesis of P(OEG/GEM-C) copolymer. 61

Figure 3.17. ^{1}H NMR spectrum of P(OEG/GEM-C) copolymer (DMSO d6). 62

Figure 3.18. GEM release profiles from P(OEG/GEM-C). 63

Figure 3.19. Cell viabilities of (a) BxPC-3 cells, (b) Capan-1 cells treated with free GEM and P(OEG/GEM-C) copolymer. 63

Figure 3.20. The synthesis of P(OEG/HCQ-E/GEM-C) copolymer. 64

Figure 3.21. ^{1}H NMR spectra of GEM-C-MA monomer (purple line) and P(OEG/HCQ-E/GEM-C copolymer (black line) (DMSO d6).....65

Figure 3.22. HCQ and GEM release from copolymer P(OEG/HCQ-E/GEM-C) at 37°C...66

Figure 3.23. Cell viabilities of (a) BxPC-3 cells, (b) Capan-1 cells treated with free GEM, the combination of GEM-HCQ and P(OEG/HCQ-E/GEM-C).....66

Figure 3.24. The synthesis of P(OEG/HCQ-C/GEM-C) copolymer.....67

Figure 3.25. ^{1}H NMR spectra of GEM-C-MA monomer (purple line) and P(OEG/HCQ-C/GEM-C) copolymer (green line) (DMSO d6).....68

Figure 3.26. HCQ and GEM release from copolymer P(OEG/HCQ-C/GEM-C) at 37°C. .69

Figure 3.27. Cell viabilities of (a) BxPC-3 cells, (b) Capan-1 cells, and (c) Panc-1 cells, treated with free GEM, the combination of GEM-HCQ and P(OEG/HCQ-E/GEM-C).....70

Figure 3.28. Synthetic pathway of disulfide-carbamate bond containing GEM-SSC-MA monomer. 71

Figure 3.29. ^{1}H NMR spectrum of GEM-SSC-MA monomer (DMSO d6). 71

Figure 3.30. Cleavage mechanism of disulfide-carbamate linkage in the presence of GSH.....72

Figure 3.31. Synthesis of P(OEG/GEM-SSC) copolymer.....73

Figure 3.32. ^{1}H NMR spectrum of P(OEG/GEM-SSC) (DMSO d6).....74

Figure 3.33. (a) GEM release profile from P(OEG/GEM-SSC at 37 ^{o}C, (b) comparison of GEM release ratio between P(OEG/GEM-SSC) and P(OEG/GEM-C) in the presence of GSH. 75

Figure 3.34. Cytotoxicity results of (a) BxPC-3 cells and (b) Capan-1 cells treated with free GEM, P(OEG/GEM-C), and P(OEG/GEM-SSC). 76

Figure 3.35. The polymerization reaction of P(OEG/HCQ-C/GEM-SSC). 77

Figure 3.36. ^{1}H NMR spectra of GEM-SSC-MA monomer (purple line) and P(OEG/HCQ-C/GEM-SSC) copolymer (black line) (DMSO d6). 78

Figure 3.37. (a) HCQ release profiles, and (b) GEM release profiles from P(OEG/HCQ-C/GEM-SSC) at 37 ^{o}C. 79

Figure 3.38. Cell viabilities of (a) BxPC-3 cells and (b) Capan-1 cells, treated with free GEM, GEM-HCQ, and P(OEG/HCQ-C/GEM-SSC). 80

Figure 3.39. The synthesis of HCQ-CB-MA monomer via carbonate linker. 81

Figure 3.40. ^{1}H NMR spectrum of HCQ-CB-MA monomer in $CDCl_3$. 82

Figure 3.41. The polymerization reaction of P(OEG/HCQ-CB). 83

Figure 3.42. ^{1}H NMR spectrum of P(OEG/HCQ-CB) copolymer in $CDCl_3$. 83

Figure 3.43. (a) HCQ release profile from P(OEG/HCQ-CB) copolymer at 37 ^{o}C, (b) and (c) cell viabilities of BxPC-3 and Capan-1 cells, treated with free HCQ and P(OEG/HCQ-CB). 85

Figure 3.44. The polymerization reaction of P(OEG/HCQ-CB/GEM-SSC) copolymer. ... 86

Figure 3.45. ^{1}H NMR spectrum of P(OEG/HCQ-CB/GEM-SSC) (DMSO d6). 87

Figure 3.46. *In vitro* (a) HCQ and (b) GEM release profiles from P(OEG/HCQ-CB/GEM-SSC) copolymer in pH = 5.4 and 7.4, GSH (10 mM), PLE enzyme, the mixture of PLE-GSH and rat plasma at 37 ^{o}C (n = 3). 88

Figure 3.47. Cell viabilities of (a) BxPC-3 cells and (b) Capan-1 cells, treated with a mixture of GEM-HCQ and P(OEG/HCQ-CB/GEM-SSC). 89

Figure 3.48. Cell viabilities of (a) PSC stellate cells and (b) PDAC cells, treated with free GEM, HCQ, GEM-HCQ, and P(OEG/HCQ-CB/GEM-SSC). 91

Figure 3.49. The synthesis of BODIPY-MA monomer. 92

Figure 3.50. ^{1}H NMR spectrum of BODIPY-MA monomer in $CDCl_3$. 92

Figure 3.51. The polymerization scheme of P(OEG/HCQ-CB/GEM-SSC/BODIPY) copolymer 93

Figure 3.52. ^{1}H NMR spectrum of P(OEG/HCQ-CB/GEM-SSC/BODIPY). 93

Figure 3.53. Representative bright-field images of BxPC-3 tumor spheroids 94

Figure 3.54. Determination of the tumor spheroid area (%) based on images. Data are expressed as mean ± SD (n = 3, ****p < 0.001, * p<0.05). 95

Figure 3.55. Fluorescence microscopy images of BxPC-3 cells treated with free BODIPY and BODIPY-conjugated and drug-containing copolymer. Cell nuclei were stained with DAPI (blue). The scale bar is 50 μm 96

Figure 3.56. (a) The fluorescence images of spheroids and penetration efficiency of free BODIPY and P(OEG/HCQ-CB/GEM-SSC/BODIPY) into BxPC-3 tumor spheroids; (b) the mean fluorescence intensity of dye-treated spheroids. 97

Figure 4.1. Schematic illustration of the fabrication of drug-loaded targeted nanogels. 101

Figure 4.2. (a, b) Size distributions of empty and DOX-loaded βCD-nanogels, (c) comparative Z-average diameter of empty and drug-loaded nanogels as determined by DLS at 37 °C, TEM micrographs of (d) empty βCD-nanogels, and (e) DOX-loaded βCD-nanogels. 107

Figure 4.3. (a) Trends in nanogel size with increasing polymer concentration where Ada-TEG-SS linker equivalence was kept as 1, (b) the nanogel size with different Ada-TEG-SS linker equivalency (the concentration of polymer is 1 mg/mL)..... 107

Figure 4.4. ^{1}H NMR spectra of Ada-TEG-SS linker (black line), βCD-Dex (blue line), and complex of βCD-Dex and Ada-TEG-SS linker (βCD-nanogel) (burgundy line) in D_2O. 108

Figure 4.5. (a) Schematic representation of βCD-nanogels with DTT (10 mM), (b) DLS measurements before and after DTT treatment, (c) DLS measurements before and after GSH (5mM) treatment, and (d) disassembly of βCD-nanogels structures in the presence of GSH (5 mM) at 37 ^{o}C. 109

Figure 4.6. (a) Synthetic pathway of NHS-Ada, (b) ^{1}H NMR spectrum of NHS-Ada ($CDCl_3$). 110

Figure 4.7. Synthesis of RGD-Ada ligand. 111

Figure 4.8. Conjugation of Ada-cRGD to βCD nanogels. 111

Figure 4.9. *In vitro* DOX release at pH 5.4 with and without GSH (5 mM) and at pH 7.4 with and without GSH (5 mM). 112

Figure 4.10. (a) Cytotoxicity assay of empty βCD nanogel on MDA-M231 cells; (b) Cell viabilities as the histogram of MDA-MB-231 cells treated with free DOX, DOX-loaded non-targeted nanogels (βCD-DOX-NG), targeted DOX-

loaded nanogels (RGD-βCD-DOX-NG), and GSH-mediated targeted DOX loaded nanogels (RGD-βCD-DOX-NG + GSH) after 48 h. 113

Figure 4.11. Fluorescence microscopy images of MDA-MB-231 cells treated with free DOX and DOX-loaded non-targeted (βCD-NG-DOX) and targeted (RGD-βCD-NG-DOX) nanogels. Cell nuclei were stained with DAPI (blue). Scale bar = 50 μm..... 114

Figure 5.1. Fabrication of drug-conjugated redox-responsive hydrogels via SPAAC reaction, illustration of injectability and drug release efficiency with the linker, and representation of cellular internalization. 118

Figure 5.2. The synthesis of P(OEG/N_3) copolymer via RAFT polymerization. 127

Figure 5.3. The ^{1}H NMR spectrum of P(OEG/N_3) copolymer ($CDCl_3$)..... 128

Figure 5.4. The synthesis of P(OEG/N_3/GEM-C) copolymer via RAFT polymerization. 129

Figure 5.5. ^{1}H NMR spectrum of P(OEG/N_3/GEM-C) copolymer. 129

Figure 5.6. The synthesis of P(OEG/N_3/GEM-SSC) copolymer via RAFT polymerization. 130

Figure 5.7. ^{1}H NMR spectrum of P(OEG/N_3/GEM-SSC) copolymer..... 131

Figure 5.8. The synthesis of P(OEG/N_3/GEM-SSC/BODIPY) copolymer..... 132

Figure 5.9. The ^{1}H NMR spectrum of P(OEG/N_3/GEMSSC/BODIPY). 132

Figure 5.10. The PEG-SS-$(DBCO)_2$ crosslinker synthesis steps..... 133

Figure 5.11. The ^{1}H NMR spectrum of PEG$(SS\text{-}OH)_2$. 134

Figure 5.12. The ^{1}H NMR spectrum of PEG-$(SSDBCO)_2$ crosslinker. 134

Figure 5.13. ^{13}C NMR spectra of PEG4K and DBCO-SS-PEG-SS-DBCO (PEG-$(SSDBCO)_2$) crosslinker. 135

Figure 5.14. The fabrication of HG-GEMSSC hydrogels via SPAAC reaction and images of them in dry and swollen forms. 136

Figure 5.15. FTIR spectra of P(OEG/N_3/GEMSSC) copolymer before gelation and HG-GEMSSC hydrogel. 137

Figure 5.16. The frequency sweep test results of HG-GEMSSC hydrogels. 138

Figure 5.17. The amplitude sweep test results of HG-GEMSSC hydrogels. 138

Figure 5.18. SEM images of 5, 10, and 15 wt % HG-GEM-SSC hydrogels and swelling graph 139

Figure 5.19. SEM images of 5, 10, and 15 wt % HG-GEM-C hydrogels and swelling graph 140

Figure 5.20. (a) Schematic representation of hydrogel degradation in the presence of GSH, (b) hydrogel images under UV-lamp before and after GSH treatment. 141

Figure 5.21. Degradation profiles of hydrogels in the presence and absence of glutathione at 37 ^{o}C. 142

Figure 5.22. Injectability testing of hydrogels: (a) BODIPY-conjugated hydrogel was injected via a 21-gauge needle, (b) injection of hydrogel into water and photographs under sunlight and UV-light, (c) investigation of self-healing behavior of hydrogel and images of before and after healing and (d) degradation of hydrogels with 1 mM GSH. 143

Figure 5.23. The fabrication of a self-healing test using deformation and fluorescence images after being treated with maleimide-containing fluorescein. 145

Figure 5.24. The diagram of the viscosity rheology as a function of the shear rate of HG-GEMSSC hydrogels. 145

Figure 5.25. (a) GEM release profiles from HG-GEMSSC hydrogel, (b) GEM release ratios from HG-GEM-C hydrogel at 37 ^{o}C. 147

Figure 5.26. Biocompatibility of blank hydrogel using cytotoxicity assay and live-dead assay on L-929 cells. 148

Figure 5.27. Cytotoxicity results of HG-GEMSSC and HG-GEMC hydrogels against BxPC3 pancreatic cancer cells. 150

Figure 5.28. Fluorescence microscopy images of cancer cells treated with dye-containing hydrogels in the presence and absence of GSH. The scale bar is 50 μm. 151

Figure 6.1. Illustration of diversification of surface functionality of polymer brushes for fabrication of functional interfaces. 156

Figure 6.2. The synthesis scheme of azobis-G0-ene. 165

Figure 6.3. ^{1}H NMR spectrum of azobis-G0-ene in $CDCl_3$ 166

Figure 6.4. The synthesis scheme of G1-alkyne-diene. 167

Figure 6.5. ^{1}H NMR spectrum of G1-alkyne-diene in $CDCl_3$. 167

Figure 6.6. Demonstration of "*click*" reaction and synthesis of azobis-G1-diene. 168

Figure 6.7. ^{1}H NMR spectrum of azobis-G1-diene in $CDCl_3$. 168

Figure 6.8. Synthetic pathway of obtaining G2-tetraene dendron. 169

Figure 6.9. ^{1}H NMR spectrum of G2-alkyne-tetraene in $CDCl_3$. 170

Figure 6.10. Synthesis of Azobis-G2-tetraene via azide-alkyne cycloaddition reaction. .. 171

Figure 6.11. ^{1}H NMR spectrum of Azobis-G2-tetraene in $CDCl_3$. 172

Figure 6.12. (a) Fabrication of DEGMA polymer brushes, (b) FTIR spectra of CTA- (black line) and polymer brush coated surface (red line), (c) AFM cross-section polymer brush, and (d) XPS analysis of polymer brush coated surface. 174

Figure 6.13. High-resolution N1s and O1s XPS spectra of DEGMA-containing brush. .. 175

Figure 6.14. Time-dependent growth of DEGMA polymer brush as a line graph. 175

Figure 6.15. Fabrication of maleimide-terminated DEGMA polymer brush. 176

Figure 6.16. XPS survey and high-resolution C1s, O1s, and N1s spectra of protected maleimide functionalized DEGMA-containing brush. 177

Figure 6.17. FTIR spectra of p-maleimide (dark blue line) and free maleimide (purple line) end group functionalized DEGMA polymer brushes. 178

Figure 6.18. XPS survey and high-resolution C1s, N1s, and O1s spectra of maleimide functionalized DEGMA-containing brush. 179

Figure 6.19. Fabrication of terminal alkene functionalized DEGMA-based polymer brush via radical cross-coupling reaction..... 180

Figure 6.20. XPS survey and high-resolution C1s, N1s, and O1s, spectra of alkene (azobis-G0-ene) functionalized DEGMA-containing brush 180

Figure 6.21. FTIR spectra of azobis-G0-ene (mint green line) and alkene (azobis-G0-ene) functionalized DEGMA-containing brush (purple line). 181

Figure 6.22. (a) Post-polymerization modification of maleimide-terminated DEGMA polymer brushes with BODIPY-SH and Biotin-SH/Streptavidin-coated Qdot nanoparticles; fluorescence image after modification with (b) BODIPY-SH, and (c) Biotin-SH/Streptavidin-coated Qdot nanoparticles (scale bar is 100 μm). 182

Figure 6.23. (a) Post-polymerization modification of alkene-terminated DEGMA polymer brushes with BODIPY-SH as well as Biotin-SH/Streptavidin-coated Qdot nanoparticles, (b) and (c) fluorescence images after modification with BODIPY-SH and Biotin-SH/Streptavidin-coated Qdot nanoparticles (scale bar is 100 μm). 184

Figure 6.24. Structures of dendritic azo-chain terminators and representative surface modification using a G2-alkene-based dendron-grafted brush. 185

Figure 6.25. XPS survey and high-resolution C1s, O1s, and N1s spectra of G1-diene functionalized DEGMA-containing brush. 186

Figure 6.26. XPS survey and high-resolution C1s, O1s, and N1s spectra of G1-diene/AIBN functionalized DEGMA-containing brush. 187

Figure 6.27. XPS survey and high-resolution C1s, O1s, and N1s spectra of G2-tetraene/AIBN functionalized DEGMA-containing brush. 188

Figure 6.28. FT-IR spectra of azobis-G0-ene functionalized DEGMA brushes (peach line), azobis-G1-diene functionalized DEGMA brushes (navy blue line), and azobis-G2-tetraene functionalized DEGMA brushes (green line). 188

Figure 6.29. XPS survey and high-resolution C1s, O1s, N1s, and S2p, spectra of mannose-SH functionalized G0 (azobis-ene)-containing brush. 189

Figure 6.30. XPS survey and high-resolution C1s, O1s, N1s, and S2p, spectra of mannose-SH functionalized G1-containing brush. 190

Figure 6.31. XPS survey and high-resolution C1s, O1s, N1s, and S2p, spectra of mannose-SH functionalized G1/AIBN-containing brush. 190

Figure 6.32. XPS survey and high-resolution C1s, O1s, N1s, and S2p, spectra of mannose-SH functionalized G2/AIBN-containing brush. 191

Figure 6.33. Immobilization of mannose-terminated brushes with *Con A*. (a) Fluorescent image of DEGMA@G0ene-mannose brush (d=51 ± 3 nm); (b), (c) and (d) Fluorescent images of DEGMA@G1diene-mannose brush (d =55 ± 2 nm), DEGMA@G1diene/AIBN-mannose brush (d=55 ± 2 nm) and DEGMA@G2tetraene/AIBN-mannose brush (d=56 ± 2 nm) after ConA binding (scale bar is 100 μm)..... 192

Figure 6.34. (a) Surface plasmon resonance (SPR) binding analysis indicating the interaction between mannose-bearing G2 polymer brushes with the two different proteins (FITC-ConA and BSA), and (b) fluorescence microscope image of SPR sensor chip after binding of FITC-ConA. (Scale bar is 100 μm). 193

Figure 7.1. Fabrication and functionalization of PDS-based thiol-reactive polymer brushes. 197

Figure 7.2. The synthesis of PDS-functionalized polymer brush via SI-RAFT. 205

Figure 7.3. The XPS survey scan spectra of P1-P5 polymer brushes. 206

Figure 7.4. The high-resolution C1s spectra of P1-P5 polymer brushes. 207

Figure 7.5. The high-resolution N1s spectra of P1-P5 polymer brushes. 208

Figure 7.6. The high-resolution S2p spectra of P1-P5 polymer brushes. 209

Figure 7.7. Time-dependent growth of P2 polymer brush (10% PDSMA) as a line graph. 209

Figure 7.8. (a) The fabrication of BODIPY-SH conjugation to PDS-containing polymer brush; (b) the fluorescence images of BODIPY-containing surface after BODIPY release in the DTT and BODIPY release line graph. 210

Figure 7.9. Functionalization of PDS-containing P2 brush with TFBM. 211

Figure 7.10. FT-IR spectra of TFBM and TFBM conjugated brush. 212

Figure 7.11. XPS high-resolution C1s, N1s, F1s, and S2p spectra of TFBM conjugated P2 brush..... 212

Figure 7.12. (a) Fabrication of mannose-containing P2 brush for lection binding affinity, (b) fluorescence microscope images of mannose-containing P2 brush treated with FITC-ConA and RhB-PNA. The scale bar is 50 µm. 213

Figure 7.13. The fluorescence microscopy images of FITC-ConA immobilized P2 brush before and after DTT treatment. The scale bar is 50 µm. 214

Figure 7.14. The modification of the P2 polymer brush with thiolated RGD peptide and functionalization with FITC. 215

Figure 7.15. The fluorescence image of the FITC-conjugated RGD-containing surface (left), (c) the fluorescence image of the control P2 surface (right). The scale bar is 500 µm. 215

Figure 7.16. (a) The fabrication of an RGD-containing polymer brush for cell attachment merged fluorescence microscopy images of cells immobilized on (b) P1 surface, (c) P2 surface, and (d) RGDC-conjugated P2 surfaces after actin

filament staining with Alexa Fluor 488 and nuclei staining with DAPI. The scale bar is 50 µm. 216

Figure 7.17. (a) Illustration of cell release from the surface with DTT, (b) the fluorescence microscopy image of calcein-AM and PI stained cells onto the peptide-conjugated brush surface, and (c) the fluorescence microscopy image of calcein-AM and PI stained cells after detachment from polymer surface. 217

Figure 7.18. (a) The illustration of DOX-SH binding to polymer brush via thiol-disulfide exchange reaction, (b) the fluorescence image of P2 brush surface after modifying with DOX-SH, and (c) the fluorescence image of control surface after treatment with DOX. The scale bar is 50 µm. 218

Figure 7.19. (a) Immobilization of 3-amino-1-propanol to reduce dithiocarbonyl groups to thiols and immobilization of maleimide-containing rhodamine and subsequent BODIPYH conjugation, (b) the fluorescence images of rhodamine and BODIPY-conjugated P2 polymer brush. The scale bar is 50 µm. 219

Figure 7.20. Fabrication of cRGD-Mal and hydroxypropyl-Mal modified P2 polymer brush and fluorescence images of attached cells after staining with Alexa Fluor Phalloidin (AF488) and DAPI. The scale bar is 50 µm. 221

Figure 7.21. The illustration of cellular uptake of DOX by cancer cells via GSH treatment using cRGD and DOX conjugated P2 polymer brush. 222

Figure 7.22. The fluorescence merged and DOX channel images of MDA-MB-231 cells attached surfaces with and without GSH treatment and illustration of DOX internalization efficiency by the cells. The scale bar is 50 µm. 223

Figure 7.23. The fluorescence and bright field images of detached cells from the surface treated with GSH and cell media. 224

Figure 8.1. Schematic illustration of reversible conjugation on reactive polymeric thin film via a thiol-disulfide exchange reaction. 228

Figure 8.2. The synthesis of BDSMA monomer. 235

Figure 8.3. The ^{1}H NMR spectrum of BDSMA monomer in $CDCl_3$. 235

Figure 8.4. ^{13}C NMR spectrum of BDSMA monomer in $CDCl_3$. 236

Figure 8.5. BDS-based copolymer (P(Px-By)) is synthesized via RAFT polymerization. 237

Figure 8.6. ^{1}H NMR spectrum of copolymer $P(P_{80}\text{-}B_{20})$ in $CDCl_3$. 238

Figure 8.7. (a) Release of benzothiazole group upon with DTT, (b) UV-Vis spectra of copolymer $P(P_{70}\text{-}B_{30})$ before and after 10 mM DTT solution, (c) Benzothiazolethione release profiles of copolymers $P(P_{90}\text{-}B_{10})$ and $P(P_{70}\text{-}B_{30})$ after treatment with 10 mM DTT. 239

Figure 8.8. (a) Post-polymerization modification of copolymer $P(P_{80}\text{-}B_{20})$ with furfuryl mercaptan via thiol-disulfide exchange reaction and (b) ^{1}H NMR spectrum of the functionalized copolymer. 240

Figure 8.9. The synthesis of surface-attachable copolymer ($P(P_x\text{-}B_y\text{-}T_z)$). 241

Figure 8.10. ^{1}H NMR spectrum of copolymer $P(P_{65}\text{-}B_{30}\text{-}T_5)$ in $CDCl_3$. 242

Figure 8.11. ^{1}H NMR spectrum of copolymer $P(P_{85}\text{-}B_{10}\text{-}T_5)$ in $CDCl_3$. 242

Figure 8.12. ^{1}H NMR spectrum of control copolymer $P(P_{95}\text{-}B_0\text{-}T_5)$ in $CDCl_3$. 243

Figure 8.13. FT-IR spectra of $P(P_{95}\text{-}B_0\text{-}T_5)$ (black line), $P(P_{85}\text{-}B_{10}\text{-}T_5)$ (red line), and $P(P_{65}\text{-}B_{30}\text{-}T_5)$ (blue line) 243

Figure 8.14. (a) Schematic illustration of polymer coatings, (b) ATR-FTIR spectrum of polymer-coated surfaces, and (c) water contact angle of polymer-coated surfaces.....244

Figure 8.15. (a) XPS survey scan of S(P_{85}-B_{10}-T_5), (b) C1s high resolution, (c) N1s high resolution, and (d) S2p high-resolution spectra of S(P_{85}-B_{10}-T_5). 245

Figure 8.16. (a) Conjugation of TFBM to the reactive polymer-coated glass surface, (b) water contact angle of polymer-coated surfaces, (c) N1s high resolution, (d) S2p high resolution, and (e) F1s high-resolution spectra of S(P_{85}-B_{10}-T_5)-TFBM. 246

Figure 8.17. (a) Schematic illustration of polymer-coated surface modification using BODIPY-SH, and fluorescence microscopy images of dye-modified surfaces, (b) S(P_{85}-B_{10}-T_5) and (c) S(P_{65}-B_{30}-T_5). Insets show a lack of any fluorescence of unmodified surfaces. The scale bar is 50 µm. 247

Figure 8.18. (a) Schematic illustration of the release of dye from BODIPY-modified surface with DTT and confirmation of thiolated interface through the attachment of maleimide-containing dye Fluo-MAL; and fluorescence microscopy images of (b) S(P_{85}-B_{10}-T_5)-BODIPY surface and (c) DTT treated surface, and (d) Fluo-MAL conjugated surface. Scale bar: 50 µm...248

Figure 8.19. Scheme of immobilization of L929 mouse fibroblast cells onto polymer-coated glass substrates. 250

Figure 8.20. Fluorescence microscopy images of cells immobilized on S(P_{85}-B_{10}-T_5)-RGD, S(P_{85}-B_{10}-T_5), and S(P_{95}-B_0-T_5) surfaces after actin filament staining with Alexa Fluor 488 and nuclei staining with DAPI. Scale bar: 50 µm 250

Figure 8.21. Fluorescence microscopy image of cells immobilized on RGD peptide attached polymer film (left), and merged fluorescence microscopy image

displaying viable (green) and dead (red) cells after detachment and removal from polymer film (right). The scale bar is 50 μm. 251

Figure 9.1. Schematic illustration of the fabrication of βCD reactive polymeric thin film and polymeric film modification via host-guest chemistry using the μCP technique. 255

Figure 9.2. Synthesis of surface attachable RAFT copolymers carrying adamantane side groups. 263

Figure 9.3. ^{1}H NMR spectrum of P(D_{75}-A_{20}-T_5) copolymer ($CDCl_3$). 263

Figure 9.4. ^{1}H NMR spectrum of P(D_{95}-A_0-T_5) copolymer ($CDCl_3$). 264

Figure 9.5. (a) Schematic illustration of coating of polymers onto a silicon surface, (b) ATR-FTIR spectrum of polymer-coated surfaces, (c) water contact angle of polymer-coated surfaces, and high-resolution XPS spectra (d) C1s, (e) N1s and (f) S2p of S(D_{75}-A_{20}-T_5) surface. 265

Figure 9.6. FTIR spectra of S(D_{75}-A_{20}-T_5) and S(D_{95}-A_0-T_5) after incubation with PBS (pH 7.4) at 37°C for 24 h. 266

Figure 9.7. The synthesis scheme of βCD-grafted lissamine rhodamine B conjugate. 266

Figure 9.8. ^{1}H NMR spectrum of βCD-lissamine rhodamine B conjugate in D_2O. 267

Figure 9.9. (a) Schematic illustration of polymer-coated surface modification via μCP using βCD-grafted lissamine-Rhodamine B dye; fluorescence microscopy images of dye-modified (b) patterned surfaces, (c) nonpatterned surfaces, and inset S(D_{95}-A_0-T_5). The scale bar is 100 μm. 268

Figure 9.10. The fluorescence images of βCD-grafted lissamine-rhodamine B modified S(D_{75}-A_{20}-T_5) surface after incubation at 37 ^{o}C in PBS buffer from 0 h to

48 h, b) the fluorescence intensity bar graph of βCD-grafted lissamine-Rhodamine B modified S(D_{75}-A_{20}-T_5) surface. 269

Figure 9.11. (a) Schematic illustration of polymer-coated surface modification with βCD-grafted biotin and immobilization of FITC-Streptavidin using μCP, fluorescence microscopy images of CdSe Qdot streptavidin-modified surfaces (b) patterned S(D_{75}-A_{20}-T_5), (c) nonpatterned S(D_{75}-A_{20}-T_5). The scale bar is 50 μm..... 270

Figure 9.12. (a) Schematic illustration of polymer-coated surface modification with βCD-grafted biotin and immobilization of CdSe Qdot-Streptavidin using μCP; fluorescence microscopy image of (b)CdSe Qdot streptavidin-modified patterned S(D_{75}-A_{20}-T_5) surface; (c) CdSe Qdot streptavidin-modified nonpatterned S(D_{75}-A_{20}-T_5) surface. The scale bar is 50 μm)..... 271

Figure 9.13. High-resolution XPS spectra (a) C1s, (b) N1s, and (c) S2p of βCD-Biotin conjugated S(D_{75}-A_{20}-T_5); and high-resolution XPS spectra (d) C1s, (e) Cd3d and N1s, and (f) S2p of βCD-Biotin conjugated S(D_{75}-A_{20}-T_5) after immobilization of CdSe-Qdot conjugated streptavidin. 272

Figure 9.14. The copper-catalyzed *click* reaction between alkyne-containing mannose and mono-azide functionalized βCD..... 273

Figure 9.15. ^{1}H NMR spectrum of mono-mannose conjugated βCD in D_2O..... 273

Figure 9.16. (a) Schematic illustration of polymer-coated surface modification with βCD- mannose and immobilization of FITC-ConA using μCP; (b) fluorescence microscopy images of FITC-ConA-modified and (c) fluorescence microscopy images of Rhodamine-PNA-modified S(D_{75}-A_{20}-T_5) before and after washing steps. The scale bar is 50 μm. 275

Figure 9.17. Regeneration and reuse of βCD-Man-S(D_{75}-A_{20}-T_5) surface. (a) (c) and (e) Adsorption of FITC-ConA on βCD-Man-S(D_{75}-A_{20}-T_5) surface; (b) and (d)

regeneration by releasing of ConA in the presence of D-mannose; (f) The cycles of reuse of βCD-Man-S(D_{75}-A_{20}-T_5) were measured by analyzing the mean fluorescence intensity of the images. 276

Figure 9.18. The synthesis of cyclic RGD-conjugated βCD via click reaction. 277

Figure 9.19. High-resolution XPS spectra (a) C1s, (b) N1s, (c) survey scan ,and (d) O1s spectra of cRGD immobilized S(D_{75}-A_{20}-T_5) surface 278

Figure 9.20. (a) Scheme of conjugation of RGD-βCD and subsequent cellular attachment; (b) merged fluorescence microscopy images of fibroblast cells immobilized on RGD-βCD-S(D_{75}-A_{20}-T_5), S(D_{95}-A_0-T_5) and S(D_{75}-A_{20}-T_5) surfaces after staining. The scale bar is 50 µm. 279

Figure A.1. ^{13}C NMR spectrum of HCQ-E-MA monomer ($CDCl_3$). 336

Figure A.2. FTIR spectrum of HCQ-E-MA monomer. 336

Figure A.3. ^{13}C NMR spectrum of HCQ-C-MA monomer ($CDCl_3$). 337

Figure A.4. FTIR spectrum of HCQ-C-MA monomer. 337

Figure A.5. ^{13}C NMR spectrum of HCQ-CB-MA monomer ($CDCl_3$). 337

Figure A.6. FTIR spectrum of HCQ-CB-MA monomer. 338

Figure A.7. ^{13}C NMR spectrum of GEM-C-MA monomer (DMSO d6). 338

Figure A.8. FTIR spectrum of GEM-C-MA monomer. 338

Figure A.9. ^{13}C NMR of GEM-SSC-MA monomer (DMSO d6). 339

Figure A.10. FTIR spectrum of GEM-SSC-MA monomer. 339

Figure A.11. ^{13}C NMR spectrum of azobis-ene ($CDCl_3$). 340

Figure A.12. FTIR spectrum of azobis-ene. 340

Figure A.13. ^{13}C NMR spectrum of G1-diene-alkyne ($CDCl_3$). 341

Figure A.14. ^{13}C NMR spectrum of Azobis-G1-diene ($CDCl_3$). 341

Figure A.15. FTIR spectrum of azobis-G1-diene. 342

Figure A.16. ^{13}C NMR spectrum of alkyne bearing G2-tetraene ($CDCl_3$). 342

Figure A.17. ^{13}C NMR spectrum of Azobis-G2-tetraene ($CDCl_3$). 343

Figure A.18. FTIR spectrum of azobis-G1-diene. 343

Figure A.19. ^{1}H NMR spectra of copolymer P(P_{90}-B_{10}) and P(P_{70}-B_{30}) in $CDCl_3$ 344

Figure B.1. Copyright license of [22]. 345

Figure B.2. Copyright license of [58]. 345

Figure B.3. Copyright license of [59]. 346

Figure B.4. Copyright license of [160]. 347

Figure B.5. Copyright license of [162]. 348

Figure B.6. Copyright license of [166]. 349

Figure B.7. Copyright license of [201]. 350

Figure B.8. Copyright license of [337]. 350

LIST OF TABLES

Table 1.1. Some chemotherapy agents target DNA replication [16]. 4

Table 3.1. Polymerization conditions of P(OEG/HCQ-E)..... 52

Table 3.2. Calculated EC_{50} values of HCQ and POEGMA-HCQ-E copolymer for pancreas cancer cell lines after 48 h incubation. 54

Table 3.3. Polymerization conditions of P(OEG/HCQ-C). 56

Table 3.4. Calculated EC_{50} values of HCQ and P(OEG/HCQ-C) copolymer for pancreas cancer cell lines after 48 h incubation. 58

Table 3.5. Polymerization conditions of P(OEG/GEM-C). 61

Table 3.6. Calculated EC_{50} values of GEM and P(OEG/GEM-C) copolymer for pancreas cancer cell lines after 48 h incubation. 63

Table 3.7. Polymerization conditions of P(OEG/HCQ-E/GEM-C)..... 65

Table 3.8. Calculated EC_{50} values of the combination of GEM-HCQ and P(OEG/HCQ-E/GEM-C) copolymer for pancreas cancer cell lines after 48 h incubation. .. 67

Table 3.9. Polymerization conditions of P(OEG/HCQ-C/GEM-C). 68

Table 3.10. Calculated EC_{50} values of the combination of GEM-HCQ and P(OEG/HCQ-E/GEM-C) copolymer for pancreas cancer cell lines after 48 h incubation. .. 69

Table 3.11. Polymerization conditions of P(OEG/GEM-SSC). 74

Table 3.12. Calculated EC_{50} values of GEM, P(OEG/GEM-SSC), and P(OEG/GEM-C) copolymer for pancreas cancer cell lines after 48 h incubation. 76

Table 3.13. Polymerization conditions and properties of P(OEG/HCQ-C/GEM-SSC). 78

Table 3.14. Calculated EC_{50} values of GEM-HCQ and P(OEG/GEM-SSC) copolymer for pancreas cancer cell lines after 48 h incubation. 80

Table 3.15. Polymerization conditions of P(OEG/HCQ-CB). 82

Table 3.16. Calculated EC_{50} values of HCQ and P(OEG/HCQ-CB) copolymer. 84

Table 3.17. Polymerization conditions and properties of P(OEG/HCQ-CB/GEM-SSC). .. 87

Table 3.18. Calculated EC_{50} values of GEM-HCQ mixture and P(OEG/HCQ-CB/GEM-SSC) copolymer for pancreas cancer cell lines after 48 h incubation. 89

Table 3.19. Calculated EC_{50} values of GEM, HCQ, GEM-HCQ, and P(OEG/HCQ-CB/GEM-SSC) copolymer for PSC and PDAC after 48 h incubation. 91

Table 5.1. Characterization and properties of P(OEG/N_3) copolymer 127

Table 5.2. The properties of P(OEG/ P(OEG/N_3/GEM-C) 129

Table 5.3. The properties of P(OEG/ P(OEG/N_3/GEM-SSC) 130

Table 5.4. The gelation conditions of HG-GEM-SSC and HG-GEMC. 137

Table 7.1. The properties of polymer brush (P1-P5) and calculated monomer composition from XPS based on N/O ratio. 207

Table 8.1. Polymerization conditions and characterization data of BDSMA-PEGMA copolymers. 237

Table 8.2. Polymerization conditions and characterization data of BDSMA-PEGMA-TMSPMA copolymers. 241

Table 9.1. Polymerization conditions of AdaMA-DEGMEMA copolymers. 263

LIST OF ACRONYMS/ABBREVIATIONS

ACVA	4’4-Azobis(4-cyanovaleric acid) (V-501)
ACN	Acetonitrile
AcOH	Acetic acid
Ada	Adamantane
AdaMA	Adamantane Methacrylate
AFM	Atomic Force Spectroscopy
AHMA	Azido-hexyl methacrylate
AIBN	2,2’-azobisisobutyronitrile
ALAL	Alanine-Leucine-Alanine-Leucine
APTES	3-Aminopropyltriethoxysilane
ATCC	American Type Culture Collection
ATR-FTIR	Attenuated Total Reflectance Fourier Transform Infrared
ATRP	Atom Transfer Radical Polymerization
AUC	Under Area Curve
βCD	Beta cyclodextrin
BDSMA	Benzothiazole-disulfide Methacrylate
BDSOH	Benzothiazole-disulfide Alcohol
Bis-MPA	2,2-Dimethoxypropane
BODIPY	4,4-difluoro-4-bora-3a,4a-diaza-s-indacene
BPDC	Brush-type Polymer Drug Conjugate
BSA	Bovine Serum Albumin
CA-4	Combrestatin A-4
CB[*n*]	Cucurbiturils
ConA	Concanavalin A
CCK-8	Cell Counting Kit Assay
$CDCl_3$	Deuterated Chloroform
CDDP	Cisplatin
CL	Clearence
Cmax	Maximum Concentration
CPT	Camptothecin

CQ	Chloroquine
cRGDfK	Cyclic Arginine-Gylcine-Aspartic acid-Phenyl alanine-Lysine
CRP	Controlled Radical Polymerization
CSC	Cancer Stem Cells
CTA	Chain Transfer Agent
CuAAc	Copper-Catalyzed Azide-Alkyne Cycloaddition
DA	Diels-Alder
DAPI	4'-6-Diamidino-2-phenylindole
DBCO	Dibenzocyclooctyne
DCC	*N,N'*-Dicyclohexylcarbodiimide
DCM	Dichloromethane
DCU	Dicyclohexyl urea
DDS	Drug Delivery System
DEGMA	Diethylene glycol Methacrylate
DEX	Dexamethasone
DIPEA	Diisopropylethylamine
DMAC	Dimethylacetamide
DMAP	4-Dimethylaminopyridine
DMEM	Dulbecco's Modified Eagle's Medium
DMF	*N,N'*-Dimethylformamide
DMPA	2,2'-Dimethoxy-2-phenylacetophenone
DMSO	Dimethyl sulfoxide
DOX	Doxorubicin
DSC	Disuccinimidyl carbonate
DTT	Dithiothreitol
DTX	Docetaxel
ECs	Endothelial Cells
ECM	Extracellular Matrix
EDCI	1-(3-(Dimethylamino)propyl)-3-ethylcarbodiimide hydrochloride
EGFR	Epidermal Growth Factor Receptor
EPR	Enhanced Permeability and Retention
Et_3N	Triethyl amine (TEA)
EtOAc	Ethyl Acetate

FBS	Fetal Bovine Serum
FDA	Food and Drug Administration
FITC	Fluorescein Isothiocyanate
FITC-ConA	Fluorescein Isothiocyanate Concanavalin A Conjugate
Fluo-Mal	N-(5-fluoresceinyl) maleimide
FRET	Fluorescence Resonance Energy Transfer
FTIR	Fourier-Transform Infrared
FuMaMA	Furan-protected Maleimide Methacrylate
GEM	Gemcitabine
GEM-C-MA	Gemcitabine Carbamate Methacrylate
GEM-SS-C-MA	Gemcitabine Disulfide-Carbamate Methacrylate
GFLG	Glycyl-phenylalanyl-leucyl-glycine
GMA	Glycidyl Methacrylate
GPC	Gel Permeation Chromatography
GSH	Glutathione
GSHOEt	Glutathione Ethyl Ester
HA	Hyaluronic Acid
HEMA	2-(Hydroxy ethyl) methacrylate
HEPES	4-(2-hydroxyethyl)-1-piperazineethanesulfonic acid
HCQ	Hydroxychloroquine
HCQ-E-MA	Hydroxychloroquine Ester Methacrylate
HCQ-C-MA	Hydroxychloroquine Carbamate Methacrylate
HCQ-CB-MA	Hydroxychloroquine Carbonate Methacrylate
HPLC	High-performance liquid chromatography
HPMA	N-(hydroxypropyl)methacrylamide
HSEMA	2-((2-Hydroxyethyl)disulfanyl)ethyl methacrylate
J	Coupling Constant
kDa	Kilo Dalton
LCMS	Liquid Chromatography–Mass Spectrometry
LCST	Lower Critical Solution Temperature
µCP	Microcontact Printing
MBTS	2,2’-Dithiobis(benzothiazole)
MeOH	Methanol

MHz	Mega Hertz
MPC	2-methacryloyloxyethyl phosphorylcholine
MRI	Magnetic Resonance Imaging
MTD	Maximum Tolerated Dose
MTX	Methotrexate
MWCO	Molecular Weight Cut-Off
NAS	N-acryloyloxysuccinimide
NHS	N-Hydroxysuccinimide
NHS-HSEMA	N-Hydroxysuccinimidiyl-2-((2-Hydroxyethyl)disulfanyl)ethyl methacrylate
NMP	Nitroxide Mediated Polymerization
NOAEL	No Obseved Adverse Effect Level
NMR	Nuclear Magnetic Resonance
OEGMA	Oligo(etlylene glycol) methyl ether metacrylate
PAA	Poly(acrylic acid)
PAMAM	Poly(amidoamine)
PBS	Phosphate-bufferedd saline
PDAC	Pancreatic Ductal Adenocarcinoma
PDC	Polymer Drug Conjugate
PDI	Polydispersity Index
PDMS	Polydimethoxysiloxane
PDSMA	Pyridyl-disulfide methacrylate
PDSOH	Pyridyl-disulfide alcohol
PEG	Poly(ethylene glycol)
PEGDA	Poly(ethylene glycol) diacrylate
PEGDMA	Poly(ethylene glycol) dimethylacrylate
PEGMA	Poly(ethylene glycol) methyl methacrylate
PEtOx	Poly(2-ethyl-2-oxazoline)
PFPA	Poly(pentafluorophenyl acrylate)
PK	Pharmacokinetic
PLA	Polylactide
PLE	Porcine Liver Esterase
PMDETA	N,N,N’-N’’-N’’ pentamethyldiethylenetriamine

PMMA	Poly (methyl methacrylate)
PNIPAm	Poly(N-isopropylacrylamide)
PREP-HPLC	Preparative High Performance Liquid Chromatograph
PSC	Pancreatic Stellate Cells
PTSA	p-Toluenesulfonic acid monohydrate
PTX	Paclitaxel
PVA	Polyvinyl alcohol
PVP	Poly(vinyl pyrrolidone)
Qdot605	Streptavidin-Coated CdSE Quantum Dots
RAFT	Reversible Addition Fragmentation Chain Transfer
RDRP	Reversible Deactivation Radical Polymerization
RGDC	Arginine-Glycine-Aspartate-Cycteine Peptide
RhB-PNA	Rhodamine B-Conjugated Peanut
RPMI	Roswell Park Memorial Institute
SAM	Self-Assembled Monolayer
SCEMA	2-(N-succinimidylcarboxyoxy)ethyl methacrylate
SEC	Size Exclusion Chromatograhpy
SEM	Scanning Electron Microscopy
SET-LRP	Single Electron Transfer–Living Radical Polymerization
SI-RAFT	Surface Initiated Reversible Addition Fragmentation Chain Transfer
SPAAC	Strain-Promoted Azide-Alkyne Cycloaddition
SPR	Surface Plasmon Resonance
SS	Disulfide
rDA	retro Diels-Alder
TAMRA-Mal	Tetramethylrhodamine-5-maleimide
TFBA	4-Trifluorobenzyl amine
TFBM	4-Trifluoromethylbenzyl mercaptan
THF	Tetrahydrofuran
TMSCI	Chlorotrimethylsilane
TMSPMA	3-(Trimethoxysilyl)propyl methacrylate
UV-Vis	Ultra-violet-Visible
VDβ	Volume of Distribution
XPS	X-Ray Photoelectron Spectroscopy

1. INTRODUCTION

The aim of this introductory chapter is to briefly discuss some of the general research areas that are related to the different topics explored in this thesis. The brief sections provides the reader with general terminologies in the area, as well as illustrates with some examples the state of the art. The aim of the subsequent sections is not to review the advances in the respective research areas. A more focused introduction related to the individual projects are provided at the beginning of each chapter.

1.1. Polymer Drug Conjugates for Delivery of Anticancer Drugs

1.1.1. Cancer

The human body consists of billions of cells. Our life started as a single cell, and that cell constituted our tissues and organs by copying itself and dividing. Normal cells grow and divide when required and undergo apoptosis, defined as programmed cell death when they grow old and suffer from unrepairable damage [1]. The general process is illustrated in Figure 1.1.

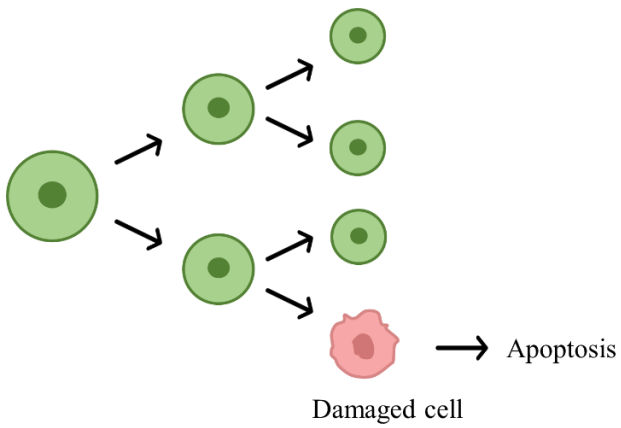

Figure 1.1. Schematic illustration of normal cell division.

DNA is the fundamental carrier of genetic information in all living cells but does not have structural stability towards physical or chemical reagents [2]. Therefore, DNA undergoes several mutations, and a normal healthy cell may turn into a cancerous cell because of mutations in the DNA. DNA damage can lead to genetic changes, and when genes that control cell growth suffer from DNA damage, these changes can cause cancer [2]. Cancer cells start to grow and divide in an out of control manner because the apoptosis mechanism does not work correctly. The reason for DNA damage can become inherited, or people may encounter it at any time during their lives. There are millions of people suffering from various forms of cancer all over the world. According to Global Cancer Incidence, Mortality and Prevalence (GLOBOCAN) cancer statistics, 19.3 million cancer cases have been reported, and 10 million people died from cancer in 2020 [3].

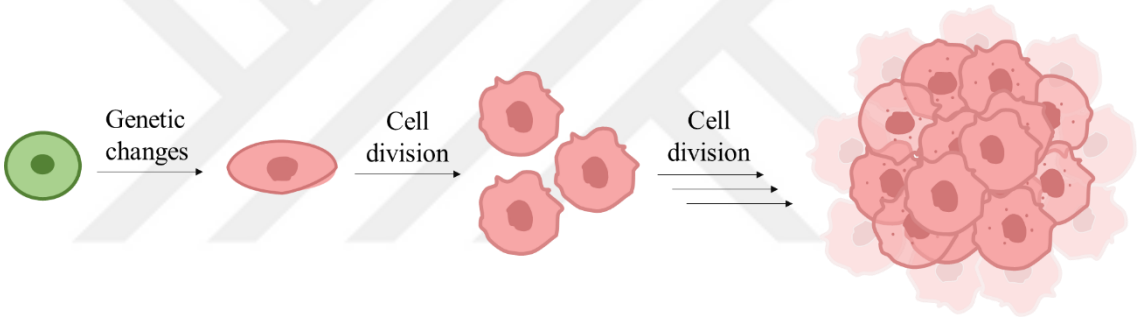

Figure 1.2. Schematic illustration of uncontrolled cell growth.

Hanahan and Weinberg summarized the hallmarks of cancer development [4,5]. Sustaining signaling for proliferation, resisting cell death and angiogenesis, and avoiding immune destruction are some cancer development hallmarks and cellular factors. Besides cellular factors, environmental factors like carcinogens and lifestyle issues such as smoking and age may play an essential role in cancer progression [6]. Cancer is not one disease; it has been described that there are more than 100 types of human cancer [7]. Recent research shows that lung, colon, stomach, liver, breast, pancreas, and esophagus cancer are the major types since these are the leading cause of death [8]. Many types of cancer start in one place in the body; therefore, they are defined as primary cancer, and this place where cancer begins is known as the primary site. Sometimes, cancer cells can leave their original place, circulate in the bloodstream, and locate in other parts of the body. This new part is called a secondary site, where a secondary tumor develops. This process is known as “metastasis” [9]. Although

the metastasis process is poorly understood, it is the leading cause of cancer death, and more than 90% of patients with cancer die due to metastasis [10]. Bone, liver, lung, and brain are regions where metastasis occurs frequently.

Tumor growth and metastasis strongly depend on the vascular network. The formation of new blood and lymphatic vessels is needed to supply oxygen and nutrients and eliminate waste products in the tumor region. The construction of new blood and lymphatic vessels occurs due to processes that are defined as angiogenesis and lymphangiogenesis, respectively [11]. Tumors suffering from the lack of vascular support may become apoptotic or necrotic. On the other hand, forming new blood vessels, including tumor angiogenesis, comprises a four-step process. In the first step, the basement membrane in the tissue undergoes damage, and hypoxia is dominant in this situation. In the second step, endothelial cells (ECs) are promoted by angiogenic signal due to hypoxia. In the third step, endothelial cells start proliferation, and they gain resistance to apoptosis. In the final step, highly proliferated and differentiated endothelial cells constitute new blood vessels [11-13]. As a result, the angiogenesis process, shown in Figure 1.3, supports tumor growth by forming new blood vessels which are responsible for supplying oxygen and nutrients.

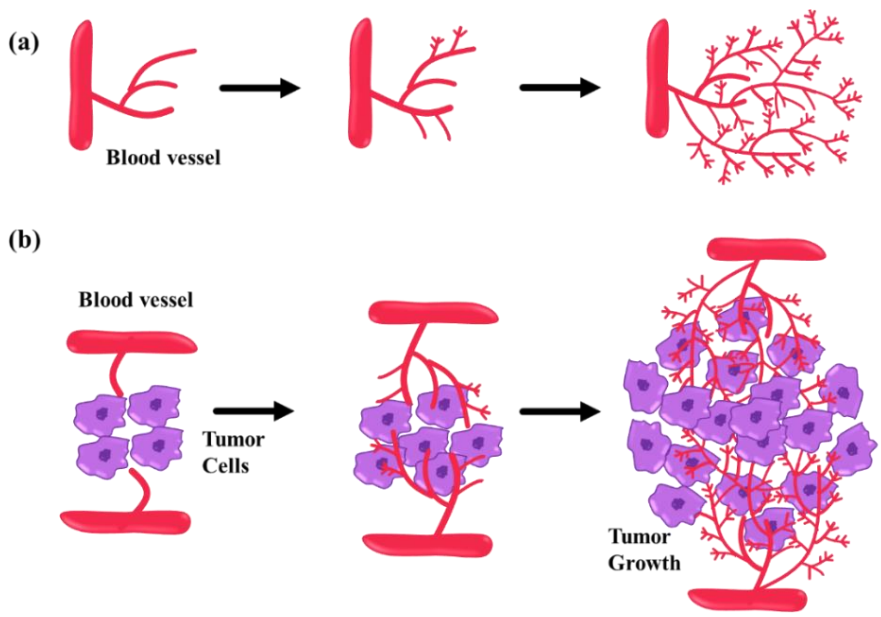

Figure 1.3. (a) Schematic illustration of angiogenesis process, (b) tumor growth via angiogenesis.

Chemotherapy, radiotherapy, and surgery are commonly used methods for cancer treatment. Other techniques and procedures include immune therapy, targeted therapy, gene therapy, hormone therapy, magnetic hyperthermia, photodynamic therapy, and bone marrow transplantation [14]. These methods aim to cure cancer, provide prolonged patient life, and improve quality of life [15]. These methods can sometimes be applied together or consecutively to increase the cancer treatment rate.

1.1.2. Chemotherapy

As mentioned above, chemotherapy is one of the most common methods for the treatment of cancer. Chemotherapy, which is a drug treatment, targets the cancer cells that divide rapidly in the body. Anticancer drugs or chemotherapy agents in chemotherapy kill cancer cells by targeting DNA replication and microtubules. Some alkylation agents and antimetabolites are used as chemotherapy agents. They block DNA, and therefore, the DNA may not make copies of itself, and as a result, a new cell may not reproduce. Some of the chemotherapy agents which interfere with DNA replication are tabulated in Table 1.1.

Table 1.1. Some chemotherapy agents target DNA replication [16].

Drugs	**Mechanism of Action**	**Therapeutic Applications**
Methotrexate (MTX)	Inhibits nucleotide synthesis and dihydrofolate reductase	Childhood leukemia and some lymphomas and solid tumors.
5-Fluorouracil (5-FU)	Prevention of nucleotide synthesis	gastrointestinal, breast neck cancers
Gemcitabine (dFdC)	Inhibits DNA polymerase, prevents DNA replication	Pancreas, lung, and bladder cancers
Doxorubicin (DOX)	Damages to the DNA template	Breast cancer, osteogenic sarcoma
Camptothecin (CPT)	Inhibits DNA topoisomerase	Colon, lung and ovarian, leukemia, and gastric cancer

Microtubule-target agents block cell cycle progression during mitosis and lead to apoptosis [18,19]. Some chemotherapy agents target microtubules via stabilization and destabilization ways. Paclitaxel (PTX), docetaxel (DTX), and cabazitaxel are responsible for the stabilization of microtubules, while eribulin, vinflunine, combretastatin-A4 (CA-4) are in charge of destabilization of microtubules [19]. In addition to DNA-blocking agents and microtubule-targeting drugs, anti-angiogenic agents have a significant role in cancer treatment. As mentioned, angiogenesis may promote cancer progression, tumor growth, and metastasis by supplying new blood vessels to carry oxygen and nutrients. Therefore, inhibition of angiogenic factors is the most effective way to treat some cancers. Bevacizumab (Avastin), cetuximab (Erbitux), erlotinib (Tarceva), panitumumab (Vectibix), and trastuzumab (Herceptin) are some FDA-approved anti-angiogenic agents [20]. For example, trastuzumab binds the extracellular domain of the HER-2 receptor in breast cancer tumors. Erlotinib inhibits the epidermal growth factor receptor (EGFR) and tyrosine kinase activity and is used for the metastatic pancreas and breast cancer. Although chemotherapy is successful to some extent, drawbacks of chemotherapy agents restrict their bioavailability and applicability. The water solubility of chemotherapy agents is poor. They are small molecules, so they spread everywhere in the body. Therefore, chemotherapy agents do not show selectivity. In addition, these agents can damage healthy tissues due to nonspecific biodistribution.

Moreover, rapid metabolism and clearance of these drugs from the kidney reduces the circulation time in the bloodstream. As a result of non-specificity and quick clearance, less drug reaches the target site; that's why chemotherapy requires higher doses. High doses bring about severe side effects such as hair loss, cardiotoxicity, nausea, and loss of appetite. Also, higher doses lead to elevated toxicity in healthy tissue and increased drug resistance [21]. Drawbacks of anticancer drugs, such as low efficacy, poor pharmacokinetic profile, and high toxicity, pave the way to developing a new area in cancer treatment: polymer therapeutics.

1.1.3. Polymer Therapeutics

The combination of polymer chemistry and biomedical sciences has created the concept of 'polymer therapeutics.' Polymer therapeutics are nanosized (5-100 nm) polymer-

based pharmaceuticals composed of polymer-protein conjugates, polymer-drug conjugates, polymer-DNA complexes, polymer-drug carriers such as micelles, nanoparticles, liposomes, and so on. In polymeric systems, the polymer increases the plasma half-life, decreases immunogenicity, provides water solubility, and increases the stability of a bioactive molecule [22]. In other words, the polymer improves the pharmacokinetic and pharmacodynamic properties of bioactive molecules like a drug or peptides.

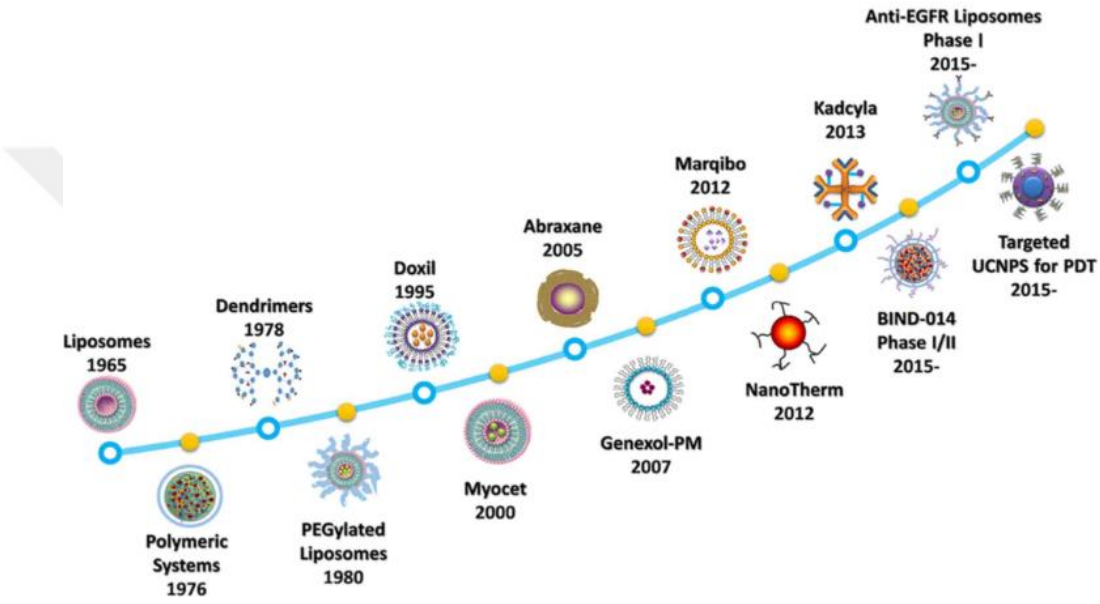

Figure 1.4. Timeline of development polymeric nanomedicine. Reprinted with permission from [22].

1.1.4. Polymer Drug Conjugates (PDCs) as Polymer Therapeutics

As indicated previously, chemotherapy agents have solubility problems in water. They show nonspecific biodistribution and high toxicity. They have a low plasma half-life. Recently, polymer-drug conjugates have been extensively studied to eliminate these drawbacks of small chemotherapy agents. Polymer drug conjugates improve drug solubility and stability, increase plasma half-life, and provide specific biodistribution in the body [23]. The concept of polymer-drug conjugates was introduced by Ringsdorf in 1975 [24]. According to the Ringsdorf model, a polymer-drug conjugate consists of a biocompatible polymer backbone to which a drug is conjugated via a suitable linker. In addition, a targeting group is attached to the polymer backbone to transport the drug carrier to the biological site.

Besides drug conjugation and targeting groups, a solubilizer is another critical component of the polymer backbone.

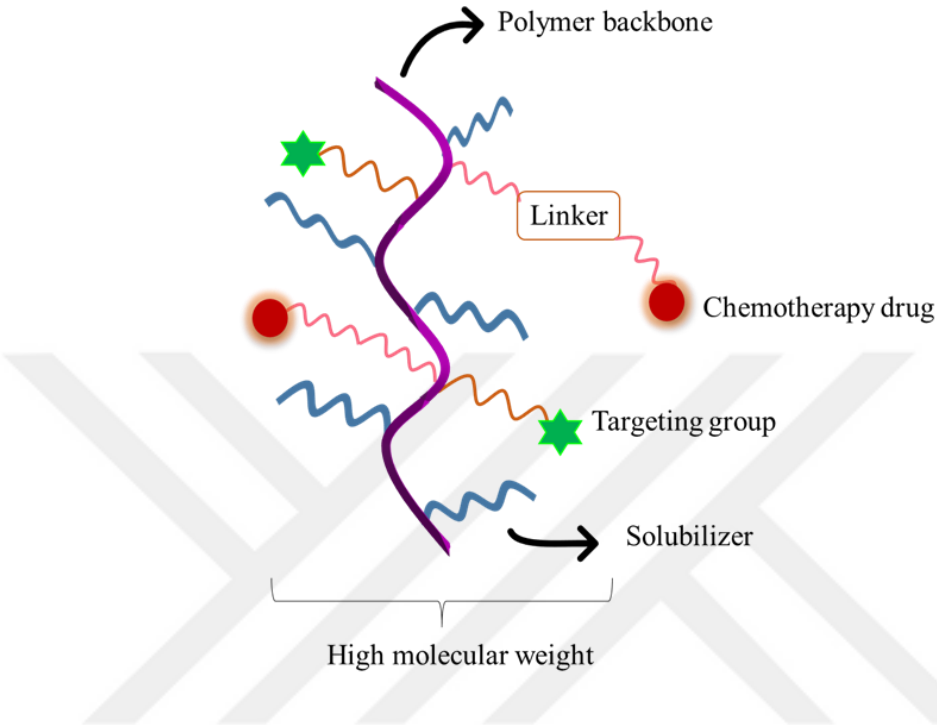

Figure 1.5. Components of a polymer-drug conjugate according to Ringsdorf's model.

1.1.5. Importance of Polymer in Polymer Drug Conjugates

In polymer-drug conjugates, the chemical conjugation of chemotherapy drugs to water-soluble polymers with high molecular weight is utilized to eliminate handicaps and improve the efficacy of the small drugs. Polymer conjugation provides water solubility to hydrophobic chemotherapy agents. Polymer chains increase longer circulation time and therapeutic efficacy. In addition, polymer chains prevent enzymatic degradation with the aid of steric hindrance. Moreover, polymer conjugation decreases drug dosing frequency and minimizes drug side effects [25]. Both natural and synthetic polymers have been used in drug conjugation. Collagen, alginic acid, chitosan, dextran, and cellulose are natural polymers used in polymer-drug conjugates [26]. They are biocompatible, biodegradable, and nontoxic and generally do not lead to an immunogenic reaction.

On the other hand, polysaccharides, chitosan, and alginates have high molecular weight; their molecular weights are above 200.000 g/mol without making any process to obtain a lower molecular weight sample. In addition, they are highly polydisperse, and polydispersity (Mw/Mn) is above 2 [27]. Higher polydispersity means more heterogeneity in all polymer-drug samples. Therefore, the utilization of synthetic polymer has attracted attention. Poly(ethylene glycol) (PEG), poly(vinyl pyrrolidone) (PVP), poly(vinyl alcohol) (PVA), polyglutamic acid (PGA), N-(2-hydroxypropyl)methacrylamide (HPMA), poly(methyl methacrylate) (PMMA) are commonly used synthetic polymers in drug conjugated polymeric systems [25]. Among these synthetic polymers, PEG is mainly used for drug conjugation due to several advantages. PEG is an FDA-approved biocompatible polymer. Because of the widespread use of PEG for drug conjugation, many functional PEGs are commercially available. Moreover, large-scale PEG can be easily synthesized with narrow polydispersity. Although these advantages, non-biodegradability is the main disadvantage of PEG [26]. Another drawback of PEG-drug conjugate is low drug loading capacity due to drug conjugation only at end chains [27]. To solve these problems, PEG-drug conjugates that can be degradable have been examined [28,29].

1.1.6. The Choice of Linker in Polymer Drug Conjugates

A linker is another vital component for the fabrication of polymer-drug conjugates. Polymer drug delivery systems that load the drug physically without using any linker have some drawbacks, such as low drug encapsulation, drug instability inside the carrier, rapid drug release due to weak physical interactions, and higher cytotoxicity due to quick release [30]. Drugs are covalently conjugated to a polymer to overcome these limitations. The chemical conjugation of the drug on the polymer backbone paves the way for the concept of “smart linker” and “targeted drug release”. A smart linker in a polymer-drug conjugate system should be stimuli-responsive and show cleavage according to internal stimuli that enable targeted drug release [30]. Smart linkers can be redox-responsive, pH-responsive, and enzyme responsive. Compared with physical drug loading, chemical/covalent conjugation enables longer circulation time and slows down drug release by preventing burst release.

Moreover, the linker provides sustained/controlled and targeted drug release. For example, a disulfide linker is a redox-responsive linker that degrades in the presence of glutathione (GSH) and DTT. GSH is a reducing agent in biochemical processes [30]. Some breast, ovarian, and lung tumors have elevated GSH concentrations compared with healthy tissue. Also, it is known that intracellular GSH concentration is higher than the extracellular version [31]. Due to these differences, GSH-mediated or redox-responsive polymer-drug conjugates have gained importance [32-34]. In addition, while the extracellular pH value of normal cells is almost 7.4, the extracellular pH of cells in tumor tissue is around 6.0. In addition, the pH value of lysosomes in cancer cells (pH 3.8 - 4.7) is lower than that of normal cells (pH 4.5 - 6.0) [35]. Therefore, pH-responsive linkers are favorable for intracellular drug release and have attracted attention in targeted drug therapy [36]. In other words, most pH-responsive linkers are unstable acidic environments and show higher drug release in endosomes and lysosomes in tumor tissue. On the other hand, pH-responsive linkers are stable under physiological conditions, and their release rates are lower.

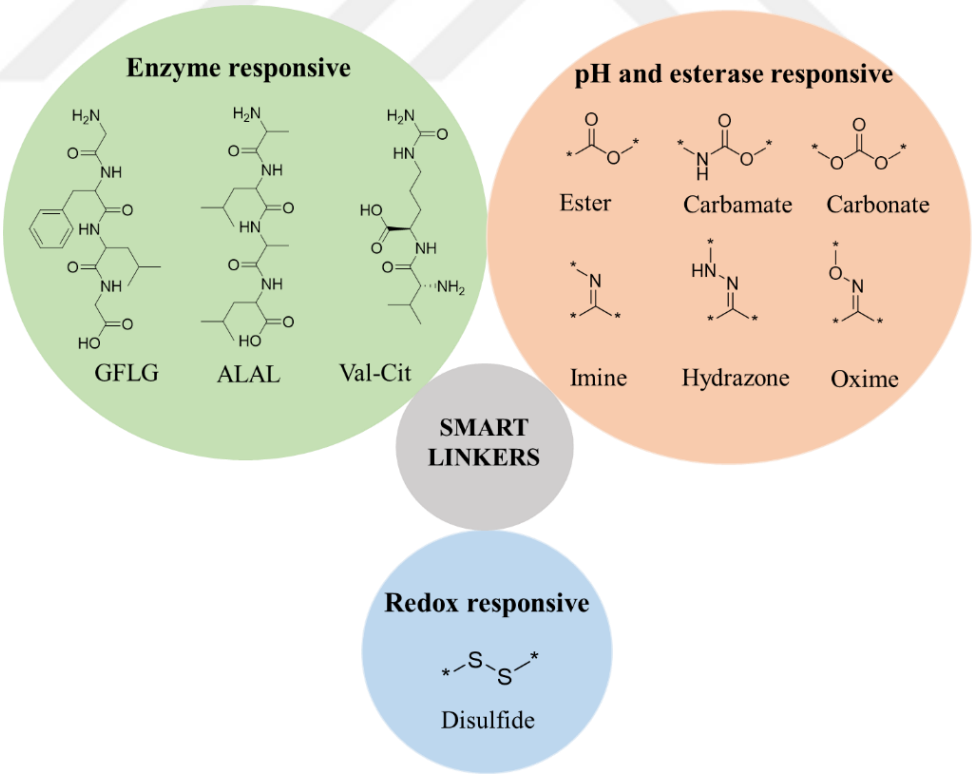

Figure 1.6. Commonly used linkers between drug and polymer backbone.

1.1.7. Molecular Weight, Size, and Enhanced Permeation and Retention (EPR) Effect

Nowadays, small molecules used for chemotherapy do not distinguish tumor sites from normal tissue. When they are introduced to the body, they spread non-specifically into the body. In addition, small anticancer drugs are immediately removed from the tumor or normal tissues. As a result of these challenges, a low percentage of the drug reaches targeted tumor tissue. Along with polymer therapeutics, passive targeting or the enhanced permeability and retention (EPR) effect was investigated as the critical role of tumor targeting macromolecular drug delivery system.

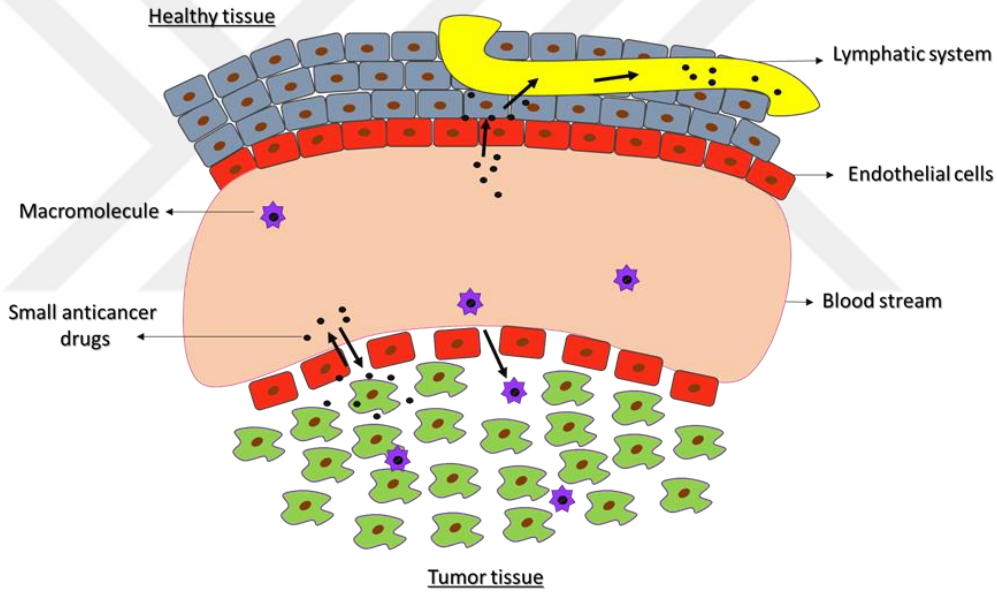

Figure 1.7. Schematic representation of the EPR effect.

Matsumura and Maeda introduced the concept of EPR effect in 1986 [37]. They showed that macromolecules accumulate in tumor tissue due to hypervasculature of tumor tissue and lack of a lymphatic recovery system [37]. It is well known that angiogenesis produces hypervasculature in tumor tissue [11]. The uncontrolled growth of cancer cells leads to the formation of highly disorganized blood vessels different from normal tissue vasculature. The tumor vasculature is disorganized and endothelial cells in the tumor vasculature are different in terms of their morphology, size, and shape [38]. In addition, the diameters of blood vessels are inconsistent, and the shape of blood vessels is uneven [39].

Thereby, large gaps exist between endothelial cells in the tumor vasculature. Due to these intercellular gaps between endothelial cells, tumor vessels show hyper-permeability. In addition to hyper-permeability, lymphatic vessels in tumor tissue are highly dilated and leaky. The recent findings established that tumor tissue has no lymphatic clearance [37]. As a result of hyper-permeability and poor lymphatic system, tumor tissue demonstrates extravasation and retention of macromolecular drugs and nanostructures. The molecular weight of the macromolecular drug should be above 40 kDa, and the size of the nanostructure should be between 50-150 nm [40,41]. The size of the intercellular gaps in the normal vessel wall is less than 10 nm; therefore, macromolecules and nanostructures will not be able to extravasate to normal healthy tissues. In contrast to normal tissue, large macromolecules and nanostructures (>10 nm) can pass through tumor vessels and accumulate in tumor tissue**.** The exceptional condition of tumor tissue has become the main principle of targeted drug delivery systems. In EPR-based drug delivery systems, chemotherapy agents are conjugated to macromolecules like polymers. Drug-conjugated macromolecules selectively accumulate in tumor tissue. They have a prolonged circulation time and show therapeutic effects by decreasing the toxicity of chemotherapy drugs via controlled release and improving the pharmacokinetic properties of a drug [42].

1.1.8. Active Targeting

There are two types of targeting strategy that is utilized in drug delivery systems: passive and active targeting. Passive targeting, or the EPR effect, as explained above benefits from the nanosized of the delivery vehicle which results in higher drug accumulation in cancerous tissues. In contrast to passive targeting, active targeting is based on receptor-ligand affiliation. An active targeting system comprises a carrier, drug, and targeting moiety/ligand. Cancer cell receptors may be different from one on normal tissue, or may be overexpressed on cancer cells compared to their normal counterparts [43]. Targeting ligands on drug carriers interact with the receptors on cancer cells, and such receptor-ligand interaction may promote their cellular internalization. In other words, active targeting, which entails providing the carrier with a cue for going to a specific address, is more cell selective than passive targeting. The most widely used targeting ligands are monoclonal antibodies [44], folic acid and lectins [45], transferrin [46], cell-adhesive peptides such as the RGD-peptide containing the arginine-glycine-aspartic acid tripeptide sequence [47]. To

summarize, passive and active targeting are cornerstones of contemporary targeted drug delivery.

1.1.9. Polymeric Nanomedicine

In today's nanomedicine, polymer conjugation of small anticancer drugs has become prominent. Many research groups and industrial companies have worked on fabricating polymeric constructs and the conjugation of chemotherapy agents in the market. As mentioned before, polymer conjugation improves the therapeutic activities of chemotherapy agents. Therefore, many scientists conjugate small chemotherapy drugs to polymeric architectures to develop pharmacokinetic properties. Most polymeric architectures/structures provide water solubility for anticancer drugs. Polymer drug conjugates may be oriented to tumor tissue via passive targeting (EPR). Moreover, targeting groups can be attached to polymeric drug macromolecules to increase targeting ability. Polymer drug conjugates in the tumor region show drug release with the aid of intelligent linkers.

There are many examples of polymer-drug conjugates. The first concept of the polymer-drug conjugate was introduced by Ringsdorf in 1975 [24,48]. He demonstrated successful drug release from polymeric structures with a cleavable linker. Ringsdorf's concept has attracted attention and paved the way for synthesizing the first synthetic HPMA-based drug-conjugated polymeric system by Kopecek and coworkers in 1976 [49]. Doxorubicin (DOX) conjugated HPMA polymer, defined as PK1, was the first clinically tried HPMA polymer-drug conjugate in 1998. In PK1, DOX was chemically conjugated to the polymer via a tetrapeptide GFLG linker. After cellular internalization via pinocytosis, the GFLG linker underwent degradation by lysosomal enzymes, and then the HPMA copolymer showed DOX release [50].

Ghandehari and coworkers have extensively studied HPMA-based polymer-drug conjugates. One of their studies is focused on evaluation of a HPMA-docetaxel conjugate for prostate cancer [51]. They synthesized targeted, and non-targeted HPMA-docetaxel conjugates, where docetaxel (DTX) was conjugated to the polymer backbone via an enzymatically cleavable GFLG linker. In addition to targeting ability, they varied the

molecular weights of the polymer-docetaxel conjugates. Their efficacies were evaluated at two concentrations (20 mg/kg and 40 mg/kg) on DU145 tumor xenografts. It was deduced that targeted HPMA-docetaxel-RGDFK conjugate (26.9 kDa) and the high molecular weight nontargeted HPMA-docetaxel conjugate (87.1 kDa) showed the highest efficacy on limiting the tumor growth when compared with free docetaxel and the non-targeted HPMA-docetaxel conjugate with low molecular weight [51].

Lammers and coworkers reported the synthesis of HPMA-based polymeric gemcitabine (GEM) and doxorubicin (DOX) carrier for anticancer therapeutic. They obtained HPMA-based polymer-drug conjugate (P-GEM-DOX), which included 6.4 wt% of GEM and 5.7 wt% of DOX. It was shown that P-GEM-DOX killed cancer cells *in vitro*. In addition, P-GEM-DOX demonstrated prolonged circulation time and selectively localized to the tumor region. Their findings revealed that P-GEM-DOX inhibited tumor growth and angiogenesis by simultaneously delivering chemotherapeutic GEM and DOX drugs to the tumor [52].

Sanyal and coworkers published the synthesis of polymer-combretastatin A-4 (CA-4) conjugate for bone targeting. In their work, targeted and nontargeted poly(oligo ethylene glycol)methacrylate (POEGMA) based polymer was used, and an anti-angiogenic drug CA4 and alendronate (ALN) targeting group were conjugated to the polymer backbone. It was observed that ALN targeting group conjugation polymers showed a high affinity to bone minerals compared with a polymer that did not include targeting the ALN group. Cytotoxicity results revealed that targeted polymer-drug conjugate demonstrated cytotoxicity towards HUVECs, U2-Os, and Saos-2 cell lines [53].

1.2. Nanogels and Hydrogels for Delivery of Anticancer Drugs

1.2.1. Nanogels

Nanogels are nanosized (from 20 nm to 250 nm) hydrophilic gels. They can be obtained using chemically or physically crosslinking strategies. Nanogels can become the

vehicles for delivery of therapeutic cargo, such as hydrophobic drugs. They can solubilize the drug molecules and allow their sustained release at the target site. Due to their hydrophilic nature, nanogels are easily dispersed in aqueous media. Due to these features, nanogels are attracting attention as promising platforms for drug delivery [54]. Besides, nanogels have demonstrated attractive potential in tissue engineering, encapsulation of biomolecules like proteins, and imaging systems [55,56]. Nanogels can be prepared via two main strategies: using self-assembly of functional polymers followed by crosslinking, or through polymerization of emulsion stabilized reactive monomers [57]. The different approaches for preparation of nanogels is illustrated in Figure 1.8. Amphiphilic or triblock copolymers are prepared in the self-assembly strategy, and these copolymers can form nanogels. In addition, reactive site-containing polymers are synthesized and can be used for chemical or physical crosslinking.

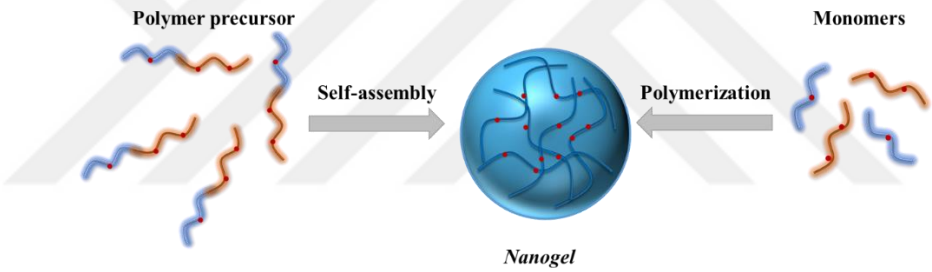

Figure 1.8. Preparation methods of nanogels.

The first approach was utilized in a recent example reported by Sanyal and coworkers. They synthesized multi-functional nanogels using thermally driven self-assembly of polymers, followed by chemical crosslinking using the thiol-maleimide chemistry [58]. These nanogels were obtained by heating maleimide-containing poly(ethylene glycol) methyl ether methacrylate (PEGMA) copolymer above their LCST and crosslinking the obtained aggregates by using a dithiol-based crosslinker. The remaining thiol and maleimide groups were functionalized with maleimide-containing dye and thiol-containing peptide. *N*-hydroxysuccinimide carbonate ester groups were introduced into the nanogels to enable the conjugation of an anticancer drug to show the potential usage of such nanogels as targeted a drug delivery and imaging system.

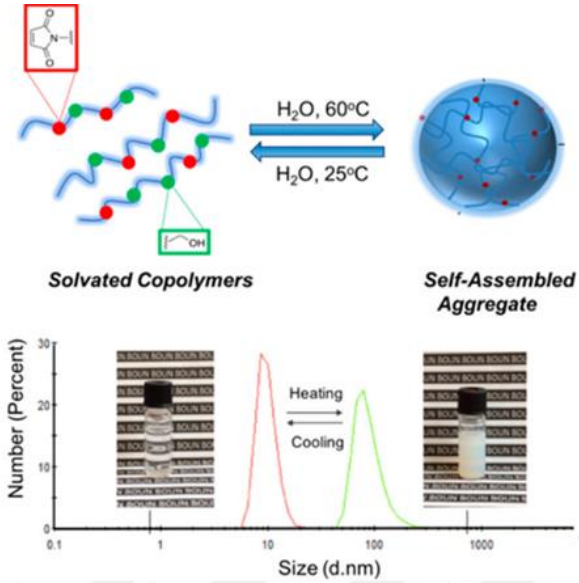

Figure 1.9. The fabrication of nanogels via self-assembly and subsequent chemical crosslinking strategy. Reprinted with permission from [58].

Another example of nanogel obtained via self-assembly and crosslinking strategy was reported by Thayumanavan and coworkers [59]. They synthesized random copolymers consisting of oligo ethylene glycol (OEG) groups and pyridyl disulfide (PDS) groups as side chain functionalities. Their system is illustrated in Figure 1.10. The presence of hydrophobic PDS groups along with thermo-responsive OEG residues, led to their self-assembly in aqueous media. The PDS groups were utilized to obtain crosslinked nanogels via the thiol-disulfide exchange reaction. Authors demonstrated that these nanogels were biodegradable and could act as delivery systems for encapsulated guest molecules.

In the second approach, nanogels can be prepared using crosslinking of reactive monomers via suitable polymerization techniques. Using the monomer-based approach, Xing and coworkers designed the thermo-responsive and pH-responsive nanogels via a one-pot laser-induced emulsion polymerization technique [60]. They obtained biocompatible nanogels via emulsion polymerization at 532 nm using temperature/pH sensitive monomers containing poly(ethylene glycol) diacrylate (PEGDA), *N*-vinyl caprolactam (NVCL) and 2-(dimethylamino) ethyl methacrylate (DMAEMA). Obtained nanogels showed an average hydrodynamic diameter of 195.9 nm with a low polydispersity index of 0.115.

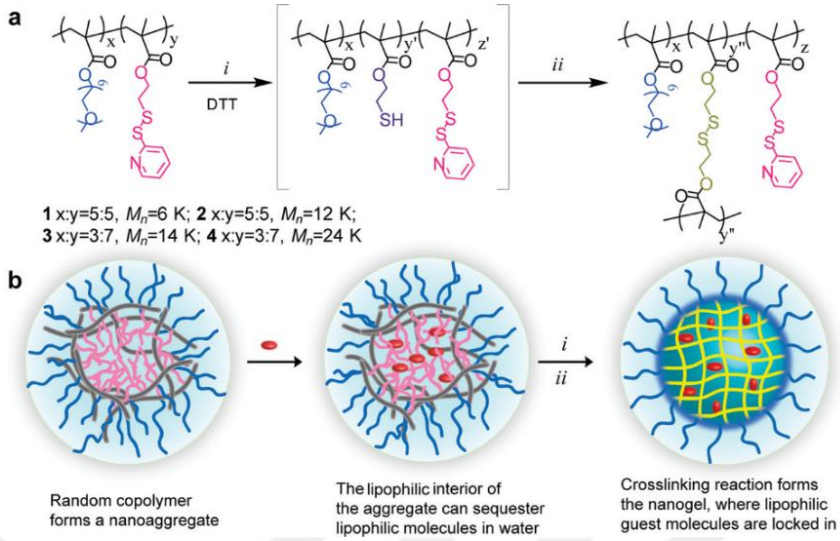

Figure 1.10. Fabrication of biodegradable nanogels via self-assembly and further chemical crosslinking via thiol-pyridyl disulfide exchange reaction. Reprinted with permission from [59].

1.2.2. Hydrogels

Hydrogels can be described as three-dimensional (3D) polymeric networks that can retain a high amount of water or biological fluids [61]. Hydrogels are generally based on hydrophilic monomers and polymers. Therefore, they show high water uptake capacity by remaining insoluble in the aqueous media. Hydrogels are porous structures; consequently, they can carry any cargo, such as drugs, proteins, cells, etc. Furthermore, the mechanical properties of hydrogels are tunable, and their viscoelastic properties may be adjusted by changing polymer or monomer concentration and crosslinking density. In addition, hydrogels can be prepared with straightforward methods. Hydrogels have attracted attention due to their distinctive properties such as porous structures, biocompatibility, biodegradability, hydrophilicity and swelling properties in the water, tunable mechanical properties, and simple fabrication procedure [62]. Due to these advantages, hydrogels have gained importance for various biomedical applications such as drug delivery, wound healing, tissue engineering, and cell encapsulation [63].

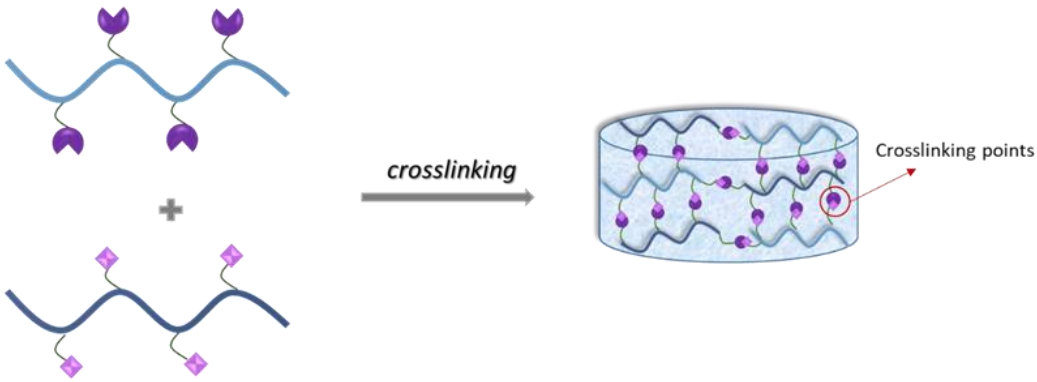

Figure 1.11. Schematic illustration for fabrication of hydrogels.

Hydrogels can be categorized into two parts according to preparation way: physically and chemically crosslinked hydrogels. Physically crosslinking or reversible hydrogels may be obtained under mild conditions without crosslinking agents, which generally lead to cytotoxicity. Ionic interactions, hydrophilic/hydrophobic interactions, host-guest chemistry, and thermo-gelation are commonly used to fabricate physically crosslinked hydrogels [64]. Physically crosslinked hydrogels are mostly biodegradable. Also, physical hydrogels do not require any functional group to provide crosslinking; therefore, complex synthesis steps do not require. On the other hand, physically crosslinked hydrogels often show poor mechanical properties thanks to weak interactions needed in their fabrication [65].

Chemically crosslinked hydrogels can be prepared using functional groups via chemical reactions., Some functional groups such as azide, alkyne, amine, thiol, and epoxy can be used to obtain chemically crosslinked hydrogels. Hence, chemical modifications are required to synthesize functional polymers. Copper-catalyzed azide-alkyne "*click*" reactions [66], copper-free "*click*" reactions [68], Schiff-base reactions [68], thiol-maleimide Michael Addition reaction [69], thiol-ene, thiol-yne chemistries [70], thiol-disulfide exchange reaction [71], Diels-Alder "*click*" reaction [72], and photo-induced crosslinking [73] are widely used methods to obtained chemically crosslinked hydrogels. In general, covalent crosslinking is more stable than physical crosslinking; thus, more stable, strong, and robust hydrogels can be obtained via chemical crosslinking.

Natural and synthetic polymers are used to fabricate hydrogels. Starch, alginate, chitin, chitosan, hyaluronic acid (HA), collagen, and gelatin are some natural polymers to fabricate

hydrogels. Hydrogels from natural polymers are mostly biocompatible, biodegradable, and nontoxic. However, they have poor mechanical properties and are not reproducible [74]. Poly(hydroxyethyl methacrylate) (PHEMA), poly(vinyl alcohol) (PVA), poly(ethylene glycol) (PEG), poly(acrylic acid) (PAA), poly(methacrylic acid) (PMMA), poly(N-isopropylacrylamide) (PNIPAm) are synthetic polymers for preparation of hydrogels [75]. Among them, poly(ethylene glycol) (PEG) was mainly used to fabricate hydrogels for biomedical applications. PEG is a hydrophilic, biocompatible, bio-inert, and nontoxic polymer that can be easily functionalized [76]. Because PEG is not degradable by hydrolysis, PEG polymer smaller than 30 kDa molecular weight is eliminated through the kidneys. Therefore, chemical reactions have gained significant importance in obtaining degradable PEG-based hydrogels [77]. For example, Hoffman and coworkers reported a hydrolytically degradable PEG-based hydrogel [78]. They used PLA (poly(lactide) to provide hydrogel degradability.

1.2.3. Chemically Crosslinked Hydrogels

As mentioned above, chemical crosslinking is widely used to fabricate hydrogels. When we compare it with physical crosslinking, chemical crosslinking has become prominent. Therefore, chemical crosslinking is permanent or irreversible; stable and robust hydrogels can be obtained via chemical crosslinking. Chemically crosslinked hydrogels show flexibility for gelation time, porosity, chemical modification, and degradability [79]. Furthermore, these hydrogels have higher mechanical properties than their physical counterparts, and mechanical properties are tunable.

The chemical crosslink formation can be achieved by adding small crosslinkers, polymer-polymer conjugation, photo-polymerization, and enzyme-catalyzed reaction. Among them, adding a small crosslinker is commonly used to obtain chemically crosslinked hydrogels. This method requires a functionalizable group-containing polymer and a small crosslinker in a suitable solvent. Crosslinkers include mainly two functional groups that allow the formation of crosslinking between reactive sites on polymer chains [80]. For example, furan groups on hyaluronic acid form covalent crosslinking with bis-maleimide functionalized PEG-based crosslinker, and furan-maleimide conjugation gives covalently crosslinked hydrogel [81]. In other cases, glutaraldehyde (GA) can act as a crosslinker, and

it reacts with amino groups on chitosan (CS) polymer and forms chemically crosslinked hydrogels by the generation of imine bonds [82]. In other cases, copper-catalyzed azide-alkyne "*click*" reaction [66] and metal-free "*click*" reactions [67-72] are used for the fabrication of chemically crosslinked hydrogels. Among these reactions, Cu(I)-catalyzed azide-alkyne "*click*" cycloaddition reaction (CuAAc) has been widely studied, and it has been used in many areas of material chemistry [83,84]. There are many examples of hydrogels prepared by CuAAc [85,86]. Although CuAAc reaction is fast and selective, it is not favorable in biomedical applications. After obtaining desired material via CuAAc reaction, removing copper metal is complicated, and the remaining copper shows a cytotoxic effect [87]. Thus, copper-free "*click*" reactions have become prominent in preparing biomaterials. New synthetic approaches to fabricate hydrogels via copper-free "click" reactions have been suggested recently. For example, Zhu and coworkers published hydrogel preparation without any catalyst or initiator [88]. They synthesized an azide-functionalized polymer. In addition to this polymer, the maleimide-functionalized polymer was also synthesized. Subsequently, the hydrogel was obtained via a chemical crosslinking reaction between azide and maleimide groups without a metal catalyst.

1.2.2.1. Strain-Promoted Azide-Alkyne Cycloaddition and Fabrication of Hydrogels. Strain-promoted azide-alkyne cycloaddition reaction (SPAAC) is a biorthogonal, site-specific, and fast reaction between azide and cycloalkyne groups. This reaction does not require any reagent or catalyst. A stable triazole product is obtained by the cycloaddition of cycloalkyne functional material with azide. The SPAAC reaction between azide and cyclooctyne is shown in Figure 1.12. In addition to these advantages, any byproduct does not form at the end of the SPAAC reaction [89]. Due to these facilities, the SPAAC reaction is an excellent method for fabricating biomaterials.

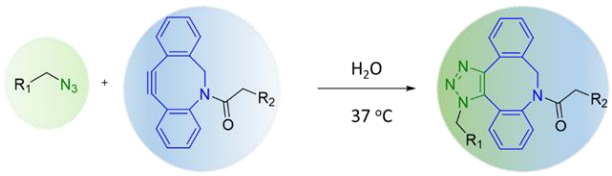

Figure 1.12. Illustration of SPAAC reaction between an azide and DBCO-based cyclooctyne.

Due to the high specificity, rapidity, and efficiency without a catalyst, SPAAC reaction has been examined in some biomedical applications such as cell imaging [90], DNA labeling [91], protein labeling [92], surface functionalization [93], fluorescent sensor [94], fabrication of material for tissue engineering [95], delivering of bioactive molecules [96]. In recent years, hydrogel fabrication via SPAAC reaction has come to the fore due to the cytotoxicity of other crosslinking strategies, which are unsuitable for biomedical applications. SPAAC reaction, which occurs without metal catalysis and does not give any byproduct, is commonly used to fabricate hydrogel for cell encapsulation. For example, Hodgson and coworkers reported reproducible PEG hydrogels via SPAAC crosslinking [97]. They used dibenzocyclooctyne-PEG (abbreviated as DBCO-PEG-DBCO) as a crosslinker. In addition to crosslinker, they synthesized azide end group functionalized first and second-generation G1 and G2 dendron-PEG conjugate. Subsequently, they obtained hydrogel via the SPAAC reaction between azide and DBCO units. They encapsulated primary human mesenchymal stem cells into the G2 hydrogel system and performed a live-dead assay to investigate cell viability. Their result showed that obtained G2 hydrogel demonstrated high cell viability over two weeks.

1.2.4. Stimuli-Responsive Hydrogels

Stimuli-responsive hydrogels can also be called “intelligent” or “smart” hydrogels. These types of hydrogels demonstrate tunable changes in swelling or mechanical properties in response to some stimuli such as pH [98], temperature [99], ionic strength [100], light [101], electric field [102], magnetic field [103], redox species [104], glucose [105]. These stimuli can change the hydrogels' phase transition, stiffness, and biochemical properties. The ability to respond to external stimuli, biocompatibility, and high water content capacity make stimuli-responsive hydrogels attractive biomaterials for biomedical applications such as drug delivery, tissue engineering, wound healing, and so on [106]. Thermoresponsive hydrogels are one of the most used stimuli-responsive hydrogels. They can be stimulated with temperature, undergo a phase transition, and show changes in swelling/ deswelling properties. For example, poly(N-isopropylacrylamide (PNIPAM) is one of the widely utilized thermoresponsive polymers [107]. It has an LCST (lower critical solution temperature) of 32 ^{o}C. Therefore, the PNIPAM solution is in a solution state at room temperature and can transform into a gel state when the temperature reaches body

temperature [108]. Redox-responsive hydrogels are another important type of smart hydrogel. In recent years, disulfide linkers containing degradable hydrogels have gained importance because they demonstrate redox-responsive degradation when treated with reducing agents such as glutathione (GSH) and dithiothreitol (DTT), and so on. Therefore, the fabrication of disulfide-containing hydrogels has been investigated to release therapeutic agents in the tumor region [109,110].

1.2.5. Injectable Hydrogels

In recent years, minimally invasive ways, including needles, catheters, endoscopes, and so on, are gaining speed to minimize traditional open surgeries because they may reduce healthcare expenses and enhance patients' recovery [111]. There is a huge demand for development over traditional scaffolds and hydrogels, especially in biomedical areas like drug delivery, regenerative medicine, cartilage regeneration, and tissue engineering. Hence, the concept of injectable hydrogels has attracted attention among researchers. Injectable hydrogels require minimally invasive procedures. The handling of injectable hydrogel is easy. They can be applied via a syringe into the body. In addition, they can complete the filling of the defect/target area. They can reach into intense tissue. Furthermore, they can deliver therapeutic agents such as drugs, proteins, and even cells to the target site [111]. Due to these advantages, the fabrication of injectable hydrogel systems has become a trend, and there are a lot of publications about injectable hydrogels [112-114].

1.3. Fabrication of Polymer Coatings on Solid Substrates

Design and fabrication of functional surfaces are of paramount engineering importance for biomedical applications because these surfaces are used in various biomedical devices such as implants, catheters, and contact lenses. Polymer coating materials are applied to many areas, such as corrosion control and protection [115], durable and self-cleaning surfaces [116], and photonic devices [117]. In particular, the concept of polymer coating is embraced by biomedical science because polymer coating is used in drug delivery, cardiovascular stents, antibacterial surface, cell culture, orthopedic devices, tissue

engineering, and biosensing [118,119]. This thesis contains four chapters about polymer coatings, where polymer coatings on solid glass and silicon surfaces were fabricated as thin films and polymer brushes.

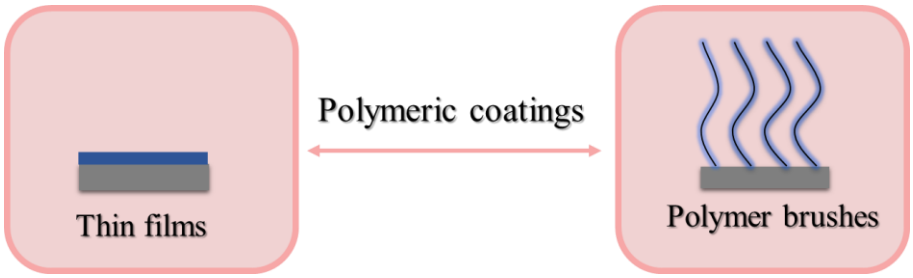

Figure 1.13. Polymeric surface coatings are studied in this thesis.

1.3.1. Polymeric Thin Films

As new technologies are introduced to develop smaller devices, polymeric thin films have become essential in thin-film transistors, semiconductor chips, biosensing materials, and organic photovoltaics [120]. The morphology and stability of polymeric thin film on a solid surface are essential for developing new polymer-based nanotechnologies, and they mainly depend upon the chemical nature of materials [121]. Self-assembled monolayers (SAMs) formation is one of the most investigated molecule-substrate interactions. SAMs have drawn attention as a versatile method to change the chemical and physical properties of solids substrates.

SAMs are generally obtained from small amphiphilic molecules. In these molecules, head groups show a specific affinity towards the surface. The molecules adsorb and bind into a monolayer on the surface via head groups. The end functional groups of the molecule do not show binding to the surface, and they remain accessible and determine hydrophobic/hydrophilic properties, reactivity, and adhesive characteristic of the monolayer surface [121]. Most SAMs have been prepared via the adsorption of n-alkanethiols onto gold surfaces [122,123]. The gold-sulfur (Au-S) interaction between thiol molecules and gold surfaces is a fundamental factor in fabricating SAMs for many applications. In particular, SAMs technology and thiol-gold chemistry are used to fabricate monomolecular films of biological molecules [123,125]. On the other hand, it has been demonstrated that organo-

thiol SAMs onto gold may oxidize to sulfonates and sulfonates when they are exposed to air for a long time, and this situation reveals their finite stability [126,127]. Trichlorosilanes [128] and trialkoxysilanes [129] have been used as alternative molecules to fabricate SAMs.

Likewise, macromolecules like polymers, including surface-attachable groups, are adsorbed onto a suitable surface to provide coatings that are in general robust compared to SAMs. Polymers are conjugated to the surface from the end group or side chain, and this depends on the position of the surface anchoring unit on the polymer backbone. There are three types of grafting modes: "full side-grafting," "random side-grafting," and "block side-grafting." First of all, "full side-grafting" occurs when all repeating units on the polymer backbone show affinity towards the surface. As for random "side-grafting," it happens when surface anchoring units are randomly distributed on the polymer backbone. When surface anchoring parts constitute a block part of a polymer structure, one block shows affinity to the surface, and another block remains free, and that's why "block side-grafting" is formed [130].

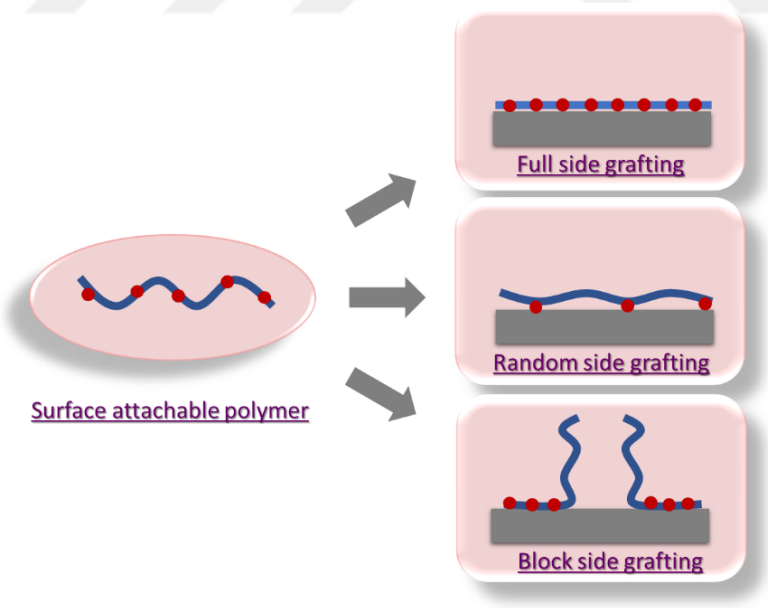

Figure 1.14. Types of the polymeric thin film in terms of the position of surface attachable groups on the polymer backbone.

Although polymeric self-assembly monolayers (PSAMs) and small molecules self-assembly monolayers (SAMs) share many properties, there exist distinctions between them. PSAMs may fully cover the surface even though the grafting density is lower. The thickness of PSAMs is not directly linked to the length of the polymer chain, but it changes with the position of the surface anchoring group on the polymer skeleton. In addition, PSAMs may demonstrate stimuli-responsive behaviors due to changes in polymer conformation along with pH, solvent, and temperature.

1.3.2. Polymer Brushes

Polymer brushes can be described as polymer chains that are densely tethered from the end group to a planar (2D) or spherical (3D) surface [131]. Grafting density is an essential element in obtaining polymer brushes. The thickness of the polymer brush layer depends on the polymerization degree and grafting density. When a low number of chains are tethered to the surface, no interaction between polymer chains occurs, and therefore, a "pancake" structure is obtained with a low grafting density [132]. When the grafting density of chains in a surface area is high, repulsive forces between polymer chains become essential, and polymer chains are pushed up from the surface. Mushrooms and brush structures are obtained with high grafting density [133]. At high grafting density, polymer chains are so dense that they are forced to each other, and polymer chains stretch from the surface, so "brush" conformation occurs [134]. There are two approaches to fabricating polymer brushes: "grafting to" and "grafting from." In the grafting to approach, the polymer that contains the surface anchoring group is synthesized, and the preformed polymer is attached to the surface. There are two advantages of the grafting to method. The chemical composition, molecular weight, and polydispersity index (PDI) of polymer are precisely known [135]. Another advantage is that the preparation of brush and surface modification with preformed polymer requires simple methods such as dip or spin coating. However, the main shortcoming of this method is low grafting density and low brush thickness due to steric hindrance caused by already tethered polymer chains [135]. In the "grafting from" approach, a self-assembled monolayer is prepared using a surface-attachable initiator, and then polymer chains are grown from the modified surface. A polymer brush with a high grafting density is obtained when the initiator is coated onto the surface with good efficiency

[136]. Also, the thickness of polymer brushes may be controlled by changing polymerization types or parameters.

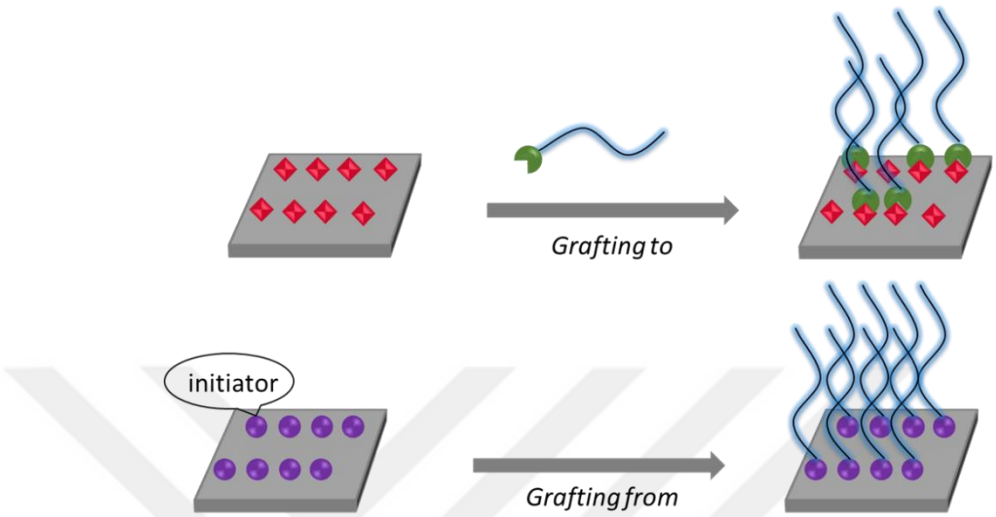

Figure 1.15. Fabrication of polymer brush via grafting from and grafting to method.

In recent years, surface-initiated controlled radical polymerization techniques such as atom-transfer radical polymerization (ATRP) [137], reversible addition-fragmentation chain transfer polymerization (RAFT) [138], nitroxide-mediated polymerization (NMP) [139] have been immensely investigated to fabricate polymer brushes because these techniques allow over polymer brush thickness and chemical composition.

1.3.3. Surface-Initiated RAFT (SI-RAFT) Polymerization

Reversible addition-fragmentation chain transfer polymerization (RAFT) is one of the most used polymerization techniques in recent years. Moad and coworkers first reported it in 1998 [140]. The RAFT process is also a reversible deactivation radical polymerization (RDRP). It mimics the characteristics of living polymerization while using the flexibility of a radical process. RAFT polymerization provides the synthesis of complex polymeric structures with predictable molecular weight, low polydispersity index (PDI), high end-group fidelity, and reactive end group, which enable chain growth [141]. RAFT polymerization requires using of a chain transfer agent (CTA). CTA is added to a free radical

system, controls the molecular weight's growth, and limits the termination process. The most popular RAFT CTAs are dithiocarbamates, trithiocarbonates, and dithiobenzoates.

One of the most critical parameters of the RAFT process is the choice of CTA with R and Z groups. Z group on CTA affects the stability of the dithioester radical intermediate and provides reactivity towards propagating radicals. The R group should be chosen as an excellent leaving group that reinitiates polymerization [142]. RAFT polymerization starts with the decomposition of the initiator, and after that, active radical gives propagating polymer radical (Pn.). Pn radical reacts with thiocarbonylthio (CTA), and a new R radical (R.) occurs. R radical reacts with monomer (M), yielding a new propagating radical (Pm.). Pm radical reacts with Pn-S-C=S-Z macro chain transfer agent, and polymer with narrow polydispersity is obtained via rapid equilibrium between propagating and dormant chains.

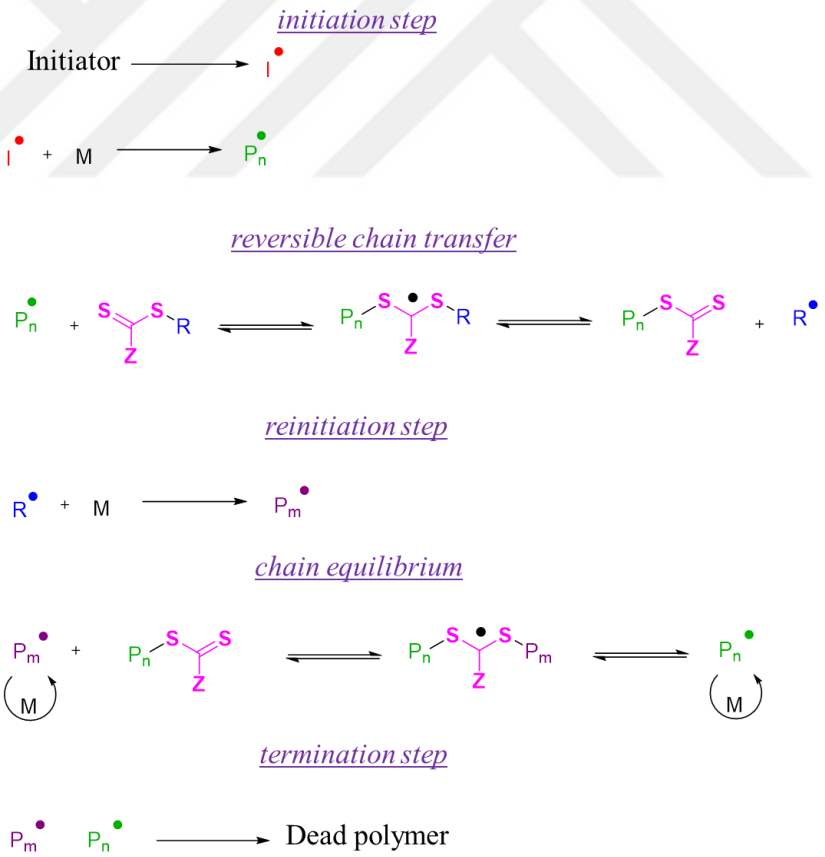

Figure 1.16. Proposed mechanism of RAFT polymerization.

RAFT polymerization has also been used for surface-tethered polymerization applications. The surface is coated with either a free radical or chain transfer agent, and polymerization takes place from the surface; hence this process can be defined as surface-initiated RAFT polymerization (SI-RAFT) [143]. Baum and Brittain reported the synthesis of polymer brushes from a silicon surface using SI-RAFT [144]. They modified the silicon surface with an azoinitiator, then synthesized styrene, methyl methacrylate, and N, N-dimethyl acrylamide-based polymer brushes via SI-RAFT. SI-RAFT polymerization can be performed by using surface-immobilized CTAs. Before the polymerization step, a self-assembled monolayer is prepared using surface attachable CTA. Surfaces are modified with CTA via R-group [145-147] and Z-group [148-149] approaches. In R-group (reinitiated group) strategy, the CTA molecule was immobilized to the surface via the R group. R group on the surface leaves and reinitiates during polymerization. In this method, RAFT polymerization carries out near the brush layer, resulting in the "grafting from" procedure [150]. In Z-group (radical stabilizing group) approach, CTA was attached to the surface via Z-group. This approach is similar to grafting to methods. Because propagating radical is close to the surface, steric hindrance happens, and a polymer brush is obtained with a low grafting density [143]. Therefore, R-group approaches are mainly used to fabricate polymer brushes [145-147], [151].

1.3.4. Post-Polymerization Modification and Biomedical Applications of Polymer Brushes

Surface-initiated polymerization techniques such as SI-ATRP and SI-RAFT provide using functional groups. However, polymer brushes with some functional groups may not be prepared via direct surface-initiated polymerization [152]. Therefore, post-polymerization modification methods are used to fabricate functionalizable polymer brushes. These methods can be applied to only the end chain, only the side chain, or both side chains of polymers. In RAFT polymerization, resulting polymer chains have thiocarbonylthio groups at the ω-end of the chain. A wide range of methods can modify these end chains to obtain desirable end groups [152-154]. Thiocarbonylthio groups at the end of polymer chains can be converted into thiol groups, and polymer chains can be modified with another molecule via a thiol-maleimide reaction [153]. Another post-polymerization modification method is a radical cross-coupling reaction that requires using

functionalized azo-based compounds. Azo-based compounds modified with the "*clickable*" functional group enable the diversification of polymer brushes.

For example, Sanyal and coworkers reported the fabrication of modifiable polymer brushes on magnetic nanoparticles [155]. In this study, they coated magnetic nanoparticles with macro-CTA, which has a trihiocarbonyl end group, and polymer brushes were obtained using grafted from approach. Azide and maleimide functionalized bis-azo compounds were synthesized. Trithiocarbonyl groups at the end chain of polymer brushes were replaced with clickable groups of bis-azo compounds. Both maleimide and azide functionalized polymer brushes were prepared for further diversification of polymer brushes.

In another example, Klok and coworkers reported the synthesis and post-polymerization modification of poly(pentafluorophenyl methacrylate) brushes [156]. They immobilized silicon wafers with surface attachable RAFT agent, and poly(pentafluorophenyl methacrylate) based brushes were obtained via SI-RAFT. Post-polymerization modification experiments were shown using many amine-containing molecules such as ethanolamine, cysteamine, 1-amino-2-propanol, and so on.

Sanyal and coworkers reported the fabrication of succinimidyl carbonate-based amine reactive polymer brushes for bioconjugation. They immobilized the silicon surface with surface attachable RAFT agent, and subsequently, succinimidyl carbonate-based polymer brushes were obtained using succinimidyl carbonate methacrylate (SCEMA) and DEGMA monomers via SI-RAFT. The succinimidyl carbonate unit was modified using an amine-containing trifluorobenzylamine (TFBA) molecule. Surfaces were characterized by FTIR and XPS analysis. Also, the reactive polymer surface was modified with biotin-amine, and the biotinylated polymer brush was immobilized with dye-conjugated streptavidin protein. The presence of streptavidin was showen using a fluorescence microscope. Succinimidyl carbonate groups allow post-polymerization modification with amine-containing biomolecules [160].

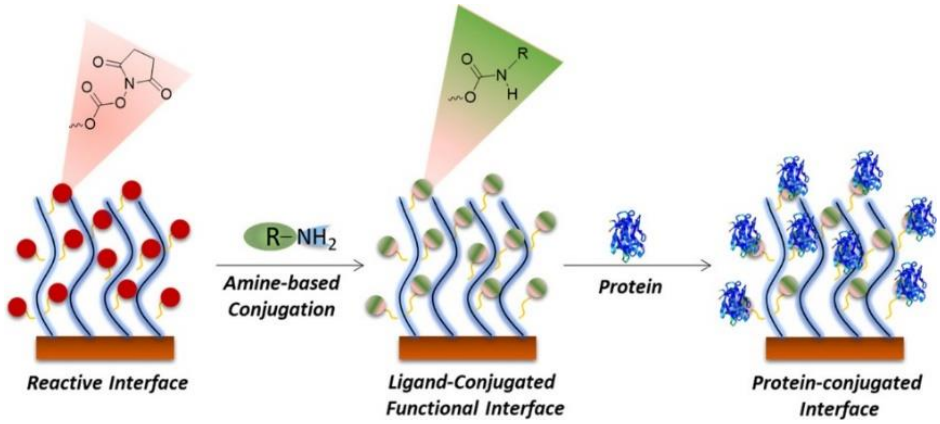

Figure 1.17. Functionalization and fabrication of succinimidyl-carbonate-containing amine reactive polymer brushes. Reprinted with permission from [160].

1.3.5. Functionalization and Biomedical Applications of Reactive Polymeric Coatings

Polymer coatings have become increasingly popular in especially biomedical applications. Tunability in the desired manner is the best property of polymer coatings. In other words, a surface can be coated to eliminate unwanted interactions and/or provide desired interactions. Polymer coatings enable strong multi-functionalities of their host molecules, and these functionalities depend on various monomers with different properties. Applications of polymer coatings are orthopedic materials, cardiovascular stents, antibacterial-antimicrobial surfaces, drug delivery, tissue engineering, biosensors, and interfaces for cellular attachment [157]. In this thesis, we have focused on the fabrication of polymer coatings that can be potential for biosensing and cellular attachment. As mentioned before, the use of polymer coatings provides the formation of a uniform surface. Post-polymerization modification techniques are essential to obtain effective modification of the surface. Consequently, "*click*" based reactions have become prominent due to their high efficiency. These reactions have many advantages like fast reaction time, high selectivity, good yield, and easy product isolation [158]. In addition, mild reaction condition is one of the most important features of click-based reactions. Many biomolecules are sensitive to harsh reaction conditions; unfortunately, they will tend to decompose if the conditions are not quite benign. Therefore, *click*-based reactions with mild reaction environments are very useful for immobilizing biomolecules onto polymer-coated surfaces. Copper-catalyzed

azide-alkyne cycloaddition reaction, strain-promoted azide-alkyne *click* reactions [159], Diels-Alder (DA) chemistry, amine-reactive chemistry [160], thiol-maleimide Michael addition [161,162], thiol-disulfide exchange reaction [163] are commonly utilized "*click*" based reaction to obtain bioactive surfaces. In addition to these reactions, supramolecular host-guest interaction is used to obtain functionalizable polymeric coatings and polymer brushes [164-165]. An attractive feature of using supramolecular host-guest type chemistry is that such immobilizations can be reversible and surfaces can be engineered to be renewable.

Sanyal and coworkers reported a thiol-reactive polymeric thin film on titanium surface to inhibit bacterial adhesion and growth. Maleimide and dopamine-containing PEG-based copolymers were synthesized using RAFT polymerization. Maleimide groups were utilized for further modification with thiol-including molecules, and dopamine groups were used to fabricate of thin film. An antibacterial peptide was conjugated to thin film using a thiol-maleimide reaction and the peptide-conjugated polymeric thin films demonstrated both antifouling and antimicrobial properties against both Gram-negative and Gram-positive bacteria [162]. One can envision that such surface coatings can also be engineered to attract and kill cancerous cells, as demonstrated in this thesis.

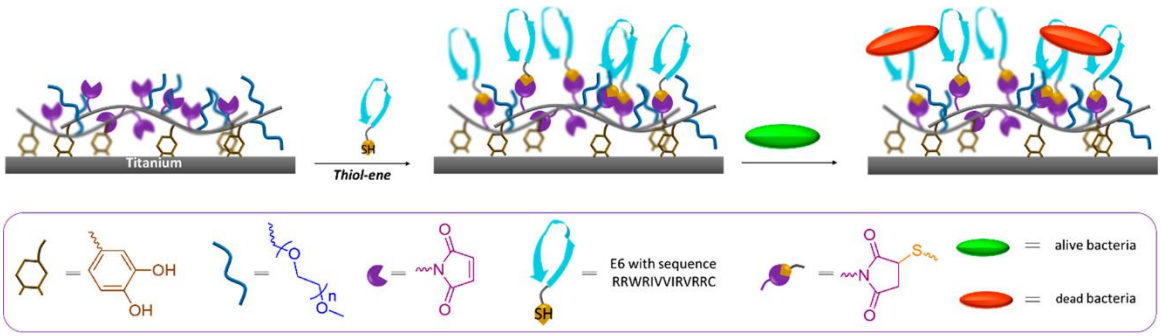

Figure 1.18. Fabrication of antibacterial thin film coating. Reprinted with permission from [162].

The same group reported surface anchoring thiol-reactive polymeric coatings for biomolecular immobilization and sensing [166]. Poly(ethylene glycol) (PEG)-based copolymers were synthesized and alkoxysilyl group and furan-protected maleimide groups were introduced to the side chains of copolymers. While alkoxysilyl group provides surface

attachment, protected maleimide groups enable functionalization with thiol-reactive molecules. After synthesis, biotin, a protein-binding ligand, was conjugated to the polymeric surface using the thiol-maleimide Michael addition reaction, and a model protein streptavidin was immobilized to the surface using biotin-streptavidin interaction. They showed that the facile fabrication and easy modification makes maleimide-containing surfaces for attractive candidates for biotechnological applications.

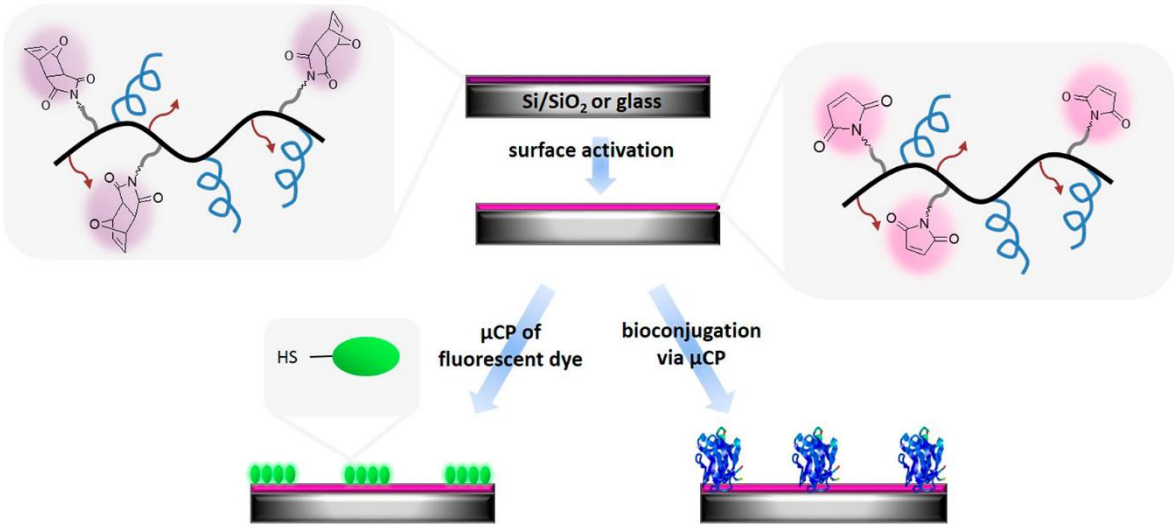

Figure 1.19. Schematic illustration of fabrication and functionalization of reactive polymeric surface. Reprinted with permission from [166].

The sections above illustrate the indispensable role played by stimuli-responsive polymeric materials in various areas of biomedical sciences ranging from effective delivery of drugs to disease sites through either systemic or local administration, as well as fabricating functional interfaces for diagnostics purposes. In this thesis, we explore the design and application of several polymeric platforms that can act as tools to address challenges faced in treatment of diseases such as cancer.

2. RESEARCH OVERVIEW

This thesis encompasses research projects on designing and fabricating novel stimuli-responsive polymeric biomaterials for therapeutic applications. The aim has been accomplished by fabricating five different kinds of polymer-based biomaterials: polymer-drug conjugates, nanogels, hydrogels, polymer brushes, and polymeric thin films.

The first part of this thesis is related to the fabrication of polymer-drug conjugates for drug delivery applications. Polymer-drug conjugates were fabricated and evaluated for potential utilization for drug delivery. Oligo (ethylene glycol) (OEG) side-chain-containing polymer-drug conjugates were synthesized using the reversible addition-fragmentation chain transfer (RAFT) polymerization technique. Drug molecules were covalently conjugated to the polymer backbone using pH, enzyme, and redox-responsive linkers. After synthesis and characterization, *in vitro* experiments were performed to investigate these polymer-drug conjugates' cellular cytotoxicity and release profiles.

Redox-responsive nanogels were fabricated for targeted drug delivery applications in the second part of this thesis. The nanogel was designed using host-guest interactions, an anticancer drug was physically loaded, and peptide-based targeting groups were attached through host-guest interactions. Disulfide linkers were introduced to the nanogel system to provide redox-responsive degradation of nanogels and trigger drug release. Following the preparation of nanogels, *in vitro* cytotoxicity and drug release experiments were performed.

In the third part, stimuli-responsive and injectable hydrogels were designed for drug delivery applications. Drug-conjugated copolymers were synthesized using RAFT polymerization and were utilized to obtain hydrogels using a metal-free strain-promoted azide-alkyne cycloaddition reaction. Disulfide linkers were introduced into hydrogels to achieve triggered drug release and provide degradability. After fabrication, biodegradability, injectability, and self-healing ability were demonstrated. In addition, *in vitro* drug release and cytotoxicity experiments were performed.

The fourth part of this thesis is related to designing polymer brushes for biomedical applications. This part of the dissertation consists of two projects. In the first project, trithiocarbonate end-group functionalized polymer brushes were grafted from silicon oxide surfaces. Post-polymerization modification of the chain end of the polymer brushes with monovalent and multivalent molecules was accomplished using a radical cross-coupling reaction. The cluster effect of sugar-appended dendrons on polymer brushes with different dendron generations was investigated through the immobilization of the Concanavalin A protein. In the other project, redox-responsive polymer brushes containing pyridyl disulfide groups were grafted from silicon surfaces to obtain thiol-reactive interfaces. Functionalization with thiol-containing molecules and biomolecules was shown. Following the fabrication of reactive brushes, biomolecule immobilization, *in vitro* cell catch and release, and drug release studies were performed.

The fifth part of this thesis is related to designing reactive polymeric thin film coatings, and this section is composed of two projects. Polymeric thin film coatings containing thiol-reactive benzothiazole-disulfide bearing surface anchorable copolymers were utilized to modify glass surfaces. Following the fabrication of reactive coatings, biomolecule immobilization and *in vitro* cell catch and release studies were performed. In the other project, host-guest chemistry-based modular surface functionalization was investigated. Hydrophilic copolymers bearing adamantane, OEG groups, and surface trimethoxysilyl groups for imparting anti-biofouling character, supramolecular functionalization, and surface anchoring, respectively, were synthesized. This polymeric thin film-coated surface was amenable to facile modification in a modular fashion using host-guest interaction.

In summary, this dissertation reports on the design and synthesis of novel biomaterials prepared using advances in organic and polymer chemistry for applications ranging from biomolecular sensing, catch and release of proteins and cells, to drug delivery.

3. FABRICATION OF POLYMER GEMCITABINE AND HYDROXYCHLOROQUINE CONJUGATES FOR PANCREATIC ADENOCARCINOMA

3.1. Introduction

Pancreatic ductal adenocarcinoma (PDAC) is the fourth leading cause of cancer deaths. The GLOBOCAN data show that 19.2 million cancer cases and 9.96 million people will die from cancer in 2020, and PDAC deaths will constitute 4.7 % of total cancer deaths [167]. The five-year survival rate of PDAC, among the lowest of all cancer types, is 9% [168]. This dramatic result is mainly caused by the lack of distinctive symptoms and credible biomarkers that interfere with early diagnosis [169]. Surgery, radiation therapy, and chemotherapy are treatment options for pancreatic cancer. Unfortunately, less than 20 % of diagnosed patients may be cured via surgery because cancer has spread into other body parts until it is diagnosed [170]. Furthermore, high local recurrence and chemoresistance caused by cancer stem cells (CSCs) are other significant challenges for the treatment [171,172]. Therefore, chemotherapy may prolong survival for advanced cancer. Gemcitabine (GEM, dFdC: 2',2'-difluorodeoxycytidine) is a nucleoside analog widely used for pancreatic cancer. Also, GEM demonstrates activity against multiple cancer types containing colon, lung, ovarian, and breast [173]. When gemcitabine is internalized by the cell, it undergoes phosphorylation three times by deoxycytidine kinase and active metabolite gemcitabine triphosphate (dFdCTP) forms. Gemcitabine triphosphate is incorporated into DNA during replication and inhibits DNA polymerase activity, which causes cell death via apoptosis [174]. Despite its anticancer effect, it has a short half-life of 8-17 min and relative plasma concentration in the tumor region. It undergoes rapid metabolic inactivation by deoxycytidine deaminase; therefore, it shows low therapeutic activity [175]. High doses of gemcitabine (1000mg/m^2) are administrated to enhance its therapeutic levels, but high doses bring severe side effects [176]. Therefore, effort should be devoted to many alternatives to protecting gemcitabine from degradation and accumulating a high amount of GEM in the tumor region. Besides short half-life and metabolic degradation, chemoresistance

progression is another drawback of GEM. In particular, upon being used for the treatment of PDAC, GEM undergoes strong chemoresistance because of cancer stem cells (CSCs) [174]. Therefore, only GEM may not provide effective therapy for PDAC. In recent years, chloroquine (CQ) and hydroxychloroquine (HCQ), antimalarial drugs, have been explored for cancer treatment for some reasons. First of all, Balic and coworkers reported that chloroquine (CQ) might eliminate pancreatic cancer stem cells [172]. Also, CQ and HCQ block $CXCR_4$ receptors essential for metastatic spread [177]. Furthermore, it has been reported that CQ and HCQ enhance cancer therapies by inhibiting autophagy in cancer cells [178,179]. Moreover, it was reported that CQ increases tumor vessel diameter and it improves delivery efficiency above 70 nm size particles [180].

In recent years, great effort has been devoted to increasing solubility, enhancing metabolic stability, and improving gemcitabine's pharmacokinetic profile and antitumor activity by eliminating side effects. For these purposes, some gemcitabine-containing nanodiamonds, nanoparticles, micelles, liposomes, and polymer-drug conjugates (PDC) have been extensively studied [171], [181-183]. Joubert and coworkers reported the synthesis of gemcitabine polymer conjugate for pancreatic cancer. Gemcitabine was conjugated to the polymer backbone via ester and amide linkages, and this polymeric conjugate formed nanoparticles. They showed promising results, including sustained GEM release by 70% after 30 days in the presence of acidic pH (5.4) and Cathepsin B enzyme, lower cytotoxicity than free GEM, and superiorly prolonged activity compared to the free drug [181].

A recent report by Kattel and coworkers demonstrated conjugation of GEM chemically to polymer backbone modified the circulation residence, biodistribution, and toxicity of GEM. They reported that GEM conjugation to amphiphilic polymer resulted in polymeric micelle formation, which provided sustained delivery of GEM to the tumor by more than 2.5-fold compared to free GEM and reduced toxicity [171]. Chitkara and coworkers demonstrated micelles via self-assembling from the polymer-gemcitabine conjugate. They showed that gemcitabine-conjugated micelles could protect GEM from rapid plasma metabolism, enable a sustained gemcitabine release, and exhibit enhanced antitumor activity [182].

Herein, we report the syntheses and evaluations of drug-conjugated monomers and polymer-drug conjugates carrying only gemcitabine, hydroxychloroquine, and both. While gemcitabine has an anti-proliferative activity for cancer cells, hydroxychloroquine may eliminate pancreatic cancer stem cells [172]. Syntheses of poly(oligo ethylene glycol) (P(OEG)) polymer-based conjugates were reported. Drug release kinetics were investigated to find the best polymer-drug conjugate using different linkers (ester, carbamate, carbonate, and disulfide) to incorporate the drug into the polymer backbone. Afterward, *in vitro* cytotoxicities of polymer-drug conjugates were evaluated against pancreatic cancer cell lines. After the excellent polymer-drug conjugate was determined, cellular internalization was shown on both monolayer and 3D spheroid models.

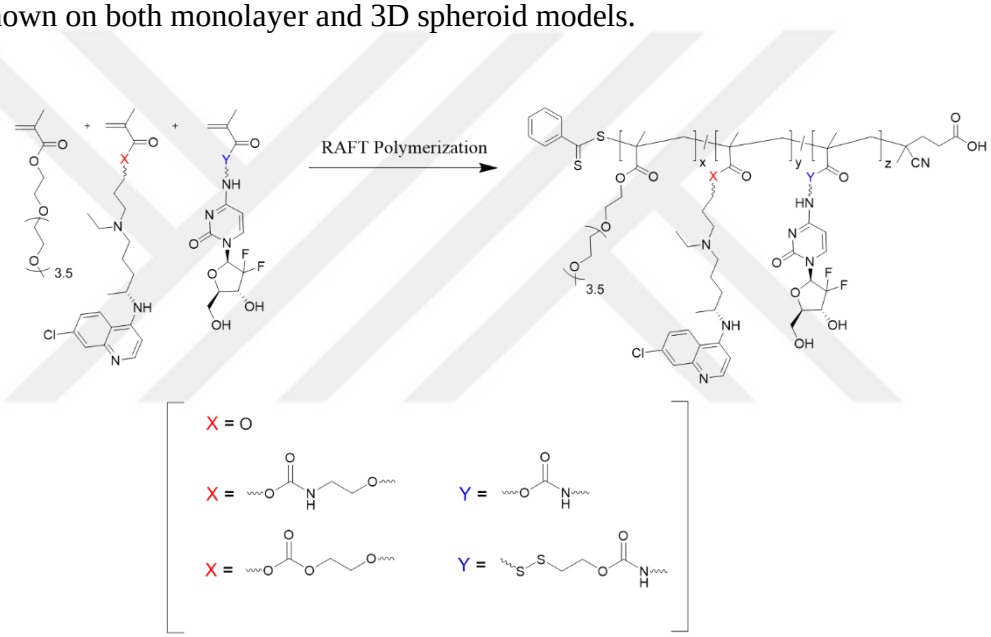

Figure 3.1. Fabrication of HCQ and GEM-containing polymer-drug conjugate, the influence of linkers on drug release.

3.2. Experimental

3.2.1. Materials

All solvents were purchased from Merck and used as obtained without further purification. Ultrapure water was obtained via Milli-Q Water Purification System (Milli-Q

system, Millipore, Billerica, MA, USA). DCM (CH_2Cl_2) was obtained from the SciMatCo purification system, and other solvents were dried over molecular sieves. 4-Dimethylaminopyridine (DMAP), reduced glutathione (GSH), esterase from the porcine liver (PLE), 2-hydroxyethyl disulfide, and *N,N'*-disuccinimidyl carbonate (DSC), and 4-cyano-4-thiobenzoylthio)pentanoic acid were purchased from Sigma-Aldrich. Hydroxychloroquine sulfate was purchased from Sigma-Aldrich and neutralized by adjusting to pH 11 before use. Gemcitabine hydrochloride was purchased from Sigma Aldrich. Pyridine and triethylamine were obtained from Merck. 2-isocyanatoethyl methacrylate, methacryloyl chloride, and chlorotrimethylsilane (TMS-Cl) were purchased from Abcr, Alfa Aesar, and Acros Organics, respectively. Oligo(ethylene glycol) methyl ether methacrylate (OEGMA, Mn = 300 g/mol) was purchased from Sigma Aldrich and filtered through a basic alumina column before use. 2,2'-Azobis(2-methylpropionitrile) (AIBN) was purchased from Sigma Aldrich, recrystallized from methanol, and dried before use. SCEMA monomer [184], HSEMA [185], NHS-activated HSEMA monomer [186], and BODIPY-OH [187] were synthesized by using a published procedure. BxPC-3 and Capan-1 cells were purchased from ATCC (LGC Standards, Germany).

3.2.2. Methods

The monomer and copolymer characterizations were performed with ^{1}H and ^{13}C NMR spectroscopy (Avancha III HD, 400 MHz, Bruker, USA), Fourier transforms infrared (ATR-FTIR) spectroscopy (Nicolet 380, Thermo Scientific, USA). HCQ and GEM monomers were characterized by liquid chromatography-mass spectrometry (LC-MS) analysis using an LCMS 2020-Mass Spectrometer System (Shimadzu, Japan) equipped with a C-18 (5 µm - 150 × 4.6 mm) column. The mobile phase consisted of deionized water and HPLC grade acetonitrile (ACN) using the following gradient; LC: 0−3 min, 50% ACN; 3.01 min, 50% ACN; 8 min, 95% ACN; 8.01−11 min, 50% ACN; MS positive scan 100−800 m/z. Disulfide-containing gemcitabine monomer (GEM-SSC-MA) monomer was purified using preparative-high performance liquid chromatography equipment (PREP-HPLC, Shimadzu, Japan) equipped with a C-18 (15 µm- 50 x 250 mm) column. The mobile phase consisted of deionized water and HPLC grade acetonitrile (ACN) using a ratio of 50:50 with a 40 mL/min flow rate at 210 nm. The molecular weights and polydispersity indexes of copolymers were estimated by size exclusion chromatography (SEC) using a PSS-SDV (length/ID 8 × 300

mm, 10 µm particle size) linear Mixed C column calibrated with poly(methyl methacrylate) (PMMA) standards using a refractive-index detector with a mobile phase solution of 0.05 M lithium bromide in *N,N'*-dimethylaceteamide (DMAc) as eluent at a flow rate of 1 mL/min at 30 ^{o}C.

3.2.3. Synthesis and Characterization of Ester-Containing Hydroxychloroquine Methacrylate Monomer (HCQ-E-MA)

Hydroxychloroquine (1.43 g, 1.26 mmol) was dissolved in anhydrous THF under N_2 atmosphere, and the solution was cooled to 0 ^{o}C using an ice bath. At 0 ^{o}C, triethylamine (0.88 mL, 645 mg, 6.38 mmol) and methacryloyl chloride (0.62 mL, 667 mg, 6.38 mmol) were added, respectively. The reaction mixture was stirred for 24 h from 0 ^{o}C to 25 ^{o}C. Then, THF was removed under reduced pressure. The crude product was re-dissolved in CH_2Cl_2 and extracted with 10% $NaHCO_3$ solution (3 x 20 mL) and H_2O (3 x 20 mL). The organic layer was dried over Na_2SO_4. The crude product was purified by column chromatography using ethyl acetate as a mobile phase (yellow viscous, 75 % yield). ^{1}H NMR (400 MHz, $CDCl_3$): δ/ppm = 8.51 (d, *J* = 5.3 Hz, 1H), 7.94 (s, 1H), 7,68 (d, *J* = 8.9 Hz, 1H), 7.33 (d, *J* = 8.9 Hz, 1H), 6.41 (d, *J* = 5.3 Hz, 1H), 6.07 (s, 1H), 5.51 (s, 1H), 5.08 (s, 1H), 4.22 (t, *J* = 6.0, 2H), 3.72 - 3.68 (m, 1H), 2.74 (t, *J* = 6.0, 2H), 2.60 - 2.50 (m, 4H), 1.91 (s, 3H), 1.75 - 1.57 (m, 4H), 1.30 (d, *J* = 6.2, 3H), 1.00 (t, *J* = 7.0, 3H). ^{13}C NMR (100 MHz, $CDCl_3$): δ/ppm = 167.5, 151.9, 149.2, 149.0, 136.1, 134.9, 128.7, 125.6, 125.1, 121.0, 117.2, 71.7, 62.8, 53.7, 51.4, 48.4, 48.2, 34.3, 24.2, 20.3, 18.3, 11.7. LCMS expected [M+H] m/z = 403 g/mol, observed [M+H] m/z = 404 g/mol.

3.2.4. Synthesis and Characterization of Carbamate-Containing Hydroxychloroquine Methacrylate Monomer (HCQ-C-MA)

Hydroxychloroquine (250 mg, 0.744 mmol), triethylamine (225 mg, 2.23 mmol), and *N,N'*-dimethylamino pyridine (DMAP) (1.81 g, 0.0148 mmol) were dissolved in anhydrous dichloromethane (CH_2Cl_2), and the mixture was cooled into 0 ^{o}C using an ice bath. At 0 ^{o}C, 2-(isocyanatoethyl methacrylate) (138.6 mg, 0.893 mmol) was dropwise added to the reaction mixture. Then the mixture was stirred from 0 ^{o}C to 25 ^{o}C for 4 h. The product was purified by column chromatography on SiO_2 (from 60:40 EtOAc: Hexane to 100:0 EtOAc:

Hexane). The product was obtained as a yellow oil with a 93 % yield. ^{1}H NMR (400 MHz, $CDCl_3$): δ/ppm = 8.49 (d, *J* = 5.3, 1H), 7.93 (s, 1H), 7.70 (d, *J* = 8.8, 1H), 7.34 (dd, *J* = 1.9, *J* = 8.9, 1H), 6.40 (d, *J* = 5.5, 1H), 6.05 (s, 1H), 5.55 (s, 1H), 5.18 (NH, 1H), 4.18 - 4.11 (m, 4H), 3.72 - 3.67 (m, 1H), 3.47 - 3.42 (m, 2H), 2.67 (t, *J* = 5.7, 2H), 2.56 (q, *J* = 6.3, 2H), 2.50 (t, *J* = 6.1, 2H), 1.89 (s, 3H), 1.29 (*J* = 6.3, 3H), 1.23 (s, 2H), 0.98 (t, *J* = 7.0, 3H), 0.87 - 0.78 (m, 2H). ^{13}C NMR (100 MHz, $CDCl_3$): δ/ppm = 167.2, 156.4, 151.2, 149.3, 149.0, 135.9, 134.8, 128.7, 126.0, 125.0, 121.0, 117.2, 99.2, 63.7, 62.8, 52.0, 48.3, 48.1, 40.1, 34.3, 29.7, 24.0, 20.3, 18.3, 11.3. FTIR (cm^{-1}): 3324, 2929, 2870, 1718, 1637, 1611, 1248, 1150, 1044. LC-MS expected [M+H] m/z = 491 g/mol; observed [M+H] m/z = 491 g/mol).

3.2.5. Synthesis and Characterization of Carbonate-Including Hydroxychloroquine Methacrylate Monomer (HCQ-CB-MA)

NHS-activated carbonate monomer (SCEMA) was first synthesized according to a published procedure [184] in the presence of disuccinimidyl carbonate (DSC) and 2-hydroxyethyl methacrylate (HEMA) for the synthesis of hydroxychloroquine methacrylate monomer via carbonate (CB) linker. SCEMA monomer (800 mg, 2.94 mmol) was dissolved in anhydrous CH_2Cl_2 (5 mL). Pyridine (0.24 mL, 232 mg, 2.94 mmol) was added to the SCEMA solution. The free base form of hydroxychloroquine (HCQ) was dissolved in anhydrous CH_2Cl_2 (5 mL) in another reaction flask and transferred into SCEMA solutions. The reaction mixture was allowed to mix for 24 h at room temperature. After 24 h, CH_2Cl_2 was removed under reduced pressure. The crude product was purified via column chromatography with a mobile phase (70:30 EtOAc: Hexane). The pure product was obtained as a yellow viscous in 42% yield. ^{1}H NMR (400 MHz, $CDCl_3$): δ/ppm = 8.51 (d, *J* = 5.3 Hz, 1H), 7.94 (s, 1H), 7,68 (d, *J* = 8.9 Hz, 1H), 7.35 (d, *J* = 8.7 Hz, 1H), 6.41 (d, *J* = 5.3 Hz, 1H), 6.09 (s, 1H), 5.55 (s, 1H), 5.01 (s, 1H), 4.40 - 4.32 (m, 4H), 4.26 - 4.17 (m, 2H), 3.75 - 3.68 (m, 1H), 2.72 (t, *J* = 5.9, 2H), 2.58 - 2.50 (m, 4H), 1.91 (s, 3H), 1.78 - 1.67 (m, 4H), 1.31 (d, *J* = 6.3, 3H), 1.00 (t, *J* = 7.1, 3H). LC-MS expected [M+H] m/z = 492 g/mol, observed [M+H]+ m/z = 493 g/mol).

3.2.6. Synthesis and Characterization of Carbamate-Containing Gemcitabine Methacrylate Monomer (GEM-C-MA)

Gemcitabine (1.36 mmol, 358 mg) was dissolved in a pyridine: acetonitrile (ACN) mixture (30: 4 mL), and the mixture was cooled to 0 ^{o}C using an ice bath. At 0 ^{o}C, chlorotrimethylsilane was slowly added to the mixture to protect OH groups on gemcitabine; then, the reaction mixture was stirred at 0 ^{o}C for 2 h. After 2 h, the SCEMA monomer was dissolved in acetonitrile (2 mL) and added to the mixture, and then the mixture was heated to 65 ^{o}C for two days. Finally, the mixture's temperature was decreased to 45 ^{o}C, and ethanol was added to deprotect TMS groups. After stirring at 45 ^{o}C for 5 h, the mixture was concentrated under reduced pressure. The product was purified by column chromatography on SiO_2 (80:20 EtOAc: Hexane), and the product was obtained as a white solid with a 52 % yield. ^{1}H NMR (400 MHz, DMSO d6) δ: 10.97 (s, NH, 1H), 8.24 (d, *J* = 7.6, 1H), 7.08 (d, *J* = 7.4, 1H), 6.18 (t, *J* = 7.2, 1H), 6.05 (s, 1H), 5.57 (s, 1H), 5.33 (s, OH, 1H), 4.40 - 4.39 (m, 2H), 4.34 - 4.33 (m, 2H), 4.24 - 4.14 (m, 1H), 3.89 (t, *J* = 5.4, 1H), 3.65 (d, *J* = 13.0, 2H), 1.88 (s, 3H). ^{13}C NMR (100 MHz, DMSO d6): δ/ppm = 166.9, 163.9, 154.5, 153.5, 144.9, 136.1, 126.7, 123.4, 95.4, 84.5 (t, *J* = 32.9), 81.4, 68.8 (t, *J* = 22.8), 63.6, 63.0, 59.3, 81.4. FTIR (cm^{-1}): 3314, 2990, 2952, 1748, 1704, 1200, 1162, 1062. LC-MS expected [M+H] m/z = 419 g/mol; observed [M+H] m/z = 420 g/mol.

3.2.7. Synthesis and Characterization of Disulfide-Carbamate-Containing Gemcitabine Methacrylate Monomer (GEM-SSC-MA)

To obtain gemcitabine methacrylate monomer with a disulfide-carbamate linker, as a first step, HSEMA and NHS-HSEMA monomers were synthesized according to published procedures [185,186]. Briefly, in the presence of triethylamine, the HSEMA monomer was obtained using bis(hydroxyethyl)disulfide and methacryloyl chloride. Then, the HSEMA monomer was activated with the NHS group using disuccinimidyl carbonate (DSC). Gemcitabine (GEM, 6.3 mmol, 1.65 g) was dissolved in a pyridine: acetonitrile mixture (40:4 mL), and the mixture was cooled to 0 ^{o}C using an ice bath. At 0 ^{o}C, chlorotrimethylsilane (2.5 mL, 2.1 g, 19 mmol) was slowly added to the mixture to protect OH groups on gemcitabine, and then the reaction mixture was stirred at 0 ^{o}C for 2 h. After 2 h, NHS-activated HSEMA monomer (3.2 g, 9 mmol) was dissolved in acetonitrile (4 mL)

was added to the mixture, and then the mixture was heated to 65 ^{o}C for two days. Finally, the mixture's temperature was decreased to 45 ^{o}C, and ethanol (30 mL) was added to deprotect TMS groups. After stirring at 45 ^{o}C for 5 h, the mixture was concentrated under reduced pressure. The product was purified by PREP-HPLC equipment as mobile phase 50/50 acetonitrile: water (v/v) at 209 nm. The product was obtained as a white solid with a 53 % yield. ^{1}H NMR (400 MHz, DMSO d6): δ/ppm = 10.96 (s, 1H), 8.22 (d, *J* = 7.2 Hz, 1H), 7.08 (d, *J* = 7.17, 1H), 6.31 (d, *J* = 5.5, 1H), 6,16 (t, *J* = 7.4 Hz, 1H), 6.04 (s, 1H), 5.69 (s, 1H), 5.30 (t, *J* = 5.0, 1H), 4.37 (q, *J* = 6.6 Hz, 4H), 4.25 - 4.14 (m, 1H), 3.88 (d, *J* = 8.4 Hz, 1H), 3.81 (d, *J* = 3.4 Hz, 1H), 3.65 (d, *J* = 3.4 Hz, 1H), 3.07 - 3.01 (m, 4H), 1.87 (s, 3H). ^{13}C NMR (100 MHz, DMSO d6): δ/ppm = 166.8, 163.8, 154.4, 153.4, 144.9, 136.1, 126.5, 123.4, 120.9, 95.4, 84.6 (t, *J* = 32.7), 81.50, 68.9 (t, *J* = 22.4), 63.6, 62.7, 59.3, 36.9, 18.4. LCMS expected [M+H] m/z = 511g/mol, observed [M+H] and [M+Na] m/z = 512 g/mol and 534 g/mol.

3.2.8. Synthesis and Characterization of BODIPY-Methacrylate Monomer

Hydroxy-terminated BODIPY-dye (BODIPY-OH) was synthesized using a published procedure [187]. BODIPY-OH (250 mg, 0.62 mmol) was dissolved in anhydrous CH_2Cl_2 (6 mL). The mixture was cooled to 0 ^{o}C and triethylamine (112 µL, 82 mg, 0.81 mmol). At 0 ^{o}C, methacryloyl chloride in anhydrous CH_2Cl_2 (1 mL) was added to the mixture. The reaction mixture was allowed to stir from 0 ^{o}C to room temperature overnight. Afterward, the mixture was added to CH_2Cl_2 (100 mL) and extracted with water (3 x 30 mL). The organic layer was dried over Na_2SO_4. The crude product was purified by column chromatography. The pure product was obtained as a red-orange solid (180 mg, 62% yield). ^{1}H NMR (400 MHz, $CDCl_3$): δ/ppm = 6.09 (s, 1H), 6.05 (s, 2H), 5.54 (s, 1H), 4.13 (t, *J* = 6.7, 2H), 2.95 - 2.91 (m, 2H), 2.51 (s, 6H), 2.41 (s, 6H), 1.94 (s, 3H), 1.70 - 1.58 (m, 4H), 1.51 - 1.45 (m, 2H), 1.41 - 1.24 (m, 10H). ^{13}C NMR (100 MHz, $CDCl_3$): δ/ppm = 167.7, 153.9, 146.9, 140.4, 136.7, 131.6, 125.3, 121.7, 64.9, 32.1, 30.5, 29.6, 29.4, 28.8, 28.7, 26.1, 18.4, 16.5, 14.6.

3.2.9. Synthesis and Characterization of Copolymer P(OEG/HCQ-E)

P(OEGMA) (637 mg, 2.12 mmol) and HCQ-E-MA (367 mg, 0.91 mmol) were dissolved in anhydrous DMF (2.5 mL), and the mixture was stirred for 30 min under N_2. 4-cyano-4-(thiobenzoylthio)pentanoic acid (4.23 mg, 0.015 mmol) as a chain transfer reagent, and AIBN (0.49 mg, 3.02 x 10^{-3} mmol) as initiator were added to polymer the polymer solution under N_2. The reaction was sealed and heated at 70 ^oC for 18 h. First, the copolymer was precipitated in diethyl ether (100 mL) to purify the copolymer. Secondly, the copolymer solution was dialyzed against acetonitrile: MeOH (95:5) using a 10kDa cutoff regenerated cellulose acetate membrane for 24 h. The product was dried under a vacuum and obtained as a yellow viscous (0.7 g, 70 % yield). ^1H NMR (400 MHz, $CDCl_3$): δ/ppm = 8.49 (br s, 1H), 7.91 (s, 1H), 7.83 (br s, 1H); 7.32 (br s,1H), 6.42 (br s, 1H), 5.42 (s, 1H), 4.07 (br s, 2H), 3.63 (br s, 14H), 3.53 (br s, 2H), 3.36 (s, 3H), 2.66 (br s, 2H), 2.51 (br s, 4H), 1.00 - 0.89 (m, CH_2 and CH_3 polymer backbone). GPC: Mn = 43 kDa; Mw / Mn = 1.62.

3.2.10. Synthesis and Characterization of Copolymer P(OEG/HCQ-C)

P(OEGMA) (523 mg, 1.74 mmol) and hydroxychloroquine methacrylate monomer with carbamate linker (HCQ-C-MA, 367 mg, 0.74) were dissolved in anhydrous DMF (2.2 mL) and the mixture was stirred for 30 min under N_2. 4-cyano-4-(thiobenzoylthio)pentanoic acid (3.44 mg, 0.012 mmol) as a chain transfer reagent and AIBN (0.40 mg, 2.46 x 10^{-3} mmol) as initiator were added to polymer solution under N_2. The reaction was sealed and heated at 70 ^oC for 18 h. First, the copolymer was precipitated in diethyl ether (100 mL) to purify the copolymer. Secondly, the copolymer solution was dialyzed against acetonitrile: MeOH (95:5) using a 10kDa cutoff regenerated cellulose acetate membrane for 24 h. The product was dried under a vacuum and obtained as a yellow viscous (0.62 g, 70 % yield). ^1H NMR (400 MHz, $CDCl_3$): δ/ppm = 8.49 (br s, 1H), 7.91 (s, 1H), 7.81 (br s, 1H), 7.32 (br s, 1H), 6.42 (br s, 1H), 5.41 (s, 1H), 4.08 (br s, 2H), 3.63 (br s, 14H), 3.53 (br s, 2H), 3.36 (s, 3H), 2.66 (br s, 2H), 2.51 (br s, 4H), 1.00 - 0.89 (m, CH_2 and CH_3 polymer backbone). GPC: Mn = 56 kDa; Mw / Mn = 1.70.

3.2.11. Synthesis and Characterization of Copolymer P(OEG/HCQ-CB)

OEGMA (243 mg, 0.81 mmol), hydroxychloroquine methacrylate monomer via carbonate (CB) linker (HCQ-CB-MA, 100 mg, 0.203 mmol) was dissolved in anhydrous DMF (1.5 mL), and purged with N_2 for 30 min. Under N_2, 4-cyano-4-(thiobenzoylthio)pentanoic acid (1.42 mg, 5.08 x 10^{-3} mmol) as a chain transfer reagent and AIBN (016 mg, 1.16 x 10^{-3} mmol) as initiator were added to the polymer solution, respectively. Then, the reaction mixture was stirred at 70 ^oC for 18 h. After 18 h, the polymer solution was transferred into a dialysis bag, and the dialysis bag was put into a mixture of ACN: MeOH (95:5). Polymer solution was dialyzed against a mixture of ACN: MeOH using 10kDa cutoff regenerated cellulose acetate membrane for 24 h. The polymer was obtained as yellow viscous containing 5.4% HCQ by weight (0.26 g, 75 % yield). ^{1}H NMR (400 MHz, $CDCl_3$): δ/ppm = 8.49 (br s, 1H), 7.91 (s, 1H), 7.81(br s, 1H), 7.32 (br s,1H), 6.42 (br s, 1H), 5.41 (s, 1H), 4.08 (br s, 2H), 3.63 (br s, 14H), 3.53 (br s, 2H), 3.37 (s, 3H), 2.67 (br s, 2H), 2.51 (br s, 4H), 1.00 - 0.89 (m, CH_2 and CH_3 polymer backbone). GPC: Mn = 57 kDa; Mw / Mn = 1.70.

3.2.12. Synthesis and Characterization of Copolymer P(OEG/GEM-C)

P(OEGMA) (768 mg, 2.56 mmol) and GEM-C-MA (460 mg, 1.09 mmol) were dissolved in anhydrous DMF (2.6 mL), and the mixture was stirred for 30 min under N_2. 4-cyano-4-(thiobenzoylthio)pentanoic acid (5.06 mg, 0.018 mmol) as a chain transfer reagent and AIBN (0.59 mg, 3.64 x 10^{-3} mmol) as initiator were added to polymer the polymer solution under N_2. The reaction was sealed and heated at 70 ^oC for 18 h. First, the copolymer was precipitated in diethyl ether (100 mL) to purify the copolymer. Secondly, the copolymer solution was dialyzed against acetonitrile: MeOH (95:5) using a 10kDa cutoff regenerated cellulose acetate membrane for 24 h. The product was dried under a vacuum and obtained as a pink viscous (0.88 g, 72 % yield). ^{1}H NMR (400 MHz, DMSO d6): δ/ppm = 10.77 (br s, 1H), 8.23 (d, *J* = 7.1 Hz, 1H), 7.10 (d, *J* = 6.8 Hz, 1H), 6.3 (d, *J* = 6.2 Hz, 1H), 6.17 (t, *J* = 7.1 Hz, 1H), 5.25 (br s, 1H), 4.02 (br s, 2H), 3.61 - 3.54 (br s, 14 H), 3.44 (br s, 2H), 3.24 (br s, 3H), 0.95 - 0.80 (m, CH_2 and CH_3 polymer backbone) GPC: Mn = 51 kDa; Mw / Mn = 1.45.

3.2.13. Synthesis and Characterization of Copolymer P(OEG/GEM-SSC)

P(OEGMA) (470 mg, 1.56 mmol) and GEM-MA-SSC (200 mg, 0.39 mmol) were dissolved in anhydrous DMF (3 mL), and the mixture was stirred for 30 min under N_2. 4-cyano-4-(thiobenzoylthio)pentanoic acid (2.72 mg, 9.75 x 10^{-3} mmol) as a chain transfer reagent and AIBN (0.32 mg, 1.95 x 10^{-3} mmol) as initiator were added to polymer the polymer solution under N_2. The reaction was sealed and heated at 70 ^oC for 18 h. First, the copolymer was precipitated in diethyl ether (100 mL) to purify the copolymer. Secondly, the copolymer solution was dialyzed against acetonitrile: MeOH (95:5) using a 10kDa cutoff regenerated cellulose acetate membrane for two days. The product was dried under a vacuum and obtained as a pink viscous (0.55 g, 82 % yield). ^{1}H NMR (400 MHz, DMSO d6): δ/ppm = 10.92 (br s, 1H), 8.22 (d, *J* = 7.1 Hz, 1H), 7.10 (d, *J* = 6.8 Hz, 1H), 6.3 (d, *J* = 6.2 Hz, 1H), 6.17 (t, *J* = 7.1 Hz, 1H), 5.26 (br s, 1H), 4.02 (br s, 2H), 3.53 (br s, 14 H), 3.43 (br s, 2H), 3.24 (br s, 3H), 0.95 - 0.80 (m, -CH_2 and CH_3 polymer backbone). Mn = 53 kDa; Mw / Mn = 1.45.

3.2.14. Synthesis and Characterization of Copolymer P(OEG/HCQ-E/GEM-C)

P(OEGMA) (375 mg, 1.25 mmol), HCQ-E-MA (200 mg, 0.50 mmol), and GEM-MA-C (314 mg, 0.75 mmol) were dissolved in anhydrous DMF (2 mL), and the mixture was stirred for 30 min under N_2. 4-cyano-4-(thiobenzoylthio)pentanoic acid (3.48 mg, 0.0125 mmol) as a chain transfer reagent and AIBN (0.41 mg, 2.5 x 10^{-3} mmol) as initiator were added to polymer the polymer solution under N_2. The reaction was sealed and heated at 70 ^oC for 18 h. First, the copolymer was precipitated in diethyl ether (100 mL) to purify the copolymer. Secondly, the copolymer solution was dialyzed against acetonitrile: methanol (95:5) using a 10kDa cutoff regenerated cellulose acetate membrane for two days. The product was dried under a vacuum and obtained as a yellow viscous (0.49 g, 55 % yield). ^{1}H NMR (400 MHz, DMSO d6): δ/ppm = 10.95 (br s, 1H), 8.35 (br s, 2H), 8.22 (br s, 1H), 7.77 (br s, 1H), 7.41 (br s, 1H), 7.07 (br s, 1H), 6.88 (br s, 1H), 6.44 (br s, 1H), 6.32 (br s, 1H), 6.17 (br s, 1H), 5.29 (br s, 1H), 4.01 (br s, 2H), 3.74 - 3.41 (m, 16H), 3.22 (br s, 3H), 0.92 - 0.79 (m, -CH_2 and CH_3 polymer backbone). Mn = 50 kDa; Mw / Mn = 1.8.

3.2.15. Synthesis and Characterization of Copolymer P(OEG/HCQ-C/GEM-C)

P(OEGMA) (375 mg, 1.19 mmol), HCQ-C-MA (234 mg, 0.48 mmol), and GEM-C-MA (300 mg, 0.72 mmol) were dissolved in anhydrous DMF (2.1 mL), and the mixture was stirred for 30 min under N_2. 4-cyano-4-(thiobenzoylthio)pentanoic acid (3.32 mg, 0.0120 mmol) as a chain transfer reagent and AIBN (0.39 mg, 2.4 x 10^{-3} mmol) as initiator were added to polymer the polymer solution under N_2. The reaction was sealed and heated at 70 ^oC for 18 hours. Copolymer solution was dialyzed against acetonitrile: methanol (95:5) using a 10kDa cutoff regenerated cellulose acetate membrane for two days. The product was dried under a vacuum and obtained as a yellow viscous (0.67 g, 75 % yield). ^1H NMR (400 MHz, DMSO d6): δ/ppm = 10.95 (br s, 1H), 8.35 (br s, 2H), 8.21 (br s, 1H), 7.76 (br s, 1H), 7.40 (br s, 1H), 7.09 (br s, 1H), 6.86 (br s, 1H), 6.47 (br s, 1H), 6.32 (br s, 1H), 6.16 (br s, 1H), 5.28 (br s, 1H), 4.30 - 3.81 (m, 6H), 3.50 - 3.41 (m, 18H), 3.24 (br s, 3H), 0.92 - 0.79 (m, -CH_2 and CH_3 polymer backbone). Mn = 55 kDa; Mw / Mn = 1.9.

3.2.16. Synthesis and Characterization of Copolymer P(OEG/HCQ-C/GEM-SSC)

P(OEGMA) (351 mg, 1.17 mmol), HCQ-C-MA (191 mg, 0.39 mmol), and GEM-SSC-MA (200 mg, 0.39 mmol) were dissolved in anhydrous DMF (3.0 mL), and the mixture was stirred for 30 min under N_2. 4-cyano-4-(thiobenzoylthio)pentanoic acid (2.72 mg, 9.75 x 10^{-3} mmol) as a chain transfer reagent and AIBN (0.32 mg, 1.95 x 10^{-3} mmol) as initiator were added to polymer the polymer solution under N_2. The reaction was sealed and heated at 70 ^oC for 18 h. Copolymer solution was dialyzed against acetonitrile: methanol (95:5) using a 10kDa cutoff regenerated cellulose acetate membrane for two days. The product was dried under a vacuum and obtained as a yellow viscous (0.5 g, 67 % yield). ^1H NMR (400 MHz, DMSO d6): δ/ppm = 10.97 (br s, 1H), 8.37 (br s, 2H), 8.24 (br s, 1H), 7.77 (br s, 1H), 7.40 (br s, 1H), 7.10 (br s, 1H), 6.89 (br s, 1H), 6.49 (br s, 1H), 6. 33 (br s, 1H), 6.17 (br s, 1H), 5.30 (br s, 1H), 4.36 (br s, 4H), 4.18-3.79 (m, 2H), 3.52 - 3.43 (m, 16H), 3.24 (br s, 3H), 0.91 - 0.79 (m, -CH_2 and CH_3 polymer backbone). Mn = 50 kDa; Mw / Mn = 1.7.

3.2.17. Synthesis and Characterization of Copolymer P(OEG/HCQ-CB/GEM-SSC)

P(OEGMA) (351 mg, 1.17 mmol), carbonate-containing hydroxychloroquine monomer (HCQ-CB-MA, 192 mg, 0.39 mmol), and disulfide-carbamate-containing gemcitabine monomer (GEM-SSC-MA, 200 mg, 0.39 mmol) were dissolved in anhydrous DMF (3 mL), and the solution was purged with N_2 for 30 min. Under N_2, 4-cyano-4-(thiobenzoylthio)pentanoic acid (2.72 mg, 9.75 x 10^{-3} mmol) as a chain transfer reagent and AIBN (0.32 mg, 1.95 x 10^{-3} mmol) as initiator were added to the polymer solution under N_2. The copolymer precursor solution was stirred at 70 ^oC for 18 h. After 18 h, the copolymer solution was transferred into a dialysis bag. It was purified via dialysis against 95:5 (ACN: MeOH) using a 12-14 kDa cutoff regenerated cellulose acetate membrane for two days. The product was dried under a vacuum and obtained as a yellow viscous (0.61 g, 82 % yield). ^1H NMR (400 MHz, DMSO d6): δ/ppm = 10.92 (br s, 1H), 8.36 (br s, 2H), 8.22 (br s, 1H), 7.77 (br s, 1H), 7.42 (br s, 1H), 7.09 (br s, 1H), 6.85 (br s, 1H), 6.47 (br s, 1H), 6.30 (br s, 1H), 6.15 (br s, 1H), 5.26 (br s, 1H), 4.36 (br s, 4H), 4.18 - 3.79 (m, 2H), 3.52 - 3.43 (m, 16H), 3.24 (br s, 3H), 0.91 - 0.79 (m, -CH_2 and CH_3 polymer backbone). Mn = 57 kDa; Mw / Mn = 1.60.

3.2.18. Synthesis and Characterization of Copolymer P(OEG/HCQ-CB/GEM-SSC/BODIPY)

P(OEGMA) (135 mg, 0.45 mmol), carbonate-containing hydroxychloroquine monomer (HCQ-CB-MA, 50 mg, 0.098 mmol), and disulfide-carbamate-containing gemcitabine monomer (GEM-SSC-MA, 48 mg, 0.098 mmol) and BODIPY-MA (3.2 mg, 6.78 x 10^{-3} mmol) were dissolved in anhydrous DMF (2 mL). The solution was purged with N_2 for 30 min. Under N_2, 4-cyano-4-(thiobenzoylthio)pentanoic acid (0.91 mg, 3.26 x 10^{-3} mmol) as a chain transfer reagent and AIBN (0.11 mg, 6.70 x 10^{-4} mmol) as initiator were added to the polymer solution under N_2. The copolymer precursor solution was stirred at 70 ^oC for 18 h. After 18 h, the copolymer solution was transferred into a dialysis bag. It was purified via dialysis against 95:5 (ACN: MeOH) using a 12-14 kDa cutoff regenerated cellulose acetate membrane for two days. The product was dried under a vacuum and obtained as an orange viscous (0.15 g, 64 % yield). ^1H NMR (400 MHz, DMSO d6): δ/ppm = 10.92 (br s, 1H), 8.36 (br s, 2H), 8.22 (br s, 1H), 7.77 (br s, 1H), 7.42 (br s, 1H), 7.09 (br

s, 1H), 6.85 (br s, 1H), 6.47 (br s, 1H), 6.30 (br s, 1H), 6.15 (br s, 2H), 5.26 (br s, 1H), 4.36 (br s, 4H), 4.18-3.79 (m, 2H), 3.52 - 3.43 (m, 16H), 3.24 (br s, 3H), 0.91 - 0.79 (m, -CH_2 and CH_3 polymer backbone). Mn = 41 kDa; Mw / Mn = 1.68.

3.2.19. Evaluation of Drug Stability

Before the drug release experiment, drug stability was investigated. GEM and HCQ solution (100 ppm) were prepared in water. The solution was incubated separately in porcine liver esterase (PLE), rat plasma, pH = 5.4, and pH = 7.4 buffers with total drug concentrations of 50 ppm. GEM-HCQ solutions were stirred at 250 rpm for 72h. Samples were taken at predetermined time points, and plasma and enzyme proteins were precipitated by adding acetonitrile (50uL). Tubes were centrifuged at 6000 g for 2 min, and supernatants were analyzed to measure HCQ-GEM concentration by LC-MS analysis.

3.2.20. *In Vitro* Drug Release Study

Drug release profiles from polymer-drug conjugates were determined via LCMS. Briefly, the drug-containing copolymer solutions were prepared separately in rat plasma, esterase from the porcine liver (PLE), glutathione (GSH) (10 mM), and the mixture of PLE-GSH with a total GEM concentration of 500 ppm. Copolymer solutions were then incubated at 37 ^{o}C while stirring at 250 rpm for 72 h. Samples were taken at predetermined time points, and plasma and enzyme proteins were precipitated by ACN addition (100 μL). Tubes were centrifuged at 6000 g for 2 min, and supernatants were analyzed for HCQ and GEM concentration by LCMS analysis.

3.2.21. Cell Culture

Pancreas cancer cell lines (BxPC-3, Capan-1, and Panc-1) were purchased from ATCC ((LGC Standards, Germany). Cells were grown in RPMI 1640 media supplemented with 10% FBS and 1% v/v MEM according to the manufacturer's culture method requirements and incubated at 37 °C in a humidified atmosphere of 5 % CO_2 and kept in the logarithmic phase of growth.

3.2.22. *In Vitro* Cytotoxicity Experiments

BxPC-3 and Capan-1 pancreatic cancer cells (purchased from ATCC (LGC Standards, Germany)) were used for cytotoxicity experiments in this study. Cells were grown in RPMI 1640 media supplemented with 10% FBS and 1% v/v MEM according to the manufacturer's culture method requirements and incubated at 37 °C in a humidified atmosphere of 5 % CO_2 and kept in a logarithmic phase of growth throughout all experiments. Cytotoxicity of copolymers was determined using a CCK-8 assay on BxPC-3 and Capan-1 cells. Cells (10000 cells/well) were seeded on a 96-well plate as triplicates in a culture medium (100 μL) and incubated at 37 ºC for 24 h for cells to grow and adhere completely. Only HCQ and GEM containing copolymers and free gemcitabine solutions were prepared with total GEM concentration 1 x 10^{-3} M and diluted between 10^{-4}-10^{-10} M. In both HCQ and GEM containing copolymers, polymer solutions were designed according to GEM amount of the polymer backbone. Cells were incubated separately in the copolymer and free drug solutions for 48 hours. After 48 hours, copolymer and drug solutions were removed, and the cells were washed with PBS (2 x 100 μL). The cells were incubated with CCK-8-bearing media for two h. After the incubation, the absorbance values at 450 nm were measured via a microplate reader. Results were gained by GraphPad prism software using nonlinear regression mode.

3.2.23. *In Vitro* Cellular Uptake of P(OEG/HCQ-CB/GEM-SSC/BODIPY) in BxPC-3 Monolayer

BxPC-3 human pancreatic adenocarcinoma cells were grown in a 5% CO_2-containing atmosphere at 37 °C and cultured in RPMI media supplemented with 10% fetal bovine serum (FBS) (PAN Biotech). BxPC-3 cells (110 000 cells/well) were seeded in 12 well-plate as triplicate in culture media (1 mL). The cells were incubated at 37 °C for 24 h. After 24-hour incubation, free BOPIPY dye and BODIPY-conjugated and drug-containing copolymer P(OEG/HCQ-CB/GEM-SS-C/BODIPY) solutions (2 μM) were added to the cells. After adding dye-containing solutions, cell media were removed from cells at several time points (1, 3, 24 h) during incubation. Then, cells were washed with 1 x PBS (1 mL x 3 times). Cells were fixed using 3.7% formaldehyde solution for 10 minutes at 37 ºC. After washing with PBS, cell nuclei were stained with DAPI for 20 min at 37 ºC. At the end of the staining step, cells were washed with 1 x PBS (1 mL x 3 times). Images of stained cells were recorded

using a Zeiss Observer Z1 fluorescence microscope and processed with Zeiss Zen Blue lite software (Carl Zeiss, Jena, Germany).

3.2.24. *In Vitro* 3D Spheroid Formation and Inhibition Ability of Free Drugs and Copolymer

In the seeding process for spheroid assay, BxPC-3 cells (5000 cells/well) were seeded on an ultra-low attachment 96-well plate at four replicates using cocktail media. Cocktail media was prepared by adding 1x B27 (diluted from 50x Neuropan 27 stock solution), 20 ug/mL insulin, 10 ng/mL FGF-2 (Fibroblast growth factor-2), 50 ng/mL EGF (Epidermal growth factor), 1 µg/mL hydrocortisone into RPMI. Before the drug treatment, spheroid images were taken using an inverted phase microscope, and the data process was started on day 0. On day 0, (D0) GEM, HCQ, GEM-HCQ mixture, and P(OEG/HCQ-CB/GEM-SSC) copolymer solutions were added to spheroids at the same GEM concentration (1×10^{-6} M). Media change was done on 2., 4., 6., and 8. days, and new drug solutions were added. Until day 14, spheroid images were recorded. Zen Lite software and a camera were used to take pictures (10x magnification and 0.2 µm/pixel resolution). Spheroid processing was done by using Matlab Software.

3.2.25. Penetration of P(OEG/HCQ-CB/GEM-SS-C/BODIPY) into BxPC-3 Spheroids

The BxPC-3 tumor spheroids were prepared as mentioned above. The spheroids (1000 cells/ well) were treated with free BODIPY and P(OEG/HCQ-CB/GEM-SSC/BODIPY) solutions (2 µM, 200 µL) to study the penetration capacity. After 1, 3, and 24 hours of incubation, 100 µL of dye solutions were removed from spheroids. Subsequently, spheroids in the remaining solutions were transferred into a 12-well plate and carefully washed with PBS. The level of permeability of free BODIPY and BODIPY-conjugated copolymer was analyzed using a Zeiss Observer Z1 fluorescence microscope and processed with Zeiss Zen Blue lite software (Carl Zeiss, Jena, Germany).

3.3. Results and Discussion

3.3.1. Synthesis of HCQ-E-MA Monomer

Hydroxychloroquine sulfate was neutralized before use. Hydroxychloroquine sulfate was dissolved in the minimum amount of water, and pH was adjusted to 11 by adding 1 M NaOH to neutralize. Then, chloroform was added and stirred for 1 h. After one hour, the chloroform layer was taken and dried. Hydroxychloroquine methacrylate monomer via ester linker (HCQ-E-MA) was synthesized using hydroxychloroquine and methacryloyl chloride in the presence of triethylamine in 75 % yield. The reaction is shown in Figure 3.2.

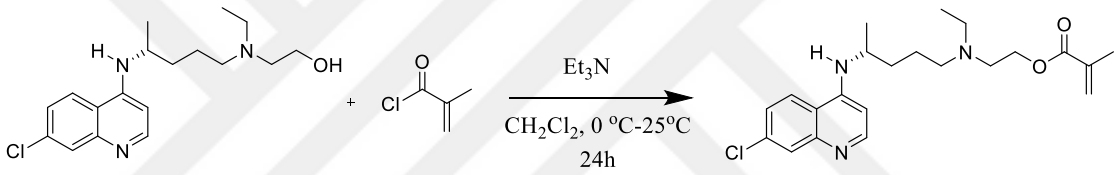

Figure 3.2. Synthesis of hydroxychloroquine monomer via ester linkers (HCQ-E-MA).

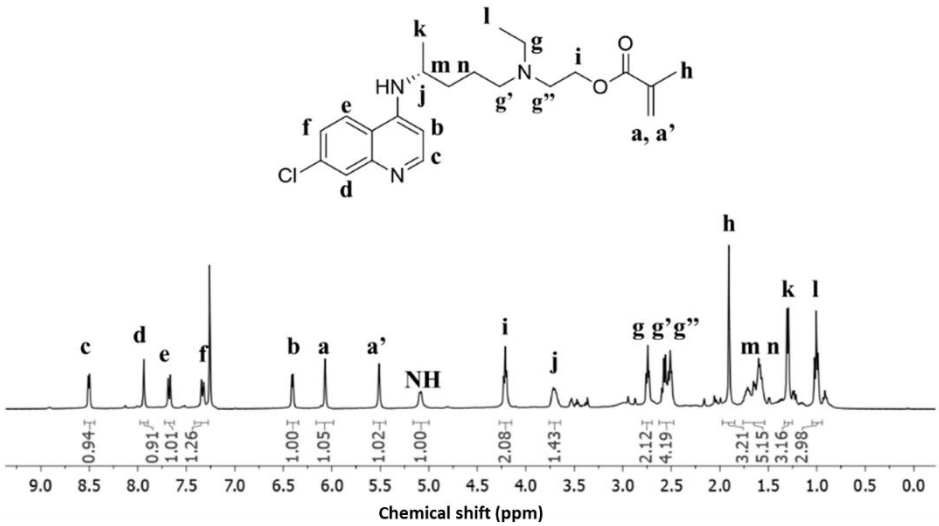

Figure 3.3. ^{1}H NMR spectrum of HCQ-E-MA monomer ($CDCl_3$).

HCQ-E-MA was analyzed with ^{1}H NMR, ^{13}C NMR, and FTIR spectroscopies. The proton resonances at 6.07 and 5.51 ppm due to the terminal alkenyl group of methacrylate monomer unit and the proton resonances between 8.51 and 6.41 ppm due to aromatic hydrogens of hydroxychloroquine were evidence of successful reaction. The full ^{1}H NMR spectrum is given in Figure 3.3. ^{13}C NMR and FTIR spectra are presented in Figure A.1 and Figure A.2.

3.3.2. Synthesis of P(OEG/HCQ-E) Copolymer via RAFT Polymerization

OEGMA (Mn = 300 g/mol) and HCQ-E-MA monomers were polymerized via reversible addition-fragmentation chain transfer (RAFT) polymerization in the presence of AIBN as an initiator and 4-cyano-4-(thiobenzoylthio)pentanoic acid as a chain transfer agent (CTA) in anhydrous DMF at 70 ^{o}C. The polymerization reaction is shown in Figure 3.4.

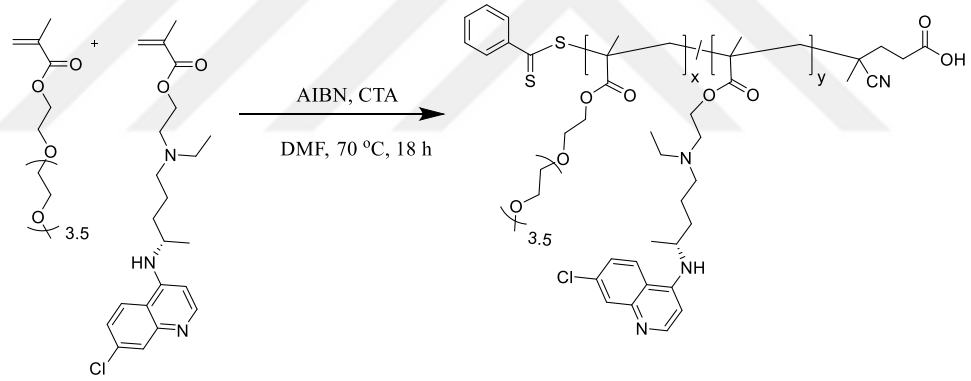

Figure 3.4. Synthesis of P(OEG/HCQ-E) via RAFT polymerization.

P(OEG/HCQ-E) analysis was done with ^{1}H NMR spectroscopy and SEC. The proton resonances between 8.5-6.4 ppm due to aromatic hydrogens of hydroxychloroquine, and the proton resonances around 3.39 ppm due to the terminal methyl ether group of the OEGMA unit and the disappearance of proton resonances at 6.07 and 5.51 ppm due to the terminal alkenyl group of methacrylate unit showed successful polymerization. ^{1}H NMR spectrum is given in Figure 3.5. The feed ratio to synthesized copolymer P(OEG/HCQ-E) was used as 80:20 with OEGMA and HCQ-E-MA monomers. This feed ratio produced a P(OEG/HCQ-E) copolymer with an 88.5:11.5 ratio of OEGMA and HCQ. The weight percent of HCQ in P(OEG/HCQ-E) conjugate was calculated using ^{1}H NMR by comparing the aromatic proton

resonances of HCQ at 6.42 ppm and the proton resonance of $–OCH_3$ in OEGMA at 3.39 ppm. Drug content for P(OEG/HCQ-E) (43 kDa) was calculated as 11.5% by weight. Polymerization conditions and properties of P(OEG/HCQ-E) conjugate are given in Table 3.1.

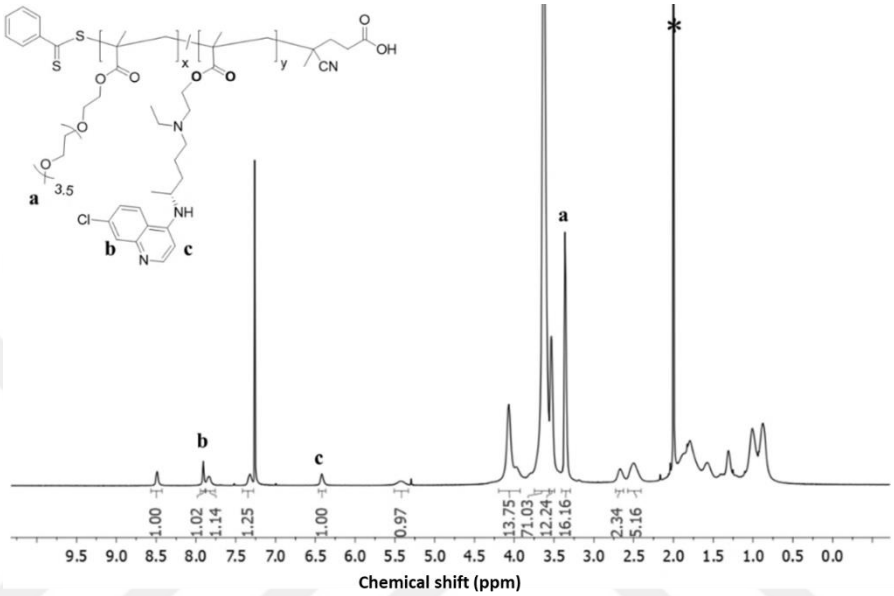

Figure 3.5. ^{1}H NMR spectrum of POEGMA-HCQ-E in $CDCl_3$.

Table 3.1. Polymerization conditions of P(OEG/HCQ-E).

No	**Feed Ratio**		**Obtained Ratio**		**CTA**	**AIBN**	**Mn(kDa)**	**Mw/Mn (PDI)**
	OEG	HCQ	OEG	HCQ				
1	80	20	88.5	11.5	5	1	43	1.6

3.3.3. *In Vitro* Drug Release Study and Cytotoxicity of P(OEG/HCQ-E) Copolymer

In the P(OEG/HCQ-E) copolymer, HCQ was linked to the polymer backbone via a pH-responsive ester linker. When drugs are attached covalently to the polymeric system through cleavable linkers, drug release profiles may be improved using some stimuli like pH, enzyme, temperature, and so on. HCQ release from P(OEG/HCQ-E) copolymer was investigated in acidic and physiological pH values, esterase enzyme (PLE), and rat plasma. P(OEG/HCQ-E) copolymer solutions were incubated separately in rat plasma and esterase

enzyme from the porcine liver (PLE) at 37°C. At certain times, samples were collected from the copolymer solutions, and the concentration of HCQ and release ratio were determined using LCMS analysis. As seen in Figure 3.6, very low HCQ release from the P(OEG/HCQ-E) copolymer was observed. At the end of 72 h, the P(OEG/HCQ-E) copolymer showed HCQ release by 0.7%, 0.48%, 0.11%, and 0.32% in pH = 5.4, pH = 7.4, PLE enzyme, and rat plasma, respectively.

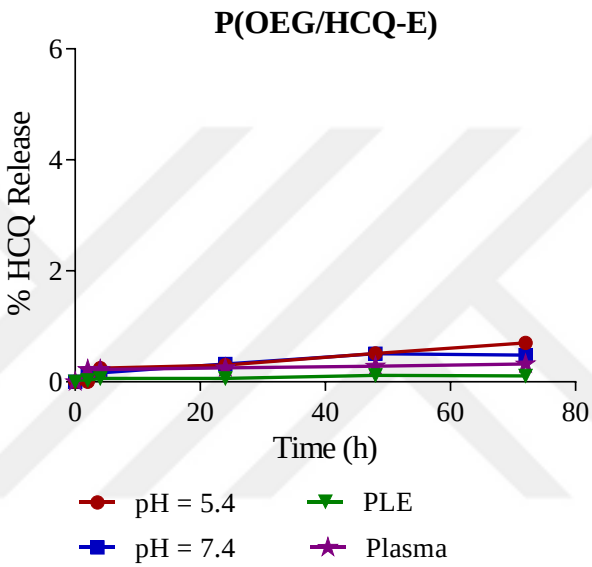

Figure 3.6. HCQ release profiles from P(OEG/HCQ-E) copolymer in pH = 5.4, pH = 7.4, PLE, and plasma at 37 °C for 72 h.

After evaluation of HCQ release, cytotoxicity of P(OEG/HCQ-E) copolymer was investigated using BxPC-3 and Capan-1 pancreatic adenocarcinoma cell lines. Both free HCQ and P(OEG/HCQ-E) copolymer were applied to cells with the same HCQ concentration (10^{-4} M to 10^{-10} M). At the end of 48 h of incubation, EC_{50} values of free HCQ and P(OEG/HCQ-E) copolymer were determined as 2.54 x 10^{-6} M and >10^{-4} M on BxPC-3 cells. EC_{50} values were tabulated in Table 3.2. When Capan-1 cells were used, EC_{50} values of free HCQ and P(OEG/HCQ-E) were calculated as 2.58 x 10^{-6} M and 1.97 x 10^{-5} M. It was clear that when HCQ was conjugated to a polymer via ester linkage, P(OEG/HCQ-E) copolymer showed 100-fold less activity toward BxPC-3 cells due to deficient HCQ release. Cytotoxicity graphs are shown in Figure 3.7.

Table 3.2. Calculated EC_{50} values of HCQ and P(OEG/HCQ-E) copolymer for pancreas cancer cell lines after 48 h incubation.

		EC_{50} (M)	
No	**Constructs**	**BxPC-3**	**Capan-1**
1	HCQ	2.54×10^{-6}	2.58×10^{-6}
2	P(OEG/HCQ-E)	$> 10^{-5}$	1.97×10^{-5}

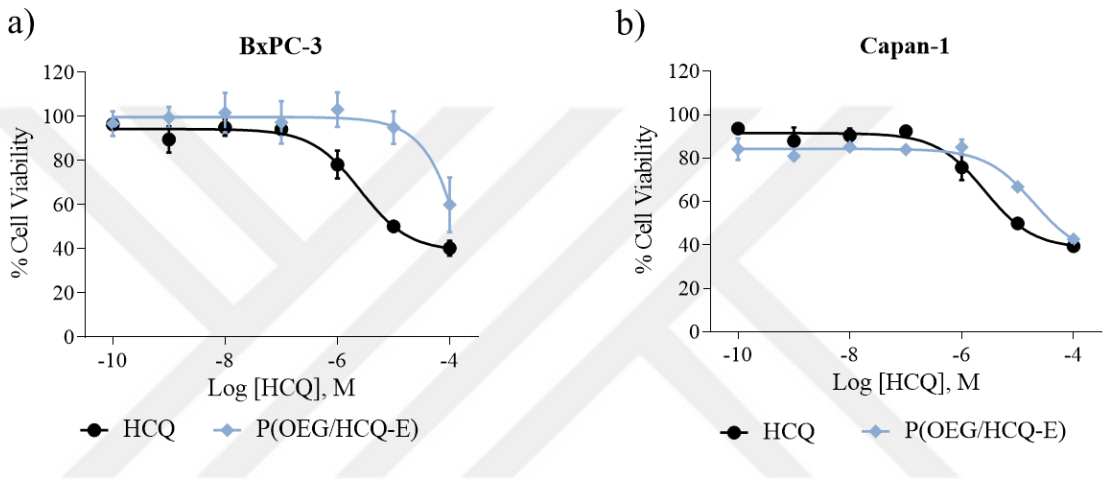

Figure 3.7. Cell viabilities of (a) BxPC-3 cells, (b) Capan-1 cells treated with free HCQ and P(OEG/HCQ-E) copolymer.

3.3.4. Synthesis of HCQ-C-MA Monomer

Due to low HCQ release from P(OEG/HCQ-E) copolymer and less cytotoxic activity against cancer cells, the linker between the polymer backbone and HCQ was changed, and pH-responsive carbamate linker (C) was introduced to the system in place of the ester linkage. pH-responsive carbamate bond-containing hydroxychloroquine methacrylate monomer (HCQ-C-MA) was synthesized using 2-isocyanataethyl methacrylate and hydroxychloroquine in 93% yield. The reaction pathway is shown in Figure 3.8.

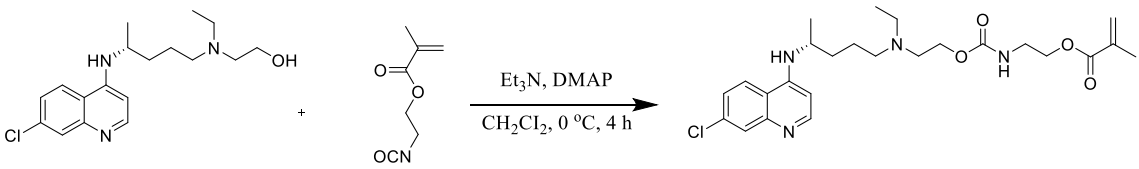

Figure 3.8. Synthesis of HCQ-C-MA monomer via carbamate linker.

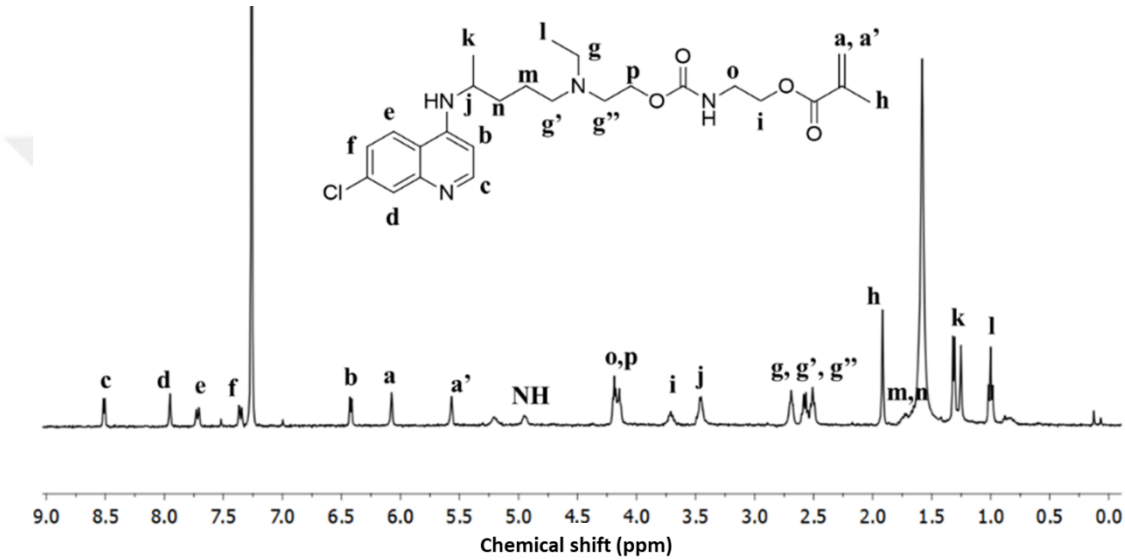

Figure 3.9. ^{1}H NMR spectrum of HCQ-C-MA monomer ($CDCl_3$).

Analysis of HCQ-C-MA was done with ^{1}H NMR, ^{13}C NMR, and FTIR. The proton resonances at 6.05 and 5.55 ppm due to the terminal alkenyl group of methacrylate monomer unit and the proton resonances between 8.49 and 6.40 ppm due to aromatic hydrogens of hydroxychloroquine were evidence of successful reaction. The full ^{1}H NMR spectrum is given in Figure 3.9. ^{13}C NMR and FTIR spectra are shown in Figure A.3 and Figure A.4.

3.3.5. Synthesis of P(OEG/HCQ-C) Copolymer via RAFT Polymerization

P(OEG/HCQ-C) copolymer was obtained using OEGMA and carbamate bond (C) containing HCQ-C-MA monomers via RAFT polymerization. AIBN and 4-cyano-4-(thiobenzoylthio)pentanoic acid were used as an initiator and chain transfer agent (CTA).

The polymerization reaction was carried out in DMF at 70 ºC for 18 h. The polymerization reaction is shown in Figure 3.10.

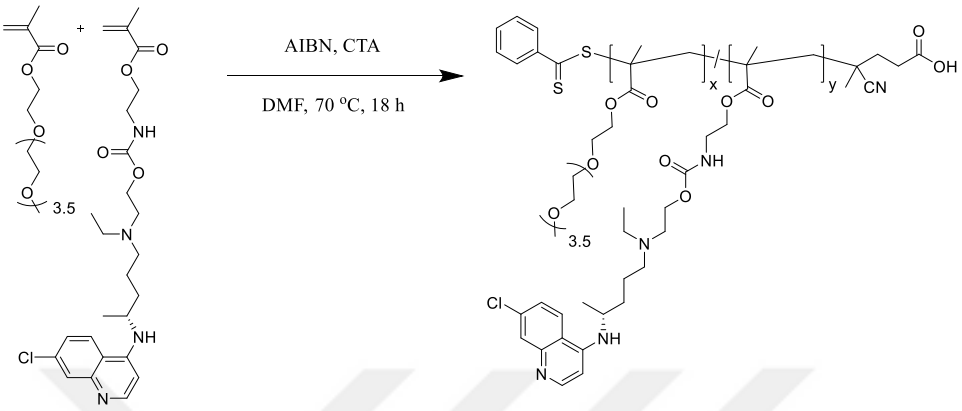

Figure 3.10. Synthesis of P(OEG/HCQ-C) via RAFT polymerization.

P(OEG/HCQ-C) copolymer was characterized via ^{1}H NMR and SEC analyses. ^{1}H NMR spectrum is given in Figure 3.11. The proton resonances of aromatic hydrogens of Hydroxychloroquine between 8.49 - 6.42 ppm, the proton resonance of $–OCH_3$ group of OEGMA unit at 3.37 ppm, and the removal of peaks of methacrylate alkenyl hydrogens at 6.05 and 5.55 ppm demonstrated that OEGMA and HCQ-C-MA monomers were successfully polymerized. The P(OEG/HCQ-C) copolymer's experimentally obtained monomer compositions are nearly the same as theoretical monomer compositions. To reach targeted copolymer P(OEG/HCQ-C), the feed ratio was used as 90:10 with OEGMA: HCQ-C-MA monomers, and it produced P(OEG/HCQ-C) copolymer with 91.8:8.2 ratio of OEGMA: HCQ. Polymerization conditions were tabulated in Table 3.3. The molecular weight and size distribution (polydispersity index, PDI) were determined as 56 kDa and 1.7 by SEC analysis. The hydroxychloroquine amount on the polymer backbone was calculated as 8.2% by weight using ^{1}H NMR.

Table 3.3. Polymerization conditions of P(OEG/HCQ-C).

No	**Feed Ratio**		**Obtained Ratio**		**CTA**	**AIBN**	**Mn (kDa)**	**Mw/Mn (PDI)**
	OEG	HCQ	OEG	HCQ				
1	90	10	91.8	8.2	5	1	56	1.7

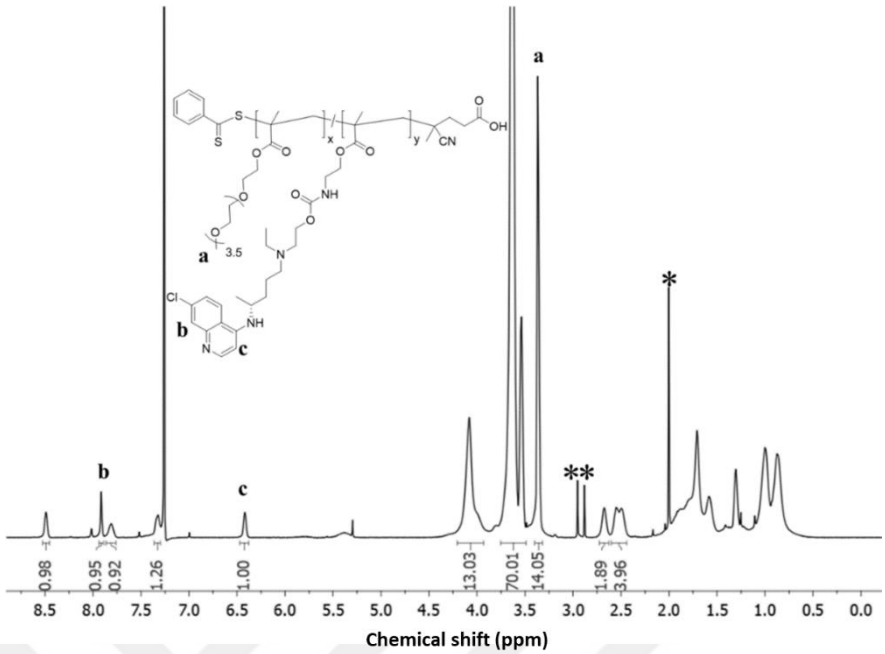

Figure 3.11. ^{1}H NMR spectrum of P(OEG/HCQ-C) copolymer ($CDCl_3$).

3.3.6. *In Vitro* Drug Release Study and Cytotoxicity of P(OEG/HCQ-C) Copolymer

After synthesis of P(OEG/HCQ-C) copolymer, HCQ release from the copolymer was evaluated in acidic and physiological pH values, esterase enzyme (PLE), and rat plasma. P(OEG/HCQ-C) copolymer was incubated with these release solutions, and samples were collected at predetermined intervals. HCQ % release was determined using LCMS analysis, and the release graph is given in Figure 3.12. At the end of 72 h, P(OEG/HCQ-C) copolymer released HCQ by 3.4% in pH = 5.4, 4.3% in pH 7.4, 1.1% in PLE enzyme, and 1.7% in rat plasma. Compared with the P(OEG/HCQ-E) copolymer, more HCQ release was observed with the carbamate-containing P(OEG/HCQ-C) copolymer. Although % HCQ release still remained under 10%, different HCQ release results were obtained when the linkage was switched from ester to carbamate.

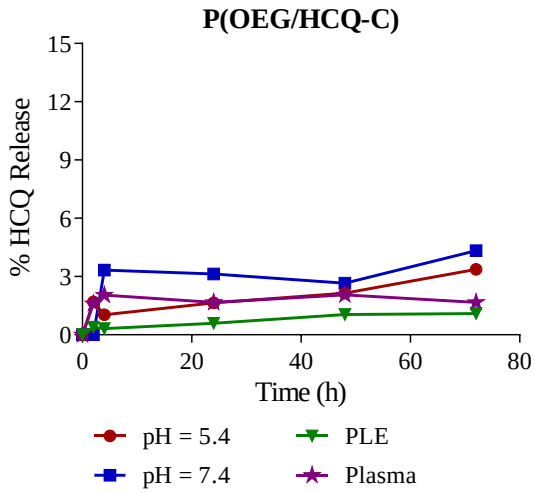

Figure 3.12. HCQ release profiles from P(OEG/HCQ-C) in pH = 5.4, pH = 7.4, PLE, and plasma at 37 ^{o}C for 72 h.

After that, the cytotoxicity of the P(OEG/HCQ-C) copolymer was explored toward BxPC-3 and Capan-1 cell lines. The cytotoxicity graph is given in Figure 3.13. We expected that the P(OEG/HCQ-C) copolymer would show more cytotoxic activity on cells because the HCQ release amount from the P(OEG/HCQ-C) copolymer was more than the P(OEG/HCQ-E) copolymer. At the end of 48 h incubation of cells with POEG/HCQ-C copolymer, EC_{50} values of the copolymer were determined as 8.87 x 10^{-6} M, and 1.77 x 10^{-5} M for BxPC-3 and Capan-1 cells, respectively and these values were tabulated in Table 3.4. Moreover, when we compared with the cytotoxicity result of the P(OEG/HCQ-E) copolymer, the (POEG/HCQ-C) copolymer showed more cytotoxicity towards BxPC-3 cells as expected. In addition to BxPC-3, two HCQ-based copolymers (ester and carbamate-containing) had almost the same EC_{50} values in Capan-1 cells.

Table 3.4. Calculated EC_{50} values of HCQ and P(OEG/HCQ-C) copolymer for pancreas cancer cell lines after 48 h incubation.

		EC_{50} (M)	
No	**Constructs**	**BxPC-3**	**Capan-1**
1	HCQ	2.54 x 10^{-6}	2.58 x 10^{-6}
2	P(OEG/HCQ-C)	8.87 x 10^{-6}	1.77 x 10^{-5}

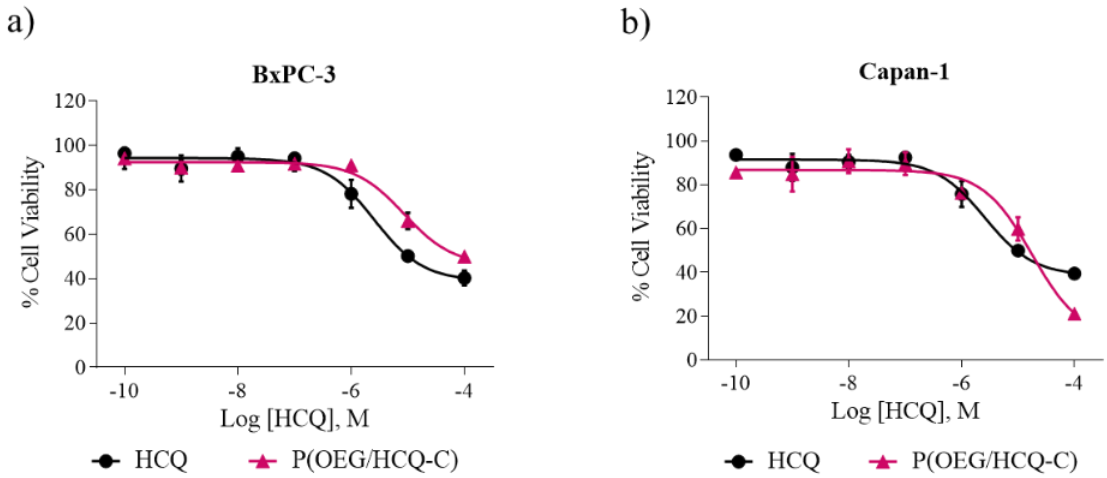

Figure 3.13. Cell viabilities of (a) BxPC-3 cells, (b) Capan-1 cells treated with free HCQ and P(OEG/HCQ-C) copolymer.

3.3.7. Synthesis of GEM-C-MA Monomer

The carbamate bond containing gemcitabine methacrylate monomer (GEM-MA-C) was synthesized in two steps. Firstly, succinimidyl carbonate-based monomer (SCEMA) was synthesized according to a published procedure [184]. Hydroxyl groups of gemcitabine were protected using chlorotrimethylsilane (TMS-CI) at 0 ^{o}C in pyridine-acetonitrile. The protected gemcitabine was used without isolation, and the reaction with SCEMA monomer was carried out for two days at 65 ^{o}C. GEM-C-MA was obtained in 52% yield after deprotection of hydroxyl groups with ethanol. The reaction is shown in Figure 3.14.

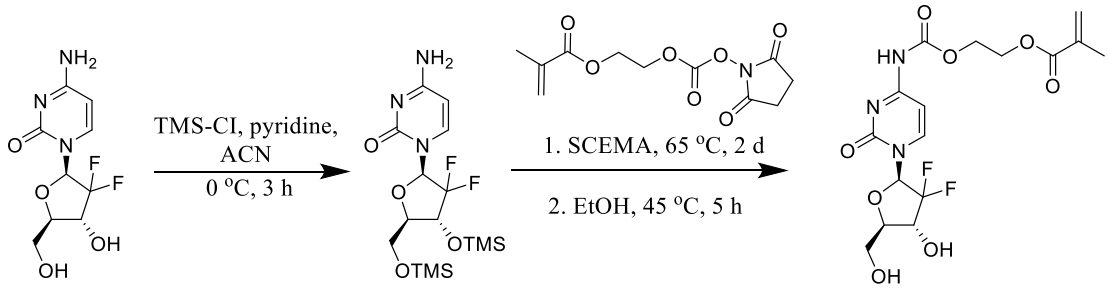

Figure 3.14. Synthetic pathway of GEM-MA-C monomer.

Analysis of the GEM-C-MA monomer was done via ^{1}H NMR. The full ^{1}H NMR is given in Figure 3.15. The proton resonances at 8.22 (e labeled) and 7.06 (d marked) ppm due to gemcitabine and the proton resonances at 6.04 and 5.70 ppm due to the terminal alkenyl hydrogens of the methacrylate group are evidence of the formation of GEM-C-MA monomer. ^{13}C NMR and FTIR spectra are given in Figure A.7 and Figure A.8.

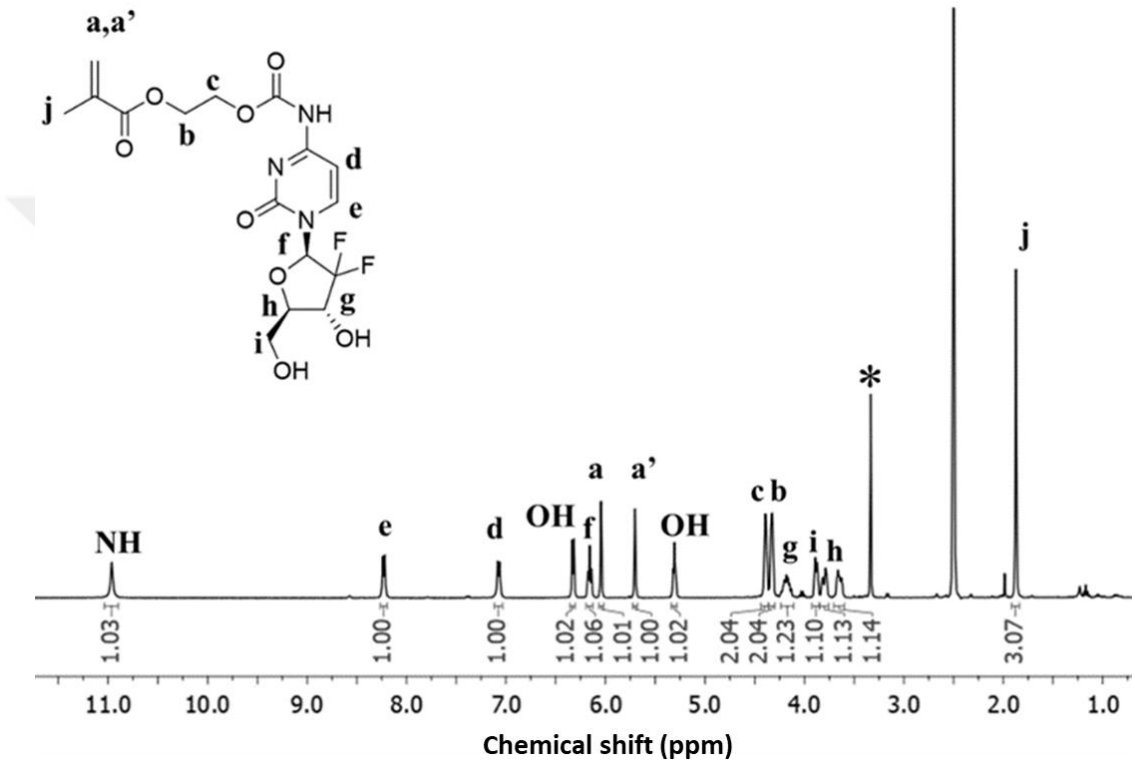

Figure 3.15. ^{1}H NMR spectrum of GEM-C-MA monomer (DMSO d6).

3.3.8. Synthesis of P(OEG/GEM-C) Copolymer via RAFT Polymerization

GEM anticancer drug was first introduced as a monomer using carbamate linkers. GEM-C-MA monomer was synthesized and polymerized with OEGMA by RAFT polymerization in the presence of AIBN and 4-cyano-4-(thiobenzoylthio)pentanoic acid as an initiator and chain transfer agent, and it was shown in Figure 3.16.

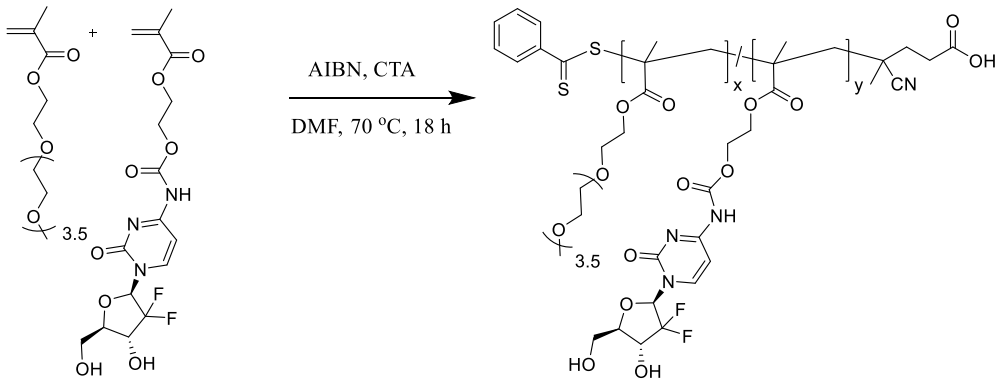

Figure 3.16. Synthesis of P(OEG/GEM-C) copolymer.

The P(OEG/GEM-C) copolymer was analyzed via ^{1}H NMR and SEC. ^{1}H NMR spectrum is given in Figure 3.17. The proton resonances at 10.76, 8.21, 7.10, 6.28, 6.16, and 5.24 ppm due to the gemcitabine unit, and the proton resonance at 3.25 ppm due to the terminal methyl ether group (-OCH_3) of POEGMA unit demonstrated that both gemcitabine and OEGMA existed together on the polymer backbone. The disappearance of proton resonances at 6.04 and 5.70 ppm due to the terminal alkenyl group of methacrylate groups of monomer was another proof of successful polymerization. To obtain P(OEG/GEM-C) copolymer, OEGMA and GEM-C-MA monomers were using a 90:10 feed ratio, which paved the way for P(OEG/GEM-C) with 94.7:5.3 chemical composition. The molecular weight and size distribution (polydispersity, PDI) were determined as 51 kDa and 1.4 via SEC analysis. GEM content on the polymer backbone was calculated as 5.3% by weight using the ratio of the proton integration of GEM and the proton integration of the methyl ether group of OEGMA in the ^{1}H NMR spectrum. The experimentally obtained monomer compositions of the P(OEG/GEM-C) demonstrate that the incorporation of the GEM-MA-C monomer is lower than targeted in the feed composition. The polymerization conditions and properties of P(OEG/GEM-C) conjugate are given in Table 3.5.

Table 3.5. Polymerization conditions of P(OEG/GEM-C).

No	**Feed Ratio**		**Obtained Ratio**		**CTA**	**AIBN**	**Mn (kDa)**	**Mw/Mn (PDI)**
	OEG	GEM	OEG	GEM				
1	90	10	94.7	5.3	5	1	51	1.4

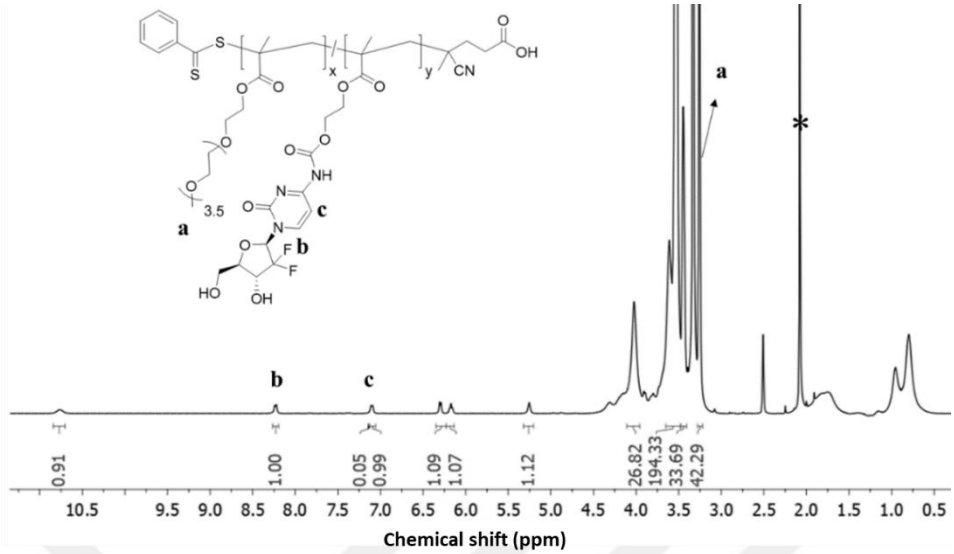

Figure 3.17. ^{1}H NMR spectrum of P(OEG/GEM-C) copolymer (DMSO d6).

3.3.9. *In Vitro* Drug Release Study and Cytotoxicity of P(OEG/GEM-C) Copolymer

P(OEG/GEM-C) copolymer, where GEM was conjugated to the polymer backbone via pH-responsive carbamate linker, was explored in terms of release profile and cytotoxicity. P(OEG/GEM-C) copolymer was incubated in pH = 5.4, pH = 7.4 buffers, PLE enzyme, GSH (10 mM), and rat plasma to explore GEM release from copolymer, and the amount of released GEM was determined by LCMS analysis. As seen in Figure 3.18, P(OEG/GEM-C) copolymer released GEM by 1.1 % in pH = 5.4, 0.78 % in pH = 7.4, 1.98% in PLE, 4.5% in plasma and 4.5% in GSH (10 mM) at the end of 72 h incubation.

After the release study, cytotoxicities of free GEM and P(OEG/GEM-C) copolymer were investigated against BxPC-3 and Capan-1 cells, and the results are represented in Figure 3.19. At the end of 48 h incubation, cell viability was determined via CCK-8 assay. While the EC_{50} value of free GEM was determined as 2.51 x 10^{-8} M, the EC_{50} value of the P(OEG/GEM-C) copolymer was calculated as 2.32 x 10^{-6} M against BxPC-3 cells. As for Capan-1 cells, EC_{50} values for free GEM and P(OEG/GEM-C) copolymer were found as 1.67 x 10^{-7} M and 4.89 x 10^{-5} M. Cytotoxicity results revealed that copolymer showed almost 100-fold less activity toward BxPC-3 cells when GEM was conjugated to the polymer backbone via carbamate linker, which was responsible for prolonged GEM release.

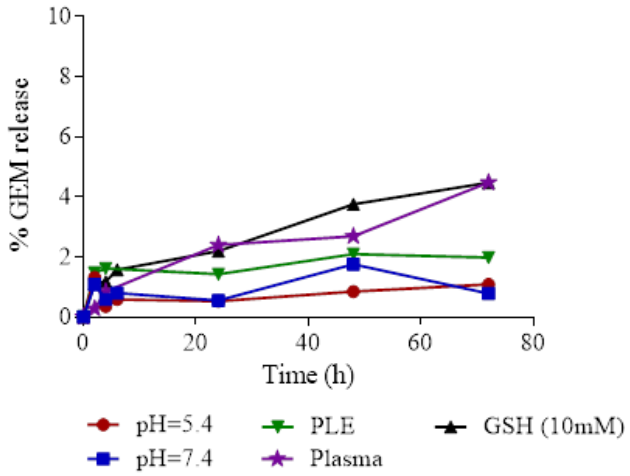

Figure 3.18. GEM release profiles from P(OEG/GEM-C).

Table 3.6. Calculated EC_{50} values of GEM and P(OEG/GEM-C) copolymer for pancreas cancer cell lines after 48 h incubation.

		EC_{50} (M)	
No	**Constructs**	**BxPC-3**	**Capan-1**
1	GEM	2.51×10^{-8}	1.67×10^{-7}
2	P(OEG/GEM-C)	2.32×10^{-6}	4.89×10^{-5}

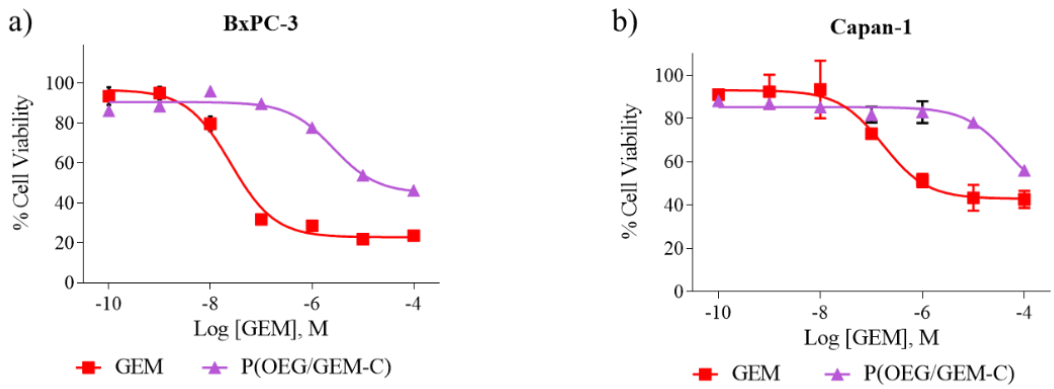

Figure 3.19. Cell viabilities of (a) BxPC-3 cells, (b) Capan-1 cells treated with free GEM and P(OEG/GEM-C) copolymer.

3.3.10. Synthesis of P(OEG/HCQ-E/GEM-C) Copolymer via RAFT Polymerization

After obtaining drug-containing monomers and one-drug-attached copolymers, two drug-attached copolymers were synthesized to find the best copolymer in release and cytotoxicity profiles. For this purpose, a P(OEG/HCQ-E/GEM-C) copolymer was synthesized using an HCQ-E-MA monomer. HCQ was attached to the methacrylate group via the ester linker and GEM-C-MA monomer, where GEM was bonded with the carbamate linker. The polymerization reaction was carried out at 70° C in anhydrous DMF via RAFT polymerization. The polymerization reaction is shown in Figure 3.20.

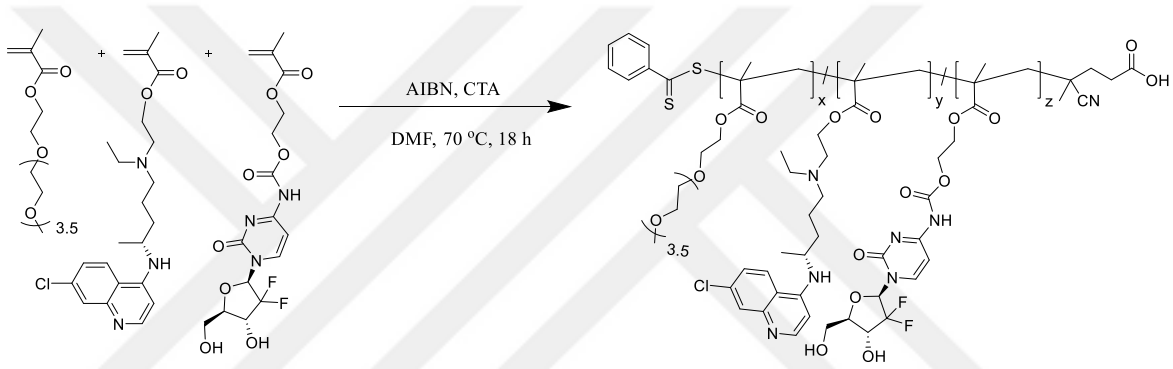

Figure 3.20. The synthesis of P(OEG/HCQ-E/GEM-C) copolymer.

Analysis of P(OEG/HCQ-E/GEM-C) was done using ^{1}H NMR and SEC. The proton resonances at 10.85, 8.35, 8.21, 7.77, 7.39, 7.08, 6.89, 6.45, 6.33, 6.16, and 5.17 due to both GEM and HCQ groups and the proton resonance at 3.24 ppm due to terminal methyl ether group of OEGMA unit showed successful polymerization. ^{1}H NMR spectrum of P(OEG/HCQ-E/GEM-C) was overlapped with that of the GEM-C-MA monomer to identify GEM peaks. The proton resonances at 8.21 (c labeled) and 7.08 (d marked) ppm came from gemcitabine. The proton resonances at 8.35, 7.77, 7.39, and 6.89 ppm were due to HCQ. The proton resonances at 6.04 and 5.70 due to the methacrylate group disappearing, as expected after polymerization. The molecular weight (Mn) and size distribution (polydispersity index, PDI) were determined as 50 kDa and 1.8, respectively, via SEC analysis. GEM and HCQ content on the polymer backbone were calculated as 8.1% and 13% by weight using proton integration in the ^{1}H NMR spectrum. The polymerization conditions

and properties of P(OEG/HCQ-E/GEM-C) conjugate are given in Table 3.7. ^{1}H NMR spectrum of P(OEG/HCQ-E/GEM-C) was demonstrated in Figure 3.21.

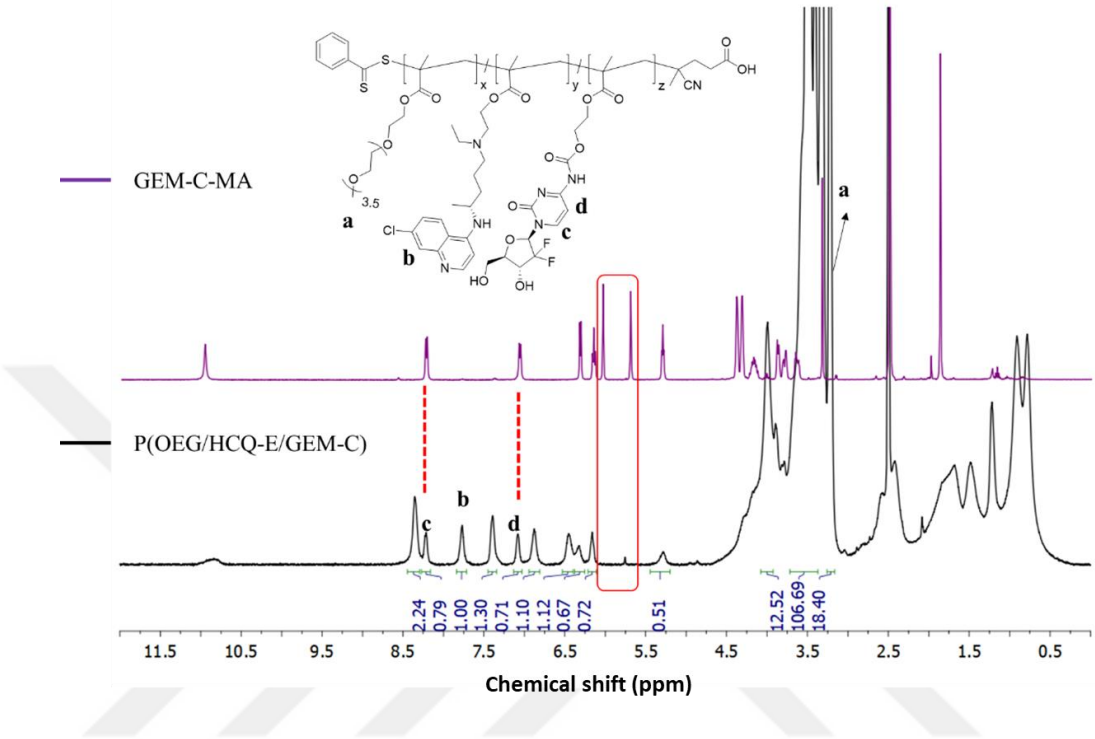

Figure 3.21. ^{1}H NMR spectra of GEM-C-MA monomer (purple line) and P(OEG/HCQ-E/GEM-C copolymer (black line) (DMSO d6).

Table 3.7. Polymerization conditions of P(OEG/HCQ-E/GEM-C).

No	Feed Ratio			Obtained Ratio			CTA	AIBN	Mn (kDa)	Mw/Mn (PDI)
	OEG	GEM	HCQ	OEG	GEM	HCQ				
1	60	20	20	78.9	8.1	13	5	1	50	1.8

3.3.11. *In Vitro* Drug Release Study and Cytotoxicity of P(OEG/HCQ-E/GEM-C) Copolymer

GEM and HCQ release profiles from P(OEG/HCQ-E/GEM-C) were investigated. Thus, acidic and neutral pH were used to examine the release of GEM and HCQ from the copolymer. PLE enzyme was used to be able to mimic cancer tissue. As seen in Figure 3.22, HCQ and GEM releases from the P(OEG/HCQ-E/GEM-C) copolymer were very low; they

remained under 5% in all conditions. The cytotoxicity of the combination of free GEM-HCQ and P(OEG/HCQ-E/GEM-C) copolymer was investigated toward BxPC-3 and Capan-1 cells. In BxPC-3 cells, whereas free GEM showed EC_{50} at 2.51 x 10^{-8} M, the combination of GEM-HCQ demonstrated EC_{50} at 2.42 x 10^{-8} M. P(OEG/HCQ-E/GEM-C) showed almost 100-fold less toxicity toward BxPC-3 cells, and it has an EC_{50} value of 4.53 x 10^{-6} M. The low cytotoxic activity could be attributed to very low GEM and HCQ release in the presence of carbamate and ester linkages. The cytotoxicity graph is given in Figure 3.23.

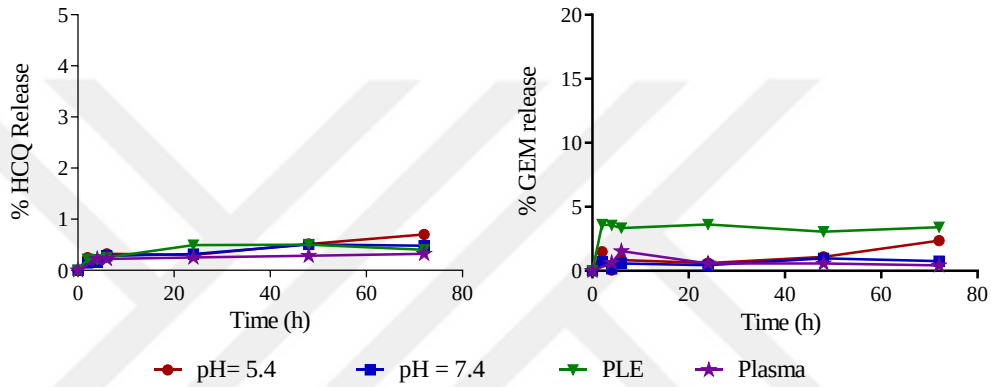

Figure 3.22. HCQ and GEM release from copolymer P(OEG/HCQ-E/GEM-C) at 37°C.

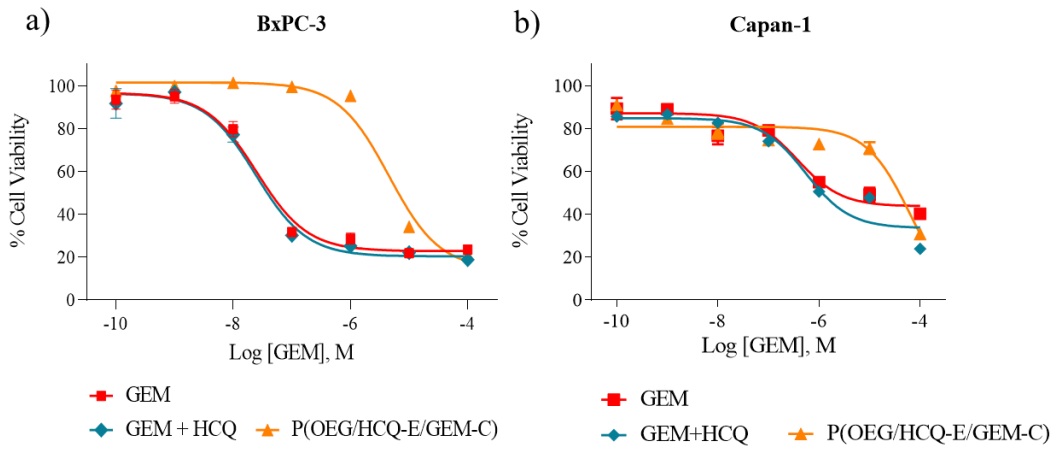

Figure 3.23. Cell viabilities of (a) BxPC-3 cells, (b) Capan-1 cells treated with free GEM, the combination of GEM-HCQ and P(OEG/HCQ-E/GEM-C).

Table 3.8. Calculated EC_{50} values of the combination of GEM-HCQ and P(OEG/HCQ-E/GEM-C) copolymer for pancreas cancer cell lines after 48 h incubation.

		EC_{50} (M)	
No	**Constructs**	**BxPC-3**	**Capan-1**
1	GEM+HCQ	2.42×10^{-8}	5.45×10^{-7}
2	P(OEG/HCQ-E/GEM-C)	4.53×10^{-6}	6.50×10^{-5}

3.3.12. Synthesis of P(OEG/HCQ-C/GEM-C) Copolymer via RAFT Polymerization

P(OEG/HCQ-C/GEM-C) copolymer was obtained via RAFT polymerization using HCQ-C-MA and GEM-C-MA, where both HCQ and GEM were conjugated to the monomer group via pH-responsive carbamate bond. The polymerization reaction was carried out at 70 ^{o}C in the presence of AIBN as an initiator and CTA as a chain transfer agent. The polymerization reaction is shown in Figure 3.24.

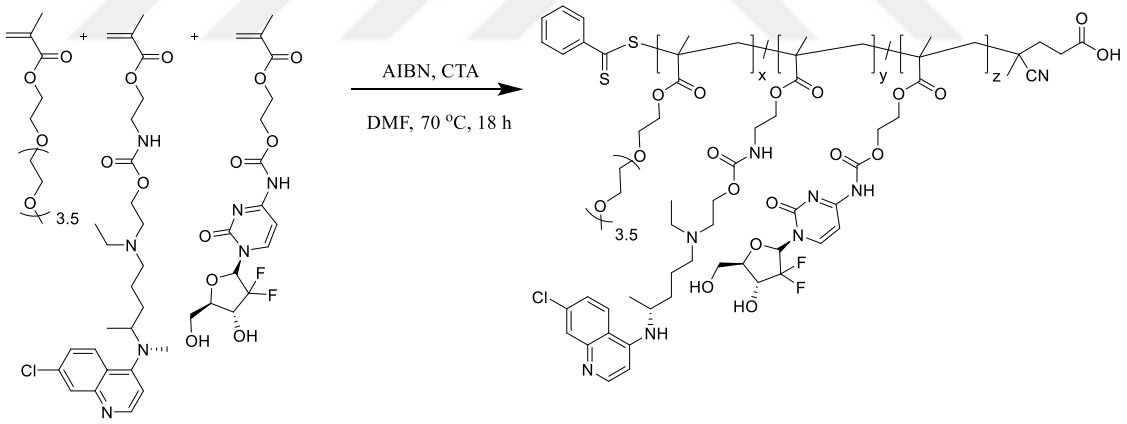

Figure 3.24. The synthesis of P(OEG/HCQ-C/GEM-C) copolymer.

The chemical composition and drug content of the P(OEG/HCQ-C/GEM-C) copolymer were determined using the ^{1}H NMR spectrum in Figure 3.25. The proton resonances 8.21 (c labeled) and 7.08 (d marked) were due to gemcitabine. In addition to these proton resonances, the proton resonance at 3.23 ppm due to the terminal methyl ether group of POEGMA and the disappearance of methacrylate alkenyl peaks at 6.04 and 5.70 ppm were evidence of successful polymerization. HCQ and GEM contents were calculated

as 12.9% and 10.7% by weight using proton integrations in the ^{1}H NMR spectrum. The polymerization conditions and properties of the copolymer were tabulated in Table 3.9.

Table 3.9. Polymerization conditions of P(OEG/HCQ-C/GEM-C).

No	**Feed Ratio**			**Obtained Ratio**			**CTA**	**AIBN**	**Mn (kDa)**	**Mw/Mn (PDI)**
	OEG	GEM	HCQ	OEG	GEM	HCQ				
1	60	20	20	76.4	10.7	12.9	5	1	55	1.9

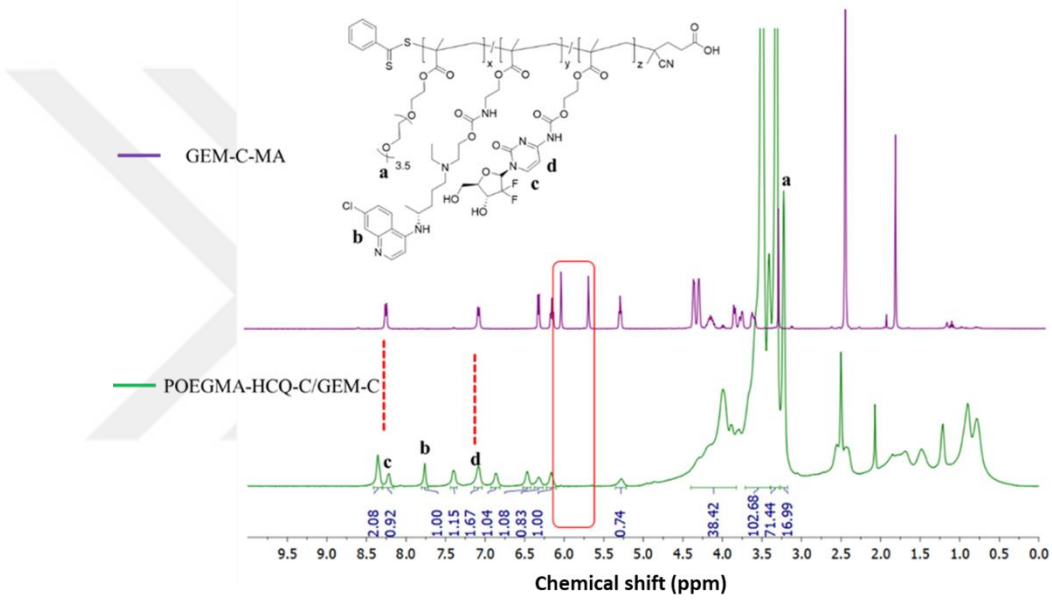

Figure 3.25. ^{1}H NMR spectra of GEM-C-MA monomer (purple line) and P(OEG/HCQ-C/GEM-C) copolymer (green line) (DMSO d6).

3.3.13. *In Vitro* Drug Release Study and Cytotoxicity of P(OEG/HCQ-C/GEM-C) Copolymer

As well as P(OEG/HCQ-E/GEM-C) copolymer, P(OEG/HCQ-C/GEM-C) copolymer was investigated in terms of drug release and cytotoxicity. Thus P(OEG/HCQ-C/GEM-C) copolymer was incubated with pH = 5.4, pH = 7.4, PLE enzyme, and plasma. The released drug amount was determined using LCMS analysis. However, the P(OEG/HCQ-C/GEM-C) copolymer showed no significant GEM and HCQ release. Due to low drug release, any improvement in cell cytotoxicity could not be obtained.

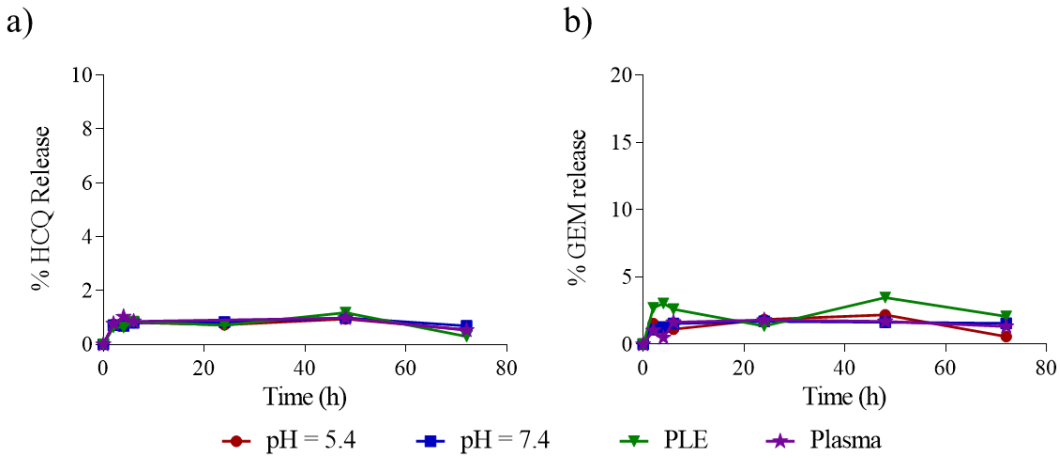

Figure 3.26. HCQ and GEM release from copolymer P(OEG/HCQ-C/GEM-C) at 37ºC.

Effects of free GEM and HCQ alone, the combination of GEM-HCQ and P(OEG/HCQ-C/GEM-C) copolymer were evaluated on pancreatic cancer cell lines (BxPC-3, Capan-1, Panc-1) via CCK-8 assay. Cytotoxicity results were given in Figure 3.27, and EC_{50} values were tabulated in Table 3.10. While free GEM and GEM-HCQ mixture were highly toxic toward BxPC-3 cells, the cytotoxicity of P(OEG/HCQ-C/GEM-C) was approximately 400-fold less toxic than that of the HCQ-GEM mixture. Apart from BxPC-3 and Capan-1 cells, free drugs and P(OEG/HCQ-C/GEM-C) were applied to Panc-1 cells. Even drug high concentrations, Panc-1 cells showed drug resistance, and the viability of Panc-1 cells remained at almost 75-80%.

Table 3.10. Calculated EC_{50} values of the combination of GEM-HCQ and P(OEG/HCQ-E/GEM-C) copolymer for pancreas cancer cell lines after 48 h incubation.

		EC_{50} (M)		
No	**Constructs**	**BxPC-3**	**Capan-1**	**Panc-1**
1	GEM	2.51×10^{-8}	1.67×10^{-7}	8.67×10^{-7}
2	HCQ	2.54×10^{-6}	2.58×10^{-6}	$>10^{-5}$
3	GEM+HCQ	2.42×10^{-8}	5.45×10^{-7}	4.05×10^{-7}
4	P(OEG/HCQ-C/GEM-C)	3.89×10^{-5}	$>10^{-5}$	1.84×10^{-5}

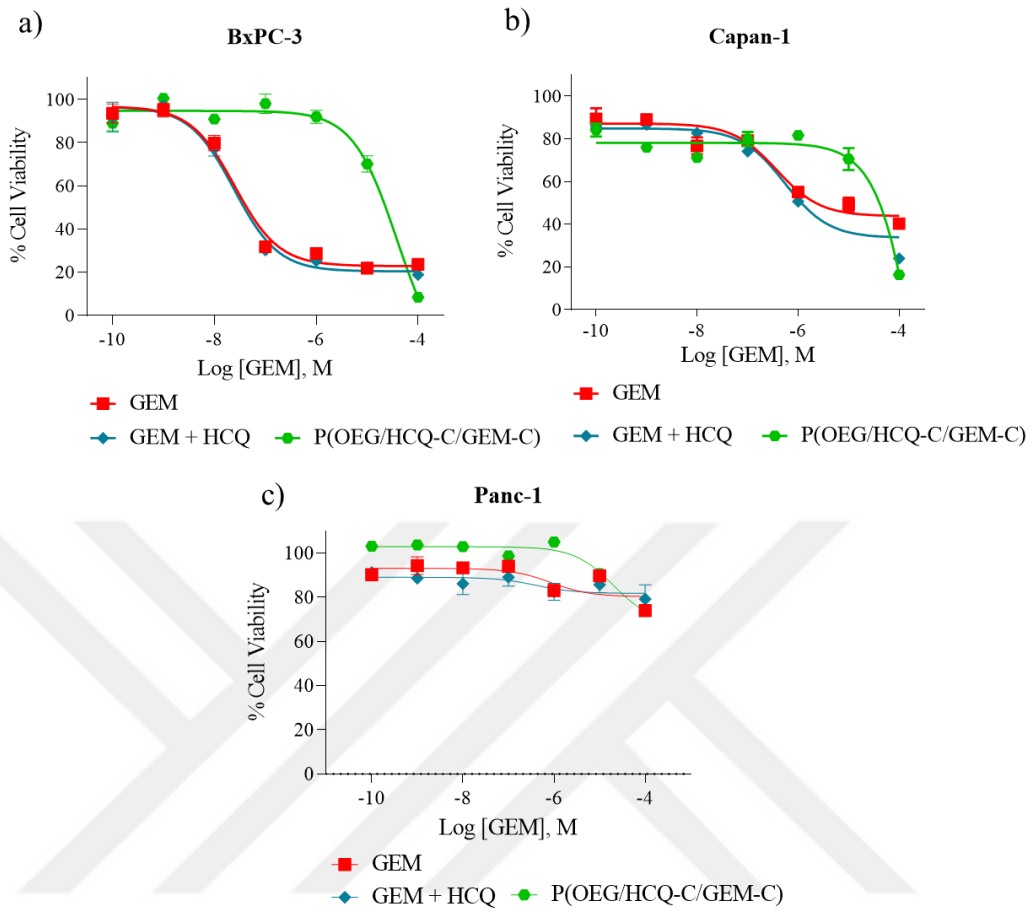

Figure 3.27. Cell viabilities of (a) BxPC-3 cells, (b) Capan-1 cells, and (c) Panc-1 cells, treated with free GEM, the combination of GEM-HCQ and P(OEG/HCQ-E/GEM-C).

3.3.14. Synthesis of Disulfide-Carbamate Containing Gemcitabine Monomer

Redox-responsive disulfide-carbamate (SSC) containing gemcitabine methacrylate monomer (GEM-SSC-MA) was prepared in three steps. In the first step, the HSEMA monomer was obtained using bis(2-hydroxyethyl) disulfide and methacryloyl chloride [185]. After synthesizing the HSEMA monomer, the NHS-activated HSEMA monomer was synthesized using disuccinimidyl carbonate (DSC) [186]. Finally, hydroxyl groups of GEM were protected with TMS groups, and the GEM-SSC-MA monomer was synthesized using NHS-HSEMA, and TMS protected GEM in pyridine at 65 ^{o}C for two days. After two days, TMS groups were deprotected using ethanol, and the GEM-SSC-MA monomer was obtained with a 53 % yield. The reaction pathway is shown in Figure 3.28.

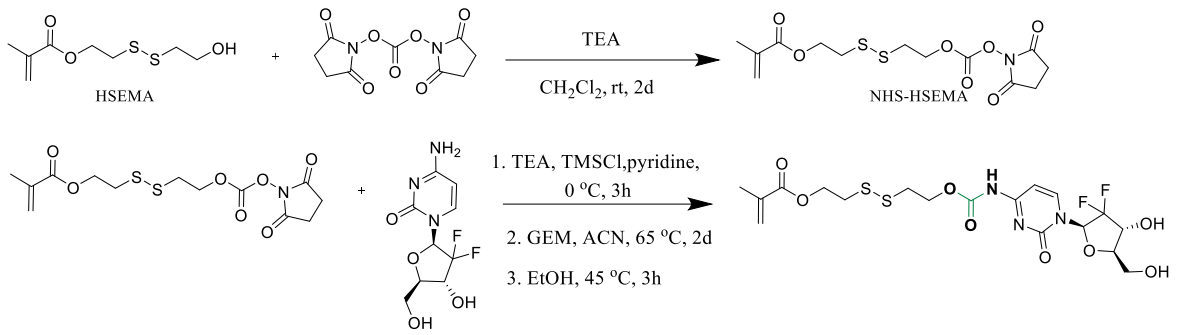

Figure 3.28. Synthetic pathway of disulfide-carbamate bond containing GEM-SSC-MA monomer.

The GEM-SSC-MA monomer was analyzed using ^{1}H NMR and ^{13}C NMR spectroscopies and FTIR analysis. The full ^{1}H NMR spectrum is shown in Figure 3.29. The proton resonances at 8.23 (b labeled) and 7.09 (c labeled) ppm come from gemcitabine. The proton resonances at 6.04 and 5.70 ppm were due to the terminal alkenyl hydrogens, and the proton resonance at 1.07 ppm due to hydrogens of the methyl group was due to the methacrylate group. These are evidence of the formation of the GEM-SSC-MA monomer. ^{13}C NMR and FTIR spectra are given in Figure A.9 and Figure A.10.

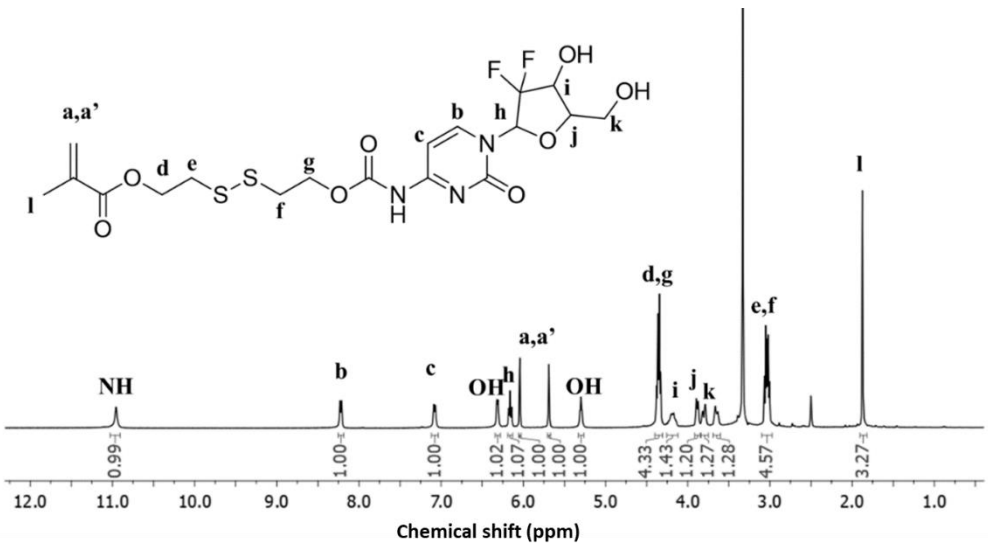

Figure 3.29. ^{1}H NMR spectrum of GEM-SSC-MA monomer (DMSO d6).

3.3.15. Synthesis of Disulfide-Carbamate Containing Gemcitabine Monomer

Disulfide exists in many natural organisms. Due to its reversibility, disulfide bonds can be easily degraded, and they can form free thiols after degradation in the presence of reducing agents such as glutathione (GSH) and DTT. Glutathione is the most abundant intracellular thiolated molecule. In living organisms, GSH and glutathione disulfide (GS-SG) play an essential role in regulating intracellular redox homeostasis and protecting organisms from oxidative stress [30]. The GSH concentration ranges from 2-10 μM in blood to 1-10 mM within the cytosol. Moreover, the GSH level is higher than that of healthy tissues [31]. Whereas GSH levels were found 100-fold high inside tumor mass, they were found 7-fold high in cancer cells. Increased GSH levels are relevant in regulating carcinogenic mechanisms, cell proliferation and tumor development, drug resistance, and DNA synthesis [188]. Therefore, the GSH level has been recognized as a biomarker for tumor formation and development [189]. Along with this knowledge, a disulfide-carbamate containing GEM-SSC-MA monomer was designed. This monomer contains two carbon spacers between disulfide and carbamate linkers. When it is incubated with GSH, disulfide starts to degrade, and sulfur anion attacks into a carbamate bond. After that, the thermodynamically stable 5-membered ring appears, and the drug or other conjugated analyte cleaves from the structure [190]. A possible cleavage mechanism of the disulfide-carbamate bond is given in Figure 3.30.

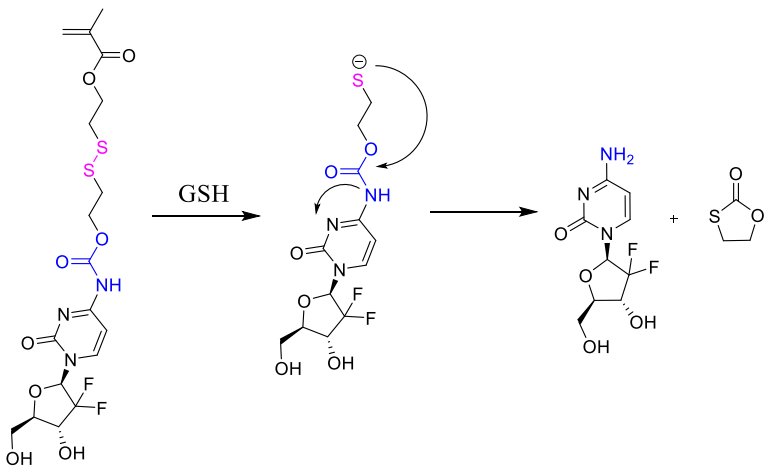

Figure 3.30. Cleavage mechanism of disulfide-carbamate linkage in the presence of GSH.

3.3.16. Synthesis of P(OEG/GEM-SSC) Copolymer via RAFT Polymerization

Disulfide-carbamate containing P(OEG/GEM-SSC) copolymer was synthesized using OEGMA and GEM-SSC-MA monomers via RAFT polymerization in the presence of CTA and AIBN in anhydrous DMF at 70 ^{o}C. After dialysis, the pure copolymer was obtained. Now, our copolymer consisted of redox-responsive disulfide and pH-responsive carbamate bonds. The polymerization is given in Figure 3.31.

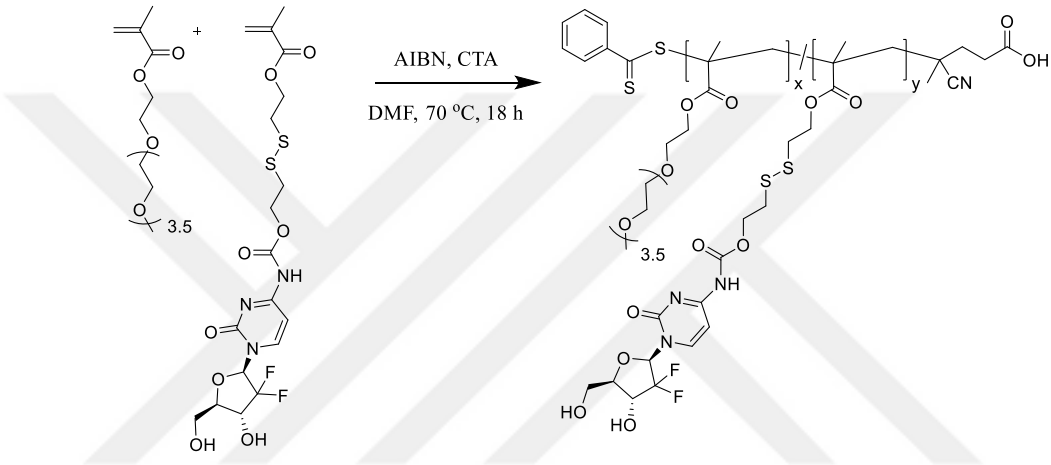

Figure 3.31. Synthesis of P(OEG/GEM-SSC) copolymer.

The P(OEG/GEM-SSC) copolymer was analyzed using ^{1}H NMR and SEC. The full spectrum is given in Figure 3.32. The proton resonances at 10.93, 8.21, 7.08, 6.29, 6.16, and 5.26 ppm came from the gemcitabine drug. The proton resonance at 3.24 ppm was due to the terminal methyl ether group (-OCH_3) of the P(OEGMA) unit. In addition, the resonances of the terminal alkenyl group of methacrylate units at 6.04 and 5.70 ppm disappeared after the polymerization reaction. All these changes demonstrated successful polymerization between GEM-SSC-MA and OEGMA. To target copolymer, OEGMA and GEM-SSC-MA monomers were using an 80:20 feed ratio, and it paved the way to P(OEG/GEM-SSC) copolymer with 87.7:12.3 chemical composition. This chemical composition was determined using ^{1}H NMR spectrum. The molecular weight and size distribution (polydispersity index, PDI) were determined as 53 kDa and 1.5 via SEC analysis. GEM content on the polymer backbone was calculated as 12.3% by weight using the ratio of the proton integration of GEM and the proton integration of the methyl ether group of OEGMA.

The polymerization conditions and properties of P(OEG/GEM-SSC) was tabulated in Table 3.11.

Table 3.11. Polymerization conditions of P(OEG/GEM-SSC).

No	Feed Ratio		Obtained Ratio		CTA	AIBN	Mn (kDa)	Mw/Mn (PDI)
	OEG	GEM	OEG	GEM				
1	80	20	87.7	12.3	5	1	53	1.5

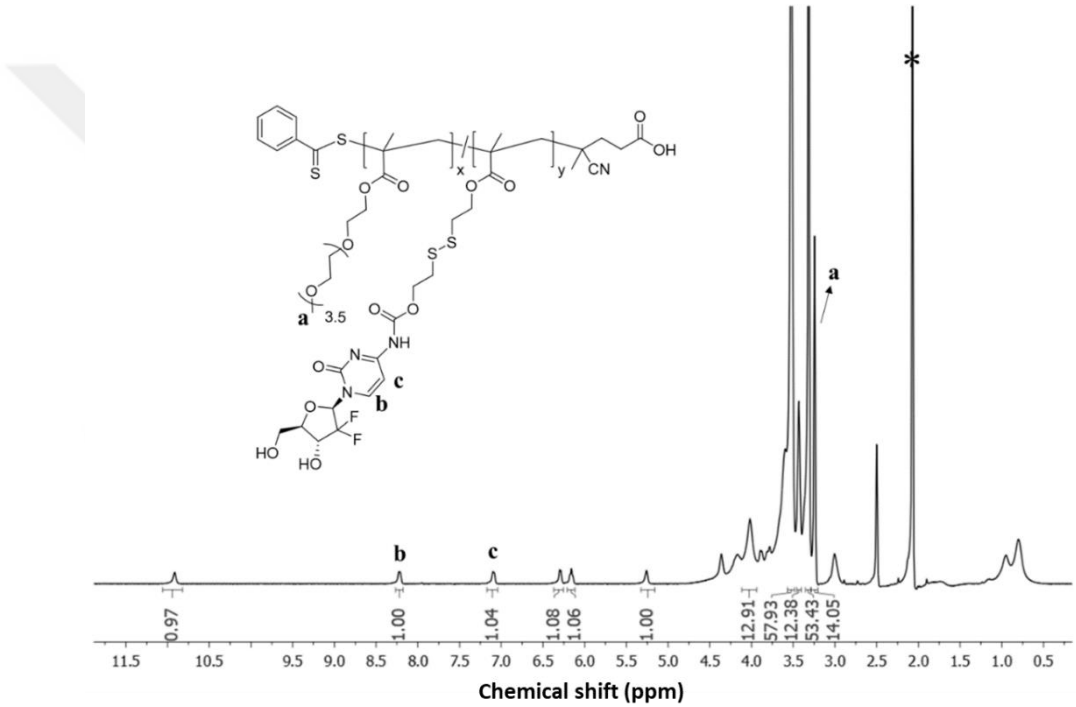

Figure 3.32. ^{1}H NMR spectrum of P(OEG/GEM-SSC) (DMSO d6).

3.3.17. *In Vitro* Drug Release Study and Cytotoxicity of P(OEG/GEM-SSC) Copolymer

For the drug release study, P(OEG/GEM-SSC) solutions were incubated separately in pH = 5.4, pH = 7.4, rat plasma, esterase enzyme from the porcine liver (PLE), and GSH (10 mM). To our best knowledge, GSH is a reducing agent and disulfide bond cleavages in the presence of GSH [191,192]. Since cancer cells and tumor regions contain high concentrations of GSH [31], [188], and esterase enzyme [193], the GEM release profile was

also investigated in the mixture of GSH-PLE to mimic the cancer cell and tumor environment. The GEM release graph is shown in Figure 3.33. Since the copolymer included disulfide and carbamate linkers, more GEM release from P(OEG/GEM-SSC) was expected in the presence of GSH due to the degradation of the disulfide linker. As expected, high GEM release profiles from P(OEG/GEM-SSC) were observed in the combination of PLE-GSH (98%) at the end of 3 days. However, the released GEM amount was 61% and 7% in only GSH and PLE, respectively. To show the importance of the disulfide bond, P(OEG/GEM-C), where GEM was linked with a carbamate bond, was incubated in the GSH solution. A small amount of GEM release (4.5%) was observed. In conclusion, the fabrication of GEM-SSC based copolymer provided us high GEM release as requested.

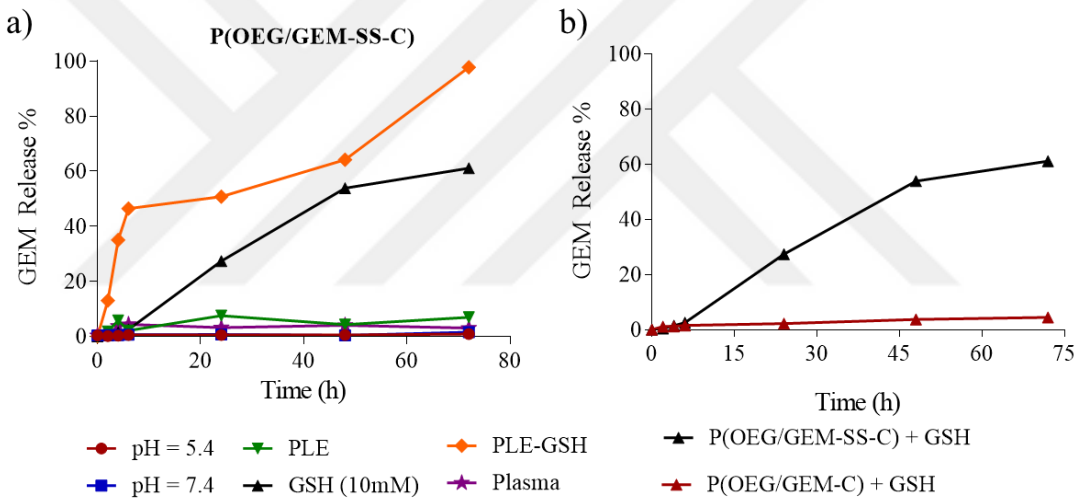

Figure 3.33. (a) GEM release profile from P(OEG/GEM-SSC at 37 ºC, (b) comparison of GEM release ratio between P(OEG/GEM-SSC) and P(OEG/GEM-C) in the presence of GSH.

After obtaining efficient GEM release results, the cytotoxicity of the P(OEG/GEM-SSC) copolymer was explored on BxPC-3 and Capan-1 cells. P(OEG/GEM-SSC) copolymer possessed EC_{50} values at 6.90 x 10^{-7} and 5.08 x 10^{-6} M towards BxPC-3 and Capan-1 cells. Thus, when GEM was conjugated with the disulfide-carbamate linkage to the polymer backbone, cytotoxic activity was lost only 10-fold. Cytotoxicities of P(OEG/GEM-SSC) and P(OEG/GEM-C) copolymer were compared, and it was found that P(OEG/GEM-SSC) copolymer was approximately 4-fold more toxic than P(OEG/GEM-C) copolymer on

BxPC-3 cells. These dramatic cytotoxicity differences resulted from high GEM release after disulfide degradation in the cell environment. The cytotoxicity graph and EC_{50} values are given in Figure 3.34 and Table 3.12.

Table 3.12. Calculated EC_{50} values of GEM, P(OEG/GEM-SSC), and P(OEG/GEM-C) copolymer for pancreas cancer cell lines after 48 h incubation.

		EC_{50} (M)	
No	**Constructs**	**BxPC-3**	**Capan-1**
1	GEM	2.51×10^{-8}	1.67×10^{-7}
2	P(OEG/GEM-C)	2.32×10^{-6}	4.89×10^{-5}
3	P(OEG/GEM-SSC)	6.50×10^{-7}	5.08×10^{-6}

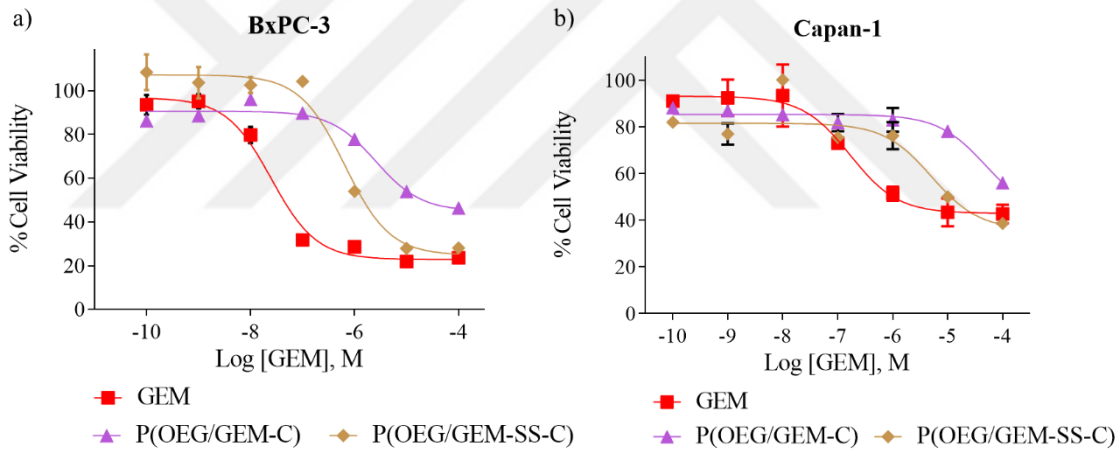

Figure 3.34. Cytotoxicity results of (a) BxPC-3 cells and (b) Capan-1 cells treated with free GEM, P(OEG/GEM-C), and P(OEG/GEM-SSC).

In conclusion, the first GEM-based copolymer had a carbamate linker between GEM and polymer backbone. Due to low GEM release, cytotoxicity was observed only at high drug concentrations. After the tumor study with the P(OEG/HCQ-C/GEM-C) copolymer, we decided to change linkers between HCQ and GEM. Therefore, we fabricated a new GEM-based monomer containing a disulfide bond, which was fabricated and synthesized and, subsequently, copolymerized. High GEM release from P(OEG/GEM-SSC) was observed in the presence of GSH. In addition, high cytotoxicity was gained using GEM

release thanks to disulfide degradation. With this knowledge, we have decided to synthesize a new GEM-HCQ-based copolymer on which HCQ will be linked with the carbamate linker while GEM will be attached using the disulfide-carbamate bond. We will explore drug release and cellular cytotoxicity.

3.3.18. Synthesis of P(OEG/HCQ-C/GEM-SSC) Copolymer via RAFT Polymerization

P(OEG/HCQ-C/GEM-SSC) copolymer was obtained via RAFT polymerization using HCQ-C-MA and GEM-C-MA, where HCQ was conjugated to the polymer backbone via pH-responsive carbamate linker, whereas GEM was attached to the polymer via redox responsive disulfide-carbamate linker. The polymerization was carried out at 70 ^{o}C in the presence of AIBN as an initiator and CTA as a chain transfer agent. The polymerization reaction is shown in Figure 3.35.

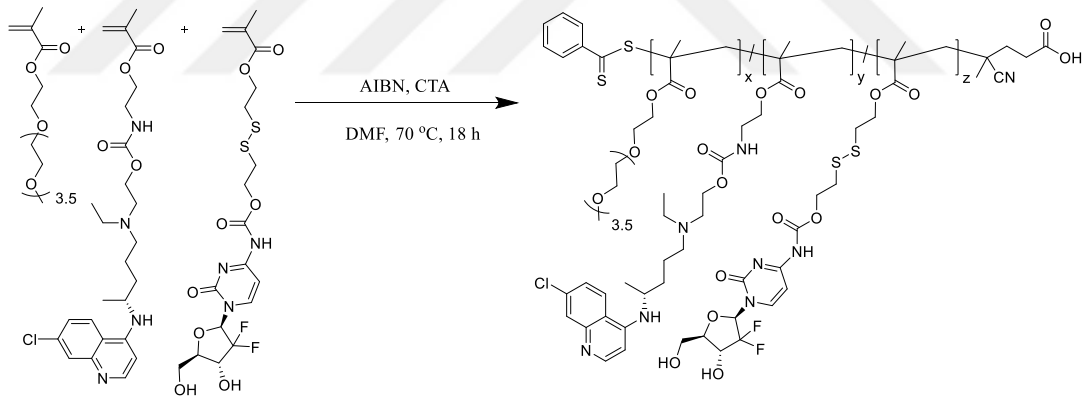

Figure 3.35. The polymerization reaction of P(OEG/HCQ-C/GEM-SSC).

The chemical composition and drug content of the P(OEG/HCQ-C/GEM-SSC) copolymer were determined using ^{1}H NMR spectrum, and the full ^{1}H NMR spectrum was given in Figure 3.36. The proton resonances coming from GEM and HCQ appeared at 10.97, 8.37, 8.24, 7.96, 7.77, 7.42, 7.10, 6.88, 6.48, 6.33, 6.17, and 5.30. In addition, the proton resonance at 3.24 ppm due to the terminal methyl ether group of POEGMA and the disappearance of methacrylate alkenyl peaks at 6.04 and 5.70 ppm were evidence of

successful polymerization and chemical composition. The polymerization conditions and properties of the copolymer were tabulated in Table 3.13.

Table 3.13. Polymerization conditions and properties of P(OEG/HCQ-C/GEM-SSC).

No	Feed Ratio			Obtained Ratio			CTA	AIBN	Mn (kDa)	Mw/Mn (PDI)
	OEG	GEM	HCQ	OEG	GEM	HCQ				
1	60	20	20	80.9	8.7	10.4	5	1	50	1.7

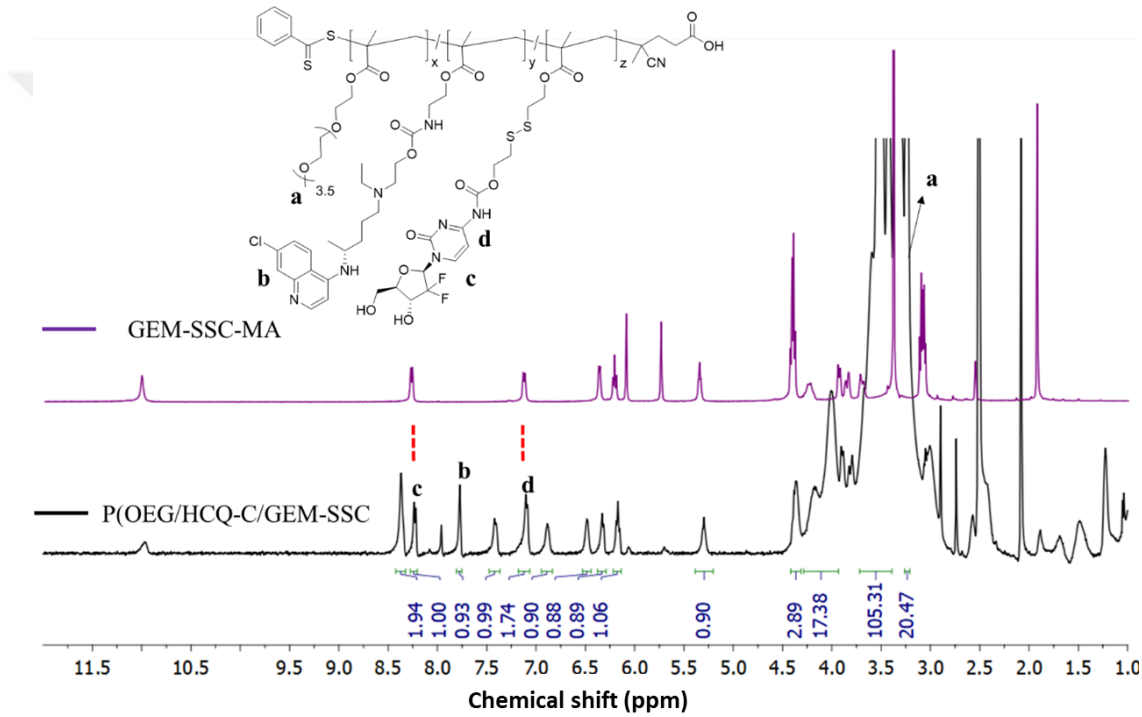

Figure 3.36. ^{1}H NMR spectra of GEM-SSC-MA monomer (purple line) and P(OEG/HCQ-C/GEM-SSC) copolymer (black line) (DMSO d6).

3.3.19. *In Vitro* Drug Release Study and Cytotoxicity of P(OEG/HCQ-C/GEM-SSC) Copolymer

HCQ and GEM release profiles from P(OEG/HCQ-C/GEM-SSC) copolymer were examined in pH = 5.4 and pH = 7.4 buffers, only PLE enzyme, only GSH (10 mM), a mixture of PLE-GSH and plasma. The release graphs are given in Figure 3.37. As seen in Figure 3.37, HCQ release ratios from the P(OEG/HCQ-C/GEM-SSC) copolymer were very low

because of the carbamate linker in all release conditions. The same results were obtained from the P(OEG/HCQ-C) copolymer and the P(OEG/HCQ-C/GEM-C) copolymer. On the other hand, high GEM release profiles (B) from P(OEG/HCQ-C/GEM-SSC) copolymer were recorded in only GSH and a mixture of PLE-GSH. Whereas GEM release reached 83% in GSH (10 mM), the release of GEM was observed by 90% at the end of 72 h. In addition, GEM releases were observed by 20% and 15% in plasma and PLE enzyme, respectively. Low drug release in plasma is crucial for us. When a drug-conjugated polymer was injected into a mouse intravenously, copolymer accumulation in the tumor generally takes 24-30 hours. At this time, less amount of drug can reach into target site because of undesirable drug release in mouse plasma. Our P(OEG/HCQ-C/GEM-SSC) copolymer showed GEM release by 5% in plasma at 48 h.

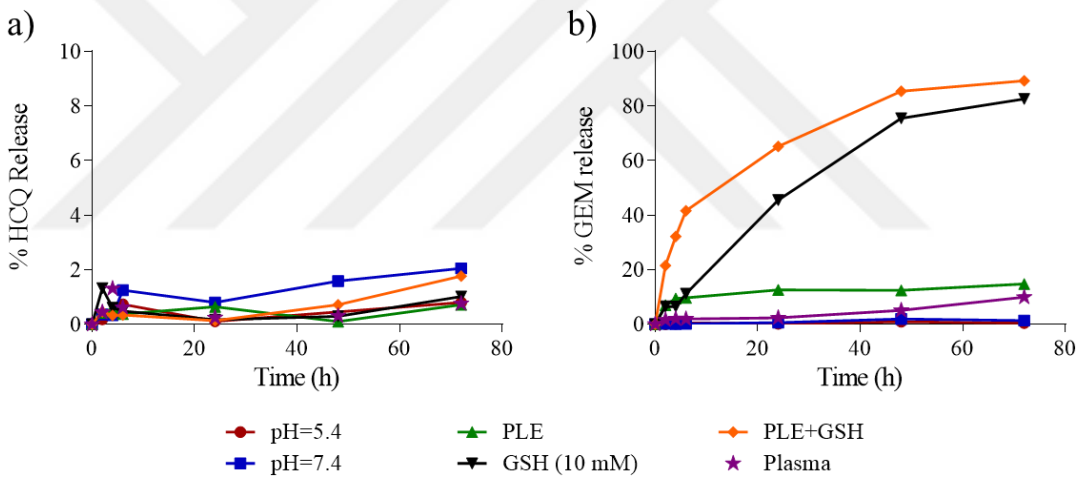

Figure 3.37. (a) HCQ release profiles, and (b) GEM release profiles from P(OEG/HCQ-C/GEM-SSC) at 37 ^{o}C.

The cytotoxicity evaluations with GEM, GEM-HCQ, and P(OEG/HCQ-C/GEM-SSC) showed high cytotoxicity against BxPC-3 cells. The EC_{50} value for P(OEG/HCQ-C/GEM-SSC) copolymer was calculated as 5.09 x 10^{-8} M. There was only an almost 2-fold cytotoxicity difference between free GEM-HCQ and copolymer. As for Capan-1 cells, EC_{50} was determined as 7.84 x 10^{-7} M, and copolymer was approximately 1.4-fold less toxic than free GEM-HCQ. Furthermore, despite nearly the same GEM release ratio, P(OEG/HCQ-C/GEM-SSC) was almost 10-fold more cytotoxic than P(OEG/GEM-SSC). It was

envisioned that even though the P(OEG/HCQ-C/GEM-SSC) copolymer did not show any significant HCQ release, the presence of HCQ led to high cytotoxicity with GEM. Cytotoxicity profiles are given in Figure 3.38.

Table 3.14. Calculated EC_{50} values of GEM-HCQ and P(OEG/GEM-SSC) copolymer for pancreas cancer cell lines after 48 h incubation.

		EC_{50} (M)	
No	**Constructs**	**BxPC-3**	**Capan-1**
1	GEM	2.51×10^{-8}	1.67×10^{-7}
2	GEM-HCQ	2.42×10^{-8}	5.45×10^{-7}
3	P(OEG/GEM-SSC)	5.09×10^{-8}	8.59×10^{-6}

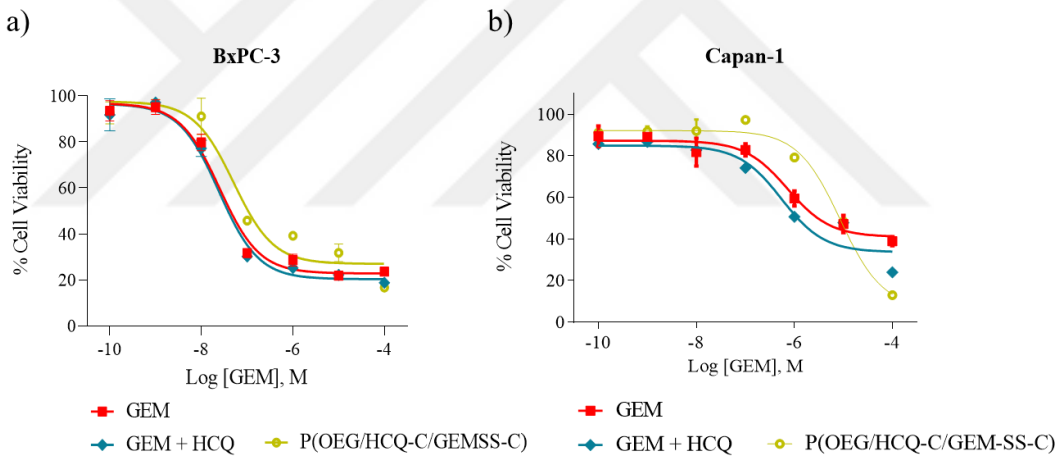

Figure 3.38. Cell viabilities of (a) BxPC-3 cells and (b) Capan-1 cells, treated with free GEM, GEM-HCQ, and P(OEG/HCQ-C/GEM-SSC).

In conclusion, we gained high cellular cytotoxicity at low concentrations despite very low HCQ release from P(OEG/HCQ-C/GEM-SSC). P(OEG/GEM-SSC) and P(OEG/HCQ-C/GEM-SSC) copolymers contain disulfide linkers between GEM and polymer backbone. HCQ release ratio from P(OEG/HCQ-C/GEM-SSC) was under 5%. Hence, the P(OEG/HCQ-C/GEM-SSC) copolymer was nearly the same as the P(OEG/GEM-SSC) in release profiles. On the other hand, their cytotoxicity profiles were different. P(OEG/HCQ-C/GEM-SSC) copolymer was 13-fold more toxic than P(OEG/GEM-SSC) toward BxPC-3

cells. If so, HCQ may release from P(OEG/HCQ-C/GEM-SSC) copolymer inside the cell, and HCQ may show toxicity with GEM towards BxPC-3 cells. Therefore, we decide to explore HCQ release from the copolymer. For this purpose, the carbamate linkage between HCQ and polymer backbone will be changed.

3.3.20. Synthesis of HCQ-CB-MA Monomer

Until now, two different hydroxychloroquine methacrylate monomers have been synthesized. One was composed of an ester linkage between HCQ and polymerizable methacrylate unit. Another monomer included a carbamate linker between HCQ and the methacrylate unit. HCQ-based copolymers from these monomers showed very low HCQ release and less cytotoxicity. Carbonate linker containing hydroxychloroquine methacrylate monomer were fabricated. Carbonate (CB) linker containing hydroxychloroquine methacrylate (HCQ-CB-MA) monomer was synthesized using succinimidyl-based SCEMA monomer [184] and neutralized HCQ in the presence of pyridine in 42% yield. The reaction is shown in Figure 3.39.

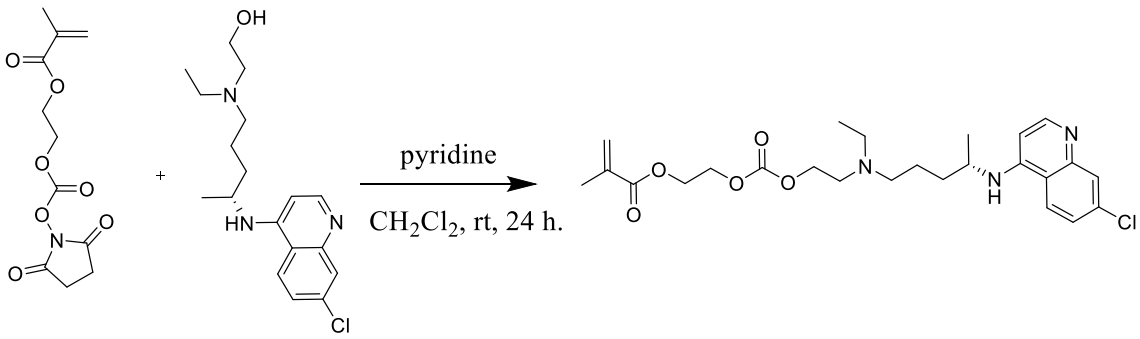

Figure 3.39. The synthesis of HCQ-CB-MA monomer via carbonate linker.

HCQ-CB-MA monomer via carbonate (CB) linker was characterized by ^{1}H NMR spectroscopy, and the full spectrum was given in Figure 3.40. The ^{1}H NMR spectrum was composed of the aromatic proton resonances due to hydroxychloroquine at 8.50, 7.94, 7.67, 7.36, and 6.45 ppm, and the terminal alkenyl proton resonances thanks to the methacrylate group at 6.09 and 5.55 ppm. ^{13}C NMR and FTIR spectra are given in Figure A.5 and Figure A.6.

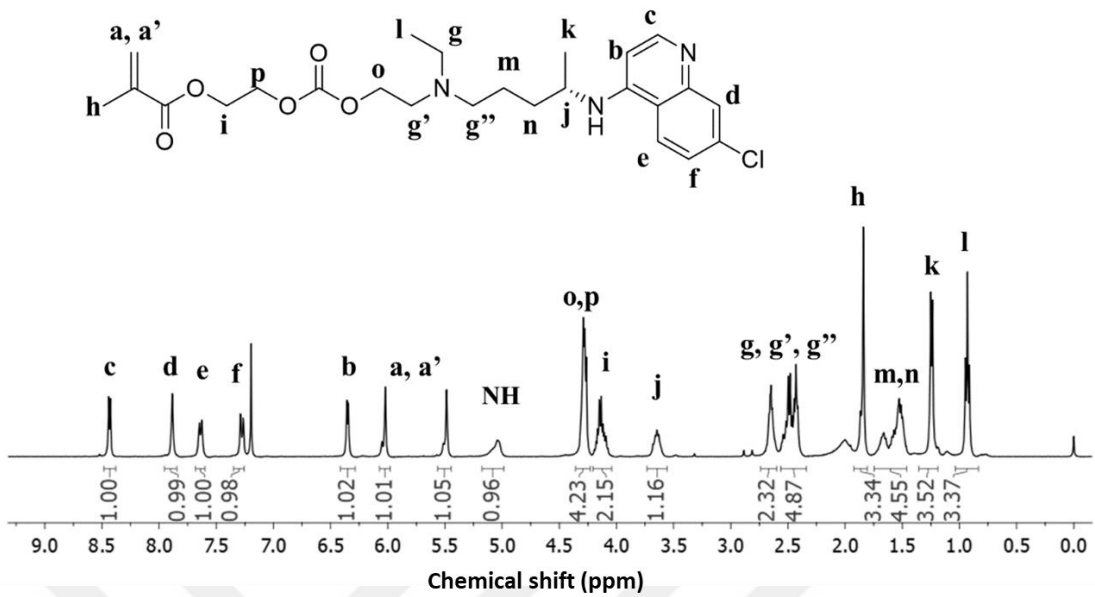

Figure 3.40. ^{1}H NMR spectrum of HCQ-CB-MA monomer in $CDCl_3$.

3.3.21. Synthesis of P(OEG/HCQ-CB) Copolymer via RAFT Polymerization

P(OEG/HCQ-CB) copolymer was obtained by using OEGMA and carbonate bond (CB) containing HCQ-CB-MA monomers via RAFT polymerization in the presence of AIBN and 4-cyano-4-(thiobenzoylthio)pentanoic acid (CTA). The polymerization reaction was carried out in DMF at 70 ^{o}C for 18 h. The polymerization reaction is shown in Figure 3.41.

Table 3.15. Polymerization conditions of P(OEG/HCQ-CB).

No	**Feed Ratio**		**Obtained Ratio**		**CTA**	**AIBN**	**Mn (kDa)**	**Mw/Mn (PDI)**
	OEG	HCQ	OEG	HCQ				
1	90	10	94.6	5.4	5	1	57	1.7

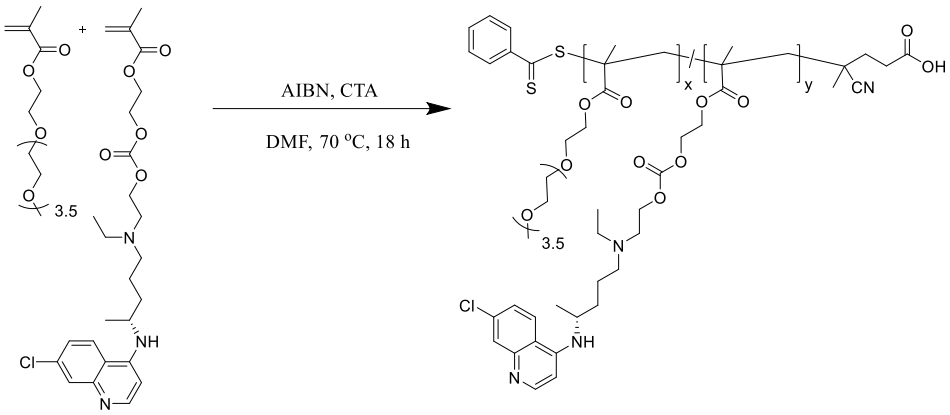

Figure 3.41. The polymerization reaction of P(OEG/HCQ-CB).

The P(OEG/HCQ-CB) copolymer was characterized using ^{1}H NMR and SEC analysis. The full ^{1}H NMR spectrum is given in Figure 3.42. The proton resonances of aromatic hydrogens appeared at 8.49, 8.02, 7.92, 7.81, and 6.44 ppm. In addition to peaks of hydroxychloroquine, the proton resonances of the terminal –OCH_3 group of the OEGMA unit appeared at 3.37 ppm. SEC analysis determined the molecular weight and size distribution (polydispersity index, PDI) as 57 kDa and 1.7. The P(OEG/HCQ-CB) copolymer properties were tabulated in Table 3.15.

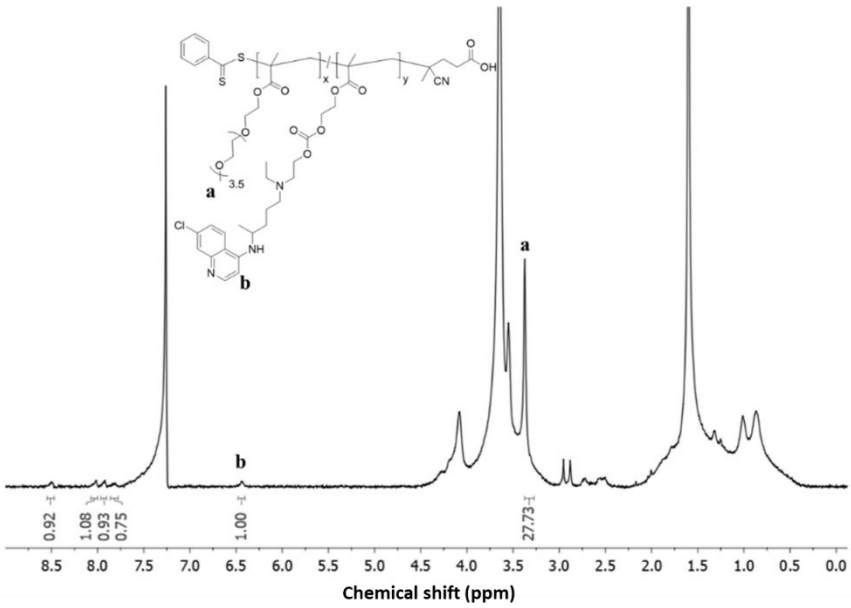

Figure 3.42. ^{1}H NMR spectrum of P(OEG/HCQ-CB) copolymer in $CDCl_3$.

3.3.22. *In Vitro* Drug Release Study and Cytotoxicity of P(OEG/HCQ-CB) Copolymer

HCQ release profile from P(OEG/HCQ-CB) copolymer, on which HCQ was conjugated to the polymer backbone via carbonate linker (CB), was examined in acidic and neutral pH, only PLE and GSH (10 mM), PLE-GSH mixture and plasma. While carbamate linker is stable, carbonate linkage is very labile. Therefore, high HCQ release from the carbonate linker was expected.

High HCQ release was obtained in pH = 5.4 acetate buffer, pH = 7.4 PBS buffer, PLE enzyme, and plasma at the end of 72 h. HCQ release percent from P(OEG/HCQ-CB) copolymer were determined as 65%, 40%, 31%, and 35% in the presence of pH = 5.4, pH = 7.4, plasma, and PLE, respectively. After 48 h, the highest HCQ release was observed in pH = 5.4 acetate buffer. HCQ release amount was 41%, and plasma HCQ release was 14%. More release in an acidic environment was desirable for us. The release graph is given in Figure 3.43.

After the release study, the cytotoxicity of P(OEG/HCQ-CB) copolymer was investigated in BxPC-3 and Capan-1 cell lines. The cytotoxicity graph is given in Figure 3.43b-c, and EC_{50} values are tabulated in Table 3.16. When the cytotoxicity of P(OEG/HCQ-CB) was compared with that of P(OEG/HCQ-C), nearly the same EC_{50} values were observed despite different HCQ release profiles.

Table 3.16. Calculated EC_{50} values of HCQ and P(OEG/HCQ-CB) copolymer.

		EC_{50} (M)	
No	Constructs	**BxPC-3**	**Capan-1**
1	HCQ	2.54×10^{-6}	2.58×10^{-6}
2	P(OEG/HCQ-CB)	5.13×10^{-5}	$>10^{-5}$

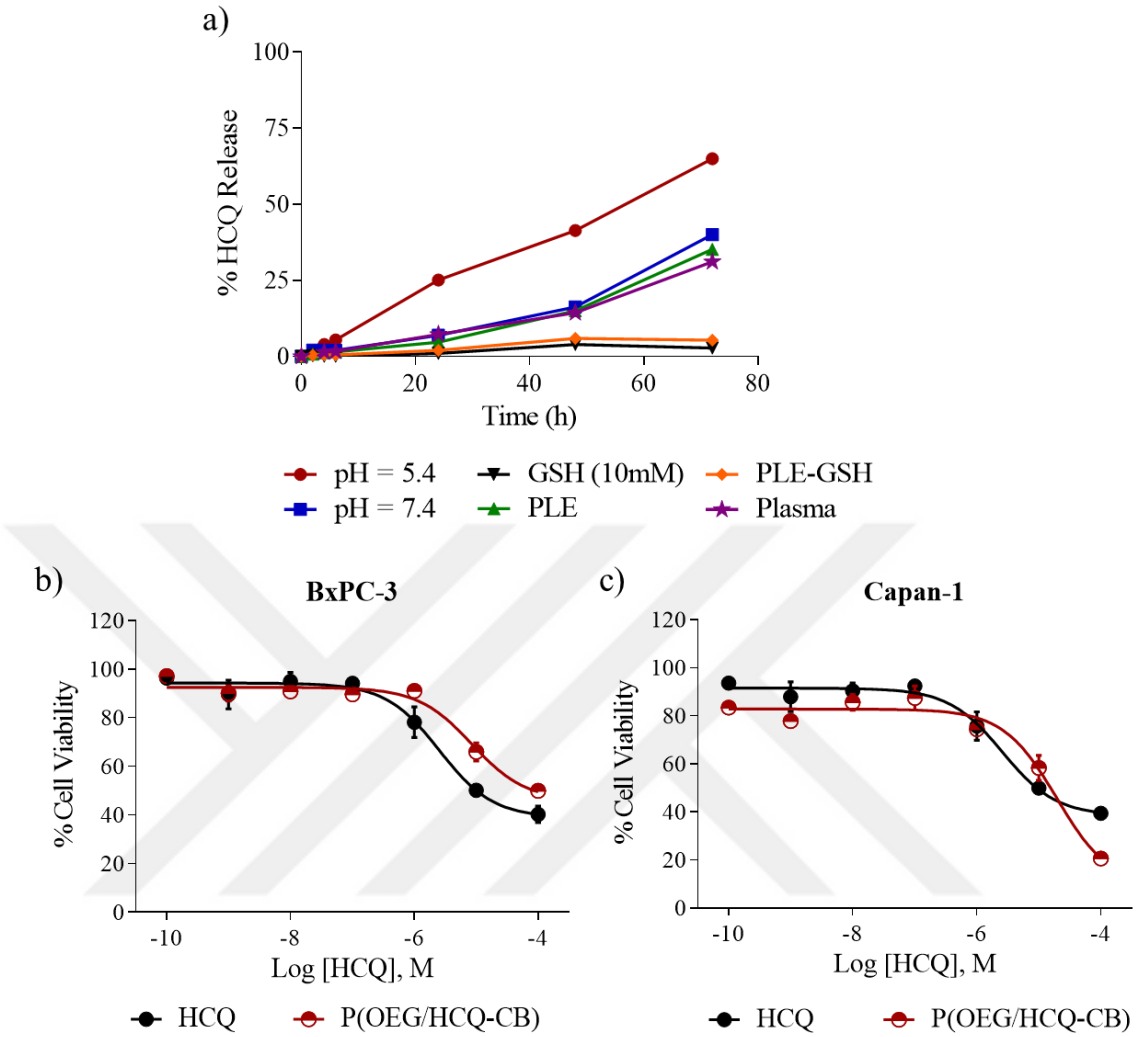

Figure 3.43. (a) HCQ release profile from P(OEG/HCQ-CB) copolymer at 37 ^{o}C, (b) and (c) cell viabilities of BxPC-3 and Capan-1 cells, treated with free HCQ and P(OEG/HCQ-CB).

In conclusion, three different HCQ-MA monomers were synthesized with various linkages. HCQ-based copolymers with carbamate and ester linkers did not show significant HCQ release. In addition, these copolymers did not have substantial cytotoxicity on pancreatic cancer cell lines. Therefore, carbonate-based HCQ monomer was synthesized and copolymerized with OEGMA. Strikingly, the P(OEG/HCQ-CB) copolymer showed a very high HCQ release, but its cytotoxicity was low. The vital key with the desired copolymer is the release profile. An effective copolymer should deliver high drug release after it accumulates in the tumor region. Therefore, many drug monomers were synthesized using

different linkages for linker optimization. Thus, the next copolymer will contain disulfide-carbamate-containing GEM and carbonate-containing HCQ.

3.3.23. Synthesis of P(OEG/HCQ-CB/GEM-SSC) Copolymer via RAFT Polymerization

P(OEG/HCQ-CB/GEM-SSC) copolymer was obtained via RAFT polymerization using HCQ-CB-MA and GEM-SSC-MA. In this system, HCQ was conjugated to the polymer backbone via a pH-responsive carbonate linker, and GEM was attached to the polymer via a redox-responsive disulfide-carbamate linker. The polymerization was carried out at 70 ^{o}C in the presence of AIBN as an initiator and CTA as a chain transfer agent. The polymerization reaction is shown in Figure 3.44.

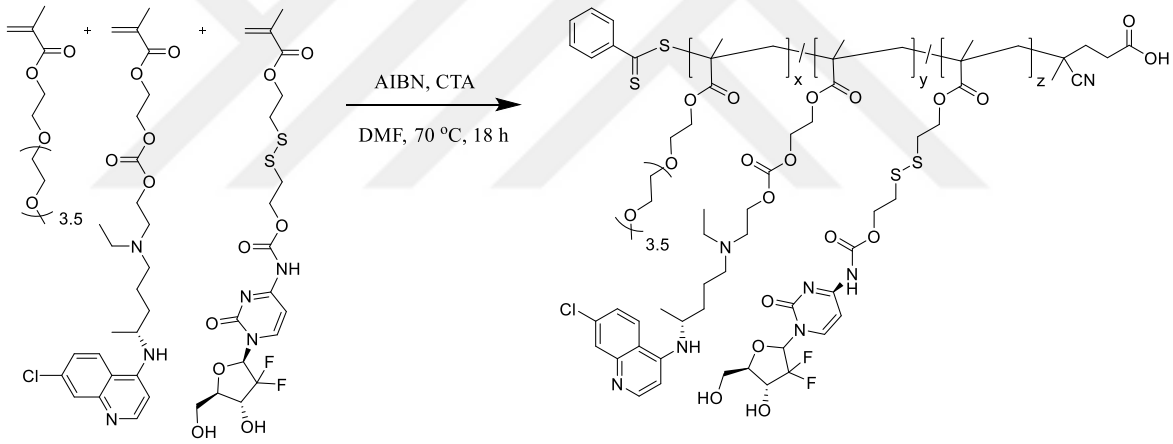

Figure 3.44. The polymerization reaction of P(OEG/HCQ-CB/GEM-SSC) copolymer.

The characterization and chemical composition of the P(OEG/HCQ-CB/GEM-SSC) copolymer was done by ^{1}H NMR spectroscopy. The full ^{1}H NMR spectrum is given in Figure 3.45. All peaks between 10.97 - 5.31 ppm came from HCQ and GEM. The c labeled proton resonances at 8.23 ppm, and the d labeled proton resonances at 7.09 ppm appeared due to gemcitabine. The b-labeled proton resonance at 7.77 ppm belonged to HCQ. The methyl ether group of POEGMA showed resonance at 3.24 ppm. Moreover, methacrylate alkenyl peaks at 6.05 and 5.70 ppm disappeared. 20:20:40 feed ratio for GEM-SSC-MA: HCQ-CB-MA: OEGMA was used to obtain the target copolymer, and this ratio produced P(OEG/HCQ-CB/GEM-SSC) copolymer with a ratio of 8:14:78 for GEM-SSC-MA: HCQ-

CB-MA: OEGMA. The average molecular weight (Mn) and size distribution of P(OEG/HCQ-CB/GEM-SSC) copolymer were determined as 57 kDa and 1.6, respectively, via SEC analysis. HCQ and GEM content were calculated as 8% and 14% by weight using proton integrations in the ^{1}H NMR spectrum. The polymerization conditions and properties of the copolymer were tabulated in Table 3.17.

Table 3.17. Polymerization conditions and properties of P(OEG/HCQ-CB/GEM-SSC).

No	**Feed Ratio**			**Obtained Ratio**			**CTA**	**AIBN**	**Mn (kDa)**	**Mw/Mn (PDI)**
	OEG	GEM	HCQ	OEG	GEM	HCQ				
1	60	20	20	78	14	8	5	1	57	1.6

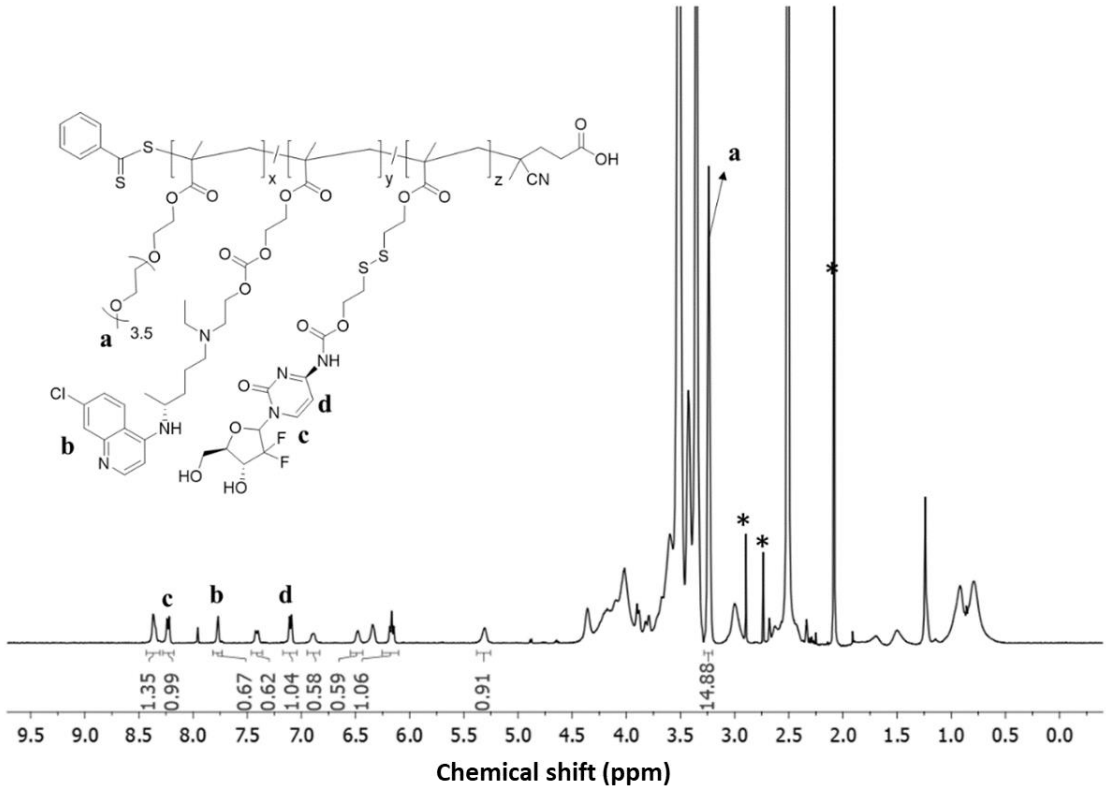

Figure 3.45. ^{1}H NMR spectrum of P(OEG/HCQ-CB/GEM-SSC) (DMSO d6).

3.3.24. *In Vitro* Drug Release Study and Cytotoxicity of P(OEG/HCQ-CB/GEM-SSC) Copolymer

P(OEG/HCQ-CB/GEM-SSC) copolymer was successfully synthesized and characterized. This copolymer is essential because drugs can release from the polymer backbone. We synthesized HCQ-based copolymer via carbonate linker and then showed the HCQ release profile. Similarly, a GEM-based monomer via a disulfide-carbamate linker and release profile was demonstrated. Both HCQ and GEM showed high release from the copolymer. Therefore, the new copolymer was obtained from these releasable monomers. The release kinetics of P(OEG/HCQ-CB/GEM-SSC) copolymer was investigated in acidic and neutral pH, in the presence of GSH and PLE enzyme, and in plasma to prove this idea. HCQ and GEM release results are given in Figure 3.46. The highest HCQ release (75%) was recorded in a pH 5.4 acidic environment. In addition to HCQ, the highest GEM release was obtained in the presence of the GSH-PLE mixture. Thus, when the P(OEG/HCQ-CB/GEM-SSC) copolymer is internalized by cancer cells, both HCQ and GEM will release from the copolymer due to the acidic and redox-responsive tumor environment.

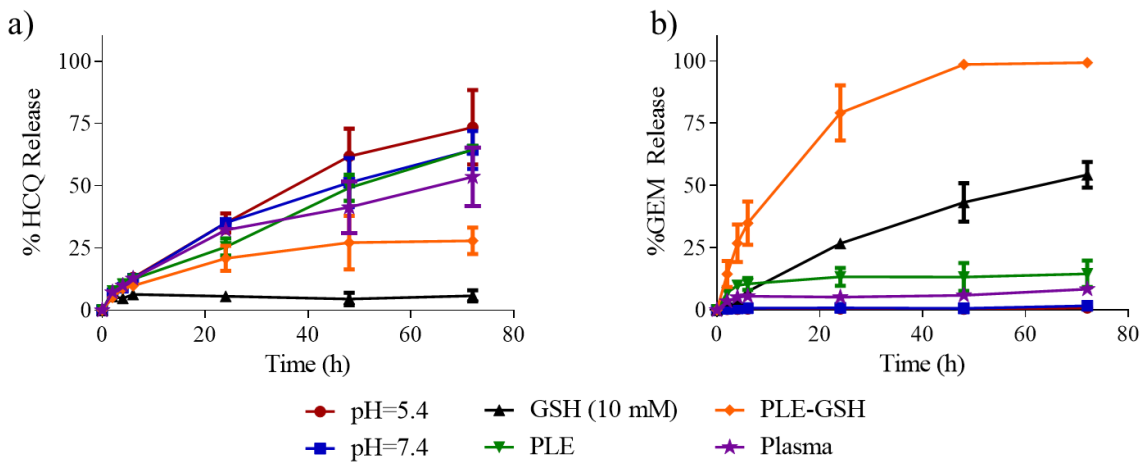

Figure 3.46. *In vitro* (a) HCQ and (b) GEM release profiles from P(OEG/HCQ-CB/GEM-SSC) copolymer in pH = 5.4 and 7.4, GSH (10 mM), PLE enzyme, the mixture of PLE-GSH and rat plasma at 37 ^{o}C (n = 3).

After successful GEM and HCQ release results, the CCK-8 cell proliferation assay was utilized to evaluate the cytotoxicity of the combination of free GEM-HCQ and GEM-HCQ-bearing copolymer P(OEG-HCQ-CB/GEMSS-C). Our results indicated that P(OEG-HCQ-CB/GEMSS-C) copolymer showed the best activity towards BxPC-3 cells like GEM-HCQ mixture, and its EC_{50} value was found as 9.80 x 10^{-8} M. Afterwards, BxPC-3 cells, high activity was observed towards Capan-1 cells. EC_{50} values of P(OEG-HCQ-CB/GEMSS-C) copolymer on Capan-1 was found as 5.73 x 10^{-6} M. EC_{50} values are tabulated in Table 3.18, and cytotoxicity graphs are given in Figure 3.47.

Table 3.18. Calculated EC_{50} values of GEM-HCQ mixture and P(OEG/HCQ-CB/GEM-SSC) copolymer for pancreas cancer cell lines after 48 h incubation.

		EC_{50} (M)	
No	**Constructs**	**BxPC-3**	**Capan-1**
1	GEM+HCQ	2.42 x 10^{-8}	5.45 x 10^{-7}
2	P(OEG/HCQ-CB/GEM-SSC)	9.80 x 10^{-8}	5.73 x 10^{-6}

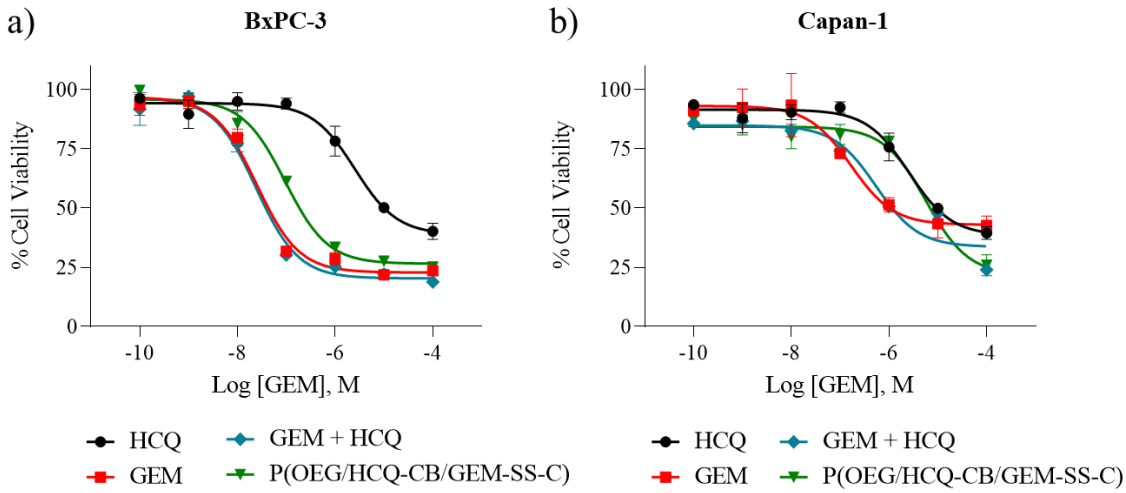

Figure 3.47. Cell viabilities of (a) BxPC-3 cells and (b) Capan-1 cells, treated with a mixture of GEM-HCQ and P(OEG/HCQ-CB/GEM-SSC).

3.3.25. *In Vitro* Cytotoxicity of P(OEG/HCQ-CB/GEM-SSC) Copolymer on PSC and PDAC Cells

After cell viability studies on BxPC-3 and Capan-1, we used another two cell lines to investigate the cytotoxicities of our free drugs and P(OEG/HCQ-CB/GEM-SSC). One of them was patient-derived cells, abbreviated as PDAC, isolated from patients with pancreatic cancer. Another cell line is pancreatic stellate cells, abbreviated as PSC. PSCs are resident cells of a healthy pancreas and exist in a non-activated state [194]. PSCs show abundant vitamin A in their cytoplasm [195]. PSC cells in diseased states expose to transformation due to the influence of growth factors, oxidative stress, etc., and PSCs transform into a myofibroblast-like phenotype. Under diseased conditions, PSCs lose their vitamin A stores and activated/transformed PSCs secrete an excess amount of extracellular matrix (ECM) proteins [196,197].

ECM is a fundamental part of the tumor microenvironment and plays a vital role in cancer. It paves the way for necessary biochemical and biophysical hints to give countenance to cancer cell proliferation, migration, and invasion [198]. In addition, it has been reported that PSCs enhance the survival of cancer cells. According to the published study, the presence of PSC protects pancreatic cancer cells against the cytotoxicity of gemcitabine [199,200].

First, the cytotoxicities of free drug and P(OEG/HCQ-CB/GEM-SSC) copolymer were investigated against PSC stellate cells. Interestingly, we found that free GEM was more cytotoxic than free HCQ. EC_{50} values of free GEM and free HCQ were determined as 0.137 μM and 4.38 μM. On the other hand, at higher concentrations (10-100 μM), HCQ was more effective than GEM. At 100 μM, while HCQ decreased the cell viability to 25%, the effect of GEM on cell viability remained 64% at the end of 48 h. The EC_{50} value of P(OEG/HCQ-CB/GEM-SSC) was found as 8.57 μM. The cytotoxicity graphs are given in Figure 3.48, and EC_{50} values are tabulated in Table 3.19.

Table 3.19. Calculated EC_{50} values of GEM, HCQ, GEM-HCQ, and P(OEG/HCQ-CB/GEM-SSC) copolymer for PSC and PDAC after 48 h incubation.

		EC_{50} (M)	
No	**Constructs**	**PSC**	**PDAC**
1	HCQ	4.38×10^{-6}	1.80×10^{-5}
2	GEM	1.37×10^{-7}	6.27×10^{-8}
3	HCQ+GEM	1.68×10^{-7}	3.52×10^{-8}
4	P(OEG/HCQ-CB/GEM-SSC)	8.57×10^{-6}	1.52×10^{-6}

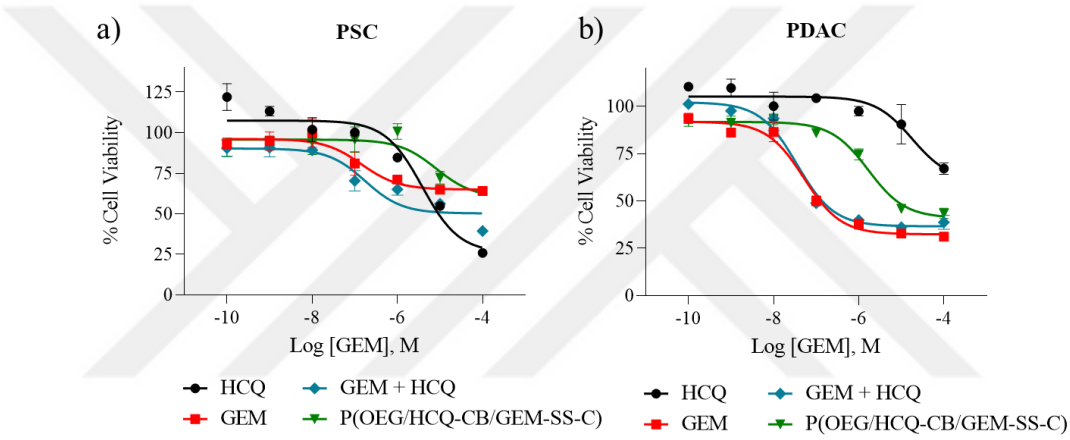

Figure 3.48. Cell viabilities of (a) PSC stellate cells and (b) PDAC cells, treated with free GEM, HCQ, GEM-HCQ, and P(OEG/HCQ-CB/GEM-SSC).

After PSC stellate cells, cytotoxicities of free drug and P(OEG/HCQ-CB/GEM-SSC) copolymer were investigated against PDAC. PDAC cells were isolated from patients with pancreas cancer, and PDAC cells contain many types of pancreas cancer cells, even PSC cells. Results are given in Figure 3.48b and Table 3.19. GEM, GEM+HCQ, and our P(OEG/HCQ-CB/GEM-SSC) showed more cytotoxicity towards PDAC cells than PSC cells. However, HCQ was 20-fold less toxic toward PDAC compared with PSC cells. In conclusion, the P(OEG/HCQ-CB/GEM-SSC) copolymer demonstrated excellent cytotoxicity toward PDAC cells, BxPC-3, Capan-1, and PSC cells because of the desired effect of HCQ and GEM release. Therefore, P(OEG/HCQ-CB/GEM-SSC) was selected as the best copolymer, and further studies were done with this copolymer.

3.3.26. Synthesis of BODIPY-MA Monomer

A fluorescent BODIPY-dye-containing monomer was synthesized using hydroxy-terminated BODIPY-OH and methacryloyl chloride in a 62% yield. This monomer was synthesized to use a cellular internalization study. The reaction scheme is shown in Figure 3.49.

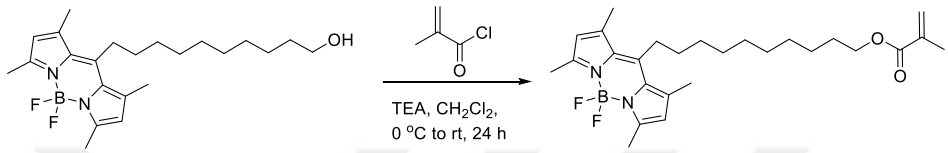

Figure 3.49. The synthesis of BODIPY-MA monomer.

NMR characterized BODIPY-MA monomer, and the ^{1}H NMR spectrum was given in Figure 3.50. The methacrylate unit's alkenyl group hydrogens appeared at 6.09 and 5.54 ppm. The characteristic BODIPY peak in the ring labeled b was observed at 6.05 ppm. In addition to these peaks, methyl group hydrogens (c and d labeled) on the BODIPY ring revealed peaks at 2.51 and 2.41 ppm.

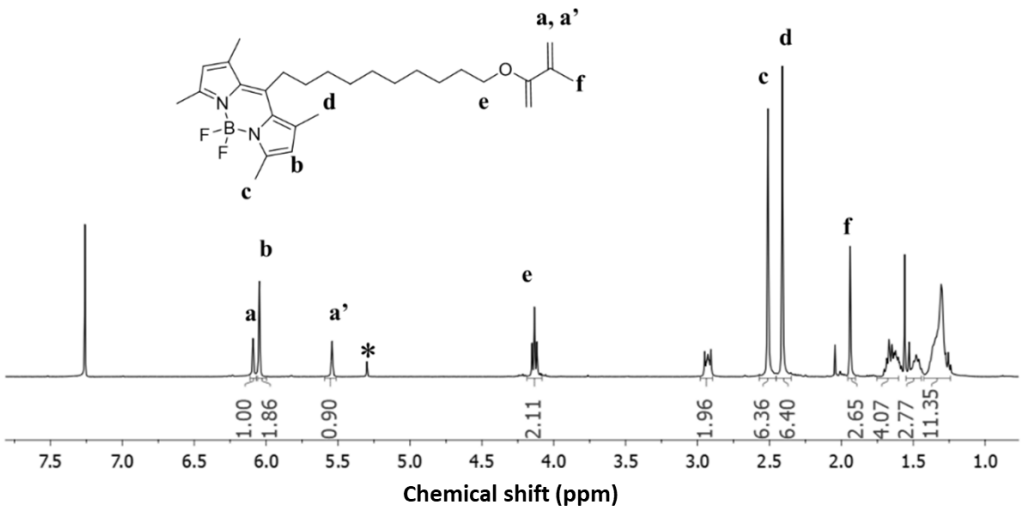

Figure 3.50. ^{1}H NMR spectrum of BODIPY-MA monomer in $CDCl_3$.

3.3.27. Synthesis of P(OEG/HCQ-CB/GEM-SSC/BODIPY) Copolymer

P(OEG/HCQ-CB/GEM-SSC/BODIPY) copolymer was obtained by using OEGMA, carbonate bond (CB) containing HCQ-CB-MA monomers, disulfide-carbamate containing GEM-SSC-MA and BODIPY-MA monomers via RAFT polymerization in the presence of AIBN and 4-cyano-4-(thiobenzoylthio)pentanoic acid (CTA). The polymerization reaction is shown in Figure 3.51.

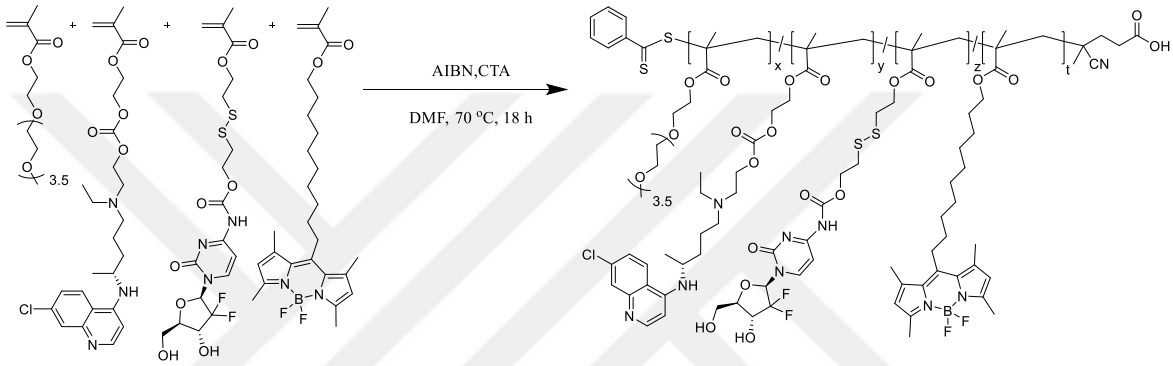

Figure 3.51. The polymerization scheme of P(OEG/HCQ-CB/GEM-SSC/BODIPY) copolymer.

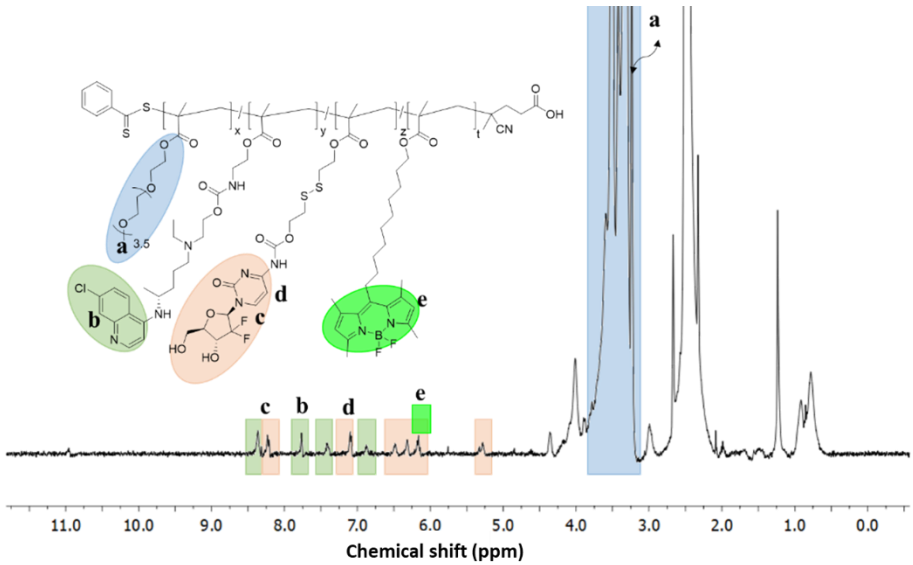

Figure 3.52. ^{1}H NMR spectrum of P(OEG/HCQ-CB/GEM-SSC/BODIPY).

3.3.28. Inhibition of Tumor Spheroid Growth

The in vitro cytotoxicities of free GEM, HCQ, and the combination of GEM-HCQ and P(OEG/HCQ-CB/GEM-SSC) copolymer were further evaluated by investigating their suppression ability on the growth of BxPC-3 tumor spheroids, may better mimic the tumor environment. As shown in Figure 3.53 and Figure 3.54, the untreated tumor spheres, incubated with only a culture medium, showed growth until 14 days. As for free drug-applied tumor spheres, the tumor spheroids treated with GEM, HCQ, and GEM-HCQ at the equivalent GEM concentrations of 1 x 10^{-6} M exhibited growth inhibition within 14 days. Furthermore, the spheroid group treated with P(OEG/HCQ-CB/GEM-SSC) copolymer showed a decrease in the spheroid area compared with other GEM groups, demonstrating the best antitumor effect.

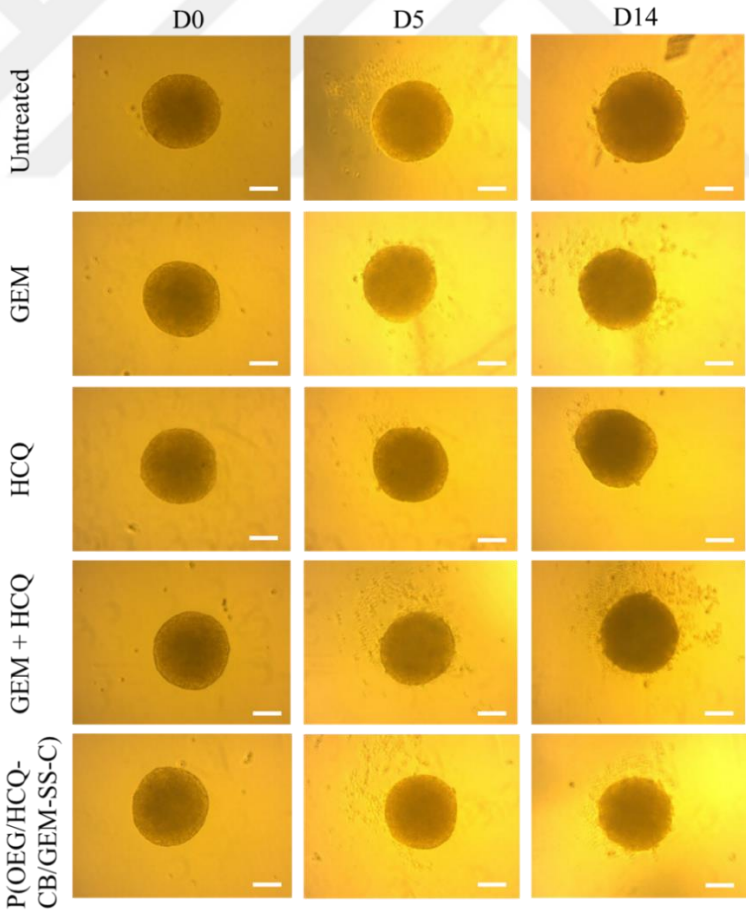

Figure 3.53. Representative bright-field images of BxPC-3 tumor spheroids.

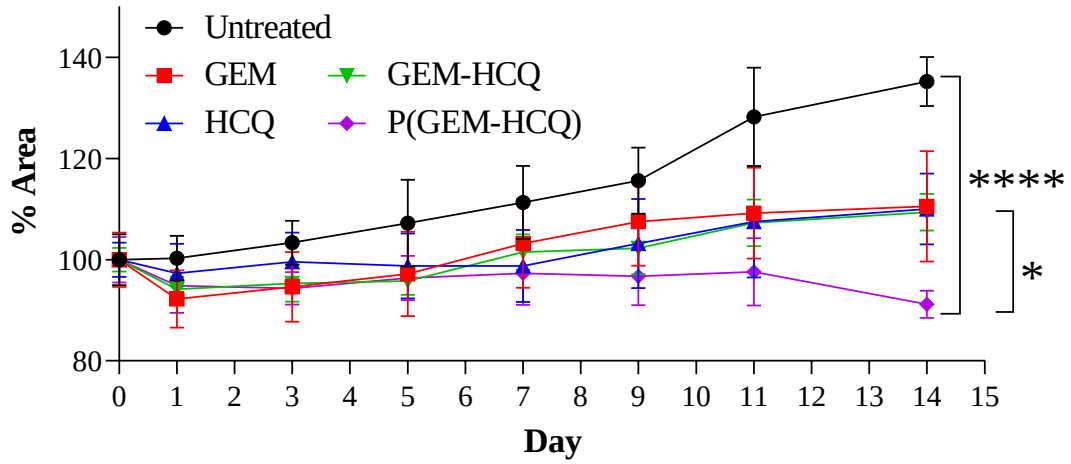

Figure 3.54. Determination of the tumor spheroid area (%) based on images. Data are expressed as mean ± SD (n = 3, ****p < 0.001, * p<0.05).

3.3.29. Cellular Uptake of P(OEG/HCQ-CB/GEM-SSC) on BxPC-3 Monolayer

BODIPY fluorescent dye was conjugated into our best copolymer (P(OEG/HCQ-CB/GEM-SSC)) to show cellular internalization. The intracellular localization of free BODIPY dye and BODIPY-conjugated and drug-bearing copolymer (P(OEG/HCQ-CB/GEM-SSC/BODIPY)) into the BxPC-3 pancreatic cancer cells were investigated using fluorescence microscopy. The BxPC-3 cells were incubated with free BODIPY and P(OEG/HCQ-CB/GEM-SSC/BODIPY) copolymer with the same BODIPY concentration (2 µM). Each group demonstrated a different level of internalization after 1, 3, and 24 h incubation. As shown in Figure 3.55, P(OEG/HCQ-CB/GEM-SSC/BODIPY) copolymer-treated cells displayed a much stronger fluorescence than the cells exposed to free BODIPY under the same concentration. Higher fluorescence intensity was observed along with increased incubation time, which means high internalization and accumulation of P(OEG/HCQ-CB/GEM-SSC/BODIPY) copolymer.

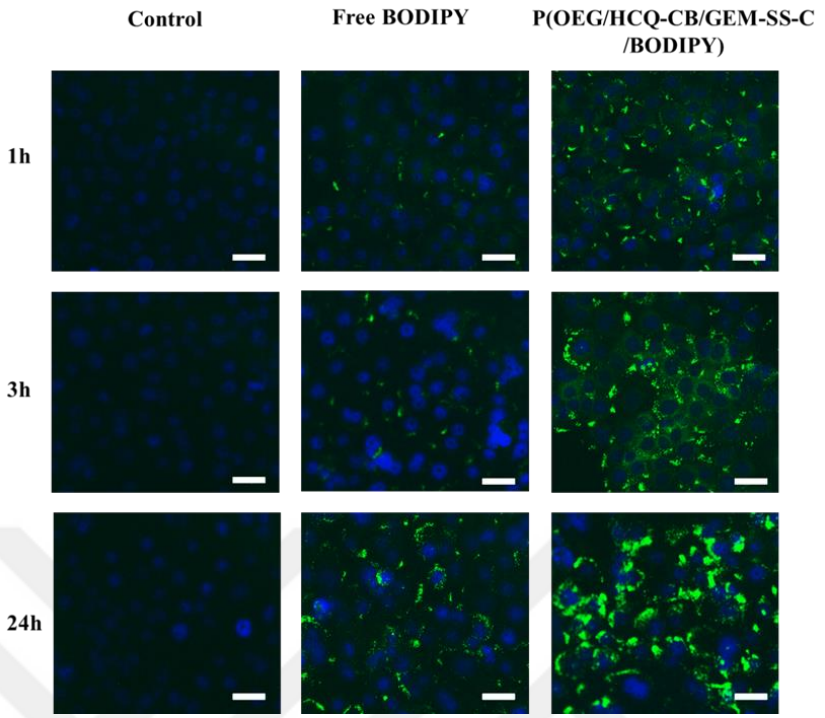

Figure 3.55. Fluorescence microscopy images of BxPC-3 cells treated with free BODIPY and BODIPY-conjugated and drug-containing copolymer. Cell nuclei were stained with DAPI (blue). The scale bar is 50 μm.

3.3.30. Penetration of BODIPY-Conjugated Copolymer into 3D Tumor Spheroids

The BxPC-3 3D tumor spheroid model was established to test the penetration efficiency of GEM-HCQ conjugated copolymer into tumor spheroids. Penetration capability was evaluated using a fluorescence microscope. BxPC-3 3D spheroids were incubated with free BODIPY and BODIPY-conjugated and drug-containing copolymer (P(OEG/HCQ-CB/GEM-SSC/BODIPY)). Control spheroids were incubated in only culture media. It was demonstrated that free BODIPY and P(OEG/HCQ-CB/GEM-SSC/BODIPY) display increased green fluorescence of BODIPY with the incubation time. Notably, the BODIPY fluorescence intensity treated with P(OEG/HCQ-CB/GEM-SSC/BODIPY) is significantly higher than that treated with free BODIPY at the same incubation time points. The cell images and data are represented in Figure 3.56. This result suggests that P(OEG/HCQ-CB/GEM-SSC) may exhibit better anticancer efficacy due to enhanced cellular internalization.

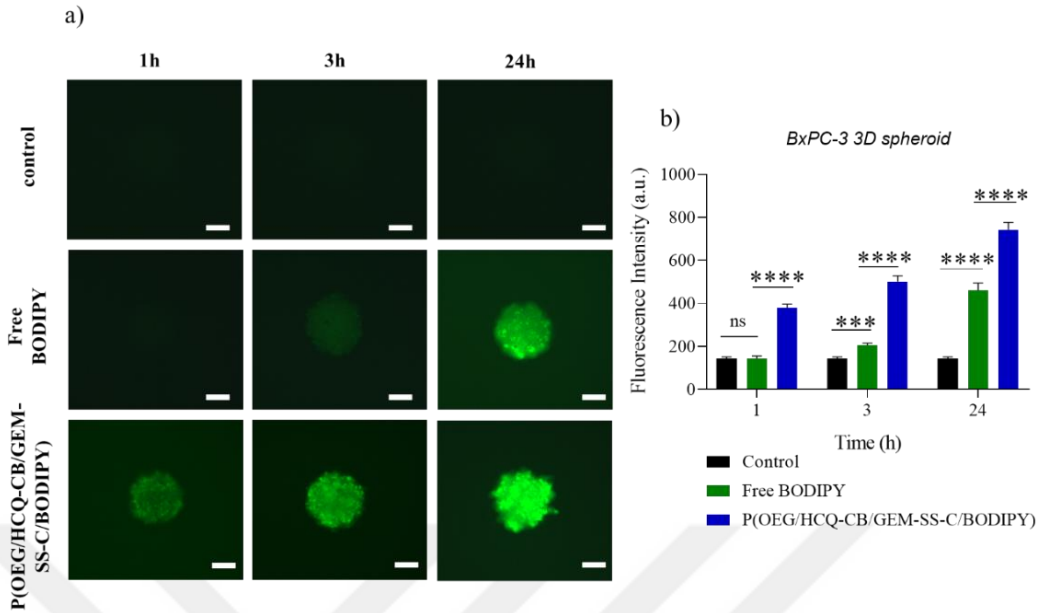

Figure 3.56. (a) The fluorescence images of spheroids and penetration efficiency of free BODIPY and P(OEG/HCQ-CB/GEM-SSC/BODIPY) into BxPC-3 tumor spheroids; (b) the mean fluorescence intensity of dye-treated spheroids.

3.4. Conclusion

In summary, we designed and synthesized oligo(ethylene glycol)-based polymeric drug carriers, which consisted of one and two drugs with different linkers. Each copolymer was evaluated in terms of drug release kinetics and cytotoxicity profile to find the best copolymer. First of all, HCQ was linked with ester linker to polymer backbone. Release study showed that P(OEG/HCQ-E) copolymer demonstrated very low HCQ release. Therefore, linker was changed from ester to carbamate bond and P(OEG/HCQ-C) copolymer was synthesized. Compared with the P(OEG/HCQ-E) copolymer, more HCQ release from P(OEG/HCQ-C) copolymer was observed but HCQ release ratio remained still under 10 %. Thereafter, hydrolysable carbonate linker was introduced between HCQ and polymer backbone. In contrast to ester and carbamate linker, carbonate linkage provided the highest HCQ release. At acidic pH, HCQ release amount from P(OEG/HCQ-CB) copolymer were determined as 65%. As a result, linker was optimized as carbonate for HCQ release.

After linker optimization for HCQ release, the same process was applied to GEM release. Firstly, pH-responsive carbamate linker was used between GEM and polymer backbone and released GEM amount remained under 10%. Therefore, carbamate linker was changed, and redox-responsive disulfide linker was chosen. Higher GEM release profiles from disulfide linker were observed in the combination of PLE-GSH (98%) at the end of 3 days. Therefore, disulfide-carbamate linker was selected for GEM release.

After linker optimization, P(OEG/HCQ-CB/GEM-SSC) copolymer was synthesized. HCQ and GEM were attached to copolymer via carbonate and disulfide-carbamate linkers, respectively, showed the best drug release and cytotoxic activity toward pancreatic cancer cell lines. In addition, while free GEM, HCQ, and GEM-HCQ suppressed the growth of tumor spheroids, the P(OEG/HCQ-CB/GEM-SSC) copolymer successfully decreased spheroid area. Furthermore, an internalization assay with BODIPY-dye conjugated copolymer (P(OEG/HCQ-CB/GEM-SSC/BODIPY) on monolayer and 3D-spheroid revealed that dye-conjugated copolymer showed better penetration ability compared to free BODIPY. These results showed that P(OEG/HCQ-CB/GEM-SSC) copolymer is a promising drug delivery system for pancreatic adenocarcinoma treatment.

4. FABRICATION OF CYCLODEXTRIN-BASED REDOX-RESPONSIVE NANOGELS FOR TARGETED DRUG DELIVERY

This chapter was adapted with permission from {Degirmenci, A., H. Ipek, R. Sanyal, and A. Sanyal, "Cyclodextrin-containing Redox-Responsive Nanogels: Fabrication of a Modular Targeting Drug Delivery System", *European Polymer Journal*, Vol. 181, p. 111645}. Copyright {2022} Elservier [201].

4.1. Introduction

Over the past decade, polymeric nanostructures have gained prominence due to their diverse applications in biomedical sciences [202-204]. Among these applications, in particular, the delivery of therapeutic agents to various types of tumors has been extensively studied since cancer remains one of the deadliest diseases facing mankind [173], [205-209]. It is well-established that polymeric nanostructures encapsulate hydrophobic drugs and provide them with the increased bioavailability and stability required for demonstrating efficacy in our biological system [210]. Furthermore, these polymeric nanocarriers enable cell-specific delivery through the conjugation of targeting moieties, increase the drug residence time in blood, and allow controlled drug release [54], [211]. Importantly, these polymeric vehicles can be fabricated in sizes ranging from tens to hundreds of nanometers, enabling the passive targeting of tumors through the enhanced permeability and retention effect (EPR) [212]. Overall, the combination of all these attractive attributes makes nanostructures ideal candidates for drug delivery. Today, various polymeric nanomaterials ranging from micelles, polymeric nanoparticles, and nanogels (NGs) are available as alternatives for drug delivery vehicles.

Recent years have witnessed an increasing interest in nanogels, and significant advancements in their synthesis and applications have been reported [213-216]. Stable

nanogels can be obtained through covalent or non-covalent crosslinking of polymers [58], [158], [217-219]. The employment of non-covalent approaches where appropriately functionalized polymers are mixed to yield nanogels in aqueous media provides a versatile fabrication method and yields dynamic soft materials that can be envisioned to undergo facile degradation. Furthermore, incorporating stimuli-responsive linkages within non-covalently assembled nanogels can be expected to enhance further the drug release in the acidic and reductive environments within cancerous cells. In this context, predominantly, the focus has been to engineer stimuli-responsive covalently-crosslinked delivery systems using a variety of acetal and disulfide-linkage-containing polymeric systems [33], [59], [220-228]. Specific host-guest interactions enable non-covalent crosslinking of different polymeric chains by simple formulation in aqueous media to yield a variety of novel supramolecular nanostructures [229,230]. To this end, various host-structures macrocyclic structures such as calixarenes, calixpyrroles, crown ethers, cucurbiturils, pillararenes, and cyclodextrins (CDs) have been employed [231-236]. Among these macrocycles, cyclodextrins (CDs) have been widely used as building blocks to fabricate self-assembled structures at various length scales [237-241] for various diagnostics and delivery applications because of their low toxicity, biocompatibility and efficient complexation with a range of guest molecules including various hydrophobic therapeutic drugs [242-244]. For example, Liu and coworkers reported synthesizing a supramolecular nanoparticle consisting of positively charged adamantane and βCD-bearing hyaluronic acid (HACD) to release pDNA, where the nanoparticle formation resulted from host-guest interaction between βCD and Ada units [245]. Seminal contribution in this area has been reported by Amiel and coworkers, who reported stable nano-assemblies formed spontaneously upon mixing βCD- and Ada-modified dextran copolymers (βCD-Dex and Ada-Dex) and demonstrated that their sizes could be tailored by varying the extent of βCD and Ada substitution levels [246]. It can be envisioned that introducing a disulfide-based redox-responsive linkage into the nanogels fabricated using βCD-Ada interactions will provide a delivery system responsive to the endogenous tripeptide glutathione (GSH), which is over-expressed in many cancerous cells [31]. Liu and coworkers have integrated disulfide-based redox chemistry with supramolecular host-guest chemistry elegantly [247,248]. In their approach, hydrophobic drugs are modified with an adamantane group through a disulfide linkage, which upon mixing with CD-containing hydrophilic polymers, leads to amphiphilicity-driven nanoparticle formation. To date, Chen, He, and coworkers have reported a redox-responsive

host-guest-based nanogel with a somewhat related approach [249]. They utilized benzimidazole-cyclodextrin complexation, where they employed a disulfide-containing cyclodextrin crosslinker. The system disclosed in the present work utilizes nanogels that contain CDs, which enables facile functionalization using a plug-and-play approach by employing adamantane-containing functional molecules, as demonstrated here by arming the delivery system with adamantane-containing peptide-based targeting groups. Thus the alternative method reported here outlines the fabrication of a delivery system that can be easily tailored for therapeutic targets in a modular fashion.

Herein, we report the fabrication and evaluation of dextran-based self-assembled redox-responsive nanogels as a modular targeted drug delivery vehicle. In particular, nanogels are obtained through the self-assembly of βCD-modified dextran polymers and a disulfide group containing bis-adamantane linker in an aqueous environment. The βCD-modified dextran polymers were readily obtained using the Huisgen type "*click*" reaction between alkyne-functionalized dextran and azide-terminated βCD. Doxorubicin (DOX) was encapsulated into nanogels during their formation. It was followed by treatment of the drug-loaded nanogels with an adamantane group containing cyclic RGD peptide, a well-known motif targeting the integrin receptors over-expressed on various cancer cells [250,251]. Finally, *in vitro* drug release under neutral and acidic conditions, in the presence and absence of GSH, and cellular internalization and cytotoxicity against MDA-MB-231 breast cancer cells were evaluated.

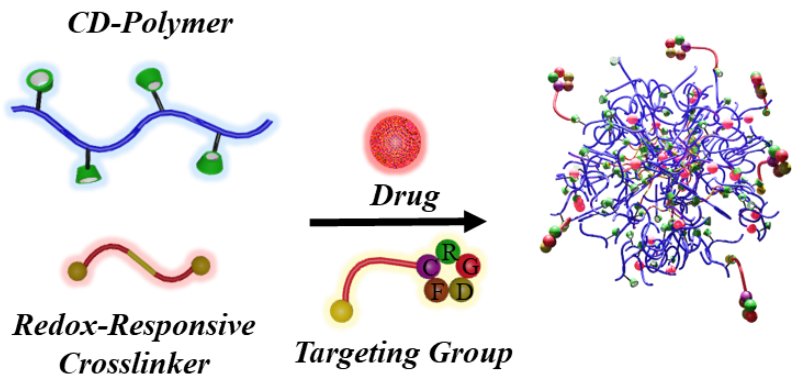

Figure 4.1. Schematic illustration of the fabrication of drug-loaded targeted nanogels.

4.2. Experimental

4.2.1. Materials

All solvents were purchased from Merck and used as obtained without further purification. Ultrapure water was obtained from a Milli-Q Water Purification System (Milli-Q system, Millipore, Billerica, MA, USA). Anhydrous CH_2Cl_2 was obtained from the SciMatCo purification system, and other solvents were dried over molecular sieves. Dextran (Dex40, MW 40 kDa) was purchased from Pharmacosmos and dried in vacuo at 80 ^oC overnight before use. 1-Bromo adamantane, 4-pentynoic acid, p-toluenesulfonyl chloride, and *N,N'*-dicyclohexylcarbodiimide (DCC) were purchased from Alfa-Aesar. Tetraethylene glycol (TEG), 4,4'-dithiobutyric acid, 4-(dimethylamino)pyridine (DMAP) and N, N, N', N'', N''- pentamethyldiethylenetriamine (PMDETA), β-Cyclodextrin (β-CD), copper(I)bromide (CuBr) and 4',6-diamidino-2-phenylindole (DAPI) were purchased from Sigma Aldrich. N,N'-Diisopropylcarbodiimide (DIC) was obtained from TCI. Triethylamine and sodium azide were purchased from Merck. Reduced L-Glutathione was purchased from Biofroxx. 6-O-Monotosyl-βCD (βCD-OTs) [252], 6-monodeoxy-6-monoazido-βCD (βCD-N_3) [252], 2-(2-{2-[2-(adamantan-1-ylmethoxy)-ethoxy]-ethoxy}-ethoxy)-ethanol (Ada-TEG) [253], and Ada-TEGSS linker [254] and βCD-Dex polymer [254] were synthesized according to literature procedures.

4.2.2. Methods

The characterization of synthesized molecules was performed with ^1H, and ^{13}C NMR spectroscopy (Avance III HD, 400 MHz, Bruker, USA), Fourier transform infrared (ATR-FTIR) spectroscopy (Nicolet 380, Thermo Scientific, USA). The hydrodynamic size of nanogels was obtained using a Zetasizer Nanoparticle analyzer (Malvern). Liquid chromatography-mass spectroscopy (LC-MS/MS) was used to analyze drug amounts and evaluate drug release. TEM imaging of dry nanogel was done on a holey carbon film-coated 300 mesh Cu-grid (Pacific Grid Tech, USA) by using transmission electron microscopy (TEM, LVEM5 microscope operated, Delong Instruments, USA). Cytotoxicity experiments were done with a plate reader (Multiscan FC, Thermo Scientific, USA) using Cell Counting

Kit-8 (CCK-8, Fluka). Images of drug internalized cells were obtained using a Zeiss Observer Z1 fluorescence microscope with an Axiocam MRc5 camera.

4.2.3. Synthesis of βCD-Dex Polymer and Bis-Ada-TEG-SS Linker

βCD-Dex polymer and bis-Ada-TEG-SS linker were synthesized according to literature procedures [254].

4.2.4. Synthesis of Empty- and DOX-loaded Nanogels (NGs)

In a vial, βCD-conjugated dextran polymer (βCD-Dex) (5 mg) and bis-Ada-TEG-SS linker (0.631 mg) were dissolved in DMSO (1 mL). The βCD and Ada functional group ratio was kept at 1:1. The solution was stirred at room temperature for 1 h. After 1 h, the solution was added to water (2 mL) and stirred for 30 min. Subsequently, the solution was dialyzed against water using a membrane (3.5kDa Mw cut-off) for 2 h to obtain nanogels. To prepare DOX-loaded nanogels, βCD-Dex (5 mg, βCD: 1eq), bis-Ada-TEG-SS linker (0.631 mg, Ada: 1 eq), and neutralized DOX (0.5 mg, %10 wt) were dissolved in DMSO. After stirring for 1 h, the solution was diluted with water (2 mL). To remove unloaded DOX, the solution was dialyzed against water using a regenerated cellulose-based dialysis membrane (Mw cut-off 3.5 kDa) for 2 h to yield a DOX-loaded nanogel-containing solution.

4.2.5. Encapsulation and *In Vitro* Drug Release

DOX was loaded into nanogels using the dialysis method. The amount of drug loading was calculated using LCMS-MS. To determine the drug loading amount, a 100 μL sample was taken from DOX-loaded nanogel solution and incubated in DTT solution (500 μL, 100 mM) for 30 min to degrade the nanogel. After that, the solution was diluted with acetonitrile (ACN) and analyzed to determine encapsulated drug concentration using LCMS-MS. To determine the release kinetics of DOX from nanogels, drug-loaded nanogel solution was divided into four parts. Each of these parts was placed into dialysis bags (3.5kDa Mw cut-off) and immersed in 12 mL acetate buffer (pH 5.4), phosphate buffer (pH 7.4), 5 mM GSH-containing acetate buffer (pH 5.4), and 5 mM GSH-containing phosphate buffer (pH 7.4), separately. The solutions were allowed to shake gently (260 rpm) at 37 ^{o}C. At predetermined

time points, a sample (500 μL) was taken from the outer phase of the dialysis membrane, and fresh buffer solutions (500 μL) were added. The amount of released DOX was determined using LCMS-MS analysis. The release results were presented as average data with standard deviations.

4.2.6. Synthesis of NHS-activated Adamantane (NHS-Ada) and RGD-conjugated Adamantane (RGD-Ada)

Adamantaneacetic acid (50 mg, 0.257 mmol) and *N*-hydroxysuccinimide (30 mg, 0.257 mmol) were dissolved in the mixture of ethyl acetate (1.5 mL) and dioxane (1.5 mL), and the mixture was cooled into 0 ^{o}C using an ice bath. At 0 ^{o}C, DCC was added to the mixture, and the reaction mixture was stirred at room temperature for 24 h. After that, DCU salts were filtrated, the reaction solvent was removed under reduced pressure, and the crude product was redissolved in ethyl acetate and extracted with 5% $NaHCO_3$ (25 mL x 2 times), water (25 mL x 2 times) and brine solution (25 mL x 2 times). The organic layer was dried over anhydrous Na_2SO_4. Ethyl acetate was removed under reduced pressure, and NHS-Ada was obtained as a white solid. (75 % yield). ^{1}H NMR ($CDCl_3$, δ, ppm) 2.84 (s, 4H), 2.34 (s, 2H), 2.01 (br s, 3H), 1.71 - 1.68 (m, 12H) ^{13}C NMR ($CDCl_3$, δ, ppm) 169.4, 166.5, 45.5, 42.2, 36.7, 33.4, 28.7, 25.8.

NHS-Ada (10 mg, 0.034 mmol) was dissolved in anhydrous DMF (0.2 mL). DIPEA (6 μL, 4.39 mg, 0.034 mmol) was added. To this mixture, cRGDfK (10 mg, 0.017 mmol) in anhydrous DMF (0.2 mL) was dropwise added and then allowed to stir for 24 hours. After that, the reaction mixture was added to cold diethyl ether (50 mL). The formed precipitates were washed with an excess amount of diethyl ether. RGD-Ada was obtained as a white solid (67% yield). LCMS m/z: calculated for $C_{39}H_{57}N_9O_8$ 779.43; found 781.0 $[M + 2H]^{+}$.

4.2.7. *In Vitro* Cytotoxicity

Cytotoxicities of empty and DOX-loaded nanogels were determined using CCK-8 assay. MDA-MB-231 human breast cancer cells (purchased from ATCC (LGC Standards, Germany) were used for cytotoxicity experiments. Cells were grown in DMEM supplemented with 10% fetal bovine serum and incubated at 37 ^{o}C. MDA-MB-231 cells

(6000 cells/well) were seeded in a 96-well plate in 100 μL DMEM and incubated at 37 ºC for 24 h to adhere completely. After 24 h incubation, βCD-based nanogels solutions between 1 mg/mL and 0.1 mg/mL were prepared and placed onto the cells (100 μL/well). DOX-loaded βCD-based nanogels solutions 10^{-6} and 10^{-12} M were placed onto the cells (100 μL/well). For free DOX treatment, DOX solution (1 x 10^{-3} M) was prepared in PBS buffer and diluted between 10^{-6} and 10^{-12} M, then DOX solutions were added to cells. For GSH-mediated cytotoxicity, the cells were incubated with 5 mM GSHOEt for 5 hours. At the end of 5h, the GSH solution was removed from the cells, and the cells were washed with 1 x PBS (1 mL x 3 times). Then the cells were treated with cRGD-appended DOX-loaded βCD-based nanogels.

After 48 h incubation, nanogels and drug solutions were removed from cell-containing wells, and the wells were washed with PBS (1 mL). CCK-8 solution %10 in DMEM was added onto cells (100 μL/well) and incubated for 2h. The absorbance measurements at 450 nm were done with a plate reader. EC_{50} values of nanogels and free DOX were calculated using Graph Pad Prism software.

4.2.8. *In Vitro* Cell Internalization

MDA-MB-231 adenocarcinoma cells (300 000 cells/well) were seeded in a 12-well plate as duplicates in 1 mL of culture media (DMEM). The cells were incubated at 37 ºC for 24 h. DOX-loaded non-targeted (βCD-NG-DOX) and targeted (RGD-βCD-NG-DOX) nanogels (0.04 mg/mL DOX concentration) were added to the wells. Free RGDfV combined with RGD-βCD-NG-DOX nanogels were used for the competitive internalization experiment. After 1 h and 3h incubation, cell media were removed, and cells were washed with 1 x PBS (1 mL x 2 times). Cells were fixed using a 3.7% formaldehyde solution for 10 minutes at 37 ºC. After fixation, cells were washed with 1 x PBS (1 mL x 2 times). After that, cell nuclei were stained by DAPI for 15 min at 37 ºC. After washing the cells, cell images were taken using a Zeiss Observer Z1 fluorescence microscope and processed with AxioVision software.

4.3. Result and Discussion

4.3.1. Synthesis and Characterization of Nanogel Precursors: βCD-Functionalized Dextran and Disulfide-Containing Bis-Ada Crosslinker

A straightforward and scalable approach reported by Larsen and coworkers was utilized to obtain the βCD-Dex copolymer [255]. Briefly, a CD-conjugated dextran copolymer was synthesized using an azide-alkyne Huisgen type "*click*" reaction between propargyl group appended dextran and azide-containing CD-derivative (βCD-N_3). For the synthesis of the Ada-based crosslinker, the reaction between Ada-TEG-OH and 4,4-dithiodibutyric acid in the presence of DMAP and DIC yielded the bis-Ada-TEG-SS linker.

4.3.2. Preparation and Characterization of Self-assembled Empty and Drug-loaded Nanogels

Nanogel formation involves aqueous media self-assembly of βCD-Dex polymer and bio-reducible bis-Ada-TEG-SS linker. A solution of βCD-Dex polymer (5 mg/mL) and bis-Ada-TEG-SS linker was prepared in DMSO and stirred for 1 h to ensure homogenous dissolution. After that, this mixture was dialyzed against water to induce the formation of stable nanogels. Obtained nanogels (1 mg/mL) were characterized using DLS and TEM, and results were represented in Figure 4.2a-e. The hydrodynamic diameter of the self-assembled nanogels in water was determined as 178 ± 20 nm and 57 ± 10 nm using DLS and TEM, respectively. As expected, the size obtained using DLS is larger than that observed in TEM since nanogels are in their hydrated form in solution, as opposed to their compact form upon drying. As seen in Figure 4.3, the nanogel size was optimized by changing the concentration of βCD-Dex polymer and equivalence of the Ada-TEG-SS linker. For obtaining drug-loaded nanogels, the nanogel formation was undertaken in the presence of doxorubicin. In this case, the hydrodynamic diameter of the drug-loaded nanogels in water was determined as 230 ± 9 nm and 38 ± 6 nm using DLS and TEM, respectively. The loaded DOX amount into nanogels was determined as 3.72 ± 0.49 % by weight using LCMS-MS analysis. The formation of an inclusion complex between βCD and DOX ($K_a = 2.1 \times 10^2\ M^{-1}$) [256] due to

host-guest interaction and the hydrogen bonding between DOX and CD grafted dextran polymer could be suggested for driving force DOX loading into the nanogels.

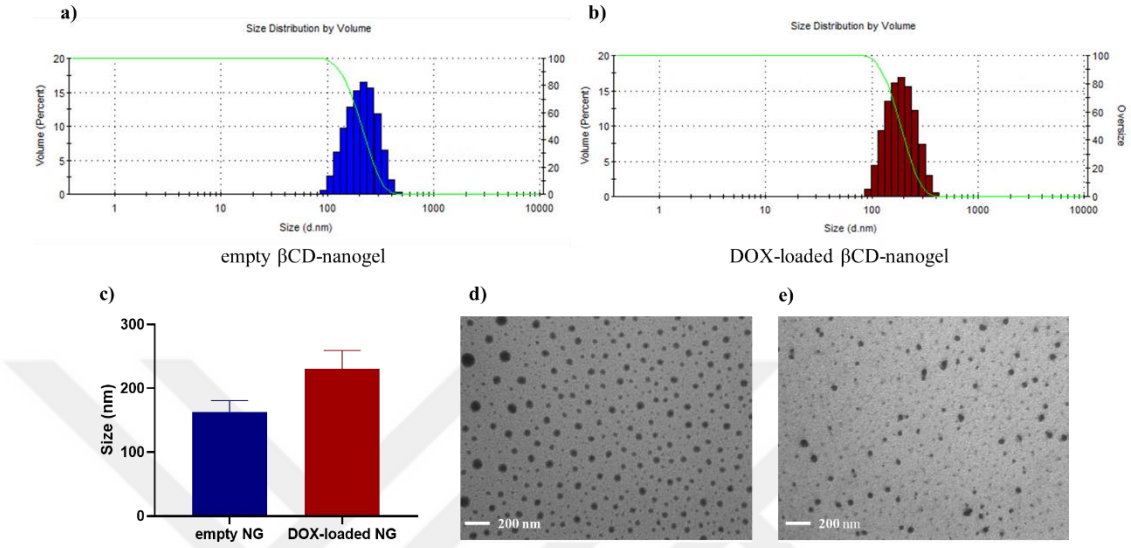

Figure 4.2. (a, b) Size distributions of empty and DOX-loaded βCD-nanogels, (c) comparative Z-average diameter of empty and drug-loaded nanogels as determined by DLS at 37 °C, TEM micrographs of (d) empty βCD-nanogels, and (e) DOX-loaded βCD-nanogels.

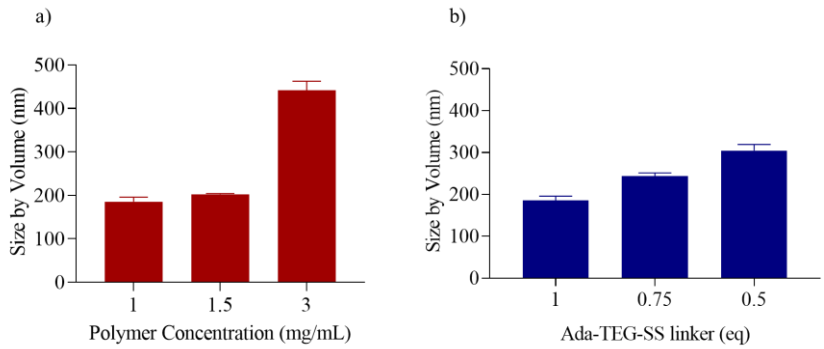

Figure 4.3. (a) Trends in nanogel size with increasing polymer concentration where Ada-TEG-SS linker equivalence was kept as 1, (b) the nanogel size with different Ada-TEG-SS linker equivalency (the concentration of polymer is 1 mg/mL).

To further confirm the formation of inclusion complex between βCD and Ada groups, a ^{1}H NMR experiment of Ada-TEG-SS linker, βCD-Dex, and (βCD-Ada nanogel) was performed using D_2O as a solvent, and H NMR spectra were given in Figure 4.4. As expected, the Ada-TEG-SS linker (black line) did not display any proton resonances since the linker did not have any solubility in water. As for βCD-Dex polymer, expected peaks were observed between 3.30 - 5.20 ppm (blue line). Importantly, in the ^{1}HNMR of the nanogels, peaks of βCD-Dex polymer between 3.30 - 5.20 ppm and as well as Ada group hydrogens at 2.23, 1.77, and 1.61 ppm were observable (burgundy line). The presence of the proton resonances from the linker suggests solubilization of the linker through complexation with the CD units of the dextran polymer in the nanogel.

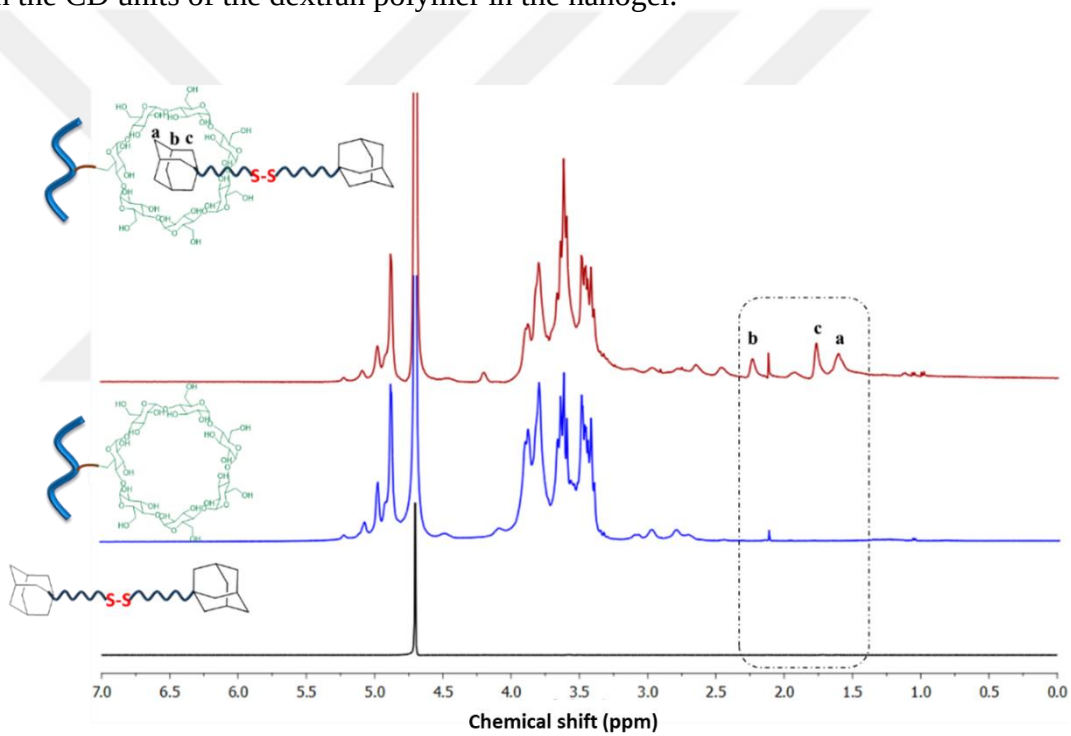

Figure 4.4. ^{1}H NMR spectra of Ada-TEG-SS linker (black line), βCD-Dex (blue line), and complex of βCD-Dex and Ada-TEG-SS linker (βCD-nanogel) (burgundy line) in D_2O.

4.3.3. Nanogel Disassembly in Reducing Environment

After preparing βCD-nanogels, their responsiveness to the thiol-containing reducing agent DTT and GSH was investigated. The hydrodynamic sizes of the nanogels before and after DTT (10 mM) treatment was compared using DLS. The size of βCD-nanogels

decreased to around 12 ± 3 nm from 179 ± 20 nm after 4 h of incubation with DTT at 37 °C. Furthermore, while the initial βCD-nanogel solution was turbid, the solution became clear after incubation with DTT, which also visually suggests the disassembly of the βCD-nanogels. Disassembly was demonstrated in Figure 4.5b.

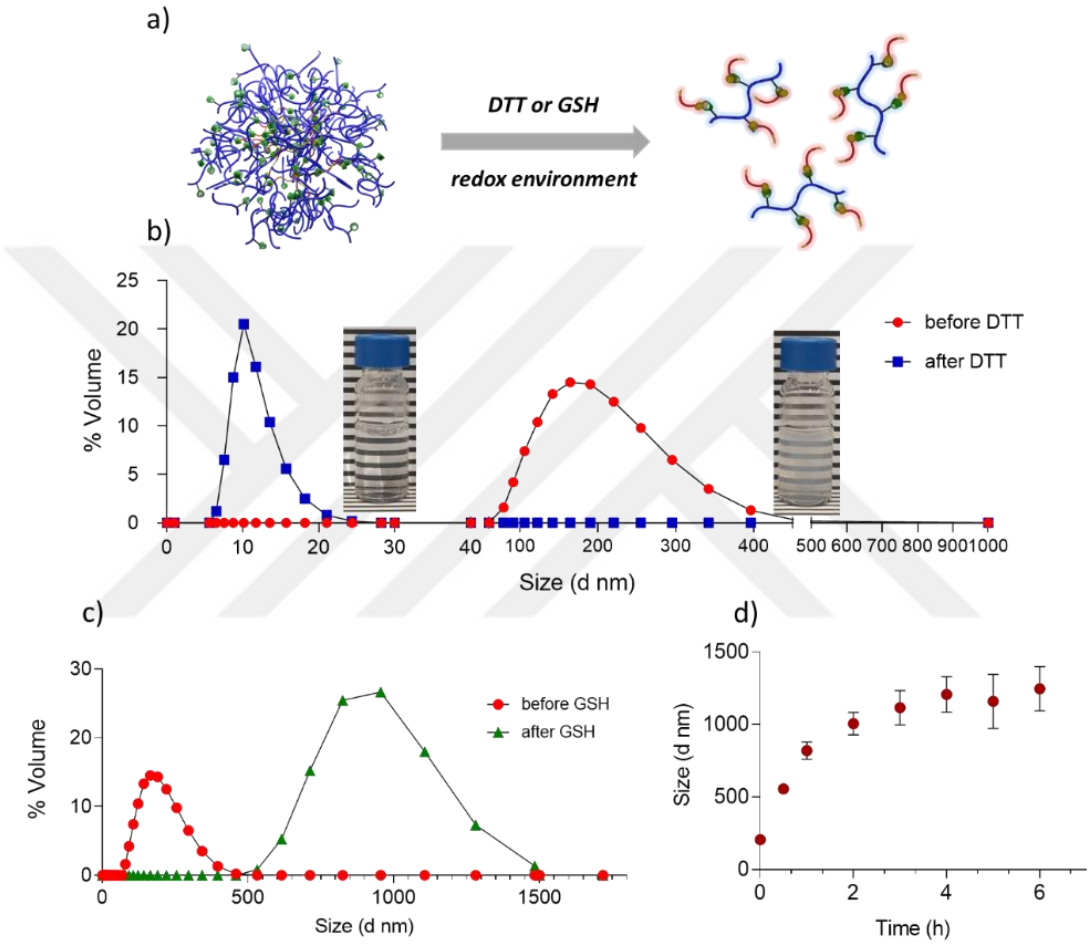

Figure 4.5. (a) Schematic representation of βCD-nanogels with DTT (10 mM), (b) DLS measurements before and after DTT treatment, (c) DLS measurements before and after GSH (5mM) treatment, and (d) disassembly of βCD-nanogels structures in the presence of GSH (5 mM) at 37 °C.

After DTT, the responsiveness of βCD-nanogels was also investigated in GSH solution (5 mM) at 37 °C. At certain times, hydrodynamic sizes of βCD-nanogels were recorded using DLS. As seen in Figure 4.5d, the size of βCD-nanogels increased to around 1246 ± 100 nm from 200 ± 2 nm after 6 h incubation with GSH at 37 °C. It can be concluded

that while a powerful reducing agent like DTT cleaves the disulfide bonds effectively and results in individual polymers, GSH causes disulfide bond cleavage to yield a larger and looser βCD-nanogel structure, and the DLS result is given in Figure 4.5c.

4.3.4. Synthesis of RGD-conjugated Adamantane (RGD-Ada)

To obtain adamantane-conjugated RGD peptide (RGD-Ada), NHS-activated adamantane (NHS-Ada) was synthesized using adamantane acetic acid and N-hydroxysuccinimide via DCC coupling reaction. The synthesis scheme and ^{1}H NMR spectrum of NHS-Ada are given in Figure 4.6. The characteristic NHS peak was observed at 2.84 ppm in ^{1}H NMR. The hydrogens of Ada units were observed between 1.5 - 2.0 ppm. After purification and characterization, NHS-Ada was reacted with cyclic-RGDfK peptide in the presence of DIPEA, and RGD-Ada was obtained with a 67% yield. The scheme is shown in Figure 4.7.

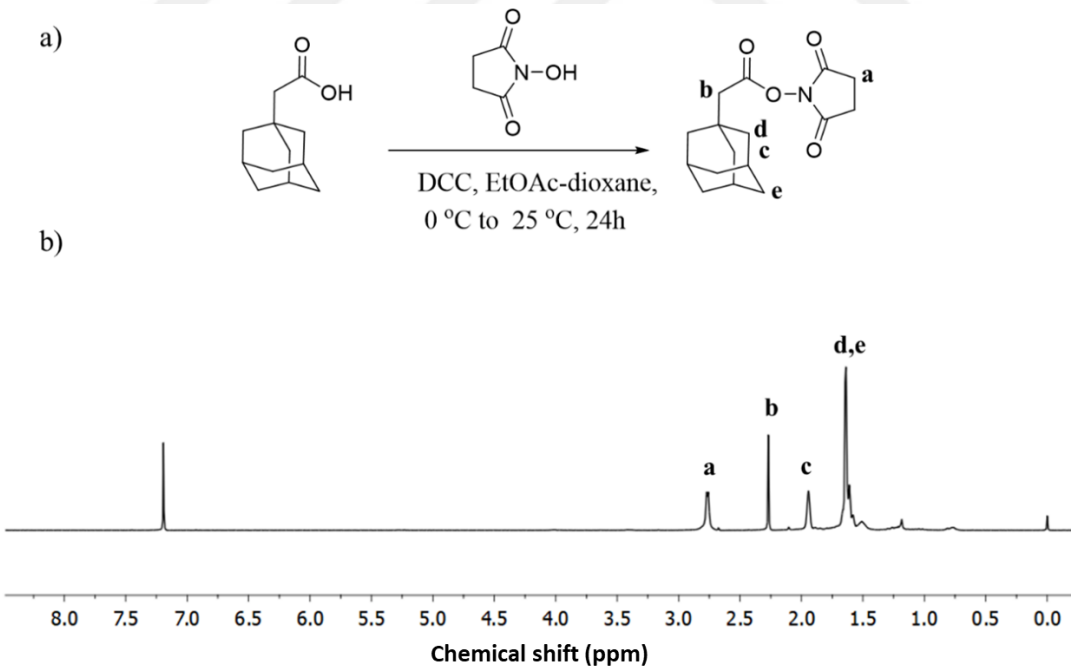

Figure 4.6. (a) Synthetic pathway of NHS-Ada, (b) ^{1}H NMR spectrum of NHS-Ada ($CDCl_3$).

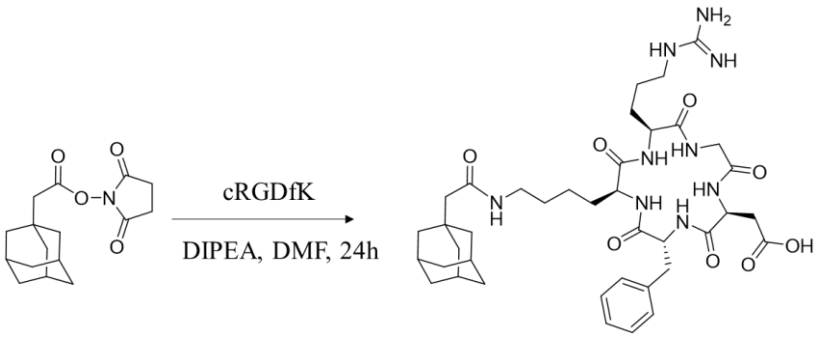

Figure 4.7. Synthesis of RGD-Ada ligand.

4.3.5. *In Vitro* Studies of Peptide-targeted Drug-loaded βCD Nanogels

Another feature of the βCD-nanogels that can be exploited further is the ability to attach an assortment of functional molecules apart from the loaded drug. Thus we evaluated simultaneous drug loading and conjugation of a cancerous cell targeting cyclic peptide during the nanogel formation. To this end, an adamantane-conjugated cRGDfK (Ada-cRGD) was added during the fabrication of drug-loaded nanogels.

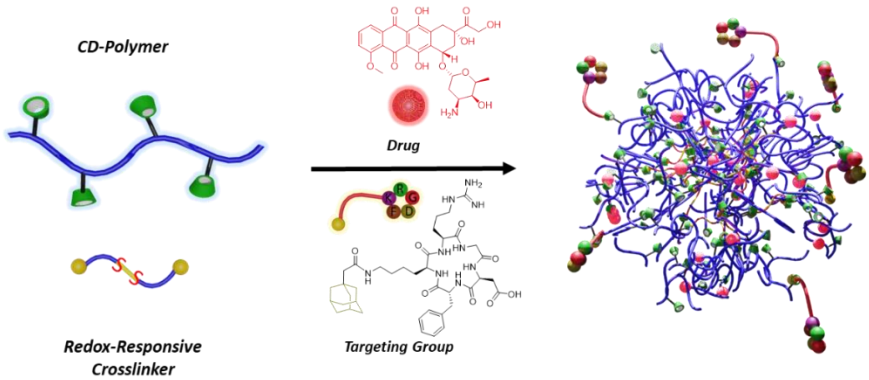

Figure 4.8. Conjugation of Ada-cRGD to βCD nanogels.

The association constant between βCD and Ada-cRGD with a 1:2 ratio was known as $1.19 \pm 0.08 \times 10^5$ M^{-1} [257]. Ka value for small Ada and βCD complexation with a 1:1 ratio is approximately 10^4 M^{-1} [258]. It was suggested that Ada-cRGD showed relatively strong binding to drug-loaded nanogels. After removing the unbound drug and targeting peptide using dialysis in water, Ada-cRGD conjugated DOX-loaded nanogels were obtained, as seen

in Figure 4.8. The presence of the cyclic peptide was confirmed using a BCA assay on drug-free nanogel, and the amount of Ada-RGD in nanogels was determined as 10 μg/mg βCD-NG using a BSA standard-based calibration curve.

In vitro drug release behavior of DOX from βCD-based nanogels was studied in buffer mimicking extracellular environment (pH 7.4) and tumor environment (pH 5.4, 1-10 mM GSH) at 37 °C. As expected, the release of DOX from the nanogels was observed to be pH and redox responsive. DOX-loaded βCD-based nanogel solutions were placed in a dialysis bag (3.5 kDa cut-off) and immersed separately in acetate buffer (pH = 5.4), 5 mM GSH-containing acetate buffer (pH = 5.4), PBS buffer (pH = 7.4), 5 mM GSH-containing PBS buffer (pH = 7.4). At certain times, the samples were taken from the outer phase of the dialysis bag, and the DOX amount was analyzed using LCMS-MS. The cumulative DOX release graph is given in Figure 4.9. For βCD-based nanogels, DOX release was higher in the acidic medium in 5 mM GSH (86%) than in acidic pH without GSH (43%). While similar DOX release trend in an acidic medium was observed at neutral pH in the presence of 5 mM GSH (44%), and a much lower DOX release was observed at pH = 7.4 (20%).

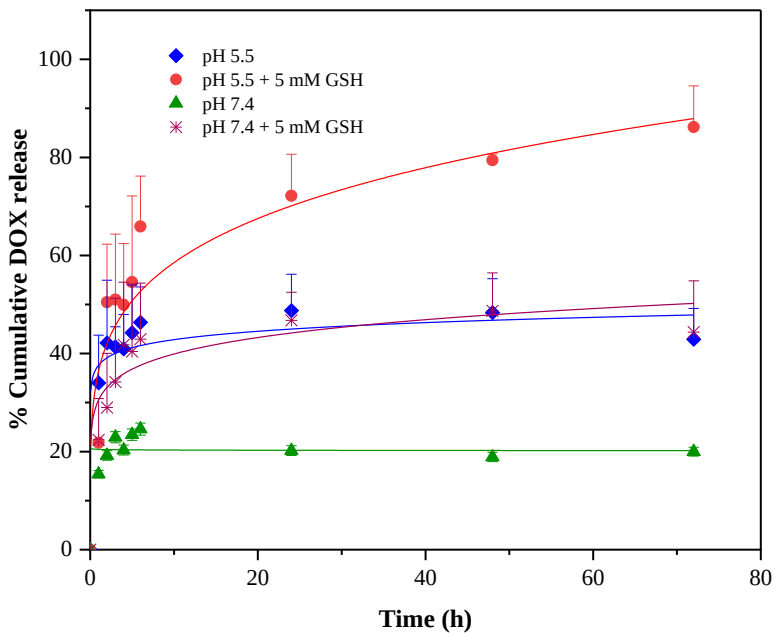

Figure 4.9. *In vitro* DOX release at pH 5.4 with and without GSH (5 mM) and at pH 7.4 with and without GSH (5 mM).

To investigate the cytotoxic effect of empty βCD-NGs and DOX-loaded βCD-NGs, in vitro CCK-8 cytotoxicity tests were performed using the MDA-MB-231 human breast adenocarcinoma cell line. MDA-MB-231 cells were treated with empty βCD-NGs, DOX-loaded βCD-NGs, and free DOX. The drug concentration was varied between $1x10^{-6}$ and $1x10^{-12}$ M, and the cells were treated with 0.1-1mg/mL of empty βCD-NGs. The CCK-8 assay indicated that empty βCD-NGs displayed no cytotoxicity even at high concentrations, as seen in Figure 4.10a.

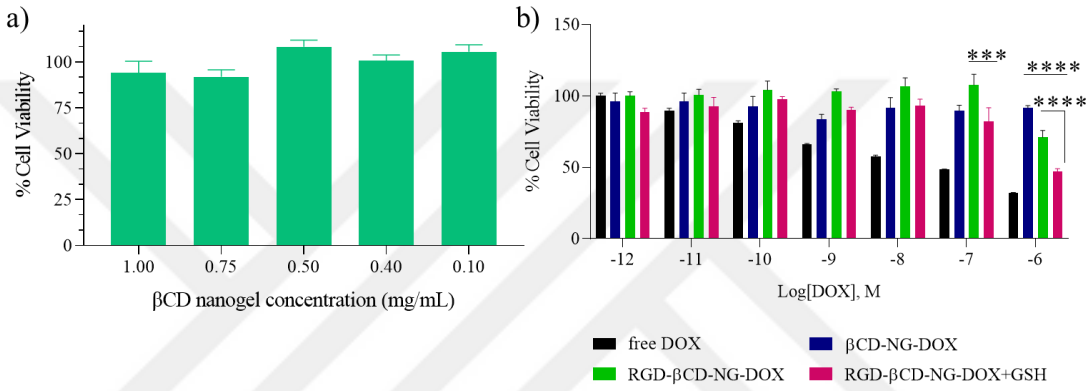

Figure 4.10. (a) Cytotoxicity assay of empty βCD nanogel on MDA-M231 cells; (b) Cell viabilities as the histogram of MDA-MB-231 cells treated with free DOX, DOX-loaded non-targeted nanogels (βCD-DOX-NG), targeted DOX-loaded nanogels (RGD-βCD-DOX-NG), and GSH-mediated targeted DOX loaded nanogels (RGD-βCD-DOX-NG + GSH) after 48 h.

Next, the cytotoxic effect of DOX-loaded βCD-NGs on cancerous cells was evaluated. In particular, MDA-MB-231 cells were treated with non-targeted and targeted nanogels and free DOX, and the drug concentration was varied between $1x10^{-6}$ and $1x10^{-12}$ M**.** In addition, the cytotoxicity of targeted DOX-loaded βCD-NGs in GSH-enriched cells was investigated. For this purpose, MDA-MD-231 cells were treated with 5 mM GSH ethyl ester (GSHOEt), a hydrophobic GSH-derivative which can rapidly penetrate cellular membranes [259-261]. After incubation for five hours with GSHOEt, cells were incubated with various amounts of targeted DOX-loaded βCD-NGs for 48 h. The cytotoxicity graph is shown in Figure 4.10b. As expected, free DOX showed the highest cytotoxic effect. It exhibited an EC_{50} = 3.43 x 10^{-8} M. Such in vitro performance of small molecule hydrophilic drugs is normal since they

can diffuse into cells faster than corresponding nanocarriers. Still, unlike nanosized carriers, they do not undergo preferential accumulation at the tumor site through the size-based EPR effect. Notably, the non-targeted (EC_{50} > 1 x 10^{-5} M) and RGD-targeted (EC_{50} > 1 x 10^{-6} M) nanogels demonstrated considerable cytotoxicity. Moreover, for the RGD-targeted βCD-NGs, the viability was lower in MDA-MB-231 cells treated with 5 mM GSHOEt (EC_{50} = 3.65 x 10^{-6} M). Here, the lower viability of MDA-MB-231 cells can be attributed to enhanced drug release through cleavage of disulfide bonds in cells with a high level of GSH concentration.

In subsequent experiments, the intracellular internalization of free DOX and DOX-loaded βCD-NGs into the MDA-MB-231 breast cancer cells was examined. The cells were incubated with free DOX, non-targeted DOX-loaded βCD-NGs (βCD-NG-DOX), and DOX-loaded targeted βCD-NGs (RGD-βCD-NG-DOX) in the absence and presence of cyclic RGDfV competitive peptide ligand. After 1h and 3h incubation, fluorescence microscopy determined internalization efficiency.

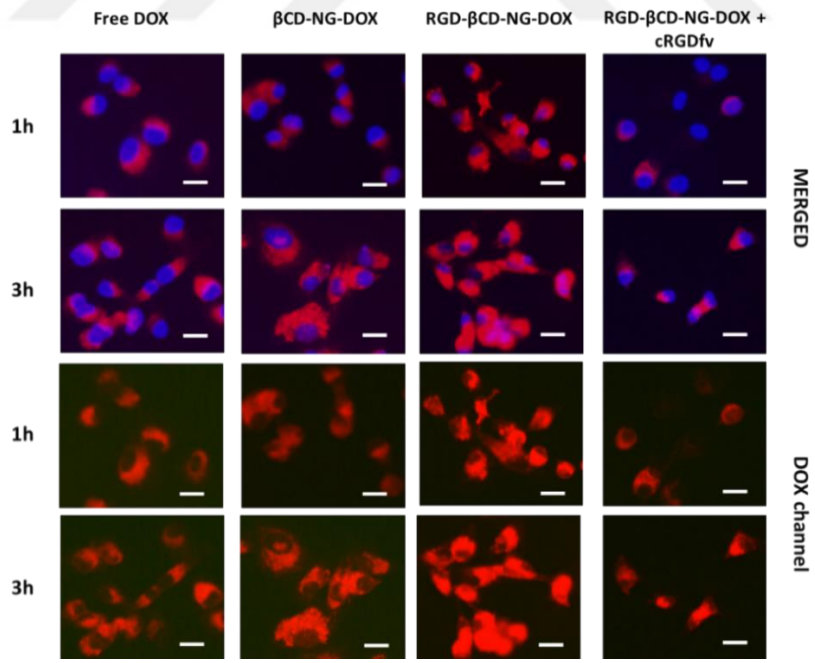

Figure 4.11. Fluorescence microscopy images of MDA-MB-231 cells treated with free DOX and DOX-loaded non-targeted (βCD-NG-DOX) and targeted (RGD-βCD-NG-DOX) nanogels. Cell nuclei were stained with DAPI (blue). Scale bar = 50 μm.

After 3h, cells incubated with DOX-loaded βCD-nanogels demonstrated significant fluorescence intensity due to internalization. Fluorescence images and internalization efficiency are shown in Figure 4.11. Additionally, a comparison of fluorescence intensities suggested that targeted DOX-loaded nanogels (RGD-βCD-NG-DOX) showed greater internalization when compared with free DOX and non-targeted nanogels. A competitive internalization experiment was done to prove that the efficient internalization of targeted RGD-βCD-NG-DOX was due to the presence of the targeting peptide. When free cRGDfV was added along with targeted RGD-βCD-NG-DOX, the internalization efficiency of RGD-βCD-NG-DOX decreased, which suggests that the free cRGDfV-based inhibitor binds to the integrin receptors on the cell surface and blocks them, thus resulting in reduced interaction of RGD-βCD-NG-DOX with cancer cells. Importantly, these experiments demonstrate that the adamantane-conjugated cyclic RGD-peptide (Ada-RGD) ligand on the βCD-NGs facilitates their intracellular uptake.

4.4. Conclusion

In summary, redox-responsive nanogels were fabricated using the self-assembly of βCD-appended dextran polymers and a disulfide group containing bis-Ada crosslinker in aqueous media. Obtained nanogels could be simultaneously loaded with an anticancer drug and a cell-targeting moiety. The drug-encapsulated nanoparticles demonstrated drug release in a stimuli-responsive manner, where the full release was obtained under an acidic and GSH-rich reducing environment. The treatment of breast cancer MDA-MB-231 cells with non-targeted and targeted βCD nanogels showed higher internalization due to targeting RGD moiety. Furthermore, in vitro cytotoxicity assay demonstrated that empty βCD nanogels show no appreciable cytotoxic effect. Additionally, targeted βCD nanogels showed higher cytotoxicity toward the GSH-enriched cancer cells than normal cancer cells. One can envision that the facile fabrication of this stimuli-responsive modular drug delivery platform will prompt interest in further evaluating this formulation for targeting other types of cancers.

5. FABRICATION OF REDOX-RESPONSIVE HYDROGEL VIA STRAIN-PROMOTED AZIDE-ALKYNE CYCLOADDITION (SPAAC) REACTION FOR DRUG DELIVERY

5.1. Introduction

Over the past decades, hydrogels have attracted increasing attention due to their utilization in various areas, such as drug and protein delivery, tissue engineering, bio-sensing, and implant coatings [63], [262,263]. Easy fabrication and modification, low cost, porous structure, and high water uptake capacity are reasons for the growing interest in hydrogels [62]. In particular, hydrogels are good candidates for controlled and local drug delivery systems.

Polymer-based injectable delivery systems, films, discs, and wafers have been used for the sustained release of anti-cancer drugs to eradicate remaining cancer cells after surgery [264]. Therefore, these systems can be used in cancer treatment along with surgery. For example, the Gliadel Wafer (MGI Pharma/Eisai Pharmaceuticals) is a biodegradable polyanhydride wafer that includes a chemotherapeutic carmustine drug. It is employed as a drug delivery implant for the treatment of brain cancer after surgery [264]. For drug delivery applications, both physically and chemically crosslinked hydrogels can be used, and chemotherapy agents can be encapsulated physically or conjugated chemically into the system.

Chemically crosslinked hydrogels with covalently attached drugs may provide sustained drug release into the targeted site by preventing burst release. The linker chemistry has gained much interest for conjugating therapeutic agents onto polymer backbone to obtain desirable release profiles. pH-responsive and hydrolyzable linkers (ester, amide, hydrazone, carbonate, carbamate), enzyme-responsive linkers (GFLG peptide), and redox-responsive linkers (disulfides) are used commonly in chemically conjugated drug delivery systems [30]. For instance, Sanyal and coworkers reported the fabrication of PEG-based hydrogel and

cryogel containing amine-responsive carbonate linker. Anticancer drug DOX was conjugated to hydrogel/cryogel using carbonate groups, and a new carbamate linker occurred between DOX and hydrogel/cryogel. Both hydrogel and cryogel showed slow DOX release. While about 6% DOX release was observed under acidic pH in the hydrogel system, a 7-fold DOX release ratio was observed for the cryogel version [265]. In another study, Wang and coworkers reported the fabrication of dendrimer hydrogel for sustained drug release. In this study, camptothecin (CPT) was covalently conjugated to polyamidoamine (PAMAM) dendrimer and subsequently reacted with polyethylene glycol diacrylate (PEGDA) to obtain dendrimer-based hydrogel. This novel hydrogel showed prolonged CPT release via ammonolysis of ester bonds [266]. In another study, CPT-conjugated injectable hydrogels were fabricated by Gao and coworkers. CPT-polymer conjugate was synthesized by using CPT and poly[oligo(ethylene glycol) maleate] (POEGM), and a carbonic ester bond occurred between CPT and polymer. Subsequently, injectable CPT hydrogel was obtained via thiol-ene "*click*" reaction using poly [oligo(ethylene glycol) mercaptosuccinate] (POEGMS), and sustained CPT release was continued for 16 days [267].

Metal-free "*click*" reactions are required to fabricate chemically crosslinked hydrogels for drug delivery applications. Although the copper-based Huisgen type cycloaddition reaction is one of the most famous click reactions to fabricate hydrogels, the toxicity of copper and purification problems restrain its usage in biomedical applications. That's why recent studies have been focused on metal-free click reactions to obtain crosslinked polymeric materials. The strain-promoted azide-alkyne cycloaddition (SPAAC) reaction [95],[97], [114], [268,269], tetrazine-norbornene reaction [270,271], Diels-Alder reaction [81], [272], epoxy-amine reaction [109], [273], thiol-Michael addition chemistry [69], [274], thiol-ene reaction [275,276], propiolic acid ester/amide-azide chemistry [277] and maleimide-azide reaction [88] are commonly used metal free "*click*" reactions to formulate hydrogels. Using such metal-free "*click*" reactions eliminates the metal impurities in the hydrogel.

This chapter focused on the synthesis of copolymers on which gemcitabine was conjugated with different linkers to the polymer backbone, the fabrication of drug-containing hydrogels, and the investigation of drug release ratios from hydrogels. GEM

containing OEGMA-based copolymers were designed, and GEM was conjugated with pH-responsive carbamate and redox-responsive disulfide linkers. In addition to the drug, azide groups on the polymer backbone were used to obtain hydrogel. Dibenzocycloocytne (DBCO) based PEG cross-linker was also synthesized, and this cross-linker also contained a disulfide linker. Strain-promoted azide-alkyne cycloaddition (SPAAC) reaction between azide and DBCO was utilized to fabricate hydrogels. The concentration of the copolymers was optimized to obtain robust and stable hydrogels. Swelling studies were investigated to understand the effect of gelation concentration. GEM release was investigated in acidic and physiological pH. In addition to pH, the release ratios were compared with and without GSH. After the release study, the cytotoxic activities of hydrogels were examined on cancer cells.

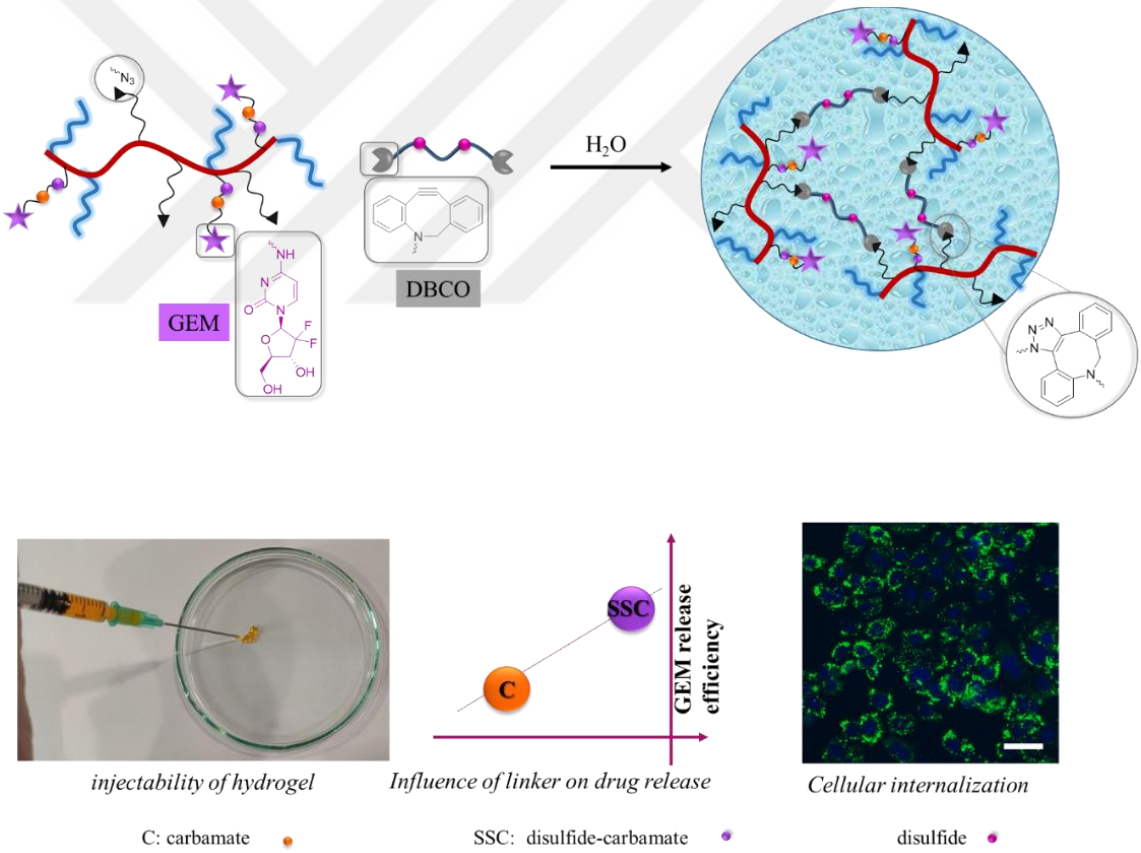

Figure 5.1. Fabrication of drug-conjugated redox-responsive hydrogels via SPAAC reaction, illustration of injectability and drug release efficiency with the linker, and representation of cellular internalization.

5.2. Experimental

5.2.1. Materials

All solvents were purchased from Merck and used as obtained without further purification. Ultrapure deionized water was obtained via Milli-Q Water Purification System (Milli-Q system, Millipore, Billerica, MA, USA). Dichloromethane (CH_2Cl_2) was obtained from the SciMatCo purification system, and other solvents were dried over molecular sieves. 4-Dimethylaminopyridine (DMAP), dibenzocyclooctyne acid, and 3-mercaptopropionic acid were purchased from Sigma Aldrich. Poly(ethylene glycol) (4000 g/mol) was purchased from Fluka. *N,N'*-Diisopropylcarbodiimide was obtained from TCI. p-Toluenesulfonic acid monohydrate (PTSA) was purchased from Alfa Aesar. Azidohexyl methacrylate monomer (AHMA) was prepared according to a published procedure [184]. 4-Cyano-4-(phenylcarbonothioylthio)pentanoic acid (CTA) was taken from Sigma Aldrich. Oligo(ethylene glycol) methyl ether methacrylate (OEGMA, Mn = 300 g/mol) was purchased from Sigma Aldrich and filtered through a basic alumina column before use. 2,2'-Azobis(2-methylpropionitrile) (AIBN) was purchased from Sigma Aldrich, recrystallized from methanol, and dried before use. The dialysis bags (Spectra/Por Biotech Regenerated Cellulose Dialysis Membranes, MWCO 3.5 kDa) were purchased from Spectrum Laboratories. DAPI and Cell Counting Kit-8 (CCK-8) were obtained from Sigma-Aldrich. Synthesis details of disulfide-containing gemcitabine methacrylate - (GEM-SSC-MA) and carbamate-containing (GEM-MA-C) monomers were given in the previous chapter. Poly(ethylene glycol) (PEG)-dithiol [278] and pyridyl disulfide alcohol (PDS-OH) [163] were synthesized according to literature procedures.

5.2.2. Methods

NMR spectra were recorded using a 400 MHz Bruker spectrometer at 25 °C. The molecular weights of the copolymers were determined by gel permeation chromatography (GPC, SEC, Shimadzu). GPC column is a PSS-SDV column (Gram linear, length/ID 8 × 300 mm, 10 μm particle size). GPC system was calibrated using poly(methyl methacrylate) standards (1−175 kDa) utilizing a refractive-index detector, and *N,N'*-dimethylacetamide

(DMAC) was used as a mobile phase at a flow rate of (1 mL/min). The gemcitabine drug release study was achieved via LCMS analysis using an LCMS 2020-Mass Spectrometer System equipped with a C-18 (5 μm -150 × 4.6 mm) column (Shimadzu, Japan). The microstructures or morphologies of obtained hydrogels were investigated using a scanning electron microscopy (SEM) instrument with an accelerating voltage of 10 kV (JEOL NeoScope JCM-5000). The rheological behaviors of hydrogels were determined by measuring the hydrogel's loss (G'') and storage (G') moduli using Anton PAAR MCR 302 rheometer. In cytotoxicity experiments, absorbance values were measured using a Multiscan FC Microplate Photometer from Thermo Scientific. Cellular internalization experiments were performed using a Zeiss Observer Z1 fluorescence microscope connected to Axiocam MRc5 and processed with Zeiss Zen Blue lite software (Carl Zeiss, Jena, Germany).

5.2.3. Synthesis of Disulfide-Containing Poly(ethylene glycol)-diol

Poly(ethylene glycol) (PEG)-dithiol was synthesized according to a published procedure using poly(ethylene glycol) (4000 g/mol) and 3-mercaptopropionic acid in the presence of PTSA catalyst [278]. Pyridiyl disulfide alcohol (PDS-OH, 52 mg, 0.276), which was synthesized using a published procedure [163], was dissolved in methanol (0.2 mL), and a catalytic amount of acetic acid (0.034 mmol, 2 μL) was added. In a separate reaction flask, PEG-dithiol (300 mg, 0.069 mmol) was dissolved in methanol (0.8 mL), and PEG-dithiol solution was dropwise added to the PDS-OH solution. The reaction mixture was stirred at room temperature for 4 hours. After 4 hours, methanol was evaporated, and the crude product was redissolved in the minimum amount of CH_2Cl_2. The solution was precipitated in cold diethyl ether (Et_2O). The solid product was washed with diethyl ether until the yellow color disappeared. ^{1}H NMR (400 MHz, $CDCl_3$): δ/ppm = 4.26 (m, 4H), 3.85 (m, 4H), 3.82 - 3.44 (m, 358H), 2.96 - 2.88 (m, 12H).

5.2.4. Synthesis of Dibenzocyclooctyne-Containing PEG Crosslinker

Disulfide containing PEG-diol ($PEG(SS\text{-}OH)_2$, 61 mg, 0.014 mmol), dibenzocyclooctyne acid (DBCO-acid, 10 mg, 0.030 mmol), and 4-(dimethylamino)pyridine (DMAP, 0.855 mg, 7 x 10^{-3} mmol) were dissolved in anhydrous CH_2Cl_2 (0.8 mL). This solution was cooled to 0 ^oC using an ice bath. At ^oC, DIC (N,N'-Diisopropylcarbodiimide)

in 0.2 mL anhydrous CH_2Cl_2 was slowly added to the mixture. After that, the reaction mixture was stirred from 0 ^oC to room temperature for 24 h. After 24 h, the mixture was poured into CH_2Cl_2 (50 mL) and extracted with 0.1 M NaCl solution (10 mL x 2). The organic layer was dried over Na_2SO_4. CH_2Cl_2 was evaporated, and the crude product was precipitated in cold diethyl ether (white solid, 75% yield). ^1H NMR (400 MHz, $CDCl_3$): δ/ppm = 7.61 (d, *J* = 7.6, 2H), 7.60 - 7.33 (m, 1H), 5.07 (d, *J* = 13.8, 2H), 3.80 - 3.37 (m, 360H), 2.83 (t, *J* = 6.9, 4H), 2.76 (t, *J* = 6.7, 4H), 2.68 (t, *J* = 7.1, 4H), 2.16 - 2.10 (m, 2H), 2.05 (t, *J* = 7.4 4H), 1.40 - 1.17 (m, 10H). ^{13}C NMR ($CDCl_3$, δ, ppm): 173.2, 171.7, 158.3, 152.0, 148.1, 132.4, 129.1, 128.5, 128.4, 128.2, 127.8, 127.3, 125.6, 123.2, 122.8, 115.2, 107.9, 70.7, 69.2, 64.0, 62.3, 55.5, 37.1, 34.5, 34.1, 33.8, 33.4, 24.9, 24.2.

5.2.5. Synthesis of P(OEG/N_3) Copolymer via RAFT Polymerization

OEGMA (1000 mg, 3.33 mmol) and AHMA monomer (31 mg, 0.149 mmol) were dissolved in anhydrous DMF (6 mL), and the mixture was stirred for 30 min under N_2. 4-cyano-4-(thiobenzoylthio)pentanoic acid (5.75 mg, 0.021 mmol) as a chain transfer reagent and AIBN (0.68 mg, 4.14 x 10^{-3} mmol) as initiator were added to polymer solution under nitrogen atmosphere. The reaction flask was sealed and heated at 70 ^oC for 18 h. After 18 h, the polymer solution was dialyzed against MeOH: ACN (5:95) for two days. The polymer was obtained as pink viscous (0.72 g, 70 % yield). GPC (SEC): Mn = 58 kDa; Mw / Mn = 1.6. ^1H NMR (400 MHz, $CDCl_3$): δ/ppm = 4.07 (br s, 2H), 3.65 (br s, 14H), 3.54 (br s, 2H), 3.37 (s, 3H), 3.30 (br s, 2H), 1.85 (br s, 3H), 1.00 - 0.89 (m, CH_2 and CH_3 polymer backbone).

5.2.6. Synthesis of P(OEG/GEM-C/N_3) Copolymer via RAFT Polymerization

OEGMA (1000 mg, 3.33 mmol), carbamate-containing gemcitabine methacrylate monomer (GEM-C-MA, 83 mg, 0.198 mmol), and AHMA monomer (31 mg, 0.149 mmol) were dissolved in anhydrous DMF (6 mL), and the mixture was stirred for 30 min under N_2. 4-cyano-4-(thiobenzoylthio)pentanoic acid (5.75 mg, 0.021 mmol) as a chain transfer reagent, and AIBN (0.68 mg, 4.14 x 10^{-3} mmol) as initiator were added to polymer solution under nitrogen atmosphere. The reaction flask was sealed and heated at 70 ^oC for 18 h. After 18 h, the polymer solution was dialyzed against MeOH: ACN (5:95) for two days. The

polymer was obtained as pink viscous containing % 3.28 GEM by weight. GPC (SEC): Mn = 45 kDa; Mw / Mn = 1.30. ^{1}H NMR (400 MHz, $CDCl_3$): δ/ppm = 8.28 (br s, 1H), 6.31 (br s, 1H), 4.07 (br s, 2H), 3.65 (br s, 14H); 3.54 (br s, 2H), 3.37 (s, 3H), 3.30 (br t, 2H), 1.85 (br s, 3H), 1.00-0.89 (m, CH_2 and CH_3 polymer backbone).

5.2.7. Synthesis of P(OEG/GEM-SSC/N_3) Copolymer via RAFT Polymerization

OEGMA (1000 mg, 3.33 mmol), disulfide-carbamate containing gemcitabine methacrylate monomer (GEM-SSC-MA, 103 mg, 0.201 mmol), and AHMA monomer (32 mg, 0.151) were dissolved in anhydrous DMF (5 mL), and the mixture was stirred for 30 min under N_2. 4-cyano-4-(thiobenzoylthio)pentanoic acid (5.86 mg, 0.021 mmol) as a chain transfer reagent, and AIBN (0.69 mg, 4.2 x 10^{-3} mmol) as initiator were added to polymer solution under nitrogen atmosphere. The reaction flask was sealed and heated at 70 ºC for 19 h. After 19 h, the polymer solution was dialyzed against MeOH: ACN (5:95) for two days. The polymer was obtained as pink viscous containing % 3.43 GEM by weight (0.99 g, 88 % yield). GPC (SEC): Mn = 50 kDa; Mw / Mn = 1.50. ^{1}H NMR (400 MHz, $CDCl_3$): δ/ppm = 8.29 (br s, 1H), 6.31 (br s, 1H), 4.08 (br s, 2H), 3.65 (br s, 14H); 3.56 (br s, 2H), 3.37 (s, 3H), 3.30 (br t, 2H), 1.80 (br s, 3H), 1.01-0.86 (m, CH_2 and CH_3 polymer backbone).

5.2.8. Synthesis of P(OEG/GEM-SS-C/N_3/BODIPY) Copolymer via RAFT

OEGMA (533 mg, 1.78 mmol), GEM-SSC-MA (57 mg, 0.112 mmol), AHMA (18 mg, 0.08 mmol), and BODIPY-MA (20 mg, 0.04 mmol) were dissolved in anhydrous DMF (4 mL) and purged with N_2 for 30 min. Under purging with nitrogen, 4-cyano-4-(thiobenzoylthio)pentanoic acid (3.26 mg, 0.012 mmol) and AIBN (0.38 mg, 2.33x10^{-3} mmol) with 100 µL anhydrous DMF. The reaction flask was sealed and heated at 70 ºC for 19 h. After 19 h, the polymer solution was dialyzed against MeOH: ACN (5:95) for two days. The polymer was obtained as orange viscous containing % 2.79 GEM by weight (0.62 g, 56 % yield). GPC (SEC): Mn = 50 kDa, Mw / Mn = 1.35. ^{1}H NMR (400 MHz, $CDCl_3$): δ/ppm = 8.31 (s, 1H), 6.32 (s, 1H), 6.06 (s, 1H), 4.08 (br s, 2H), 3.66 (br s, 14H), 3.55 (br s, 2H), 3.38 (s, 3H), 3.33 (br s, 2H), 1.88-0.87 (m, CH_2 and CH_3 polymer backbone).

5.2.9. Preparation of Hydrogels via SPAAC Reaction

Hydrogels were prepared using a P(OEG/GEM-SSC/N_3) copolymer and different polymer concentrations (5%, 10%, and 15% by weight). The ratio of DBCO and azide was kept at 1:1. P(OEG/GEM-SSC/N_3) (10 mg, 1.90 x10^{-3} mmol N_3) was dissolved in deionized water. In a separate eppendorf, DBCO-SS-PEG-SS-DBCO crosslinker (4.88 mg, 9.52x10^{-4} mmol) was dissolved in deionized. The solution of the DBCO crosslinker was added to the copolymer solution. Water amounts were determined according to final polymer concentration by weight percent. The mixture was immediately sonicated to get a homogeneous hydrogel network. Later 2-3 min, hydrogel formation was observed when the eppendorf tube was tilted. Gelation was continued overnight at 37 ^{o}C by shaking to provide complete crosslinking. The resulting hydrogels were purified by washing with the excess amount of deionized water at 37 °C shaking. After purification, hydrogels were lyophilized to get the dry gel.

Another hydrogel system was prepared using P(OEG/GEM-C/N_3) copolymer and DBCO-SS-PEG-SS-DBCO crosslinker with the same weight percent. After obtaining hydrogels, they were dried using a lyophilizer after purification.

5.2.10. Swelling Study

At room temperature, lyophilized dry hydrogel samples (5 mg) were immersed in deionized water (15 mL). At periodic time points, the hydrogel was taken from the water, and water on the surface of the hydrogel was removed and subsequently weighed. The swelling experiment was continued until obtaining a constant hydrogel weight. The degree of swelling was calculated as [(M_s-M_{dry})/M_{dry}] x 100, where M_{dry} and M_s refer to the weight of dry and swollen hydrogels, respectively. The swelling experiment was repeated three times.

5.2.11. Rheological Study

Hydrogels' rheological analysis was evaluated using an Anton Paar MCR 302 rheometer. A circular plate (15 mm diameter) was utilized as test geometry. An amplitude

sweep test was applied on swollen state hydrogels to examine strain amplitude dependence of hydrogel's sol-gel behavior, and it gives information about the viscoelastic characteristic of hydrogels. Time sweep and frequency sweep tests (0.1-100 Hz, 1% strain) were performed. The Frequency sweep measurement also gives information on the behavior of hydrogel below critical strain. A frequency-independent G' value shows a more solid state of hydrogels. A closed system was used to prevent water evaporation from hydrogels during measurements

5.2.12. Degradation, Injectability, and Self-Healing Properties of Hydrogel

BODIPY dye-conjugated and GEM-containing polymer was used for degradation and injectability studies. BODIPY-containing HG-GEMSSC hydrogel (5 wt %) was prepared. Hydrogel degradation was investigated in two GSH concentrations: 1 mM and 5 mM. Visual degradation of hydrogels was shown under UV-lamp.

For the injectability test, BODIPY-conjugated HG-GEMSSC hydrogel (5 wt %) was prepared in a syringe. After 24 hours, the hydrogel was injected from a 21-gauge needle onto a petri dish. In addition, the hydrogel was injected into water.

The self-healing behavior of HG-GEMSSC was investigated using two pieces of hydrogels. Two spherical hydrogels were prepared, and each hydrogel was colored with rhodamine B (RhB) and bromophenol blue (BPB). The hydrogels were cut, and newly obtained hydrogels were rejoined at room temperature. For visualization of the self-healing ability of the HG-GEMSSC hydrogel, the tensile strength test was applied to the healed hydrogel using a tweezer.

5.2.13. Gemcitabine Release Study

GEM release profiles from obtained hydrogels were investigated at pH 7.4 and pH 6.8 with and without 1 mM GSH. The freeze-dried hydrogel samples were put into a dialysis bag along with (a 400 µL release buffer), and subsequently, the dialysis bags were immersed in the release buffer containing vials. The samples were incubated by shaking at 37 ^{o}C. The

release media were replaced with 2 mL fresh buffer each hour. The released GEM amount was determined using LCMS analysis.

5.2.14. Biocompatibility of Hydrogels on L-929 Mouse Fibroblast Cells

Cytotoxicity of the blank hydrogels (no GEM on polymer backbone) was investigated via CCK-8 viability assay on L929 fibroblast cells. L929 cells were grown in DMEM media supplemented with 10% FBS and 1% v/v DMEM according to the manufacturer's culture method requirements and incubated at 37 °C under 5 % CO_2. L929 cells (7000 cells/well) were seeded on the 96 well-plate with culture medium (100 μL) and incubated at 37 °C for 24 h. After 24 h incubation, dried hydrogel samples (from 0.5 mg to 2 mg) were added to cell-containing wells) (n = 4), and 100 μL DMEM was added to wells. After that, cells were incubated with hydrogels for 24 hours. At the end of 1day, hydrogel samples were removed from the cells, and the cells were washed with 1 x PBS (100 μL). CCK-8 solution (10%) was added to cells to measure cell viability. After incubation for 2 hours, the absorbance values at 450 nm were recorded using a microplate reader. Cytotoxicity results were analyzed using GraphPad Prism Software. Biocompatibility of blank hydrogels was also shown using the live-dead assay. L929 fibroblast cells were treated with blank hydrogel (2 mg) for 24 h. After that, the live-dead assay was performed, and the viability of cells was visualized under the fluorescence microscope.

5.2.15. Cytotoxicity Experiment on BxPC-3 Pancreatic Adenocarcinoma Cells

Human pancreatic adenocarcinoma BxPC-3 cells were grown in RPMI media supplemented with 10% FBS and 1% v/v MEM according to the manufacturer's culture method requirements and incubated at 37 °C under 5 % CO_2. BxPC-3 cells (7000 cells/well) were seeded on a 96-well plate as triplicates with RPMI (100 μL), and cells were incubated at 37 °C for 24 h for cells. After 24 h, the cell-containing wells were divided into five groups. Two groups are control groups, and they were incubated with cell media and glutathione ethyl ester (GSHOEt, 1 mM). The remaining groups were experimental groups. In the experimental group, hydrogel samples on which gemcitabine was conjugated with disulfide (HG-GEMSSC) linkages were put into cell-containing wells (n = 3), and 200 μL RPMI was added.

The other experimental group was incubated with HG-GEMSSC hydrogels in the presence of 1 mM GSHOEt containing RPMI (n = 3). The last group of cells was treated with free GEM. GEM concentration was kept at $1x10^{-5}$ M for free GEM and GEM-containing hydrogel samples. All groups were incubated for 24 h. After 24 h incubation, hydrogel samples and cell media were removed from the cells, and cells were washed with 1xPBS. CCK-8 assay was applied to cells to determine viability, and the processing was done with GraphPad Prism Software. The same experiment was done with another hydrogel system where GEM was conjugated via only carbamate linkers (HG-GEMC).

5.2.16. Cellular Internalization

For the cellular internalization experiment, BxPC-3 pancreatic adenocarcinoma cells (150000 cells/well) were seeded in a 12-well plate as triplicates in 1 mL culture media (RPMI). The cells were incubated at 37 °C for 24 h. After 24 h, one group of cells was incubated with 1 mM GSHOEt for 3 hours. After 3 h, the solution of GSHOEt was removed from the cells, and the cells were washed with the excess amount of PBS. A fluorescent BODIPY-containing-hydrogels, which were prepared using P(OEG/GEM-SS/N_3/BODIPY) copolymer, were applied to cells and the BODIPY concentration was 2 µM. The first cell group was incubated with BODIPY-containing hydrogels. The second group, which was treated with GSHOEt, was treated with BODIPY-hydrogels. In the third group, BODIPY-hydrogel samples were added to cells, and cell media contained 1 mM GSHOEt. Control group cells were incubated with only RPMI. In addition, another cell group was treated with free BODIPY-OH (2 µM). The cells were incubated for 24 hours at 37 ^oC.

After 24 h, BODIPY dye solutions and dye-containing hydrogels were removed from the cells, and the cells were washed with PBS (3 x 1 mL). After washing, the cells were fixed using a 3.7% formaldehyde solution for 10 min at 37 ^oC. After washing with PBS, cell nuclei were stained with DAPI for 20 min at 37 ^oC. After the staining process, the cells were washed with PBS (3 times x 1 mL). Cell images were recorded using a Zeiss Observer Z1 fluorescence microscope. Image processing was done with Zeiss Zen Blue lite software (Carl Zeiss, Jena, Germany).

5.3. Results and Discussion

5.3.1. Synthesis of Azide (N_3)-containing PEG-based Copolymer P(OEG/N_3)

The synthesis of the azide group containing hydrophilic copolymer was accomplished using RAFT polymerization of PEG-based methacrylate (OEGMA) monomer and azide-containing methacrylate (AHMA) monomer. Briefly, AHMA was polymerized with commercially available OEGMA (Mn = 300 g/mol) at 70 ^oC via RAFT polymerization. The PEG-based monomer was selected to synthesize hydrophilic copolymers with an anti-biofouling character. AHMA monomer was chosen to use a click-based reaction for further experiments. The polymerization reaction is shown in Figure 5.2.

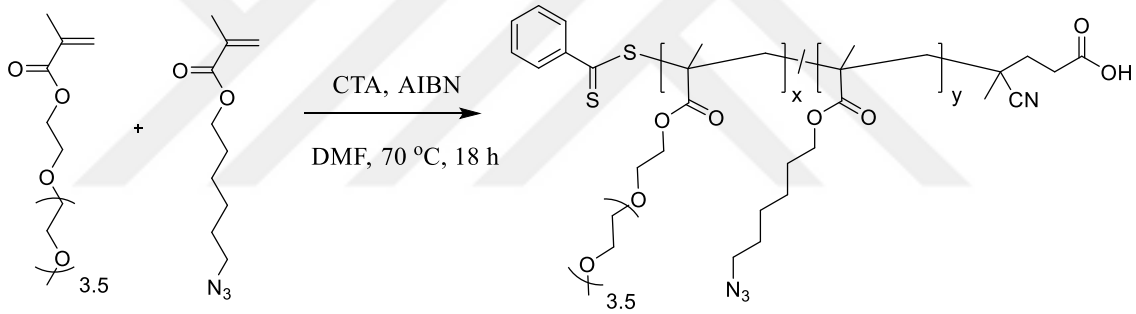

Figure 5.2. The synthesis of P(OEG/N_3) copolymer via RAFT polymerization.

Table 5.1. Characterization and properties of P(OEG/N_3) copolymer.

No	Feed Ratio (#)		Obtained Ratio (#)		CTA	AIBN	Mn (kDa)	Mw/Mn (PDI)
	OEG	-N_3	OEG	-N_3				
1	96	4	94.6	4.07	5	1	58	1.6

^1H NMR and SEC analysis achieved the characterization of the P(OEG/N_3) copolymer. The full ^1H NMR spectrum is given in Figure 5.3. The characteristic peak of methoxy group hydrogens due to the OEG unit was observed at 3.38 ppm. In addition to this peak, the hydrogen resonance at 3.26 ppm due to methylenic hydrogens, which was adjacent

to the azide group (b marked), demonstrated clearly that AHMA monomer was successfully copolymerized with OEGMA monomer. The number of azide units on the polymer backbone was calculated as 4.07 using proton integrations of methoxy group hydrogens and methylenic hydrogens. The molecular weight and molecular weight distribution were determined as 58 kDa and 1.60 via SEC analysis.

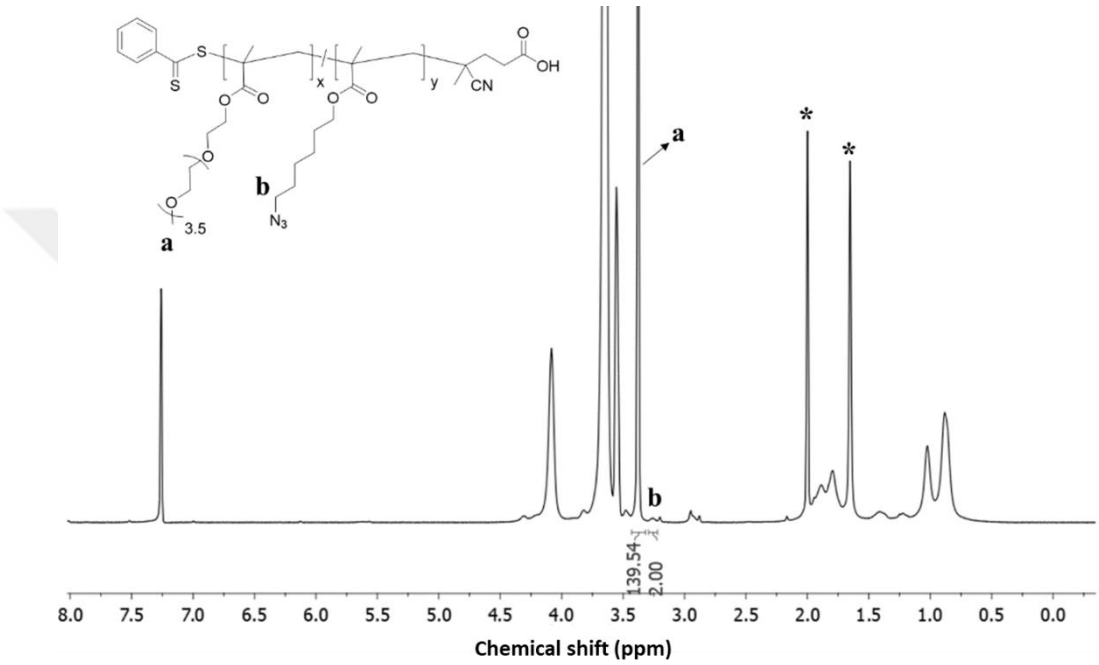

Figure 5.3. The ^{1}H NMR spectrum of P(OEG/N_3) copolymer ($CDCl_3$).

5.3.2. Synthesis of Azide (N_3) and Carbamate-containing Gemcitabine-including PEG-based Copolymer P(OEG/N_3/GEM-C)

The synthesis of azide and GEM containing hydrophilic copolymer was accomplished using RAFT polymerization. The synthesis of carbamate containing GEM-MA-C monomer was shown in the previous chapter (chapter 3). For this purpose, AHMA and GEM-MA-C monomers were copolymerized randomly with OEGMA monomer using RAFT polymerization. In this formulation, GEM anticancer drug was conjugated to a polymer backbone via a pH-responsive carbamate linker. The obtained random copolymer was characterized via ^{1}H NMR and SEC analysis. The synthesis scheme of the P(OEG/N_3/GEM-C) copolymer is shown in Figure 5.4.

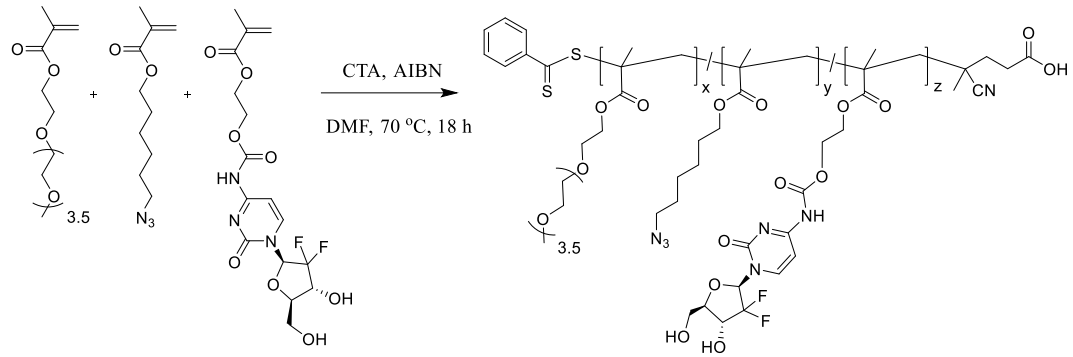

Figure 5.4. The synthesis of P(OEG/N_3/GEM-C) copolymer via RAFT polymerization.

Table 5.2. The properties of P(OEG/N_3/GEM-C).

No	**Feed Ratio (#)**			**Obtained Ratio (#)**			**CTA**	**AIBN**	**Mn (kDa)**	**Mw/Mn (PDI)**
	OEG	-N_3	GEM	OEG	-N_3	GEM				
1	88	4	8	90.3	4.2	5.5	5	1	45	1.3

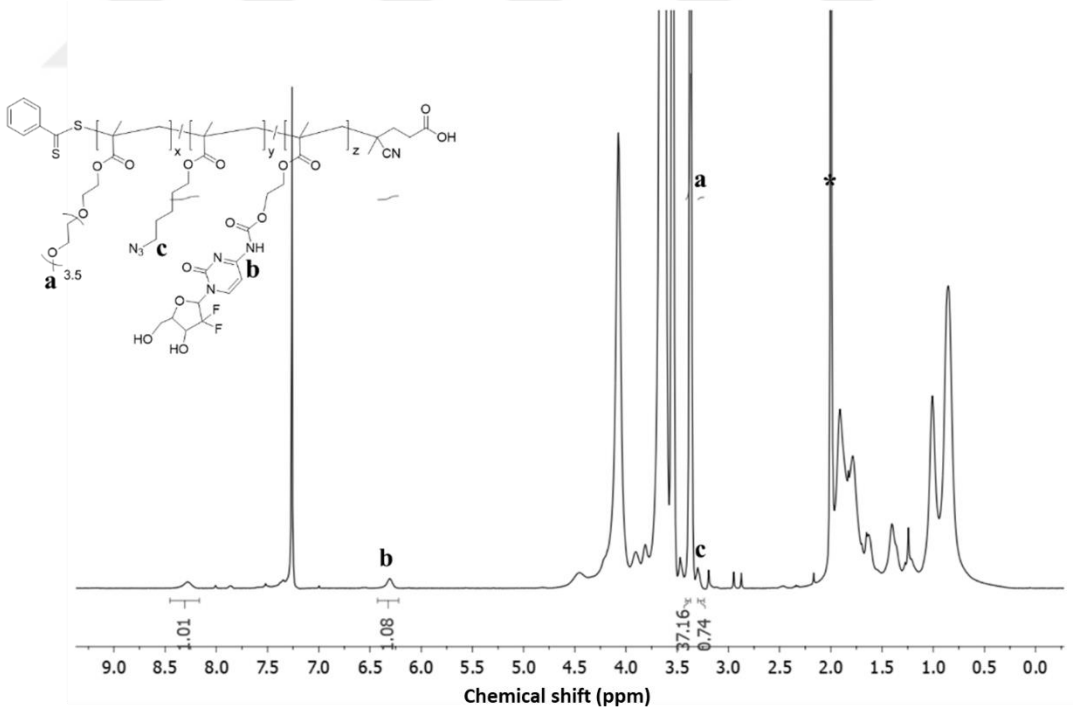

Figure 5.5. ^{1}H NMR spectrum of P(OEG/N_3/GEM-C) copolymer.

The full ^{1}H NMR spectrum of the P(OEG/N_3/GEM-C) copolymer is shown in Figure 5.5. The proton resonances at 8.27 and 6.30 ppm were due to the aromatic region of gemcitabine. The proton resonance of the terminal methyl ether unit (-OCH_3) was observed at 3.37 ppm. Additionally, the signal of the methylene group adjacent to the azide group (-CH_2-N_3) emerged at 3.30 ppm. These peaks showed successful copolymerization among OEGMA, AHMA, and GEM-C-MA.

5.3.3. Synthesis of Azide (N_3) and Disulfide-carbamate-containing Gemcitabine-including PEG-based Copolymer P(OEG/N_3/GEM-SSC)

OEGMA monomer was randomly copolymerized with AHMA and GEM-SSC-MA monomers using RAFT polymerization to synthesize P(OEG/N_3/GEM-SSC) copolymer. Polymerization reaction was carried out at 70 ^{o}C for 18-19 h. In this case, gemcitabine was conjugated to the polymer backbone via pH-responsive carbamate and redox-responsive disulfide bonds. The synthesis scheme is shown in Figure 5.6.

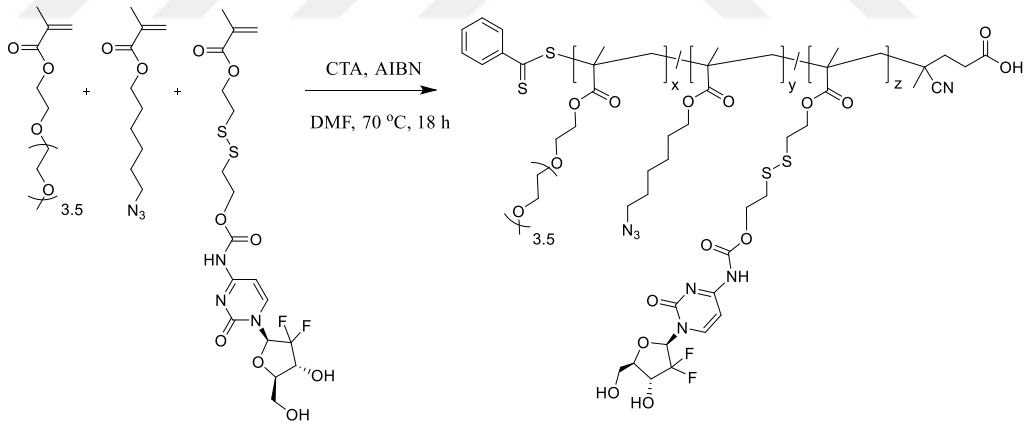

Figure 5.6. The synthesis of P(OEG/N_3/GEM-SSC) copolymer via RAFT polymerization.

Table 5.3. The properties of P(OEG/N_3/GEM-SSC).

No	Feed Ratio (#)			Obtained Ratio (#)			CTA	AIBN	Mn (kDa)	Mw/Mn (PDI)
	OEG	-N_3	GEM	OEG	-N_3	GEM				
1	88.0	4.0	8.0	88.0	4.0	8.0	5	1	50	1.5

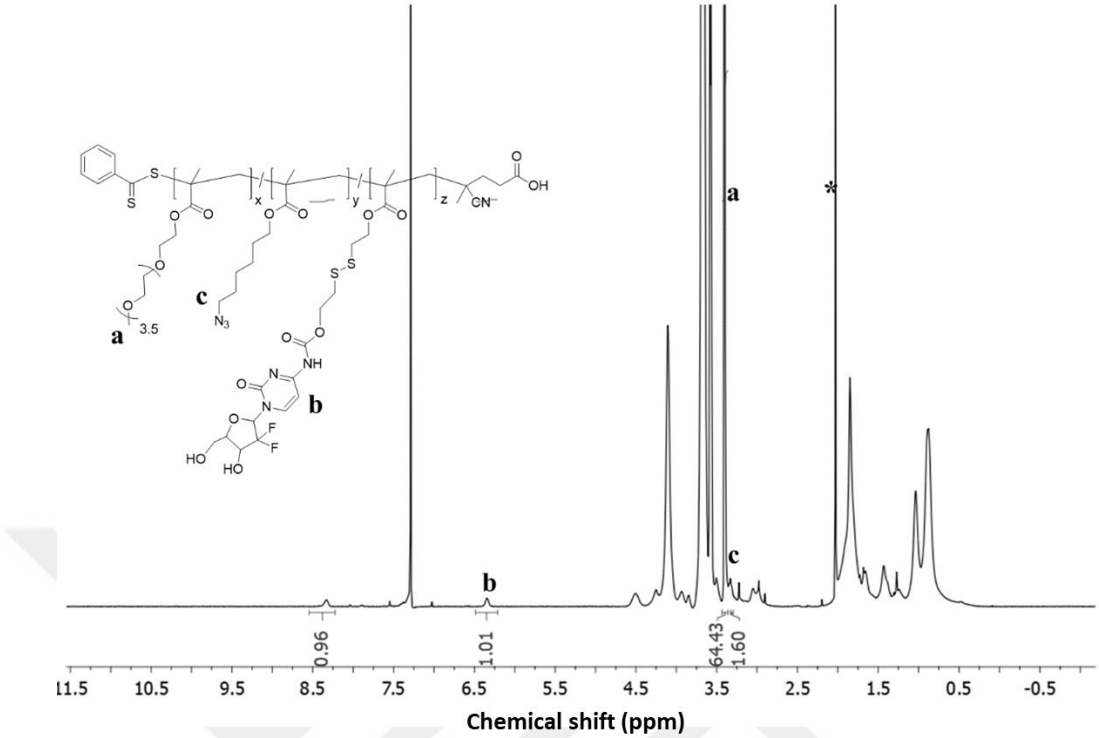

Figure 5.7. ^{1}H NMR spectrum of P(OEG/N_3/GEM-SSC) copolymer.

The P(OEG/N_3/GEM-SSC) copolymer was characterized via SEC and ^{1}H NMR. The ^{1}H NMR spectrum is demonstrated in Figure 5.7. The peak at 8.30 and 6.33 ppm, coming from gemcitabine, and the other peaks at 3.37 and 3.30 ppm due to the methoxy group and methylene group (-CH_2-N_3), respectively, demonstrated incorporation of all monomers on the polymer backbone. The molecular weight of the P(OEG/N_3/GEM-SSC) copolymer was determined as 50 kDa via SEC analysis.

5.3.4. Synthesis of Azide (N_3) and GEM and BODIPY-containing PEG-based Copolymer P(OEG/N_3/GEM-SSC/BODIPY)

The BODIPY-dye conjugated copolymer P(OEG/N_3/GEM-SSC/BODIPY) was synthesized using OEGMA, AHMA, GEM-SSC-MA, and BODIPY-MA monomers via RAFT polymerization at 70 ^{o}C for 19 h. The polymerization scheme is shown in Figure 5.8. BODIPY dye was conjugated to the polymer backbone via an ester linker. The copolymer was characterized with ^{1}H NMR, SEC.

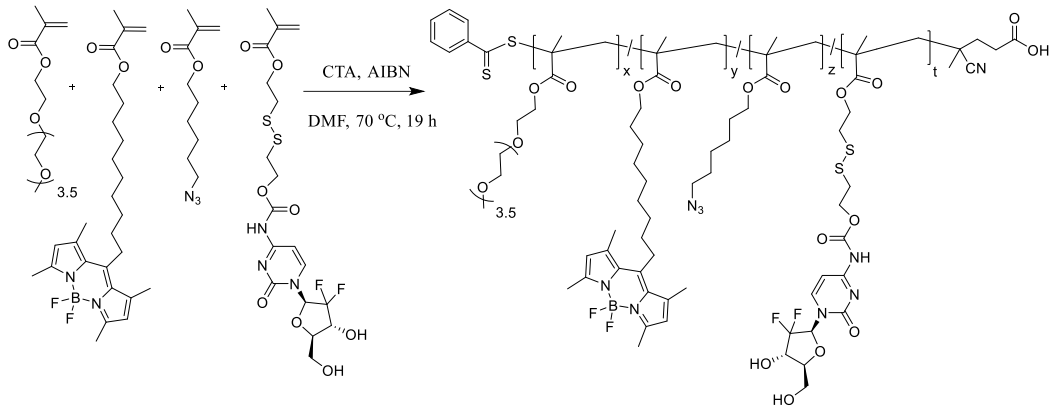

Figure 5.8. The synthesis of P(OEG/N_3/GEM-SSC/BODIPY) copolymer.

The ^{1}H NMR spectrum of P(OEG/N_3/GEM-SSC/BODIPY) was demonstrated in Figure 5.9. In addition to peaks at 8.31, 3.38, and 3.33 ppm coming from gemcitabine, methoxy of OEG unit and methylene group of AHMA unit (-CH_2N_3), the new peak at 6.06 ppm was observed, and this peak originated from BODIPY ring (d labeled). The molecular weight of the copolymer was determined as 50 kDa via SEC analysis.

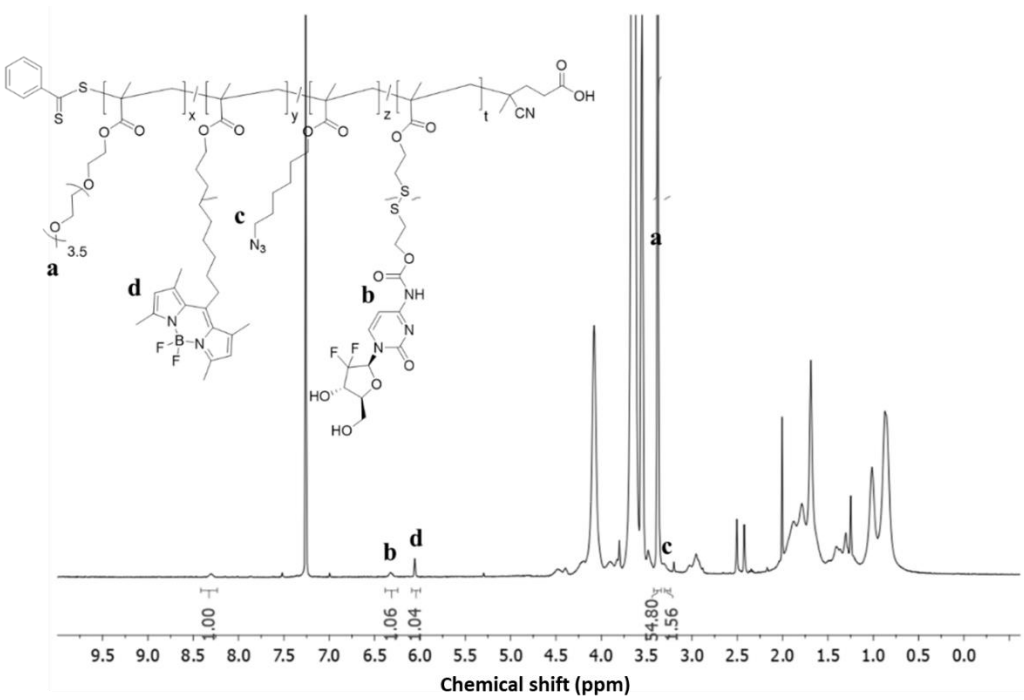

Figure 5.9. The ^{1}H NMR spectrum of P(OEG/N_3/GEMSSC/BODIPY).

5.3.5. Synthesis of Disulfide-Containing DBCO-PEG Crosslinker

The other polymeric precursor, PEG-SS-$(DBCO)_2$ or DBCO-SS-PEG-SS-DBCO was synthesized in 3 steps. In the first step, PEG (4000 g/mol) was reacted with 3-mercaptopropionic acid, and PEG-dithiol was obtained [278]. In the second step, pyridyl disulfide alcohol (PDS-OH) was synthesized according to the literature procedure [163]. The obtained PDS-OH was reacted with PEG-dithiol in the presence of acetic acid as a catalyst. The end of the reaction gave disulfide containing PEG-diol ($PEG(SS\text{-}OH)_2$). In the final step, DBCO-acid was introduced on both ends of a PEG-diol ($PEG(SS\text{-}OH)_2$) using an EDCI-mediated esterification reaction.

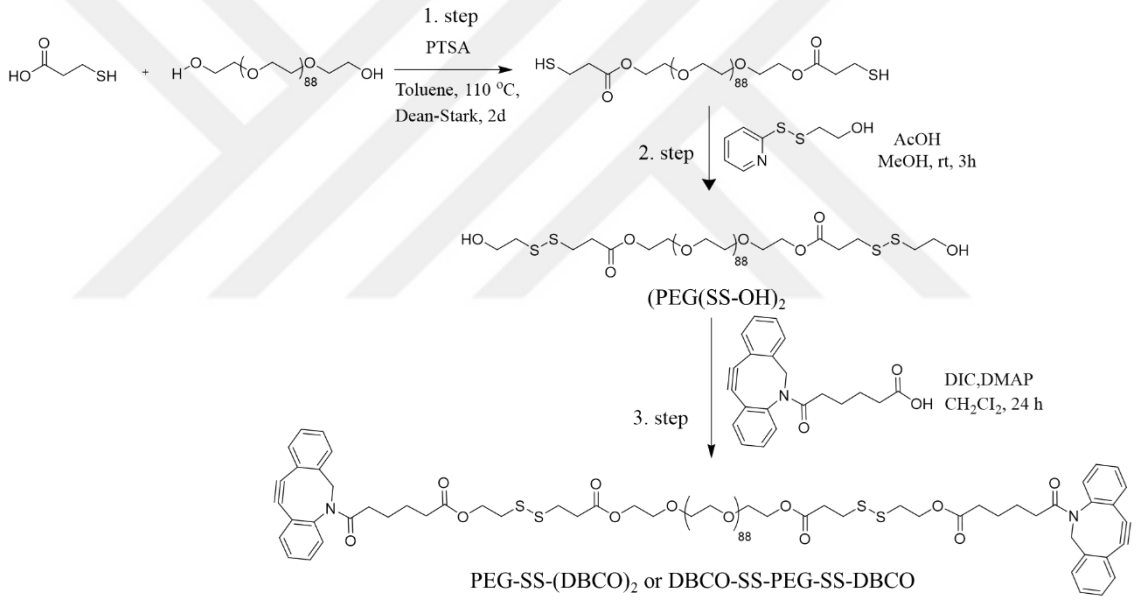

Figure 5.10. The PEG-SS-$(DBCO)_2$ crosslinker synthesis steps.

$PEG(SS\text{-}OH)_2$ and PEG-SS-$(DBCO)_2$ were characterized by ^1H NMR analysis. The full spectra are given in Figure 5.11 and Figure 5.12. In the ^1H NMR spectrum of $PEG(SS\text{-}OH)_2$, the hydrogen signal (a labeled) at 4.20 ppm coming from the methylene group adjacent to the ester group and the b labeled peak at 3.79 ppm due to the methylenic hydrogens adjacent to hydroxy end group (-CH_2-OH) showed successful thiol-pyridyl disulfide exchange reaction between PDS-OH and PEG-dithiol groups. The end group functionalization was calculated as 97% using integrations of a labeled peak and peak of PEG.

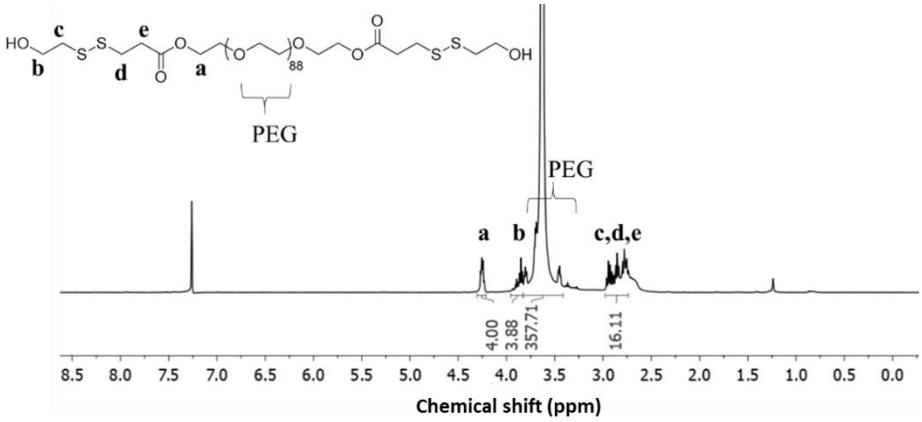

Figure 5.11. The ^{1}H NMR spectrum of PEG(SS-OH)$_2$.

As for the ^{1}H NMR spectrum of PEG-SS-(DBCO)$_2$ crosslinker, the proton resonances between 7.69 - 7.60 ppm (labeled with star) originated from the DBCO group. In addition to these aromatic hydrogens, another peak (a labeled) at 5.14 ppm was due to DBCO. The peak of methylene hydrogens adjacent to the ester group was observed at 4.25 ppm. The disappearance of the PEG-OH resonance at 3.79 ppm showed the complete esterification between PEG(SS-OH)$_2$ and DBCO acid group.

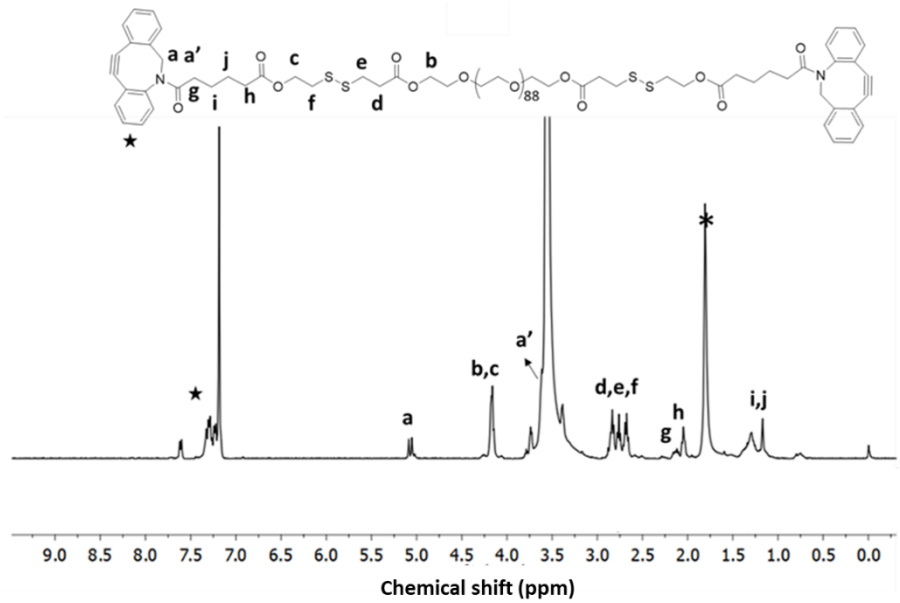

Figure 5.12. The ^{1}H NMR spectrum of PEG-(SSDBCO)$_2$ crosslinker.

After ^{1}H NMR, PEG-$(SSDBCO)_2$ crosslinker was characterized with ^{13}C NMR, and spectra were shown in Figure 5.13. PEG4000 (PEG4K) was compared with PEG-$(SSDBCO)_2$ crosslinker. The complete esterification of the PEG end group was proved by the disappearance of the characteristic carbon signal for -CH_2OH at 61.7 ppm.

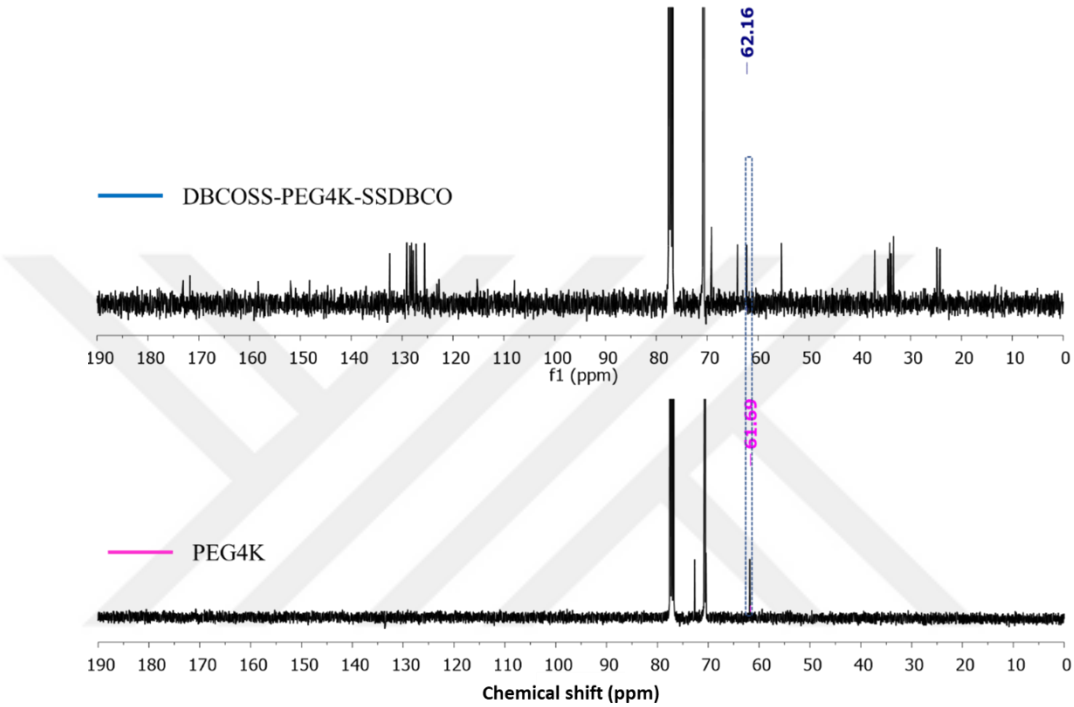

Figure 5.13. ^{13}C NMR spectra of PEG4K and DBCO-SS-PEG-SS-DBCO (PEG-$(SSDBCO)_2$) crosslinker.

5.3.6. Preparation and Characterization of SPAAC Hydrogels

Hydrogels were prepared via strain-promoted azide-alkyne cycloaddition (SPAAC) reaction between azide-containing OEGMA-based copolymers and dibenzocyclooctyne-conjugated PEG-based crosslinker. Hydrogel formation was studied in water at 37 ^{o}C. Two different hydrogels were prepared: HG-GEMSSC and HG-GEM-C. P(OEG/N_3/GEMSSC) copolymer was used to synthesize HG-GEM-SSC. The click reaction between P(OEG/N_3/GEMSSC) and DBCO-containing crosslinker (DBCO-SS-PEG-SS-DBCO) gave HG-GEMSSC hydrogels. Hydrogels were prepared by rapidly mixing a DBCO-based crosslinker and P(OEG/N_3/GEMSSC) copolymer. In all hydrogel formulations, the

functional group ratio of DBCO to azide remained 1:1. HG-GEMSSC hydrogels were prepared in three different concentrations 5 %, 10 %, and 15 % wt of total polymer concentration. The gelation conditions and conversion were tabulated in Table 5.4. Unsurprisingly, the gelation times are much faster for the 15 % wt hydrogels than 10 % wt and 5 wt% hydrogels. While hydrogel formation happened after almost 2 minutes with 5 % wt polymer concentration, 15 % wt polymer concentration gave hydrogel after 10 seconds. The obtained hydrogels were clear, colorless, and transparent. The fabrication of hydrogel and images of them are shown in Figure 5.14.

Another hydrogel system (HG-GEMC) was obtained using a P(OEG/GEM-C/N_3) copolymer, which included the carbamate linker between GEM and polymer backbone and DBCO-containing crosslinker. HG-GEMC hydrogels were also prepared in the same formulations as well as the HG-GEMSSC system. DBCO and azide ratio was kept at 1:1, and HG-GEMC hydrogels were prepared in 5 %, 10 %, and 15 % wt of total polymer concentrations.

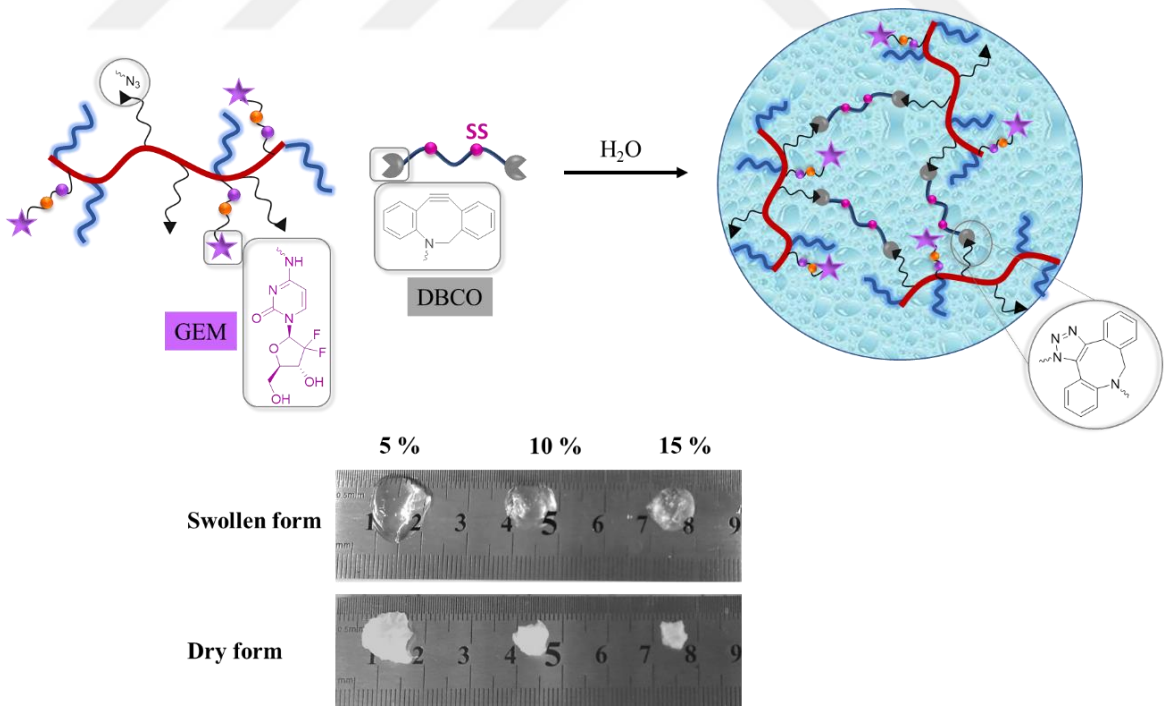

Figure 5.14. The fabrication of HG-GEMSSC hydrogels via SPAAC reaction and images of them in dry and swollen forms.

Table 5.4. The gelation conditions of HG-GEMSSC and HG-GEMC.

Copolymer type	N_3: DBCO	Solvent	Temperature (^oC)	Wt % Polymer	Conversion (%)
P(OEG)/N_3/GEM-SSC)	1:1	H_2O	37	5	88
P(OEG)/N_3/GEM-SSC)	1:1	H_2O	37	10	81
P(OEG)/N_3/GEM-SSC)	1:1	H_2O	37	15	75
P(OEG)/N_3/GEM-C)	1:1	H_2O	37	5	87
P(OEG)/N_3/GEM-C)	1:1	H_2O	37	10	81
P(OEG)/N_3/GEM-C)	1:1	H_2O	37	15	60

After obtaining HG-GEMSSC hydrogel, the first characterization was employed using FTIR analysis. The FTIR spectrum was given in Figure 5.15. While P(OEG/N_3/GEMSSC) copolymer showed an azide peak at 2098 cm^{-1} before gelation, there was no azide peak after gelation. This data showed that gelation happened 1:1 ratio between azide and DBCO.

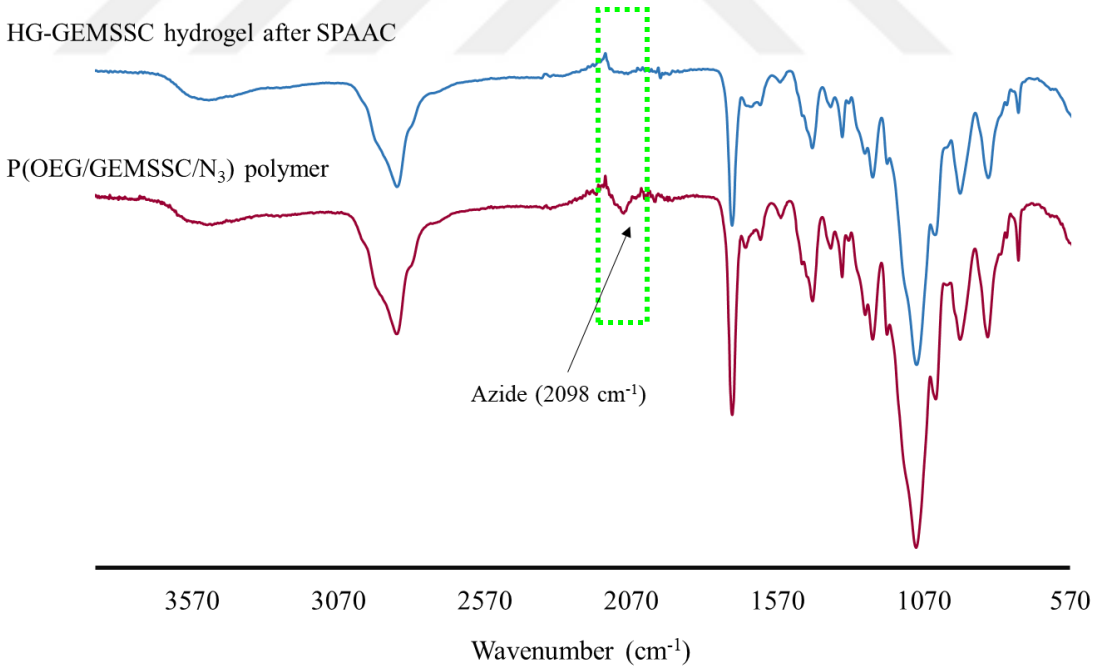

Figure 5.15. FTIR spectra of P(OEG/N_3/GEMSSC) copolymer before gelation and HG-GEMSSC hydrogel.

HG-GEMSSC hydrogels were also characterized by rheological analysis to examine the effect of total polymer concentration on the physical properties of hydrogels, like mechanical strength. 5%, 10%, and 15% wt HG-GEMSSC hydrogels were prepared with the same crosslinker and copolymer amount, and the total polymer concentration was changed. The frequency sweep and amplitude sweep tests were applied on swollen state hydrogels. Test results are given in Figure 5.16 and Figure 5.17.

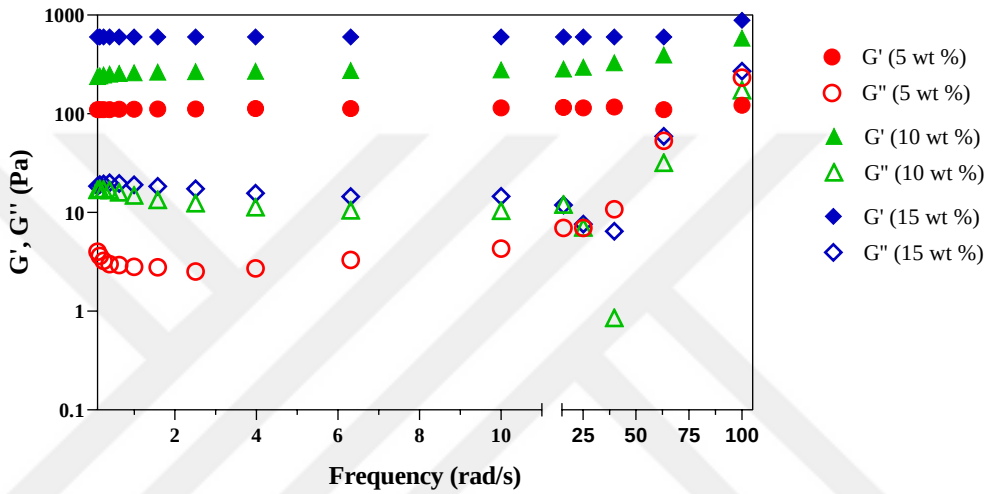

Figure 5.16. The frequency sweep test results of HG-GEMSSC hydrogels.

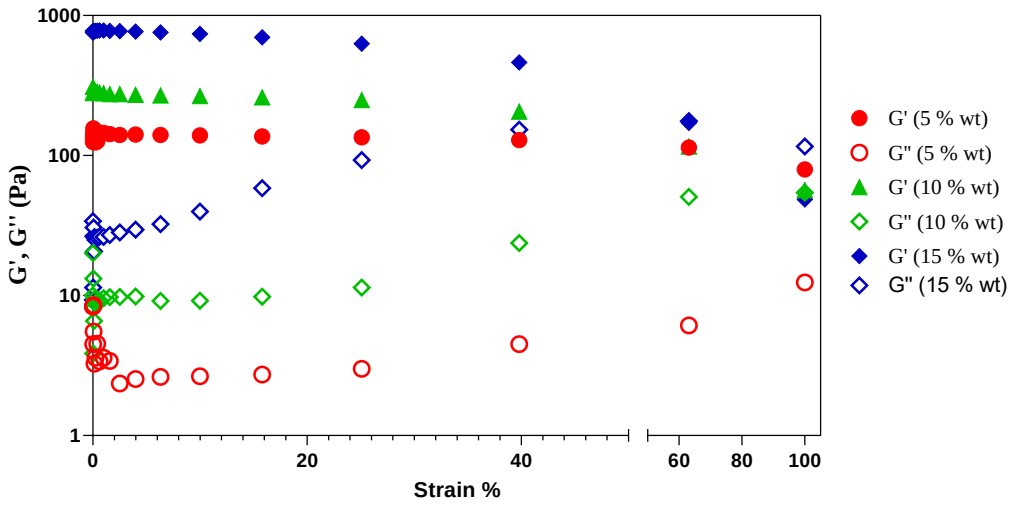

Figure 5.17. The amplitude sweep test results of HG-GEMSSC hydrogels.

Rheology analysis indicated that all hydrogels (5 %, 10 %, and 15 % wt) showed gel-like structure, G' value was higher than G'' for all hydrogels. It was observed that G' value increased with total polymer concentration. 15 % wt hydrogel showed the highest G' value, and 5% wt gel had the lowest G' value. It was concluded that total polymer concentration induced a higher G' value and stiffer gel.

5.3.7. Hydrogel Swelling

Swelling of hydrogels (HG-GEMSSC and HG-GEM-C) at 5, 10, and 15 % wt was measured by weighing the hydrogels at predetermined time intervals because they swelled in water at room temperature. The mass-based swelling ratios over time were calculated were plotted in Figure 5.18.

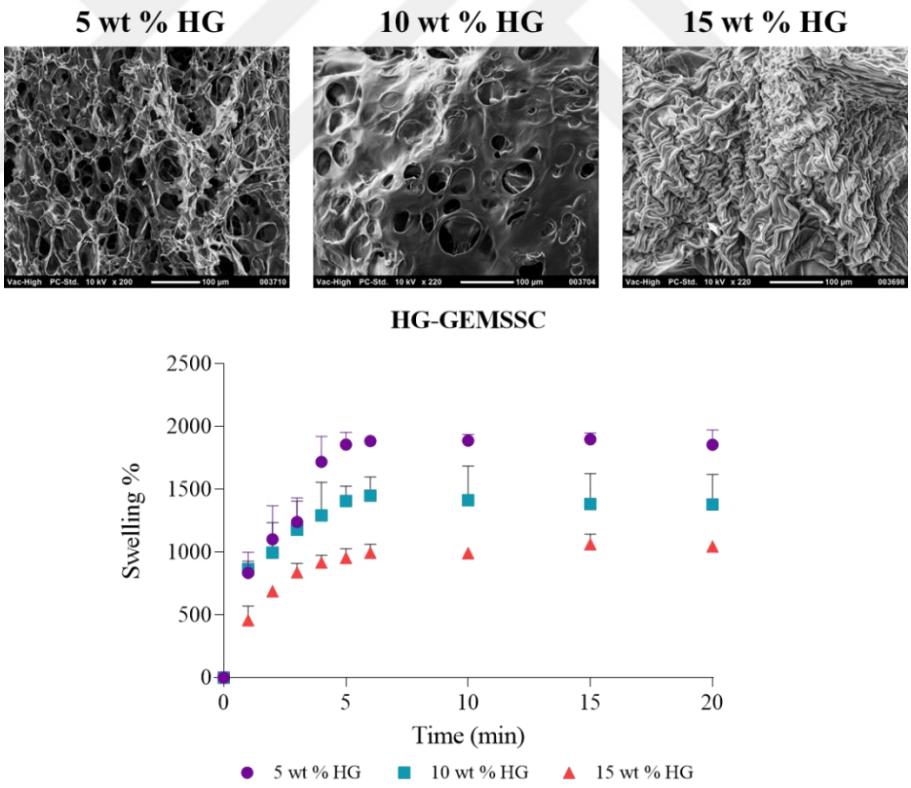

Figure 5.18. SEM images of 5, 10, and 15 wt % HG-GEM-SSC hydrogels and swelling graph.

As seen in Figure 5.18, the overall swelling characteristics of hydrogels were different. The swelling ratios of 5, 10, and 15 wt % hydrogels increased over time. The 5 wt % hydrogel showed the highest swelling ratio due to more porous structures. 5, 10, and 15 wt % hydrogels were characterized using SEM to investigate their porosities, and SEM images were shown in Figure 5.18. It was important to note that the porosity of hydrogels and swelling ratios were directly proportional. 5 wt % HG system had more porosity than 10 and 15 wt %, and it also had the highest water uptake capacity. Unsurprisingly, 15 wt% HG had the lowest porous structure, but it showed swelling.

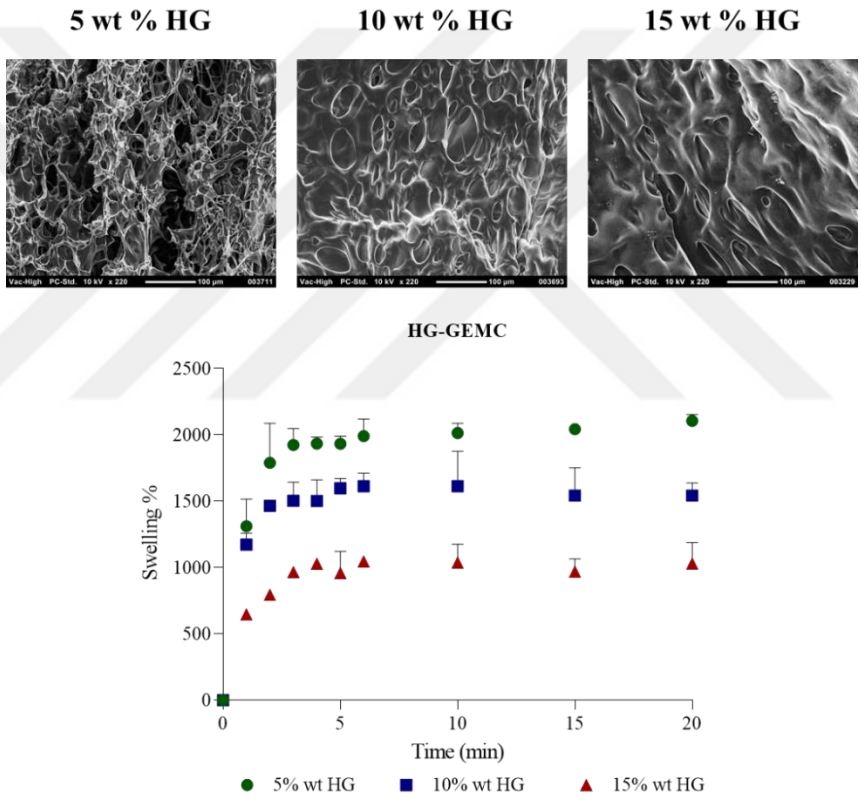

Figure 5.19. SEM images of 5, 10, and 15 wt % HG-GEM-C hydrogels and swelling graph.

The mechanical strength and porosity of hydrogel effects the water uptake capacity. Figures 5.18 and 5.19 show that hydrogel porosity decreased from 5% wt to 15 % wt polymer concentration. Compared to water uptake capacity, 5 % wt hydrogel showed more swelling in water. 15 % wt hydrogel had a higher G' value than 10 % and 5 % wt hydrogel, it indicated that 15 % wt was stiffer and 15 % hydrogel had less water uptake capacity.

5.3.8. Degradation of Redox-Responsive Hydrogels

Disulfide-containing hydrogels are expected to be degradable when they are exposed to reducing agents such as glutathione (GSH) and dithiothreitol (DTT). To this end, BODIPY dye-conjugated disulfide-containing hydrogels were prepared using BODIPY-containing copolymer and disulfide-incorporated DBCO crosslinker. For the degradation study, BODIPY-conjugated hydrogels were treated with PBS and GSH-containing PBS solution (5 mM) at 37 ºC. A piece of dye-containing hydrogel sample was immersed in PBS solution, and no green fluorescence was observed in the solution after 24 h. However, a bright green fluorescence in the solution was observed under UV illumination (365 nm) in the GSH-containing vial due to the degradation of dye-containing hydrogel. Along with the green fluorescent solution, the hydrogel sample disappeared at the end of 24 hours of incubation in 5 mM GSH solution. Images under UV light were given in Figure 4x. These observations showed that dye-containing hydrogel was degradable under reductive conditions, as expected. Degradation of hydrogel was also shown in the presence of 1 mM GSH. The dye-conjugated hydrogel was treated with 1 mM GSH (50 µL) in a vial, and after incubation for 24 hours, hydrogel dissolution was observed, as seen in Figure 5.20b.

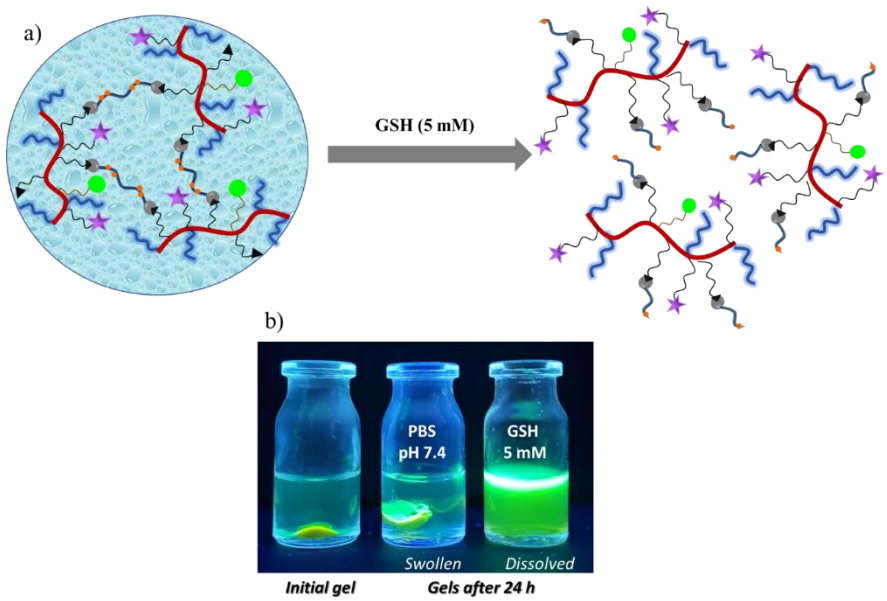

Figure 5.20. (a) Schematic representation of hydrogel degradation in the presence of GSH, (b) hydrogel images under UV-lamp before and after GSH treatment.

The degradation ability of hydrogels was also shown in rheology analysis. HG-GEMSSC hydrogel samples (5 % and 10 % wt) were placed in a rheometer at 37 ^{o}C in the presence of glutathione solution (1 mM) in PBS (pH 7.4). Degradation was investigated by following G' and G'' values using the time sweep test. This experiment was also done in the absence of glutathione. In the presence of glutathione, G' value started to decrease, demonstrating the disintegration of disulfide bonds and dissolution of the hydrogel. G' and G'' crossover is a sign of the destruction of the strength and stiffness of hydrogel, and hydrogel became a sol form at this point.

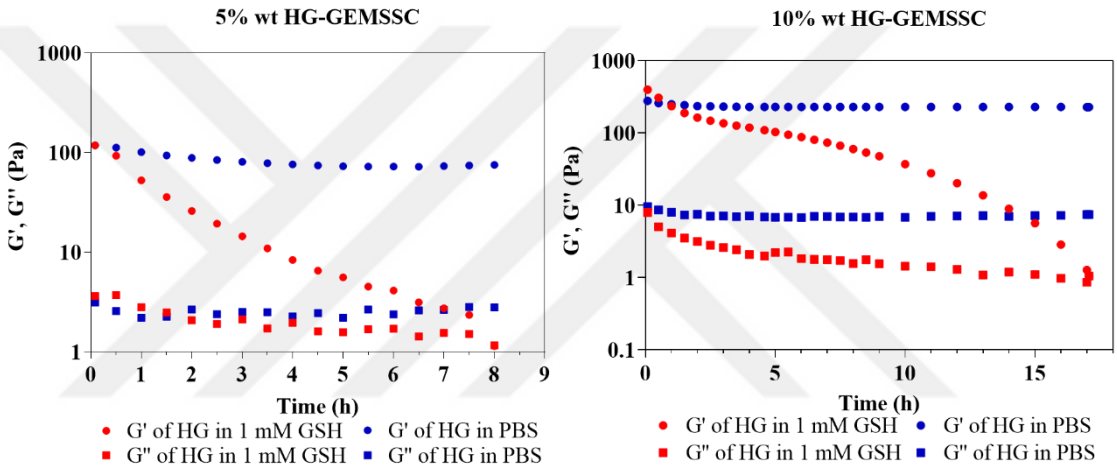

Figure 5.21. Degradation profiles of hydrogels in the presence and absence of glutathione at 37 ^{o}C.

As expected, degradation time showed changes with total polymer concentration. While 5% wt hydrogel degraded at the end of 7.5 h, 10 % hydrogel showed degradation at the end of 17 h.

5.3.9. Injectability and Self-Healing Behaviour of Hydrogel

Injectable and self-healable hydrogels enable unique advantages for biomedical applications. First, they may be easily used for local applications and do not require invasive strategies. In addition, these types of hydrogels can heal their structures after any damage. Therefore, injectable and self-healable hydrogels are good candidates for local drug delivery systems. To this end, the injectability of HG-SS-GEM hydrogel was tested using a 21-gauge

needle. To provide visualization, BODIPY-dye conjugated polymer was used for gelation. The injectability of hydrogel (BODIPY-HG-SS-GEM) was shown in Figure 5.22a-b.

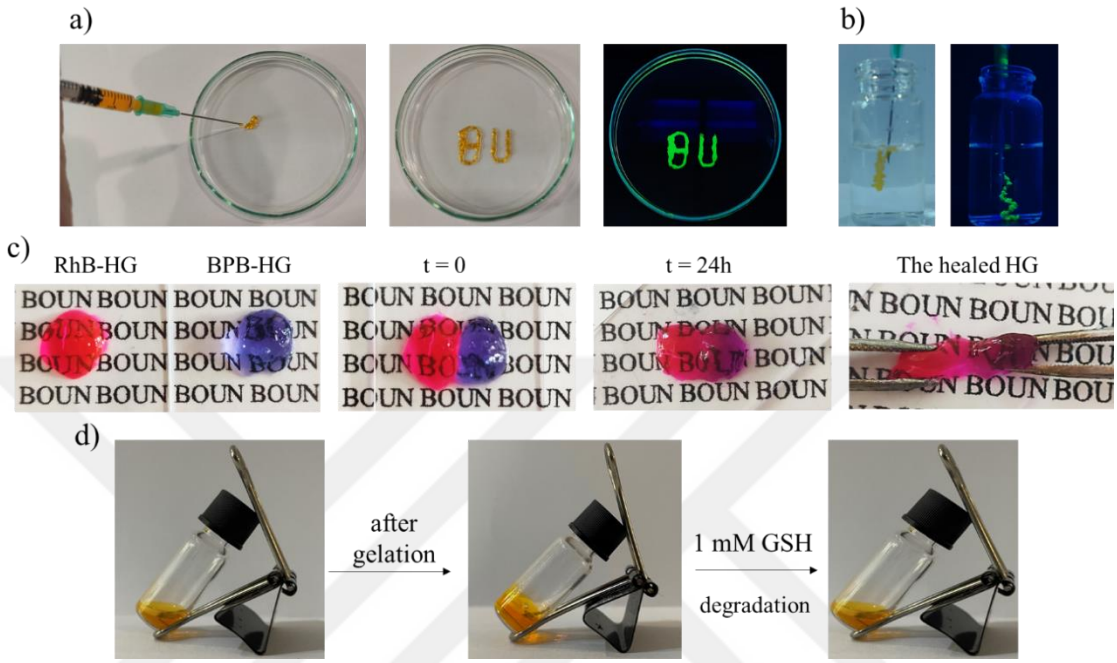

Figure 5.22. Injectability testing of hydrogels: (a) BODIPY-conjugated hydrogel was injected via a 21-gauge needle, (b) injection of hydrogel into water and photographs under sunlight and UV-light, (c) investigation of self-healing behavior of hydrogel and images of before and after healing and (d) degradation of hydrogels with 1 mM GSH.

As seen in Figure 5.22a, the hydrogel was easily injected through a needle. We could write the letters “BU” using HG-SS-GEM hydrogel through a 21-gauge needle. The injected hydrogels were visualized under a UV lamp. In addition, the hydrogel was injected into water, and as seen in Figure 5.22b, the hydrogel remained intact and did not dissolve.

To investigate the self-healing property of HG-GEMSSC hydrogels, they were prepared in a spherical form with two different colors (rhodamine B, RhB, and bromophenol blue, BPB). These hydrogels were cut, and the new pieces with different colors were put together. After incubation for 24 hours at room temperature, these colored hydrogel pieces were bound each other via self-healing. After that, the stretching test was applied to the

healed hydrogel using a tweezer. As seen in Figure 5.22c, the healed hydrogel could endure stretching.

The self-healing behavior of disulfide-containing HG-GEMC hydrogel, in which GEM was connected to a polymer backbone with the carbamate linker, and there were no disulfide bonds on the polymer backbone, was investigated by deforming hydrogel structure. There was an idea that when HG-GEMC hydrogel was injected using a 21-gauge needle, the hydrogel structure may be subjected to deformation due to the breaking of disulfide linkages. After a certain time, hydrogel recovers due to the disulfide bonds' dynamic nature. To investigate this idea, HG-GEMSSC hydrogel was injected into a petri dish in two parts using a 21-gauge needle, and subsequently, injected hydrogel was treated with maleimide-containing fluorescein dye (0.1 mg/mL) for 1 h. The remained injected hydrogel piece was also treated after 24 hours. As the control experiment, the hydrogel was prepared in Eppendorf. This hydrogel was treated with maleimide-containing fluorescein dye. All groups were treated with the same maleimide-containing fluorescein dye solution and the same incubation time. After incubation, hydrogels were washed with PBS solution and lyophilized. The dry hydrogel samples were visualized under a fluorescence microscope, and images were represented in Figure 5.23.

As seen, the hydrogel sample in Eppendorf (before injection) revealed no fluorescence because this sample did not contain free thiol to react with maleimide-containing fluorescein. However, injected hydrogel showed green fluorescence. This data proved hydrogel deformation as a result of disulfide bonds during the injection. While injecting, free thiols formed, and these thiols gave a reaction with maleimide-containing fluorescein via thiol-maleimide Michael addition. As we expected, there was no green fluorescence after injection for 24 hours. This showed that hydrogel recovered itself due to the dynamic nature of disulfide bonds. It was concluded that hydrogel showed self-healing behavior due to the presence of disulfide bonds.

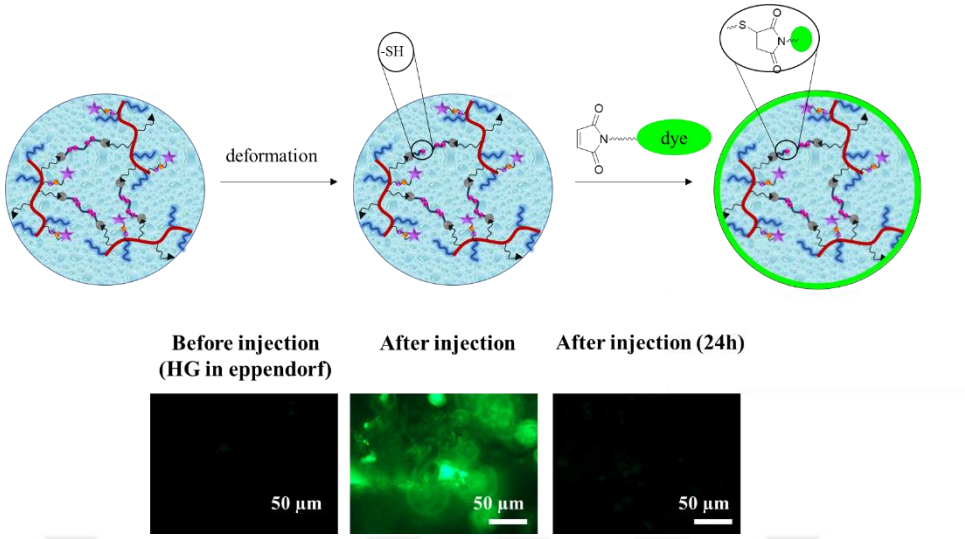

Figure 5.23. The fabrication of a self-healing test using deformation and fluorescence images after being treated with maleimide-containing fluorescein.

The injectability performance of HG-GEMSSC hydrogel (5%wt) was also examined by monitoring the shear-thinning ability. The shear-thining ability of injectable hydrogels is an essential parameter for *in vivo* use since the injectable hydrogel should be easily injected into the desired area, and it should preserve its gel structure by self-healing under the shear stress. As expected, the viscosity of the HG-GEMSSC hydrogel decreased when the shear rate increased, and the viscosity diagram is shown in Figure 5.24.

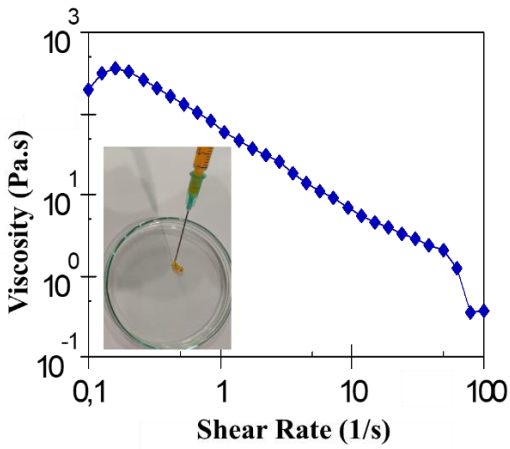

Figure 5.24. The diagram of the viscosity rheology as a function of the shear rate of HG-GEMSSC hydrogels.

5.3.10. GEM Release from Hydrogels

Gemcitabine release profiles from hydrogels were explored at pH 6.8 and pH 7.4 in the absence and presence of GSH. Gemcitabine was introduced into copolymers via a pH-responsive carbamate linker and redox-responsive disulfide bond to compare their release efficiency. As mentioned in the previous chapter, GSH is abundant in cancer cells and breaks the disulfide bond [191,192]. Therefore, it was expected that hydrogel-containing disulfide linkage (HG-GEMSSC) would show more GEM release than hydrogel-including carbamate bond. In addition to reducing the environment, two different pHs were selected. The pH of the extracellular microenvironment (pH_e) of the tumor is between 6.5-6.9, and the pH_e of normal tissue is almost 7.2-7.5 [35]. Hydrogels are bulky materials and cannot penetrate the inside of tumor tissue. After degradation, degradation products like polymer can enter into tumor tissue. Therefore, we selected pH 6.8 for our injectable hydrogel system. Hydrogel samples (HG-GEMC and HG-GEM-SSC, 5%wt) were put into a dialysis bag with a release buffer, and these dialysis bags were placed inside the release buffer and incubated at 37 ^{o}C. GEM release from hydrogels was determined by LCMS analysis.

GEM release graphs were demonstrated in Figure 5.25. GEM release kinetics from HG-GEM-SSC were given in Figure 5.25a. The amount of released GEM from hydrogels was very low at pH 6.8 and 7.4, and it remained under 10%. On the other hand, when HG-GEM-SSC hydrogels were incubated at pH 6.8 and 7.4 in the presence of GSH (1 mM), they showed significantly more GEM release. Thus, HG-GEM-SSC hydrogel released GEM by 97 % and 70 % at pH 7.4 and 6.8, along with 1 mM GSH. These dramatic release profiles can be attributed to the degradation of the disulfide linker with GSH.

GEM release amounts from another hydrogel system (HG-GEM-C) were explored in the same release conditions, and the release graph was given in Figure 5.25b. Unfortunately, HG-GEM-C hydrogel showed very slow GEM release at our conditions. At the end of 96 hours, the released amount of GEM remained under 2 % percent. It was concluded that the carbamate linker was not broken to release GEM. Moreover, the hydrogel system that can selectively release anticancer drug on it was obtained by taking advantage of the tumor region's disulfide linker and redox environment.

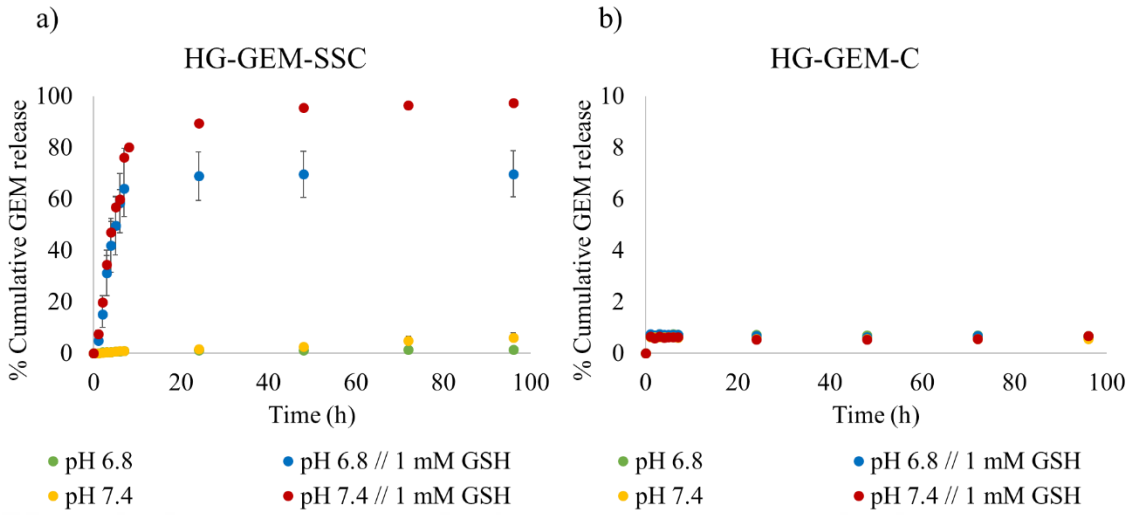

Figure 5.25. (a) GEM release profiles from HG-GEMSSC hydrogel, (b) GEM release ratios from HG-GEM-C hydrogel at 37 ºC.

5.3.11. Biocompatibility of Hydrogels *In Vitro* Cytotoxicity towards Healthy and Cancer Cells

Biocompatible hydrogels are important in especially biomedical applications. If the hydrogels are formed in situ, biocompatible polymers and metal-free biorthogonal reactions are required. In a seminal contribution, Adronov and coworkers fabricated a PEG-based hydrogel using SPAAC crosslinking strategy, and showed that obtained hydrogels are nontoxic and support cell growth [97]. To confirm the benign nature of the SPAAC-based hydrogel obtained in this study, we synthesized gels using an OEG-based azide-containing copolymer, which is devoid of any drug. For the cytotoxicity experiment, L-929 mouse fibroblast cells were incubated with different amounts (from 0.5 to 2 mg) of obtained hydrogel samples for 48 h. Thereafter, CCK-8 assay was performed to determine the cell viability. As seen in Figure 5.26, hydrogels did not show any significant toxicity even at high amounts.

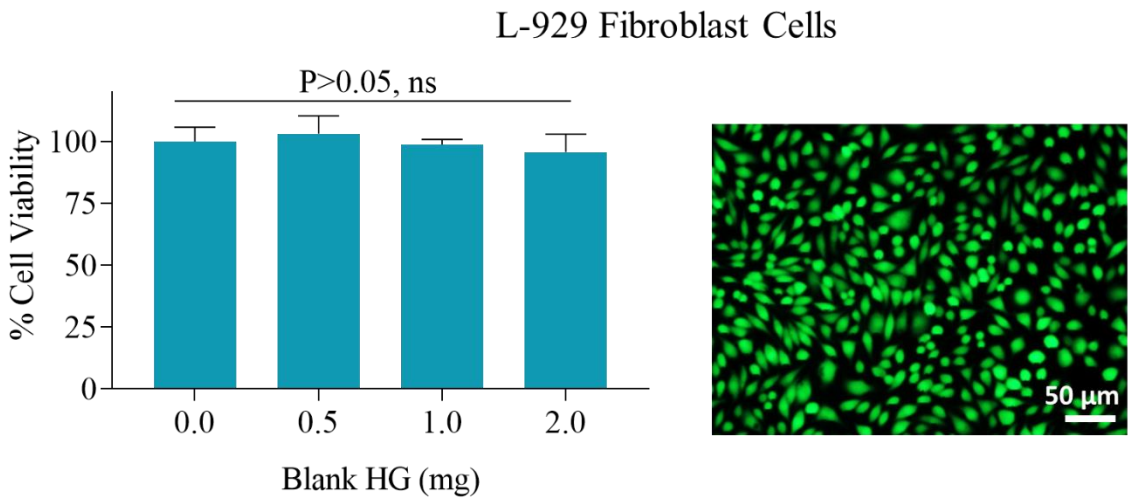

Figure 5.26. Biocompatibility of blank hydrogel using cytotoxicity assay and live-dead assay on L-929 cells.

The biocompatibility of blank hydrogel was also tested using a live-dead assay kit. The fibroblast cells were treated with a hydrogel sample for 24 h. After 24 h, cells were incubated with live (Calcein-AM)-dead (propidium iodide) assay solution. Cells were visualized under the fluorescence microscope. Calcein-AM shows the esterase activity of healthy cells and gives bright green fluorescence. Propidium iodide binds to the DNA of dead cells and presents red fluorescence. As seen in Figure 5.26, cells showed green fluorescence, indicating that cells are alive, thus highlighting the excellent biocompatibility of these hydrogels.

5.3.12. *In Vitro* Cytotoxicity towards Cancer Cells

BxPC-3 cells (human pancreatic adenocarcinoma cells) were used in cytotoxicity experiments. In this experiment, cells were divided into five groups. Two groups were control groups incubated with cell media and 1mM GSHOEt. In the third group, HG-GEMSSC hydrogels were put into cell-containing wells, and the final RPMI volume was 200 µL. Fourth group cells were incubated with HG-GEMSSC hydrogels in the presence of 1 mM GSHOEt containing RPMI solution (200 µL). When hydrogels were fully degraded, and GEM was released from hydrogels and copolymers, GEM concentration would be $1x10^{-5}$ M in 200 µL cell media. Therefore, the fifth group cells were incubated with free GEM

($1x10^{-5}$ M). The cytotoxicity experiment was also done with HG-GEMC hydrogels with the same experimental design ($1x10^{-5}$ M, GEM). After 24 h incubation, cell viability was measured using CCK-8 assay, and cytotoxicity graphs were shown in Figure 5.27.

BxPC3 cells showed high viability (93%) when incubated with HG-GEMSSC hydrogels without GSH. HG-GEMSSC hydrogel showed no cytotoxicity because it did not degrade to form a free GEM-containing polymer and free GEM. On the other hand, HG-GEMSSC hydrogel showed more cytotoxicity, and cell viability decreased to % 62 when applied with 1 mM GSH. After 24 h incubation, HG-GEMSSC hydrogel samples remained in the cell-containing wells without GSH, but there were no HG-GEMSSC hydrogel samples in the wells containing 1 mM GSH. This observation showed that HG-GEMSSC hydrogel samples showed complete degradation due to breaking disulfide bonds in the presence of GSH. Also, GEM was integrated into the polymer backbone via disulfide linkers; therefore, copolymer and hydrogel released GEM in the presence of GSH. Both hydrogel degradation and GEM release from copolymer forming degradation of hydrogel led to more cytotoxicity against BxPC3 cells. When it came to free GEM, the cytotoxic effect of it in the same concentration was 65% after 24 h incubation. Notably, HG-GEMSSC hydrogel showed almost the same cytotoxicity as free GEM in the presence of GSH.

HG-GEMC hydrogels also did not show significant cytotoxicity (98% cell viability) in the absence of GSH. HG-GEMC hydrogels did not show degradation without GSH. However, cell viability decreased to 72% when HG-GEMC hydrogels were applied with 1 mM GSH. In the HG-GEMC hydrogel system, hydrogels were fully degraded with GSH but forming copolymer released less amount of GEM because GEM was attached to the polymer backbone via the carbamate linker. We knew the P(OEG/N_3/GEM-C) copolymer showed GEM release under 2%. However, the forming copolymer after degradation of HG-GEMC hydrogel demonstrated cytotoxicity because this copolymer could be internalized by cells. In summary, HG-GEMSSC hydrogels were more cytotoxic than HG-GEMC in the presence of GSH, and they had nearly the same cytotoxic activity as free GEM.

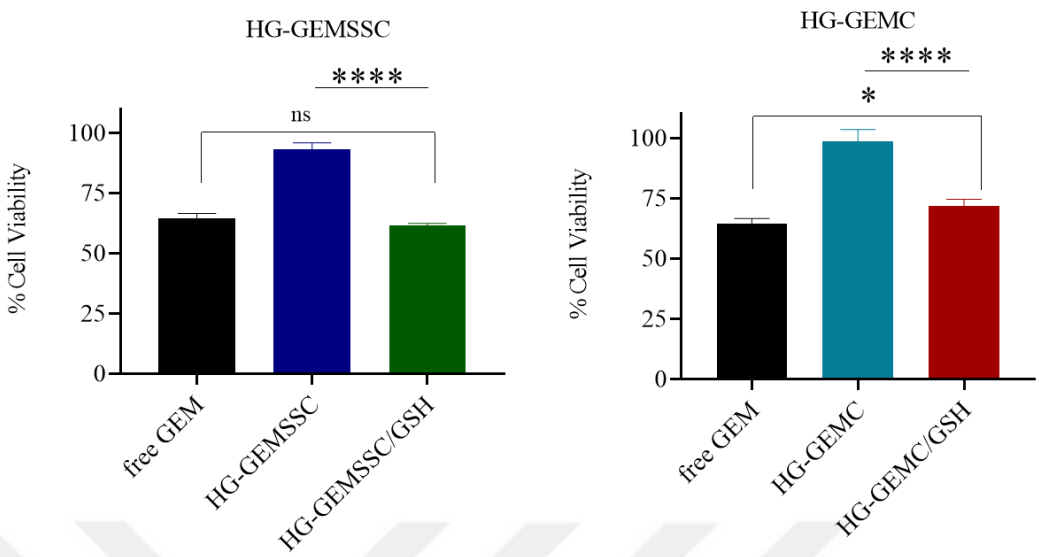

Figure 5.27. Cytotoxicity results of HG-GEMSSC and HG-GEMC hydrogels against BxPC3 pancreatic cancer cells.

5.3.13. *In Vitro* Cellular Internalization

After the GEM release study, in vitro cellular uptake study was achieved. A fluorescent BODIPY-containing copolymer was synthesized for the cellular uptake study, and subsequently, BODIPY-containing degradable hydrogels were prepared.

Hydrogels are bulky materials; hence they do not penetrate inside cancer cells and tumor region. However, when hydrogel shows degradation, the polymer coming from hydrogel degradation can be internalized by cancer cells and may show accumulation to the tumor site. Therefore, the cellular uptake of hydrogel was investigated. The cells were divided into three groups. One group was only treated with dye-containing hydrogels in the presence of cell media. Another cell group was first treated with glutathione ethyl ester (GSHOEt, 1 mM) for 3 hours to enrich cells in terms of GSH. After 3 hours of GSH treatment, GSH was removed from cells, and the cells were washed excess amount of PBS. After that, dye-containing hydrogel samples were added to GSH-enriched cells with only cell media. The third group of cells was incubated with dye-containing cells in the presence of 1 mM GSH solution prepared in cell media. After 24 hours of incubation, cell nuclei were stained by DAPI after washing steps. The internalization efficiency was characterized using

fluorescence microscopy. The fluorescence microscopy images of cells were given in Figure 5.28. Surprisingly, green cells were observed when dye-containing hydrogels were applied with only cell media on them. This result showed that our dye-containing hydrogel displayed degradation due to some enzymes in cell media, but the degradation ratio was low, as expected. As for the second group cells, green-colored cells were again observed. However, a higher BODIPY fluorescence intensity was observed. This result revealed that GSH-enriched cells provided GSH into cell media and GSH broke disulfide bonds, and dye-containing polymer due to hydrogel degradation was internalized by cancer cells. Regarding the third group cells, these cells showed the most internalization efficiency due to the presence of GSH. At the end of 24 hours of incubation, all hydrogels degraded, and there was no hydrogel sample on the cells. This meant that the cells were exposed to a high amount of dye-containing polymer, which formed after degradation with GSH. Therefore, the highest internalization was obtained using GSH. In summary, dye-containing hydrogel degradation and cellular internalization demonstrated an increase along with GSH.

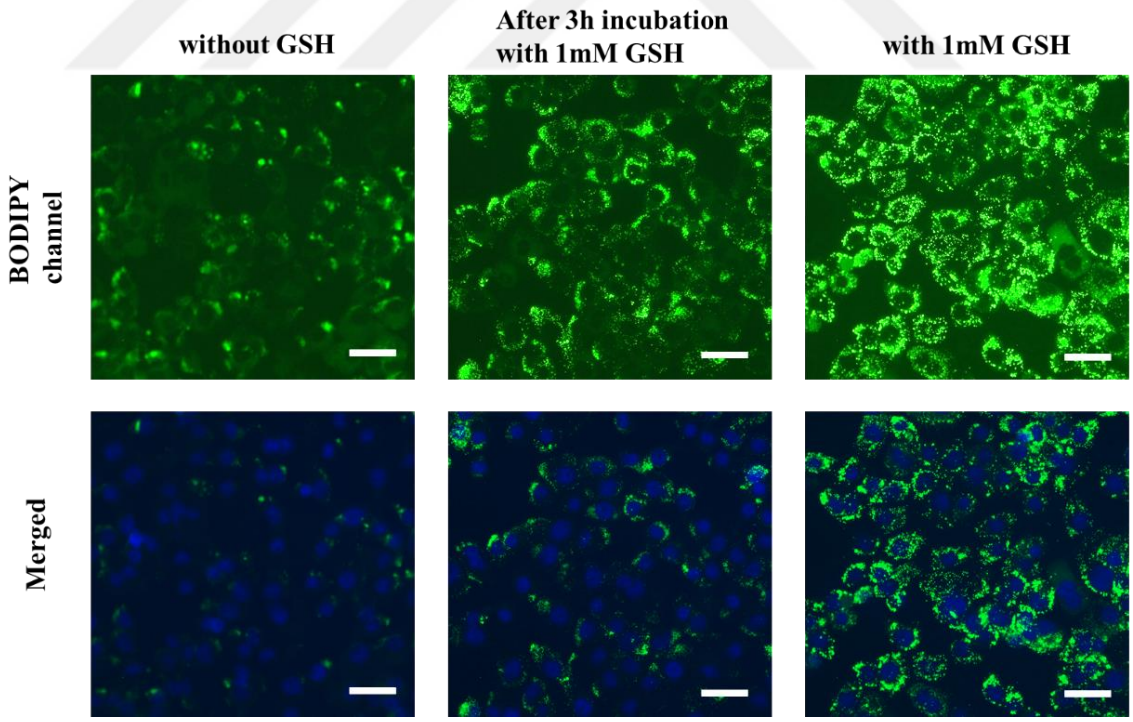

Figure 5.28. Fluorescence microscopy images of cancer cells treated with dye-containing hydrogels in the presence and absence of GSH. The scale bar is 50 μm.

5.4. Conclusions

A novel strategy for fabrication of redox-responsive injectable hydrogels using a combination of SPAAC and thiol-disulfide exchange reaction is disclosed. A copolymer containing OEGMA and azide-containing AHMA monomer was synthesized using RAFT polymerization. Drug-containing copolymers were synthesized using OEGMA, AHMA, and GEM-based methacrylate monomers, and two different GEM-containing copolymers were prepared. GEM was conjugated to the polymer backbone via carbamate and disulfide-carbamate linkers to investigate the effect of the linker on drug release and cytotoxicity. An azide group reactive DBCO-disulfide-containing PEG-based crosslinker was synthesized. Strain-promoted azide-alkyne cycloaddition reaction (SPAAC) between the azide groups on the copolymer and the DBCO groups on the crosslinker led to hydrogel formation. Hydrogels were characterized using FTIR, SEM, and rheometer. Hydrogels fabricated with low polymer concentration had a more porous structure and higher water uptake capacity. Rheology analysis showed that hydrogel with a high polymer concentration (15 % wt) was stiffer than hydrogel obtained with a lower polymer concentration. The degradation of hydrogels was investigated in the absence and presence of glutathione, and degradation profiles were monitored using a rheometer. Hydrogels showed degradation with glutathione, and degradation time increased from 5 % wt hydrogel to 15% wt hydrogel. Visual degradation of hydrogel was also shown using BODIPY-conjugated hydrogels in the presence of GSH. The injectability of hydrogel was shown using BODIPY-conjugated hydrogels. We could easily write “BU” using a 21-gauge needle. The self-healing ability of hydrogel was shown by applying a stretching test to cut and healed hydrogels using a tweezer. In addition, the self-healing ability of hydrogel was due to rupture of the disulfide linkages was demonstrated using a maleimide-containing dye. The ruptured linkages formed during the injection process, self-heals over time after injecting the hydrogel.

In vitro GEM release profiles were investigated at pH 6.8 and 7.5 in the absence and presence of GSH. HG-GEMSSC hydrogel, in which GEM was conjugated to the polymer backbone via disulfide bonds, showed more GEM release in the presence of GSH, compared to HG-GEMC hydrogel, in which GEM was conjugated onto the polymer via a carbamate linker. Excellent biocompatibility of blank hydrogel (no GEM on hydrogel) was established

using CCK-8, and live-dead assay on healthy fibroblast cells. Cytotoxic evaluations of GEM-containing hydrogels were performed using BxPC-3 pancreatic adenocarcinoma cells. When cells were treated with HG-GEMSSC hydrogel along with GSH (1 mM), HG-GEMSSC hydrogel showed almost the same cytotoxic activity as free GEM due to the breaking of disulfide bonds. GSH led to the degradation of hydrogels and the release of GEM. For cell internalization efficiency of hydrogels, BxPC-3 cells were treated with BODIPY-dye conjugated hydrogel samples with and without GSH. In the presence of GSH, hydrogel degraded and release of the BODIPY-dye conjugated polymer occurred, and this polymer was internalized by cancer cells. In conclusion, this chapter reported a novel example of a redox-responsive, biocompatible, biodegradable, injectable and self-healable hydrogel. When the anticancer drug was conjugated to a hydrogel system via a stimuli-responsive linker, this system is promising for local drug delivery applications by taking advantage of its injectable nature.

6. MULTIVALENT POLYMER BRUSHES FOR BIOMOLECULAR IMMOBILIZATION

This chapter was adapted with permission from {Degirmenci, A., G.Y. Bas, R. Sanyal and A. Sanyal, "Clickable Polymer Brush Interfaces: Tailoring Monovalent to Multivalent Ligand Display for Protein Immobilization and Sensing", *Bioconjugate Chemistry*, Vol. 33, No. 9, pp. 1672-1684}. Copyright {2022} American Chemical Society [279].

6.1. Introduction

The past decade has witnessed the evolution of polymeric surface coatings from a simple protection barrier to a functional interface, which imparts functional attributes to the material through specific interactions and communication with its environment. In particular, polymeric coatings bearing bioactive ligands ranging from small molecules to biomacromolecules are critical in realizing various diagnostic and biosensing platforms [280-284]. For such applications, a polymeric layer that is stable in an aqueous environment, inherently anti-biofouling, and can be easily conjugated with biological probes is often desirable. In light of the demand for workability under aqueous conditions, as a general approach, hydrophilic polymers are chemically tethered onto the underlying inorganic substrate through either a 'graft-to' or 'graft-from' approach. Due to widespread applications of functional surfaces, polymer brushes have emerged as an attractive coating platform due to their versatile nature [131,132], [152], [285].

The 'graft-from' approach entails the growth of polymer chains directly from surfaces immobilized with polymerization initiators or chain transfer agents (CTAs) [136], [286]. The employment of contemporary controlled/living radical polymerization techniques allows control over their thickness and architecture. Also, these techniques furnish coatings with diverse chemical compositions due to the high tolerance of recent polymerization techniques toward various functional groups. Furthermore, effective post-polymerization

modification of polymeric materials can be undertaken using reactions from the '*click*' chemistry toolbox [287-291]. In this regard, the introduction of various 'clickable' functional groups in polymer brushes has been exploited for their modification using diverse 'click' reactions. Commonly used transformations include the Huisgen-type copper-catalyzed [3+2] azide-alkyne cycloaddition [159], [292,293] and metal-free "*click*" reactions such as thiol-ene [294], thiol-yne, [295,296], thiol-maleimide [161], [297], and the Diels-Alder cycloaddition [298]. In particular, methods such as nitroxide-mediated polymerization (NMP) [139], [299-301], atom-transfer radical polymerization (ATRP) [302-305], and reversible addition-fragmentation chain transfer (RAFT) polymerization [149], [160], [306,307] have been widely used for obtaining polymer brushes. There is an increasing interest in employing RAFT polymerization to fabricate polymeric brushes due to its metal-catalyst-free nature, high compatibility with various functional groups, and efficient polymerization at moderate temperatures with a high level of oxygen tolerance. While clickable handles can be introduced as side-chain residues or at the chain end in a dense surface tethered polymer brush, it is the latter position at the top of the surface that mainly interacts with the external environment. These positions act as the location of choice for installing bioactive functional molecules that can enable specific recognition of proteins, cells, and bacteria. Thus, a facile methodology to establish various reactive groups at the chain end of polymer brushes will allow one to readily obtain such functional interfaces. RAFT polymerization in this context appears to be a suitable candidate since, apart from advantages like its metal-free nature, the chain end of polymers obtained using this method bears the thioester or trithio-carbonate groups, which can undergo a variety of chemical transformations [308-310]. The azo group containing molecules that decompose either through thermal or photochemical activation furnish radical intermediates which can act as polymerization initiators [311], fragmentation units [312], or chain-terminating agents for polymers obtained through RAFT polymerization [313,314].

Herein, we demonstrate that polymer brushes fabricated on a Si/SiO_2 glass-like surface using RAFT polymerization are amenable to the facile transformation of their thioester-based chain end group into a variety of monovalent or multivalent reactive clickable groups. These clickable handles can be subsequently conjugated with various functional molecules ranging from fluorescent dyes to bioactive ligands for biomolecular immobilization and sensing. In particular, poly(ethylene glycol)-based polymer brushes were obtained using

surface-initiated RAFT polymerization (SI-RAFT), followed by a radical-exchange reaction with azo-containing molecules for their end groups transformation. Maleimide and alkene groups are installed at the brush interface for subsequent functionalization using thiol-maleimide, and radical thiol-ene *click* reactions, respectively. Effective conjugation of fluorescent dyes and bioactive ligands such as biotin and mannose are demonstrated. Additionally, the method uses dendritic molecules to install clustered multivalent functional groups at the interface. Functionalization of obtained dendritic structures at the surface is used to display mannose, a motif specific for recognition of ConA. The advantage of installing such multivalent ligand clusters is demonstrated by efficient sensing of target lectin.

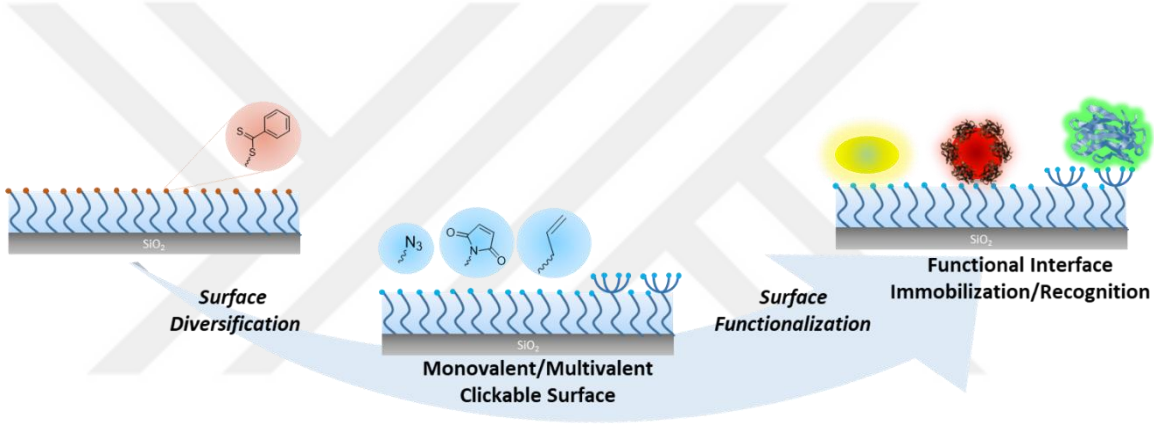

Figure 6.1. Illustration of diversification of surface functionality of polymer brushes for fabrication of functional interfaces.

6.2. Experimental

6.2.1. Materials

All chemicals were used as received unless specified. 4-Cyano-4-(phenylcarbonothioylthio)pentanoic acid and N,N'-Dimethylamino pyridine (DMAP) were purchased from Sigma-Aldrich. 3-Aminopropyltriethoxysilane was obtained from Across Organics. Di(ethylene glycol) methyl ether methacrylate (DEGMA) was purchased from Sigma Aldrich and filtered over basic aluminum oxide before use. Azobisisobutyronitrile

(AIBN, Sigma Aldrich) was recrystallized from methanol and dried under a vacuum. 4,4'-Azobis(4-cyanovaleric acid) (V-501) was purchased from Fluka. For dendron synthesis, 2,2-Bis(hydroxymethyl)propionic acid (Bis-MPA), 2,2-Dimethoxypropane, and 4-Pentenoic anhydride were obtained from Sigma Aldrich. 1-(3-(Dimethylamino)propyl)-3-ethylcarbodiimide hydrochloride (EDCI) and *N,N'*-Dicyclohexylcarbodiimide (DCC) were purchased from Alfa-Aesar and Sigma Aldrich, respectively. Biotinylated hexa(ethylene glycol)-undecanethiol ($HS(CH_2)_{11}(OCH_2CH_2)_6NH$-Biotin, Biotin-SH) was purchased from Nanoscience Instrument (Phoenix, AZ). Qdot 605 streptavidin conjugate was obtained from Invitrogen molecular probes. DBCO-PEG_4-carboxyrhodamine and dibenzocyclooctyne-PEG_4-biotin were obtained from Click Chemistry Tools. Texas Concanavalin A-Texas Red and Conjugate and Concanavalin A–FITC conjugate were purchased from Thermo Fisher. Surface attachable RAFT agent [156], G1-OH [315], G2-OH [315], BODIPY-SH [219], azobis-p-MAL [314], mannose-SH [316,317] and azobis-azide [155] were synthesized according to previously described literature examples. Dichloromethane (CH_2Cl_2), ethanol, chloroform, dimethylformamide (DMF), n-hexane, toluene, and 1,4-dioxane were purchased from Merck. Anhydrous toluene, tetrahydrofuran (THF), and CH_2Cl_2 were obtained from the SciMatCo purification system, and other solvents were dried over molecular sieves.

6.2.2. Methods

^1H and ^{13}C NMR spectra were recorded on Bruker Avance Ultrashield 400 (400 MHz). X-ray photoelectron spectroscopy (XPS) was carried out using a K-Alpha instrument (Thermo Scientific). Fourier transform infrared (FT-IR) spectroscopy analyses were performed on a Nicolet 380 (Thermo Fisher Scientific, Inc.) instrument equipped with a Harrick Scientific GATR accessory and a Ge crystal. Atomic Force Microscopy was obtained from Nanosurf. ^1H NMR and ^{13}C NMR spectra were obtained using a Varian 400 MHz spectrometer. Fluorescence microscopy was performed using LD-A-Plan 10x/0.30 objective in Zeiss Axio Observer inverted microscope (ZEISS Fluorescence Microscopy, Carl Zeiss Canada Ltd., Canada). SPR study was performed using BioNavis (MP-SPR Navi 210A VASA) instrument.

6.2.3. Synthesis and Characterization of Double Bond End Group Functionalized G0 Dendron (Azobis-G0-ene)

4,4′-Azobis(4-cyanovaleric acid) (V-501, 840 mg, 3 mmol), DMAP (146 mg, 1.2 mmol), and 5-Hexen-1ol (660.4 mg, 6.6 mmol) were purged with N_2 for 15 min, and anhydrous dichloromethane (3 mL) was added under N_2. In a separate flask, DCC (1.26 g, 6.1 mmol) was purged with N_2 and dissolved in anhydrous dichloromethane (5 mL) under N_2, and the solution of DCC was cooled at 0 ^oC. At 0 ^oC, the solution of DCC was added to the solution of V-501/DMAP/5-Hexen-1-ol. The reaction mixture was stirred at room temperature for 24 h. Afterward, the reaction mixture was filtered to remove DCU, and then dichloromethane was evaporated. The crude product was redissolved in dichloromethane (50 mL) and extracted with $NaHSO_4$ solution (1 x 10 mL), Na_2CO_3 solution (1 x 10 mL), and brine (1 x 10 mL), respectively. The organic layer was dried over Na_2SO_4. The organic layer was concentrated under a vacuum. The crude product was purified by column chromatography (EtOAc/Hexane, 4:6, v/v). The pure product was obtained in 76 ± 4 % yield. ^1H NMR (400 MHz, $CDCl_3$) δ/ppm: 5.82 - 5.72 (m, 2H), 5.01 - 4.94 (m, 4H), 4.08 (br s, 4H), 2.49 - 2.25 (m, 8H), 2.08 - 2.01 (m, 4H), 1.7 (s, 3H), 1.65 - 1.59 (m, 6H), 1.44 - 1.41 (m, 4H); ^{13}C NMR (100 MHz, $CDCl_3$) δ/ppm: 171.4, 138.2, 117.1, 114.9, 71.9, 65.0, 60.4, 33.2, 29.1, 27.9, 25.1, 23.9. FTIR (cm^{-1}): 3065, 2938, 2857, 1730, 1678, 1177.

6.2.4. Synthesis and Characterization of Double Bond End Group Functionalized G1[alkyne] Dendron (G1- alkyne-diene)

Prop-2-yn-1-yl 3-hydroxy-2-(hydroxymethyl)-2-methylpropanoate (G1-OH, 400 mg, 2.32 mmol), 4-Pentenoic anhydride (2.1 g, 2 mL, 11.6 mmol), DMAP (113 mg, 0.93 mmol) and pyridine (917 mg, 0.94 mL, 11.6 mmol) were dissolved in dichloromethane (10 mL), and the reaction mixture was stirred at room temperature for 24 h. After that, deionized water (1 mL) was added, stirring the mixture for three hours. After that, the mixture was poured into dichloromethane (50 mL) and extracted with $NaHSO_4$ solution (1 x 10 mL), Na_2CO_3 solution (1 x 10 mL), and brine (1 x 10 mL), respectively. The organic layer was dried over Na_2SO_4. The organic layer was concentrated under a vacuum. The crude product was purified by column chromatography (EtOAc/Hexane, 30:70, v/v). The pure product was obtained in 72 ± 2 % yield. ^1H NMR (400 MHz, $CDCl_3$) δ/ppm: 5.82 - 5.72 (m, 2H), 5.04 -

4.96 (m, 4H), 4.68 (s, 2H), 4.21 (s, 4H), 3,68 (s, 1H), 2.44-2.32 (m, 8H), 1.24 (s, 3H); ^{13}C NMR (100 MHz, $CDCl_3$) δ/ppm: 172.6, 172.4, 136.2, 115.6, 75.2, 65.2, 52.6, 46.4, 33.3, 28.7, 17.71.

6.2.5. Synthesis and Characterization of Azobis-G1-diene

2-methyl-2-((prop-2-yn-1-yloxy)carbonyl)propane-1,3-diyl bis(pent-4-enoate) (G1-alkyne-diene, 250 mg, 0.74 mmol) and azobis-N_3 (180mg, 0.34 mmol) were purged with N_2 and dissolved in anhydrous THF (2 mL) under N_2. In a separate flask, Cu(I)Br (9 mg, 0.067 mmol) and PMDETA (14 μL, 0,067 mmol) were purged with N_2 and dissolved in anhydrous THF (4 mL). The solution of G1-diene and azobis-N_3 was added to the solution of Cu(I)Br and PMDETA under N_2. The reaction mixture was stirred at 40 ^{o}C for 24 h. After completion of the reaction, THF was removed under vacuum, and the crude product was dissolved in dichloromethane (50 mL) and then extracted with brine (3 x 10 mL). The organic layer was dried over Na_2SO_4. The crude product was purified by column chromatography (EtOAc/Hexane, 70:30, v/v); the yield was 82%. ^{1}H NMR (400 MHz, $CDCl_3$) δ/ppm: 7.57 (s, 2H), 5.83 - 5.73 (m, 4H), 5.25 (s, 4H), 5.05 - 4.98 (m, 8H), 4.34 (t, *J* = 7.1, 4H), 4.20 (q, *J1* =11.0, *J2* = 6.3, 8H), 4.12 - 4.04 (bs, 4H), 2.54 - 2.31 (m, 20H), 1.94 - 1.86 (m, 4H), 1.73 (s, 3H), 1.65 - 1.57 (m, 11H), 1.38 (bs, 8H), 1.2 (s, 6H); ^{13}C NMR (100 MHz, $CDCl_3$) δ/ppm: 172.7, 172.4, 171.3, 142.3, 136.4, 123.7, 117.5, 115.7, 71.8, 65.2, 64.8, 58.4, 50.3, 46.3, 33.3, 30.1, 29.1, 28.7, 28.4, 26.12, 25.3, 24.0, 23.7, 17.8. FT-IR (cm^{-1}): 3081, 2938, 1724, 1676, 1641, 1156, 1131, 1050.

6.2.6. Synthesis and Characterization of Double Bond End Group Functionalized G2[alkyne] Dendron (G2- alkyne-tetraene)

G2-OH-alkyne (450 mg, 1.11 mmol), 4-pentenoic anhydride (1.6 mL, 1.67 g, 8.91 mmol, DMAP (86 mg, 0.71 mmol), and pyridine (0.72 mL, 704 mg, 8.91 mmol) were dissolved in dichloromethane (8 mL), and this mixture was stirred at room temperature for 24 hours. Afterward, the reaction mixture was poured into dichloromethane (50 mL) and extracted with $NaHSO_4$, Na_2CO_3, and brine solution (1 x 10 mL). The organic layer was dried over Na_2SO_4. The crude product was purified using column chromatography (EtOAc/ Hexane 30:70 v/v). G2-tetraene-alkyne was obtained in 67 ± 5 % yield. ^{1}H NMR (400 MHz,

$CDCl_3$) δ/ppm: 5.83-5.73 (m, 4H), 5.05 - 4.96 (m, 8H), 4.67 (s, 2H), 4.29 - 4.16 (m, 12H), 2.48 - 2.32 (m, 16H), 1.26 (s, 3H), 1.21 (s, 6H); ^{13}C NMR (100 MHz, $CDCl_3$) δ/ppm: 172.4, 172.0, 171.4, 136.4, 115.6, 75.6, 65.7, 65.2, 52.8, 46.7, 46.4, 33.3, 28.7, 17.9, 17.5.

6.2.7. Synthesis and Characterization of Azobis-G2-tetraene

G2-tetraene-alkyne (150 mg, 0.22 mmol) and azobis-N_3 (52 mg, 0.098 mmol) were purged with N_2 for 10 min. In a separate flask, Cu(I)Br (2.81 mg, 0.02 mmol) and PMDETA (4.2 μL, 3.47 mg, 0.02 mmol) were purged with N_2 for 10 min. Then, anhydrous THF (4+4 mL) was added to two containers. Finally, the solution of G2-tetraene-alkyne and Azobis-N_3 was added to the solution of PMDETA and Cu(I)Br under nitrogen. The reaction mixture was stirred at 40 ^{o}C for 24 h. Afterward, the reaction mixture was poured into dichloromethane (50 mL) and extracted with $NaHSO_4$, Na_2CO_3, and brine solution (1 x 10 mL). The organic layer was dried over Na_2SO_4. The crude product was purified using column chromatography (EtOAc/ Hexane 60:40 v/v). The pure product was obtained as a colorless liquid with a 76±5 % yield. ^{1}H NMR (400 MHz, $CDCl_3$) δ/ppm: 7.65 (s, 2H), 5.82 - 5.72 (m, 8H), 5.23 (s, 4H), 5.04 - 4.96 (m, 16H), 4.35 (t, J = 7.0, 4H), 4.25 - 4.07 (m, 26H), 2.53 - 2.30 (m, 38H), 1.95 - 1.88 (m, 4H), 1.71 (s, 3H), 1.65 (s, 6H), 1.36 (s, 10H), 1.21 (s, 6H), 1.17 (s, 12H); ^{13}C NMR (100 MHz, $CDCl_3$) δ/ppm: 172.5, 172.2, 172.0, 142.0, 136.4, 124.1, 115.7, 72.0, 65.6, 65.1, 64.9, 58.5, 50.3, 46.7, 46.3, 33.2, 30.2, 29.2, 29.1, 28.7, 28.3, 26.2, 25.4, 24.0, 23.7, 17.8, 17.5. FT-IR (cm^{-1}): 3081, 2938, 1724, 1676, 1641, 1156, 1131, 1050.

6.2.8. Synthesis and Immobilization of Surface Anchoring RAFT Reagent

The surface RAFT agent was synthesized using a previously reported procedure [156]. Initiator-modified substrates were prepared by following a previously reported method [156]. Briefly cleaned silicon wafers (0.8 x 1.0 cm) were immersed into RAFT agent solution (1 mM) in anhydrous toluene and kept in solution for 19 hours. Next, the silicon wafers were washed with toluene and CH_2Cl_2. Finally, they were dried under a stream of nitrogen.

6.2.9. Surface Initiated RAFT Polymerization (SI-RAFT) of DEGMA

Di(ethylene glycol) methyl ether methacrylate (DEGMA, 1.5 g, 8 mmol) and AIBN (2.16 mg, 0.013 mmol) were dissolved in anhydrous DMF and purged with N_2 for 20 min. In a separate vial, the RAFT agent-coated wafers were purged with N_2 for 10 min, and wafers were treated with the solution of DEGMA/AIBN under nitrogen at 70 ^oC for 6 h. After that, wafers were washed with DMF and CH_2Cl_2 with the aid of sonication, and subsequently, they were dried under a flow of nitrogen. The DEGMA brushes were stored under nitrogen for post-polymerization modification.

6.2.10. Typical Radical Cross-Coupling End Group Modification of DEGMA Brush with Azobis-p-maleimide

Azobis-p-maleimide (0.18 mg, 0.025 mmol) was dissolved in a mixture of DMF/1,4-Dioxane (1 mL, v/v) and purged with N_2 for 20 min. In a separate vial, the DEGMA polymer surface was purged with N_2 for 10 min, and the brush was treated with the solution of azobis-p-maleimide. Afterward, the surface was washed with DMF, dichloromethane, and deionized water and dried under a nitrogen flow.

6.2.11. Activation of Maleimide Group via Retro Diels-Alder Reaction

Protected-maleimide terminated polymer brush was placed into a vacuum oven and heated at 110 ^oC for 4 h. Maleimide-containing surface was washed with ethanol and dichloromethane with the aid of sonication and dried under a stream of nitrogen.

6.2.12. Post-polymerization Modification of Maleimide-containing DEGMA Brush with BODIPY-Thiol via Michael Addition

Maleimide-containing polymer brush surface was immersed in a solution of BODIPY-thiol in THF (1mg/mL, 2.3 mM) and left overnight. Afterward, the surface was washed with THF to remove unreacted BODIPY-thiol and dried under a nitrogen stream.

6.2.13. Maleimide-containing Brush Modification with Biotin-thiol and Immobilization Streptavidin-Coated Quantum Dot Nanoparticles

Biotinylated hexa(ethylene glycol) undecanethiol (Biotin-SH) was dissolved in methanol (0.5 mg/mL), and the maleimide containing DEGMA polymer surface was treated with a solution of Biotin-SH for 24 h. Afterward, the surface was washed with methanol and dichloromethane and dried under a stream of nitrogen; subsequently, a solution of Qdots (10 µL, 1 µM) dissolved in 10 µL of water was placed onto the biotinylated surface and incubated for 4 h. After this, the surface was rinsed with deionized water several times and dried under a stream of nitrogen.

6.2.14. Post-polymerization Modification of DEGMA Brush with Azobis-G0-ene

Azobis-G0-ene (22 mg, 0.05 mmol) was dissolved in anhydrous 1,4-dioxane and purged with nitrogen, and then the DEGMA polymer brush surface was put into a vial and purged with nitrogen for 10 min. After degassing step, the reaction mixture was added to the vial, including the DEGMA brush surface. The reaction vial was immersed in an oil bath, and the reaction was carried out at 70 ^{o}C for 24 hours. After the reaction, the modified surface was washed with a gentle amount of dioxane and CH_2Cl_2. The surface was dried under nitrogen steam and kept at 4 ^{o}C for further reaction.

6.2.15. Post-polymerization Modification of DEGMA Brush with Azobis-G1-diene

Azobis-G1-diene (30 mg, 0.025 mmol) was dissolved in anhydrous 1,4-dioxane and purged with nitrogen, and then the DEGMA polymer brushes surface was put into a vial and purged with nitrogen for 10 min. After the degassing step, the reaction mixture was added to the vial, including the DEGMA brush surface. The reaction vial was immersed in an oil bath, and the reaction was carried out at 70 ^{o}C for 24 hours. After the reaction, the modified surface was washed with a gentle amount of dioxane and CH_2Cl_2. The surface was dried under a nitrogen stream and kept at 4 ^{o}C for further reaction

6.2.16. Post-polymerization Modification of DEGMA Brush with Azobis-G1-diene and AIBN

Azobis-G1-diene (30 mg, 0.025 mmol) and AIBN (4 mg, 0.025 mmol) were dissolved in anhydrous 1,4-dioxane, and the mixture was degassed with nitrogen for 30 min. DEGMA polymer brush surface was put into a vial and purged with nitrogen for 10 min. Afterward, azobis-G1-diene and AIBN mixture was added to the brush surface vial. The vial was sealed in an oil bath at 70 ^{o}C for 24 h. After the reaction, the surface was washed with dioxane and CH_2Cl_2. The modified surface was dried under N_2 steam and kept at 4 ^{o}C for further reaction.

6.2.17. Post-polymerization Modification of DEGMA Brush with Azobis-G2-tetraene and AIBN

Azobis-G2-tetraene (25 mg, 0.0125 mmol) and AIBN (2 mg, 0.0125 mmol) were dissolved in anhydrous 1,4-dioxane, and the mixture was degassed with nitrogen for 30 min. DEGMA polymer brushes surface wafer was put into a reaction vial and purged with nitrogen for 10 min. After that, the reaction mixture was added to the reaction vial, and the vial was sealed into an oil bath, and the reaction was carried out at 70 ^{o}C for 24 h. Next, the modified DEGMA surface was washed with a gentle amount of dioxane and CH_2Cl_2. The surface was kept at 4 ^{o}C under nitrogen for further reaction.

6.2.18. Modification of Reactive Dendron Grafted Surfaces with Fluorescent Dye

A fluorescent dye BODIPY-SH (4 mg, 8.4 x 10^{-3} mmol) and DMPA (0.51 mg, 1.68 x 10^{-3} mmol) were dissolved in DMF (60 μL). This solution was dropped onto a double bond end group functionalized dendron-modified polymer surface (G0), and the surface was exposed to UV light for 30 min. After that, surfaces were washed with DMF and CH_2Cl_2 with sonication. The same protocol was applied to the DEGMA polymer surface's control surface. After the modification step, the dye-modified surface was kept under nitrogen in the dark at 4 ^{o}C.

6.2.19. Post-polymerization Modification of Alkene Grafted Dendrons with Mannose-SH

Mannose-thiol (Mannose-SH) was synthesized in three steps [316,317]. Mannose-SH (3 mg, 0.01 mmol) and DMPA (0.5 mg, 2 x 10^{-3} mmol) were dissolved in DMF (60 μL), and this solution was divided into four parts. Each part was dropped onto double bond end group functionalized dendron-modified DEGMA polymer surfaces. Only the DEGMA brush surface was used as the control surface. All surfaces were exposed to UV light for 30 min. Next, surfaces were washed with DMF and CH_2Cl_2. Finally, they were dried under N_2 steam and kept at 4 ^oC for further modification.

6.2.20. Immobilization of ConA onto Mannose Functionalized Brushes

Mannose functionalized polymer surfaces (G0, G1, G1/AIBN, and G2/AIBN) were treated with 50 uL Con A-Texas red conjugate solution in PBS buffer (0.5 mg/mL) in the presence of Mn^{2+} and Ca^{2+} ions for 6 hours. After 6 hours, surfaces were washed with excess PBS buffer. For the control experiment, a double bond grafted G2 dendron functionalized polymer surface was used, and this surface was also treated with Con A-Texas red conjugate in the same manner.

6.2.21. Preparation of Mannose Conjugated Polymer Brush on SiO_2-Coated Gold SPR Surface

The mannose-containing polymer brushes on the SPR chip were prepared using the same reaction pathway along with a normal SiO_2 surface. A clean SiO_2-coated gold SPR chip was immersed in 1 mM dry toluene solution of the surface RAFT agent and kept in solution under a nitrogen atmosphere for 4 h at room temperature. After that, DEGMA polymer brushes were obtained from RAFT polymerization. End-group modification of DEGMA brushes on the SPR chip was carried out using azobis-G2-tetraene. Mannose-bearing G2 grafted polymer brushes were obtained using thiol-ene *click* chemistry in mannose-thiol.

6.2.22. Surface Plasmon Resonance and Immobilization of ConA

Surface plasmon resonance (SPR) was performed for mannose–ConA binding affinity constant assay on an SPR biosensor instrument BioNavis (MP-SPR Navi 210A VASA). G2 dendron grafted polymer brushes were prepared using a SiO_2-coated gold SPR sensor chip. Mannose decorated SPR chip was obtained by conjugating mannose-thiol to end groups of G2 polymer brushes. In the SPR biosensor, the mannose-containing gold SPR chip was exposed to HEPES buffer (20 mM) until a stable baseline was obtained. To assess the binding of ConA to mannose units on the chip, an FTIC-ConA solution (0.8 mg/mL) in an aqueous buffer solution (20 mM HEPES, 1.0 mM $MnCI_2$, 1.0 mM $CaCI_2$, 0.15 M NaCl, adjusted to pH 7.4) was injected three times (250 µL from 0.8 mg/mL FTIC-ConA solution) over the sensor chip surface. The flow rate was set to 50 $\mu L.min^{-1}$, and the contact and dissociation/washing times were set to 5 and 5 min, respectively. The bovine serum albumin (BSA) protein solution was injected over the mannose-bearing SPR chip with the same concentration as a control experiment.

6.3. Results and Discussion

6.3.1. Synthesis and Characterization of Azobis-G0-ene

Azobis-G0-ene dendron was synthesized using 5-hexen-1ol and 4,4′-azobis(4-cyanovaleric acid) via DCC-DMAP coupling reaction in 76 ± 4 % yield. The reaction was outlined in Figure 6.2, and product characterization was shown with ^1H NMR in Figure 6.3.

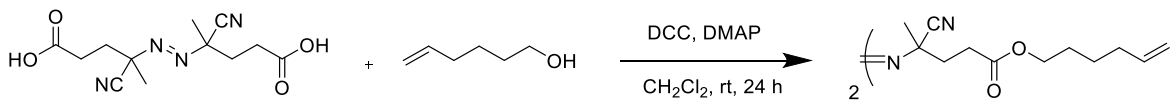

Figure 6.2. The synthesis scheme of azobis-G0-ene.

As seen in Figure 6.3, hydrogens of the alkene group on structure (a and b labeled) were observed in 5.82 - 5.72 ppm and 5.01 - 4.94 ppm. In addition to these peaks, the characteristic $–CH_2$ peak adjacent to ester carbonyl came at around 4.08 ppm. ^{13}C NMR spectrum consisted of carbon peaks at 171.4, 138.2, 117.1, 114.9, 71.9, 65.0, 60.4, 33.2, 29.1, 27.9, 25.1, and 23.9. ^{13}C NMR and FTIR spectra were reported in Figure A.11 and Figure A.12.

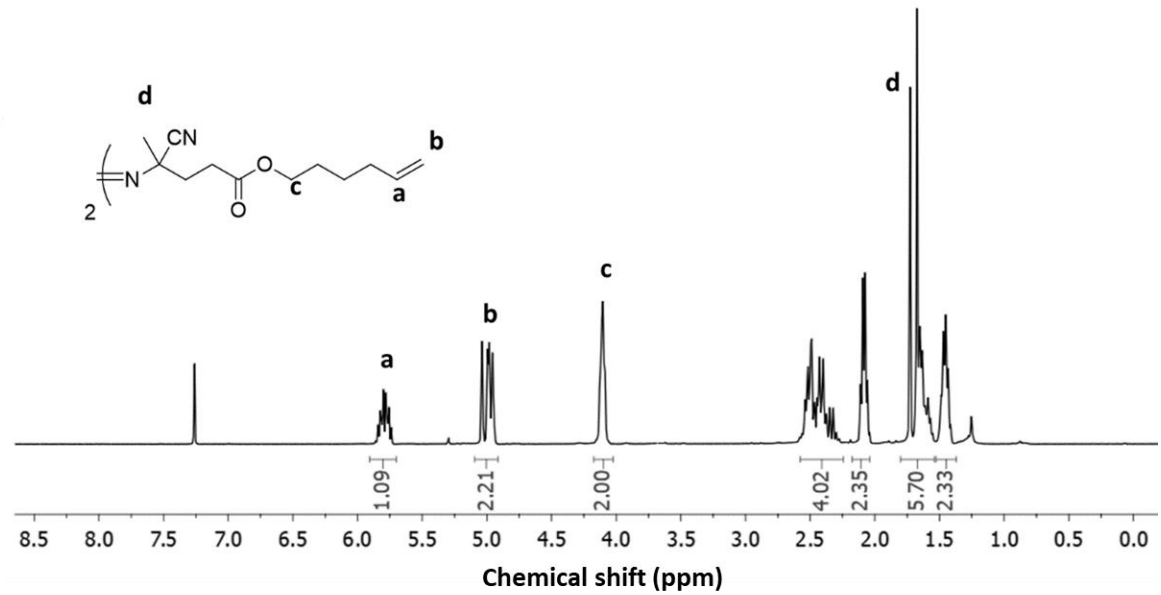

Figure 6.3. ^1H NMR spectrum of azobis-G0-ene in $CDCl_3$.

6.3.2. Synthesis and Characterization of Alkyne-bearing G1-diene

Alkyne-bearing G1-OH polyester dendron was synthesized using a published procedure [315]. G1-alkyne-diene dendron, which has two alkenes on the periphery, was synthesized using alkyne bearing G1-OH and 4-pentenoic anhydride in the presence of DMAP and pyridine in 72% yield. The reaction is demonstrated in Figure 6.4.

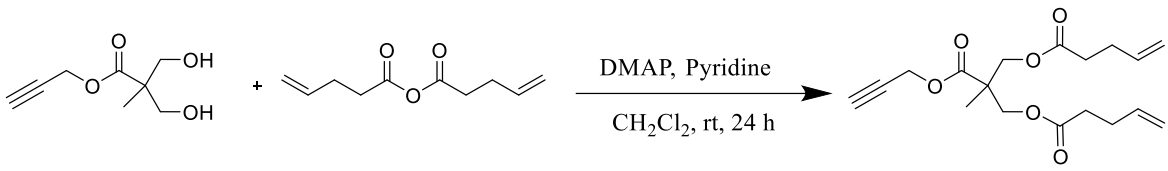

Figure 6.4. The synthesis scheme of G1-alkyne-diene.

^{1}H NMR confirmed the grafting of alkyne groups on G1 dendron, and the full ^{1}H NMR spectrum was given in Figure 6.5. One of the proton resonances of the alkene group on the periphery of the dendron appeared between 5.84 - 5.74 ppm (a labeled), and another proton resonance of the alkene group was revealed at 5.01 ppm. Proton resonances of the propargyl group appeared at 4.71 ppm (c labeled) and between 2.46 - 2.32 (i labeled). Along with these proton resonances, the presence of d and e labeled proton resonances confirmed the G1-alkyne-diene structure. ^{13}C NMR spectrum of G1-alkyne-diene was composed of carbon peaks at 172.5, 172.2, 172.0, 142.0, 136.4, 124.1, 115.7, 72.0, 65.6, 65.1, 64.9, 58.5, 50.3, 46.7, 46.3, 33.2, 30.2, 29.2, 29.1, 28.7, 28.3, 26.2, 25.4, 24.0, 23.7, 17.8 and 17.5. ^{13}C NMR spectrum was given in Figure A.13.

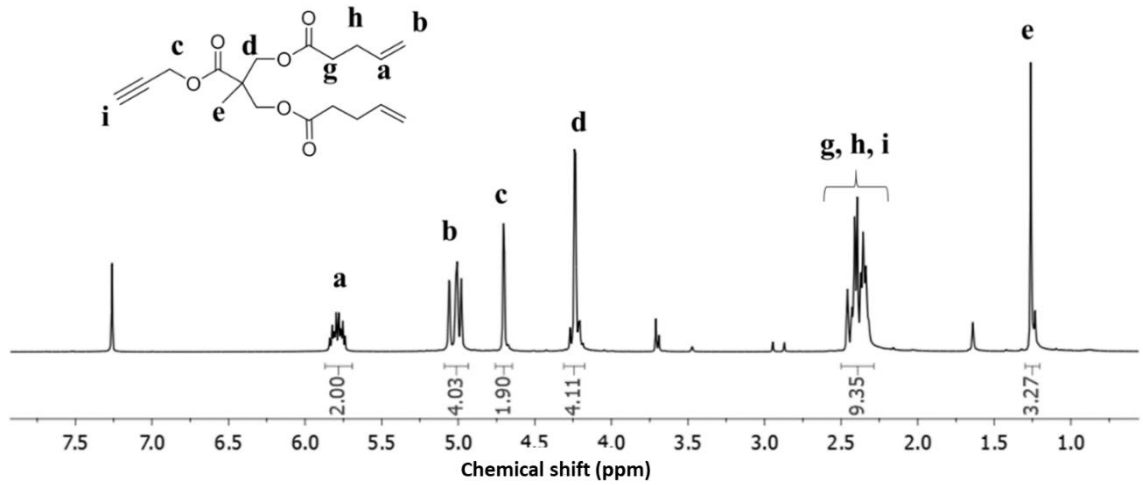

Figure 6.5. ^{1}H NMR spectrum of G1-alkyne-diene in $CDCl_3$.

6.3.3. Synthesis and Characterization of Azobis-G1-diene "*Click*" Reaction

Azobis-G1-diene was synthesized using azobis-azide, which was prepared according to a known procedure [155], and G1-alkyne-diene via copper-catalyzed "*click*" reaction. PMDETA and Cu(I)Br were used as catalysts. The reaction was carried out in anhydrous THF at 40 ^{o}C for 48h. The "*click*" reaction between azide-alkyne groups is shown in Figure 6.6.

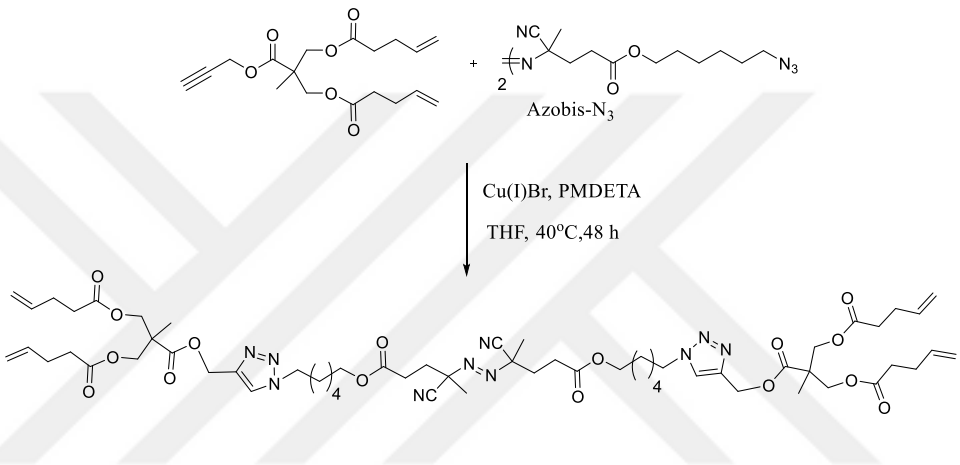

Figure 6.6. Demonstration of "*click*" reaction and synthesis of azobis-G1-diene.

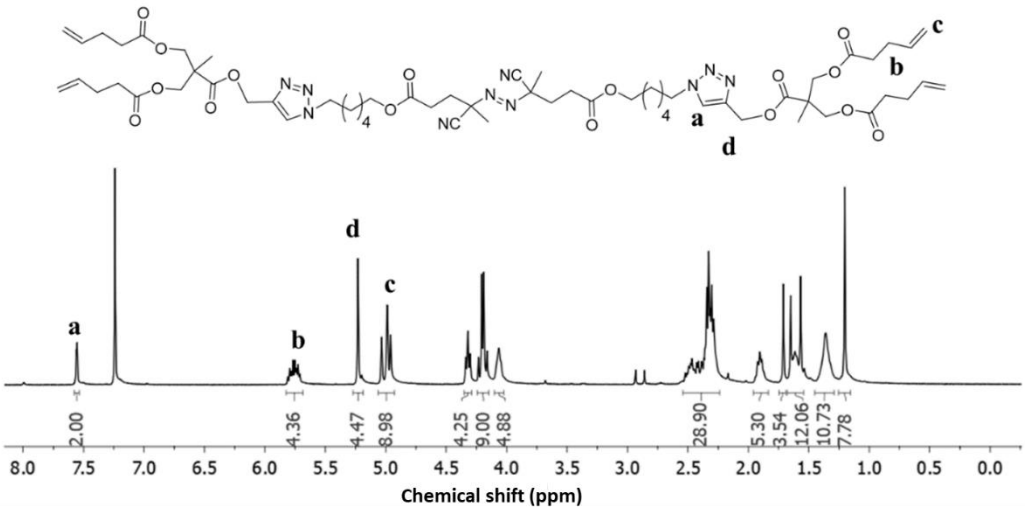

Figure 6.7. ^{1}H NMR spectrum of azobis-G1-diene in $CDCl_3$.

Analysis of azobis-G1-diene was done with ^{1}H NMR and ^{13}C NMR. ^{1}H NMR spectrum was given in Figure 6.7. Resonances of alkenyl hydrogens appeared between 5.83 - 5.73 ppm and 5.01 ppm. The resonance of the triazole ring proton, which came from the cycloaddition of alkyne and azide, appeared at 7.57 ppm. In addition, propargylic hydrogen (-O$\underline{CH_2}$CCH) showed resonances at 4.71 ppm before the reaction. After the cycloaddition reaction, this peak shifted from 4.71 to 5.25 ppm. All these proton resonances confirmed a successful cycloaddition reaction. ^{13}C NMR spectrum of G1-alkyne-diene was composed of carbon peaks at 172.7, 172.4, 171.3, 142.3, 136.4, 123.7, 117.5, 115.7, 71.8, 65.2, 64.8, 58.4, 50.3, 46.3, 33.3, 30.1, 29.1, 28.7, 28.4, 26.12, 25.3, 24.0, 23.7 and 17.8. ^{13}C NMR and FTIR spectra were reported in Figure A.14 and Figure A.15.

6.3.4. Synthesis and Characterization of Alkyne-bearing G2-tetraene

Alkyne-bearing G2-OH polyester dendron was synthesized according to a published procedure [298]. G2-alkyne-tetraene dendron, which has four alkenes on the periphery, was synthesized using alkyne bearing G2-OH and 4-pentenoic anhydride in the presence of DMAP and pyridine in 67% yield. The reaction is demonstrated in Figure 6.8.

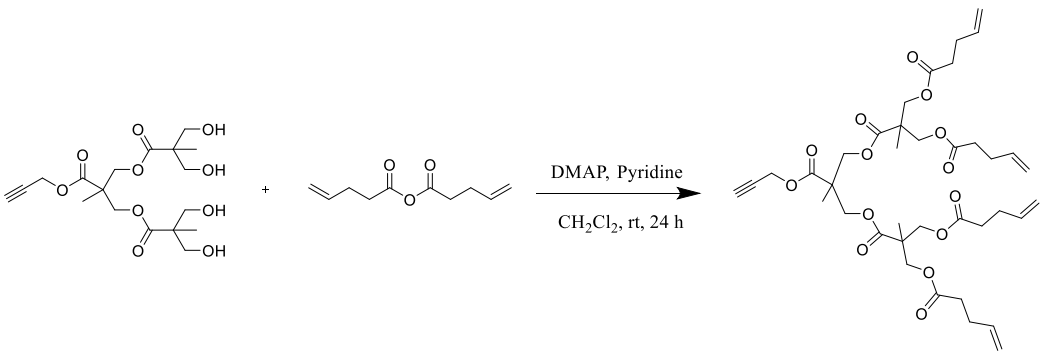

Figure 6.8. Synthetic pathway of obtaining G2-tetraene dendron.

The synthesis of G2-tetraene dendron was confirmed by NMR analysis. ^{1}H NMR spectrum was given in Figure 6.9. When the ^{1}H NMR spectrum was investigated, it was observed that the proton resonance of the alkenyl group on the periphery appeared at 5.85 - 5.75 ppm and integration of this peak corresponded to four hydrogens. In addition, another proton resonance of the terminal alkenyl group came at 5.02 ppm, where integration

corresponded to eight hydrogens. Proton resonance of the terminal alkyne group appeared at 2.50 ppm, and its integration was one hydrogen. As a result, the integral ratio between core terminal alkyne hydrogen and terminal alkene hydrogens on the periphery was 1:8, and this ratio was evidence of the successful conjugation of pentenoic acid to four hydroxyl groups on the periphery. Proton resonances of propargylic -CH_2 group (c labeled) gave a peak at 4.72 ppm.^{13}C NMR spectrum of G2-alkyne-tetraene consisted of carbon signals at 172.4, 172.0, 171.4, 136.4, 115.6, 75.6, 65.7, 65.2, 52.8, 46.7, 46.4, 33.3, 28.7, 17.9 and 17.5. ^{13}C NMR spectrum was reported in Figure A.16.

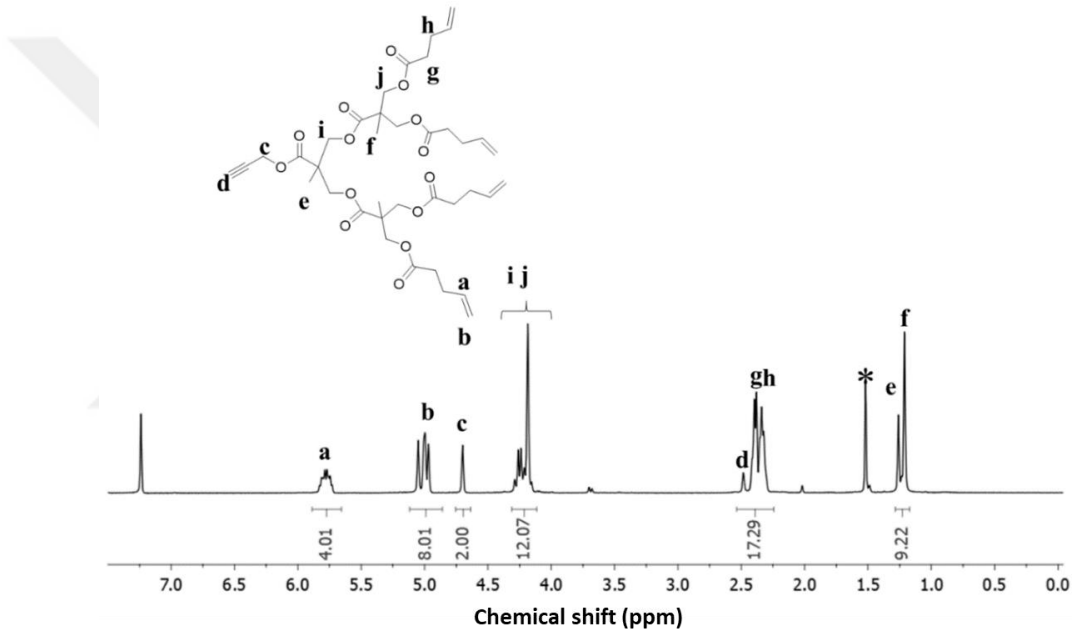

Figure 6.9. ^{1}H NMR spectrum of G2-alkyne-tetraene in $CDCl_3$.

6.3.5. Synthesis and Characterization of Azobis-G2-tetraene

Azobis-G2-tetraene was obtained from a cycloaddition reaction between azobis-azide and G2-alkyne-tetraene using the "*click*" reaction. In this reaction, PMDETA and Cu(I)Br were used as a catalyst, and the reaction was carried out in anhydrous THF at 40 ^{o}C for 48 h. Azobis-G2-tetraene was obtained in a 76% yield. The reaction pathway is shown in Figure 6.10.

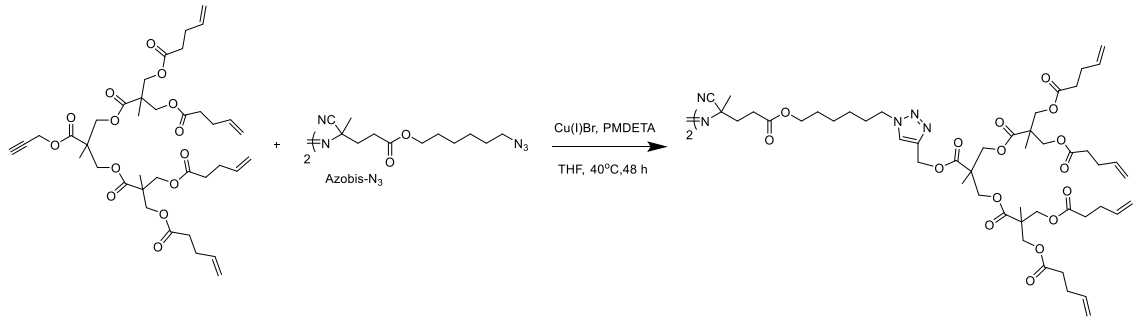

Figure 6.10. Synthesis of Azobis-G2-tetraene via azide-alkyne cycloaddition reaction.

Analysis of azobis-G2-tetraene was done via ^{1}H NMR and ^{13}C NMR. ^{1}H NMR spectrum was given in Figure 6.11. The resonances of alkenyl hydrogens on the dendron periphery showed two peaks. The first alkenyl resonances came between 5.84 - 5.75 ppm, and integration of this peak corresponded to eight hydrogens. Another alkenyl proton resonance gave a peak at 5.03 ppm with an integral ratio consisting of sixteen hydrogens. Triazole ring proton (d labeled), which formed after cycloaddition reaction between azide and alkyne groups, appeared at 7.67 ppm. In addition, propargylic hydrogen (-OCH_2CCH) showed resonance at 4.72 ppm before the "*click*" reaction. After the azide-alkyne cycloaddition reaction, this peak shifted from 4.72 ppm to 5.25 ppm. As a result, the integral ratio between triazole hydrogens and terminal alkene hydrogens on the periphery was 2:16, and this ratio was evidence of a successful cycloaddition reaction between two azide groups and two alkyne units. These ^{1}H NMR data confirmed the expected chemical structure after the reaction.

^{13}C NMR spectrum of azobis-G2-tetraene consisted of carbon peaks at 172.5, 172.2, 172.0, 142.0, 136.4, 124.1, 115.7, 72.0, 65.6, 65.1, 64.9, 58.5, 50.3, 46.7, 46.3, 33.2, 30.2, 29.2, 29.1, 28.7, 28.3, 26.2, 25.4, 24.0, 23.7, 17.8 and 17.5. ^{13}C NMR and FTIR spectra were reported in Figure A.17 and Figure A.18.

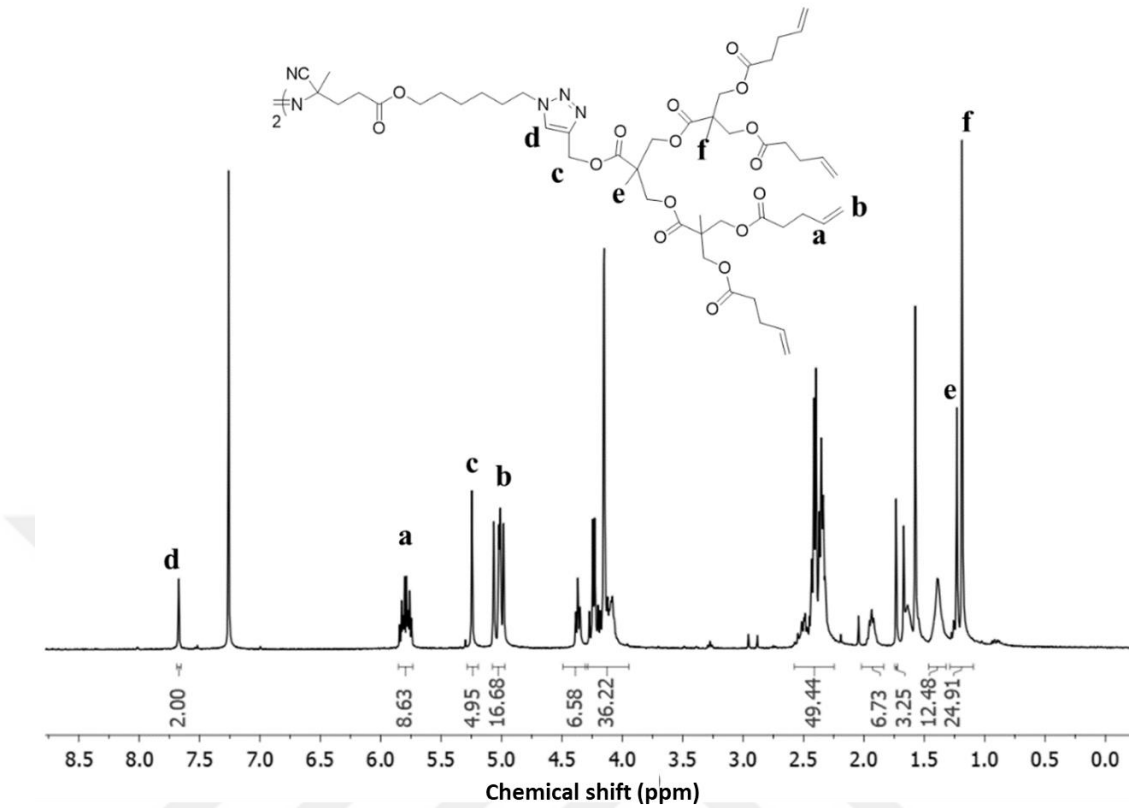

Figure 6.11. ^{1}H NMR spectrum of Azobis-G2-tetraene in $CDCl_3$.

6.3.6. Fabrication of DEGMA Polymer Brush via SI-RAFT Polymerization

The first step to preparing DEGMA based polymer brush via RAFT polymerization is to synthesize a surface-attachable RAFT agent. For this purpose, the surface-attachable RAFT agent was according to a published procedure by using APTES and 4-cyano-4-(thiobenzoylthio)pentanoic acid (CTA) [156]. After that, the cleaned Si/SiO_2 surfaces were immobilized with this surface-attachable RAFT agent, where the silane group may form a strong bond between organic compounds and inorganic materials. Afterward, RAFT-coated surfaces were photolithographically micro-patterned using a previously reported method to allow AFM analysis of the polymer brush thickness [318]. DEGMA was chosen as the main monomer to obtain polymer brushes due to its anti-biofouling character and hydrophilicity.

Surface-initiated RAFT polymerization was carried out in the presence of DEGMA and AIBN under a nitrogen atmosphere at 70 ^{o}C for six hours (Figure 6.12a). After the

reaction, surfaces were washed with DMF, CH_2Cl_2, and water to remove monomers and dried under nitrogen steam.

The DEGMA polymer brush was characterized with FT-IR, XPS, and AFM analyses. Immobilization of the RAFT agent and formation of the DEGMA polymer brush were confirmed by the FTIR spectrum, which was given in Figure 6.12b. The amide peak at 1651 cm^{-1} demonstrated that the silicon surface was coated with RAFT agent via silane groups (black line). In addition, a new peak at 1721 cm^{-1} showed successful polymerization with DEGMA from the silicon surface, and the DEGMA spectrum was shown as the red line in Figure 6.12b.

In addition to FT-IR, the DEGMA polymer brush was investigated by XPS. XPS survey scan of the DEGMA polymer brush was given in Figure 6.12d. XPS survey scan composed a carbon atom signal of around 285 eV and an oxygen atom signal of around 531 eV. The oxygen atom signal is evidence of a DEGMA brush on the silicon surface. Although the RAFT agent included a nitrogen atom, we did not observe a nitrogen signal around 400 nm in the XPS survey scan because the average depth of an XPS measurement is approximately 5 nm. The high-resolution N1s spectra of the DEGMA polymer brush are given in Figure 6.13. DEGMA polymer brush thickness was determined using AFM analysis by evaluating step heights of the cross-sectional profile of the micro-patterned surface, and polymer brush thickness (*d*) was found as 52 ± 2 nm.

In XPS analysis, the C1s high resolution, which was shown in Figure 6.12d, could be deconvoluted into 3 Gaussians with the expected relative areas for three carbon atoms at 288.9, 286.5, and 285.0 eV C=O, C-O-C/C-S/ C-N, and C-C, respectively. As seen in Figure 5.12d, the C-O count in terms of CPS (count per second) is higher than that of C-C/C-H due to $–OCH_2CH_2O-$ units in DEGMA. In addition, the C-O signal and O-C=O signal at 288.9 eV is due to the presence of DEGMA.

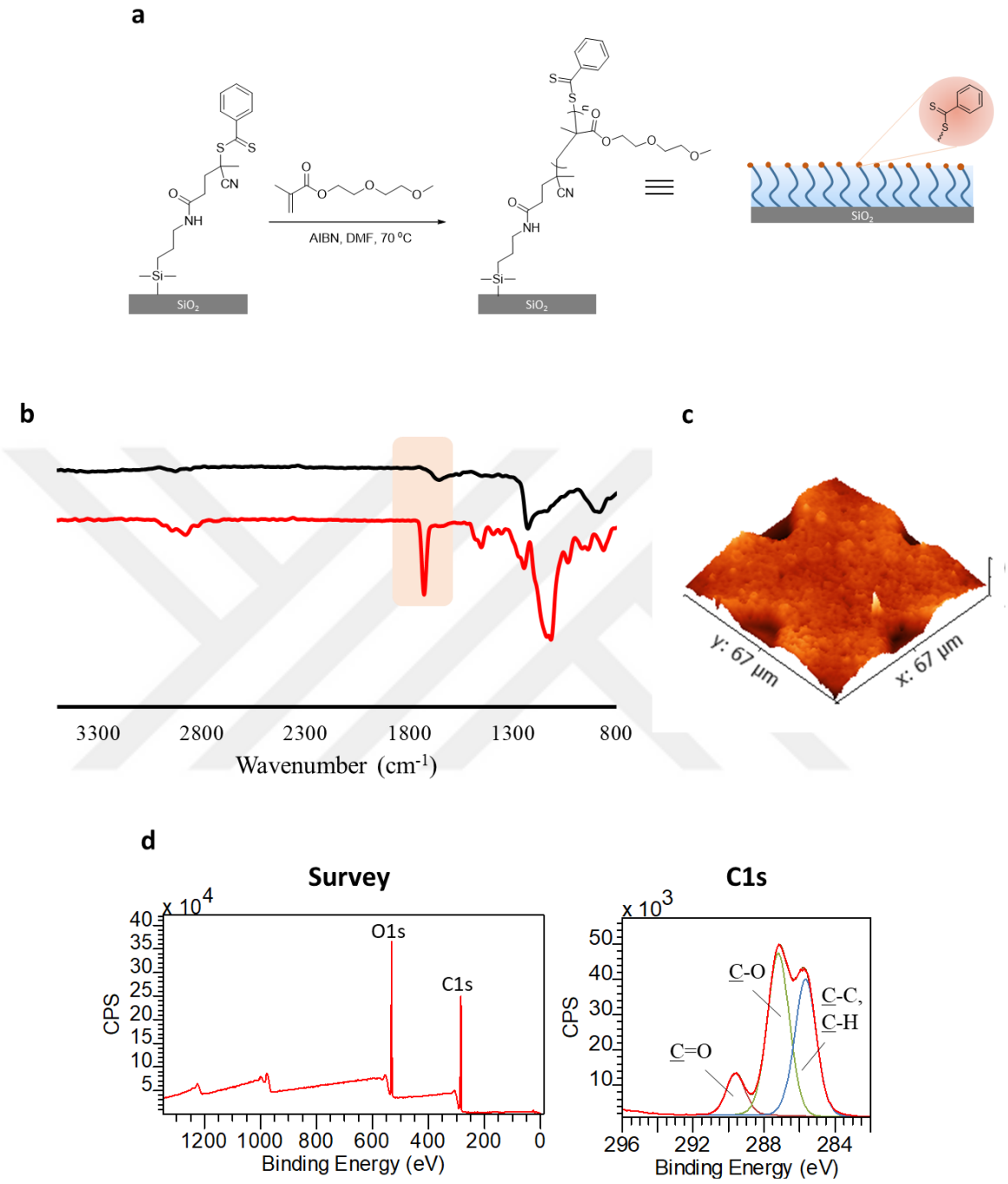

Figure 6.12. (a) Fabrication of DEGMA polymer brushes, (b) FTIR spectra of CTA-(black line) and polymer brush coated surface (red line), (c) AFM cross-section polymer brush, and (d) XPS analysis of polymer brush coated surface.

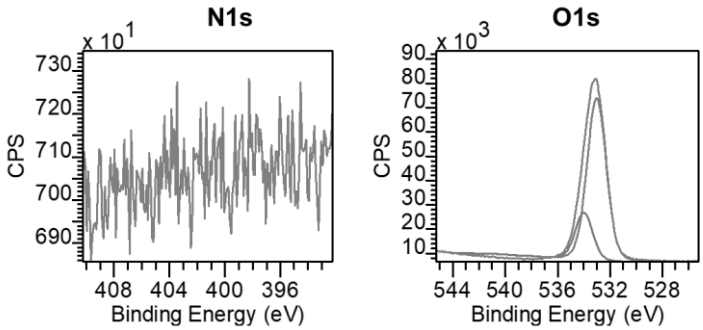

Figure 6.13. High-resolution N1s and O1s XPS spectra of DEGMA-containing brush.

The correlation of brush height with polymerization time indicated that the extent of polymerization could control the thickness of the polymeric coating. Thus, the time-dependent growth of the DEGMA polymer brush was demonstrated in Figure 6.14.

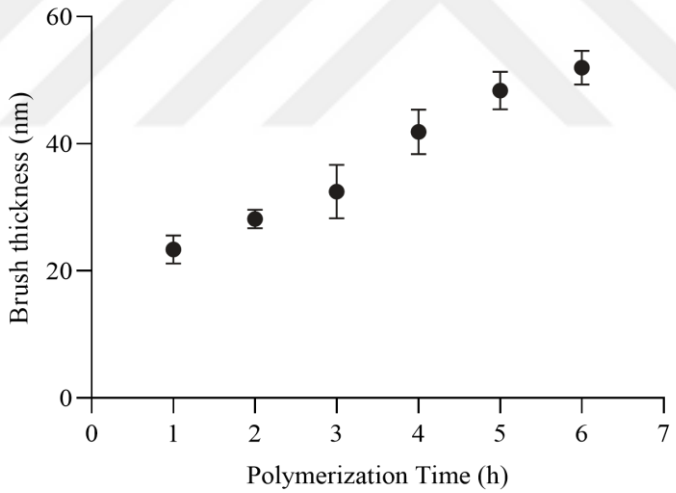

Figure 6.14. Time-dependent growth of DEGMA polymer brush as a line graph.

In addition to these characterization data, the grafting density (σ, chains/nm^2) of DEGMA polymer brush was calculated as 0.64 from AFM thickness (*h*, nm) and number-average molecular weight (M_n, g/mol) of free polymers in solution [319]. To determine the number-average molecular weight (M_n), surface RAFT polymerization was carried out in the presence of free CTA and the equimolar ratio of [AIBN]/[CTA]. After 6 h

polymerization, the M_n value was determined as 50 000 g/mol via SEC analysis (M_w/M_n = 1.60).

6.3.7. Installation of 'Clickable' Maleimide Functional Group at the Interface

The strategy of end-group functionalization with maleimide was outlined in Figure 6.15. First, to obtain the maleimide end group functionalized DEGMA polymer brush, the DEGMA polymer surface was treated with protected azobis-p-Mal at 70 °C for 24 h under N_2. During this time, the protected maleimide group (p-Mal) was conjugated to the end group of DEGMA brushes using a radical cross-coupling approach.

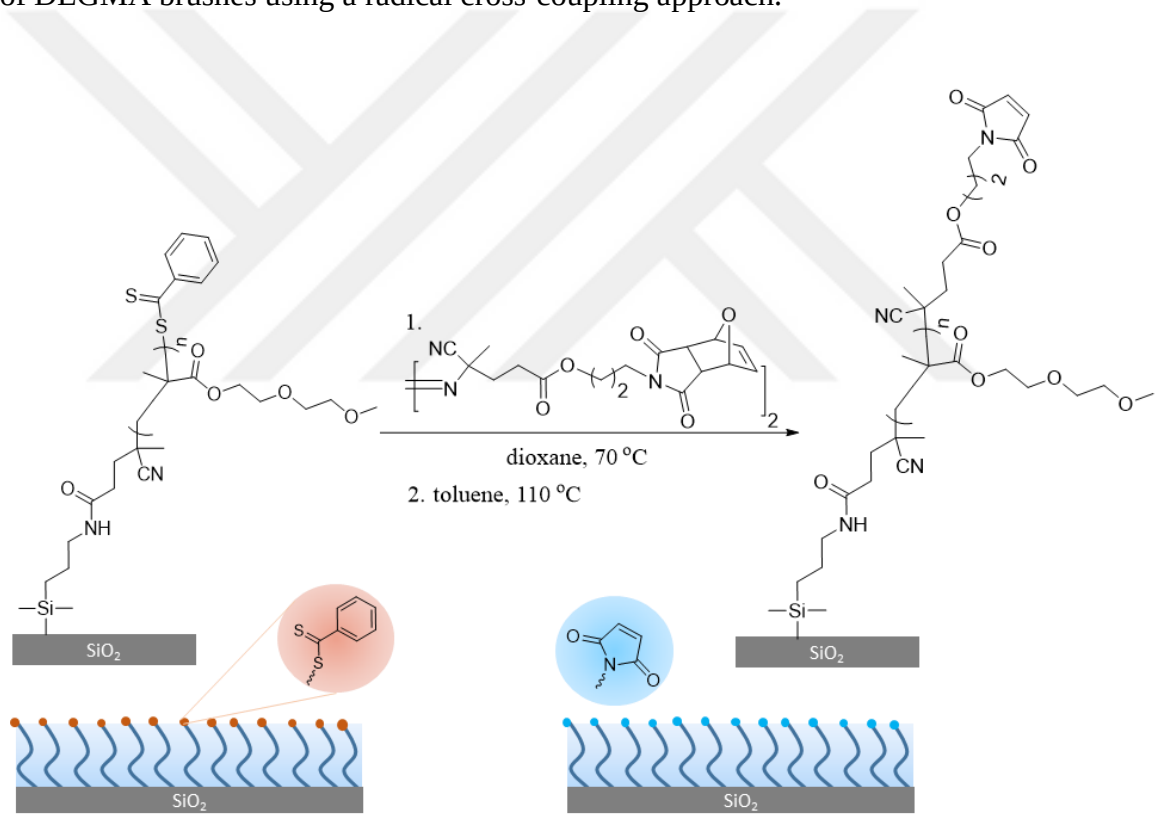

Figure 6.15. Fabrication of maleimide-terminated DEGMA polymer brush.

The successful end-group modification of brushes was confirmed using XPS and FTIR spectroscopy. The C1s high resolution, which was reported in Figure 6.16b, could be deconvoluted into 3 Gaussians with the expected relative areas for three carbon atoms at 288.5, 286.1, and 285.0 eV C=O, C-O-C, and C-C, respectively. The high-resolution O1s and N1 spectra were given in Figure 6.16c-d. The O1s high-resolution scan survey into 2

Gaussians at 533.5 and 532.5 eV for the O=C and C-O groups, respectively. The N1s high-resolution scan survey may be deconvoluted into one Gaussians at 400.0 eV due to the amide (O=C-N) group.

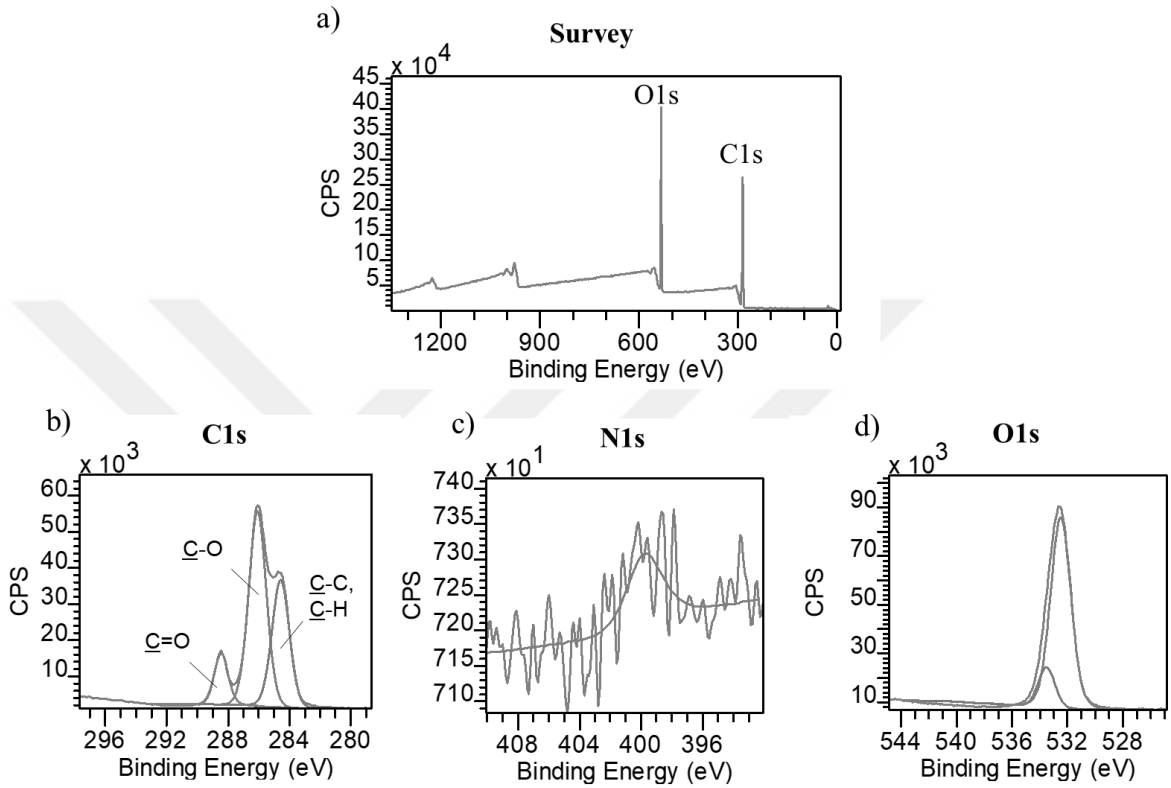

Figure 6.16. XPS survey and high-resolution C1s, O1s, and N1s spectra of protected maleimide functionalized DEGMA-containing brush.

Investigation of the FTIR spectrum of furan-protected maleimide terminated surface indicated a new carbonyl peak at 1698 cm^{-1} belonging to the masked maleimide group. Consequently, the FTIR spectrum showed two C=O and one C-O stretching vibrations at 1727 cm^{-1}, 1698 cm^{-1}, and 1110 cm^{-1}, respectively.

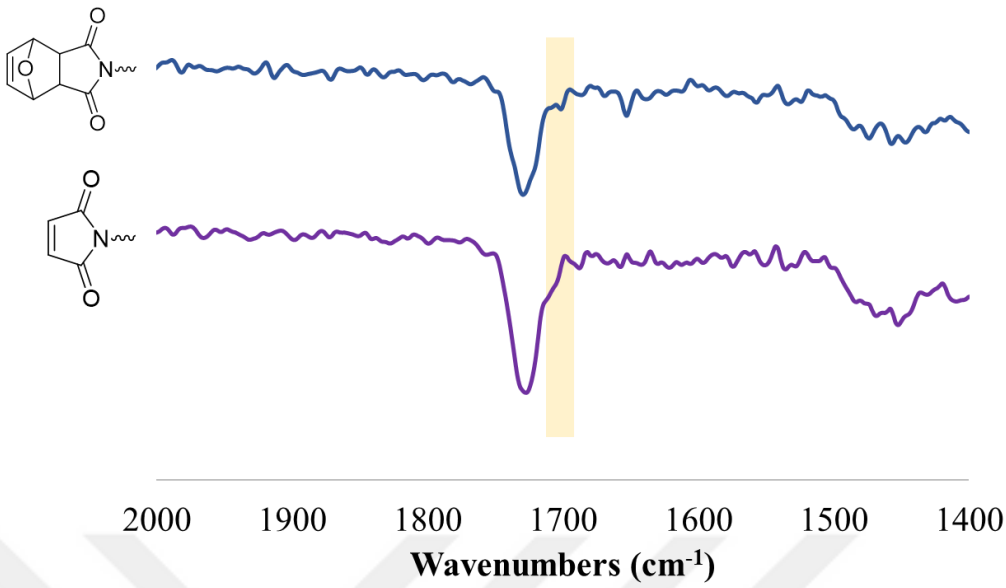

Figure 6.17. FTIR spectra of p-maleimide (dark blue line) and free maleimide (purple line) end group functionalized DEGMA polymer brushes.

In the next step, the polymer brushes were activated using the retro Diels-Alder reaction by removing the furan groups by heating the polymer brushes at 110 ^{o}C for four hours. The unmasking of the maleimide group was confirmed using XPS and FTIR spectroscopy. The C1s high resolution could be deconvoluted into 3 Gaussians with the expected relative areas for three carbon atoms at 288.8, 286.4, and 285.0 eV C=O, C-O-C, and C-C, respectively, and the C1s, N1s and O1s high-resolution spectra were given in Figure 6.18. The O1s high-resolution scan survey could be deconvoluted into 2 Gaussians at 533.6 and 532.6 eV due to O=C and C-O groups, respectively. The N1s high-resolution scan survey was fitted with a Gaussian at 399.7 eV due to the amide (O=C-N) group. Notably, the characteristic peak of the protected maleimide carbonyl group at 1700 cm^{-1} shifted to 1704 cm^{-1} after the deprotection of furan groups, similar to previous reports [161], and the IR spectrum was reported as the purple line in Figure 6.17. The thickness of the furan-protected maleimide-terminated polymer brush and the maleimide-terminated brush was 52 ± 2 nm using AFM, thus suggesting no detrimental effect of the thermal activation step on the polymer chains.

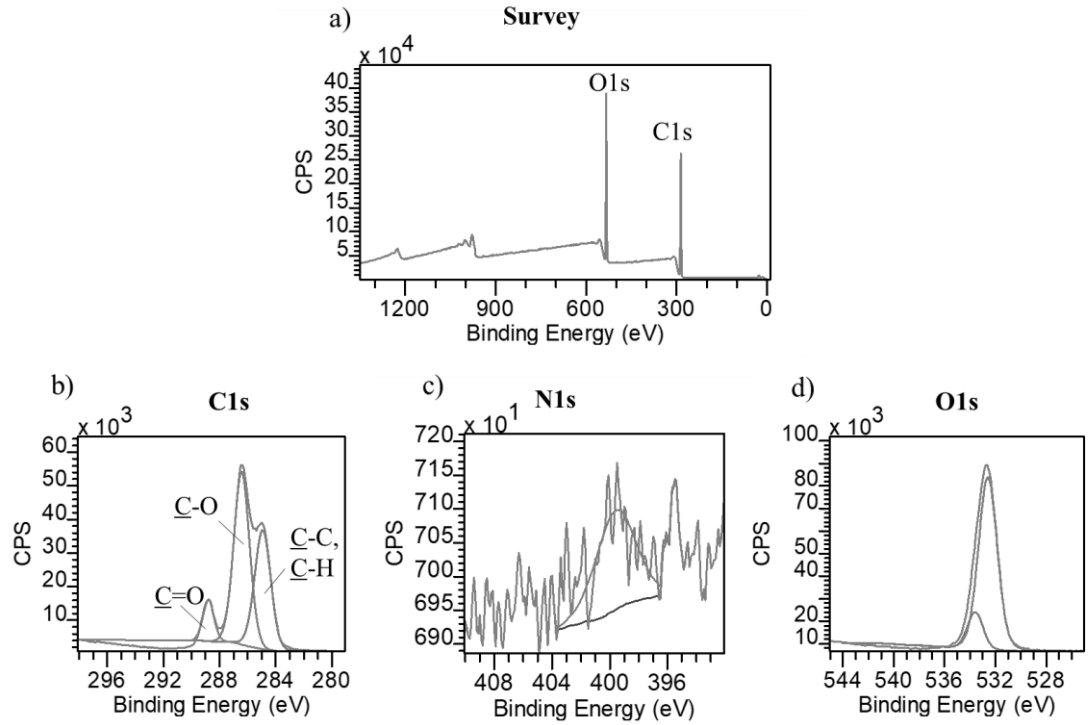

Figure 6.18. XPS survey and high-resolution C1s, N1s, and O1s spectra of maleimide functionalized DEGMA-containing brush.

6.3.8. Installation of 'Clickable' Alkene Functional Group at the Interface

A DEGMA-containing brush was functionalized with azobis-G0-ene under a nitrogen atmosphere for 24 h to obtain thiol-reactive inactivated alkene functional groups as end chains on polymer brushes. The fabrication of an alkene-containing DEGMA brush was shown in Figure 6.19.

The successful end-group modification of brushes was confirmed using XPS and FTIR spectroscopy. The high-resolution C1s, N1s, and O1s spectra of the alkene functionalized brush were demonstrated in Figure 5.20. The C1s XPS high-resolution could be deconvoluted into 3 Gaussians with the expected relative areas for three carbon atoms at 288.9, 286.5, and 285.0 eV C=O, C-O-C, and C-C, respectively. Likewise, the O1s high-resolution scan survey could be deconvoluted into expected Gaussians.

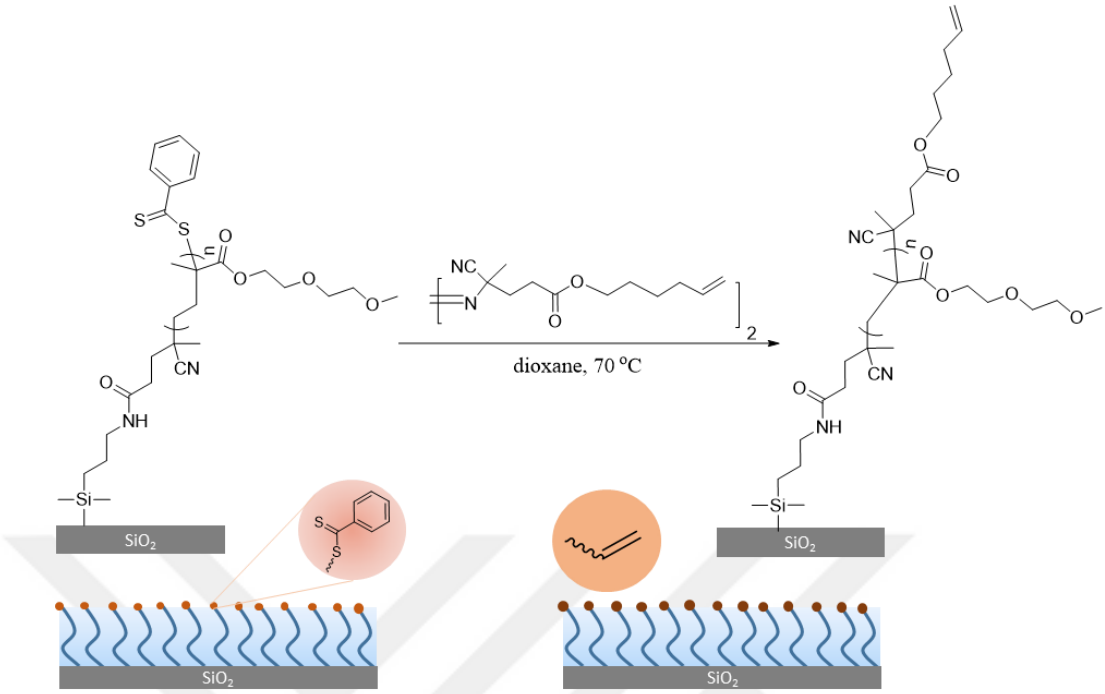

Figure 6.19. Fabrication of terminal alkene functionalized DEGMA-based polymer brush via radical cross-coupling reaction.

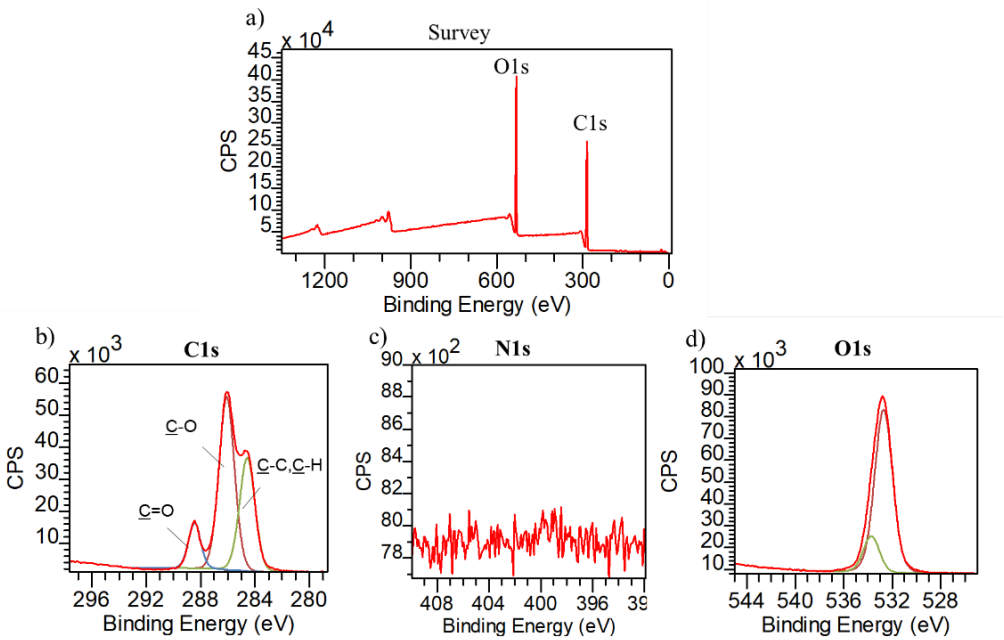

Figure 6.20. XPS survey and high-resolution C1s, N1s, and O1s, spectra of alkene (azobis-G0-ene) functionalized DEGMA-containing brush

Additionally, a comparison of the FTIR spectra of a pure azobis-G0-ene small molecule (mint green line) and azobis-G0-ene (alkene) functionalized DEGMA brush (purple line) indicated the presence of the C=C stretching on the polymer brush at 1642 cm^{-1}, which implied the successful installation of the alkene unit and FT-IR graph was shown in Figure 6.21.

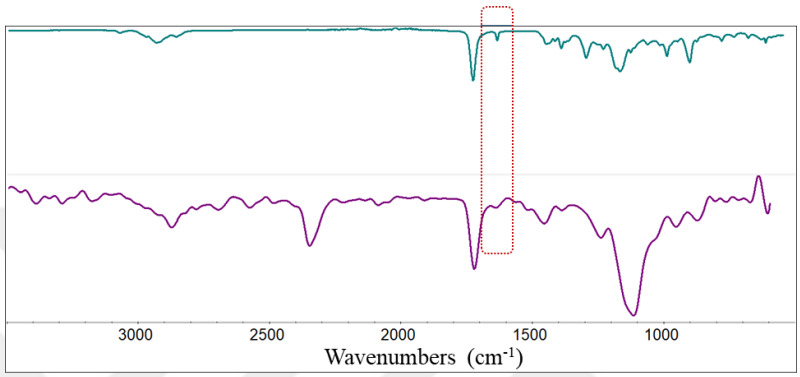

Figure 6.21. FTIR spectra of azobis-G0-ene (mint green line) and alkene (azobis-G0-ene) functionalized DEGMA-containing brush (purple line).

6.3.9. Functionalization of Maleimide-containing Brushes

The electron-deficient alkene group in the maleimide moiety is known to undergo efficient conjugate addition with thiol-containing nucleophiles under mild conditions. It has been extensively used to functionalize polymeric coatings [320]. The first post-polymerization modification of the maleimide terminated brush was undertaken using Michael addition of a thiol-containing fluorescent dye, namely, BODIPY-SH. Since the dye is hydrophobic, the polymer brush-coated surface was immersed in a solution of BODIPY-SH in THF. A furan-protected maleimide terminated polymer brush was used as a control surface and treated with BODIPY-SH under the same conditions. After rinsing off any physically adhering dye on the brushes using organic solvents, samples were examined using fluorescence microscopy. While the typical bright green fluorescence due to the BODIPY moiety was evident on the maleimide-containing brushes, thus suggesting successful conjugation, shown in Figure 6.22b, the masked maleimide group-containing brushes did not show any observable fluorescence, which was demonstrated in Figure 6.22b, inset.

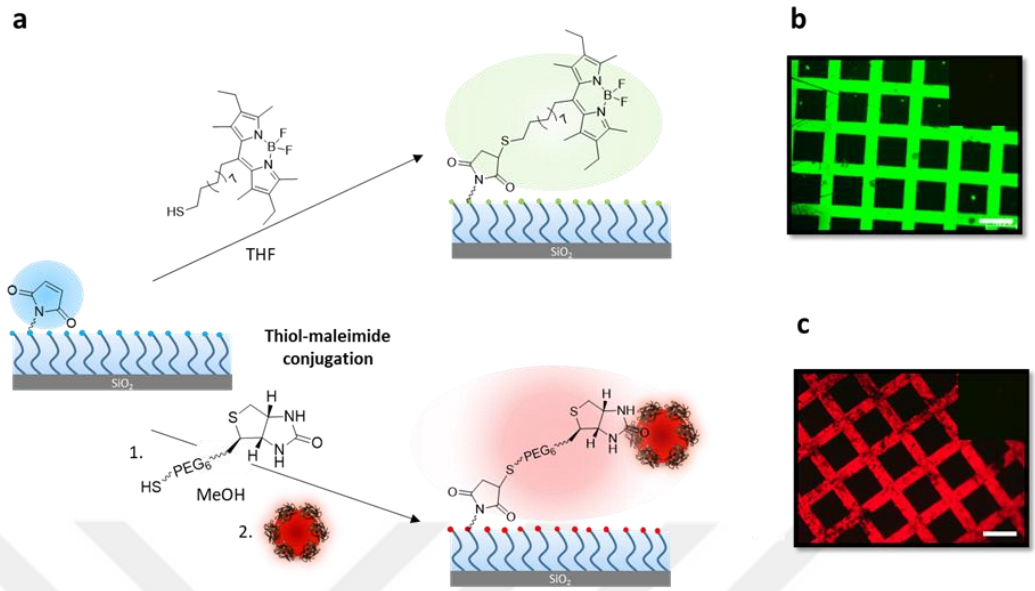

Figure 6.22. (a) Post-polymerization modification of maleimide-terminated DEGMA polymer brushes with BODIPY-SH and Biotin-SH/Streptavidin-coated Qdot nanoparticles; fluorescence image after modification with (b) BODIPY-SH, and (c) Biotin-SH/Streptavidin-coated Qdot nanoparticles (scale bar is 100 μm).

We then utilized the thiol-maleimide conjugation to install biotin, a bioactive ligand. The polymer brush was treated with biotinylated hexa(ethylene glycol)undecanethiol (Biotin-SH) in methanol. After rinsing off any unbound biotin, the biotinylated polymeric interface was incubated in a solution of streptavidin-coated quantum dots. As a control experiment, the thioester-terminated parent polymer brush, devoid of any maleimide groups, was also treated with a solution of biotin-thiol and streptavidin-coated CdSe nanoparticles under the same conditions. Upon analysis of thus treated surfaces with fluorescence microscopy, successful immobilization of streptavidin-coated nanoparticles was evident from the presence of red fluorescence, and the result was shown in Figure 6.22c. On the other hand, the polymer brush-coated surface in the control experiment did not show any noticeable fluorescence, thus suggesting specific immobilization was directed by the presence of the ligand. A fluorescence image of the control surface was given as an inset in Figure 6.22c.

6.3.10. Functionalization of Alkene-containing Brushes

The alkene functional group presenting polymer brushes is amenable to modification using the radical thiol-ene ‘click’ reaction. In this regard, a photochemical radical thiol-ene addition of a thiol-containing BODIPY dye was investigated. The polymer brush-coated surface was immersed in a solution containing the thiol-containing dye and DMPA as a photoinitiator, followed by exposure to UV irradiation. A thioester-terminated DEGMA-containing brush was utilized as a control reaction and treated with thiolated dye under similar conditions. After the functionalization, surfaces were washed with organic solvents to remove any unbound reagents, followed by their examination using fluorescence microscopy. The green fluorescence that was given in Figure 6.23b suggested successful conjugation of the thiol-containing dye to the alkene-containing brushes. As expected, the control surface with DEGMA-containing brushes did not display any significant fluorescence, shown as an inset in Figure 6.23b.

Like the previous surface functionalizations, the conjugation of biotin using thiol-ene chemistry was also examined. Alkene end group terminated brushes were conjugated with Biotin-SH in the presence of DMPA under UV light. As a control surface, thioester-terminated DEGMA-containing brushes were used and treated with Biotin-SH under the same condition. Thus, treated surfaces were washed with copious amounts of organic solvents to remove unbound biotin.

After that, the biotinylated and control polymer brushes were incubated in a solution of streptavidin-coated quantum dots. As seen in Figure 6.23c, the appearance of red fluorescence indicated the successful immobilization of streptavidin-coated nanoparticles onto the biotinylated polymer brushes. Moreover, there was no observable fluorescence on the thioester-terminated control polymer brushes, and a fluorescence image of the control surface was given as an inset in Figure 6.23c.

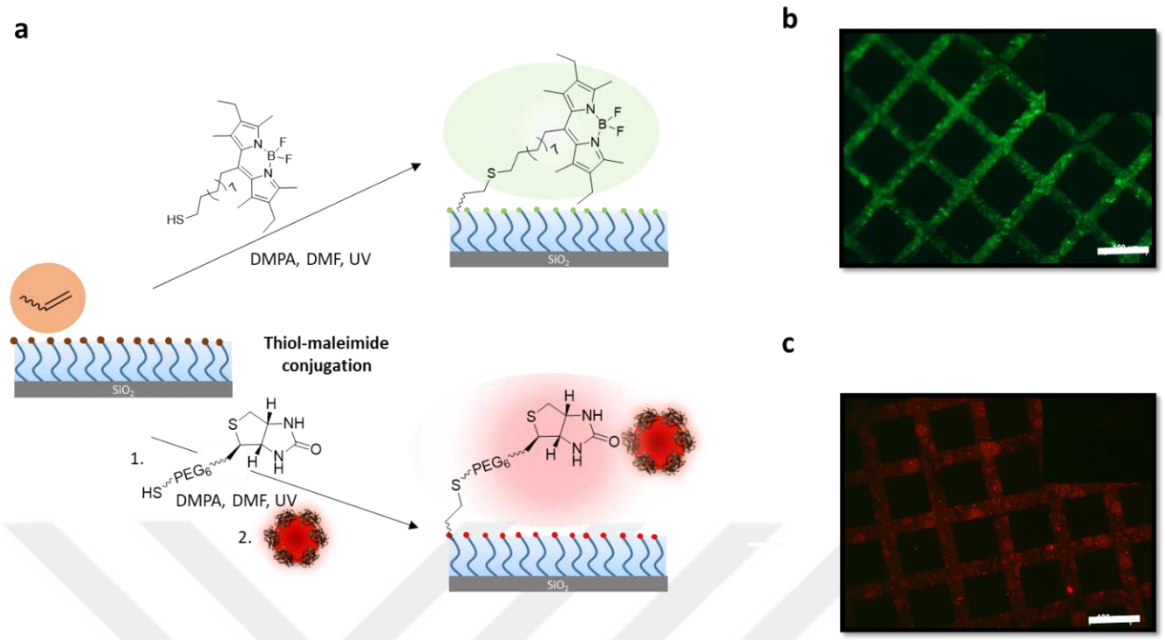

Figure 6.23. (a) Post-polymerization modification of alkene-terminated DEGMA polymer brushes with BODIPY-SH as well as Biotin-SH/Streptavidin-coated Qdot nanoparticles, (b) and (c) fluorescence images after modification with BODIPY-SH and Biotin-SH/Streptavidin-coated Qdot nanoparticles (scale bar is 100 µm).

6.3.11. Preparation and Characterization of Multivalent Dendron-based Brushes

After successfully installing and functionalizing the 'clickable' reactive groups at the interface, we envisioned that this approach could be utilized to install clusters of a functional group using dendritic azo-based chain end modifiers. To this end, we synthesized the azobis-G1-diene and azobis-G2-tetraene for utilization in post-polymerization modification and preparation, which is outlined in Figure 6.24. Using the protocol established for the DEGMA polymer surfaces with azobis-ene (G0), surfaces were modified with azobis-G1-diene. A fixed amount of AIBN was added during the modification of brushes with azobis-G1-diene and azobis-G2-tetraene to reduce functional group crowding at the interface. After modification of the interface, surfaces were characterized using FTIR and XPS spectroscopy. Expected carbonyl (at 1724 cm^{-1}) and alkene (at 1634 cm^{-1}) stretching bands were observed in the FTIR spectra, and the appearance of N-atoms (at ca. 400 eV) in XPS spectra indicated successful surface modification.

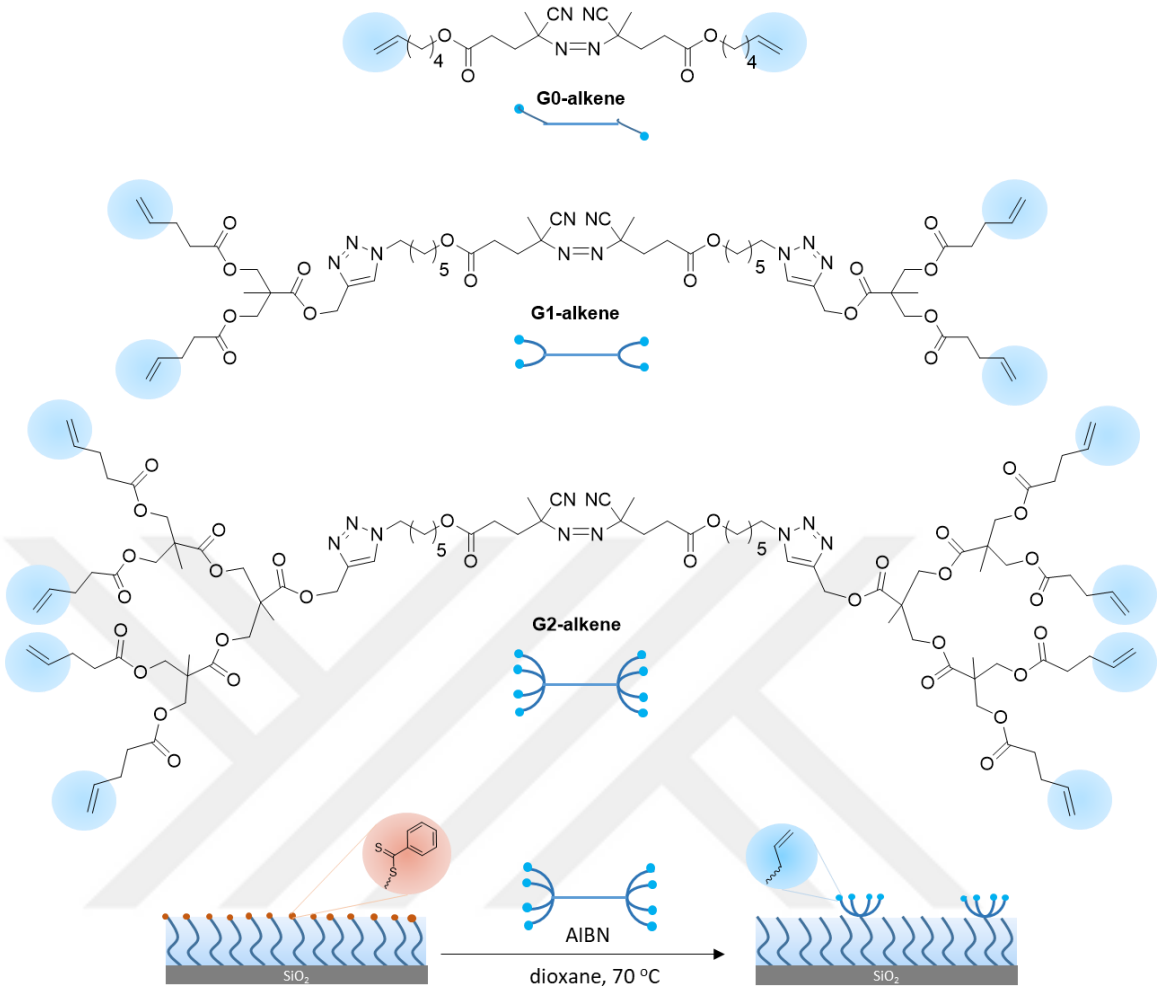

Figure 6.24. Structures of dendritic azo-chain terminators and representative surface modification using a G2-alkene-based dendron-grafted brush.

XPS data of the azobis-G0-ene functionalized brush were already given in Figure 6.20. The C1s XPS high-resolution in Figure 6.20b could be deconvoluted into 3 Gaussians with the expected relative areas for three carbon atoms at 288.9, 286.5, and 285.0 eV C=O, C-O-C, and C-C, respectively.

The XPS survey scan spectrum of azobis-G1-diene modified DEGMA brush was composed of C1s and O1s peaks, as shown in Figure 6.25a. C1s high-resolution spectrum and its deconvolution result are given in Figure 6.25b. C1s high-resolution spectra belonging to azobis-G1-diene modified DEGMA brush could be deconvoluted into 3 Gaussians at 288.5 (C=O), 286.1 (C-O-C), and 285 eV (C-C). Although the survey scan spectrum did not

include an N1s peak around 400 eV, a small peak was observed at 400 eV, which belongs to nitrogen atoms, when the high-resolution N1s spectrum was investigated in Figure 6.25c.

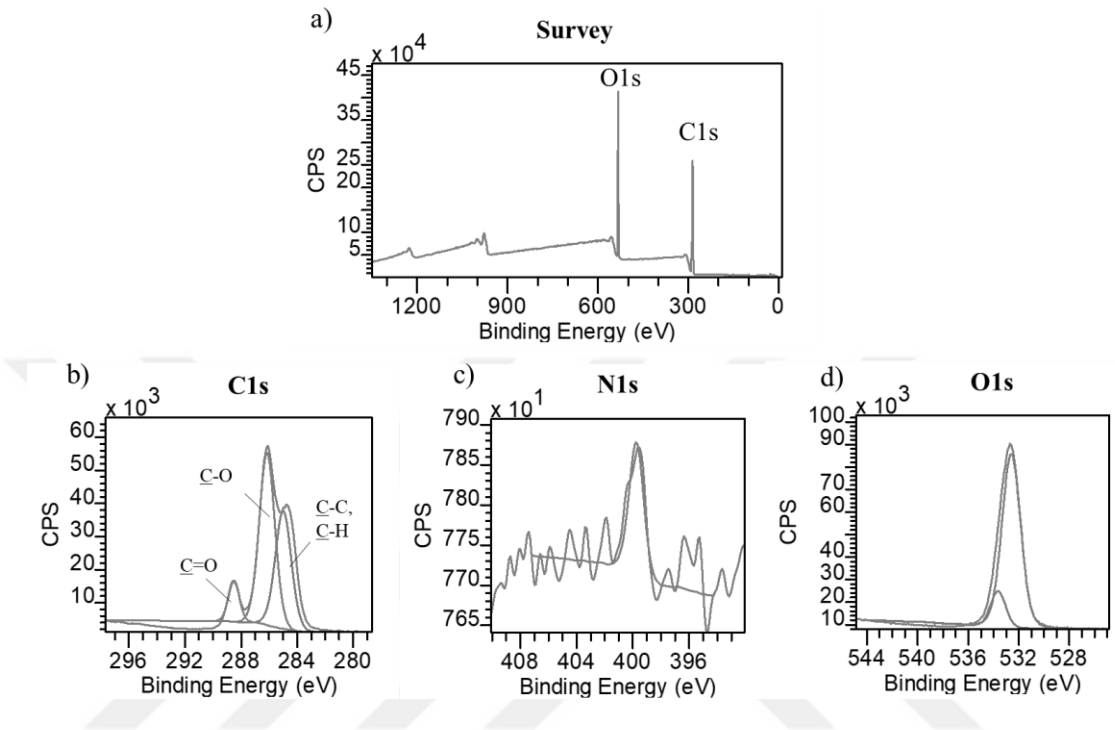

Figure 6.25. XPS survey and high-resolution C1s, O1s, and N1s spectra of G1-diene functionalized DEGMA-containing brush.

XPS analysis of Azobis-G1-diene/AIBN modified DEGMA brush is similar to that of azobis-G1-diene incorporated DEGMA brush. These two brushes are similar to each other in terms of preparation. The use of AIBN is the only difference between them. As mentioned before, AIBN was used to decrease steric hindrance between polymer chains. Therefore, similar XPS results were expected. C1s high-resolution spectra, which were shown in Figure 6.26b, belonging to azobis-G1-diene/AIBN modified DEGMA brush could be deconvoluted into 3 Gaussians at 288.9 (C=O), 286.5 (C-O-C) and 285 eV (C-C). When the N1s high-resolution spectrum in Figure 6.26c was investigated, a small N1s peak was observed at 400 eV due to the triazole ring in the dendron structure.

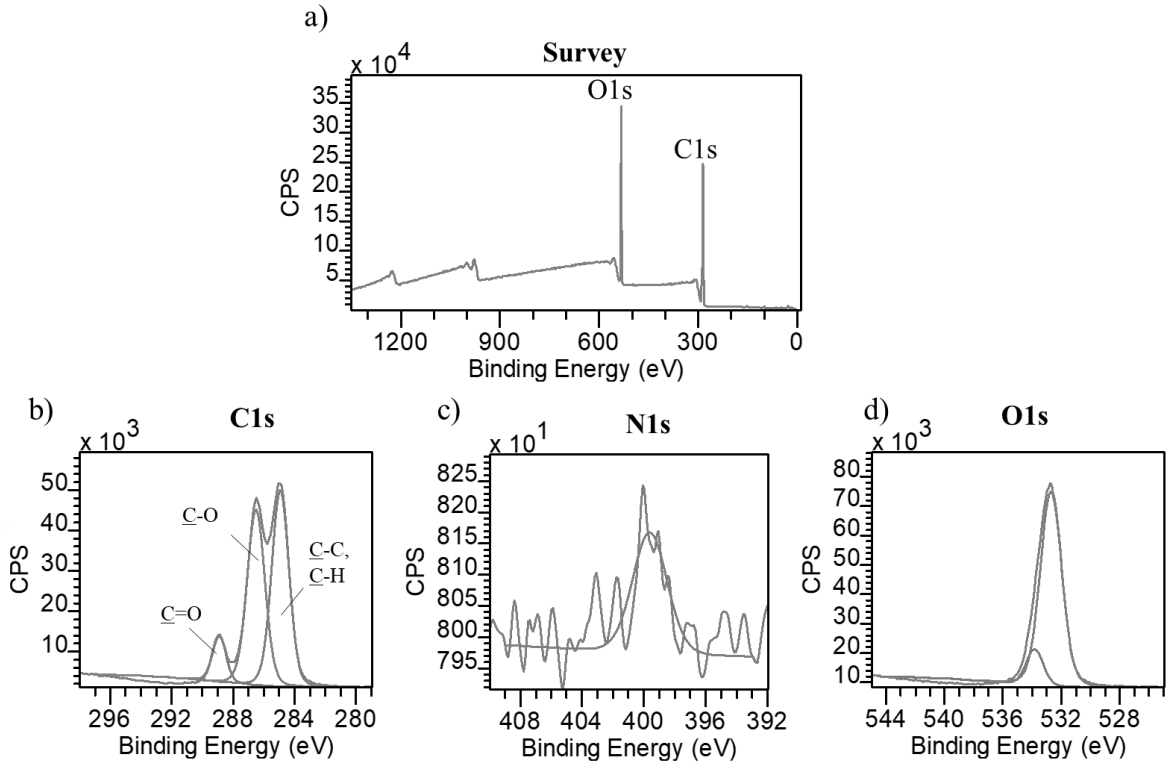

Figure 6.26. XPS survey and high-resolution C1s, O1s, and N1s spectra of G1-diene/AIBN functionalized DEGMA-containing brush.

XPS survey scan of azobis-G2-tetraene modified DEGMA brush includes C1s and O1s peak at 285.0 eV and 532.9 eV, respectively. High-resolution C1s elemental scan spectrum included 3 Gaussians at 288.9, 286.5, and 285 eV for C=O, C-O-C, and C-C, respectively. Also, when the high-resolution C1s spectrum was analyzed, it was an observation that the peak intensity of the C-O-C group was higher than that of C-C due to C-O bonds in the G2 group. In addition to C1s, the nitrogen signal around 400 eV in Figure 6.27c showed successful G2-tetraene conjugation to the DEGMA polymer brush.

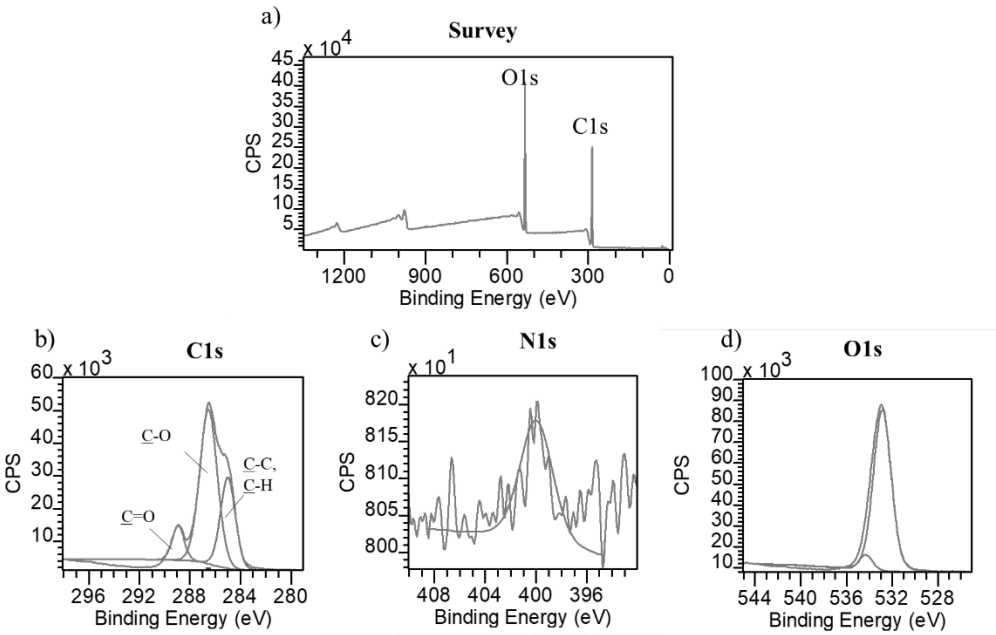

Figure 6.27. XPS survey and high-resolution C1s, O1s, and N1s spectra of G2-tetraene/AIBN functionalized DEGMA-containing brush.

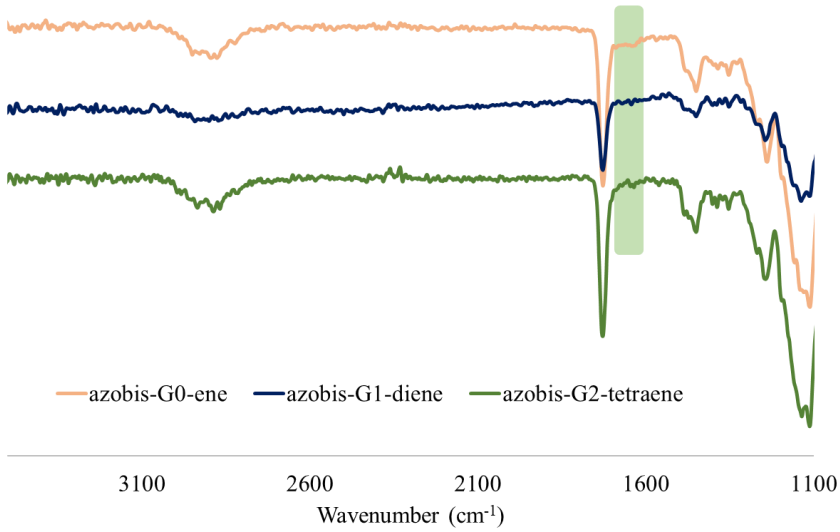

Figure 6.28. FT-IR spectra of azobis-G0-ene functionalized DEGMA brushes (peach line), azobis-G1-diene functionalized DEGMA brushes (navy blue line), and azobis-G2-tetraene functionalized DEGMA brushes (green line).

6.3.12. Functionalization of Dendron Conjugated Brushes with Mannose-SH via Thiol-Ene "*Click*" Chemistry

Mannose-thiol (mannose-SH) was conjugated with an alkene-bearing dendron grafted DEGMA brush via a thiol-ene click reaction in the presence of DMPA under UV light. After the reaction, surfaces were characterized with XPS spectroscopy. After modification of the G0-alkene interface, in the high-resolution XPS, the C1s peak could be deconvoluted into 4 Gaussians with the expected relative areas for three carbon atoms at 288.8, 286.4 and 285.0 eV C=O, C-O-C, and C-C, respectively along with the anomeric carbon O-C-O peak at 287.8 eV of the mannose moiety and high-resolution C1s spectra was demonstrated in Figure 6.29b.

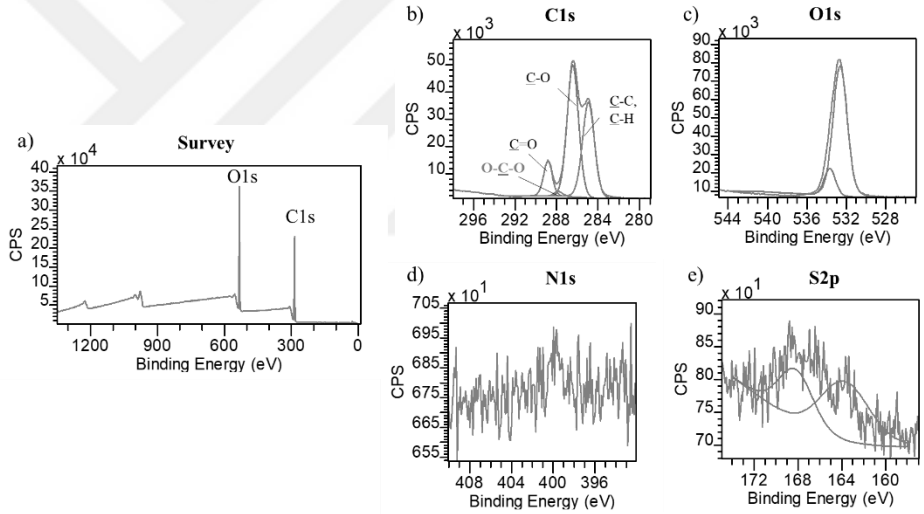

Figure 6.29. XPS survey and high-resolution C1s, O1s, N1s, and S2p, spectra of mannose-SH functionalized G0 (azobis-ene)-containing brush.

XPS result of the mannose functionalized G1-containing polymer brush was similar to that of the mannose functionalized G0-functionalized brush, given in Figure 6.30. For mannose bearing G1 modified DEGMA brush, the C1s high resolution could be deconvoluted into 4 Gaussians with the expected relative areas for three carbon atoms at 288.8, 286.4, and 285.0 eV C=O, C-O-C, and C-C, respectively. Anomeric carbon O-C-O peak was revealed at 287.6 eV due to mannose functionalization. In addition, mannose-SH functionalized G1-diene/AIBN containing brush showed similar XPS results in Figure 6.31.

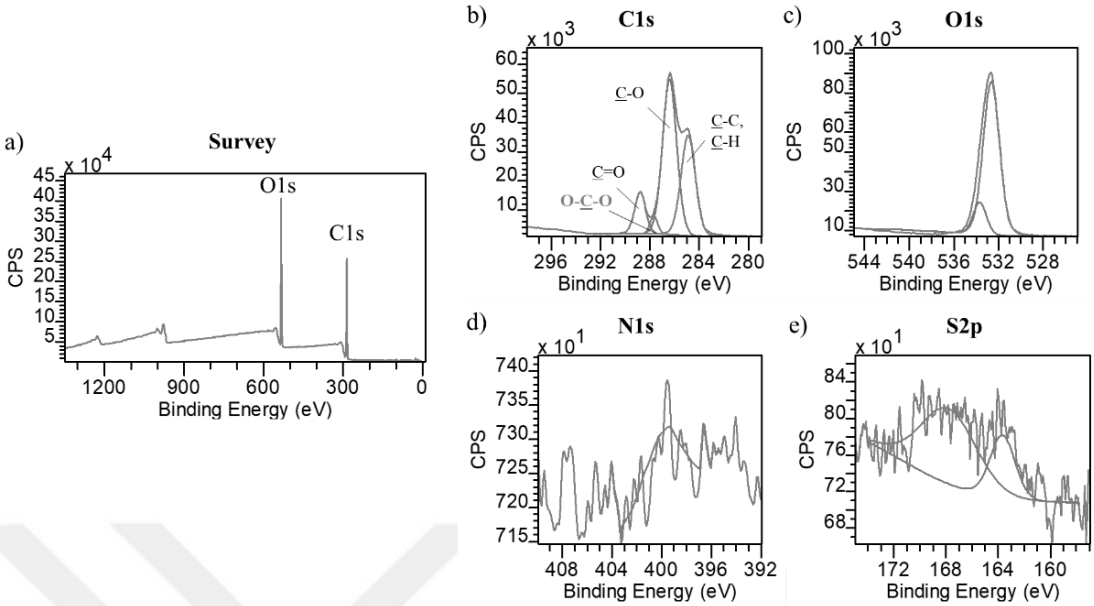

Figure 6.30. XPS survey and high-resolution C1s, O1s, N1s, and S2p, spectra of mannose-SH functionalized G1-containing brush.

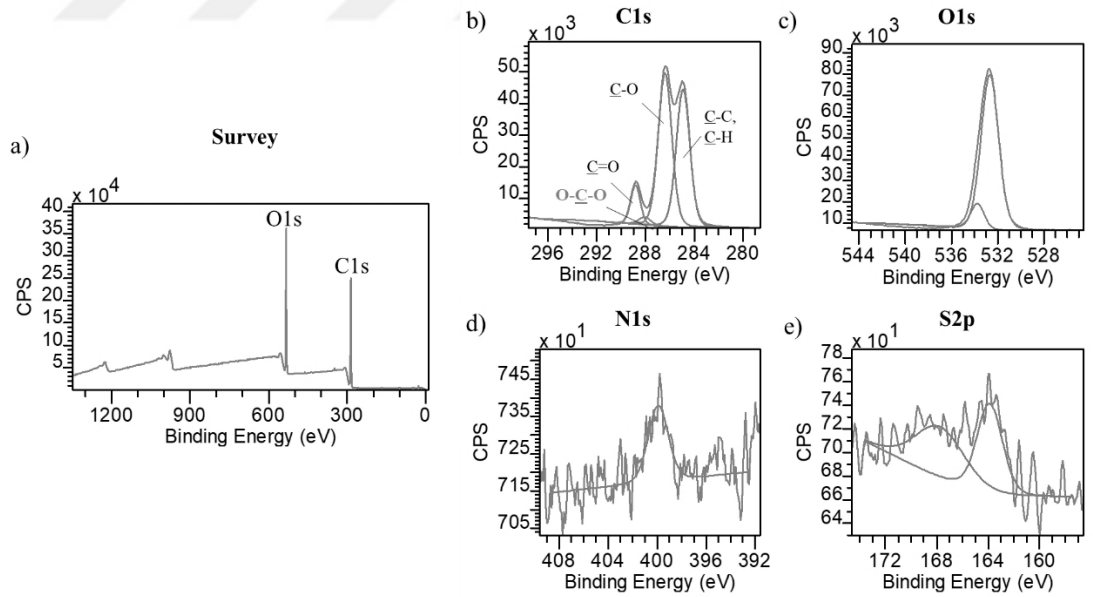

Figure 6.31. XPS survey and high-resolution C1s, O1s, N1s, and S2p, spectra of mannose-SH functionalized G1/AIBN-containing brush.

The C1s high resolution of mannose bearing G2/AIBN modified DEGMA brush that was given in Figure 6.32 could be deconvoluted into 4 Gaussians with the expected relative areas for three carbon atoms at 288.9, 286.5, and 285.0 eV C=O, C-O-C, and C-C, respectively. Anomeric carbon O-C-O peak was revealed at 287.8 eV due to mannose functionalization.

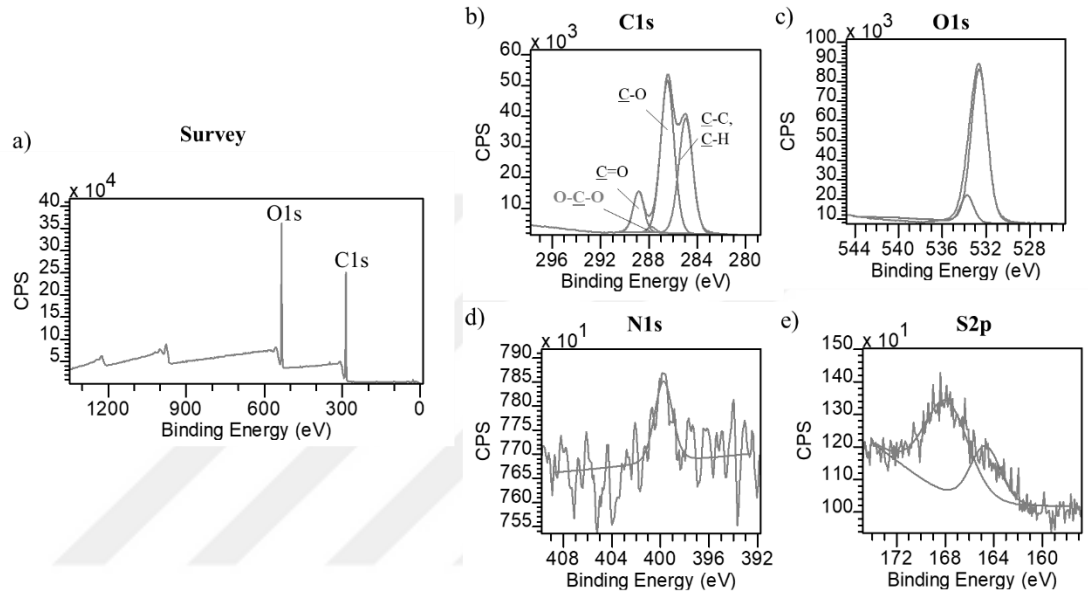

Figure 6.32. XPS survey and high-resolution C1s, O1s, N1s, and S2p, spectra of mannose-SH functionalized G2/AIBN-containing brush.

6.3.13. Immobilization of Concanavalin A on Dendron Functionalized Polymer Brushes

Mannose-functionalized surfaces were treated with the Texas Red conjugated ConA protein solution in PBS buffer (pH 7.4, $Mn^{2+,}$ and Ca^{2+}-containing buffer). The surface was characterized with fluorescence microscopy after rinsing with copious amounts of water to remove any unbound protein. While there was no significant attachment of ConA on surfaces devoid of the mannose group, there was almost no protein immobilization on the interface where single mannose units were installed. This is in contrast to the successful immobilization of streptavidin as demonstrated earlier, but not surprising considering the relatively poor binding of the mannose-ConA couple as compared to the biotin-streptavidin couple (K_d = 2.89 x 10^{-6} M and 1 x 10^{-14} M, respectively) [321,322]. Although the

fluorescence microscopy analysis showed that for the surface obtained using mannose modification of the G1-alkene, a slightly higher amount of ConA binding took place, it did not appear to be effective. To understand if the crowding of functional groups leads to this lack of enhanced protein binding, we decided to dilute the mannose clusters by adding AIBN during the attachment of the alkene units. As seen in Figure 6.33, to our surprise, the diluted mannose-conjugated dendritic surfaces performed significantly better. There was a considerably higher amount of protein immobilization on the G1-ene/AIBN-modified surface compared to the surface modified with G1-ene alone. These experiments demonstrate that the presentation of the protein-binding ligands in a dendritic fashion, without overcrowding, can significantly improve ligand-directed protein immobilization and detection.

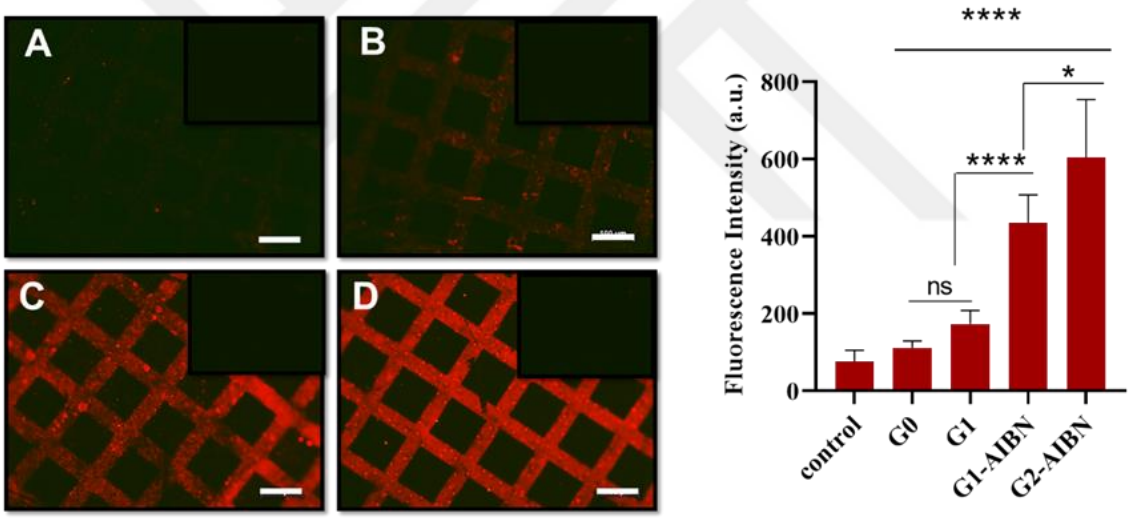

Figure 6.33. Immobilization of mannose-terminated brushes with *Con A*. (a) Fluorescent image of DEGMA@G0ene-mannose brush (d=51 ± 3 nm); (b), (c) and (d) Fluorescent images of DEGMA@G1diene-mannose brush (d =55 ± 2 nm), DEGMA@G1diene/AIBN-mannose brush (d=55 ± 2 nm) and DEGMA@G2tetraene/AIBN-mannose brush (d=56 ± 2 nm) after ConA binding (scale bar is 100 μm).

Additionally, the specific ligand-directed attachment of the protein ConA was also probed using SPR analysis. It is well known that the carbohydrate recognition site of ConA is specific for mannose and glucose. Also, no interaction with other proteins, such as BSA, is anticipated due to the underlying PEG-based matrix. Hence, we compared the difference

in the interaction between ConA and BSA proteins to a mannose-decorated SPR chip. A FITC-ConA aqueous buffer solution (20 mM HEPES, 1.0 mM $MnCI_2$, 1.0 mM $CaCI_2$, 0.15 M NaCl, adjusted to pH 7.4) was injected three times with a continuous flow over the polymer brush-coated SPR chip. The same protocol was used to access the mannose-conjugated brush-coated SPR chip surface interaction with BSA. As seen in Figure 6.34a, while FITC-ConA binds to the mannose-conjugated G2-based polymer brushes on the chip surface, BSA does not show any binding to the mannose-modified surface. This observation is in accordance with earlier observations for similar SPR studies in the literature [323]. Also, a green fluorescence, which was reported in Figure 6.34b, was observed upon inspection of the FITC-ConA treated mannose-coated SPR chip using fluorescence microscopy.

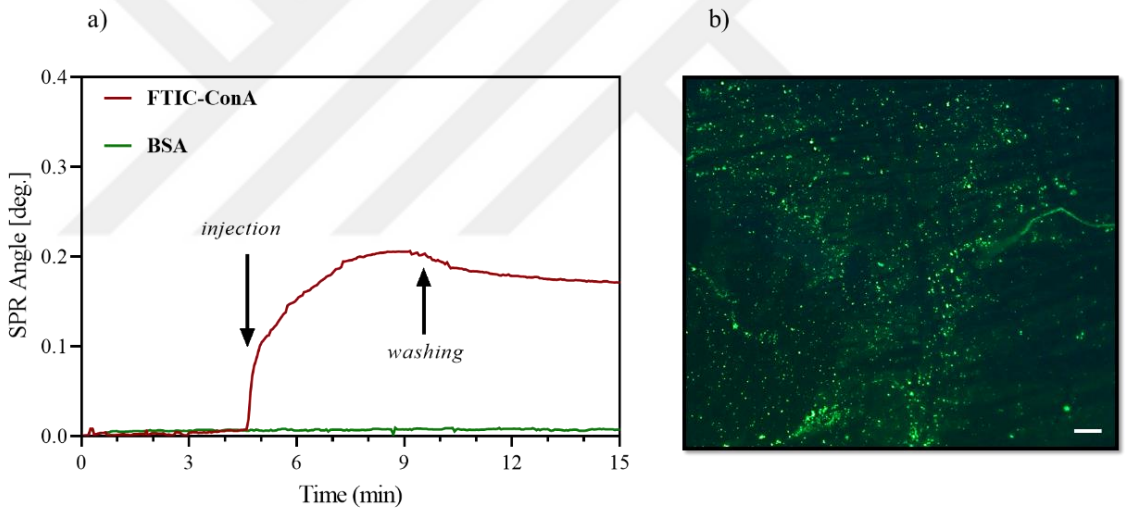

Figure 6.34. (a) Surface plasmon resonance (SPR) binding analysis indicating the interaction between mannose-bearing G2 polymer brushes with the two different proteins (FITC-ConA and BSA), and (b) fluorescence microscope image of SPR sensor chip after binding of FITC-ConA. (Scale bar is 100 μm).

6.4. Conclusions

This chapter reported discloses a versatile approach for obtaining a variety of functionalizable polymer brush interfaces that can be readily conjugated with various small molecules and ligands, using different '*click*' reactions. Notably, the approach preserves the underlying polymer brush matrix while only tailoring the surface, thus affording a library of surfaces that only vary in their surface functionalities. The radical cross-coupling exchange reaction with appropriately functionalized azo-containing reactive molecules is employed to install maleimide and terminal-alkene groups on the brush surface. The maleimide and terminal alkene groups allow conjugation through thiol-maleimide and radical thiol-ene chemistry. Successful attachment of fluorescent dye, as well as biotin ligands are undertaken. The latter also allows ligand-based immobilization/detection of the FITC-labelled protein Streptavidin.

Additionally, we demonstrate that biotin can also be used to direct the immobilization of nanostructures such as Streptavidin-coated quantum dots. The versatility of this approach is shown finally through the immobilization of dendritic functional group motifs at the interface. Alkene-terminated dendrons of two generations are conjugated at the interface using the azo-exchange reaction. Functionalization of these with mannose-thiol shows the enhanced effectiveness of dendritic interfaces toward target protein recognition. We envision that the facile and versatile approach outlined here will be of interest in functional engineering interfaces for various biomedical applications.

7. PYRIDYL-DISULFIDE CONTAINING REDOX-RESPONSIVE THIOL-REACTIVE POLYMER BRUSHES

7.1. Introduction

Over the past decades, polymeric surfaces with the reactive functional group have gained a lot of interest due to their usage in biomedical applications and material science. Among various methods for the preparation of the polymeric thin film, the utilization of polymer brushes has gradually increased in recent years [324]. Polymer brushes can be surface-confined macromolecules where polymer chains are covalently tethered to the surface [131]. Polymer brushes have applications in the biomedical area, such as bio-sensing, analyte detection, biomolecule immobilization, bioseparation, drug delivery, interfaces for cell attachment and growth, and antibacterial surfaces [325-327].

Polymer brushes can be fabricated via “grafting-to” and “grafting-from”. The grafting- to method requires polymer synthesis, and subsequently, the synthesized surface reactive polymer is tethered to a surface. Due to steric hindrance between polymer chains, thin polymer brushes are obtained with low grafting density [135]. The grafting to method first involves preparing surface coating with an initiator. Because the surface is coated with a surface-attachable initiator, polymerization occurs on the surface. When the initiator coating step becomes efficient, thick polymer brushes are obtained with high grafting density [136]. Therefore, polymer brush thickness and grafting density are tunable for desired applications.

Functional polymer brushes can be prepared in two ways: direct surface-initiated controlled radical polymerization (SI-CRP) using functional monomer and post-polymerization modification of brushes with reactive groups. Among these techniques, direct surface-initiated polymerization with functional monomers can often be used to fabricate functional polymer brushes. On the other hand, a wide range of functional groups are suitable for direct surface-initiated polymerization. Many functional monomers can not

be polymerized using SI-CRP because they can interfere with radical species during polymerization [156]. Consequently, post-polymerization techniques have become prominent in obtaining functional polymer brushes with desired side chain functional groups. Post-polymerization modification of reactive polymer brushes offers an alternative strategy to obtain polymer brushes with desired functional groups that are not suitable for direct-SI-CRP. To date, azide [328], alkene [329], alkyne [159], NHS-activated ester [160], epoxide [330], and maleimide [156,161] functionalized polymer brushes using post-polymerization modification techniques have been demonstrated.

Immobilizing biomolecules to the solid surface via their thiol groups is one of the most widely used approaches to provide bioconjugation. Surfaces that include the maleimide functional group are widely used to immobilize thiol-bearing small molecules and biomolecules. Sanyal and coworkers reported many examples of maleimide-containing polymeric surfaces conjugating thiol-bearing molecules [156], [161]. As an alternative thiol-reactive group, utilization of the pyridyl disulfide (PDS) group has gradually increased in recent years to provide the conjugation of thiolated molecules. In contrast to thiol-maleimide conjugation, the PDS-thiol exchange reaction is reversible; therefore, this exchange reaction has been exploited from reversible conjugation of biomolecules to the fabrication of redox-responsive materials [225]. To date, PDS-containing redox-responsive polymeric materials such as nanogels [59], micelles [331], and hydrogels [332] have been reported. On the other hand, the fabrication of PDS functionalized redox-responsive polymer coating has been much less explored. As an alternative, Sanyal and coworkers reported the fabrication PDS group containing micropatterned hydrogel on a silicon oxide surface for biomedical applications. They synthesized thiol-reactive hydrogel on a silicon surface using PDSMA and PEGMEMA monomers in the presence of PEGDMA crosslinkers via free radical photo-crosslinking. They showed that PDS-containing hydrogel could be functionalized with cell adhesive thiol-bearing RGD peptide to provide cell attachment [333]. In another example, Pich and coworkers reported preparing a PDS group functionalized polymeric film on a silica surface. They demonstrated synthesis details of a series of reactive copolymers based on N-vinyl lactams and pyridyl disulfide ethyl methacrylate by RAFT polymerization. After synthesis, they prepared a biocompatible thin polymer film on a silica surface using a thiol-reactive PDS functionalized copolymer. They then showed a successful thiol-disulfide exchange reaction using some thiol-containing

molecules [163]. In another example, Iwasaki and coworkers prepared polymer brushes on silicon surfaces to immobilize antibody fragments. They synthesized polymer brushes composed of 2-methacryloyloxyethyl phosphorylcholine (MPC) and glycidyl methacrylate (GMA) via surface-initiated atom transfer radical polymerization (ATRP). After obtaining polymer brushes, they introduced the PDS group into polymer brushes via epoxy groups in GMA units. They showed the immobilization of antibody fragments onto PDS-functionalized polymer brushes via a thiol-disulfide exchange reaction [334].

In this chapter of the thesis, pendant pyridyl disulfide (PDS) bearing reactive polymer brushes that are modifiable with thiol-containing molecules are demonstrated in Figure 7.1. A pyridyl disulfide methacrylate (PDSM) monomer was copolymerized with hydrophilic DEGMA monomers via SI-RAFT polymerization. Although PDS-bearing thin films on the solid substrate were reported, there is no example of PDS-containing polymer brushes fabricated using surface-initiated RAFT polymerization. Direct polymerization of PDS monomer would be easier and more homogenous on a solid substrate than the post-polymerization functionalization method. In this study, the density of reactive PDS units on the polymer brushes was tunable by changing the monomer ratios. PDS-grafted polymer brushes with different PDS ratios were characterized with XPS spectroscopy. The functionalization of polymer brushes using a pyridyl-disulfide exchange reaction with a fluorescent dye and various biomolecules was demonstrated.

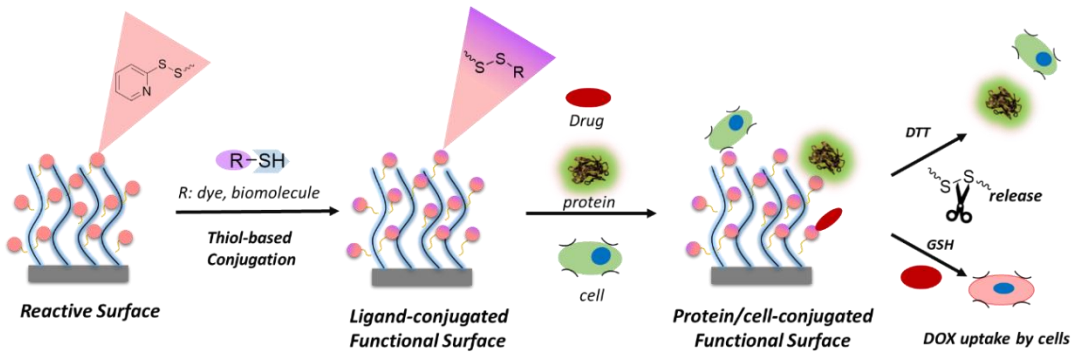

Figure 7.1. Fabrication and functionalization of PDS-based thiol-reactive polymer brushes.

7.2. Experimental

7.2.1. Materials

Di(ethylene glycol) methyl ether methacrylate (DEGMEMA) was obtained from Sigma-Aldrich and filtered through the basic aluminum oxide to get rid of the inhibitor before use. AIBN was purchased from Sigma Aldrich and was used after recrystallization from methanol. 2-Mercaptoethanol was purchased from Merck. 2,2'-Dipyridyl disulfide was obtained from IS Chemical. The linear arginine-glycine-aspartate-cysteine (RGDC) peptide, 4′,6-diamidino-2-phenylindole (DAPI), 4-trifluoromethylbenzyl mercaptan (TFBM), tetramethylrhodamine-5-maleimide (TAMRA) were obtained from Sigma Aldrich. Alexa Fluor 488 Phalloidin was obtained from Invitrogen. Live-dead assay kit consisting of calcein-AM (live) and propidium iodide (dead) was purchased from Sigma Aldrich. FITC-ConcanavalinA and Rhodamine-PNA were purchased from Molecular Probes and Vector. Pyridiyl disulfide alcohol (PDS-OH) [163], pyridyl disulfide methacrylate (PDSMA) monomer [163], and thiol-containing mannose [316,317] were synthesized following previously described procedures. Thiol-bearing BODIPY dye (BODIPY-SH) and DOX-SH were synthesized using published methods [335,336]. Surface attachable RAFT agent and RAFT agent-coated silicon surfaces (Si-RAFT-CTA) were prepared according to a literature procedure [156].

7.2.2. Methods

^{1}H NMR spectrum of PDSMA monomer was recorded in $CDCl_3$ on Bruker Avance Ultrashield 400 (400 MHz). Surface characterization was done using X-ray photoelectron spectroscopy (XPS) (K-Alpha, Thermo Scientific). Nicolet 380 (Thermo Fisher Scientific, Inc.) instrument equipped with a Harrick Scientific GATR accessory and a Ge crystal was used for FTIR analysis. The thickness of the polymer brush was measured using AFM, obtained from Nanosurf. Fluorescence microscopy was performed using LD-A-Plan 10x/0.30 objective in Zeiss Axio Observer inverted microscope (ZEISS Fluorescence Microscopy, Carl Zeiss Canada Ltd., Canada).

7.2.3. Fabrication of Polymer Brush P1 (100/0) (Homopolymer Brush)

DEGMA (686 mg, 3.65 mmol, 0.64 mL), and AIBN (0.0073 mmol, 1.2 mg), were dissolved in anhydrous DMF (2.0 mL). The solution was purged with nitrogen gas for 30 minutes. The surface-attachable RAFT-CTA (Si-RAFT-CTA) modified Si/SiO_2 surface was placed in a vial and purged with N_2 for 15 min. The monomer solution was transferred to the surface-including vial under N_2, and this vial was heated at 75 ^oC for 5 h. After that, the solution was removed, and brush coated surface was washed with DMF and CH_2Cl_2 and dried using a nitrogen stream.

7.2.4. Fabrication of Copolymer Brush P2 (90/10) (DEGMA/PDSMA)

PDSMA (100 mg, 0.39 mmol), DEGMA (660 mg, 3.51 mmol), and AIBN (1.28 mg, 7.8×10^{-3} mmol) were dissolved in anhydrous DMF (1.5 mL). The solution was degassed by using nitrogen gas bubbling for 30 minutes. The surface-attachable RAFT-CTA (Si-RAFT-CTA) modified Si/SiO_2 surface was put into a vial and purged with N_2 for 15 min. The monomer solution was transferred to a surface-including vial under N_2, and this vial was heated at 75 ^oC for 5 h. After that, the solution was removed, and brush coated surface was washed with DMF and CH_2Cl_2 and dried using a nitrogen stream.

7.2.5. Preparation of Copolymer Brush P3 (80/20) (DEGMA/PDSMA)

PDSMA (100 mg, 0.39 mmol), DEGMA (293 mg, 1.56 mmol), and AIBN (0.63 mg, 3.9×10^{-3} mmol) were dissolved in anhydrous DMF (1.2 mL). The solution was degassed by using nitrogen gas bubbling for 30 min. The surface-attachable RAFT-CTA (Si-RAFT-CTA) modified Si/SiO_2 surface was put into a vial and purged with N_2 for 15 min. The monomer solution was transferred to this vial under N_2, and this vial was heated at 75 ^oC for 5 h. After that, the solution was removed, and brush coated surface was washed with DMF and CH_2Cl_2 and dried using a nitrogen stream.

7.2.6. Preparation of Copolymer Brush P4 (70/30) (DEGMA/PDSMA)

PDSMA (100 mg, 0.39 mmol), DEGMA (171 mg, 0.91 mmol), and AIBN (0.43 mg, 2.6 x 10^{-3} mmol) were dissolved in anhydrous DMF (1 mL). The solution was degassed by using nitrogen gas bubbling for 30 min. The surface-attachable RAFT-CTA (Si-RAFT-CTA) modified Si/SiO_2 surface was put into a vial and purged with N_2 for 15 min. The monomer solution was transferred to this vial under N_2, and this vial was heated at 75 ^oC for 5 h. After that, the solution was removed, and brush coated surface was washed with DMF and CH_2Cl_2 and dried using a nitrogen stream.

7.2.7. Preparation of Copolymer Brush P5 (0/100) (DEGMA/PDSMA)

PDSMA (100 mg, 0.39 mmol) and AIBN (0.128 mg, 7.8 x 10^{-4} mmol) were dissolved in anhydrous DMF (0.5 mL). The solution was degassed by using nitrogen gas bubbling for 30 min. The surface-attachable RAFT-CTA (Si-RAFT-CTA) modified Si/SiO_2 surface was put into a vial and purged with N_2 for 15 min. The monomer solution was added to this vial under N_2, and this vial was heated at 75 ^oC for 5 h. After that, the solution was removed, and brush coated surface was washed with DMF and CH_2Cl_2 and dried using a nitrogen stream.

7.2.8. Functionalization of the Polymer Brush with BODIPY-SH

A BODIPY-SH solution was prepared in anhydrous DMF, and a catalytic amount of AcOH was added. Copolymer brush P2 was treated with this solution for 5 h. After that, the surface was washed with DMF and THF and dried under a stream of nitrogen.

7.2.9. Cleavage of BODIPY from Polymer Brush

BODIPY-conjugated polymer brush P2 was treated with 10 mM DTT solution in PBS for 24 h. The fluorescence microscopy images were recorded during the predetermined time interval.

7.2.10. Functionalization of the Polymer Brush with TFBM

Polymer brush P2 was treated with a TFBM solution (10 mg/mL in DMF) containing AcOH (52 µL) for 24 h. Afterward, the surface was washed with a gentle amount of DMF and THF and dried under a nitrogen flow.

7.2.11. Functionalization of the Polymer Brush with Mannose-SH for Protein Immobilization

Polymer brush P2 was treated with mannose-SH solution (10 mg/mL in DMF) containing AcOH (40 µL) for 5 h. After that, the surface was washed with DMF and THF and dried under a stream of nitrogen. Then, mannose containing surface was incubated with a mixture of FITC-ConA (0.075 mg/mL) and Rhodamine-PNA (0.075 mg/mL) in 20 mM HEPES (1.0 mM $MnCI_2$, 1.0 mM $CaCI_2$, 0.15 M NaCl, adjusted to pH 7.4) for 60 min. Subsequently, the surface was washed with 20 mM HEPES solution and dried under a nitrogen flow.

7.2.12. Functionalization of the Polymer Brush with Thiol-containing Peptide

Linear RGD-SH was dissolved in anhydrous DMF (1 mg/mL), and the catalytic amount of acetic acid (50 µL) was added. Polymer brushes (P2) were incubated with this solution for 4 h. After that, RGD-modified brushes were washed with a gentle amount of DMF and THF and dried using a nitrogen stream.

7.2.13. FITC Conjugation on Peptide Functionalized Polymer Brush

Fluorescein isothiocyanate (FITC) (1 mg, 0.0026 mmol) was dissolved in anhydrous DMF, and triethylamine (8.4 µL, 0.06 mmol) was added. RGD functionalized P2 polymer surface was immersed into this solution and incubated for 4 h. As a control experiment, RGD unmodified P2 polymer brush was treated with FITC solution under the same conditions. Subsequently, dye conjugated surface and control surface were washed with a gentle amount of DMF and THF and dried under a nitrogen stream.

7.2.14. Cell Attachment on Peptide Functionalized Polymer Brush and Actin Filament Staining

L929 mouse fibroblast cells were used, which were grown in a 5% CO2-containing atmosphere at 37 °C. Cells were cultured in Dulbecco's Modified Eagle's Medium (DMEM) media supplemented with 10% fetal bovine serum (FBS) (PAN Biotech). L929 mouse fibroblasts (15000 cells) were seeded onto prepared RGD-SH functionalized P2 surfaces. P2 polymer brush and bare DEGMA polymer brush P1 were used as control surfaces. After dropping the cell suspensions onto polymer brush surfaces, they were incubated at 37 °C in a 5% CO_2-containing atmosphere for two h. Afterward, cell media (1 mL) was added to each well-containing polymer brush surface. After incubation (24 h), cell media was removed, polymer interfaces were rinsed with 1 x PBS (3 times), and the cells were fixed with 3.7 % formaldehyde solution for 10 min at 37 ^oC. For staining filamentous actins (F-actins), cells were incubated with 0.1% Triton X-100 in PBS for 5 min. Then polymer brush surfaces were washed with 1 x PBS (1 mL x 3 times), and they were incubated in Alexa Fluor 488 phalloidin solution (5 units/mL concentration containing 1% bovine serum albumin (BSA) in 1 x PBS) for 20 min at 37^oC. After that, polymer brush surfaces were washed with 1 x PBS (1 mL x 3 times) to remove the dye. Finally, cell nuclei were stained with DAPI for 15 min at room temperature, and polymer brush surfaces were washed with 1 x PBS (1 mL x 3 times). The resulting images of cells were taken via Zeiss AxioVision and processed via Zen Lite software.

7.2.15. Cell Detachment from Peptide Functionalized Brush and Live-Dead Assay

L929 fibroblast cells (45000 cells/350µL) were seeded on the RGD functionalized polymer brush surfaces and incubated at 37 ^oC with 5% CO_2 for 3 h. After 3 h, DMEM (1 mL) was added to each surface, and incubation was continued for 24 h. After that, cell-attached surfaces were incubated with 5 mM DTT solution for 25 min, and released cells from polymer surfaces were washed with 1 x PBS (1 mL x 3 times) and stained via a live/dead assay kit. Solution A (calcein-AM, 10 µL) and solution B (propidium iodide, 5 µL) were diluted with 5 mL 1 x PBS to prepare the assay solution. Cells were incubated with this assay solution at 37 ^oC with 5% CO_2 for 25 min. Subsequently, stained cells were

washed with 1 x PBS (1 mL x 3 times). Live/dead cell viability was visualized by fluorescence microscopy and processed via Zen Lite software.

7.2.16. Functionalization of the Polymer Brush with Thiol-containing Doxorubicin

Polymer brush P2 was treated with thiolated doxorubicin (DOX-SH solution (1 mg/0.2 mL in DMF) containing AcOH (3 μL) for 5 h. After that, the surface was washed with DMF and THF and dried under a stream of nitrogen. As the control experiment, DOX was used.

7.2.17. Orthogonal Functionalization with Aminopropanol and Maleimide-containing Molecules and Cell Adhesive Peptide

Copolymer brush P2 was treated with aminopropanol (0.0576 mmol, 4.4 μL) in DMF (0.5 mL) in the presence of triethylamine (0.0576 mmol, 8.4 μL) for 18 h. After the washing step, a solution of tetramethylrhodamine maleimide (30 μL from 1 mg/mL in THF) was dropped onto this surface and incubated for 4 h. Then, the surface was washed with THF. After the drying step, this surface was incubated with a BODIPY-SH solution (30 μL from 1 mg/mL in DMF) containing the catalytic amount of AcOH for 5 h. At the end of 5 h, the interface was washed with DMF and THF and dried under a stream of nitrogen. Another functionalization was done using N-(3-hydroxypropyl) maleimide. For this, the RAFT end group containing the PDS polymer brush was treated with aminopropanol. Then, this surface was incubated with the solution of N-(3-hydroxypropyl) maleimide (40 μL, 1 mg/0.5 mL) in DMF for 5h. For cell adhesive cyclic RGD functionalization, the thiol end group containing surface, which was immobilized with 3-amino-1-propanol, was treated with maleimide-containing cyclic RGD peptide (cRGD-Mal) solution (1 mg/0.5mL) in DMF for 5 h. After the conjugation reaction, the surface was washed with THF and dried under a nitrogen flow.

7.2.18. Fabrication of Both DOX and cRGD-containing Polymer Brush

Polymer brush P2 was treated with aminopropanol and was immobilized with cRGD-Mal peptide for 5h. After 5h, the surface was washed with THF, and subsequently, it was

conjugated with DOX-SH in the presence of triethylamine for 3 h. At the end of 3 h, the surface was washed with THF and dried with a nitrogen flow.

7.2.19. Cell Culture on the cRGD End Group Functionalized Polymer Brushes

For the actin staining experiment, L929 mouse fibroblast cells (20000 cells) were seeded on the cRGD end group functionalized PDS brush and incubated at 37 ^{o}C under a 5% CO_2 atmosphere for 24 h. N-(3-hydroxypropyl) maleimide functionalized PDS brush was used as a control surface. After 24 h, surfaces were washed with 1 x PBS (1 mL x 2 times). The cells were fixed with a 3.7 % formaldehyde solution for 10 min. Then, surfaces were cleaned with 1 x PBS (1 mL x 2 times). The surfaces were incubated with 0.1% Triton X-100 solution for 5 min. After the washing step, surfaces were incubated in Alexa Fluor 488 phalloidin solution (5 units/mL concentration containing 1% bovine serum albumin (BSA) in 1 x PBS) for 20 min at 37°C. DAPI stained cell nuclei after the washing step. The resulting images of cells were taken via Zeiss AxioVision and processed via Zen Lite software. MDA-MB-231 human breast cancer cells purchased from ATCC were used for the DOX release and DOX internalization experiment. The cells were grown in a DMEM medium at 37 ^{o}C under a CO_2 atmosphere.

MDA-MB-231 cells (20 000 cells) were seeded onto cRGD and DOX-containing polymer brush surfaces and incubated for 24 h. Only cRGD containing PDS brush surface was also used as the control surface. After 24 h incubation, these surfaces were treated with GSH solution (5 mM) for 5 h. Then, the GSH solution was removed, surfaces and cells were washed with 1 x PBS (1 mL x 2 times), and cells were fixed with 3.7% formaldehyde solution for 10 min at 37 ^{o}C. After washing with PBS, the cell nuclei were stained by DAPI. After staining, cells were washed with PBS, and the resulting images of cells were taken via Zeiss AxioVision and processed via Zen Lite software. For the control experiment, after cell-attached surfaces were treated with GSH and cell media for 5 h, surfaces were exposed to trypsin, and detached cells were collected and visualized under the fluorescence microscope.

7.3. Results and Discussion

7.3.1. Fabrication of PDS-Containing Polymer Brushes

Synthesis of thiol-reactive pyridyl-disulfide (PDS)-containing polymer brush was shown in Figure 7.2. Di(ethylene glycol)methyl ether methacrylate (DEGMA) and pyridyl disulfide (PDSMA) monomers were used to synthesize side chain PDS-bearing polymer brush. While PDSMA was used as a thiol-reactive monomer, DEGMA was used anti-biofouling comonomer to minimize nonspecific adsorption.

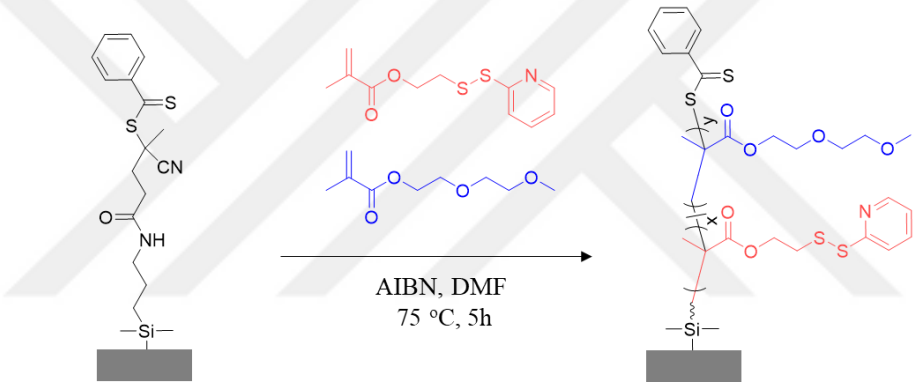

Figure 7.2. The synthesis of PDS-functionalized polymer brush via SI-RAFT.

Polymer brushes were prepared on phenylthioester-based RAFT reagent-coated silicon surface using PDSMA and DEGMA monomer in the presence of AIBN at 75 °C in DMF for 5 h. RAFT CTA-coated silicon surfaces were prepared using the literature procedure [172]. Briefly, cleaned Si/SiO_2 surfaces were immobilized with the solution of the silyltriethoxy group-including the phenylthioester molecule. Copolymer brushes, including four different molar ratios of DEGMA/PDSMA in the feed (P2: 90/10, P3:80/20, and P4:70:30), were synthesized and used in modification studies with thiol-containing molecules. Additionally, PDEGMA (P1) and PPDSMA (P5) were prepared for copolymer brush characterization, and PDEGMA (P1) homopolymer brush was used for control experiments.

A series of P[DEGMAy-*co*-PDSMAx] copolymer brushes (the y and x refer to the monomer composition in feed) containing various amounts of PDSMA were synthesized using surface-initiated RAFT polymerization. The polymer brushes (P1-P5) were characterized using AFM and XPS. The polymer brush thicknesses were measured using AFM, and thicknesses were determined by evaluating of step heights of cross-sectional profiles of patterned polymer brush samples. The composition of the P[DEGMAy-*co*-PDSMAx] copolymer brushes were determined by using XPS analysis. Figure 7.3 shows survey scan spectra of the PDEGMA (P1) homopolymer brush, P[DEGMAy-*co*-PDSMAx] (P2-P4), and PPDSMA homopolymer brush (P5). The nitrogen atom signal at around 399.7 eV and the sulfur atom signal at around 164 eV are evident for successfully incorporating PDSMA into polymer brushes. The properties of polymer brushes were tabulated in Table 7.1. The increasing PDS ratio in the copolymer brush composition increased the N and S ratios. On the other hand, there were no N and S peaks in the survey scan of PDEGMA homobrush, as expected. PDSMA: DEGMA incorporation was calculated using N1s/O1s ratio from XPS. Additionally, polymer brushes showed an increase in contact angle along with an increasing amount of hydrophobic PDS group.

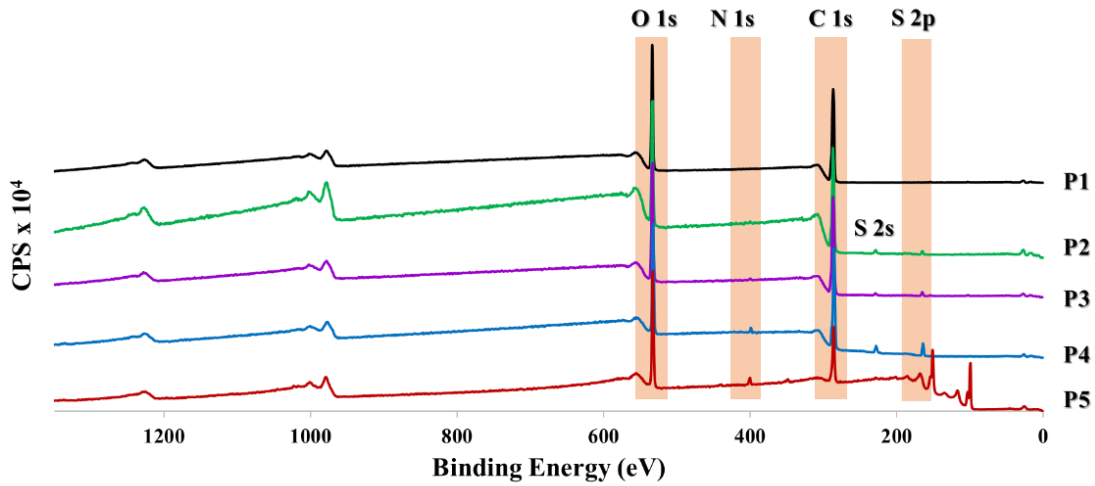

Figure 7.3. The XPS survey scan spectra of P1-P5 polymer brushes.

For representative polymer brushes, C1s high-resolution spectra and their deconvolution results were given in Figure 7.4. The C1s high-resolution spectra of DEGMA

homopolymer brush P1 could be deconvoluted to three Gaussians at 288.9, 286.5, and 285.0 eV C=O, C-O-C/C-S/C-N, and C-C, respectively.

Table 7.1. The properties of polymer brush (P1-P5) and calculated monomer composition from XPS based on N/O ratio.

Sample	DEGMA/PDS (y/x) feed ratio	DEGMA/PDS (y/x) calcd from XPS (N/O)	Thickness (nm)	Contact Angle
P1	100/0	100/0	52 ± 2	63 ± 4
P2	90/10	93.3/ 6.7	53.66 ± 2.3	71 ± 3
P3	80/20	85.6/14.4	41.46 ± 4.5	72 ± 3
P4	70/30	74.6/25.4	10.32 ± 1.2	76 ± 3
P5	0/100	0/100	5.0	82 ± 4

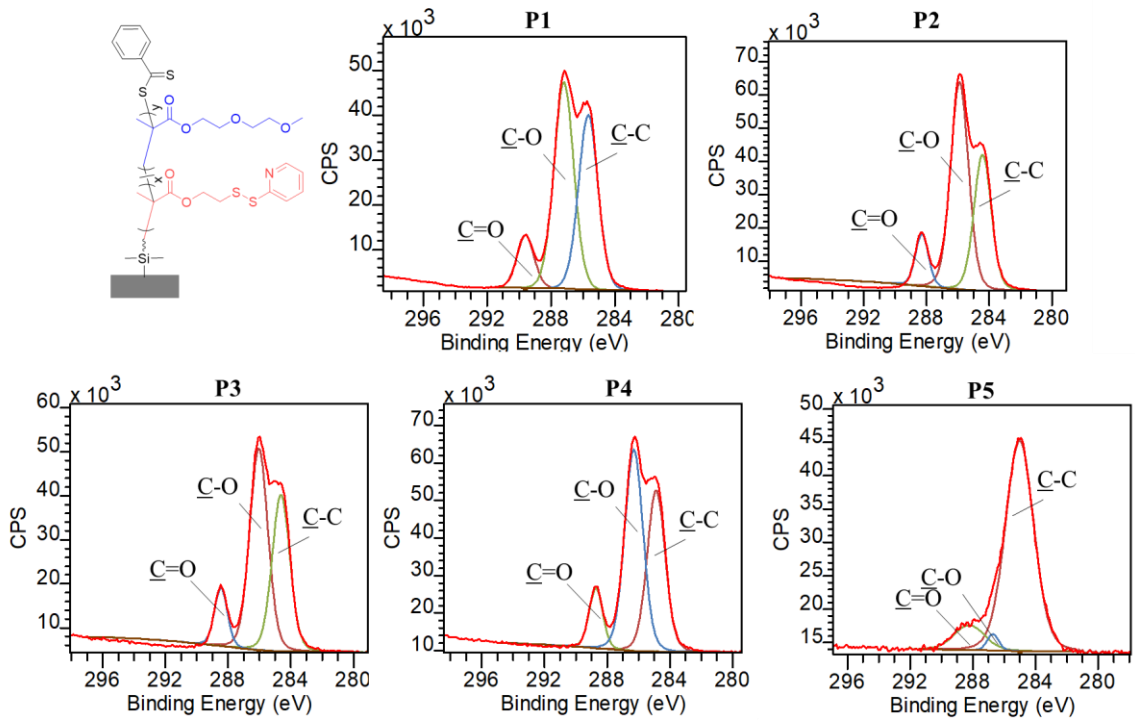

Figure 7.4. The high-resolution C1s spectra of P1-P5 polymer brushes.

The N1s high-resolution spectra of P1-P5 polymer brushes were given in Figure 7.5. DEGMA homopolymer brush P1 did not show N1s peak. This result suggested that the N atoms in the RAFT initiator was covered by DEGMA polymer chains. Copolymer brush P2-P4 and PDSMA homobrush P5 showed N1s peak at 399.7 eV due to the PDS group. As expected, the composition intensity of the N1s peak increased along with the increased ratio of PDSMA monomer in the polymer brush. The S2p high-resolution spectra of P1-P2 polymer brushes were demonstrated in Figure 7.6. While the DEGMA P1 homopolymer brush did not show any S2p peak, P2-P5 brushes demonstrated an S2p peak at 164.2 eV. S2p peak could be deconvoluted into two Gaussians with the expected relative areas for two sulfur atoms at 165.1 eV and 163.8 eV, S-S, and C-S, respectively. As well as N1s, S2p peak intensity showed an increase with the increased ratio of PDSMA monomer in copolymer brush. In addition, the P5 PDSMA homopolymer brush showed S peak at 168 eV, belonging to the RAFT group, due to very low brush thickness.

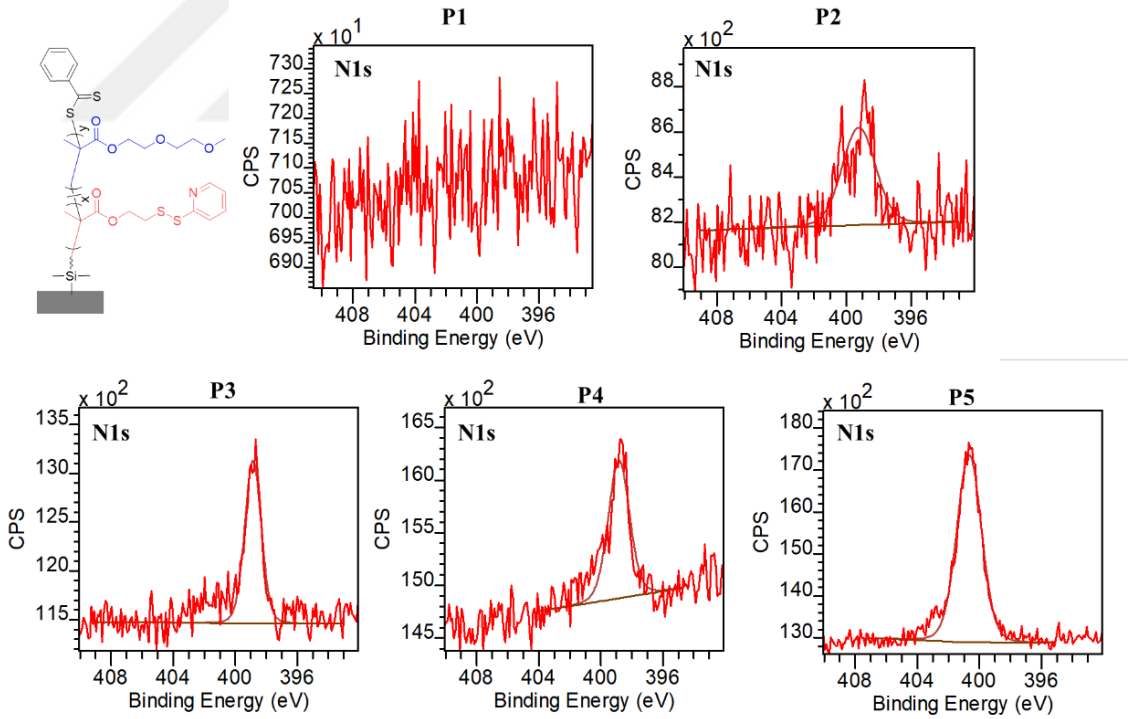

Figure 7.5. The high-resolution N1s spectra of P1-P5 polymer brushes.

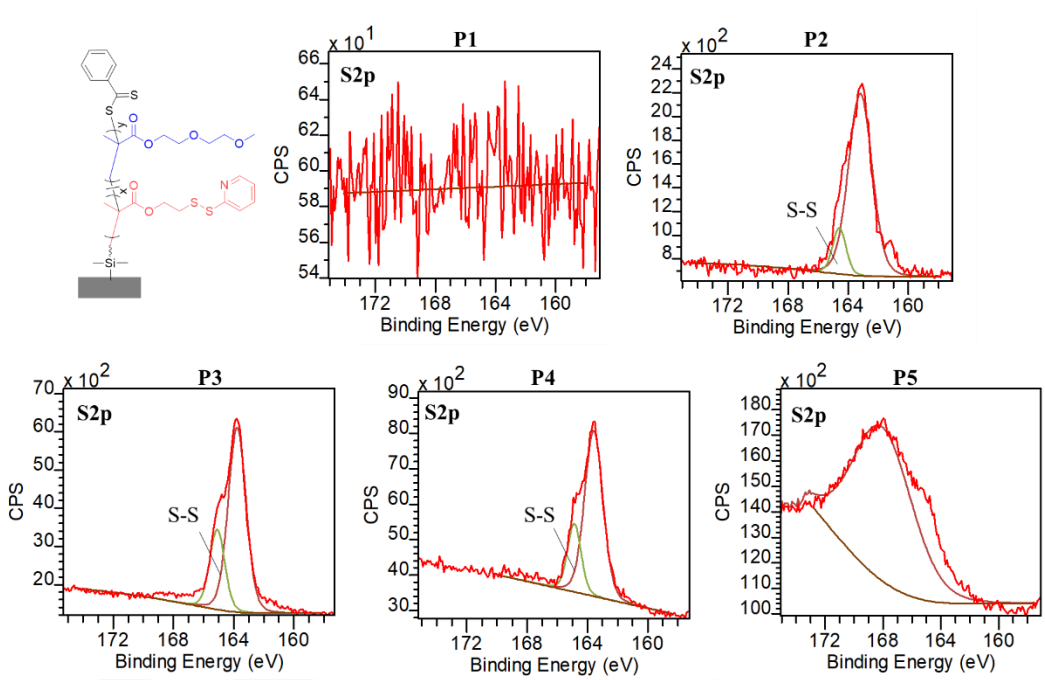

Figure 7.6. The high-resolution S2p spectra of P1-P5 polymer brushes.

The correlation of brush height with polymerization time indicated that the extent of polymerization could control the thickness of the polymeric coating. Thus, the time-dependent growth of the DEGMA polymer brush was demonstrated in Figure 7.7.

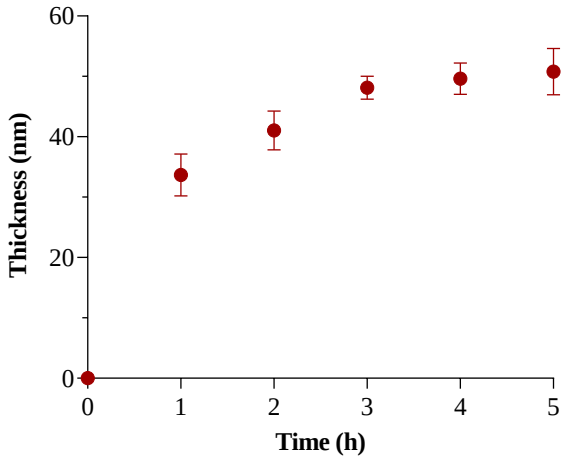

Figure 7.7. Time-dependent growth of P2 polymer brush (10% PDSMA) as a line graph.

7.3.2. Functionalization of the Copolymer Brush P2 with BODIPY-SH

To explore PDS-containing polymer brushes toward thiol-containing molecules, the copolymer brush P2 surface was functionalized with BODIPY-SH solution, and the fabrication of the dye-containing P2 brush was shown in Figure 7.8a. The P2 polymer brush surface was treated with a solution BODIPY-SH in the presence of a catalytic amount of AcOH. As a control experiment, homopolymer brush P1 (100 % DEGMA) was used and treated with BODIPY-SH under the same conditions.

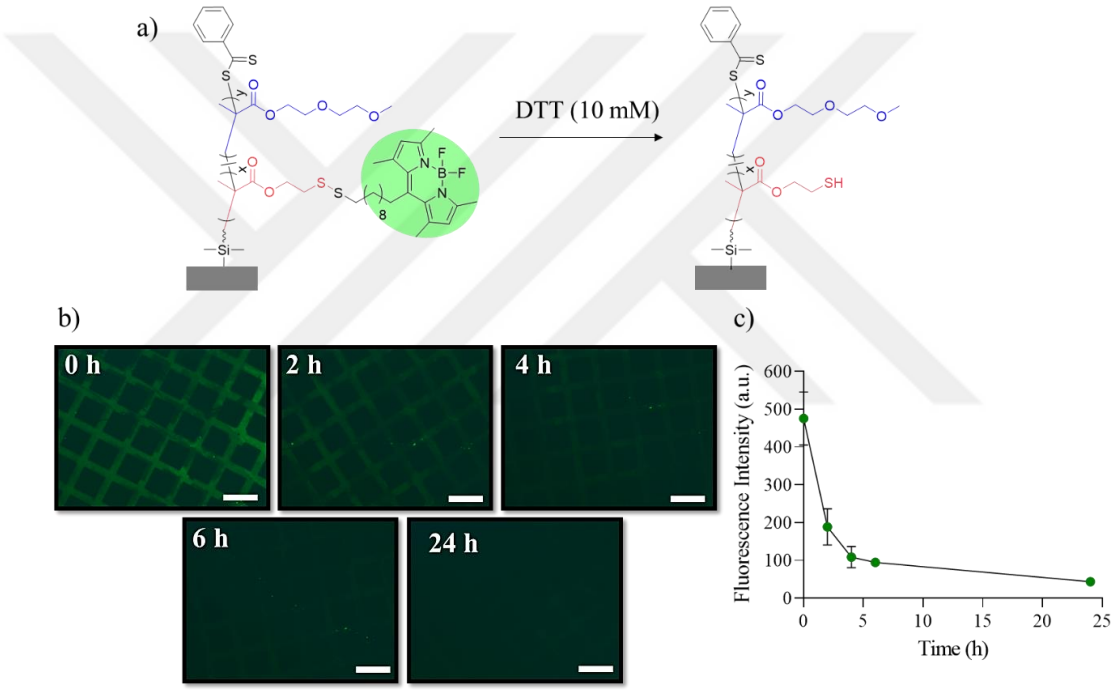

Figure 7.8. (a) The fabrication of BODIPY-SH conjugation to PDS-containing polymer brush; (b) the fluorescence images of BODIPY-containing surface after BODIPY release in the DTT and BODIPY release line graph.

The surface characterization was performed with a fluorescence microscope. The treatment of polymer brush surfaces with BODIPY-SH resulted in the thiol-disulfide exchange reaction to provide a fluorescent surface. As seen in Figure 7.8a, the green fluorescent patterned surface resulted from an exchange reaction between PDS and thiolated BODIPY. As expected, the control surface showed no fluorescence due to lacking PDS groups. The fluorescence image was also shown as an inset in Figure 7.8b. This result

revealed that the source of green fluorescence was not due to the physical adsorption of the BODIPY dye. After the BODIPY-containing copolymer brush was fabricated, the BODIPY-conjugated P2 polymer brush was treated with DTT solution (10 mM) in PBS to investigate BODIPY release from the surface. BODIPY release was determined using fluorescence microscope analysis. At predetermined time points, the surface was removed from the DTT solution, the fluorescence image was recorded after washing, and the surface was put into the DTT solution again. The time-dependent BODIPY release from the surface was demonstrated in Figure 7.8. As expected, green BODIPY fluorescence decreased due to the degradation of disulfide bonds in the presence of DTT.

7.3.3. Functionalization of the Copolymer Brush P2 with 4-Trifluoromethylbenzyl mercaptan (TFBM)

The P2 brush surface was incubated with a solution of TFBM in the presence of the catalytic amount of acetic acid. TFBM conjugated polymer brush was obtained via a thiol-disulfide exchange reaction. FTIR, contact angle measurements, and XPS analysis characterized TFBM-modified polymer brush surface. The TFBM conjugated surface FTIR spectrum was compared with TFBM, and FTIR spectra were given in Figure 7.10. After modification with TFBM, peaks at 1327 and 1067 cm^{-1} were observed [195].

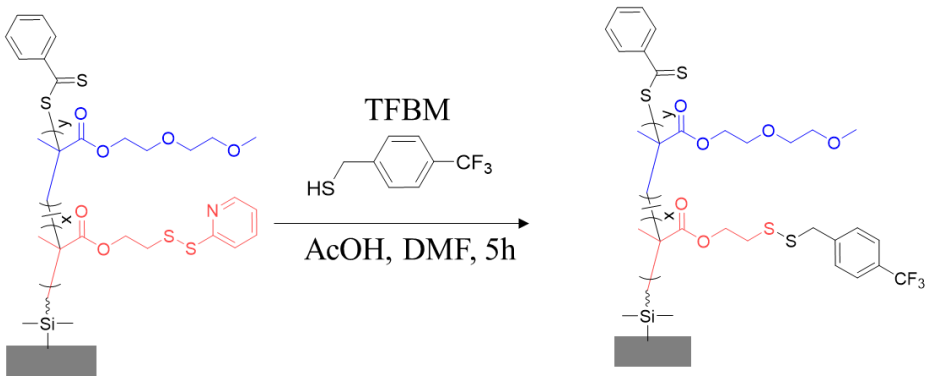

Figure 7.9. Functionalization of PDS-containing P2 brush with TFBM.

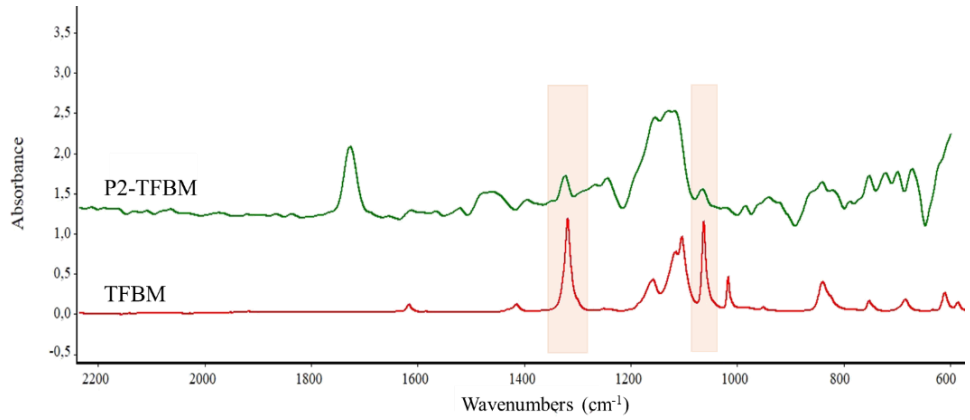

Figure 7.10. FT-IR spectra of TFBM and TFBM conjugated brush.

After FTIR characterization, the successful post-polymerization modification was also supported with XPS analysis, and spectra were demonstrated in Figure 7.11. The existence of F1s peak at 688 eV showed modification PDS groups with TFBM units. Conversion of modification was estimated as 95% from the area of the N1s signal related to TFBM ($A_{F1s}/3$) to the total area of N1s signals in the high XPS spectra, that is, ($A_{F1s}/3)/A_{N1s}$) x 100.

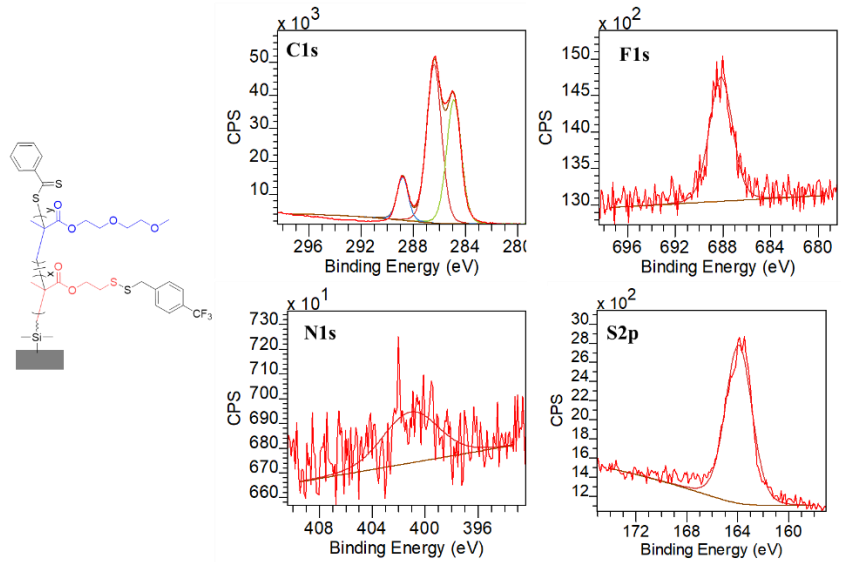

Figure 7.11. XPS high-resolution C1s, N1s, F1s, and S2p spectra of TFBM conjugated P2 brush.

7.3.4. Functionalization of Polymer Brush with Mannose-Thiol and Evaluation of Lectin Binding Efficiency

Mannose-thiol (mannose-SH), synthesized according to the literature [316,317], was conjugated to a PDS-containing polymer brush (P2) surface via the thiol-disulfide exchange reaction to obtain the mannose-containing P2 brush. After the conjugation of mannose-thiol, the lectin binding efficiency of this surface was evaluated. Fluorescein labeled Concanavalin A (FITC-ConA) and rhodamine B labeled Peanut Agglutinin (RhB-PNA) were selected as model lectins. A mixture of FITC-ConA (0.075 mg/mL) and RhB-PNA (0.075 mg/mL) in Mn^{2+} and Ca^{2+} containing HEPES buffer saline (10 mM) and mannosylated P2 surface was treated with this solution for 1h. As the control experiment, the P2 surface was used and treated with ConA-PNA solution under the same conditions. After 1 h, the surface was washed with HEPES buffer to remove unbound lectin, and lectin binding efficiency was investigated using fluorescence microscope analysis.

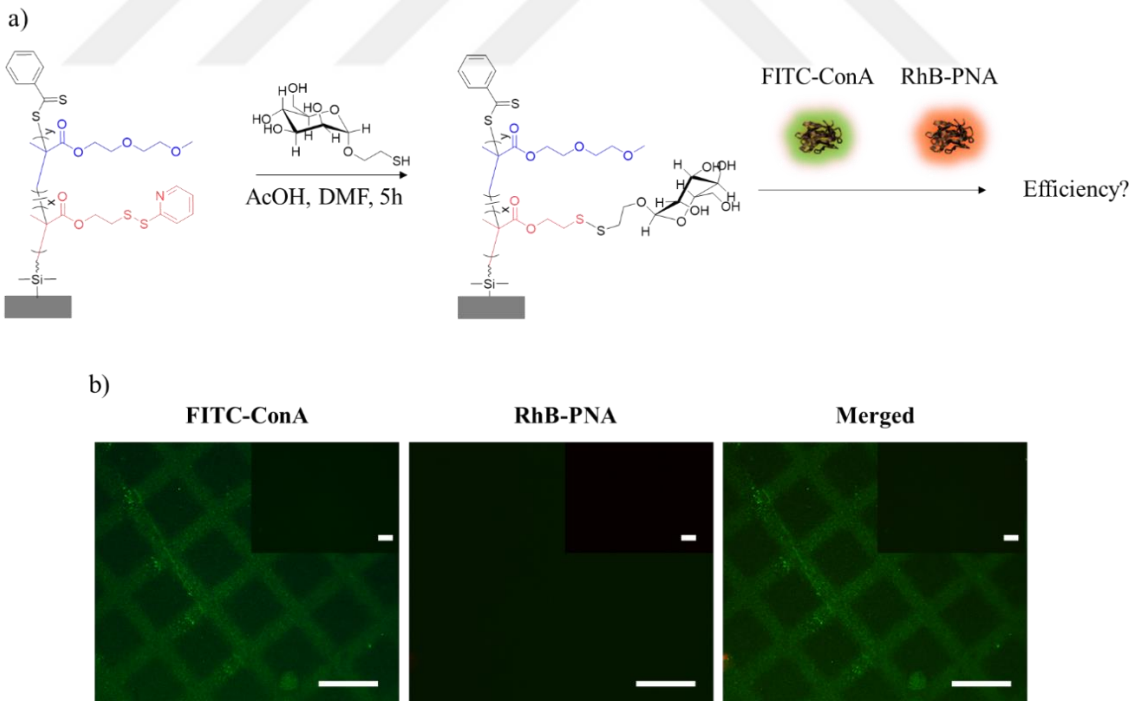

Figure 7.12. (a) Fabrication of mannose-containing P2 brush for lection binding affinity, (b) fluorescence microscope images of mannose-containing P2 brush treated with FITC-ConA and RhB-PNA. The scale bar is 50 µm.

As seen in Figure 7.12b, green fluorescence showed successful immobilization of ConA lection onto mannose-containing P2 brush due to ConA-mannose interaction efficiency. On the other hand, there was no red fluorescence coming from Rhodamine-PNA. This meant that PNA did not show binding to the mannose-containing surface. P2 surface was used as the control surface, and the results of the control surface were given as inset in Figure 7.12b. Notably, using a mannose-containing polymer brush surface showed that ConA can be specifically targeted and captured.

After successfully immobilizing FITC-ConA to mannose-containing P2 brush, this brush was incubated with 10 mM DTT solution in DMSO for 24 hours. The removal of FITC-ConA intensity was investigated using a fluorescence microscope, and green fluorescence disappeared due to disulfide degradation in the presence of DTT.

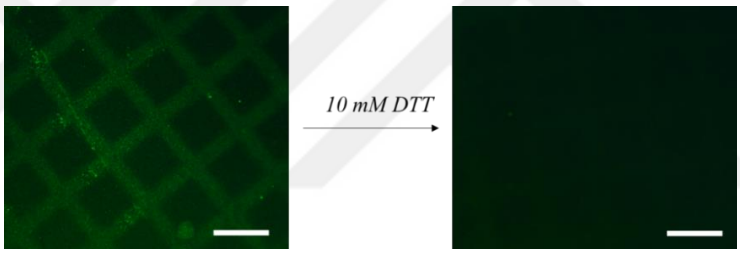

Figure 7.13. The fluorescence microscopy images of FITC-ConA immobilized P2 brush before and after DTT treatment. The scale bar is 50 µm.

7.3.5. Conjugation of Polymer Brushes with Thiol-containing Peptide and Cell Attachment and Release

After showing the reversible modification capabilities of PDS-containing polymer brushes with thiolated molecules, the PDS-containing polymer brush surfaces' efficiency on cell attachment and release was investigated using actin staining and live-dead assays. PDS-containing P2 polymer brushes were treated with linear RGD thiol (1 mg/mL) (RGDC, RGD-SH) peptide in a catalytic amount of acetic acid to promote cell attachment and proliferation. The existence of RGD on the polymer surface was proved using FITC dye. RGD conjugated surface was treated with FITC solution. The scheme was shown in Figure 7.14.

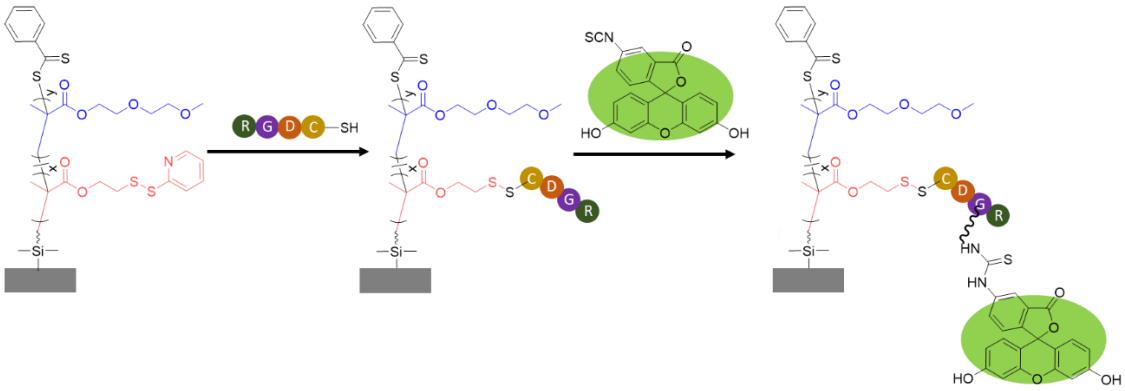

Figure 7.14. The modification of the P2 polymer brush with thiolated RGD peptide and functionalization with FITC.

Free amine groups of RGD peptide reacted with FITC, green fluorescence was obtained, and a fluorescence image was given as the left picture in Figure 7.15. RGD unmodified P2 polymer brush was also utilized as a control surface. As expected, there was no green fluorescence due to the lack of an amino group, and the image is shown in Figure 7.15 (right).

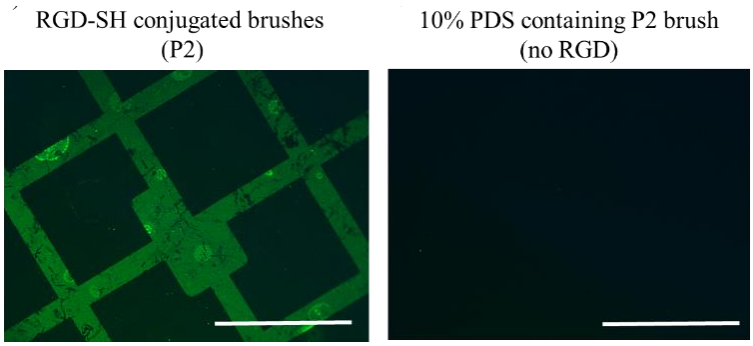

Figure 7.15. The fluorescence image of the FITC-conjugated RGD-containing surface (left), (c) the fluorescence image of the control P2 surface (right). The scale bar is 500 µm.

7.3.6. Cell Attachment and Release from RGD-Conjugated Brush

L929 mouse fibroblast cells were grown in DMEM at 37 ^{o}C under a 5% CO_2 atmosphere for cell experiments. L929 cells were seeded on linear RGD-conjugated surfaces. RGD unmodified P2 polymer brush and 100% DEGMA P1 brushes were used as

control groups. The effect of RGDC conjugation on cell attachment was compared in the presence and absence of RGD peptide. After L929 cells were seeded onto surfaces, polymer brushes were incubated for 24 h. After 24 h of incubation, the actin and nuclei of cells were stained with Alexa Fluor-phalloidin 488 and DAPI, respectively. After the staining steps, fluorescence microscopy analysis was performed to show cell attachment and proliferation on different surfaces. A clear difference was observed between the RGD-modified P2 brush and the control P1 DEGMA brush. As seen in Figure 7.16d, modifying the P2 brush with RGD-SH promoted cell attachment and proliferation. On the other hand, as seen in Figure 7.16b, the control P1 brush became bio-inert due to the anti-biofouling property of DEGMA polymer. Interestingly, P2 polymer brush bearing PDS groups displayed slightly higher efficiency than P1 brush.

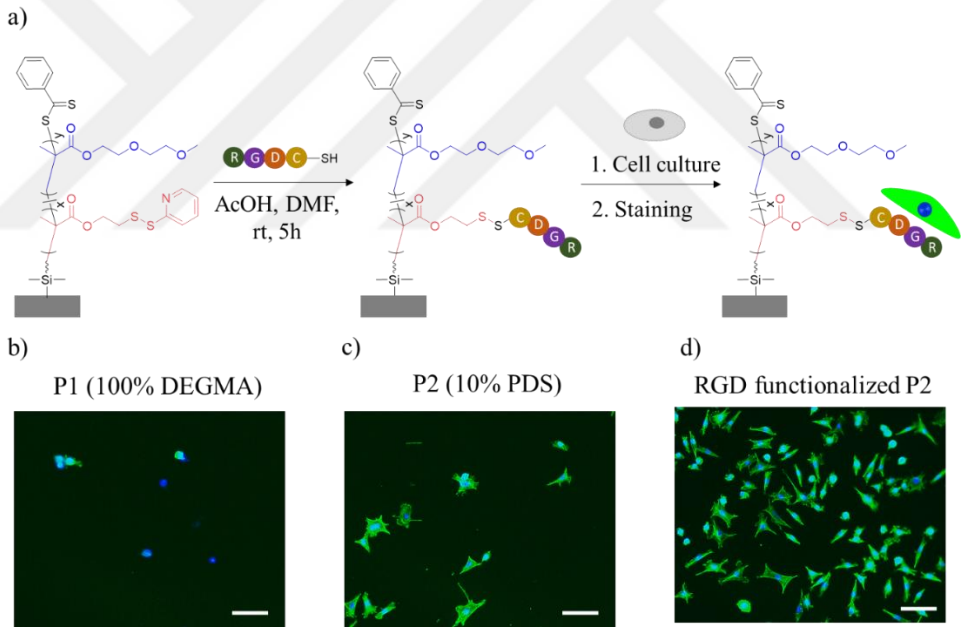

Figure 7.16. (a) The fabrication of an RGD-containing polymer brush for cell attachment merged fluorescence microscopy images of cells immobilized on (b) P1 surface, (c) P2 surface, and (d) RGDC-conjugated P2 surfaces after actin filament staining with Alexa Fluor 488 and nuclei staining with DAPI. The scale bar is 50 µm.

After successful attachment of cells onto peptide conjugated surface, cell release from the surface was assessed without compromising their viabilities. A live-dead assay was used to monitor cell viability after detachment from the surface. L929 mouse fibroblast cells were

seeded onto an RGD-conjugated polymer brush surface and incubated for 24 hours. After incubation, surface-attached cells were stained with calcein-AM and propidium iodide (PI), and cells were visualized under a fluorescence microscope. As seen in Figure 7.17b, the green fluorescence and cell morphology indicated their viable nature. L929 cells were seeded onto an RGD-modified surface for cell release and viability assay. After 24 hours of incubation, surface attached cells were exposed to 5 mM DTT solution. The cells detached from the surface due to breaking redox-responsive disulfide bonds with DTT. The surface detached cells were collected and stained with calcein-AM and propidium iodide after transferring them into a well plate. In this assay, calcein-AM showed esterase activity in viable cells and gave green fluorescence. Propidium iodide demonstrated binding to the DNA of dead cells and gave red fluorescence. As seen in Figure 7.17c, fluorescence microscopy analysis displayed that the viability of cells was not compromised after release from the polymer brush surface.

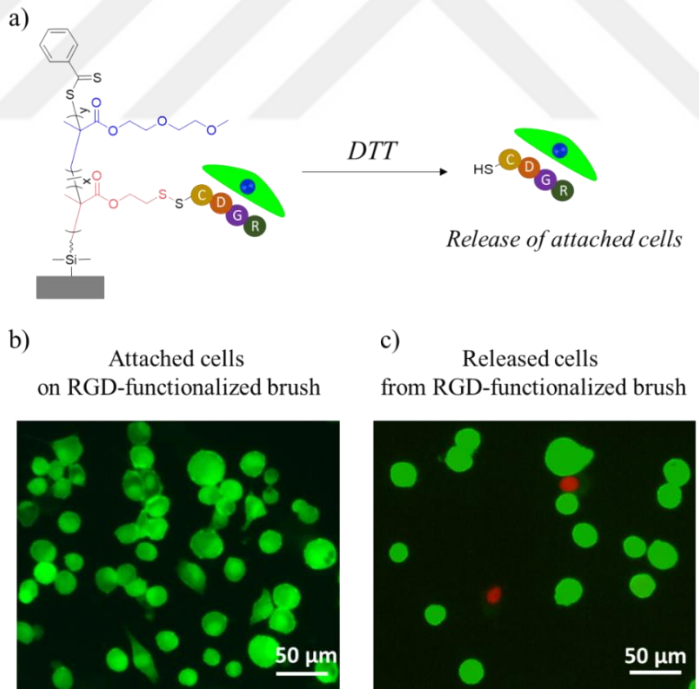

Figure 7.17. (a) Illustration of cell release from the surface with DTT, (b) the fluorescence microscopy image of calcein-AM and PI stained cells onto the peptide-conjugated brush surface, and (c) the fluorescence microscopy image of calcein-AM and PI stained cells after detachment from polymer surface.

7.3.7. The Fabrication of DOX Conjugated Polymer Brush for Delivery into Cells

Thiolated DOX (DOX-SH) was prepared according to the literature [336]. The polymer brush P2 surface was treated with DOX-SH solution in the presence of a catalytic amount of acetic acid. As a control experiment, the P2 surface was incubated with DOX solution under the same reaction conditions. The characterization of surfaces was performed with a fluorescence microscopy analysis. As seen in Figure 7.18b, red nonpatterned fluorescence showed DOX-SH conjugation to the P2 brush via the thiol-disulfide exchange reaction. On the other hand, the fluorescence image of the control group, given in Figure 7.18c, did not give red fluorescence due to lacking a thiol functional group on only the DOX molecule.

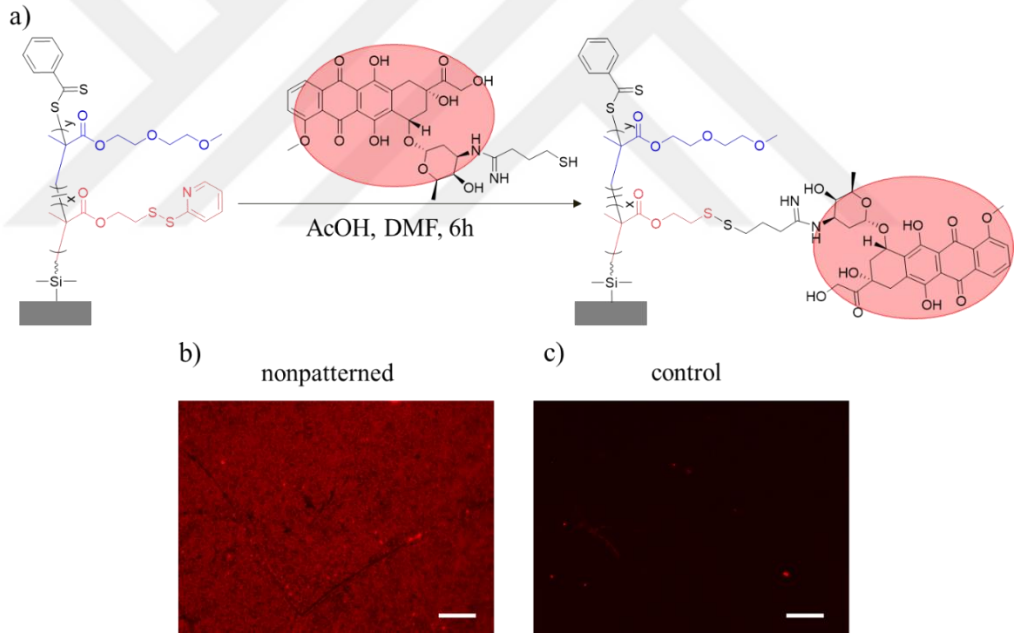

Figure 7.18. (a) The illustration of DOX-SH binding to polymer brush via thiol-disulfide exchange reaction, (b) the fluorescence image of P2 brush surface after modifying with DOX-SH, and (c) the fluorescence image of control surface after treatment with DOX. The scale bar is 50 µm.

7.3.8. The End Group Functionalization Using Orthogonal Reaction

Because polymer brushes were prepared using SI-RAFT with the R group approach, thiocarbonate functional units were located at the top of polymer chains on the surface. Post-polymerization modification methods may diversify the phenyl thioester groups at the top of polymer chains. In particular, phenyl carbonothioyl thio functional groups may be reduced into thiols in the presence of amine groups. This paves the way for orthogonal modification of polymer brushes via thiol-maleimide chemistry. Along with this knowledge, polymer brushes P2 were treated with 3-amino-1-propanol to form thiol groups from phenyl carbonothioyl thio units. Subsequently, the surface was immobilized with maleimide-bearing rhodamine dye (TAMRA-Mal, 1 mg/mL). The conjugation of rhodamine dye via thiol-maleimide chemistry was characterized by fluorescence microscopy analysis.

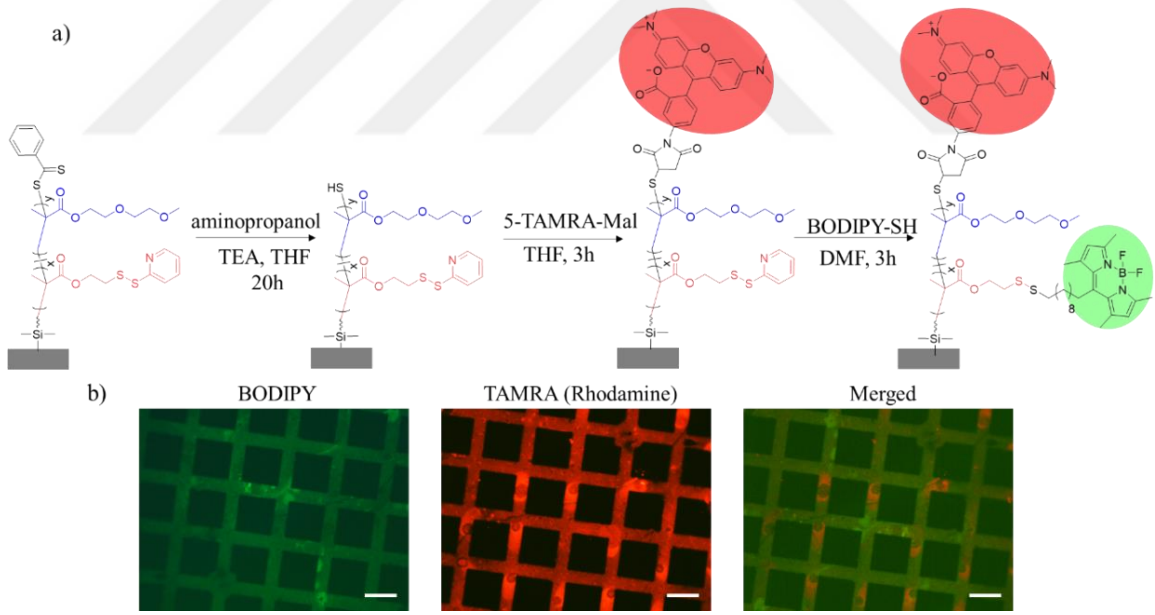

Figure 7.19. (a) Immobilization of 3-amino-1-propanol to reduce dithiocarbonyl groups to thiols and immobilization of maleimide-containing rhodamine and subsequent BODIPYH conjugation, (b) the fluorescence images of rhodamine and BODIPY-conjugated P2 polymer brush. The scale bar is 50 µm.

After that, the rhodamine-conjugated surface was immersed in BODIPY-SH solution (1 mg/mL) containing acetic acid to functionalize PDS groups on the side chains of the polymer brush. The BODIPY and rhodamine dye conjugated polymer brush P2 surface was visualized under the fluorescence microscope. As seen in Figure 7.17 b, TAMRA-Mal reacted with the thiol part and gave red fluorescence, and BODIPY-SH reacted with the PDS side of brush and revealed green fluorescence.

7.3.9. Cell Adhesive Peptide Functionalization Using Orthogonal Reaction

After successfully modifying the polymer brush using orthogonal reactions, another functionalization was performed using maleimide-containing peptide and organic molecule. After immobilizing the P2 surface with 3-amino-propanol, the thiol-containing surface was immersed in a maleimide-containing cyclic RGD peptide solution (1 mg/0.5 mL in DMF). The presence of cRGD at the top of the polymer brush was proved by XPS analysis. Moreover, the thiol-containing surface was treated with a 3-hydroxypropyl maleimide solution (1 mg/0.5 mL in DMF). After the conjugation of the P2 brush with cyclic RGD peptide, cell attachment efficiency was investigated with actin filament staining. The maleimide-containing hydroxypropyl functionalized P2 brush surface was used as a control surface.

It was well known that the cyclic RGD peptide demonstrates specific binding to integrin receptors expressed on the surface of fibroblast cells and promotes cell attachment [319]. L929 mouse fibroblast cells were seeded onto cRGD-containing and hydroxypropyl-including P2 surface and incubated for 24 h. After incubation, actins and nuclei were stained with Alexa Fluor 488 and DAPI, respectively. A clear difference was observed between the cRGD-containing P2 surface and the control hydroxypropyl functionalized surface. After the staining step, cell-attached surfaces were visualized under a fluorescence microscope, and images were given in Figure 7.20. As expected, enhanced cell immobilization and proliferation were observed on the cRGD-conjugated P2 polymer brush surface. Cell attachment and spreading remained significantly lower without modifying the P2 polymer brush surface with cRGD-Mal.

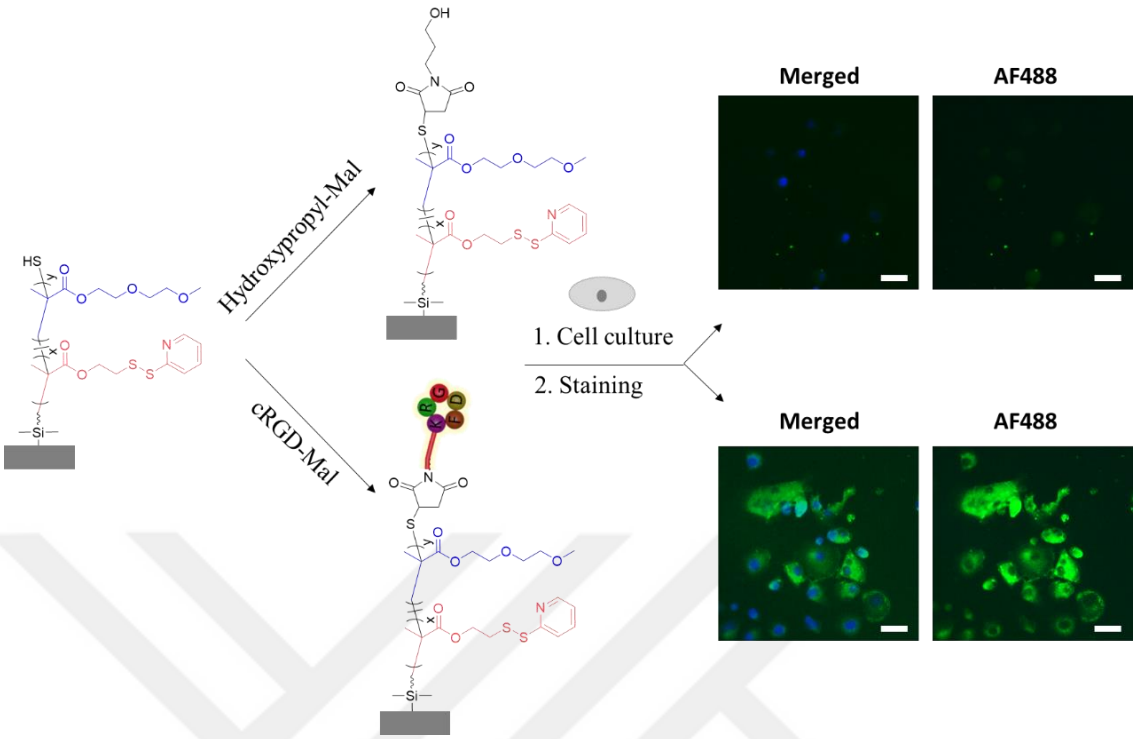

Figure 7.20. Fabrication of cRGD-Mal and hydroxypropyl-Mal modified P2 polymer brush and fluorescence images of attached cells after staining with Alexa Fluor Phalloidin (AF488) and DAPI. The scale bar is 50 µm.

7.3.10. DOX Release from Polymer Brush and Cellular Internalization

DOX-conjugated P2 polymer brush was prepared using DOX-SH via a disulfide-exchange reaction. It is well known that disulfide linker breaks in the presence of reducing agents like GSH or DTT [30]. Therefore, the DOX-conjugated P2 brush may show DOX release in the presence of GSH. In this part of the project, we wanted to show DOX internalization into cancer cells, which were proliferated onto a polymer brush surface, and this idea was illustrated in Figure 7.21. To provide cell attachment and growth, cyclic RGD (cRGD) was conjugated at the top of the polymer brush via thiol-maleimide chemistry. Subsequently, DOX-SH were conjugated to side chains of polymer brush using pyridyl disulfide groups. After preparing DOX and cRGD containing P2 polymer brush, MDA-MB-231 breast cancer cells were seeded onto this surface. A cRGD-containing P2 polymer brush (cRGD-P2) was used as a control surface without conjugating with DOX-SH. After 24 h incubation, the surfaces were incubated with 5 mM GSH solution for 5 h. At the end

of 5 h, the nuclei of cells were stained with DAPI, and cells were visualized under the fluorescence microscope. As a control experiment, a cRGD-containing P2 brush was used, cancer cells were seeded on it, the surface was treated with 5 mM GSH and cells were subsequently stained by DAPI. The cRGD and DOX-containing P2 polymer brush was used as another critical control experiment. After the cell seeding process, the surface was not incubated in GSH solution and DAPI stained cell nuclei. Finally, all surfaces were visualized under the fluorescence microscope. The fluorescence DOX and merged channel images were given in Figure 7.22.

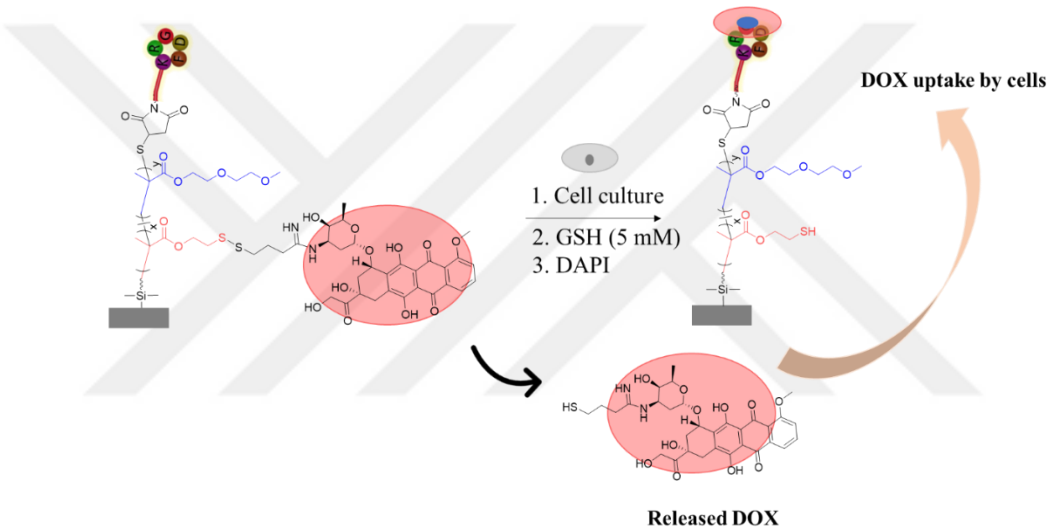

Figure 7.21. The illustration of cellular uptake of DOX by cancer cells via GSH treatment using cRGD and DOX conjugated P2 polymer brush.

As seen in Figure 7.22, MDA-MB-231 cells seeded on cRGD and DOX conjugated P2 brush surface (cRGD-DOX-P2) gave red fluorescence when cRGD-DOX-P2 surface was treated with GSH solution. This image revealed that the cRGD-DOX-P2 surface released DOX due to breaking disulfide bonds in the presence of GSH and the released DOX internalized by the cells. Furthermore, MDA-MB-231 cells on the cRGD-DOX-P2 surface did not demonstrate red fluorescence because this surface was used for the control experiment and was not incubated with GSH. Along with this, the surface remained red, as expected, showing that DOX still existed on the surface. Moreover, the cells on the cRGD-P2 surface did not show red fluorescence. They gave only blue fluorescence due to DAPI

nuclei staining. This surface was incubated with GSH (5 mM). Because the surface did not include DOX, any internalization was not observed.

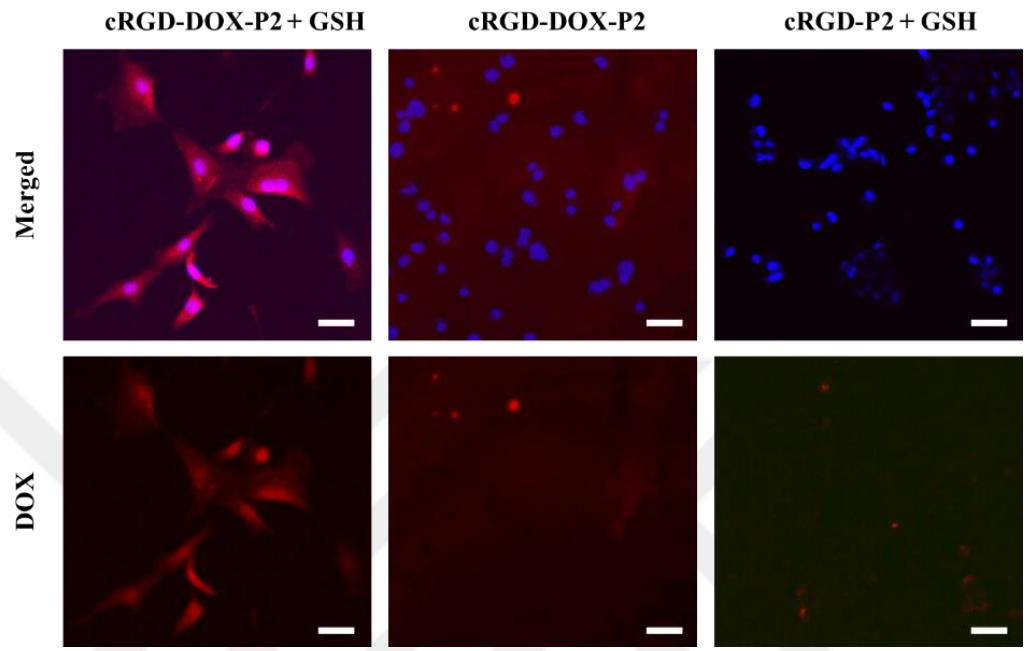

Figure 7. 22. The fluorescence merged and DOX channel images of MDA-MB-231 cells attached surfaces with and without GSH treatment and illustration of DOX internalization efficiency by the cells. The scale bar is 50 µm.

As seen in Figure 7.22, the cRGD-DOX-P2 surface remained red without GSH, but MDA-MB-231 cells appeared on this surface. It is not clear whether DOX was internalized by these cells or not. Therefore, a control experiment was conducted. MDA-MB-231 cells were seeded on c-RGD-DOX-P2 surfaces. After incubation for 24 h, one of these surfaces was treated with GSH for 5 hours. Another surface was only treated with cell media. After incubation, these surfaces were exposed to trypsin, detached cells were collected after the centrifuge step, and cells were visualized under the fluorescence microscope. Fluorescence images were given in Figure 7.23. The fluorescence images were overlapped with bright field images. As seen in Figure 7.23, cells showed red fluorescence due to DOX internalization after trypsinization of the GSH-treated surface. On the other hand, detached cells from the GSH-nontreated surface did not reveal any significant red fluorescence. Importantly, this result demonstrated DOX release and internalization in the presence of GSH.

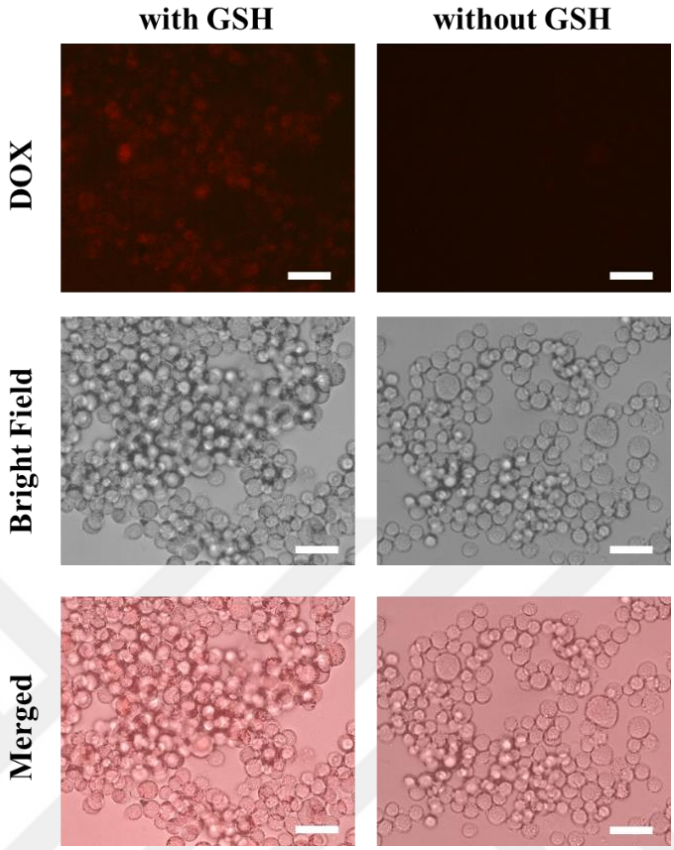

Figure 7.23. The fluorescence and bright field images of detached cells from the surface treated with GSH and cell media.

7.4. Conclusion

In conclusion, this chapter reported the fabrication of redox-responsive PDS-containing polymer brushes via SI-RAFT polymerization. We demonstrated that the amount of incorporation of reactive PDSMA monomer in polymer brush could be tuned by changing the feed ratio. Conjugation with different thiol-containing molecules was performed under mild conditions. Selective functionalization with thiolated molecules was demonstrated using a thiol-containing fluorescent dye, thiol-containing chemotherapy drug, thiolated and florine-including benzyl thiol, and thiolated sugar via thiol-disulfide exchange reaction. In addition, cell adhesive linear RGD-SH peptide was conjugated to a polymer brush to enable

cellular attachment. We demonstrated that surface-bound cells could be released in the presence of a reducing agent to collect them with high viability.

Moreover, we used the R-group approach in SI-RAFT to fabricate a polymer brush. Therefore, the R-group approach provided us with reducing RAFT end groups into thiol units. Reducing RAFT groups paves the way for the secondary functionalization of polymer brushes. RAFT groups were reduced to thiol units and maleimide-containing fluorescent dye and maleimide-conjugated cell adhesive peptide via thiol-maleimide chemistry. With this approach, the chemotherapy drug was conjugated to the side chains of the polymer brush using the thiol-disulfide exchange reaction; cell adhesive cyclic RGD peptide was conjugated to top of polymer brush chains using the Michael type thiol-maleimide addition reaction. With drug and peptide conjugating surface, cell attachment and drug internalization by cells was performed.

Notably, the critical result is one stone and three birds. Redox-responsive PDS-containing polymer brush will be attractive for bio-sensing and protein immobilization, cellular attachment, and drug release and internalization study.

8. FABRICATION OF BENZOTHIAZOLE-DISULFIDE-BASED REDOX-RESPONSIVE POLYMER COATINGS

This chapter was adapted with permission from {Degirmenci, A., R. Sanyal, M. Arslan and A. Sanyal, “Benzothiazole-Disulfide Based Redox-Responsive Polymers: Facile Access to Reversible Functionalizable Polymeric Coatings”, *Polymer Chemistry*, Vol. 13, No. 18, pp. 2595-2607, 2022}. Copyright {2022} Royal Society of Chemistry [337].

8.1. Introduction

Functional polymers' technological and scientific relevance has been the source of inspiration in developing new materials that respond to changing chemical-physical stimuli [338,339]. Such polymeric materials are stimuli-responsive, smart, or intelligent systems that can respond to an external or internal interaction in a controllable and predictable manner [340,341]. In physicochemical response, pH, temperature, and electromagnetic radiation are well-recognized stimuli that can be deliberately used to cognitively drive macromolecular structure in generating desired responsiveness [342-345]. In the biochemical aspect of stimuli-responsiveness, polymeric materials are expected to interact with physicochemical stimuli and organic cues such as glucose, enzymes, peptides, antigens, or receptors to give photo-, electro-, magneto response or structural change [224], [346]. Inherent similarities of polymeric materials with nature-based entities and pathways, as well as distinct differences in structural and compositional gradients of biological systems, have prompted considerable scientific interest in responsive polymeric materials in numerous applications such as fabrication of reactive surfaces [347], crosslinked networks [71], [348], self-healing materials [349,350], drug-delivery systems [351], sensors [352], and actuators [353].

Redox-/thiol-sensitive macromolecules are an essential class of stimuli-responsive polymeric materials with a unique potential in biomedical applications [225], [354]. In living cells, thiols play many vital roles in biological processes, especially in maintaining protein stability and conformational rigidity [355]. In exchange reactions between thiols and their oxidized forms, disulfides are governed by biochemical redox reactions by employing cellular oxidation enzymes and antioxidants such as glutathione [356]. By mimicking the chemical transformations of thiols and disulfides in living systems and benefiting from the redox sensitivity, the thiol-disulfide exchange reaction has emerged as an indispensable tool for the fabrication of thiol-responsive polymers and polymer-conjugates [357-362], nanogels [363], hydrogels [109], [364], micelles [223],[366] and coatings [163], [333]. The reversibility of disulfide bonds to form constituent thiols upon exposure to reducing agents is the critical design paradigm for preparing polymeric materials utilized as nanocarriers of drugs [367], proteins [368], and nucleic acids [369].

Functional polymeric coating surfaces are essential in enabling new technologies for various biomedical, materials science, and nanomaterial applications [370,371]. Biomedical applications involving biosensing, analyte detection, bioimmobilization, and aligned cell growth often necessitate the presence of reactive groups on interfaces to selectively attach the desired functional moiety [372]. Installation of reactive groups at interfaces that can be used as a handle for efficient functionalization, particularly in metal-free transformations, is quite attractive [373]. Interfaces with the ability to undergo reversible conjugation efficiently and specifically are desirable for applications involving surface renewability or a catch-release sequence. In this regard, the thiol-disulfide exchange reaction was an effective method for immobilizing antibodies on polymer brush-coated silicon surfaces [334]. Most studies to date employ the pyridyl disulfide group as an exchangeable handle. The benzothiazole disulfide moiety employed in this study is a cheaper and equally effective alternative to the widely used pyridyl disulfide moiety, which is synthesized using 2,2′-dipyridyl disulfide. Also, we envision that a thiol-reactive polymer that covalently anchors onto a solid platform and allows specific and reversible conjugation of thiol-containing functional molecules would be a helpful tool for various applications.

Herein, we disclose the preparation of redox-responsive benzothiazole disulfide-containing methacrylate polymers for the reversible surface functionalization of the glass

surface. It is demonstrated that reactive copolymers can be obtained with good control over molecular weight, dispersity, and composition using reversible addition-fragmentation chain transfer (RAFT) polymerization. Obtained polymers were shown to undergo facile functionalization with thiols through the thiol-disulfide exchange reaction revealing their post-polymerization modification amenity. We demonstrated the application of these benzothiazole disulfide groups containing copolymers to fabricate reversibly functionalizable surface coatings. To this end, poly(ethylene glycol) based copolymers containing PEG-monomethyl ether methacrylate (OEGMA, OEGMEMA), benzothiazole disulfide methacrylate (BDSMA), and 3-(trimethoxysilyl)propyl methacrylate (TMSPMA) monomers were used for coating of glass slides. These thiol-reactive polymeric surfaces could be functionalized using thiol-containing fluorescent dyes and cell-adhesive ligands. The reversible nature of the conjugation of fluorescent dyes is established by their release upon treatment with thiol-containing reducing agents such as dithiothreitol (DTT). The reversible nature of attachment is also exploited to attach cells onto peptide-modified polymeric coatings and their release under a reducing environment. One can envision that the ready availability of such thiol-reactive reactive polymers and interfaces obtained using them can find potential utilization in various biomedical applications where the reversible attachment is desirable.

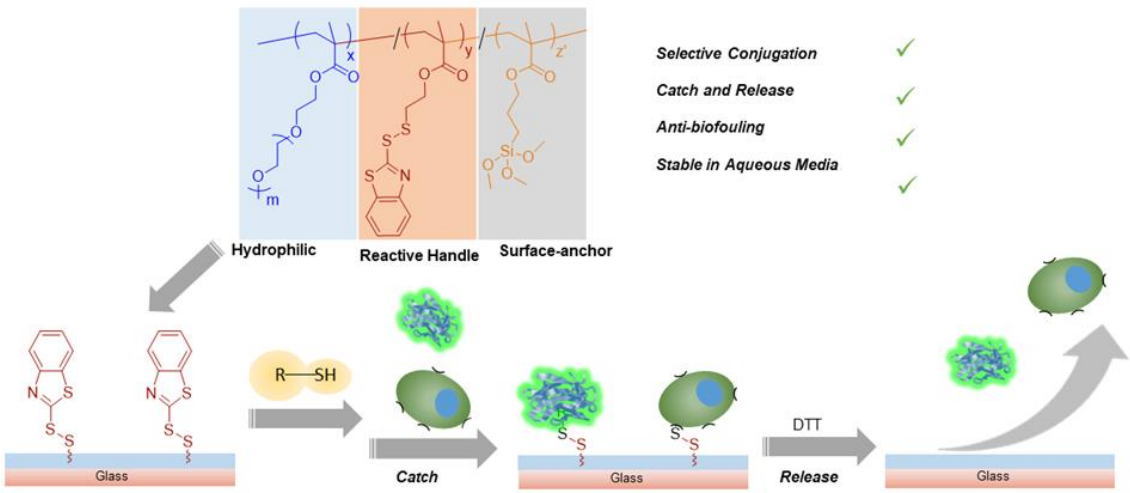

Figure 8.1. Schematic illustration of reversible conjugation on reactive polymeric thin film via a thiol-disulfide exchange reaction.

8.2. Experimental

8.2.1. Materials

Poly(ethylene glycol) methyl ether methacrylate (PEGMEMA, M_n = 300 g/mol) was obtained from Sigma-Aldrich and used after purification through activated aluminum oxide filtration. 2,2′-Dithiobis(benzothiazole) (MBTS), 2-mercaptoethanol, methacryloyl chloride, triethylamine, 2,2′-azobis(2-methylpropionitrile) (AIBN), 4-cyano-4-(phenylcarbonothioylthio)pentanoic acid, furfuryl mercaptan, 4′,6-diamidino-2-phenylindole (DAPI), 1,4-dithiothreitol (DTT), 3-(trimethoxysilyl)propyl methacrylate (TMSPMA), N-(5-fluoresceinyl)maleimide and 4-trifluoromethylbenzyl mercaptan were purchased from Sigma-Aldrich. The linear arginine-glycine-aspartate-cysteine (RGDC) peptide and 4',6-diamidino-2-phenylindole (DAPI) were obtained from Sigma-Aldrich. Alexa Fluor 488 Phalloidin was purchased from Invitrogen. A Live (calcein AM)-dead (propidium iodide) assay kit was obtained from Sigma-Aldrich. All the solvents and inorganic materials were obtained from Merck and used without further purification. Benzothiazole disulfide alcohol (BDSOH) [374] and thiol-bearing dye (BODIPY-SH) [335] were synthesized according to reported procedures.

8.2.2. Methods

^{1}H and ^{13}C NMR spectra were recorded on Bruker Avance Ultrashield 400 (400 MHz). Molecular weights of the synthesized polymers were estimated by size exclusion chromatography (SEC) using a PSS-SDV (length/ID 8 × 300 mm, 10 μm particle size) gram linear column calibrated with poly(methyl methacrylate) (PMMA) standards using a refractive-index detector with a mobile phase solution of 0.05 M lithium bromide in DMAc as eluent at a flow rate of 1 mL/min at 30 °C. Attenuated total reflectance Fourier transform infrared (ATR-FTIR) spectroscopy was collected on a Thermo Scientific Nicolet 380 FT-IR spectrophotometer. ATR-FTIR was equipped with a Harrick Scientific GATR accessory and a Ge crystal for surface analysis. Static water contact angle measurements via the sessile-drop method were performed in the air using a CAM 101 KSV goniometer. Images were obtained by an integrated digital camera observing the deionized water (5 μL)

deposited surface. Data process and contact angle determination were carried out by using CAM2008 software. Contact angle values were taken from three different locations of each sample, and average data was reported. Ultraviolet-visible spectroscopy studies were conducted on a Shimadzu UV 1800 spectrophotometer. Cytotoxicity experiments were done with a plate reader (Multiscan FC, Thermo Scientific, USA), using Cell Counting Kit-8 (CCK-8, Fluka). Images of attached and released cell images were obtained using a Zeiss Observer Z1 fluorescence microscope with Axiocam MRc5 camera with a Zeiss Filter set 38. Atomic force microscopy determined polymer film thickness using a CoreAFM instrument (Nanosurf, Switzerland).

8.2.3. Synthesis of Benzothiazole-Disulfide Methacrylate Monomer (BDSMA)

The monomer synthesis was carried out following a previously reported procedure with slight modifications [375]. BDSOH (1.00 g, 4.10 mmol) was dissolved in anhydrous dichloromethane (30 mL) trimethylamine (1.70 mL, 12.30 mmol) was added. The solution was cooled to 0 ^{o}C, and at 0 ^{o}C, methacryloyl chloride (0.5 mL, 5.3 mmol) was dropwise added to the mixture. The reaction mixture was stirred for two h at 0 °C and subsequently at ambient temperature for 16 h under nitrogen. After the reaction, the solution was washed with saturated $NaHCO_3$ (2 × 20 mL) and H_2O (2 × 20 mL). The organic layer was separated and dried over Na_2SO_4, concentrated in vacuo to yield a yellow residue. The residue was purified by column chromatography (EtOAc: Hexane 1: 9) to yield 0.92 g (72 % yield). ^{1}H NMR (400 MHz, $CDCl_3$) δ/ppm: 7.87 (d, l H, *J* = 8.0 Hz), 7.80 (d, l H, *J* = 8.0 Hz), 7.44 (t, l H, *J* = 8.0 Hz), 7.34 (t, l H, *J* = 8.0 Hz), 6.13 (s, 1H), 5.58 (m, 1H), 4.48 (t, 2 H, *J* = 8 Hz), 3.25 (t, 2 H, *J* = 8.0 Hz), 1.93 (s, 3H); ^{13}C NMR (100 MHz, $CDCl_3$) δ/ppm: 171.76, 167.17, 155.13, 136.02, 135.96, 126.50, 126.42, 124.91, 122.43, 121.30, 62.61, 38.21, 18.61. MS (ESI^+): *m/z* 312.20 (calcd. for $[M]^+$ 312.0108).

8.2.4. Synthesis of PEGMA-BDSMA Copolymer (P(P_x-B_y))

For the synthesis of P(P_{80}-B_{20}) copolymer, BDSMA (100 mg, 0.32 mmol), PEGMEMA (385 mg, 1.28 mmol), AIBN (0.32 mg, 0.002 mmol), and 4-cyano-4-(phenyl carbonothioylthio)pentanoic acid (5.5 mg, 0.02 mmol) were dissolved in 1,4-dioxane (1.6 mL). The mixture was purged with argon gas for 15 min. After purging, the mixture was

stirred at 70 ^{o}C for 16 h. After polymerization, the polymer was precipitated in cold diethyl ether. The obtained copolymer was characterized ^{1}H NMR, SEC, and FTIR. Other copolymers, P(P_{90}-B_{10}) and P(P_{70}-B_{30}), were synthesized using the same procedure by varying the monomer ratios in the feed.

8.2.5. Synthesis of PEGMA-BDSMA-TMSPMA Copolymer (P(P_x-B_y-T_z))

Given the RAFT polymerization procedure for P(P_x-B_y), copolymers are applied in terms of temperature, time, and monomer concentration. Copolymers P(P_{85}-B_{10}-T_5) and P(P_{65}-B_{30}-T_5) were synthesized by varying the monomer ratios in the feed. Thus, obtained copolymers were characterized by using SEC and ^{1}H NMR.

8.2.6. Release of Benzothiazolethione Moiety under Reducing Conditions

The release of benzothiazolethione from P(P_{90}-B_{10}) and P(P_{70}-B_{30}) copolymers was studied. For this purpose, 5 mg copolymer was taken in a UV cuvette and incubated with 3 mL of 1 x PBS solution containing 10 mM DTT as a reducing agent. At pre-determined time intervals, UV-Vis analysis was performed to read the absorbance at 320 nm, which belongs to the released benzothiazolethione group. The release graph was drawn using a calibration curve.

8.2.7. Post-Polymerization Modification of P(P_{80}-B_{20}) using Thiol-containing Molecule

Copolymer (100 mg, 0.009 mmol) and furfuryl mercaptan (3.0 mol equivalent of BDS groups) were dissolved in dichloromethane (5 mL) under an argon atmosphere. A catalytic amount of glacial acetic acid was added, and the mixture was stirred at ambient temperature for 3 hours. Purification by precipitating the reaction mixture into cold diethyl ether afforded the side chain disulfide functionalized polymer.

8.2.8. Fabrication of Polymeric Coatings on Glass Surfaces

Glass surfaces (22 × 22 mm) were cleaned sequentially using water (5 mL), acetone (5 mL), and isopropanol (5 mL). They were sonicated in these solvents for 10 minutes and then dried under a stream of nitrogen. Finally, glass surfaces were cleaned by placing them in a Novascan PSD series UV/Digital ozone system for 15 min.

Polymer solution (50 µL, 20 mg/mL in anhydrous DMF) was spread over each surface. They were left open to air for 24 hours at room temperature to let the solvent evaporate. Surfaces were placed into the vacuum oven at 60 ^{o}C for 1 h. After that, surfaces were washed and sonicated in DMF and THF for 2 minutes to remove non-adhered polymer from the surface, and then surfaces were dried under a stream of nitrogen. Surfaces were kept under nitrogen.

8.2.9. Functionalization of Polymer Coatings with 4-Trifluoromethylbenzyl Mercaptan (TFBM)

4-trifluoromethylbenzyl mercaptan (TFBM) solution (10 mg/mL) was prepared in anhydrous DMF, and a catalytic amount of AcOH (0.91 mmol, 52 µL) was added. 100 µL from this solution was spread over S(P_{85}-B_{10}-T_5), S(P_{65}-B_{30}-T_5), and S(P_{95}-B_0-T_5) surfaces. They were left for 24 h. Afterward, surfaces were washed with DMF and THF several times and dried under a nitrogen stream.

8.2.10. Functionalization of Polymer Coatings with Thiol-containing Dye

BODIPY-SH solution (1 mg/mL) in anhydrous DMF containing catalytic amount AcOH (2.4 µL) was spread over each BDS functionalized surface. They were left for 5 h. Afterward, surfaces were washed with DMF and THF several times and dried under a nitrogen stream.

8.2.11. Cleavage of Dye from Surface

$S(P_{95}\text{-}B_0\text{-}T_5)$, $S(P_{85}\text{-}B_{10}\text{-}T_5)$, and $S(P_{65}\text{-}B_{30}\text{-}T_5)$ polymer film surfaces were immersed in DTT solution in DMSO (10 mM) for 3 h. After washing with a copious amount of DMSO and THF, they were dried under a stream of nitrogen.

8.2.12. Functionalization of Thiol-containing Polymer Film with Maleimide-conjugated Fluorescein

Thiol functionalized $S(P_{85}\text{-}B_{10}\text{-}T_5)$ surface after cleaving with DTT was immersed in maleimide-functionalized fluorescein (Fluo-MAL) solution in DMF (1mg/mL) for 3 h. After washing with a gentle amount of DMF and THF, the dye-conjugated surface was dried under a stream of nitrogen.

8.2.13. Functionalization of Polymer Coatings with Thiol-containing Peptide

Cell adhesive peptide linear RGD-SH solution (1 mg/mL) in anhydrous DMF containing catalytic amount AcOH was spread over $S(P_{85}\text{-}B_{10}\text{-}T_5)$ surfaces. They were left for 5 h. Afterward, surfaces were washed with DMF and THF several times and dried under a nitrogen stream.

8.2.14. Cell Attachment on Peptide Functionalized Films

In this experiment, L929 mouse fibroblast cells were used. Fibroblast cells were grown in a 5% CO_2-containing atmosphere at 37 °C and cultured in Dulbecco's Modified Eagle's Medium (DMEM) media supplemented with 10% fetal bovine serum (FBS) (PAN Biotech). L-929 fibroblast cells (75000 cells/600µL) were seeded onto polymer-coated glass slides (22 x 22 mm) and incubated at 37 °C in a 5% CO_2-containing atmosphere for two h. After 2 hours, cell media (1 mL) was added to each well which contained polymer-coated glass slides. After 24 h incubation duration, cell media was removed, glass slides were washed with 1 x PBS (1 mL, 3 times), and cells were fixed with 3.7% formaldehyde solution in PBS for 10 min at room temperature. After fixation, cells were washed with 1 x PBS (1 mL, three times). For staining filamentous actins (F-actins), cells were incubated with 0.1%

Triton X-100 in PBS for 5 min. After washing with 1 x PBS (1 mL, three times), cells were incubated with Alexa Fluor 488 phalloidin solution (5 units/mL) in PBS containing 1% bovine serum albumin (BSA) for 20 min at room temperature. After being washed three times with PBS, cell nuclei were stained with DAPI for 10 min at room temperature. After DAPI staining, cells were washed with 1 x PBS. The resulting images of cells attached to glass surfaces were taken using a fluorescence microscope and processed via Zeiss Zen Blue lite software (Carl Zeiss, Jena, Germany).

8.2.15. Cell Detachment from Peptide Functionalized Films and Live-Dead Assay

L929 fibroblast cells (350000 cells) were seeded on the RGD functionalized polymer film ($S(P_{85}\text{-}B_{10}\text{-}T_5)$-RGD) and incubated at 37 ^oC with 5% CO_2 for 24 h. Subsequently, cell-attached surfaces were set with 5 mM DTT solution for 20 min. Afterward, detached cells were washed with 1 x PBS (3 times) and stained with a live/dead assay kit. For the assay solution, 10 µL calcein-AM and 5 µL propidium iodide solutions were taken from the assay kit and diluted with 1 x PBS (5 mL). Subsequently, cells were incubated with this assay solution at 37 ^oC with 5% CO_2 for 20 min. Finally, cells were washed with 1 x PBS (3 times), and live/dead cell viability was visualized by fluorescence microscopy.

8.3. Results and Discussion

8.3.1. Synthesis and Characterization of BDSMA Monomer

BDS-alcohol (BDS-OH) was prepared according to a literature procedure using 2,2'-dithiobis(benzothiazole) (MBTS) and 2-mercaptoethanol [374]. For BDSMA monomer synthesis, a previously reported technique with slight modifications was adapted [375]. The reaction between BDS-OH and methacryloyl chloride gave BDSMA monomer a 72% yield, and the synthesis scheme is shown in Figure 8.2.

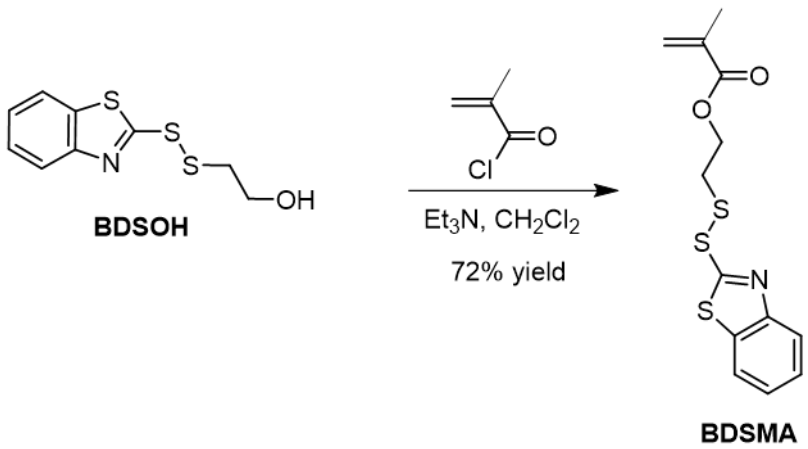

Figure 8.2. The synthesis of BDSMA monomer.

The BDSMA monomer was characterized by ^{1}H NMR and ^{13}C NMR,). As seen in Figure 8.3, the hydrogen signals of the methacrylate group (e,f labeled) were observed at 6.13 and 5.58 ppm. Hydrogens (i marked) of the methyl group in the methacrylate part were resonance at 1.93 ppm. In addition to these peaks, aromatic hydrogen signals (a, b, c, and d labeled) belonging to the BDS group revealed between 7.89 - 7.32 ppm.

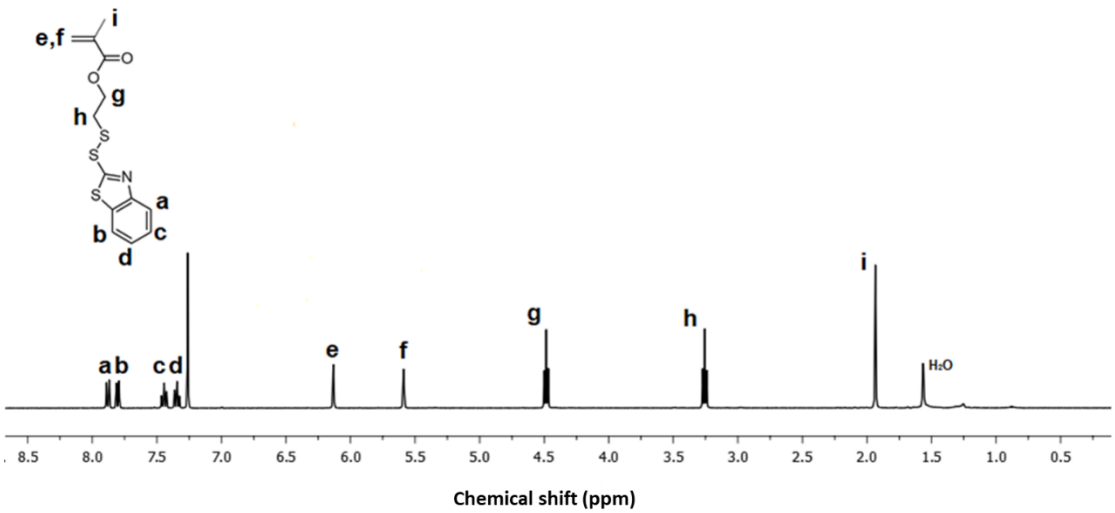

Figure 8.3. The ^{1}H NMR spectrum of BDSMA monomer in $CDCl_3$.

In addition to ^{1}H NMR, carbon NMR showed 13 different carbon atoms. ^{13}C NMR spectrum is shown in Figure 8.4. Therefore, NMR analysis put forward a successful synthesis of the BDSMA monomer.

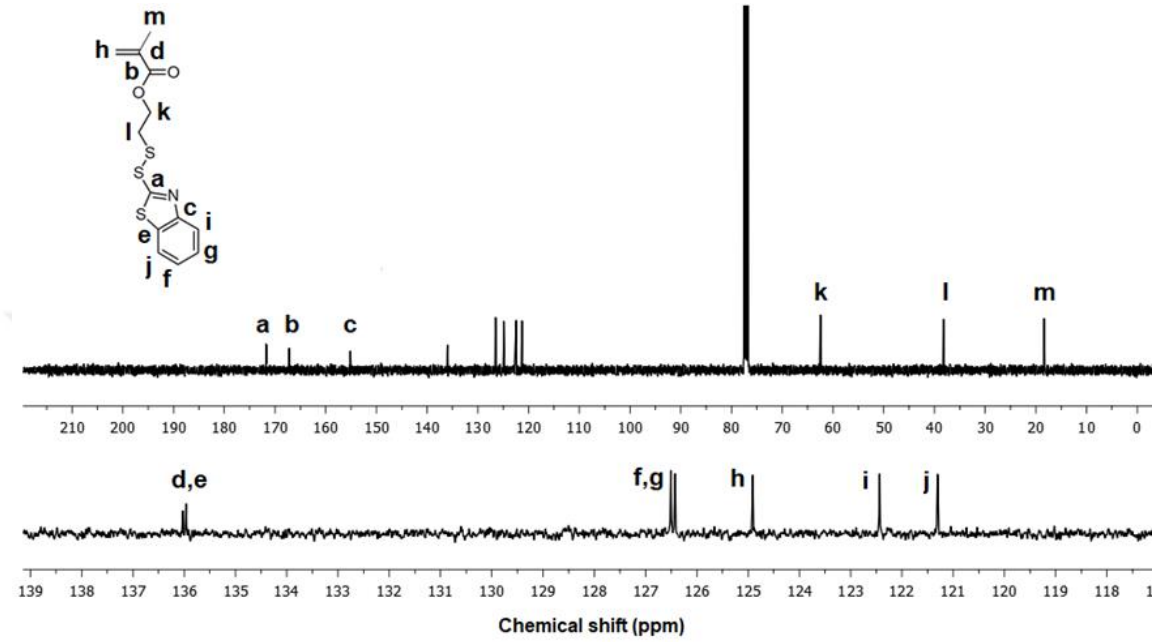

Figure 8.4. ^{13}C NMR spectrum of BDSMA monomer in $CDCl_3$.

8.3.2. Synthesis and Characterization of BDSMA-containing Copolymers

RAFT copolymerization of BDSMA monomer with hydrophilic PEGMEMA monomer under AIBN-initiated conditions was investigated. Copolymers employing varying amounts of the thiol-reactive monomer were synthesized using a benzodithioate derivative chain transfer agent. Moderately high monomer conversions were attained at 70 °C reaction temperature using dioxane ($[M]_o$: 1 M) as a solvent. ^{1}H NMR and SEC analysis characterized obtained copolymers.

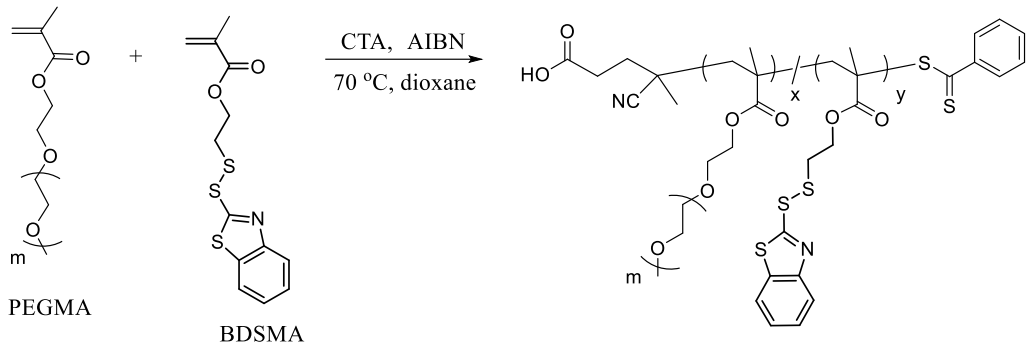

Figure 8.5. BDS-based copolymer (P(Px-By)) is synthesized via RAFT polymerization.

Table 8.1. Polymerization conditions and characterization data of BDSMA-PEGMA copolymers.

No	**Polymer**	$F_{theo.}$ **(%)**	$F_{calc.}$ **(%)**	**Conv. (%)**	$M_{n,theo}$ **(g/mol)**	$M_{n,NMR}$ **(g/mol)**	$M_{n,SEC}$ **(g/mol)**	M_w/M_n
1	$P(P_{90}\text{-}B_{10})$	90: 10	91.9: 8.1	82	19750	14800	18100	1.22
2	$P(P_{80}\text{-}B_{20})$	80: 20	85.2: 15.8	78	18800	11300	16900	1.26
3	$P(P_{70}\text{-}B_{30})$	70: 30	78.6: 23.4	72	17400	14100	13600	1.31
4	$P(P_{0}\text{-}B_{100})$	100: 0	-	69	17200	13800	10200	1.53

Structural analysis of copolymers was done with ^{1}H NMR. The NMR spectrum of $P(P_{80}\text{-}B_{20})$ copolymer is given in Figure 8.6. Proton signals belonging to the benzothiazole unit were observed at 7.86 ppm, 7.45 ppm, and 7.36 ppm. In addition to these peaks, methyl hydrogens of the methoxy end group of PEGMEMA revealed at 3.37 ppm. Characteristic methylene protons of BDSMA monomer adjacent to the ester group were observed at 4.28 ppm. Furthermore, hydrogens of methacrylate groups disappeared after polymerization. These observations demonstrated that BDSMA and PEGMA monomers were successfully copolymerized. Various incorporation degrees of BDSMA into copolymers were determined by integrating the proton signal of the functional monomer at 4.28 ppm with the terminal methoxy group signal of the PEGMA monomer at 3.37 ppm. Also, copolymers were characterized by SEC analysis. Polymerization conditions and characterization results

were tabulated in Table 8.1. In addition, ^{1}H NMR spectra of P(P_{90}-B_{10}) and P(P_{70}-B_{30}) copolymer were given in Figure A19.

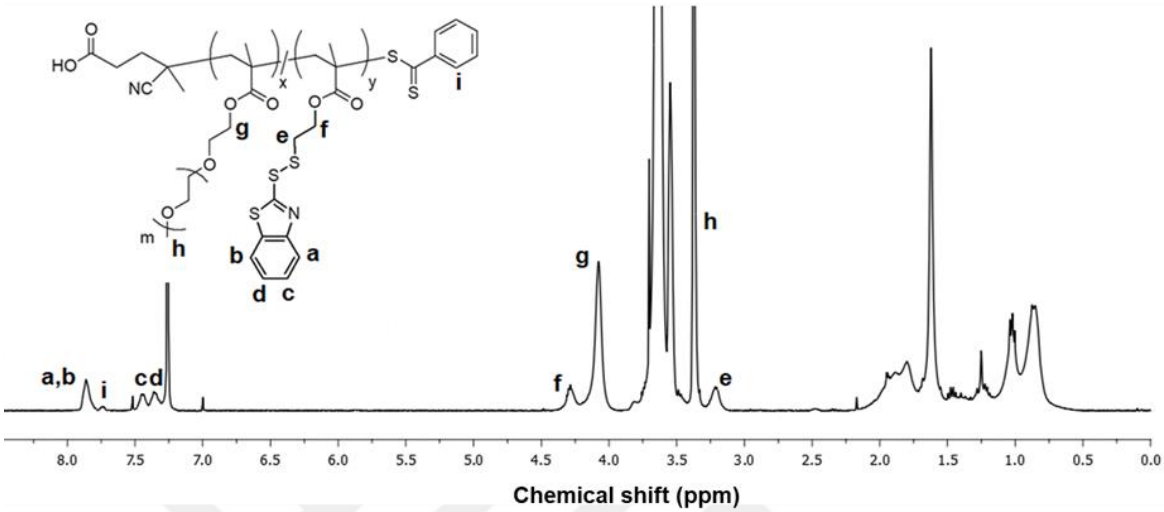

Figure 8.6. ^{1}H NMR spectrum of copolymer P(P_{80}-B_{20}) in $CDCl_3$.

8.3.3. Release of Benzothiazolethione from Copolymers

The release of the benzothiazolethione group from copolymer was studied in pH 7.4 PBS buffer in the presence of 1,4-dithiothreitol (DTT). The cleavage of the benzothiazolethione group was due to the thiol-disulfide exchange reaction. The spectroscopic signature of the released benzothiazolethione (λ_{max}: 320 nm) in Figure 8.7b shows a distinctly different absorption band from the spectrum of the benzothiazole disulfide group (λ_{max}: 253 nm) in the copolymer P(P_{70}-B_{30}). Upon treatment of the copolymers P(P_{90}-B_{10}) and P(P_{70}-B_{30}) carrying different amounts of BDS groups with DTT (10 mM), a fast release of benzothiazolethione was accounted for in the first hour. The release continued over time, reaching a total release of >95% for P(P_{90}-B_{10}) and >85% for P(P_{70}-B_{30}) after 16 h, and it was shown in Figure 8.7c. The slightly slower disulfide reduction of copolymer carrying higher BDS functionality could be attributed to the hydrophobic nature of the BDS group resulting in increased hydrophobicity-induced folding of polymer chains, thus limiting accessibility in the aqueous medium.

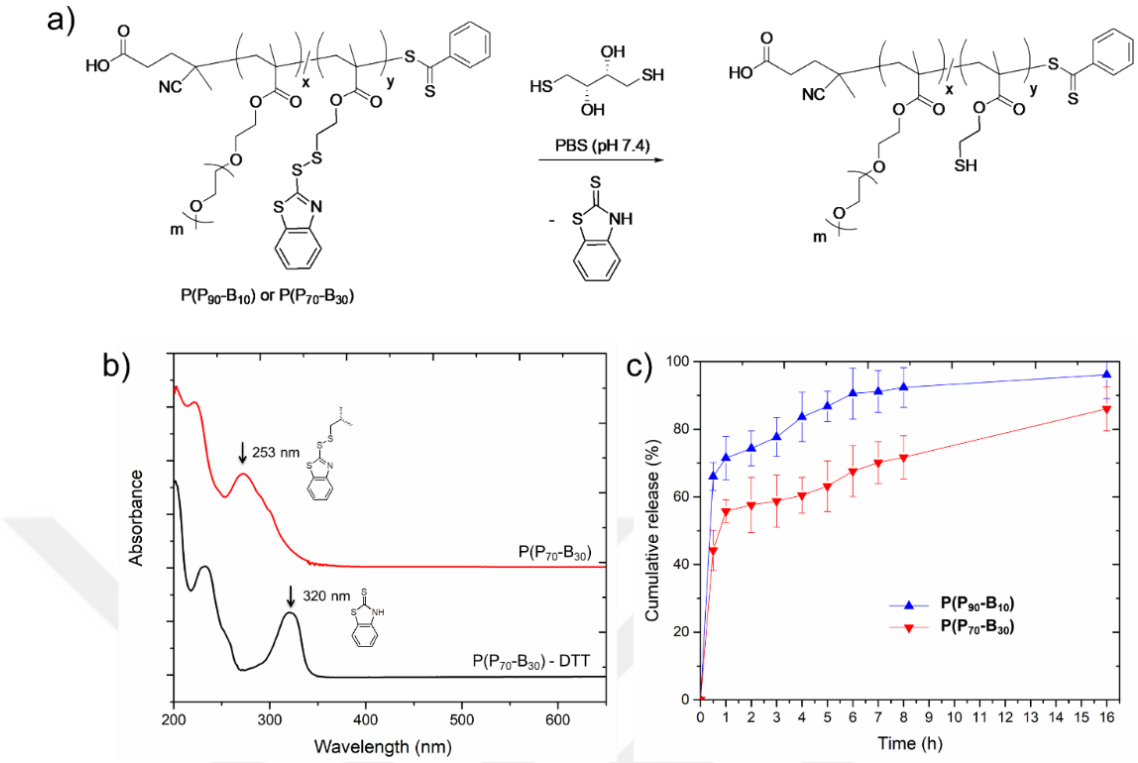

Figure 8.7. (a) Release of benzothiazole group upon with DTT, (b) UV-Vis spectra of copolymer P(P_{70}-B_{30}) before and after 10 mM DTT solution, (c) Benzothiazolethione release profiles of copolymers P(P_{90}-B_{10}) and P(P_{70}-B_{30}) after treatment with 10 mM DTT.

8.3.4. Post-Polymerization Modification of P(P_{80}-B_{20}) Copolymer

The modification of the P(P_{80}-B_{20}) copolymer was investigated using a thiol-disulfide exchange reaction. For that purpose, furfuryl mercaptan was used and reacted with P(P_{80}-B_{20}) in the presence of the catalytic amount of acetic acid. ^{1}H NMR characterized the functionalized copolymer. The functionalized copolymer demonstrated characteristic furan proton signals at 7.43, 6.35, and 6.30 ppm chemical shifts in the spectrum shown in Figure 8.8b. The disappearance of aromatic benzothiazole proton signals at 7.86, 7.45, and 7.36 ppm also suggested the high functionalization efficiency.

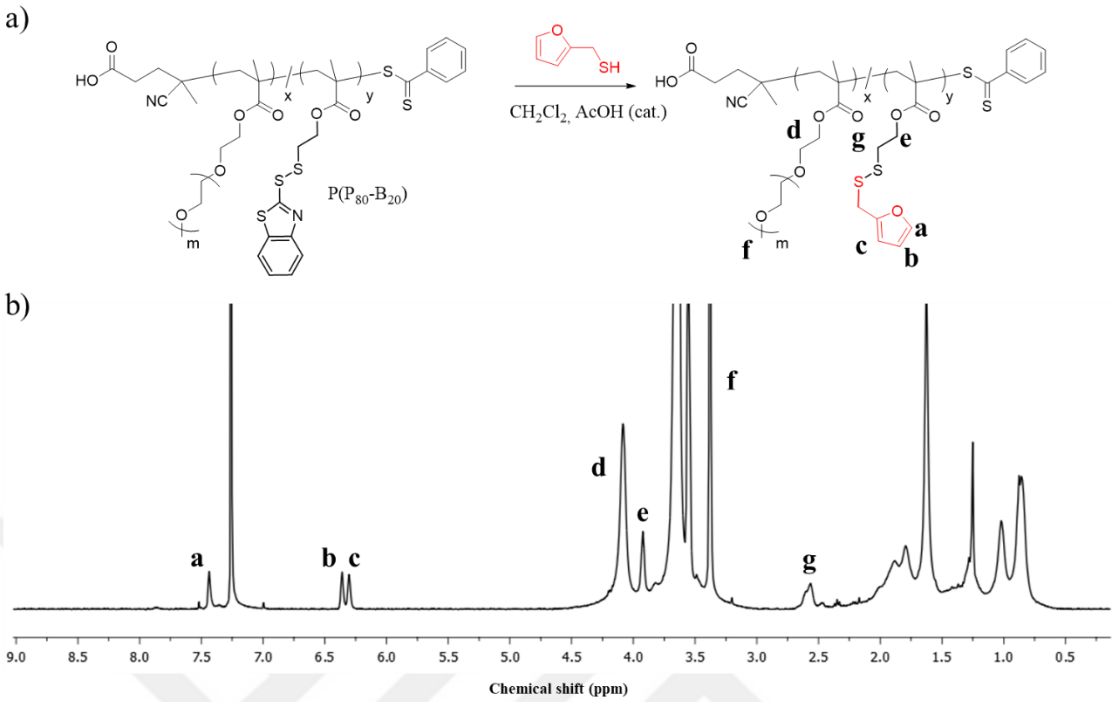

Figure 8.8. (a) Post-polymerization modification of copolymer P(P_{80}-B_{20}) with furfuryl mercaptan via thiol-disulfide exchange reaction and (b) ^{1}H NMR spectrum of the functionalized copolymer.

8.3.5. Synthesis and Characterization of Surface Reactive Copolymers

PEGMA, BDSMA, and TMSPMA-containing copolymers were synthesized with different monomer ratios via RAFT polymerization. TMSPMA unit, which provides surface attachment, was kept constant in these copolymers. PEGMA monomer provided these copolymers with anti-biofouling properties. BDSMA monomer was responsible for polymer modification in the presence of thiol-containing molecules. Their different surface attachable copolymers were prepared. The first copolymer was composed of PEGMA:BDSMA:TMSPMA with an 85:10:5 feed ratio, and the copolymer was named P(P_{85}-B_{10}-T_5). The second copolymer consisted of PEGMA:BDSMA:TMSPMA with a 65:30:5 feed ratio, and the copolymer was named P(P_{65}-B_{30}-T_5). The third copolymer contained only PEGMA and TMSPMA monomers with a 95:5 feed ratio, and this copolymer was abbreviated as P(P_{95}-B_0-T_5). To prevent any unwanted crosslinking, the

surface-attachable alkoxysilane-containing monomer was maintained to 5% in the feed, sufficient to anchor the functional copolymer onto glass surfaces [376].

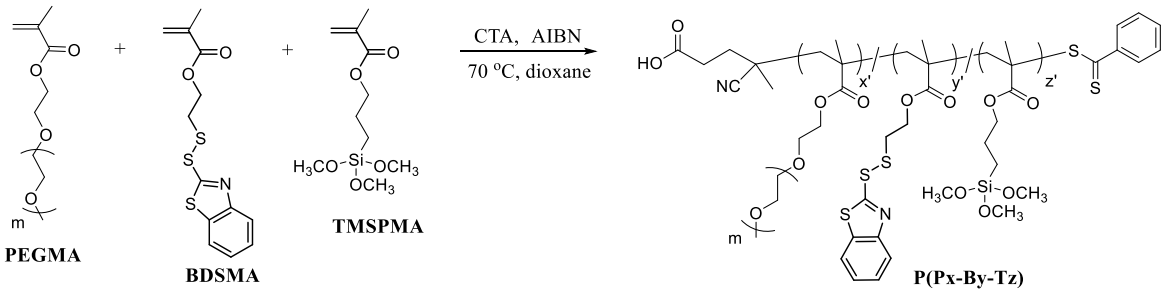

Figure 8.9. The synthesis of surface-attachable copolymer ($P(P_x\text{-}B_y\text{-}T_z)$).

Table 8.2. Polymerization conditions and characterization data of BDSMA-PEGMA-TMSPMA copolymers.

No	**Polymer**	$F_{theo.}$ **(%)**	$F_{calc.}$ **(%)**	**Conv. (%)**	$M_{n,theo}$ **(g/mol)**	$M_{n,NMR}$ **(g/mol)**	$M_{n,SEC}$ **(g/mol)**	M_w/M_n
1	$P(P_{95}\text{-}B_0\text{-}T_5)$	95: 0	-	84	21100	16700	19200	1.42
2	$P(P_{85}\text{-}B_{10}\text{-}T_5)$	85: 10	85: 8.8	81	19600	13300	14700	1.36
3	$P(P_{65}\text{-}B_{30}\text{-}T_5)$	65: 30	65: 26.2	74	18100	14100	15400	1.39

Copolymer $P(P_{95}\text{-}B_0\text{-}T_5)$ was synthesized for control experiments. After synthesis and purifications, all copolymers were characterized by NMR and SEC analysis. The polymerization conditions and SEC results were tabulated in Table 8.2. Obtained polymers showed moderately high monomer conversions, and SEC analysis revealed good molecular weight control on polymerization with relatively narrow polydispersities.

The ^{1}H NMR analysis of these copolymers revealed efficient incorporation of BDSMA monomer into the structure. Benzothiazole proton signals were observed between 7.85-7.35 ppm. Copolymer content determination via integration of signature PEGMA and BDSMA protons showed comparable incorporation of these monomers to the copolymers devoid of alkoxysilane-containing monomer.

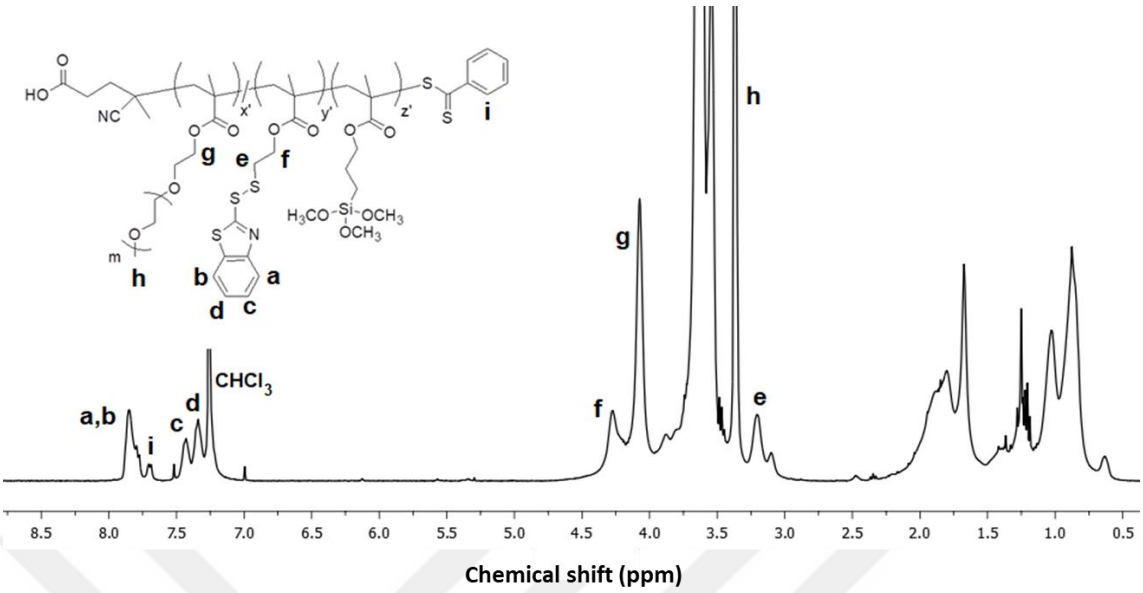

Figure 8.10. ^{1}H NMR spectrum of copolymer P(P_{65}-B_{30}-T_5) in $CDCl_3$.

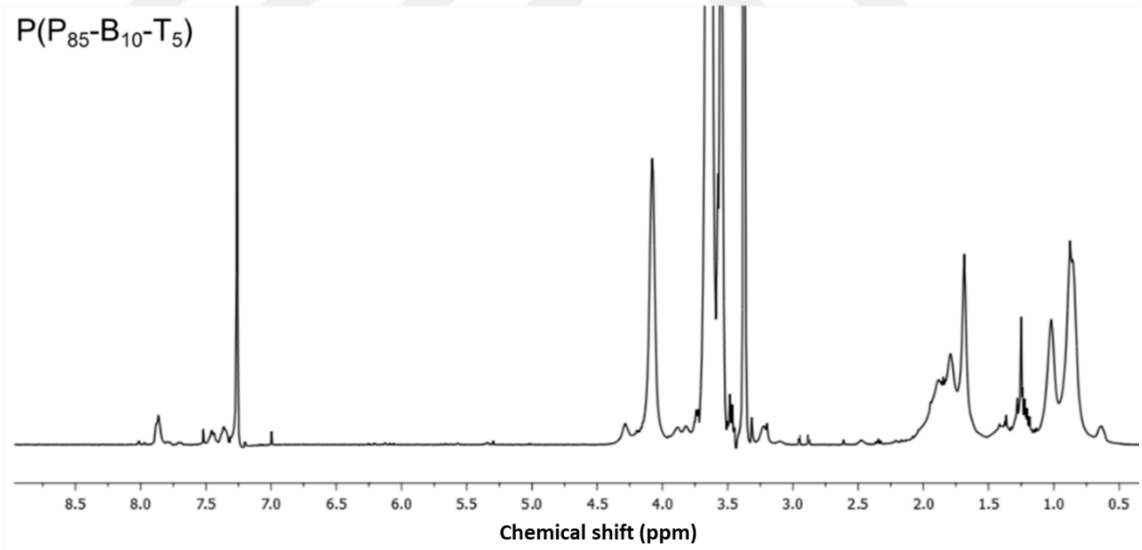

Figure 8.11. ^{1}H NMR spectrum of copolymer P(P_{85}-B_{10}-T_5) in $CDCl_3$.

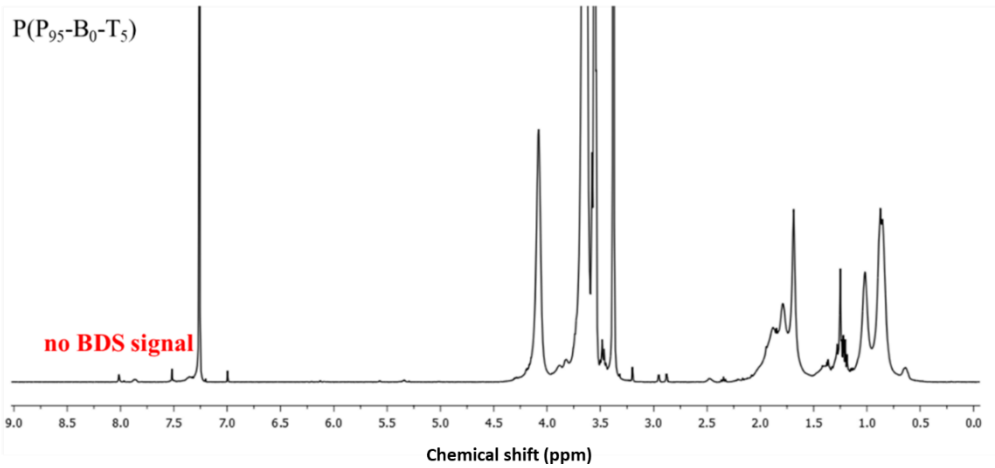

Figure 8.12. ^{1}H NMR spectrum of control copolymer P(P_{95}-B_0-T_5) in $CDCl_3$.

Incorporation of the BDSMA monomer in copolymers was also examined by using FT-IR. As expected, higher vibrational bands of C-N stretchings at 1425 cm^{-1} and C-S stretchings at 1005 cm^{-1} group were observed by increasing the BDSMA content in the copolymers. FT-IR spectra are shown in Figure 8.13.

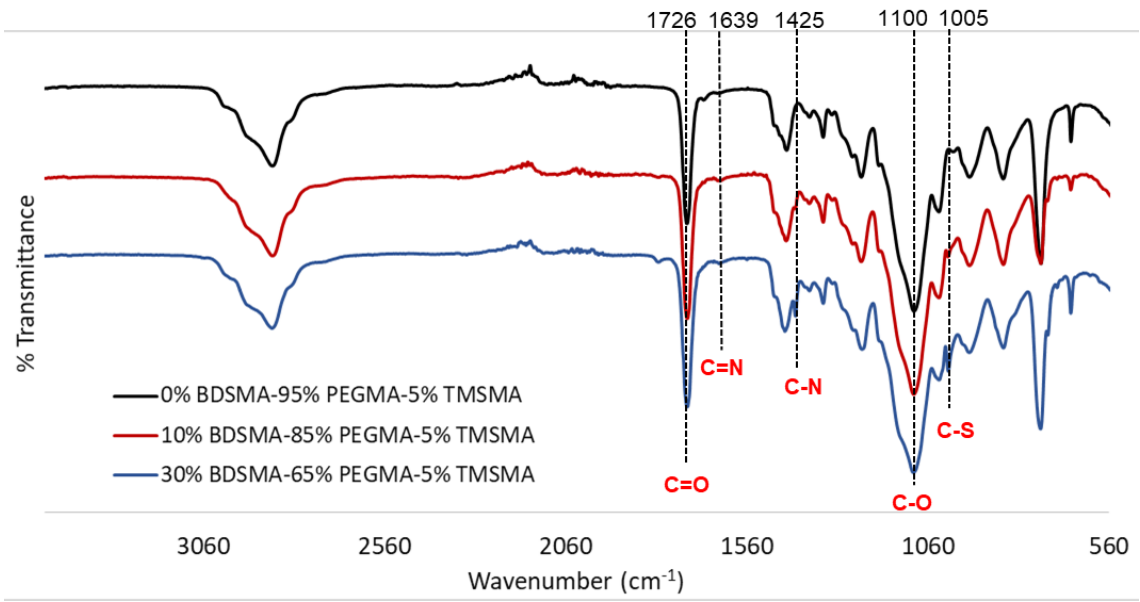

Figure 8.13. FT-IR spectra of P(P_{95}-B_0-T_5) (black line), P(P_{85}-B_{10}-T_5) (red line), and P(P_{65}-B_{30}-T_5) (blue line).

8.3.6. Fabrication and Characterization of Polymer Coating on Glass Surface

Cleaned glass surfaces were treated with copolymer solution for reversible thiol-reactive polymer coatings. For this purpose, three different copolymer solutions (20 mg/mL) were prepared and spread over each glass surface. After keeping open air overnight, surfaces were put into a vacuum oven at 60 ^{o}C for 1 h. Polymer film formation and covalent attachment were due to the TMSPMA monomer that reacted trialkyl silane groups with hydroxyl groups on the glass surface. After the preparation of polymer films, they were named as S(P_{95}-B_0-T_5), S(P_{85}-B_{10}-T_5), and S(P_{65}-B_{30}-T_5).

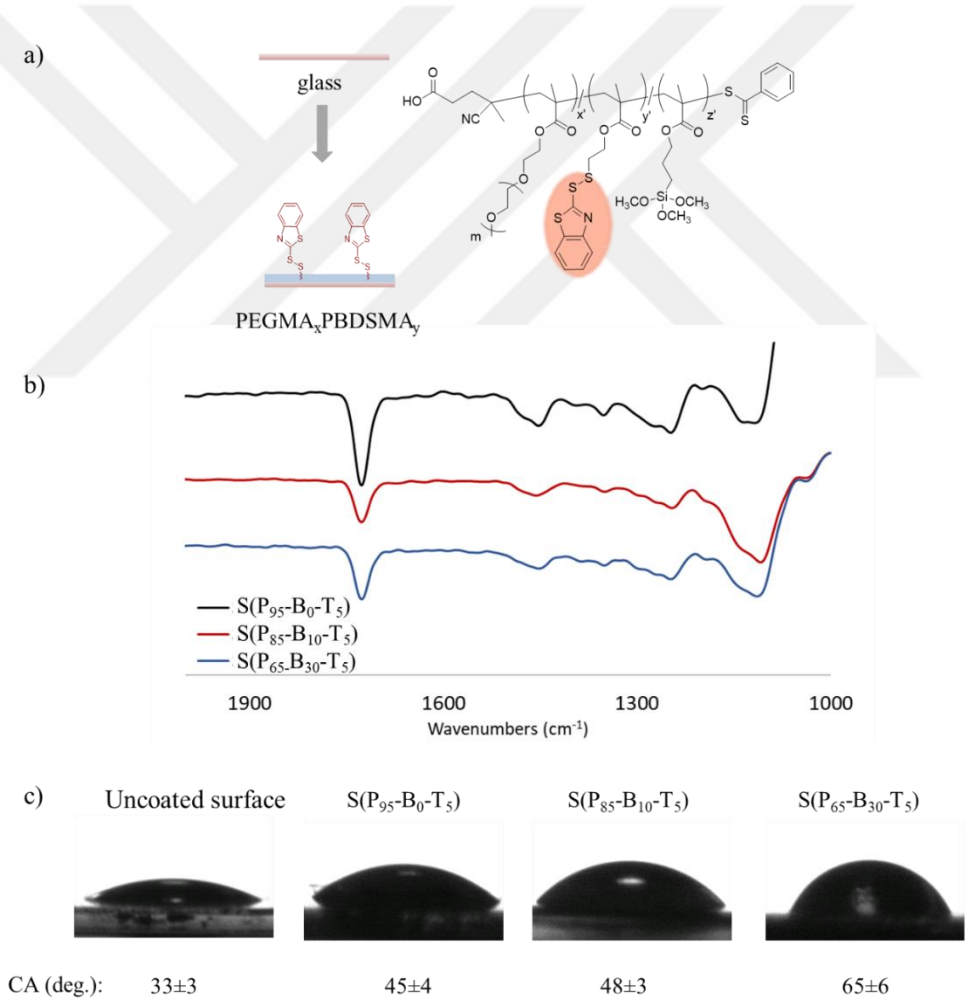

Figure 8.14. (a) Schematic illustration of polymer coatings, (b) ATR-FTIR spectrum of polymer-coated surfaces, and (c) water contact angle of polymer-coated surfaces.

The characterization of polymer-coated surfaces was achieved by FTIR analysis, contact angle, and AFM measurements. FTIR data is shown in Figure 8.14b. The average film thickness of polymer coatings was determined as 255 ± 2 nm by AFM analysis. Polymer-coated surfaces displayed high water contact angles by increasing the hydrophobic BDS groups in the copolymer structure, and data were shown in Figure 8.14c.

In addition to FTIR and contact angle measurements, polymer-coated surface (S(P_{85}-B_{10}-T_5) was characterized by XPS analysis. The XPS survey scan of S(P_{85}-B_{10}-T_5) revealed C1s and O1s signals at 285.0 and 532.0 eV, respectively. The C1s high resolution could be deconvoluted into 3 Gaussians with the expected relative areas for three carbon atoms at 288.9 eV (C=O), 286.5 (C-O-C/C-S/C-N), and 285 eV (C-C). Figure 8.15c shows S's high-resolution XPS N1s spectra (P_{85}-B_{10}-T_5), where the characteristic N atom peak was visible at 400.0 eV. The S2p peak of sulfur in the BDS groups was observed at 164.2 eV, and data were given in Figure 8.15d.

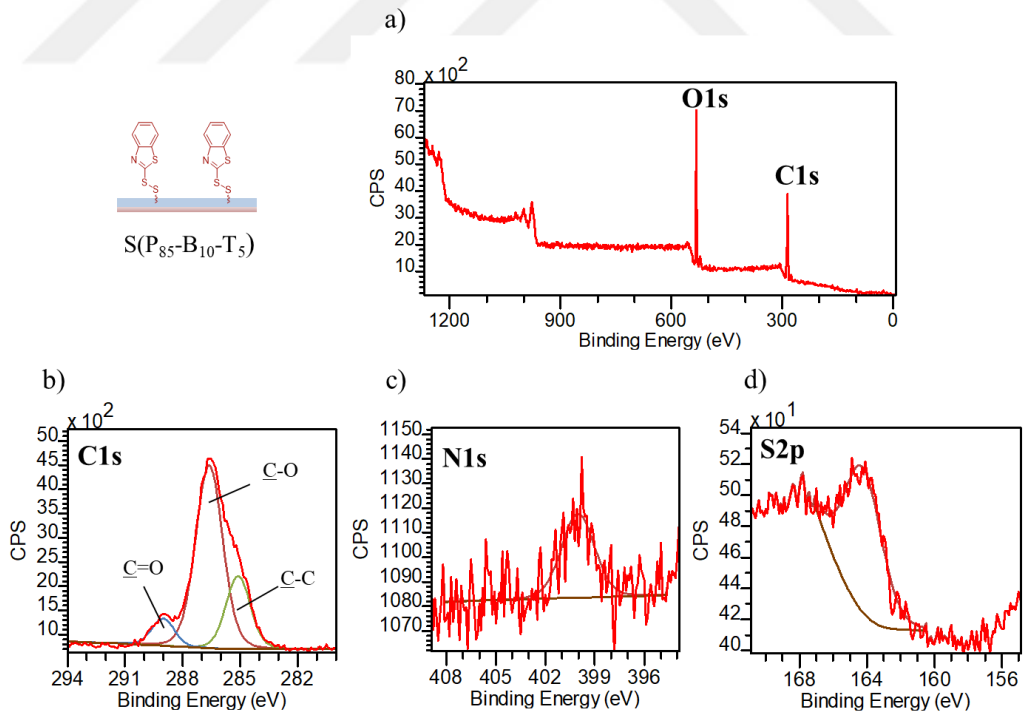

Figure 8.15. (a) XPS survey scan of S(P_{85}-B_{10}-T_5), (b) C1s high resolution, (c) N1s high resolution, and (d) S2p high-resolution spectra of S(P_{85}-B_{10}-T_5).

8.3.7. Surface Modification with TFBM via Thiol-Disulfide Exchange Reaction

$S(P_{95}\text{-}B_0\text{-}T_5)$, $S(P_{85}\text{-}B_{10}\text{-}T_5)$, and $S(P_{65}\text{-}B_{30}\text{-}T_5)$ polymer surfaces were treated with thiol-containing trifluoromethylbenzyl mercaptan (TFBM). Surface modification was achieved in the presence of the catalytic amount of acetic acid via the thiol-disulfide exchange reaction. After the reaction, all surfaces were washed with DMF and THF, and then they were characterized by contact angle measurement and XPS analysis.

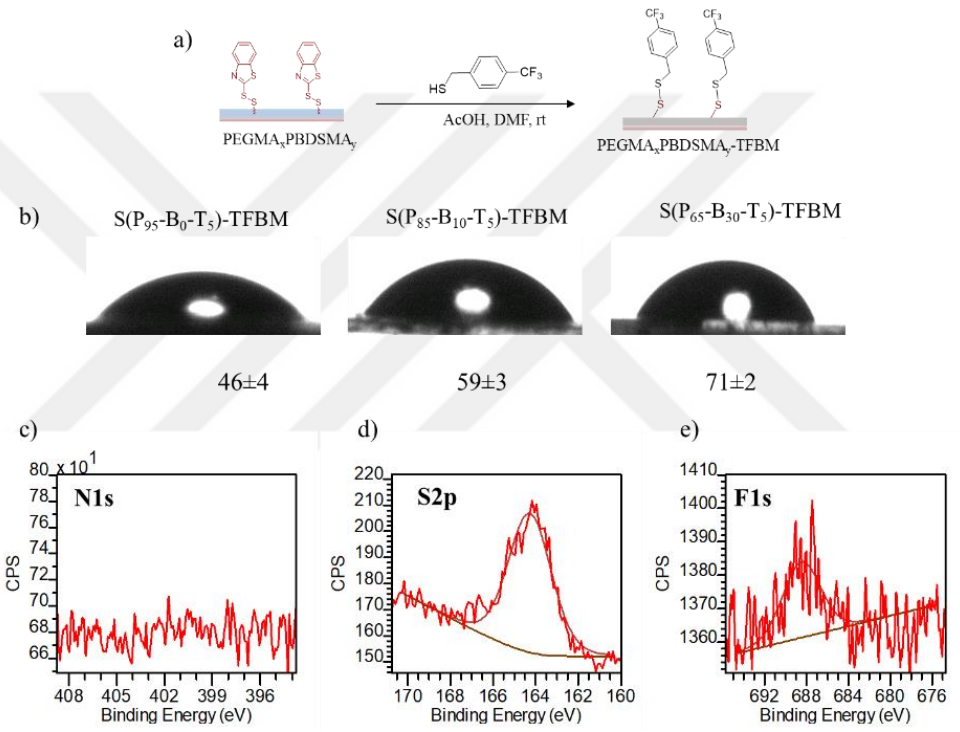

Figure 8.16. (a) Conjugation of TFBM to the reactive polymer-coated glass surface, (b) water contact angle of polymer-coated surfaces, (c) N1s high resolution, (d) S2p high resolution, and (e) F1s high-resolution spectra of $S(P_{85}\text{-}B_{10}\text{-}T_5)$-TFBM.

TFBM-conjugated glass surfaces showed an increase in water contact angle with an increasing amount of the hydrophobic BDSMA monomer. While the contact angle values of $S(P_{85}\text{-}B_{10}\text{-}T_5)$ and $S(P_{65}\text{-}B_{30}\text{-}T_5)$ were 48 ± 3 and 65 ± 6, respectively, these values were found as 59 ± 3 and 71 ± 2 after conjugation of hydrophobic TFBM moiety. In addition, the functionalization of $S(P_{85}\text{-}B_{10}\text{-}T_5)$ with TFBM was confirmed using XPS spectroscopy. While $S(P_{85}\text{-}B_{10}\text{-}T_5)$ showed N1s signal at 400 eV, this characteristic peak in Figure 8.16c

disappeared after the conjugation of TFBM. The existence of F1s peak in XPS also supported successful conjugation. The high-resolution F1s scan revealed a signal at 688 eV.

8.3.8. Reversible Attachment of Thiol-containing Dye on Polymer Coated Surfaces

The reversibility of polymer coating was explored with BODIPY-thiol. S(P_{95}-B_0-T_5), S(P_{85}-B_{10}-T_5), and S(P_{65}-B_{30}-T_5) polymer surfaces were reacted with thiol-containing fluorescent BODIPY dye in the presence of acetic acid via thiol-disulfide exchange reaction. The surface characterization was done by fluorescence microscopy. The controlled experiment of dye conjugation onto polymer-coated surface S(P_{95}-B_0-T_5) lacking BDS groups resulted in no appreciable fluoresce intensity, which demonstrated that the origin of fluorescence is not due to the physically adsorbed dye molecules on the surface. It was an observation that as BDS groups on the polymer surface increased, fluorescence intensity also increased. This data supported successful dye conjugation onto the polymer surface via a thiol-disulfide exchange reaction.

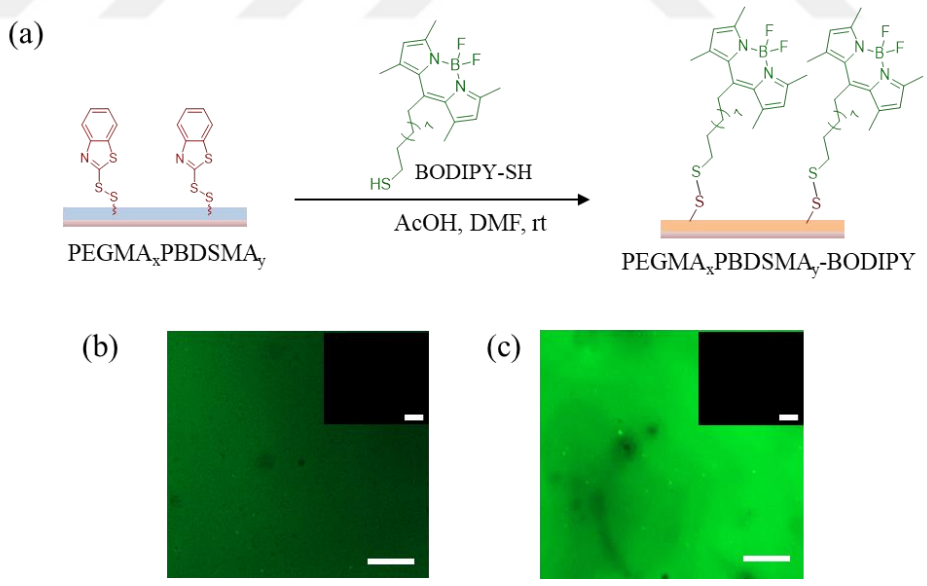

Figure 8.17. (a) Schematic illustration of polymer-coated surface modification using BODIPY-SH, and fluorescence microscopy images of dye-modified surfaces, (b) S(P_{85}-B_{10}-T_5) and (c) S(P_{65}-B_{30}-T_5). Insets show a lack of any fluorescence of unmodified surfaces. The scale bar is 50 µm.

The reversible attachment of BODIPY dye onto the polymer surface was investigated. Because BODIPY dye was conjugated to the polymer surface via a thiol-disulfide exchange reaction, disulfide linkage provided dye release from the polymer surface in the presence of DTT. BODIPY conjugated S(P_{85}-B_{10}-T_5) surface was treated with 10 mM DTT solution to prove this idea. Detachment of BODIPY dye from the surface was controlled via fluorescence microscopy.

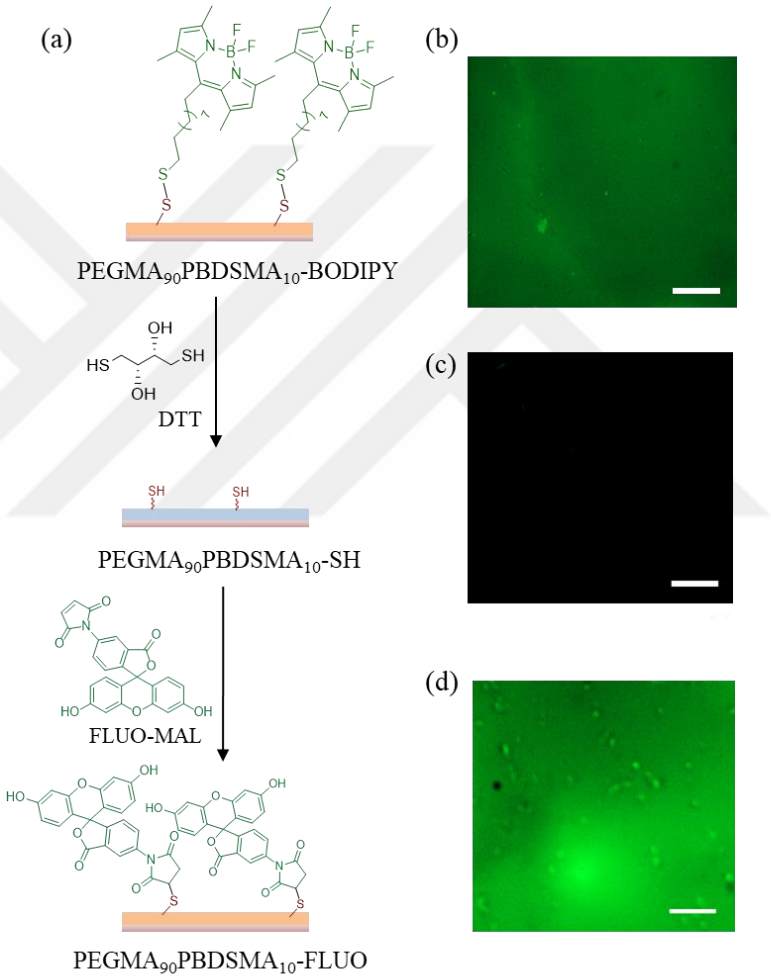

Figure 8.18. (a) Schematic illustration of the release of dye from BODIPY-modified surface with DTT and confirmation of thiolated interface through the attachment of maleimide-containing dye Fluo-MAL; and fluorescence microscopy images of (b) S(P_{85}-B_{10}-T_5)-BODIPY surface and (c) DTT treated surface, and (d) Fluo-MAL conjugated surface. Scale bar: 50 µm.

The result in Figure 8.18c demonstrated that the fluorescence intensity was significantly reduced. After the release of BODIPY dye, further functionalization of the same surface was investigated. When BODIPY showed release with DTT, free thiol groups remained polymer surface. The polymer surface was treated with maleimide-functionalized fluorescein dye solution using a thiol-Michael addition reaction to test this. Successful conjugation of dye molecules was confirmed by the reappearance of fluorescence intensity, shown in Figure 8.18d, on the polymer-coated surface.

8.3.9. Cell Attachment and Release from Peptide-conjugated Surface

After demonstrating the reversible functionalization capabilities of polymer coatings with thiol-bearing molecules, the efficiency of the BDS functionalized surfaces on cell attachment and their release was investigated through actin staining and live-dead assays. Mouse L929 fibroblast cells demonstrated cell attachment and proliferation on a linear RGDC peptide-conjugated polymer coating. It is well known that the RGD peptide shows specific binding to integrin receptors expressed on fibroblasts. Therefore, RGD-containing peptide–polymer conjugates have been widely employed to obtain bioactive materials with enhanced cell attachment. Various polymers prepared via controlled radical polymerization have recently been modified with RGD-containing peptides to promote cell interaction [377-382]. Although in our case, a linear RGD sequence was sufficient to attach cells, in principle, successfully, one can also utilize the cyclic RGD-containing sequences. The glass surface S(P_{85}-B_{10}-T_5) coated with the BDS-containing polymer P(P_{85}-B_{10}-T_5) was treated with a thiol-containing cell adhesion linear peptide (RGDC-SH) to promote the adhesion and growth of L929 mouse fibroblast cells. The effect of RGDC conjugation on cell adherence was compared with the attachment on surfaces S(P_{85}-B_{10}-T_5) and S(P_{95}-B_0-T_5), which were devoid of the peptide. Mouse fibroblast cells were seeded onto the RGDC-modified surface S(P_{85}-B_{10}-T_5). Unmodified S(P_{85}-B_{10}-T_5) and S(P_{95}-B_0-T_5) surfaces were used for control experiments to assess the effect of the presence of the peptide. After incubation for 24 h, the actins and nuclei of the cells were stained using Alexa Fluor 488-phalloidin and DAPI, respectively. A clear difference was observed between the RGDC-functionalized surface S(P_{85}-B_{10}-T_5) and control polymer films S(P_{85}-B_{10}-T_5) and S(P_{95}-B_0-T_5). After the staining process, fluorescence microscopy analysis was conducted to determine the adherence and spreading of cells on different surfaces in Figure 8.20. In the

case of modification of the glass surface with RGDC-SH, enhanced cell immobilization and spreading were observed, highlighting the advantageous effect of the cell adhesive peptide on cellular attachment. Without modifying polymer-coated surfaces with RGDC-SH, cell adherence and spreading on the rather bio-inert surfaces remained significantly lower. Interestingly, the glass surface S(P_{85}-B_{10}-T_5) bearing BDS units displayed slightly higher efficiency to adhere cells compared to the surface S(P_{95}-B_0-T_5) lacking BDS functionalities due to the anti-biofouling character of PEG groups.

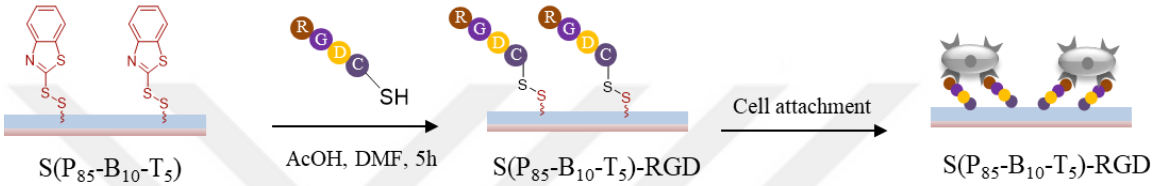

Figure 8.19. Scheme of immobilization of L929 mouse fibroblast cells onto polymer-coated glass substrates.

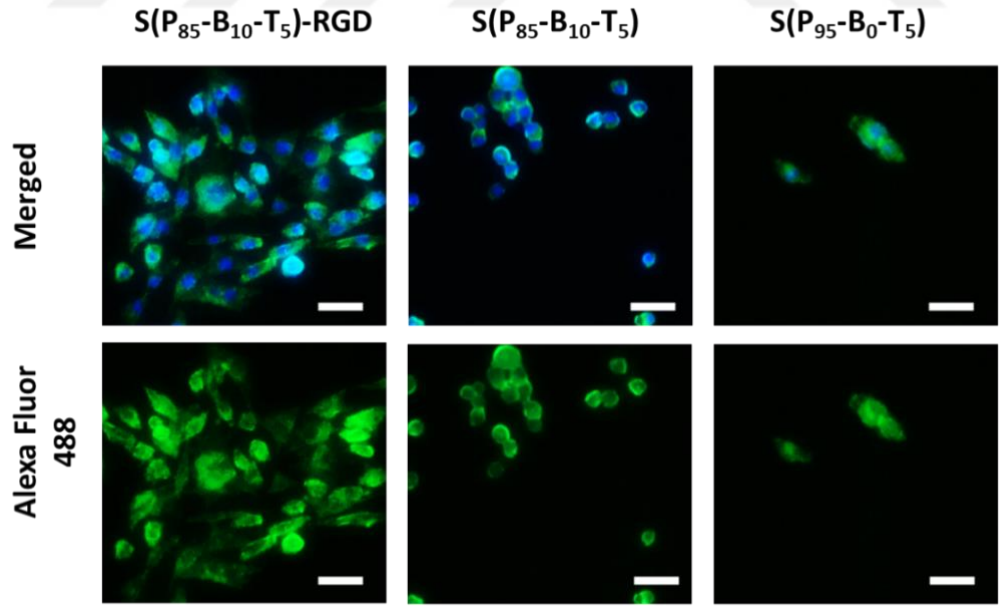

Figure 8.20. Fluorescence microscopy images of cells immobilized on S(P_{85}-B_{10}-T_5)-RGD, S(P_{85}-B_{10}-T_5), and S(P_{95}-B_0-T_5) surfaces after actin filament staining with Alexa Fluor 488 and nuclei staining with DAPI. Scale bar: 50 µm

Apart from the ability of these peptide-modified polymeric coatings to promote attachment, we also wanted to assess if the cells could be harvested without compromising their viability. A live–dead assay was utilized to monitor the cells' viability before and after detachment from surfaces. In particular, mouse fibroblast L929 cells were seeded on the RGDC-functionalized polymer-coated glass surface S(P_{85}-B_{10}-T_5). After incubation for 24 h, the surface attached cells were stained with calcein-AM and visualized under a fluorescence microscope. The bright green fluorescence in the left image in Figure 8.21 and the spread-out morphology of the cells indicated their viable nature and suitable surface attachment. Upon exposure of cell-immobilized surfaces to a 5 mM DTT solution, the cells detached from the surface. This detachment could be explained by the scissoring of the cell adhesion peptide moiety, which was tethered to the polymer coating through a redox cleavable disulfide bonding. Surface-detached cells were transferred into a well plate and immediately stained with calcein-AM, which stains viable cells (green fluorescence), and propidium iodide (PI), an indicator of dead cells (red fluorescence), and the image was shown on the right side of Figure 8.21. Importantly, fluorescence microscopy analysis revealed that cells' viability was not compromised upon detachment from the polymeric coating.

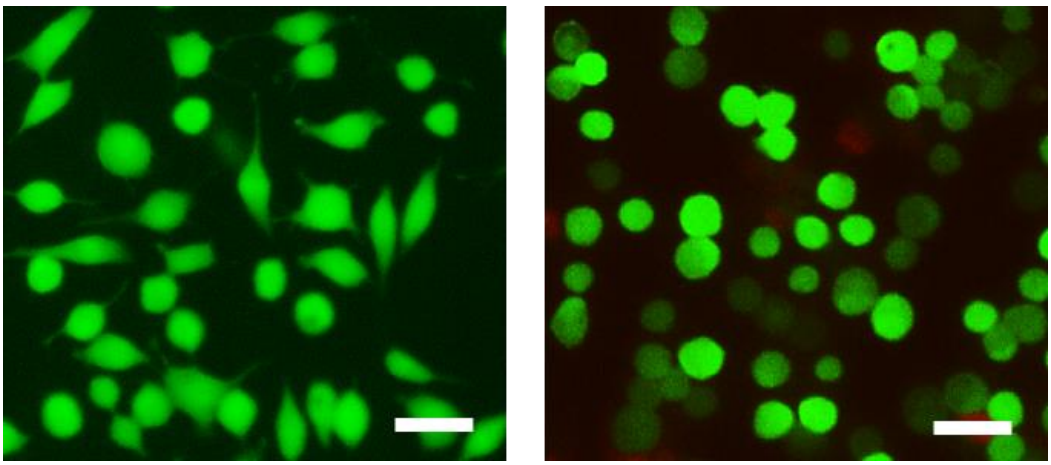

Figure 8.21. Fluorescence microscopy image of cells immobilized on RGD peptide attached polymer film (left), and merged fluorescence microscopy image displaying viable (green) and dead (red) cells after detachment and removal from polymer film (right). The scale bar is 50 μm.

8.4. Conclusion

In summary, this chapter reports the facile synthesis of a benzothiazole disulfide-based copolymer that can be conjugated with thiol-containing molecules to afford redox-responsive functional copolymers. Using RAFT polymerization, copolymers with varying amounts of the thiol-reactive monomer can be obtained with good control over molecular weight and dispersity. To demonstrate the application of these copolymers, stimuli-responsive functionalizable polymeric coatings were fabricated on glass surfaces. Selective functionalization with thiol-containing molecules was displayed using a fluorine-tagged benzyl thiol. Finally, cell adhesive peptides were conjugated onto the polymer-coated surfaces to enable cellular adhesion. Importantly, surface-bound cells could be released using a thiol-containing reducing agent to harvest them with high viability. One can envision that such redox-responsive copolymers will be helpful for various biomedical applications entailing a release-on-demand attribute.

9. PLUG-AND-PLAY BIOINTERFACES: HARNESSING HOST-GUEST INTERACTIONS FOR FABRICATION OF FUNCTIONAL POLYMERIC COATINGS

9.1. Introduction

Over the past decades, functional polymeric coatings on surfaces have become prominent due to their widespread use in biomedical sciences [372], [383-386]. Applications involving biomolecular immobilization, analyte detection, bio-sensing, targeted drug delivery, cell adhesion, and proliferation often require the installation of appropriate functional molecules and ligands onto solid surfaces to fabricate functional devices [372]. Polymeric coatings on solid surfaces offer a versatile interface for enabling these applications mentioned above [297], [333], [337], [387-390]. In general, two methods for incorporating functional molecules on a polymeric interface are utilized: covalent conjugation or immobilization of non-covalent interactions. While covalent methods for surface immobilization are robust [279], [391], non-covalent approaches offer flexibility, such as facile reversibility and renewability/reusability of functional interfaces [392-395].

To date, supramolecular host-guest interactions have been extensively explored for versatile and facile modification of various interfaces. Fabrication methods using host-guest supramolecular interactions have attracted a great deal of attention since self-assembly processes drive the association of building blocks at the molecular level [231], [396,397]. Among reported macrocyclic host molecules, crown ethers [398], cyclodextrins (CD) [237], and calixarenes [399] were among the most widely explored ones. In addition to them, more macrocyclic host molecules such as cucurbiturils (CB[*n*]) [233], blue box [400], pillar[*n*]arenes [401], resorcinarene [402] were reported. Among these macrocyclic structures, CDs have been widely used to fabricate polymeric self-assembled materials for biomedical applications due to their ready availability, low toxicity, excellent biocompatibility, and ability to make strong complexation with a variety of guests [238], [403-406].

The adamantane/βCD duo is a well-known couple among CD-based host-guest pairs. Adamantane is a rigid hydrophobic molecule and is known to be complex with βCD with a high association in an aqueous environment [258]. Therefore, the assembly of βCD and adamantane has been extensively used in various areas such as drug and gene delivery, biomolecule immobilization, bio-separation, and fabrication of sensors. [239], [407-410]. Among these applications, the construction of functional polymeric interfaces to enable the reversible immobilization of biomolecules has been explored in recent years. [164,165], [411-415].

Chen and coworkers reported seminal contribution in polymeric surface coatings in this area, who fabricated adamantane (Ada)-containing polymer brushes to construct molecular recognition surfaces. [164,165]. They fabricated Ada-containing thermo-responsive polymer brushes and showed tunable and reversible integration of biomolecules onto their platform via host-guest interactions [164]. In addition, the same group reported copolymer surfaces with different thermo-sensitivity and surface wettability by adjusting the Ada ratio on the surface [165]. While polymer brushes offer fine-tuned interfaces, their fabrication on surfaces often involves multiple steps, such as initiator immobilization and polymerization under controlled environments, as opposed to simply coating a surface with polymer by incubation in the polymer solution, followed by mild baking and drying, not to mention the relative ease in chemical characterization of the polymeric component before coating, compared to characterization of surface tethered polymeric structures. Hence, one can envision that a polymeric surface coating capable of facile and modular plug-and-play integration of functional motifs such as bioactive ligands would be an attractive approach for functional engineering interfaces for a variety of biomedical and biotechnological applications.

Herein, we report the fabrication of adamantane-containing polymeric coating to modify silicon surfaces and render them functionalizable in a modular fashion using CD-based host-guest interactions. In particular, a surface-reactive copolymer was synthesized using an adamantane-containing methacrylate (AdaMA), di(ethylene glycol) based methacrylate (DEGMEMA), and 3-(trimethoxysilyl)propyl methacrylate (TMSPMA) monomers. While the Ada-based monomer is required for host-guest interaction-based specific functionalization, the ethylene glycol-based monomer imparts the necessary anti-

biofouling characteristic to the coating. Incorporation of the alkoxysilyl monomer enables robust anchoring of the copolymer onto the glass-like interfaces. A series of copolymers capable of varying degrees of host-guest complexation are prepared, and facile surface functionalization using a variety of functional molecules such as fluorescent dyes, bioactive ligands, and cell adhesive peptides are demonstrated to highlight the versatile nature of the polymeric coating. Using simple techniques like microcontact printing [416], spatially controlled functionalization at the interfaces is achieved. We also demonstrate that the modification approach enables selective biomolecular immobilization in a reversible manner, thus rendering these interfaces as renewable.

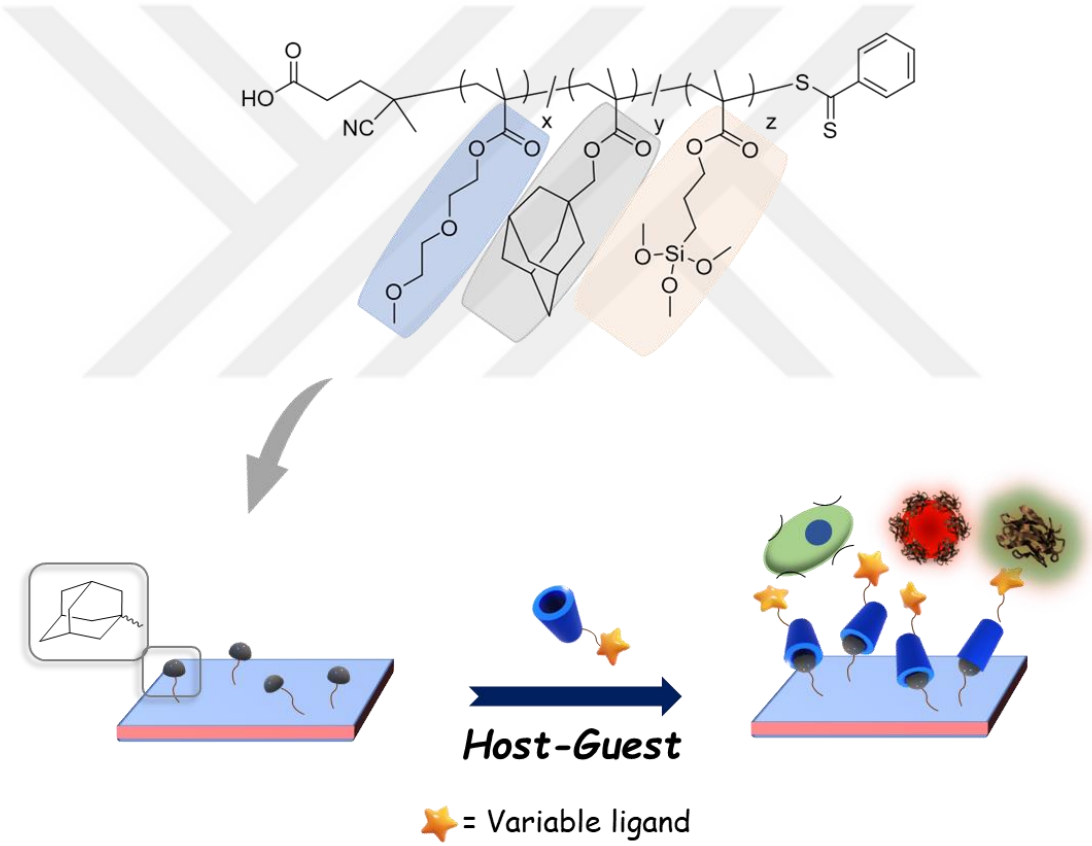

Figure 9.1. Schematic illustration of the fabrication of βCD reactive polymeric thin film and polymeric film modification via host-guest chemistry using the μCP technique.

9.2. Experimental

9.2.1. Materials

All solvents were purchased from Merck and used as obtained without further purification. Ultrapure water was obtained from a Milli-Q Water Purification System (Milli-Q system, Millipore, Billerica, MA, USA). Anhydrous toluene, tetrahydrofuran (THF), and dichloromethane (CH_2Cl_2) were obtained from the SciMatCo purification system, and other solvents were dried over molecular sieves. Di(ethylene glycol) methyl ether methacrylate (DEGMEMA) was obtained from Sigma-Aldrich and used after purification through activated aluminum oxide filtration. 2,2'-Azobis(2-methylpropionitrile) (AIBN) was purchased from Sigma Aldrich, recrystallized from methanol, and dried before use. 3-(Trimethoxysilyl)propyl methacrylate (TMSPMA), 4-cyano-4-(thiobenzoylthio)pentanoic acid and beta-cyclodextrin (βCD), *N, N, N′, N″, N‴*- pentamethyldiethylenetriamine (PMDETA), copper (I) bromide (CuBr) and FITC-streptavidin conjugate were purchased from Sigma-Aldrich. Concanavalin A (FITC conjugate) was purchased from Thermo Fisher. CdSeQdot 605 Streptavidin conjugate was purchased from Invitrogen. Rhodamine-PNA conjugate was purchased from Vector. D-mannose was obtained from Alfa-Aesar. AdaMA monomer [417], alkyne-bearing D-mannose [417] 6-O-Monotosyl-βCD (βCD-OTs) [252], 6-monodeoxy-6-monoazido-βCD (βCD-N_3) [252], 6-monodeoxy-6-monoamino-βCD (βCD-NH_2) [252], NHS-activated biotin (Biotin-NHS) [418], βCD-Biotin [418], alkyne-bearing cRGDfK [419] were synthesized according to literature procedures.

9.2.2. Methods

^1H and ^{13}C NMR spectra were recorded on Bruker Avance Ultrashield 400 (400 MHz). Molecular weights of the synthesized polymers were estimated by size exclusion chromatography (SEC) using a PSS-SDV (length/ID 8 × 300 mm, 10 μm particle size) gram linear column calibrated with poly(methyl methacrylate) (PMMA) standards using a refractive-index detector with a mobile phase solution of 0.05 M lithium bromide in DMAc as eluent at a flow rate of 1 mL/min at 30 °C. Attenuated total reflectance Fourier transform infrared (ATR-FTIR) spectroscopy was collected on a Thermo Scientific Nicolet 380 FT-

IR spectrophotometer. ATR-FTIR was equipped with a Harrick Scientific GATR accessory and a Ge crystal for surface analysis. Static water contact angle measurements were performed using a CAM 101 KSV goniometer. Images were obtained by an integrated digital camera observing the deionized water (5 µL) deposited surface. Data process and contact angle determination were carried out by using CAM2008 software. Contact angle values were taken from three different locations of each sample, and average data was reported. Atomic force microscopy determined polymer film thickness using a CoreAFM instrument (Nanosurf, Switzerland). X-ray photoelectron spectroscopy (XPS) was carried out using a K-Alpha instrument (Thermo Scientific).

9.2.3. RAFT Synthesis of Copolymers Carrying DEGMA-AdaMA-TMSPMA monomers (P(D_x-A_y-T_z))

For the synthesis of poly(DEGMEMA$_{75}$-AdaMA$_{20}$-TMSPMA$_5$) (P(D_{75}-A_{20}-T_5)), DEGMEMA (604 mg, 3.21 mmol), TMSPMA (53 mg, 0.215 mmol) and adamantane containing AdaMA (200 mg, 0.854 mmol) were taken in a round bottom flask with a magnetic bar and purged with nitrogen. Under nitrogen, anhydrous DMF (8 mL) was added, and the monomer solution was continued to degas with nitrogen. Under nitrogen, 4-cyano-4-(thiobenzoylthio)pentanoic acid (9.4 mg, 0.033 mmol) as a chain transfer reagent, and AIBN (1.08 mg, 6.6 x 10^{-3} mmol) as initiator were added the mixture. Subsequently, the reaction flask was sealed and heated at 70 ^{o}C for 19 h. After 19 h, the reaction mixture was cooled to room temperature, and DMF was removed under reduced pressure. The crude was redissolved with minimum CH_2Cl_2, and the polymer was precipitated in cold diethyl ether to remove unreacted monomers (pink viscous, 0.6 g, 70 % yield). Molecular weight (Mn) and molecular weight distribution (polydispersity index, PDI) were determined by size exclusion chromatography (SEC) (Mn = 20 kDa; PDI (Mw/Mn) = 1.36). For the synthesis of poly(DEGMEMA$_{95}$-AdaMA$_0$-TMSPMA$_5$) (P(D_{95}-A_0-T_5)), DEGMEMA (604 mg, 3.21 mmol), TMSPMA (42 mg, 0.17 mmol) were taken in a round bottom flask with a magnetic bar and purged with nitrogen. Under nitrogen, anhydrous DMF (8 mL) was added, and the monomer solution was continued to degas with nitrogen. Under nitrogen, 4-cyano-4-(thiobenzoylthio)pentanoic acid (7.4 mg, 0.026 mmol) as a chain transfer reagent, and AIBN (0.87 mg, 5.3 x 10^{-3} mmol) as initiator were added the mixture. Subsequently, the reaction flask was sealed and heated at 70 ^{o}C for 19 h. After 19 h, the reaction mixture was cooled

to room temperature, and DMF was removed under reduced pressure. The crude was redissolved with minimum CH_2Cl_2, and the polymer was precipitated in cold diethyl ether to remove unreacted monomers pink viscous, 0.55 g, 80 % yield. Molecular weight (Mn) and molecular weight distribution (polydispersity index, PDI) were determined by size exclusion chromatography (SEC) (Mn = 23 kDa; PDI (Mw/Mn) = 1.40).

9.2.4. Cleaning Procedure for Silicon Surfaces

Silicon surfaces (1 x 1 cm^2) were cleaned using water (5 mL), acetone (5 mL), and ethanol (5 mL), respectively. They were sonicated in these solvents for 15 minutes and then dried under a stream of nitrogen. Finally, silicon surfaces were cleaned using the Novascan PSD series UV/Digital ozone system for 15 min.

9.2.5. Fabrication of Polymeric Coatings on Silicon Surfaces

Two polymer solutions of P(D_{75}-A_{20}-T_5) and P(D_{95}-A_0-T_5) (50 µL, 20 mg/mL in anhydrous DMF) were spread over each silicon surface. They were left open to air for 24 hours at room temperature to let the solvent evaporate. Surfaces were placed into the vacuum oven at 60 ºC for 1 h. Finally, surfaces were washed and sonicated in DMF and THF for 2 minutes to remove non-adhered polymer from the surface, and then wafers were dried under a stream of nitrogen.

9.2.6. Stability Experiment of Polymeric Coatings

S(D_{75}-A_{20}-T_5) and S(D_{95}-A_0-T_5) surfaces were incubated in PBS solution (pH 7.4) at 37 ºC for 24 h. After that, surfaces were washed with water, and subsequently, they were lyophilized. The surfaces were characterized by FTIR analysis.

9.2.7. Synthesis of β-CD and Lissamine-Rhodamine B conjugate

βCD (40 mg, 0.034 mmol), lissamine rhodamine B sulfonyl chloride (30 mg, 0.05 mmol) were dissolved in 0.8 mL of anhydrous DMF. After adding *N*,*N*-diisopropylethyl amine (DIPEA) (24 µL, 17.5 mg, 0.136 mmol) in 0.2 mL of anhydrous DMF, the mixture

was stirred for 2 days at room temperature. At the end of 2 days, the mixture was added to acetone (50 mL), and the precipitated solid residue was centrifuged and washed with the excess amount of acetone. The product was obtained as a purple solid. ^{1}H NMR (D_2O, δ, ppm) 8.51 (s, 1H), 8.17 (d, *J* = 9.5, 1H), 7.54 (d, *J* = 7.8, 1H), 7.05 - 6.88 (m, 5H), 6.77 (s, 1H), 5.05 (s, 7H), 3.91 - 3.44 (m, 50H), 1.34 - 1.24 (m, 12H). MALDI-TOF (m/z) calcd. for $C_{69}H_{99}N_3O_{40}S_2$ $[M]^+$ 1675, found [M+Na] 1698 g/mol.

9.2.8. Synthesis of Mono-mannose Conjugated β-Cyclodextrin

Mono-mannose substituted beta-cyclodextrin was synthesized by adapting a literature procedure [420]. Briefly, the mixture of mannose-alkyne and 6-monodeoxy-6-monoazido-βCD (βCD-N_3) in DMF was mixed with $CuSO_4.5H_2O$ and sodium ascorbate in H_2O. The mixture was stirred at 60 ^{o}C for overnight. Afterward, DMF was removed, and the concentrated mixture was added to acetone (50 mL). The formed residue was washed with acetone (50 mL x 3 times). The solid product was redissolved in water (5 mL), and the copper-removing resin (CupriSorb) was added. The mixture was stirred until the color mixture transformed from blue to colorless. Finally, the mixture was filtered to remove resin and lyophilized after freezing (pale yellow solid, 90 % yield). ^{1}H-NMR (D_2O, δ, ppm) 8.46 (s, 1H), 5.08 (br s, 8H), 4.02 - 3.81 (m, 30H), 3.67 - 3.57 (m, 18H).

9.2.9. Synthesis of β-Cyclodextrin Conjugated RGD Peptide

Alkyne-bearing cRGD (10 mg, 0.0146 mol) βCD-N_3 and (18.7 mg, 0.016 mmol) were weighed in a round bottom flask and purged with N_2 for 15 min. Then, they were dissolved in anhydrous DMF (0.8 mL) under N_2. In another flask, PMDETA (2.9 µL, 2.53 mg, 0.0146 mmol) and Cu(I)Br (2.12 mg, 0.0146 mmol) were purged with N_2 for 15 min, and they dissolved in anhydrous DMF (0.4 mL) under N_2. After the purging step, the solution of PMDETA and Cu(I)Br was added to the round bottom flask, including alkyne-bearing cRGD and βCD-N_3 under purge. The mixture was stirred at 50 ^{o}C for 24 h. After 24 h, the reaction mixture was added to acetone (50 mL). The formed residue was washed with acetone (50 mL x 3 times). The solid product was redissolved in water (5 mL), and the copper-removing resin (CupriSorb) was added. The mixture was stirred until the color of the mixture transformed from blue to colorless. Finally, the mixture was filtered to remove

resin and lyophilized after freezing (white solid, 18 mg, 69% yield). MALDI-TOF MS m/z: calculated for $C_{74}H_{114}N_{12}O_{42}$ 1842.72; found 1881.81 $[M + K]^+$.

9.2.10. β-CD-Lissamine B Conjugation to Polymer Coating via Microcontact Printing

Solution of βCD grafted Lissamine-Rhodamine-B dye in water (1 mg/mL) was used to wet a 1x1 cm^2 PDMS stamp. The stamp was left to dry for 60 min, followed by further drying under a gentle stream of N_2. The stamp was placed on the polymer-coated S(D_{75}-A_{20}-T_5) surfaces for 60 minutes. After printing, surfaces were washed with cold water to remove non-conjugated materials. S(D_{95}-A_0-T_5) surface was used as a control because it did not include the adamantane group to make a complex with βCD ligand.

9.2.11. βCD grafted-Biotin Functionalization for Qdot-Streptavidin Immobilization

βCD grafted-Biotin solution (50 μL, 2 mg/mL in water) was spread over Ada-containing S(D_{75}-A_{20}-T_5) surfaces and control S(D_{95}-A_0-T_5) surfaces and incubated for 24 hours. After incubation, surfaces were washed with cold water to remove unconjugated βCD grafted-biotin. For the immobilization of streptavidin, 10 μL Qdots-streptavidin was diluted with 90 μL water, and 10 μL from this solution was spread over a 1x1 cm^2 PDMS stamp. The stamp was left to dry for 60 min, followed by further drying under a gentle stream of N_2. The stamp was placed onto the polymer-coated surfaces for 60 min. After printing, surfaces were washed with cold water to remove non-conjugated materials.

9.2.12. Surface Functionalization with βCD grafted-Mannose and Immobilization of Dye-labeled ConA and PNA Conjugates

βCD grafted-mannose solution (50 μL, 2 mg/mL in water) was spread over the Ada-containing polymer S(D_{75}-A_{20}-T_5) surface and control S(D_{95}-A_0-T_5) surfaces and incubated for 24 hours. After incubation, surfaces were washed with cold water to remove unconjugated βCD-Man. FITC-ConA and Rhodamine-PNA conjugates were used to explore lection-sugar interaction. FITC-ConA (10 μL, 0.1 mg/mL in 20 mM HEPES buffer) was spread over 1x1 cm^2 PDMS stamps. The stamps were left to dry for 60 min, followed

by further drying under a gentle stream of N_2. The stamp was placed onto the S(D_{75}-A_{20}-T_5) and S(D_{95}-A_0-T_5) polymer-coated surfaces for 60 min. After printing, surfaces were washed with cold water to remove non-conjugated materials. RhB-PNA solution (0.15 μg/mL in 20 mM HEPES buffer) was spread over a 1 x 1 cm^2 PDMS stamp for PNA immobilization. The stamps were left to dry for 60 min, followed by further drying under a gentle stream of N_2. The stamp was placed on the S(D_{75}-A_{20}-T_5) surface for 60 min. After printing, surfaces were washed with cold water to remove non-conjugated materials.

9.2.13. Surface Functionalization with βCD grafted-RGD Peptide

βCD grafted-cRGD solution (50 μL, 2 mg/mL in water) was spread over Ada-containing S(D_{75}-A_{20}-T_5) surfaces and control S(D_{95}-A_0-T_5) surfaces and incubated for 24 h. After incubation, surfaces were washed with cold water to remove unconjugated cRGD-βCD.

9.2.14. Cell Culture on Peptide Functionalized Films: Actin Filament Staining

L929 mouse fibroblast cells were grown in a 5% CO_2-containing atmosphere at 37 °C and cultured in Dulbecco's Modified Eagle's Medium (DMEM) media supplemented with 10% fetal bovine serum (FBS) (PAN Biotech). Cells (15000 cells/ 30 μL) were seeded onto polymer-coated silicon surfaces (1 x 1 cm^2) and incubated at 37 °C in a 5% CO_2-containing atmosphere for 2 h. Subsequently, DMEM (1 mL) was added to each well containing the polymer-coated silicon wafers. After 24 h and 72 h incubation, cell media was removed, silicon surfaces were washed with 1 x PBS (0.5 mL, two times), and cells were fixed with 3.7% formaldehyde solution in PBS for 10 min at room temperature. After fixation, cells were washed with 1 x PBS (0.5 mL, two times). For staining filamentous actins (F-actins), cells were incubated with 0.1% Triton X-100 in PBS for 5 min at 37 ^oC. After washing with 1 x PBS (0.5 mL, two times), cells were incubated with Alexa Fluor 488 phalloidin solution (5 units/mL) in PBS, including 1% bovine serum albumin (BSA) for 15 min at 37 ^oC. After washing with PBS, cell nuclei were stained with DAPI for 10 min at 37 ^oC. After the staining steps, the stained cells were washed with 1 x PBS. The resulting images of stained cells on polymer-coated silicon surfaces were taken using a fluorescence microscope, and processing was carried out using Zeiss Zen Blue lite software (Carl Zeiss, Jena, Germany).

9.3. Results and Discussion

9.3.1. Synthesis and Characterization of Adamantane-Containing Copolymer

For the synthesis of copolymers bearing Ada units, adamantane methacrylate (AdaMA) was synthesized [417] and polymerized with a hydrophilic di(ethylene glycol) based methacrylic monomer (DEGMEMA) and surface active trimethoxysilyl-based methacrylic monomer (TMSPMA) using RAFT polymerization. Copolymers containing AdaMA, TMSPMA, and DEGMEMA monomers (($P(P_x\text{-}A_y\text{-}T_z)$) where x, y, and z subscript numbers show their mol percentage in the feed) were synthesized using RAFT polymerization scheme was given in Figure 9.2.

Two different copolymers, $P(D_{95}\text{-}A_0\text{-}T_5)$ and $P(D_{75}\text{-}A_{20}\text{-}T_5)$, with 0 % and 20 % AdaMA groups, respectively, were synthesized. Polymerization conditions and properties of copolymers were tabulated in Table 9.1. The TMSPMA monomer ratio was kept at 5 %, a sufficient amount necessary for surface attachment [376]. Copolymer $P(D_{95}\text{-}A_0\text{-}T_5)$, devoid of any AdaMA groups, was synthesized for control experiments to deduce the role of the Ada group in surface functionalization. After polymerization, copolymers were purified by precipitating in cold diethyl ether and characterized by SEC and ^{1}H NMR. Obtained copolymers showed high monomer conversions, and SEC analysis demonstrated reasonable control on molecular weight during polymerization with a relatively narrow molecular weight distribution.

Successful incorporation of all monomers in the obtained copolymers was deduced using ^{1}H NMR spectroscopy, given in Figure 9.3. For copolymer $P(D_{75}\text{-}A_{20}\text{-}T_5)$, proton resonance from the methoxy groups ($\text{-}OCH_3$) of DEGMEMA was observed at 3.39 ppm, along with the proton resonances of adamantane hydrogens between 2.01 - 1.54 ppm.

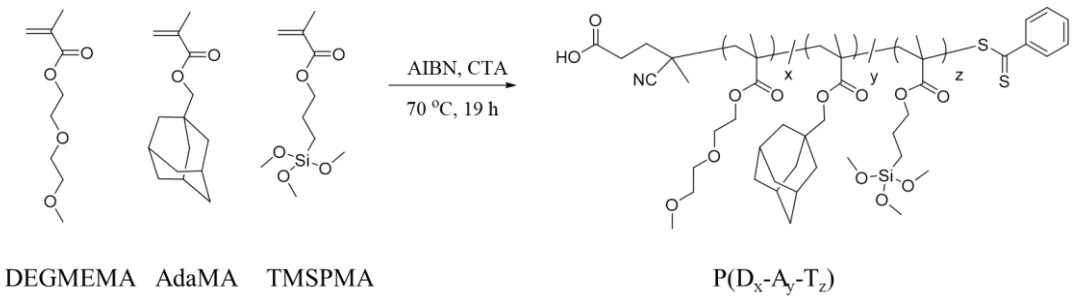

Figure 9.2. Synthesis of surface attachable RAFT copolymers carrying adamantane side groups.

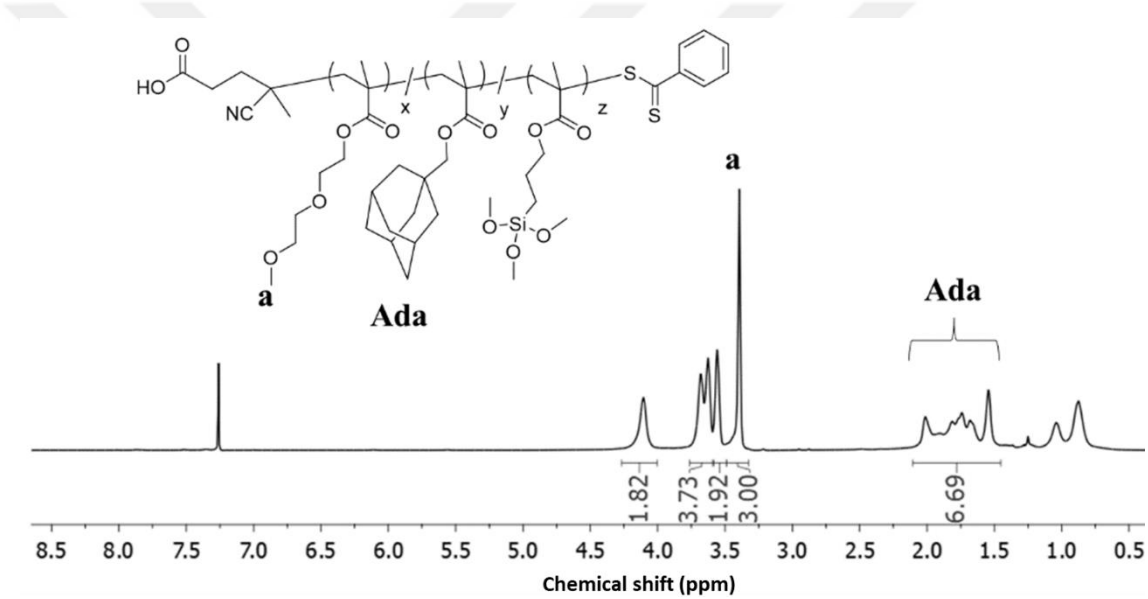

Figure 9.3. ^{1}H NMR spectrum of $P(D_{75}\text{-}A_{20}\text{-}T_5)$ copolymer ($CDCl_3$).

Table 9.1. Polymerization conditions of AdaMA-DEGMEMA copolymers.

No	**Polymer**	$F_{theo.}$ (%)	F_{calcd} (%)	**Conv.** (%)	$M_{n,theo}$ (g/mol)	$M_{n,NMR}$ (g/mol)	$M_{n,SEC}$ (g/mol)	M_w/M_n
1	$P(D_{75}\text{-}A_{20}\text{-}T_5)$	75: 20	74: 21	82	21275	23581	20000	1.36
2	$P(D_{95}\text{-}A_0\text{-}T_5)$	100: 0	100: 0	85	20301	24040	23000	1.40

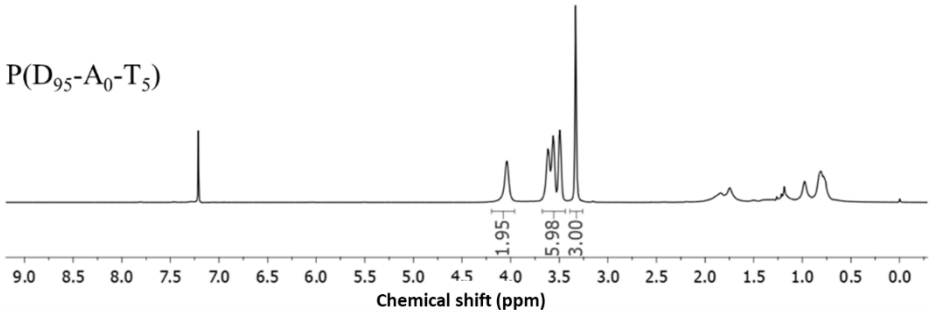

Figure 9.4. ^{1}H NMR spectrum of P(D_{95}-A_0-T_5) copolymer ($CDCl_3$).

9.3.2. Fabrication and Characterization of Polymer Coatings on Silicon Surfaces

Cleaned Si/SiO_2 surfaces were used to fabricate polymer coating on surfaces. P(D_{75}-A_{20}-T_5) and P(D_{95}-A_0-T_5) polymer solutions were prepared in anhydrous DMF (20 mg/mL). After spreading polymer solutions over Si/SiO_2 surfaces, incubation, and heating at 60 ^{o}C for 60 min, surfaces were rinsed with copious amounts of organic solvents to remove any unbound polymers. Polymer-coated surfaces obtained using P(D_{75}-A_{20}-T_5) and P(D_{95}-A_0-T_5) are referred to as S(D_{75}-A_{20}-T_5) and S(D_{95}-A_0-T_5) in subsequent sections, and "S" stands for "surface". The coated surfaces were analyzed using FTIR spectroscopy. The characteristic carbonyl bands around 1727 cm^{-1} suggested the successful attachment of polymers onto the Si/SiO_2 surfaces. In addition to the FTIR analysis, contact angle measurements recorded for S(D_{75}-A_{20}-T_5) and S(D_{95}-A_0-T_5) also suggested the same. While the water contact angle of S(D_{95}-A_0-T_5) was found as 57 ± 4, that of S(D_{75}-A_{20}-T_5) was determined as 74 ± 4 due to the hydrophobicity of adamantane groups, and data were given in Figure 9.5c. Further characterization of S(D_{75}-A_{20}-T_5) was undertaken with XPS analysis. The survey scan of S(D_{75}-A_{20}-T_5) comprises C1s, and O1s signals 285.0 eV and 532.5 eV. The high-resolution C1s spectrum in Figure 9.5d could be deconvoluted to three Gaussians with the expected relative areas for three carbon atoms at 285.0 eV (C-C/C-H), 286.4 eV (C-O-C/C-N/C-S) and 289.3 eV (C=O). Importantly, as seen in Figure 9.5e-f, no significant peaks of N and S atoms were visible, presumably due to very low concentration since they are present as only end groups in the copolymer synthesized using RAFT polymerization. The lack of peaks from these atoms in the native polymer coating will be critical to our analysis after their subsequent functionalization using host-guest interactions.

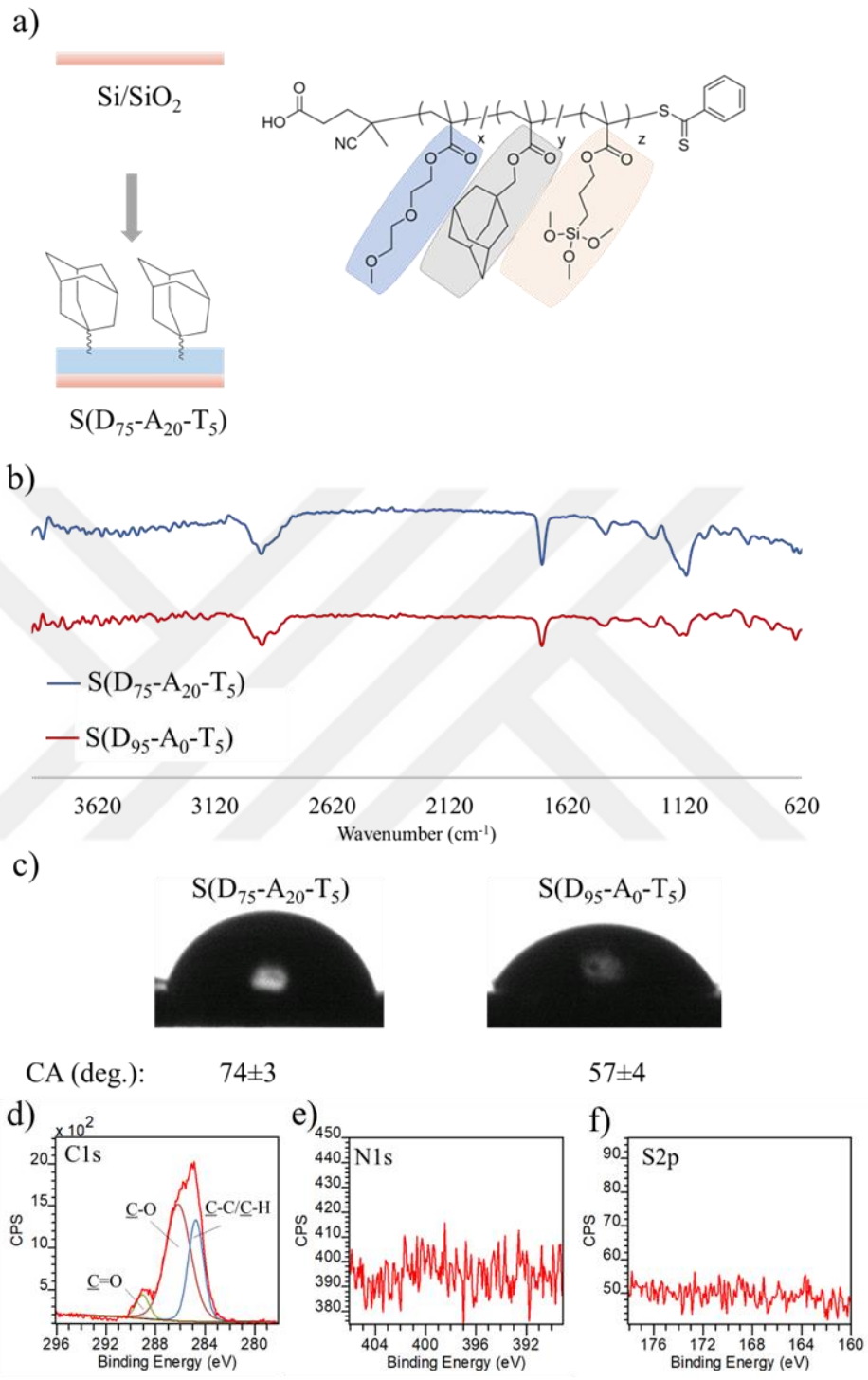

Figure 9.5. (a) Schematic illustration of coating of polymers onto a silicon surface, (b) ATR-FTIR spectrum of polymer-coated surfaces, (c) water contact angle of polymer-coated surfaces, and high-resolution XPS spectra (d) C1s, (e) N1s and (f) S2p of S(D_{75}-A_{20}-T_5) surface.

After characterization, the stability of polymer coatings in aqueous media was investigated. S(D_{75}-A_{20}-T_5) and S(D_{95}-A_0-T_5) surfaces were incubated in PBS solution (pH = 7.4) at 37 °C for 24 h. Dried surfaces were characterized using FT-IR spectroscopy. No significant change in the carbonyl peaks after incubation with PBS suggested that polymer coatings were stable in an aqueous environment, and data were shown in Figure 9.6.

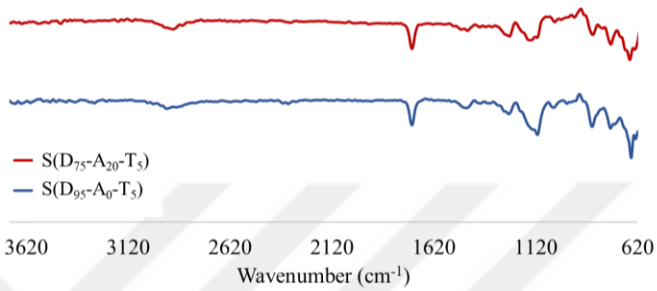

Figure 9.6. FTIR spectra of S(D_{75}-A_{20}-T_5) and S(D_{95}-A_0-T_5) after incubation with PBS (pH 7.4) at 37°C for 24 h.

9.3.3. Synthesis of βCD-Lissamine Rhodamine B Conjugate

βCD-conjugated lissamine rhodamine B was synthesized using mono-amine containing βCD and lissamine rhodamine B sulfonyl chloride in the presence of DIPEA.

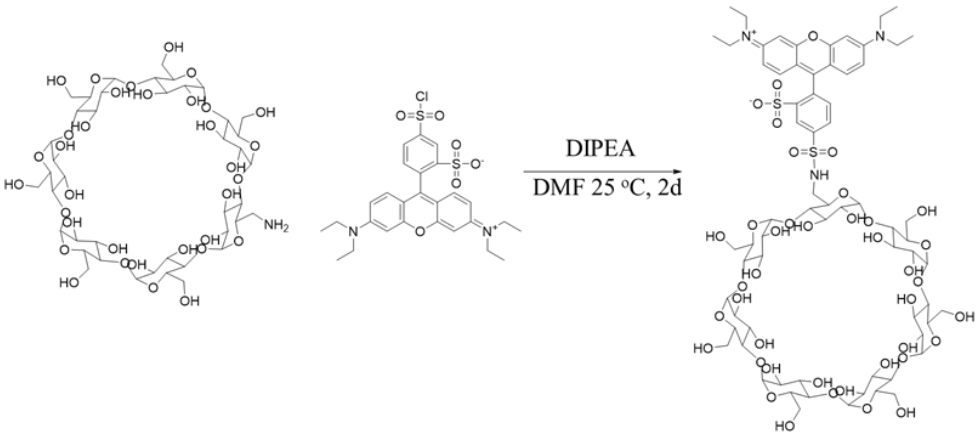

Figure 9.7. The synthesis scheme of βCD-grafted lissamine rhodamine B conjugate.

The synthesis scheme was shown in Figure 9.7. The characterization was done with ^{1}H NMR, demonstrated in Figure 9.8. The signals of aromatic hydrogens belonging to the rhodamine B group were observed between 8.51 - 6.77 ppm. The anomeric proton of βCD showed resonance at 5.05 ppm. Other peaks coming from βCD parts were observed between 3.91 - 3.44 ppm.

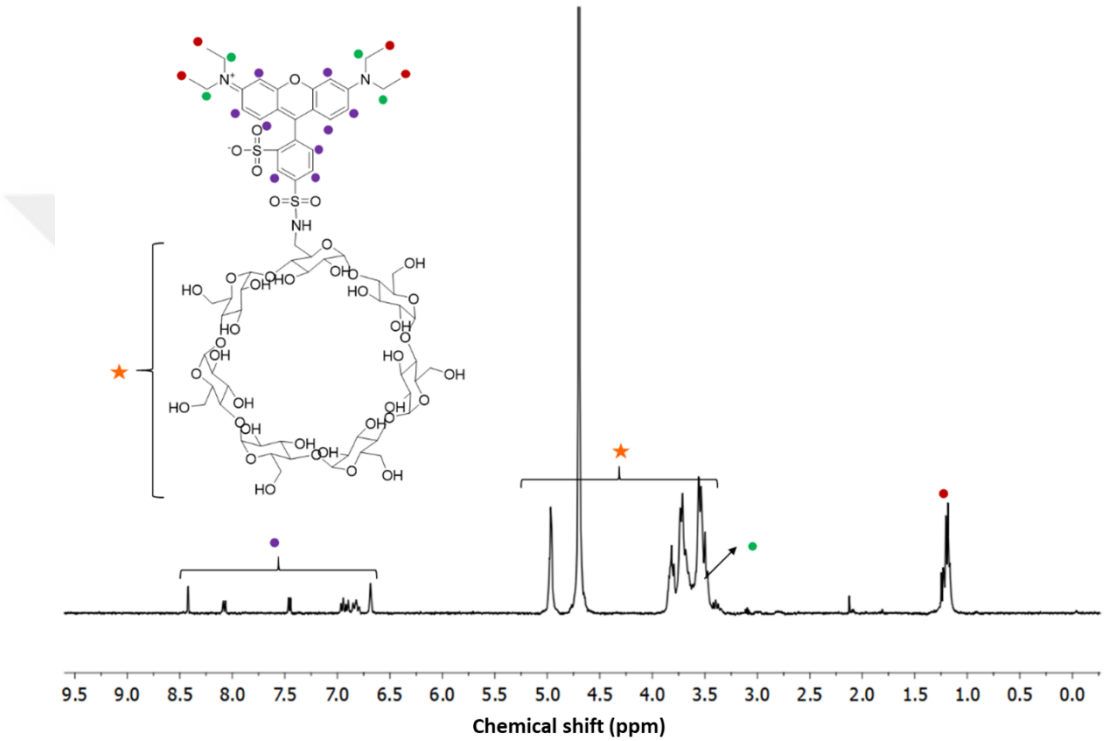

Figure 9.8. ^{1}H NMR spectrum of βCD-lissamine rhodamine B conjugate in D_2O.

9.3.4. Surface Functionalization with βCD-Lissamine-Rhodamine-B Dye

Initial functionalization of S(D_{75}-A_{20}-T_5) and S(D_{95}-A_0-T_5) was undertaken with βCD-lissamine-Rhodamine-B via the μCP method using a PDMS stamp. S(D_{75}-A_{20}-T_5) surface was brought in conformal contact with a patterned PDMS stamp inked with the dye. After printing, the surface was washed with cold water to remove any unbound dye. For the control experiment, S(D_{95}-A_0-T_5) surface was used and treated with βCD-lissamine-Rhodamine-B dye in the same manner. After printing, surfaces were visualized under the fluorescence microscope. While S(D_{75}-A_{20}-T_5) surface revealed red fluorescence, as seen in Figure 9.9b-c, S(D_{95}-A_0-T_5) did not show any fluorescent pattern, presumably due to the

lack of host-guest interaction on the surface devoid of any adamantane group and control image was given in Figure 9.9c, inset. These results suggest that obtained polymer-coated interfaces are amenable to facile functionalization using specific non-covalent interactions in an aqueous environment.

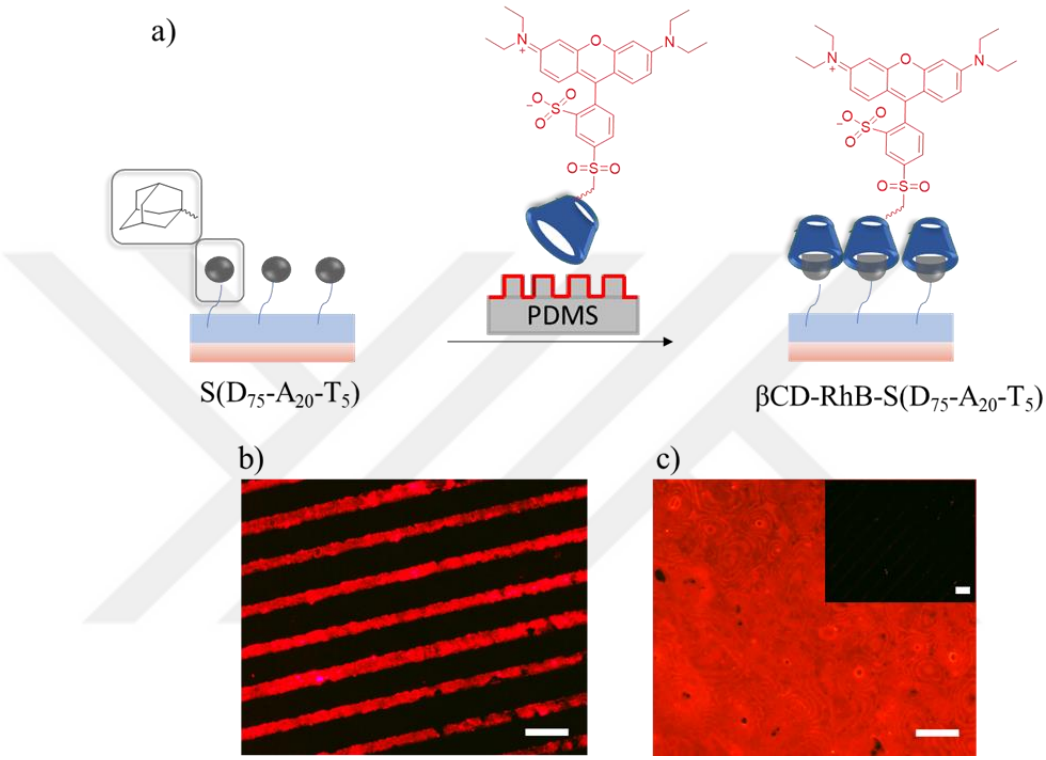

Figure 9.9. (a) Schematic illustration of polymer-coated surface modification via μCP using βCD-grafted lissamine-Rhodamine B dye; fluorescence microscopy images of dye-modified (b) patterned surfaces, (c) nonpatterned surfaces, and inset S(D_{95}-A_0-T_5). The scale bar is 100 μm.

Surface S(D_{75}-A_{20}-T_5) modified with βCD-grafted lissamine-Rhodamine B dye was immersed in PBS buffer (pH 7.4) and incubated at 37 ^{o}C for 48 hours. The fluorescence microscope images were recorded at a predetermined time interval. As seen in Figure 9.10, the fluorescence intensity of βCD-grafted lissamine-Rhodamine B modified S(D_{75}-A_{20}-T_5) surface showed no significant change when incubated at 37 ^{o}C for 48 h. Observations suggest significant stability of thus modified polymer surface βCD/Ada-based host-guest interactions.

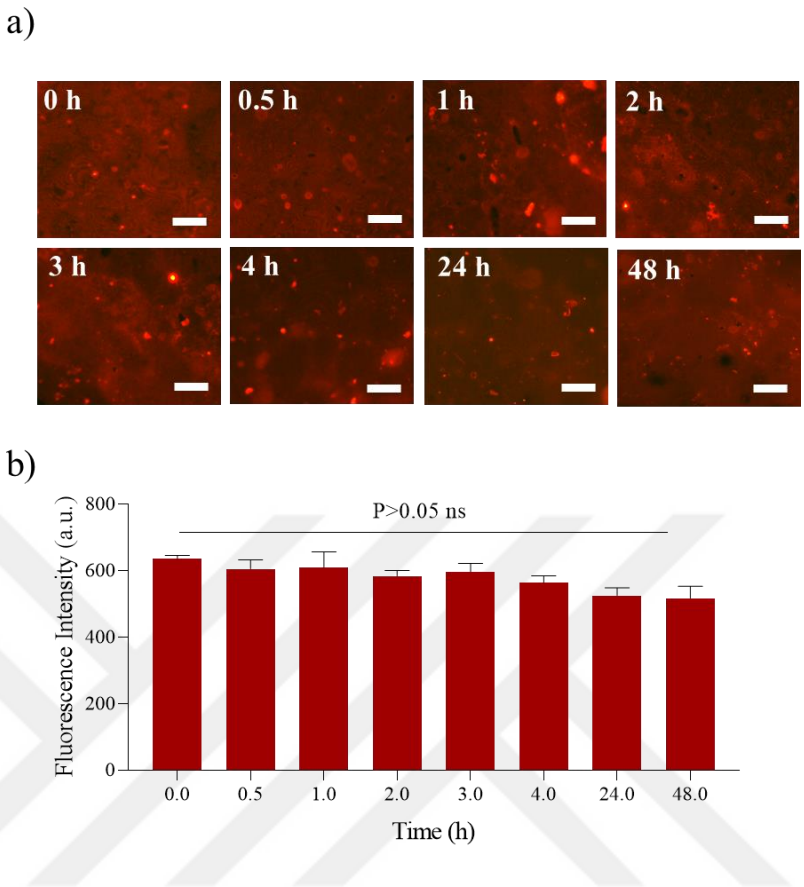

Figure 9.10. The fluorescence images of βCD-grafted lissamine-rhodamine B modified S(D_{75}-A_{20}-T_5) surface after incubation at 37 °C in PBS buffer from 0 h to 48 h, b) the fluorescence intensity bar graph of βCD-grafted lissamine-Rhodamine B modified S(D_{75}-A_{20}-T_5) surface.

9.3.5. Surface Functionalization with βCD-Biotin for Protein Immobilization

After the successful demonstration of the immobilization of fluorescent dye, an FTIC-Streptavidin conjugate was selected as a model protein to investigate biomolecular immobilization. To this end, a βCD-Biotin conjugated S(D_{75}-A_{20}-T_5) surface was modified with FITC-streptavidin with and without a pattern and scheme was illustrated in Figure 9.11a. Surface S(D_{95}-A_0-T_5), devoid of any adamantyl group, was used for control experiments. In addition to S(D_{95}-A_0-T_5) surface, S(D_{75}-A_{20}-T_5) surface, which was not modified with βCD-Biotin, was also utilized for the control experiment. After treatment of the biotinylated surface with FITC-Streptavidin, surfaces were washed with PBS to remove any unconjugated material, and surfaces were visualized under the fluorescence

microscope. As seen in Figure 9.11b-c, green fluorescence was obtained for both patterned and non-patterned biotinylated surfaces upon visualization under a fluorescence microscope. As expected, control surfaces did not exhibit significant green fluorescence, and the image was shown as an inset in Figure 9.11c.

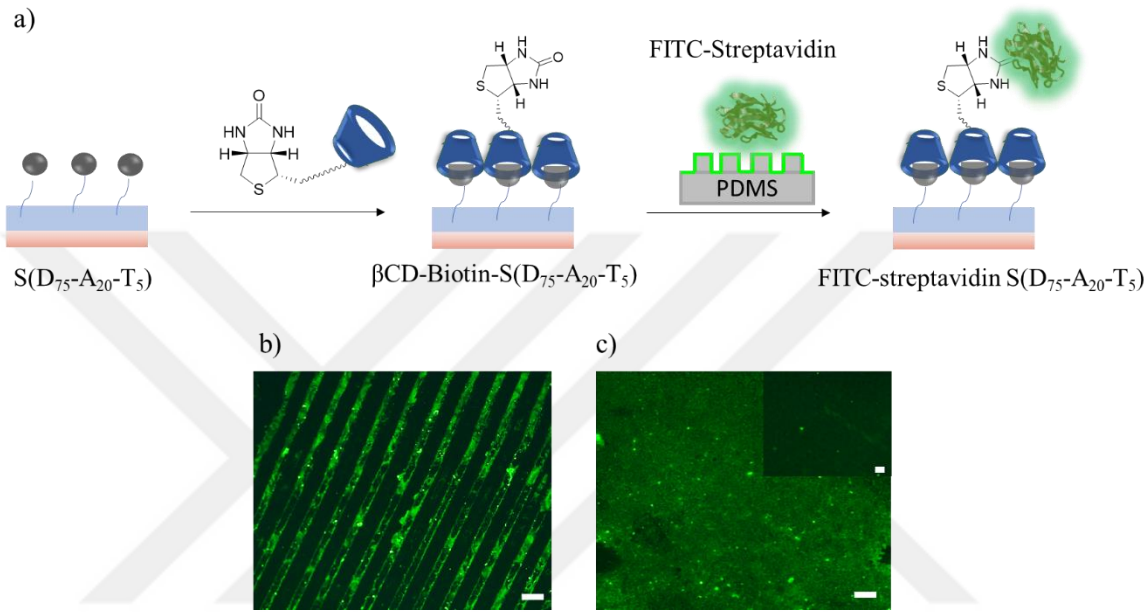

Figure 9.11. (a) Schematic illustration of polymer-coated surface modification with βCD-grafted biotin and immobilization of FITC-Streptavidin using μCP, fluorescence microscopy images of CdSe Qdot streptavidin-modified surfaces (b) patterned S(D_{75}-A_{20}-T_5), (c) nonpatterned S(D_{75}-A_{20}-T_5). The scale bar is 50 μm.

After applying FTIC-streptavidin onto biotin-immobilized S(D_{75}-A_{20}-T_5), further modification was demonstrated using CdSe Qdot-streptavidin conjugate. In the first step, βCD-grafted biotin (βCD-Biotin) was immobilized onto S(D_{75}-A_{20}-T_5) by host-guest interaction. After immobilization, the surface was washed with cold water to remove unbound βCD-Biotin. Also, control surface S(D_{95}-A_0-T_5) was treated with βCD-Biotin in the same manner. After conjugation of βCD-Biotin, Qdot-Streptavidin conjugate was immobilized onto a biotinylated and control surface with μCP. The conjugation was illustrated in Figure 9.12a. After printing, wafers were washed with cold water to remove non-conjugated materials. As seen in Figure 9.12b, upon visualization under a fluorescence microscope, a nice red fluorescence was observed on both patterned and non-patterned

biotinylated surface S(D_{75}-A_{20}-T_5). As expected, the control surface S(D_{95}-A_0-T_5) revealed no fluorescence, shown as an inset in Figure 9.12c, since no binding occurred due to the lack of adamantane groups

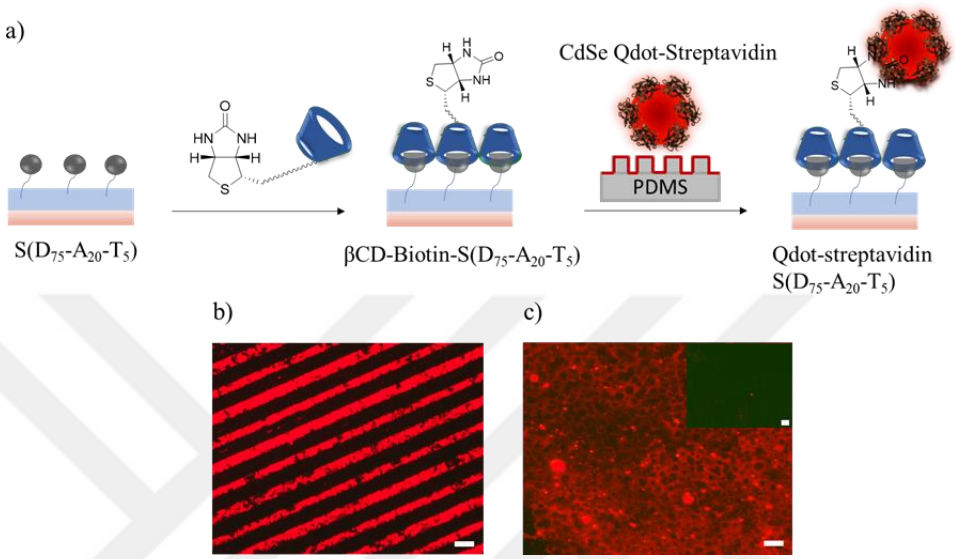

Figure 9.12. (a) Schematic illustration of polymer-coated surface modification with βCD-grafted biotin and immobilization of CdSe Qdot-Streptavidin using μCP; fluorescence microscopy image of (b)CdSe Qdot streptavidin-modified patterned S(D_{75}-A_{20}-T_5) surface; (c) CdSe Qdot streptavidin-modified nonpatterned S(D_{75}-A_{20}-T_5) surface. The scale bar is 50 μm).

Biotin conjugated surface S(D_{75}-A_{20}-T_5) was characterized by XPS analysis. The survey scan of biotin-conjugated S(D_{75}-A_{20}-T_5) is composed of C1s and O1s signals 285.0 eV and 532 eV. The high-resolution C1s spectrum, given in Figure 9.13a, could be deconvoluted to three Gaussians with the expected relative areas for three carbon atoms at 285.0 eV (C-C/C-H), 286.2 eV (C-O-C/C-N/C-S) and 288.8 eV (C=O). Figure 9.13b shows the high-resolution XPS N1s spectra of the biotin-conjugated S(D_{75}-A_{20}-T_5) surface, where the characteristic N atom peak was visible at 400.0 eV. In addition, the S2p peak coming from biotin was observed at 164.2 eV, as seen in Figure 9.13c. N1s and S2p signals suggest successful immobilization of βCD-Biotin onto Ada-containing S(D_{75}-A_{20}-T_5) via host-guest interaction.

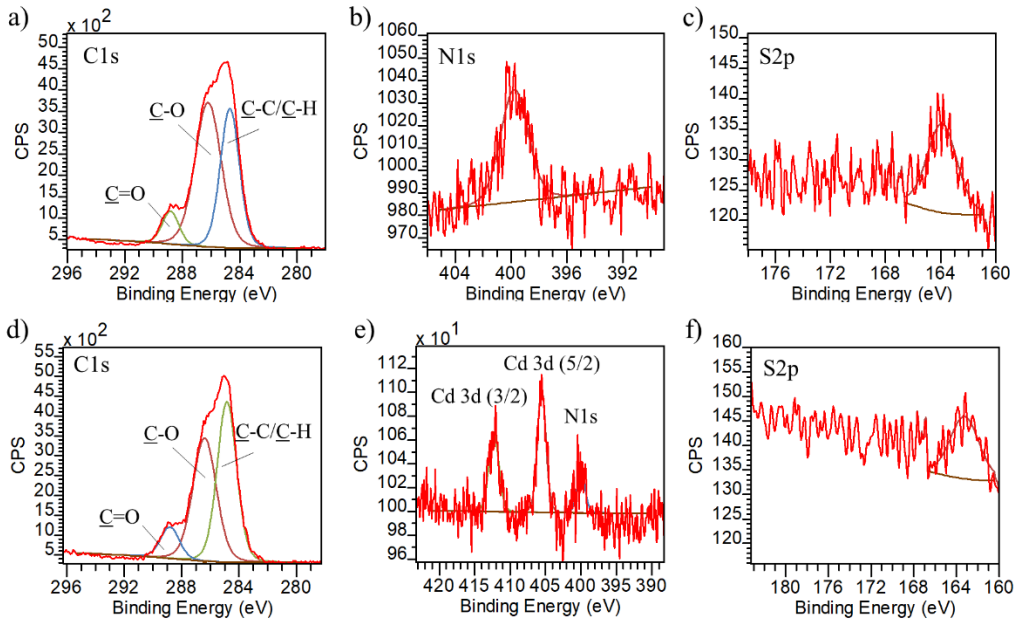

Figure 9.13. High-resolution XPS spectra (a) C1s, (b) N1s, and (c) S2p of βCD-Biotin conjugated S(D_{75}-A_{20}-T_5); and high-resolution XPS spectra (d) C1s, (e) Cd3d and N1s, and (f) S2p of βCD-Biotin conjugated S(D_{75}-A_{20}-T_5) after immobilization of CdSe-Qdot conjugated streptavidin.

In addition to visualization via fluorescence microscope, CdSe Qdot-Streptavidin conjugated biotin-S(D_{75}-A_{20}-T_5) was characterized by XPS analysis. The characteristic N1s and S2p peaks from biotin were still observed at 400 eV and 164.2 eV, respectively, and high-resolution N1s and S2p spectra were demonstrated in Figure 9.13e and Figure 9.13f. In addition to these peaks, the characteristic Cd signals, shown in Figure 9.13e, were visible at 412.2 eV (Cd 3d 3/2) and 405.3 eV (Cd 3d 5/2). The N1s and S2p signals proved the presence of biotin, and Cd3d signals showed successful interaction between CdSe Qdot-streptavidin and biotin-conjugated S(D_{75}-A_{20}-T_5) surface.

9.3.6. Synthesis of Mono-Mannose Containing βCD Conjugate

Alkyne-containing mannose and mono-azide functionalized βCD were prepared using literature procedures [417], [252]. A copper-catalyzed *click* reaction between alkyne-mannose and mono-azide functionalized βCD gave mannose-βCD conjugates in 90% yield

in the presence of $CuSO_4$ and sodium ascorbate. The reaction between the alkyne and azide groups is shown in Figure 9.14.

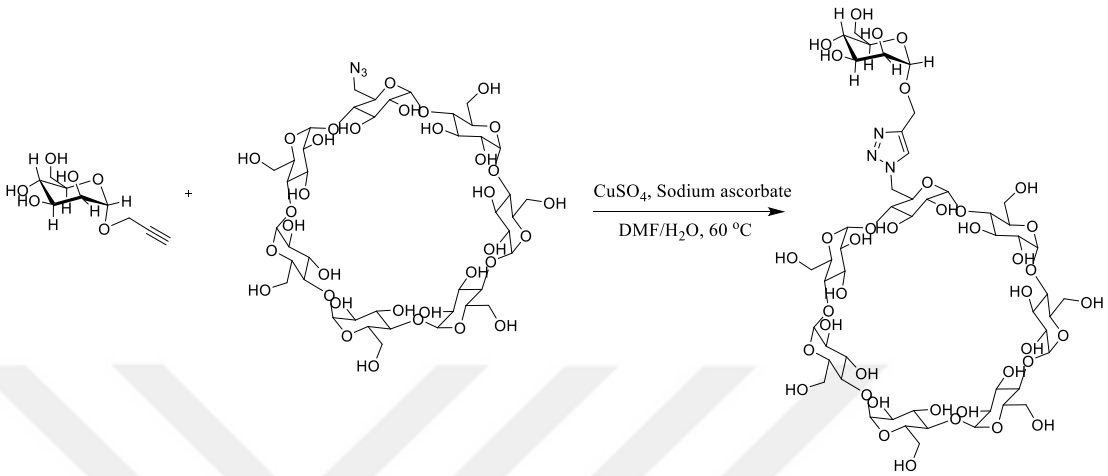

Figure 9.14. The copper-catalyzed *click* reaction between alkyne-containing mannose and mono-azide functionalized βCD.

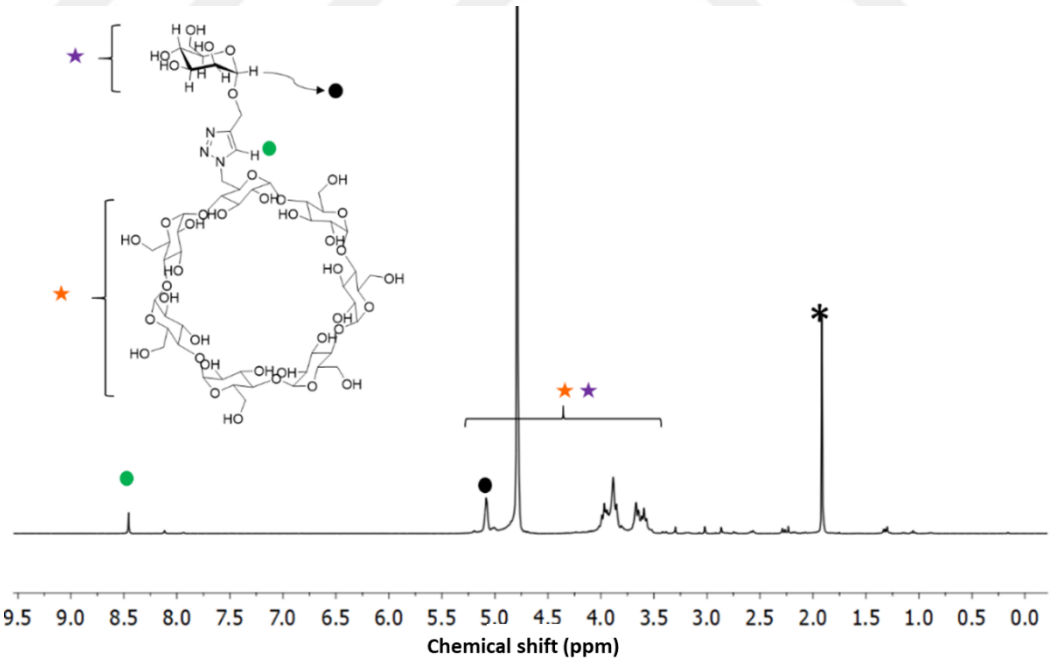

Figure 9.15. ^{1}H NMR spectrum of mono-mannose conjugated βCD in D_2O.

^{1}H NMR characterized the mannose-conjugated βCD, and the full spectrum was demonstrated in Figure 9.15. The hydrogen resonance of the triazole group at 8.46 ppm was the first proof of a successful *click* reaction between azide and alkyne groups. In addition to this characteristic peak, the signal of anomeric hydrogen coming from both mannose and βCD was another evidence of the reaction.

9.3.7. Lectin Binding to Mannose-Containing Polymer Coatings

A surface decorated with mannose was fabricated using host-guest mediated immobilization of a mannose-containing CD, followed by probing their ability to bind selectively to a dye-labeled lectin, namely, fluorescein-labeled Concanavalin A (FITC-ConA). For this purpose, Ada-containing surface S(D_{75}-A_{20}-T_5) and control surface S(D_{95}-A_0-T_5) were treated with βCD-bearing mannose to obtain a mannose displaying surface. Unbound βCD-bearing mannose was removed from the surface by rinsing the surfaces with water. βCD-Man-S(D_{75}-A_{20}-T_5) and control S(D_{95}-A_0-T_5) surfaces were subsequently utilized to evaluate Con A binding, and scheme was shown in Figure 9.16a. βCD-Man-S(D_{75}-A_{20}-T_5) and control S(D_{95}-A_0-T_5) surfaces were treated with FITC-ConA using μCP. After washing with HEPES (20 mM) solution, to remove any physically adhered FITC-ConA, the surface was visualized under a fluorescence microscope, and fluorescence image was given in Figure 9.16b. As expected, while the βCD-Man-S(D_{75}-A_{20}-T_5) surface displayed green fluorescence with clear patterns, the control S(D_{95}-A_0-T_5) surface did not show any fluorescence, shown as an inset in Figure 9.16b, when treated with FITC-ConA.

In another demonstration of FITC-ConA lectin binding, the specificity of this immobilization was demonstrated using Rhodamine B-PNA (RhB-PNA). βCD-Man-S(D_{75}-A_{20}-T_5) and control S(D_{95}-A_0-T_5) surfaces were treated with RhB-PNA using μCP method. After printing, the surface was visualized under the fluorescence microscope. As seen in Figure 9.16c, a nice pattern with red fluorescence was obtained. Subsequently, upon rinsing the surface with cold water, the red fluorescent pattern disappeared as expected since the lectin PNA does not possess any binding affinity towards mannose.

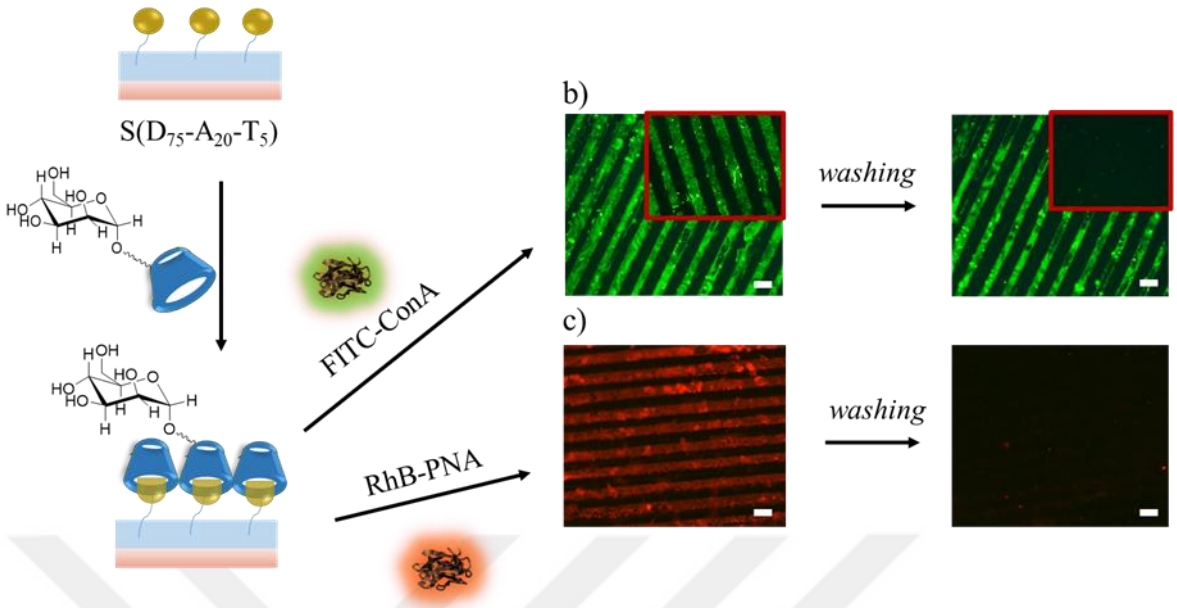

Figure 9.16. (a) Schematic illustration of polymer-coated surface modification with βCD-mannose and immobilization of FITC-ConA using μCP; (b) fluorescence microscopy images of FITC-ConA-modified and (c) fluorescence microscopy images of Rhodamine-PNA-modified S(D_{75}-A_{20}-T_5) before and after washing steps. The scale bar is 50 μm.

After demonstrating ConA binding to the βCD-Man-S(D_{75}-A_{20}-T_5) surface, we investigated if ConA can be released from the βCD-Man-S(D_{75}-A_{20}-T_5) surface. Interactions between βCD-Man-S(D_{75}-A_{20}-T_5) surface and conjugated ConA should decrease in the presence of a high concentration of a competitive ligand such as free sugar, and reduced interaction should lead to the release of ConA from the surface. To this end, FITC-ConA printed βCD-Man-S(D_{75}-A_{20}-T_5) surfaces were incubated with D-(+)-mannose solution (10 mg/mL in HEPES) to enable ConA release. Upon visualization under a fluorescence microscope, as seen in Figure 9.17b,d shows no green fluorescence after treatment with D-(+)-mannose solution, resulting from ConA release from the surface. Subsequently, regeneration/reutilization of the βCD-Man-S(D_{75}-A_{20}-T_5) surface was also investigated, and it was observed that FITC-ConA could be immobilized onto regenerated βCD-Man-S(D_{75}-A_{20}-T_5) surfaces. As seen in Figure 9.17a,c,e, the regenerated βCD-Man-S(D_{75}-A_{20}-T_5) surface could immobilize FITC-ConA in subsequent cycles with almost similar efficiency.

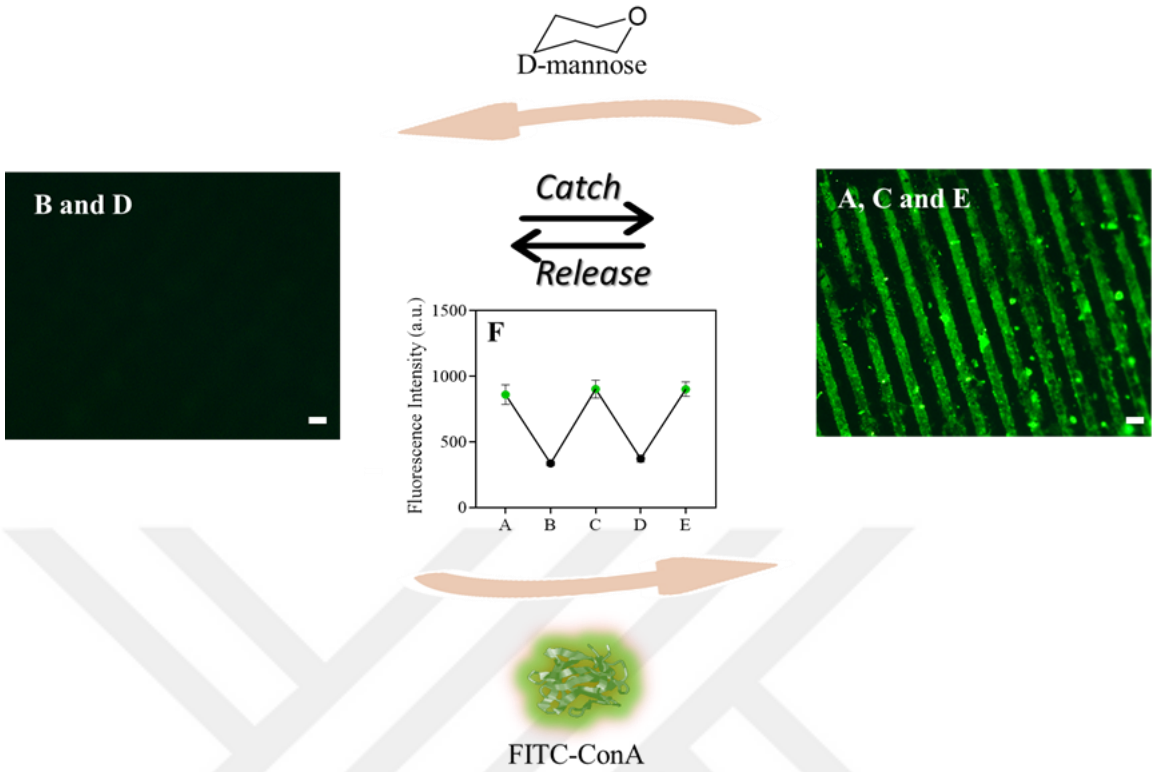

Figure 9.17. Regeneration and reuse of βCD-Man-S(D_{75}-A_{20}-T_5) surface. (a) (c) and (e) Adsorption of FITC-ConA on βCD-Man-S(D_{75}-A_{20}-T_5) surface; (b) and (d) regeneration by releasing of ConA in the presence of D-mannose; (f) The cycles of reuse of βCD-Man-S(D_{75}-A_{20}-T_5) were measured by analyzing the mean fluorescence intensity of the images.

9.3.8. The Synthesis of Cyclic-RGD-containing βCD Conjugate

To synthesize cRGD-βCD conjugate, alkyne-bearing cRGD and mono-azide functionalized βCD were used and prepared using literature procedures [402], [404]. The cRGD-βCD conjugate was synthesized by *click* reaction between azide and alkyne groups in the presence of Cu(I)Br and PMDETA. The reaction was shown in Figure 9.18. Cuprisorb was used to remove copper. The characterization of cRGD-βCD conjugate was done with mass analysis.

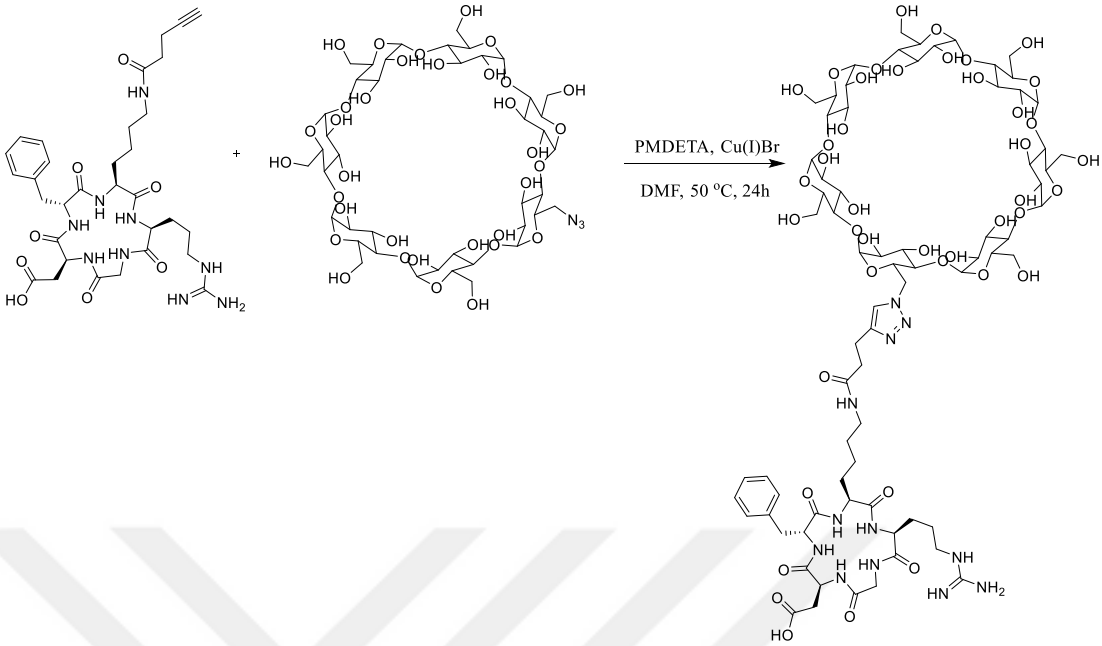

Figure 9.18. The synthesis of cyclic RGD-conjugated βCD via click reaction.

9.3.9. cRGD-βCD Immobilization and Evaluation of Cell Attachment

Finally, we wanted to investigate if polymer-coated surfaces could be rendered amenable for cell attachment through non-covalent decoration with cell-adhesive peptides. To this end, S(D_{75}-A_{20}-T_5) surfaces were treated with cRGD-conjugated βCD to obtain an interface displaying the cRGD peptide. After incubation of the surface with peptide-containing CD solution, unbound βCD-derivative was rinsed from the surface by rinsing the surfaces with water. To confirm that the peptide was immobilized onto the surface through host-guest interactions, the peptide-decorated surface S(D_{75}-A_{20}-T_5) was characterized by XPS. The survey scan cRGD peptide conjugated S(D_{75}-A_{20}-T_5) comprises C1s and O1s signals 285.0 eV and 533 eV. The high-resolution C1s spectrum, given in Figure 9.19a, could be deconvoluted to three Gaussians with the expected relative areas for three carbon atoms at 285.0 eV (C-C/C-H), 286.0 eV (C-O-C/C-N), and 289.1 eV (C=O). Notably, the characteristic N1s peak, shown in Figure 9.19b, from the cRGD peptide was observed at 400 eV, which confirmed the successful attachment of the peptide onto the surface.

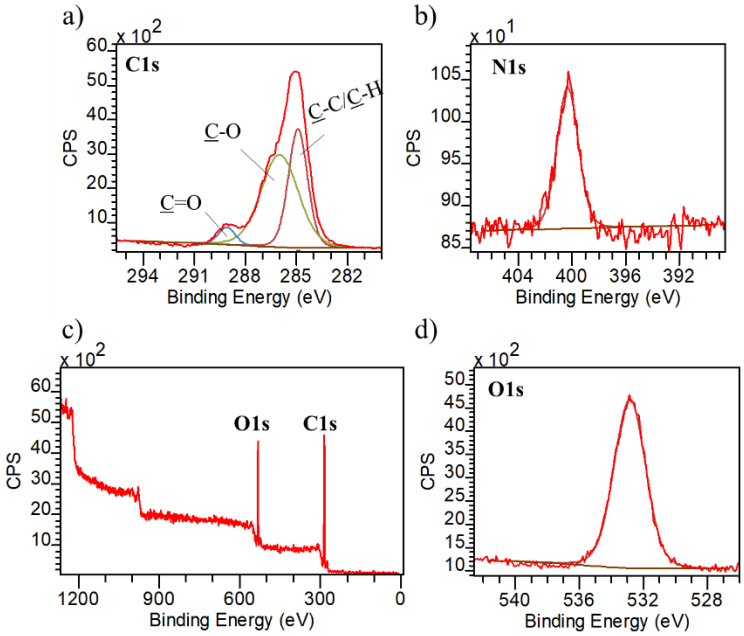

Figure 9.19. High-resolution XPS spectra (a) C1s, (b) N1s, (c) survey scan ,and (d) O1s spectra of cRGD immobilized S(D_{75}-A_{20}-T_5) surface.

After the immobilization of cRGD-βCD, L929 mouse fibroblast cells were seeded onto the peptide-modified surface (RGD-βCD-S(D_{75}-A_{20}-T_5)). S(D_{75}-A_{20}-T_5) without RGD immobilization and S(D_{95}-A_0-T_5) surfaces were utilized for the control experiment. After 24 h and 72 h incubation**,** the actin and nuclei of attached cells were stained using an Alexa fluor-phalloidin-488 kit and DAPI, respectively. After the staining processes, images of cells on the polymer-coated surfaces were obtained using a fluorescence microscope. In the case of immobilization of polymer surface with cRGD-βCD, enhanced cell attachment and proliferation were observed after 24 h and 72 h. As seen in Figure 9.20b, cell adhesive peptide affects cellular attachment onto the polymer surface. As a comparison, the attachment of cells onto S(D_{75}-A_{20}-T_5) (not treated with cRGD-βCD) and the control surface S(D_{95}-A_0-T_5) remained significantly low due to the anti-biofouling character of the PEG-based copolymer coating.

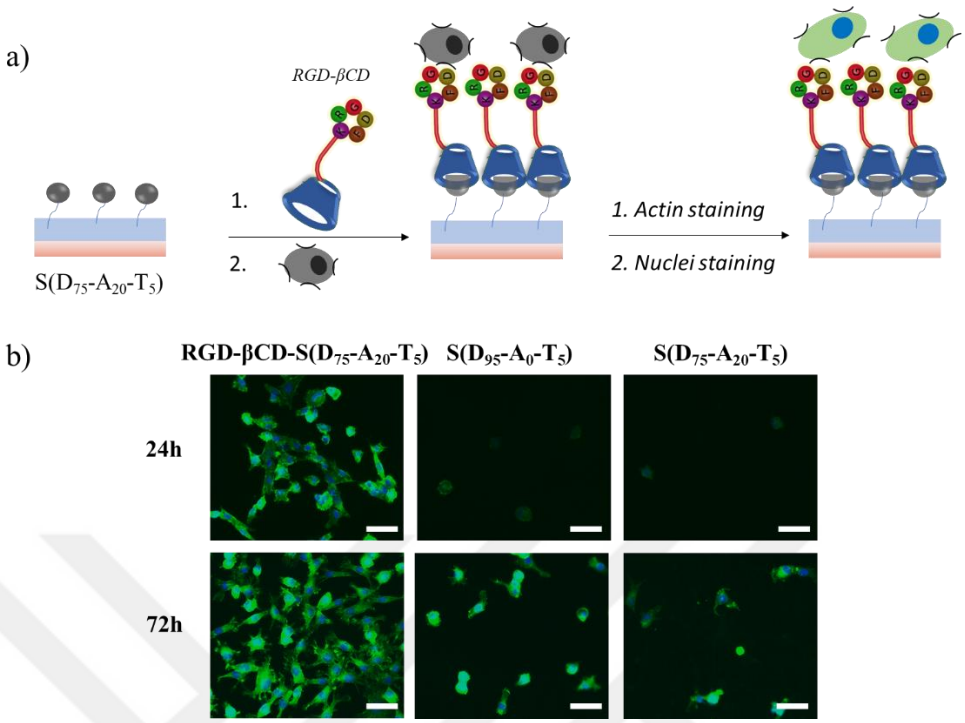

Figure 9.20. (a) Scheme of conjugation of RGD-βCD and subsequent cellular attachment; (b) merged fluorescence microscopy images of fibroblast cells immobilized on RGD-βCD-S(D_{75}-A_{20}-T_5), S(D_{95}-A_0-T_5) and S(D_{75}-A_{20}-T_5) surfaces after staining. The scale bar is 50 µm.

9.4. Conclusion

In summary, the fabrication of a versatile polymeric coating amenable to facile functionalization in a plug-and-play modular manner to immobilize various functional molecules ranging from fluorescent dyes to bioactive ligands is demonstrated. An Ada-CD-based host-guest complexation on a polymeric interface enables a variety of functionalization in a robust manner. Examples here demonstrate the modification of polymer-coated surfaces for immobilizing specific proteins and protein-coated inorganic nanocrystals. Protein immobilization/sensing can be undertaken in a selective manner by appropriate choice of the functional molecules immobilized at the interface. Through catch-and-release cycles, we demonstrate that obtained interface is robust enough for regeneration and reusability in certain applications. Finally, we show that the inherently anti-biofouling

polymeric interface can be tailored for the attachment of cells through modification with cell-adhesive peptides. One can envision that the facile fabrication and versatile and modular nature of the interface engineering demonstrated here will be deemed attractive for the fabrication of functional devices for various biomedical applications.

10. CONCLUSION

This thesis covers the design and fabrication of polymer-drug conjugates, polymer-based nanogels and hydrogels for drug delivery applications, and polymeric coatings on solid interfaces for biomedical applications. RAFT polymerization was utilized for obtaining polymer-drug conjugates, and linker optimization was performed to obtain desired *in vitro* drug release and cytotoxicity profiles. Supramolecular host-guest interactions and click-based reactions in formulation strategies were used to fabricate nanogels. Advanced techniques were utilized to characterize nanogels, and *in vitro* drug release and cell studies were performed for nanogel formulations. Metal-free "*click*" reactions were employed to fabricate hydrogels for drug delivery applications. In the other projects, polymer coatings were prepared as polymer brushes and thin film layers. While polymer brushes were prepared using a 'grafting from' method using different monomers, thin film coatings were prepared using a 'grafting to' approach using preformed polymers. Polymer brushes were obtained using SI-RAFT methods. Using polymeric coatings, biomolecular immobilization, drug delivery, cellular attachment, and cell release studies were performed. This thesis comprises seven projects related to the design, fabrication, and evaluation of different polymeric materials.

In the first project, polymer-drug conjugates with different linkers were synthesized. The linker optimization was done to obtain better drug release. For HCQ release, pH-responsive ester, carbamate, and carbonate linkers were used for optimization. According to release profiles, the carbonate linker was selected as the optimal linker to achieve a high level of HCQ release. For GEM release, pH-responsive carbamate and redox-responsive disulfide linkers were evaluated, and the disulfide-based linkage was chosen for subsequent studies. After the linker optimization, copolymers containing HCQ and GEM were synthesized using the carbonate and disulfide linkers, respectively. It was gratifying to note that desired drug release profile and high level of cytotoxicity against BxPC-3 cells and 3D-spheroid were observed.

In the second project, we reported the fabrication of redox-responsive nanogels for drug delivery applications. βCD-based nanogels were obtained using self-assembly and

host-guest supramolecular interaction. Anticancer drug DOX was physically loaded into prepared nanogels. The targeting peptide cRGD was introduced into the nanogel system to obtain targeted and drug-loaded nanogels. Nanogel characterization was achieved using DLS and TEM. *In vitro* drug release study was performed pH and redox-responsive environment. As expected, nanogels showed the highest DOX release at acidic pH in the presence of GSH. MDA-MB-231 breast cancer cells were used for the cytotoxicity experiment, and RGD-targeted and DOX-loaded nanogels demonstrated the highest cytotoxicity when cells were enriched with GSH. In addition, due to RGD moiety, RGD-targeted nanogels showed higher cellular internalization than the non-targeted version.

The third project focused on fabricating injectable hydrogels for drug delivery applications. OEGMA-based random copolymers were synthesized via RAFT polymerization. Azide ($-N_3$)-containing monomers were used for further cross-linking. Anticancer drug gemcitabine (GEM) was conjugated to the polymer backbone using carbamate and disulfide-carbamate linkers. Dibenzocyclooctyne (DBCO)-containing disulfide containing PEG-based redox-responsive crosslinker was synthesized. Strain-promoted azide-alkyne cycloaddition reaction between $-N_3$ and DBCO groups gave hydrogel. Hydrogel characterization was performed using FTIR, SEM, and rheometer. Injectability, self-healing ability, and degradability were shown. Drug release profiles were investigated at pH 6.8 and 7.4 with and without GSH. While hydrogel containing GEM with disulfide linker (HG-GEMSSC) showed significant GEM release in the presence of GSH, the same hydrogels did not release in the absence of GSH. However, the hydrogel system containing GEM with carbamate linker (HG-GEMC) showed a low amount of GEM with and without GSH. The cytotoxic activities of HG-GEMSSC and HG-GEMC hydrogels were compared in the presence and absence of GSH. Although these two hydrogels showed moderate cytotoxicity toward BxPC3 pancreatic cancer cells, HG-GEMSSC hydrogels demonstrated higher cytotoxicity than HG-GEMC hydrogels in the presence of GSH (1 mM). GSH provided hydrogel degradation and GEM release by breaking disulfide linkers.

Hydrophilic polymer brushes were fabricated and evaluated for biomolecular immobilization in the fourth project. For this purpose, DEGMA-based polymer brushes were synthesized using SI-RAFT polymerization. Maleimide, alkene, and alkene functionalized polyester dendron-conjugated azo-containing molecules were synthesized,

and radical-exchange cross-coupling reactions were employed to modify the CTA-containing end groups of polymer brushes. Copolymer brushes were characterized with AFM, XPS, FTIR, and fluorescence microscope. Maleimide-end group modified polymer brushes were functionalized with fluorescent BODIPY-SH dye and biotin-SH using a thiol-maleimide "click" reaction. Qdot-Streptavidin immobilization onto biotin-containing polymer brushes was demonstrated as an example of ligand-directed interface functionalization. Alkene-end group functionalized polymer brushes were modified with BODIPY-SH and biotin-SH using DMPA-initiated thiol-ene click reactions. Alkene functionalized G0, G1, and G2 polyester dendrons were conjugated to end groups of polymer brushes and modified with mannose-SH using the thiol-ene "click" reaction. Polymer brushes with mannose-conjugated G2 dendrons showed more effective protein recognition than G1 and G0 dendrons with lower multivalency.

In the fifth project, redox-responsive and thiol-reactive polymer brushes were fabricated. Copolymer brushes were synthesized using DEGMA and PDSMA monomers via SI-RAFT polymerization, and side-chain PDS-bearing polymer brushes were obtained with different PDS content. Copolymer brush characterization was done with AFM, XPS, FTIR, and fluorescence microscope. The PDS content of the copolymer brush was determined by XPS analysis. PDS-containing copolymer brushes were modified with thiol-containing molecules using a thiol-pyridyl disulfide exchange reaction. The copolymer brush was modified with BODIPY-SH dye, which could be released in the presence of GSH. As another demonstration of excellent functionalization, brushes were conjugated with trifluoromethyl benzyl mercaptan (TFBM), and the functionalization efficiency was investigated by XPS analysis. As another example, functionalization was done with linear RGD-SH peptide to achieve cellular attachment. Mouse fibroblast L929 cells showed higher attachment to RGD-containing surface, and the attachment of cells was shown using actin filament and DAPI staining. A live dead assay was applied to cells on an RGD-containing polymer brush, and cells showed high viability. After that, the cell-attached polymer brush was exposed to DTT, the released cells from the surface were collected, and a live-dead assay was applied. We showed that surface bounded cells could be released using a reducing environment to harvest them with high viability. In addition, another type of polymer brush modification was undertaken using end groups of polymer brushes to enable orthogonal functionalization. The CTA at the chain ends of polymer brushes was converted into thiol

groups. A maleimide-functionalized rhodamine dye was conjugated using the thiol-maleimide click reaction to investigate the orthogonal functionalization of brushes. Subsequently, BODIPY-SH was introduced to side chains of polymer brushes via the thiol-disulfide exchange reaction. The presence of two dyes was proved by fluorescence microscope analysis. With the same approach, maleimide-containing cyclic RGD was conjugated to the end group of polymer brushes, and thiol-containing DOX derivative was added to the side chains of polymer brushes. MDA-MB-231 breast cancer cells showed attachment on RGD and DOX-containing polymer brushes as expected. In the presence of GSH, cells demonstrated DOX internalization due to DOX release from the polymer brush surface. In this scenario, RGD moiety helped catch cancer cells, and DOX killed attached cells by release from polymer brush due to cleavage of the disulfide linkages when exposed to a reducing environment.

In the sixth project, benzothiazole disulfide (BDS) based redox-responsive copolymers were synthesized modification of polymers were shown with thiol-containing polymers. After that, redox-responsive polymeric coatings were fabricated on the glass surface, and polymeric coatings were obtained using the 'grafting to' approach. Functionalization with thiol-containing molecules was demonstrated using a thiol-containing fluorescent dye, fluorine-tagged benzyl thiol, and cell adhesive RGD-thiol peptide via the thiol-disulfide exchange reaction. Polymer coatings were characterized using XPS, FTIR, contact angle, and fluorescence microscope. RGD-conjugated polymeric coatings showed higher cellular attachment and cell viability. Upon exposure to DTT, surface bounded cells were collected alive to harvest them.

In the seventh and last project, βCD reactive and adamantane-containing polymeric coatings were fabricated and obtained using the 'grafted to' approach. Adamantane-containing polymeric coatings were functionalized with βCD-decorated molecules using supramolecular host-gues interaction. βCD-decorated fluorescent dye, biotin, mannose sugar, and RGD peptide were introduced onto the polymeric coatings for biomolecular immobilization and cell culture applications. Adamantane-containing polymeric coating was functionalized with βCD-biotin to provide protein immobilization, and biotin-streptavidin interaction was demonstrated using the polymeric coating. To investigate lectin binding affinity, mannose-conjugated βCD was introduced to the polymer surface, and the

mannose-grafted surface captured ConA lectin from a mixture of ConA and PNA lectins. Lastly, cyclic RDG was integrated onto polymeric coating using adamantane-βCD interaction. While the RGD-grafted surface enabled high cellular attachment, the surface without the RGD targeting group showed minimal cell attachment, as expected.

In the scope of this thesis, a total of seven projects focused on a common theme of creating functional polymeric materials for potential application in biomedical sciences were successfully evaluated. The work disclosed in this thesis demonstrates that combining fundamental organic transformations with advances in contemporary polymer science provides a powerful tool to create biomaterials that can provide solutions to the challenges encountered in several arenas of health sciences.

REFERENCES

1. Elmore, S., "Apoptosis: A Review of Programmed Cell Death", *Toxicologic Pathology*, Vol. 35, No. 4, pp. 495–516, 2007.

2. Wiesmuller, L., J. M. Ford and R. H. Schiestl, "DNA Damage, Repair, And Diseases", *Journal of Biomedicine and Biotechnology*, Vol. 2, No. 2, p. 45, 2002.

3. "International Agency for Research on Cancer", *WHO Chronicle*, Vol. 23, pp. 323–326, 1969.

4. Hanahan, D. and R. A. Weinberg, "Hallmarks of Cancer: The Next Generation", *Cell*, Vol. 144, No. 5, pp. 646–674, 2011.

5. Leong, S. P., A. Aktipis and C. Maley, "Cancer Initiation and Progression Within the Cancer Microenvironment", *Clinical and Experimental Metastasis*, Vol. 35, No. 5-6, pp. 361–367, 2018.

6. Parsa, N., "Environmental Factors Inducing Human Cancers", *Iranian Journal of Public Health*, Vol. 41, No. 11, pp. 1–9, 2012.

7. Grizzi, F., A. Di Ieva, C. Russo, E. E. Frezza, E. Cobos, P. C. Muzzio and M. Chiriva-Internati, "Cancer Initiation and Progression: an Unsimplifiable Complexity", *Theoretical Biology and Medical Modelling*, Vol. 3, No. 37, 2006.

8. Obenauf, A. C. and J. Massague, "Surviving at A Distance: Organ-Specific Metastasis", *Trends in Cancer*, Vol. 1, No. 1, pp. 76–91, 2015.

9. Fares, J., M. Y. Fares, H. H. Khachfe, H. A. Salhab and Y. Fares, "Molecular Principles of Metastasis: A Hallmark of Cancer Revisited", *Signal Transduction and Targeted Therapy*, Vol. 5, No. 28, pp. 1–7, 2020.

10. Steeg, P. S., "Tumor Metastasis: Mechanistic Insights and Clinical Challenges", *Nature Medicine*, Vol. 12, pp. 895–904, 2006.

11. Nishida, N., H. Yano, T. Nishida, T. Kamura and M. Kojiro, “Angiogenesis in Cancer”, *Vascular Health and Risk Management,* Vol. 2, No. 3, pp. 213–219, 2006.

12. Madu, C. O., S. Wang, C. O. Madu and Y. Lu, “Angiogenesis in Breast Cancer Progression, Diagnosis, and Treatment”, *Journal of Cancer,* Vol. 11, pp. 4474–4494, 2020.

13. Munoz-Chapuli, R., A. R. Quesada and M. A. Medina, “Angiogenesis and Signal Transduction in Endothelial Cells”, *Cellular and Molecular Life Sciences,* Vol. 61, No. 17, pp. 2224–2243, 2004.

14. Pucci, C., C. Martinelli and G. Ciofani, “Innovative Approaches for Cancer Treatment: Current Perspectives and New Challenges”, *Ecancermedicalscience,* Vol. 13, pp. 1–26, 2019.

15. Verhoef, M. J., R. J. Hilsden and M. O’Beirne, “Complementary Therapies and Cancer Care: An Overview”, *Patient Education and Counseling*, Vol. 38, No. 2, pp. 93–100, 1999.

16. Pommier, Y. and D. Robert, “Pharmacological and Therapeutics Agents That Target DNA Replication”, *DNA Replication in Eukaryotic Cells (2nd Edition),* Vol. 26, pp. 1–28, 2001.

17. Bhat, K. M. R. and V. Setaluri, “Microtubule-Associated Proteins as Targets in Cancer Chemotherapy”, *Clinical Cancer Research,* Vol. 13, No. 10, pp. 2849–2854, 2007.

18. Jordan, M. A. and L. Wilson, “Microtubules as A Target for Anticancer Drugs”, *Nature Reviews Cancer,* Vol. 4, pp. 253–265, 2004.

19. Van Vuuren, R. J., M. H. Visagie, A. E. Theron and A. M. Joubert, “Antimitotic Drugs in The Treatment of Cancer”, *Cancer Chemotherapy and Pharmacology,* Vol. 76, pp. 1101–1112, 2015.

20. Samant, R. S. and L. A. Shevde, “Recent Advances in Anti-Angiogenic Therapy of Cancer”, *Oncotarget,* Vol. 2, No. 3, pp. 122–134, 2011.

21. Senapati, S., A. K. Mahanta, S. Kumar and P. Maiti, “Controlled Drug Delivery Vehicles for Cancer Treatment and Their Performance”, *Signal Transduction and Targeted Therapy*, Vol. 3, No. 7, pp. 1–19, 2018.

22. Li, Z., S. Tan, S. Li, Q. Shen, K. Wang, “Cancer Drug Delivery in the Nano-era: An Overview and Perspectives”, *Oncology Reports*, Vol. 38, No. 2, pp. 611–624, 2017.

23. Liu, S., R. Maheshwari and K. L. Kiick, “Polymer-Based Therapeutics”, *Macromolecules*, Vol. 42, No. 1, pp. 3–13, 2009.

24. Ringsdorf, H., “Structure and Properties of Pharmacologically Active Polymers”, *Journal of Polymer Science: Polymer Symposia*, Vol. 51, No. 1, pp. 135–153, 1975.

25. Larson, N. and H. Ghandehari, “Polymeric Conjugates for Drug Delivery”, *Chemistry of Materials*, Vol. 24, No. 5, pp. 840–853, 2012.

26. Coelho, J. F., P. C. Ferreira, P. Alves, R. Cordeiro, A. C. Fonseca, J. R. Gois and M. H. Gil, “Drug Delivery Systems: Advanced Technologies Potentially Applicable in Personalized Treatments”, *EPMA Journal*, Vol. 1, No. 1, pp. 164–209, 2010.

27. Duncan, R., “The Dawning Era of Polymer Therapeutics”, *Nature Reviews Drug Discovery*, Vol. 2, pp. 347–360, 2003.

28. Qian, Q., L. Zhu, X. Zhu, M. Sun and D. Yan, “Drug-Polymer Hybrid Macromolecular Engineering: Degradable PEG Integrated by Platinum(IV) for Cancer Therapy”, *Matter*, Vol. 1, No. 6, pp. 1618–1630, 2019.

29. Yu, Y., C. -K. Chen, W. -C. Law, H. Sun, P. N. Prasad and C. Cheng, “A Degradable Brush Polymer–Drug Conjugate for pH-Responsive Release of Doxorubicin”, *Polymer Chemistry*, Vol. 6, pp. 953–961, 2015.

30. Chang, M., F. Zhang, T. Wei, T. Zuo, Y. Guan, G. Lin and W. Shao, “Smart Linkers in Polymer–Drug Conjugates for Tumor-Targeted Delivery”, *Journal of Drug Targeting*, Vol. 24, No. 6, pp. 475–491, 2016.

31. Gamcsik, M. P., M. S. Kasibhatla, S. D. Teeter and O. M. Colvin, “Glutathione Levels in Human Tumors”, *Biomarkers*, Vol. 17, No. 8, pp. 671–691, 2012.

32. Chen, W., L. A. Shah, L. Yuan, M. Siddiq, J. Hu and D. Yang, “Polymer–Paclitaxel Conjugates Based on Disulfide Linkers for Controlled Drug Release”, *RSC Advances*, Vol. 5, No. 10, pp. 7559–7566, 2015.

33. Zhang, P., H. Zhang, W. He, D. Zhao, A. Song and Y. Luan, “Disulfide-Linked Amphiphilic Polymer-Docetaxel Conjugates Assembled Redox-Sensitive Micelles for Efficient Antitumor Drug Delivery”, *Biomacromolecules*, Vol. 17, No. 5, pp. 1621–1632, 2016.

34. Xu, C., R. -J. Song, P. Lu, J. -C. Chen, Y. -Q. Zhou, G. Shen, M. -J. Jiang and W. Zhang, “pH-Triggered Charge-Reversal and Redox-Sensitive Drug Release Polymer Micelles Co-Deliver Doxorubicin and Triptolide for Prostate Tumor Therapy”, *International Journal of Nanomedicine*, Vol. 13, pp. 7229–7249, 2018.

35. Song, Y., H. Zhang, X. Wang, X. Geng, Y. Sun, J. Liu and Z. Li, “One Stone, Three Birds: pH Triggered Transformation of Aminopyronine and Iminopyronine Based Lysosome Targeting Viscosity Probe for Cancer Visualization”, *Analytical Chemistry*, Vol. 93, No. 3, pp. 1786–1791, 2020.

36. Choy, C. J., J. J. Geruntho, A. L. Davis and C. E. Berkman, “Tunable pH-Sensitive Linker for Controlled Release”, *Bioconjugate Chemistry*, Vol. 27, No. 3, pp. 824–830, 2016.

37. Yasuhiro M. and H. Maeda, “New Concept for Macromolecular Therapeutics in Cancer Chemotherapy: Mechanism of Tumoritropic Accumulation of Proteins and The Antitumor Agent Smancs”, *Cancer Research*, Vol. 46, No. 12, pp. 6387–6392, 1986.

38. M. A. Konerding, A. J. Miodonski, and A. Lamethschwandtner, “Microvascular Corrosion Casting in The Study of Tumor Vascularity: A Review”, *Scanning Microscopy*, Vol. 9, No. 4, pp. 1233–1244, 1995.

39. Greish, K., “Enhanced Permeability and Retention of Macromolecular Drugs in Solid Tumors: A Royal Gate for Targeted Anticancer Nanomedicines”, *Journal of Drug Targeting*, Vol. 15, No. 7-8, pp. 457–464, 2007.

40. Nakamura, Y., A. Mochida, P. L. Choyke and H. Kobayashi, “Nanodrug Delivery: Is the Enhanced Permeability and Retention Effect Sufficient for Curing Cancer?”, *Bioconjugate Chemistry*, Vol. 27, No. 10, pp. 2225–2238, 2016.

41. Maeda, H., K. Tsukigawa and J. Fang, “A Retrospective 30 Years After Discovery of The Enhanced Permeability and Retention Effect of Solid Tumors: Next-Generation Chemotherapeutics and Photodynamic Therapy—Problems, Solutions, and Prospects”, *Microcirculation,* Vol. 23, No. 3, pp. 173–182, 2016.

42. Yu, B., H. C. Tai, W. Xue, L. J. Lee and R. J. Lee, “Receptor-Targeted Nanocarriers for Therapeutic Delivery to Cancer”, *Molecular Membrane Biology*, Vol. 27, No. 7, pp. 286–298, 2010.

43. Anarjan, F. S., “Active Targeting Drug Delivery Nanocarriers: Ligands”, *Nano-Structures & Nano-Objects*, Vol. 19, p. 100370, 2019.

44. Iqbal, N. and N. Iqbal, “Human Epidermal Growth Factor Receptor 2 (HER2) In Cancers: Overexpression and Therapeutic Implications”, *Molecular Biology International*, Vol. 2014, pp. 1–9, 2014.

45. Zwicke, G. L., G. Ali Mansoori and C. J. Jeffery, “Utilizing the Folate Receptor for Active Targeting of Cancer Nanotherapeutics”, *Nano Reviews*, Vol. 3, p. 18496, 2012.

46. Shreya, A. B., S. Y. Raut, R. S. Managuli, N. Udupa and S. Mutalik, “Active Targeting of Drugs and Bioactive Molecules Via Oral Administration by Ligand-Conjugated Lipidic Nanocarriers: Recent Advances”, *Journal of the American Association of Pharmaceutical Scientists,* Vol. 20, No. 1, p. 15, 2019.

47. Ganguly, K. K., S. Pal, S. Moulik and A. Chatterjee, “Integrins And Metastasis”, *Cell Adhesion & Migration,* Vol. 7, No. 3, pp. 251–261, 2013.

48. Gros, L., H. Ringsdorf and H. Schupp, “Polymeric Antitumor Agents on A Molecular and on a Cellular Level?”, *Angewandte Chemie International Edition*, Vol. 20, No. 4, pp. 305–325, 1981.

49. Drobnik, J., J. Kopecek, J. Labsky, P. Rejmanova, J. Exner, V. Saudek and J. Kalal, "Enzymatic Cleavage of Side Chains of Synthetic Water-soluble Polymers", *Die Makromolekulare Chemie*, Vol. 177, No. 10, pp. 2833–2848, 1976.

50. Vasey, P. A., S. B. Kaye, R. Morrison, C. Twelves, P. Wilson, R. Duncan, A. H. Thomson, L. S. Murray, T. E. Hilditch, T. Murray, S. Burtles, D. Fraier, E. Frigerio and J. Cassidy, "Phase I Clinical And Pharmacokinetic Study of PK1 [N-(2-Hydroxypropyl)Methacrylamide Copolymer Doxorubicin]: First Member of A New Class of Chemotherapeutic Agents—Drug-Polymer Conjugates", *Clinical Cancer Research*, Vol. 5, pp. 83–94, 1999.

51. Ray, A., N. Larson, D. B. Pike, M. Gruner, S. Naik, H. Bauer, A. Malugin, K. Greish and H. Ghandehari, "Comparison of Active and Passive Targeting of Docetaxel for Prostate Cancer Therapy by HPMA Copolymer–RGDfK Conjugates", *Molecular Pharmaceutics*, Vol. 8, No. 4, pp. 1090–1099, 2011.

52. Lammers, T., V. Subr, K. Ulbrich, P. Peschke, P. E. Huber, W. E. Hennink and G. Storm, "Simultaneous Delivery of Doxorubicin and Gemcitabine to Tumors in Vivo Using Prototypic Polymeric Drug Carriers", *Biomaterials*, Vol. 30, pp. 3466–3475, 2009.

53. Karacivi, M., B. S. Bolu and R. Sanyal, "Targeting to The Bone: Alendronate-Directed Combretastatin A-4 Bearing Antiangiogenic Polymer–Drug Conjugates", *Molecular Pharmaceutics*, Vol. 14, No. 5, pp. 1373–1383, 2017.

54. Kabanov, A. V. and S. V. Vinogradov, "Nanogels As Pharmaceutical Carriers: Finite Networks of Infinite Capabilities", *Angewandte Chemie - International Edition*, Vol. 48, pp. 5418–5429, 2009.

55. González-Toro, D. C. J. -H. Ryu, R. T. Chacko, J. Zhuang, and S. Thayumanavan, "Concurrent Binding and Delivery of Proteins and Lipophilic Small Molecules Using Polymeric Nanogels," *Journal of the American Chemical Society*, Vol. 134, No. 16, pp. 6964–6967, 2012.

56. Lux, J., A. G. White, M. Chan, C. J. Anderson and A. Almutairi, “Nanogels from Metal-Chelating Crosslinkers as Versatile Platforms Applied to Copper-64 PET Imaging of Tumors and Metastases,” *Theranostics*, Vol. 5, No. 3, pp. 277–288, 2015.

57. Zhang, H., Y. Zhai, J. Wang and G. Zhai, “New Progress and Prospects: The Application of Nanogel in Drug Delivery”, *Material Science and Engineering*, Vol. 60, pp. 560–568, 2016.

58. Chambre, L. A. Degirmenci, R. Sanyal and A. “Sanyal, Multi-Functional Nanogels as Theranostic Platforms: Exploiting Reversible and Nonreversible Linkages for Targeting, Imaging, and Drug Delivery”, *Bioconjugate Chemistry*, Vol. 29, No. 6, pp. 1885–1896, 2018.

59. Ryu, J. -H., R. T. Chacko, S. Jiwpanich, S. Bickerton, R. P. Babu and S. Thayumanavan, “Self-Cross-Linked Polymer Nanogels: A Versatile Nanoscopic Drug Delivery Platform”, *Journal of American Chemical Society*, Vol. 132, No. 48, pp. 17227–17235, 2010.

60. Du, X., Y. Peng, C. Zhao and J. Xing, “Temperature/pH-responsive carmofur-loaded nanogels rapidly prepared via one-pot laser-induced emulsion polymerization”, *Colloids and Surfaces B: Biointerfaces*, Vol. 217, p. 112611, 2022.

61. Peppas, N. A., J. Z. Hilt, A. Khademhosseini and R. Langer, “Hydrogels in Biology and Medicine: From Molecular Principles to Bionanotechnology”, *Advanced Materials*, Vol. 18, No. 11, pp. 1345–1360, 2006.

62. Bashir, S., M. Hina, J. Iqbal, A. H. Rajpar, M. A. Mujtaba, N. A. Alghamdi, S. Wageh, K. Ramesh and S. Ramesh, “Fundamental Concepts of Hydrogels: Synthesis, Properties, And Their Applications”, *Polymers*, Vol. 12, No. 11, pp. 1–60, 2020.

63. Cabral, J. and S. C. Moratti, “Hydrogels for Biomedical Applications”, *Future Medicinal Chemistry*, Vol. 3, No. 15, pp. 1877–1888, 2011.

64. Li, X., Q. Sun, Q. Li, N. Kawazoe and G. Chen, “Functional Hydrogels with Tunable Structures and Properties for Tissue Engineering Applications”, *Frontiers in Chemistry*, Vol. 6, 2018.

65. Echalier, C., L. Valot, J. Martinez, A. Mehdi and G. Subra, “Chemical Cross-Linking Methods for Cell Encapsulation in Hydrogels”, *Materials Today Communications*, Vol. 20, p. 100536, 2019.

66. Finetti, C., L. Sola, J. Elliott and M. Chiari, “Synthesis of Hydrogel via Click Chemistry for DNA Electrophoresis”, *Journal of Chromatography A*, Vol. 1513, pp. 226–234, 2017.

67. Zhan, H., S. Jiang, A. M. Jonker, I. A. B. Pijpers and D. W. P. M. Lowik, “Self-Recovering Dual Cross-Linked Hydrogels Based on Bioorthogonal Click Chemistry and Ionic Interactions”, *Journal of Materials Chemistry B*, Vol. 8, pp. 5912–5920, 2020.

68. Yang, L., Y. Li, Y. Gou, X. Wang, X. Zhao and L. Tao, “Improving Tumor Chemotherapy Effect Using an Injectable Self-Healing Hydrogel as Drug Carrier”, *Polymer Chemistry*, Vol. 8, No. 34, pp. 5071–5076, 2017.

69. Arslan, M., T. N. Gevrek, A. Sanyal and R. Sanyal, “Cyclodextrin Mediated Polymer Coupling Via Thiol–Maleimide Conjugation: Facile Access to Functionalizable Hydrogels”, *RSC Advances*, Vol. 4, No. 101, pp. 57834–57841, 2014.

70. Sawicki, L. A. and A. M. Kloxin, “Design of Thiol–Ene Photoclick Hydrogels Using Facile Techniques for Cell Culture Applications”, *Biomaterials Science*, Vol. 2, No. 11, pp. 1612–1626, 2014.

71. Arslan, M., “Fabrication and Reversible Disulfide Functionalization of PEGylated Chitosan-Based Hydrogels: Platforms for Selective Immobilization and Release of Thiol-Containing Molecules”, *European Polymer Journal*, Vol. 126, p. 109543, 2020.

72. Nimmo, C. M., S. C. Owen and M. S. Shoichet, “Diels−Alder Click Cross-Linked Hyaluronic Acid Hydrogels for Tissue Engineering”, *Biomacromolecules*, Vol. 12, No. 3, pp. 824–830, 2011.

73. Beninatto, R., C. Barbera, O. De Lucchi, G. Borsato, E. Serena, C. Guarise, M. Pavan, C. Luni, S. Martewicz, D. Galesso and N. Elvassore, “Photocrosslinked Hydrogels

from Coumarin Derivatives of Hyaluronic Acid for Tissue Engineering Applications", *Materials Science and Engineering: C*, Vol. 96, pp. 625–634, 2019.

74. Ruedinger, F., A. Lavrentieva, C. Blume, I. Pepelanova and T. Scheper, "Hydrogels for 3D Mammalian Cell Culture: A Starting Guide for Laboratory Practice", *Applied Microbiology and Biotechnology*, Vol. 99, No. 2, pp. 623–636, 2015.

75. Lensen, M. C, V. A. Schulte, and M. Diez, "Cell Adhesion and Spreading on An Intrinsically Anti-Adhesive PEG Biomaterial", *Biomaterials - Physics and Chemistry* 2011.

76. Wang, Y., S. Zhang and D. S. W. Benoit, "Degradable Poly(Ethylene Glycol) (PEG)-Based Hydrogels for Spatiotemporal Control of SiRNA/Nanoparticle Delivery", *Journal of Controlled Release*, Vol. 287, pp. 58–66, 2018.

77. Knauf, M. J., D. P. Bell, P. Hirtzer, Z. P. Luo, J. D. Young and N. V Katre, "Relationship of Effective Molecular Size to Systemic Clearance in Rats of Recombinant Interleukin-2 Chemically Modified with Water-Soluble Polymers", *Journal of Biological Chemistry*, Vol. 263, No. 29, pp. 15064–15070, 1988.

78. Hoffman, M. D., A. H. Van Hove and D. S. W. Benoit, "Degradable Hydrogels for Spatiotemporal Control of Mesenchymal Stem Cells Localized at Decellularized Bone Allografts", *Acta Biomaterialia*, Vol. 10, No. 8, pp. 3431–3441, 2014.

79. Parhi, R., "Cross-Linked Hydrogel for Pharmaceutical Applications: A Review", *Advanced Pharmaceutical Bulletin*, Vol. 7, pp. 515–530, 2017.

80. Berger, J., M. Reist, J. M. Mayer, O. Felt, N. A. Peppas and R. Gurny, "Structure and Interactions in Covalently and Ionically Crosslinked Chitosan Hydrogels for Biomedical Applications", *European Journal of Pharmaceutics and Biopharmaceutics*, Vol. 57, No. 1, pp. 19–34, 2004.

81. Smith, L. J., S. M. Taimoory, R. Y. Tam, A. E. G. Baker, N. Binth Mohammad, J. F. Trant and M. S. Shoichet, "Diels–Alder Click-Cross-Linked Hydrogels with Increased Reactivity Enable 3D Cell Encapsulation", *Biomacromolecules*, Vol. 19, No. 3, pp. 926–935, 2018.

82. Martinez-Mejia, G., N. A. Vazquez-Torres, A. Castell-Rodriguez, J. M. del Rio, M. Corea and R. Jimenez-Juarez, "Synthesis of New Chitosan-Glutaraldehyde Scaffolds for Tissue Engineering Using Schiff Reactions", *Colloids and Surfaces A: Physicochemical and Engineering Aspects*, Vol. 579, p. 123658, 2019.

83. McBride, M. K., T. Gong, D. P. Nair and C. N. Bowman, "Photo-Mediated Copper(I)-Catalyzed Azide-Alkyne Cycloaddition (CuAAC) 'Click' Reactions for Forming Polymer Networks as Shape Memory Materials", *Polymer*, Vol. 55, No. 23, pp. 5880–5884, 2014.

84. Hou, J., X. Liu, J. Shen, G. Zhao and P. G. Wang, "The Impact of Click Chemistry in Medicinal Chemistry", *Expert Opinion on Drug Discovery*, Vol. 7, No. 6, pp. 489–501, 2012.

85. Crescenzi, V., L. Cornelio, C. Di Meo, S. Nardecchia and R. Lamanna, "Novel Hydrogels via Click Chemistry: Synthesis and Potential Biomedical Applications", *Biomacromolecules*, Vol. 8, No. 6, pp. 1844–1850, 2007.

86. Altin, H., I. Kosif and R. Sanyal, "Fabrication of 'Clickable' Hydrogels Via Dendron−Polymer Conjugates", *Macromolecules*, Vol. 43, No. 8, pp. 3801–3808, 2010.

87. Ornelas, C., J. Broichhagen and M. Weck, "Strain-Promoted Alkyne Azide Cycloaddition for The Functionalization of Poly(Amide)-Based Dendrons and Dendrimers", *Journal of the American Chemical Society*, Vol. 132, No. 11, pp. 3923–3931, 2010.

88. Zhu, H. -Z., G. Wang, H. -L. Wei, H. -J. Chu and J. Zhu, "Click Synthesis of Hydrogels by Metal-Free 1,3-Dipolar Cycloaddition Reaction between Maleimide and Azide Functionalized Polymers", *Macromolecular Research*, Vol. 24, pp. 793–799, 2016.

89. Dommerholt, J., F. P. J. T. Rutjes and F. L. van Delft, "Strain-Promoted 1,3-Dipolar Cycloaddition of Cycloalkynes and Organic Azides", *Topics in Current Chemistry*, Vol. 374, No. 16, 2016.

90. Beatty, K. E., J. D. Fisk, B. P. Smart, Y. Y. Lu, J. Szychowski, M. J. Hangauer, J. M. Baskin, C. R. Bertozzi and D. A. Tirrell, “Live-Cell Imaging of Cellular Proteins by A Strain-Promoted Azide-Alkyne Cycloaddition”, *ChemBioChem*, Vol. 11, No. 15, pp. 2092–2095, 2010.

91. Marks, I. S., J. S. Kang, B. T. Jones, K. J. Landmark, A. J. Cleland and T. A. Taton, “Strain-Promoted ‘Click’ Chemistry for Terminal Labeling of DNA”, *Bioconjugate Chemistry*, Vol. 22, No. 7, pp. 1259–1263, 2011.

92. Kurra, Y., K. A. Odoi, Y. -J. Lee, Y. Yang, T. Lu, S. E. Wheeler, J. Torres-Kolbus, A. Deiters and W. R. Liu, “Two Rapid Catalyst-Free Click Reactions for in Vivo Protein Labeling of Genetically Encoded Strained Alkene/Alkyne Functionalities”, *Bioconjugate Chemistry*, Vol. 25, No. 9, pp. 1730–1738, 2014.

93. Manova, R., T. A. van Beek and H. Zuilhof, “Surface Functionalization by Strain-Promoted Alkyne-Azide Click Reactions”, *Angewandte Chemie International Edition*, Vol. 50, No. 24, pp. 5428–5430, 2011.

94. Friscourt, F., C. J. Fahrni and G. -J. Boons, “A Fluorogenic Probe for The Catalyst-Free Detection of Azide-Tagged Molecules”, *Journal of the American Chemical Society*, Vol. 134, No. 45, pp. 18809–18815, 2012.

95. Liu, X., A. L. Miller, K. A. Fundora, M. J. Yaszemski and L. Lu, “Poly(ε-Caprolactone) Dendrimer Cross-Linked Via Metal-Free Click Chemistry: Injectable Hydrophobic Platform for Tissue Engineering”, *ACS Macro Letters*, Vol. 5, No. 11, pp. 1261–1265, 2016.

96. Liu, X., P. Gong, P. Song, F. Xie, A. L. Miller II, S. Chen and L. Lu, “Rapid Conjugation of Nanoparticles, Proteins and SiRNAs to Microbubbles by Strain-Promoted Click Chemistry for Ultrasound Imaging and Drug Delivery”, *Polymer Chemistry*, Vol. 10, pp. 705–717, 2019.

97. Hodgson, S. M., S. A. McNelles, L. Abdullahu, I. A. Marozas, K. S. Anseth and A. Adronov, “Reproducible Dendronized PEG Hydrogels via SPAAC Cross-Linking”, *Biomacromolecules*, Vol. 18, No. 12, pp. 4054–4059, 2017.

98. Hu, J., Z. Zheng, C. Liu, Q. Hu, X. Cai, J. Xiao and Y. Cheng, "A pH-Responsive Hydrogel with Potent Antibacterial Activity Against Both Aerobic and Anaerobic Pathogens", *Biomaterials Science*, Vol. 7, pp. 581–584, 2019.

99. Werzer, O., S. Tumphart, R. Keimel, P. Christian and A. M. Coclite, "Drug Release from Thin Films Encapsulated by A Temperature-Responsive Hydrogel", *Soft Matter*, Vol. 15, pp. 1853–1859, 2019.

100. Xiang, T., T. Lu, W. -F. Zhao and C. -S. Zhao, "Ionic-Strength Responsive Zwitterionic Copolymer Hydrogels with Tunable Swelling and Adsorption Behaviors", *Langmuir*, Vol. 35, No. 5, pp. 1146–1155, 2019.

101. Stoychev, G., A. Kirillova and L. Ionov, "Light-Responsive Shape-Changing Polymers", *Advanced Optical Materials*, Vol. 7, No. 16, p. 1900067, 2019.

102. Mallawarachchi, S., V. Gejji, L. S. Sierra, H. Wang and S. Fernando, "Electrical Field Reversibly Modulates Enzyme Kinetics of Hexokinase Entrapped in An Electro-Responsive Hydrogel", *ACS Applied Bio Materials*, Vol. 2, No. 12, pp. 5676–5686, 2019.

103. Manjua, A. C., V. D. Alves, J. G. Crespo and C. A. M. Portugal, "Magnetic Responsive PVA Hydrogels for Remote Modulation of Protein Sorption", *ACS Applied Materials & Interfaces*, Vol. 11, No. 23, pp. 21239–21249, 2019.

104. Choh, S. -Y., D. Cross and C. Wang, "Facile Synthesis and Characterization of Disulfide-Cross-Linked Hyaluronic Acid Hydrogels for Protein Delivery and Cell Encapsulation", *Biomacromolecules*, Vol. 12, No. 4, pp. 1126–1136, 2011.

105. Walter, S. V., F. Ennen-Roth, D. Büning, D. Denizer and M. Ulbricht, "Glucose-Responsive Polymeric Hydrogel Materials: From A Novel Technique for The Measurement of Glucose Binding Toward Swelling Pressure Sensor Applications", *ACS Applied Bio Materials*, Vol. 2, No. 6, pp. 2464–2480, 2019.

106. Sood, N., A. Bhardwaj, S. Mehta and A. Mehta, "Stimuli-Responsive Hydrogels in Drug Delivery and Tissue Engineering", *Drug Delivery*, Vol. 23, No. 3, pp. 748–770, 2016.

107. Karimi, M., P. S. Zangabad, A. Ghasemi, M. Amiri, M. Bahrami, H. Malekzad, H. G. Asl, Z. Mahdieh, M. Bozorgomid, Amir Ghasemi, M. R. R. T. Boyuk and M. R. Hamblin, "Temperature-Responsive Smart Nanocarriers for Delivery of Therapeutic Agents: Applications and Recent Advances", *ACS Applied Materials & Interfaces*, Vol. 8, No. 33, pp. 21107–21133, 2016.

108. Oak, M., R. Mandke and J. Singh, "Smart Polymers for Peptide and Protein Parenteral Sustained Delivery", *Drug Discovery Today: Technologies*, Vol. 9, pp. e131–e140, 2012.

109. Cengiz, N., "Glutathione-Responsive Multifunctionalizable Hydrogels Via Amine-Epoxy 'Click' Chemistry", *European Polymer Journal*, Vol. 123, p. 109441, 2020.

110. Legros, C., M. -C. De Pauw-Gillet, K. C. Tam, S. Lecommmandoux and D. Taton, "pH and Redox Responsive Hydrogels and Nanogels Made from Poly(2-Ethyl-2-Oxazoline)", *Polymer Chemistry*, Vol. 4, No. 17, pp. 4801–4808, 2013.

111. Sivashanmugam, A., R. A. Kumar, M. V. Priya, S. V. Nair and R. Jayakumar, "An Overview of Injectable Polymeric Hydrogels for Tissue Engineering", *European Polymer Journal*, Vol. 72, pp. 543–565, 2015.

112. Liu, S., T. Jiang, R. Guo, C. Li, C. Lu, G. Yang, J. Nie, F. Wang, X. Yang and Z. Chen, "Injectable and Degradable PEG Hydrogel with Antibacterial Performance for Promoting Wound Healing", *ACS Applied Bio Materials*, Vol. 4, No. 3, pp. 2769–2780, 2021.

113. Cao, L., B. Cao, C. Lu, G. Wang, L. Yu and J. Ding, "An Injectable Hydrogel Formed by in Situ Cross-Linking of Glycol Chitosan and Multi-Benzaldehyde Functionalized PEG Analogues for Cartilage Tissue Engineering", *Journal of Materials Chemistry B*, Vol. 3, No. 7, pp. 1268–1280, 2015.

114. Xu, L., R. C. Cooper, J. Wang, W. A. Yeudall and H. Yang, "Synthesis and Application of Injectable Bioorthogonal Dendrimer Hydrogels for Local Drug Delivery", *ACS Biomaterials Science & Engineering*, Vol. 3, No. 8, pp. 1641–1653, 2017.

115. Kaliyannan, G. V., M. K. K. Velusamy, S. K. Palaniappan, M. K. Anandraj and R. Rathanasamy, “Polymer Coatings for Corrosive Protection”, *Polymer Coatings*, pp. 371–395, 2020.

116. Khan, F., M. Rabnawaz, Z. Li, A. Khan, M. Naveed, M. O. Tuhin and F. Rahimb, “Simple Design for Durable and Clear Self-Cleaning Coatings”, *ACS Applied Polymer Materials*, Vol. 1, No. 10, pp. 2659–2667, 2019.

117. Velazquez-Benitez, A. M., M. Reyes-Medrano, J. R. Velez-Cordero and J. Hernandez-Cordero, “Controlled Deposition of Polymer Coatings on Cylindrical Photonic Devices”, *Journal of Lightwave Technology*, Vol. 33, No. 1, pp. 176–182, 2015.

118. Smith, J. R. and D. A. Lamprou, “Polymer Coatings for Biomedical Applications: A Review”, *Transactions of the IMF*, Vol. 92, No. 1, pp. 9–19, 2014.

119. Chen, L., C. Yan and Z. Zheng, “Functional Polymer Surfaces for Controlling Cell Behaviors”, *Materials Today*, Vol. 21, No. 1, pp. 38–59, 2018.

120. Rahman, M. U., Y. Xi, H. Li, F. Chen, D. Liu and J. Wei, “Dynamics and Structure Formation of Confined Polymer Thin Films Supported on Solid Substrates”, *Polymers*, Vol. 13, No. 10, p. 1621, 2021.

121. Smith, R. K., P. A. Lewis and P. S. Weiss, “Patterning Self-Assembled Monolayers”, *Progress in Surface Science*, Vol. 75, pp. 1–68, 2004.

122. Bain, C. D. and G. M. Whitesides, “Formation of Monolayers by The Coadsorption of Thiols on Gold: Variation in The Length of The Alkyl Chain”, *Journal of the American Chemical Society*, Vol. 111, No. 18, pp. 7164–7175, 1989.

123. Laibinis, P. E., M. A. Fox, J. P. Folkers and G. M. Whitesides, “Comparisons of Self-Assembled Monolayers on Silver and Gold: Mixed Monolayers Derived from $HS(CH_2)_{21}X$ and $HS(CH_2)_{10}Y$ (X, Y = CH_3, CH_2OH) Have Similar Properties”, *Langmuir*, Vol. 7, No. 12, pp. 3167–3173, 1991.

124. Ferretti, S., S. Paynter, D. A. Russell, K. E. Sapsford and D. J. Richardson, "Self-Assembled Monolayers: A Versatile Tool for The Formulation of Bio-Surfaces", *TrAC - Trends in Analytical Chemistry*, Vol. 19, No. 9, pp. 530–540, 2000.

125. Frasconi, M., F. Mazzei and T. Ferri, "Protein Immobilization at Gold–Thiol Surfaces and Potential for Biosensing", *Analytical and Bioanalytical Chemistry*, Vol. 398, No. 4, pp. 1545–1564, 2010.

126. Schoenfisch, M. H. and J. E. Pemberton, "Air Stability of Alkanethiol Self-Assembled Monolayers on Silver and Gold Surfaces", *Journal of the American Chemical Society*, Vol. 120, No. 18, pp. 4502–4513, 1998.

127. Li, Y., J. Huang, R. T. McIver and J. C. Hemminger, "Characterization of Thiol Self-Assembled Films by Laser Desorption Fourier Transform Mass Spectrometry", *Journal of the American Chemical Society*, Vol. 114, No. 7, pp. 2428–2432, 1992.

128. Sagiv, J., "Organized Monolayers by Adsorption. 1. Formation and Structure of Oleophobic Mixed Monolayers on Solid Surfaces", *Journal of the American Chemical Society*, Vol. 102, No. 1, pp. 92–98, 1980.

129. Tanaka, M., T. Sawaguchi, M. Kuwahara and O. Niwa, "Surface Modification of Silicon Oxide with Trialkoxysilanes Toward Close-Packed Monolayer Formation", *Langmuir*, Vol. 29, No. 21, pp. 6361–6368, 2013.

130. Park, J. -W., H. Kim and M. Han, "Polymeric Self-Assembled Monolayers Derived from Surface-Active Copolymers: A Modular Approach to Functionalized Surfaces", *Chemical Society Reviews*, Vol. 39, pp. 2935, 2010.

131. Feng, C. and X. Huang, "Polymer Brushes: Efficient Synthesis and Applications", *Accounts of Chemical Research*, Vol. 51, No. 9, pp. 2314–2323, 2018.

132. Zoppe, J. O., N. C. Ataman, P. Mocny, J. Wang, J. Moraes and H. -A. Klok, "Surface-Initiated Controlled Radical Polymerization: State-Of-The-Art, Opportunities, And Challenges in Surface and Interface Engineering with Polymer Brushes", *Chemical Reviews*, Vol. 117, No. 3, pp. 1105–1318, 2017.

133. Brittain, W. J. and S. Minko, “A Structural Definition of Polymer Brushes”, *Journal of Polymer Science Part A: Polymer Chemistry*, Vol. 45, No. 16, pp. 3505–3512, 2007.

134. Miao, L., H. Guo and M. J. Zuckermann, “Conformation of Polymer Brushes Under Shear: Chain Tilting and Stretching”, *Macromolecules*, Vol. 29, No. 6, pp. 2289–2297, 1996.

135. Zdyrko, B. and I. Luzinov, “Polymer Brushes by the ‘Grafting to’ Method”, *Macromolecular Rapid Communications*, Vol. 32, No. 12, pp. 859–869, 2011.

136. Zhao, B. and W. J. Brittain, “Polymer Brushes: Surface-Immobilized Macromolecules”, *Progress in Polymer Science*, Vol. 25, No. 5, pp. 677–710, 2000.

137. Wei, Q., B. Yu, X. Wang and F. Zhou, “Stratified Polymer Brushes from Microcontact Printing of Polydopamine Initiator on Polymer Brush Surfaces”, *Macromolecular Rapid Communications*, Vol. 35, No. 11, pp. 1046–1054, 2014.

138. Pourjavadi, A., M. Kohestanian and C. Streb, “pH And Thermal Dual-Responsive Poly(NIPAM-Co-GMA)-Coated Magnetic Nanoparticles via Surface-Initiated RAFT Polymerization for Controlled Drug Delivery”, *Materials Science and Engineering: C*, Vol. 108, p. 110418, 2020.

139. Matsuno, R., K. Yamamoto, H. Otsuka and A. Takahara, “Polystyrene- And Poly(3-Vinylpyridine)-Grafted Magnetite Nanoparticles Prepared Through Surface-Initiated Nitroxide-Mediated Radical Polymerization”, *Macromolecules*, Vol. 37, No. 6, pp. 2203–2209, 2004.

140. Chiefari, J., Y. K. Chong, F. Ercole, J. Krstina, J. Jeffery, T. P. T. Le, R. T. A. Mayadunne, G. F. Meijs, C. L. Moad, G. Moad, E. Rizzardo and S. H. Thang, “Living Free-Radical Polymerization by Reversible Addition−Fragmentation Chain Transfer: The RAFT Process”, *Macromolecules*, Vol. 31, No. 16, pp. 5559–5562, 1998.

141. Perrier, S., “50th Anniversary Perspective: RAFT Polymerization—A User Guide”, *Macromolecules*, Vol. 50, No. 19, pp. 7433–7447, 2017.

142. Perrier, S., P. Takolpuckdee, J. Westwood and D. M. Lewis, “Versatile Chain Transfer Agents for Reversible Addition Fragmentation Chain Transfer (RAFT) Polymerization to Synthesize Functional Polymeric Architectures”, *Macromolecules*, Vol. 37, No. 8, pp. 2709–2717, 2004.

143. Chen, W. -L., R. Cordero, H. Tran and C. K. Ober, “50th Anniversary Perspective: Polymer Brushes: Novel Surfaces for Future Materials”, *Macromolecules,* Vol. 50, No. 11, pp. 4089–4113, 2017.

144. Baum, M. and W. J. Brittain, “Synthesis of Polymer Brushes on Silicate Substrates Via Reversible Addition Fragmentation Chain Transfer Technique”, *Macromolecules*, Vol. 35, No. 3, pp. 610–615, 2002.

145. Li, C. and B. C. Benicewicz, “Synthesis of Well-Defined Polymer Brushes Grafted onto Silica Nanoparticles via Surface Reversible Addition−Fragmentation Chain Transfer Polymerization”, *Macromolecules*, Vol. 38, No. 14, pp. 5929–5936, 2005.

146. Li, C., J. Han, C. Y. Ryu and B. C. Benicewicz, “A Versatile Method to Prepare RAFT Agent Anchored Substrates and The Preparation of PMMA Grafted Nanoparticles”, *Macromolecules*, Vol. 39, No. 9, pp. 3175–3183, 2006.

147. Tsujii, Y., M. Ejaz, K. Sato, A. Goto and T. Fukuda, “Mechanism and Kinetics of RAFT-Mediated Graft Polymerization of Styrene on A Solid Surface. 1. Experimental Evidence of Surface Radical Migration”, *Macromolecules,* Vol. 34, No. 26, pp. 8872–8878, 2001.

148. Peng, Q., D. M. Y. Lai, E. T. Kang and K. G. Neoh, “Preparation of Polymer−Silicon(100) Hybrids via Interface-Initiated Reversible Addition-Fragmentation Chain-Transfer (RAFT) Polymerization”, *Macromolecules,* Vol. 39, No. 16, pp. 5577–5582, 2006.

149. Stenzel, M. H., L. Zhang and W. T. S. Huck, “Temperature-Responsive Glycopolymer Brushes Synthesized via RAFT Polymerization Using the Z-Group Approach”, *Macromolecular Rapid Communications*, Vol. 27, No. 14, pp. 1121–1126, 2006.

150. Cimen, D., E. Yildirim and T. Caykara, “Synthesis of Dual-Functional Poly(6-Azidohexylmethacrylate) Brushes by A RAFT Agent Carrying Carboxylic Acid End Groups”, *Journal of Polymer Science Part A: Polymer Chemistry*, Vol. 53, No. 14, pp. 1696–1706, 2015.

151. Rungta, A., B. Natarajan, T. Neely, D. Dukes, L. S. Schadler and B. C. Benicewicz, “Grafting Bimodal Polymer Brushes on Nanoparticles Using Controlled Radical Polymerization”, *Macromolecules*, Vol. 45, No. 23, pp. 9303–9311, 2012.

152. Barbey, R., L. Lavanant, D. Paripovic, N. Schüwer, C. Sugnaux, S. Tugulu and H. -A. Klok, “Polymer Brushes via Surface-Initiated Controlled Radical Polymerization: Synthesis, Characterization, Properties, and Applications”, *Chemical Reviews*, Vol. 109, No. 11, pp. 5437–5527, 2009.

153. Li, H., B. Yu, H. Matsushima, C. E. Hoyle and A. B. Lowe, “The Thiol−Isocyanate Click Reaction: Facile And Quantitative Access to ω-End-Functional Poly(N,N-Diethylacrylamide) Synthesized by RAFT Radical Polymerization”, *Macromolecules*, Vol. 42, No. 17, pp. 6537–6542, 2009.

154. Scales, C. W., A. J. Convertine and C. L. McCormick, “Fluorescent Labeling of RAFT-Generated Poly(N-Isopropylacrylamide) via A Facile Maleimide−Thiol Coupling Reaction”, *Biomacromolecules*, Vol. 7, No. 5, pp. 1389–1392, 2006.

155. Oz, Y., M. Arslan, T. N. Gevrek, R. Sanyal and A. Sanyal, “Modular Fabrication of Polymer Brush Coated Magnetic Nanoparticles: Engineering the Interface for Targeted Cellular Imaging”, *ACS Applied Materials & Interfaces*, Vol. 8, No. 30, pp. 19813–19826, 2016.

156. Gunay, K. A., N. Schuwer and H. -A. Klok, “Synthesis and Post-Polymerization Modification of Poly(Pentafluorophenyl Methacrylate) Brushes”, *Polymer Chemistry*, Vol. 3, pp. 2186–2192, 2012.

157. Smith, J. R., D. A. Lamprou, C. Larson and S. J. Upson, “Biomedical Applications of Polymer and Ceramic Coatings: A Review of Recent Developments”, *Transactions of the IMF*, Vol. 100, pp. 25–35, 2022.

158. Mauri, E., S. M. Giannitelli, M. Trombetta and A. Rainer, “Synthesis of Nanogels: Current Trends and Future Outlook”, *Gels*, Vol. 7, No. 2, p. 36, 2021.

159. Orski, S. V., A. A. Poloukhtine, S. Arumugam, L. Mao, V. V. Popik and J. Locklin, “High-Density Orthogonal Surface Immobilization via Photoactivated Copper-Free Click Chemistry”, *Journal of the American Chemical Society*, Vol. 132, No. 32, pp. 11024–11026, 2010.

160. Gevrek, T. N., A. Degirmenci, R. Sanyal, H. -A. Klok and A. Sanyal, “Succinimidyl Carbonate-Based Amine-Reactive Polymer Brushes: Facile Fabrication of Functional Interfaces”, *ACS Applied Polymer Materials*, Vol. 3, No. 5, pp. 2507–2517, 2021.

161. Gevrek, T. N., T. Bilgic, H. -A. Klok and A. Sanyal, “Maleimide-Functionalized Thiol Reactive Copolymer Brushes: Fabrication and Post-Polymerization Modification”, *Macromolecules*, Vol. 47, No. 22, pp. 7842–7851, 2014.

162. Gevrek, T. N., K. Yu, J. N. Kizhakkedathu, and A. Sanyal, “Thiol-Reactive Polymers for Titanium Interfaces: Fabrication of Antimicrobial Coatings”, *ACS Applied Polymer Materials*, Vol. 1, No. 6, pp. 1308-1316, 2019.

163. Peng, H., K. Rübsam, X. Huang, F. Jakob, M. Karperien, U. Schwaneberg and A. Pich, “Reactive Copolymers Based on N-Vinyl Lactams with Pyridyl Disulfide Side Groups via RAFT Polymerization and Postmodification via Thiol–Disulfide Exchange Reaction”, *Macromolecules*, Vol. 49, No. 19, pp. 7141–7154, 2016.

164. Shi, X., W. Zhan, G. Chen, Q. Yu, Q. Liu, H. Du, L. Cao, X. Liu, L. Yuan and H. Chen, “Regulation of Protein Binding Capability of Surfaces via Host–Guest Interactions: Effects of Localized and Average Ligand Density”, *Langmuir*, Vol. 31, No. 22, pp. 6172–6178, 2015.

165. Shi, X. -J., G. -J. Chen, Y. -W. Wang, L. Yuan, Q. Zhang, D. M. Haddleton and H. Chen, “Control The Wettability of Poly(N-Isopropylacrylamide-Co-1-Adamantan-1-Ylmethyl Acrylate) Modified Surfaces: The More Ada, The Bigger Impact?”, *Langmuir*, Vol. 29, No. 46, pp. 14188–14195, 2013.

166. Gevrek, T. N., I. Kosif and A. Sanyal, “Surface-Anchored Thiol-Reactive Soft Interfaces: Engineering Effective Platforms for Biomolecular Immobilization and Sensing”, *ACS Applied Materials & Interfaces*, Vol. 9, No. 33, pp. 27946–27954, 2017.

167. Sung, H., J. Ferlay, R. L. Siegel, M. Laversanne, I. Soerjomataram, A. Jemal and F. Bray, “Global Cancer Statistics 2020: GLOBOCAN Estimates of Incidence and Mortality Worldwide for 36 Cancers in 185 Countries”, *CA. A Cancer Journal of Clinicians*, Vol. 71, No. 3, pp. 209–249, 2021.

168. Tarannum, M., K. Holtzman, D. Dreau, P. Mukherjee and J. L. Vivero-Escoto, “Nanoparticle Combination for Precise Stroma Modulation and Improved Delivery for Pancreatic Cancer”, *Journal of Controlled Release*, Vol. 347, pp. 425–434, 2022.

169. Adamska, A., A. Domenichini and M. Falasca, “Pancreatic Ductal Adenocarcinoma: Current and Evolving Therapies”, *International Journal of Molecular Sciences*, Vol. 18, No. 7, p. 1338, 2017.

170. Ducreux, M., A. S. Cuhna, C. Caramella, A. Hollebecque, P. Burtin, D. Goere, T. Seufferlein, K. Haustermans, J. L. Van Laethem, T. Conroy and D. Arnold on behalf of the ESMO Guidelines Committee, “Cancer of the Pancreas: ESMO Clinical Practice Guidelines for Diagnosis, Treatment and Follow-up”, *Annals of Oncology*, Vol. 26, pp. v56-v68, 2015.

171. Kattel, K., G. Mondal, F. Lin, V. Kumar and R. I. Mahato, “Biodistribution of Self-Assembling Polymer–Gemcitabine Conjugate After Systemic Administration into Orthotopic Pancreatic Tumor Bearing Mice”, *Molecular Pharmaceutics*, Vol. 14, No. 5, pp. 1365–1372, 2017.

172. Balic, A., M. D. Sorensen, S. M. Trabulo, B. Sainz, M. Cioffi, C. R. Vieira, I. Miranda-Lorenzo, M. Hidalgo, J. Kleeff, M. Erkan and C. Heeschen, “Chloroquine Targets Pancreatic Cancer Stem Cells Via Inhibition of $CXCR_4$ And Hedgehog Signaling”, *Molecular Cancer Therapeutics*, Vol. 13, No. 7, pp. 1758–1771, 2014.

173. Heyder, R. S., F. S. Sunbul, R. M. Almuqbil, C. B. Fines, S. R. P. da Rocha, “Poly(anhydride-ester) gemcitabine: Synthesis and Particle Engineering of a High

Payload Hydrolysable Polymeric Drug for Cancer Therapy", *Journal of Controlled Release*, Vol. 330, pp.1178–1190, 2021.

174. Amrutkar, M. and I. Gladhaug, "Pancreatic Cancer Chemoresistance to Gemcitabine", *Cancers*, Vol. 9, No. 11, p. 157, 2017.

175. Liang, T. -J., Z. -M. Zhou, Y. -Q. Cao, M. -Z. Ma, X. -J. Wang and K. Jing, "Gemcitabine-Based Polymer-Drug Conjugate for Enhanced Anticancer Effect in Colon Cancer", *International Journal of Pharmaceutics*, Vol. 513, No. 1-2, pp. 564–571, 2016.

176. Moysan, E., G. Bastiat and J. -P. Benoit, "Gemcitabine Versus Modified Gemcitabine: A Review of Several Promising Chemical Modifications", *Molecular Pharmaceutics*, Vol. 10, No. 2, pp. 430–444, 2013.

177. Burger, J. A. and T. J. Kipps, "$CXCR_4$: A Key Receptor in the Crosstalk Between Tumor Cells and Their Microenvironment", *Blood*, Vol. 107, No. 5, pp. 1761–1767, 2006.

178. Liu, T., J. Zhang, K. Li, L. Deng and H. Wang, "Combination of an Autophagy Inducer and an Autophagy Inhibitor: A Smarter Strategy Emerging in Cancer Therapy", *Frontiers of Pharmacology*, Vol. 11, p. 408, 2020.

179. Li, Y., M. H. Cho, S. S. Lee, D. -E. Lee, H. Cheong and Y. Choi, "Hydroxychloroquine-Loaded Hollow Mesoporous Silica Nanoparticles for Enhanced Autophagy Inhibition and Radiation Therapy", *Journal of Controlled Release*, Vol. 325, pp. 100–110, 2020.

180. Inoue, Y., Y. Matsumoto, K. Toh, K. Miyano, H. Cabral, K. Igarashi, S. Iwasaki, K. Kataoka and T. Yamasoba, "Manipulating Dynamic Tumor Vessel Permeability to Enhance Polymeric Micelle Accumulation", *Journal of Controlled Release*, Vol. 329, pp. 63–75, 2021.

181. Joubert, F., L. Martin, S. Perrier and G. Pasparakis, "Development of a Gemcitabine-Polymer Conjugate with Prolonged Cytotoxicity against a Pancreatic Cancer Cell Line", *ACS Macro Letters*, Vol. 6, No. 5, pp. 535–540, 2017.

182. Chitkara, D., A. Mittal, S. W. Behrman, N. Kumar and R. I. Mahato, “Self-Assembling, Amphiphilic Polymer–Gemcitabine Conjugate Shows Enhanced Antitumor Efficacy Against Human Pancreatic Adenocarcinoma”, *Bioconjugate Chemistry*, Vol. 24, No. 7, pp. 1161–1173, 2013.

183. Emamzadeh, M., M. Emamzadeh and G. Pasparakis, “Dual Controlled Delivery of Gemcitabine and Cisplatin Using Polymer-Modified Thermosensitive Liposomes for Pancreatic Cancer”, *ACS Applied Bio Materials*, Vol. 2, No. 3, pp. 1298–1309, 2019.

184. Cengiz, N., H. Kabadayioglu and R. Sanyal, “Orthogonally Functionalizable Copolymers Based on A Novel Reactive Carbonate Monomer”, *Journal of Polymer Science Part A: Polymer Chemistry*, Vol. 48, No. 21, pp. 4737–4746, 2010.

185. Danial, M., S. Telwatte, D. Tyssen, S. Cosson, G. Tachedjian, G. Moad and A. Postma, “Combination anti-HIV Therapy via Tandem Release of Prodrugs from Macromolecular carriers”, *Polymer Chemistry*, Vol. 7, No. 48, pp. 7477–7487, 2016.

186. Dunn, S. S., S. Tian, S. Blake, J. Wang, A. L. Galloway, A. Murphy, P. D. Pohlhaus, J. P. Rolland, M. E. Napier and J. M. DeSimone, “Reductively Responsive siRNA-Conjugated Hydrogel Nanoparticles for Gene Silencing”, *Journal of American Chemical Society*, Vol. 134, No. 17, pp. 7423–7430, 2012.

187. Canham, S. M., J. Y. Bass, O. Navarro, S. -G. Lim, N. Das and S. A. Blum, “Toward the Single-Molecule Investigation of Organometallic Reaction Mechanisms: Single-Molecule Imaging of Fluorophore-Tagged Palladium(II) Complexes”, *Organometallics*, Vol. 27, No. 11, pp. 2172–2175, 2008.

188. Estrela, J. M., A. Ortega and E. Obrador, “Glutathione in Cancer Biology and Therapy”, *Critical Reviews in Clinical Laboratory Sciences*, Vol. 43, No. 2, pp. 143–181, 2006.

189. Takenaka, M., T. Furui, N. Suzuki, T. Koike, H. Aoki and K.-I. Morishige, “Glutathione as A Prognostic Biomarker and A Potential Therapeutic Target for Ovarian Cancer”, *Open Journal of Obstetrics and Gynecology*, Vol. 12, pp. 56–66, 2022.

190. El Aissi, R., I. Miladi, J. -M. Chezal, O. Chavignon, E. Miot-Noirault and E. Moreau, "Melanoma-Targeted Delivery System (Part 2): Synthesis, Radioiodination and Biological Evaluation in B16F0 Bearing Mice", *European Journal of Medicinal Chemistry*, Vol. 120, pp. 304–312, 2016.

191. Lee, M. H., Z. Yang, C. W. Lim, Y. H. Lee, S. Dongbang, C. Kang and J. S. Kim, "Disulfide-Cleavage-Triggered Chemosensors and Their Biological Applications", *Chemical Reviews*, Vol. 113, No. 7, pp. 5071–5109, 2013.

192. Liu, X., Y. Li, K. Wang, Y. Chen, M. Shi, X. Zhang, W. Pan, N. Li and B. Tang, "GSH-Responsive Nanoprodrug to Inhibit Glycolysis and Alleviate Immunosuppression for Cancer Therapy", *Nano Letters*, Vol 21, No. 18, pp. 7862–7869, 2021.

193. Dong, H., L. Pang, H. Cong, Y. Shen and B. Yu, "Application and Design of Esterase-Responsive Nanoparticles for Cancer Therapy", *Drug Delivery*, Vol. 26, No. 1, pp. 416–432, 2019.

194. Vonlaufen, A., P. A. Phillips, Z. Xu, D. Goldstein, R. C. Pirola, J. S. Wilson and M. V. Apte, "Pancreatic Stellate Cells and Pancreatic Cancer Cells: An Unholy Alliance", *Cancer Research*, Vol. 68, No. 19, pp. 7707–7710, 2008.

195. Xu, Z., A. Vonlaufen, P. A. Phillips, E. Fiala-Beer, X. Zhang, L. Yang, A. V. Biankin, D. Goldstein, R. C. Pirola, J. S. Wilson and M. V. Apte, "Role of Pancreatic Stellate Cells in Pancreatic Cancer Metastasis", *The American Journal of Pathology*, Vol. 177, No. 5, pp. 2585–2596, 2010.

196. Apte, M. V, R. C. Pirola and J. S. Wilson, "Battle-Scarred Pancreas: Role of Alcohol and Pancreatic Stellate Cells in Pancreatic Fibrosis", *Journal of Gastroenterology and Hepatology*, Vol. 21, pp. S97–S101, 2006.

197. McCarroll, J. A., "Vitamin A Inhibits Pancreatic Stellate Cell Activation: Implications for Treatment of Pancreatic Fibrosis", *Gut*, Vol. 55, No. 1, pp. 79–89, 2006.

198. Xiong, G. -F. and R. Xu, “Function of Cancer Cell-Derived Extracellular Matrix in Tumor Progression”, *Journal of Cancer Metastasis and Treatment*, Vol. 2, pp. 357, 2016.

199. Hwang, R. F., T. Moore, T. Arumugam, V. Ramachandran, K. D. Amos, A. Rivera, B. Ji, D. B. Evans and C. D. Logsdon, “Cancer-Associated Stromal Fibroblasts Promote Pancreatic Tumor Progression”, *Cancer Research*, Vol. 68, No. 3, pp. 918–926, 2008.

200. Pham, K., D. Delitto, A. E. Knowlton, E. R. Hartlage, R. Madhavan, D. H. Gonzalo, R. M. Thomas, K. E. Behrns, T. J. George, S. J. Hughes, S. M. Wallet, C. Liu and J. G. Trevino, “Isolation of Pancreatic Cancer Cells from a Patient-Derived Xenograft Model Allows for Practical Expansion and Preserved Heterogeneity in Culture”, *The American Journal of Pathology*, Vol. 186, No. 6, pp.1537-1546, 2016.

201. Degirmenci, A., H. Ipek, R. Sanyal and A. Sanyal, “Cyclodextrin-containing redox-responsive nanogels: Fabrication of a modular targeted drug delivery system”, *European Polymer Journal*, Vol. 181, p. 111645, 2022.

202. Aisida, S. O., P. A. Akpa, I. Ahmad, T. -k. Zhao, M. Maaza and F. I. Ezema, “Bio-inspired encapsulation and functionalization of iron oxide nanoparticles for biomedical applications”, *European Polymer Journal*, Vol. 122, p. 109371, 2020.

203. Dong, R., H. Chen, D. Wang, Y. Zhuang, L. Zhu, Y. Su, D. Yan and X. Zhu, “Supramolecular Fluorescent Nanoparticles for Targeted Cancer Imaging”, *ACS Macro Letters*, Vol. 1, No. 10, pp. 1208–1211, 2012.

204. Tu, C., L. Zhu, P. Li, Y. Chen, Y. Su, D. Yan, X. Zhu, G. Zhou, “Supramolecular Polymeric Micelles by the Host-Guest Interaction of Star-like Calix[4]Arene and Chlorin E6 for Photodynamic Therapy”, *Chemical Communication*, Vol. 47, No. 21, pp. 6063–6065, 2011.

205. Pooresmaeil, M., H. Namazi and R. Salehi, “Dual anticancer drug delivery of D-galactose-functionalized stimuli-responsive nanogels for targeted therapy of the liver hepatocellular carcinoma”, *European Polymer Journal*, Vol. 167, p. 111061, 2022.

206. Khan, M. I., M. I. Hossain, M. K. Hossain, M. H. K. Rubel, K. M. Hossain, A. M. U. B. Mahfuz and M. I. Anik, "Recent Progress in Nanostructured Smart Drug Delivery Systems for Cancer Therapy: A Review", *ACS Applied Bio Materials*, Vol. 5, No. 3, pp. 971–1012, 2022.

207. Singh, V., S. Md, N. A. Alhakamy and P. Kesharwani, "Taxanes loaded polymersomes as an emerging polymeric nanocarrier for cancer therapy", *European Polymer Journal*, Vol. 162, p. 11088, 2022.

208. Cisterna, B. A., N. Kamaly, W. II. Choi, A. Tavakkoli, O. C. Farokhzad and C. Vilos, "Targeted Nanoparticles for Colorectal Cancer", *Nanomedicine*, Vol. 11, pp. 2443–2456, 2016.

209. Sun, W., Y. Deng, M. Zhao, Y. Jiang, J. Gou, Y. Wang, T. Yin, Y. Zhang, H. He and X. Tang, "Targeting Therapy for Prostate Cancer by Pharmaceutical and Clinical Pharmaceutical Strategies", *Journal of Controlled Release*, Vol. 333, pp. 41–64, 2021.

210. Patra, J. K., G. Das, L. F. Fraceto, E. V. R. Campos, M. D. P. Rodriguez-Torres, L. S. Acosta-Torres, L. A. Diaz-Torres, R. Grillo, M. K. Swamy, S. Sharma, S. Habtemariam and H. -S. Shin, "Nano based drug delivery systems: recent developments and future prospects", *Journal of Nanobiotechnology*, Vol. 16, p. 71, 2018.

211. Molina, M., M. Asadian-Birjand, J. Balach, J. Bergueiro, E. Miceli, M. Calderon, "Stimuli-responsive nanogel composites and their application in nanomedicine", *Chemical Society Reviews*, Vol. 44, No. 17, pp. 6161–6186, 2015.

212. Maeda, H., J. Wu, T. Sawa, Y. Matsumura and K. Hori, "Tumor vascular permeability and the EPR effect in macromolecular therapeutics: a review", *Journal of Controlled Release*, Vol. 65, No. 1-2, pp. 271–284, 2000.

213. Li, Y., D. Maciel, J. Rodrigues, X. Shi and H. Tomas, "Biodegradable polymer nanogels for drug/nucleic acid delivery", *Chemical Reviews*, Vol. 115, No. 16, pp. 8564–8608, 2015.

214. Yin, Y., B. Hu, X. Yuan, L. Cai, H. Gao and Q. Yang, "Nanogel: A Versatile Nano-Delivery System for Biomedical Applications", *Pharmaceutics*, Vol. 12, p. 290, 2020.

215. Kaewruethai, T., C. Laomeephol, Y. Pan and J. A. Luckanagul, "Multifunctional Polymeric Nanogels for Biomedical Applications", *Gels*, Vol. 7, p. 228, 2021.

216. Wu, H. -Q. and C. -C. Wang, "Biodegradable Smart Nanogels: A New Platform for Targeting Drug Delivery and Biomedical Diagnostics", *Langmuir*, Vol. 32, No. 25, pp. 6211–6225, 2016.

217. Bhattacharya, K., S. L. Banerjee, S. Das, S. Samanta, M. Mandal and N. K. Singha, "Redox Responsive Fluorescence Active Glycopolymer Based Nanogel: A Potential Material for Targeted Anticancer Drug Delivery", *ACS Applied Bio Materials*, Vol. 2, No. 6, pp. 2587–2599, 2019.

218. Aktan, B., L. Chambre, R. Sanyal and A. Sanyal, ""Clickable" Nanogels via Thermally Driven Self-Assembly of Polymers: Facile Access to Targeted Imaging Platforms using Thiol–Maleimide Conjugation", *Biomacromolecules*, Vol. 18, No. 2, pp. 490–497, 2017.

219. Chambre, L. W. S. Saw, G. Ekineker, L. V. Kiew, W. Y. Chong, H. B. Lee, L. Y. Chung, Y. Bretonniere, F. Dumoulin and A. Sanyal, A, "Surfactant-Free Direct Access to Porphyrin-Cross-Linked Nanogels for Photodynamic and Photothermal Therapy", *Bioconjugate Chemistry*, Vol. 29, No. 12, pp. 4149–4159, 2018.

220. Ramasamy, T., H. B. Ruttala, B. Gupta, B. K. Poudel, H. -G. Choi, C. S. Yong and J. O. Kim, "Smart chemistry-based nanosized drug delivery systems for systemic applications: A comprehensive review", *Journal of Controlled Release*, Vol. 258, pp. 226–253, 2017.

221. Gannimani, R., P. Walvekar, V. R. Naidu, T. M. Aminabhavi and T. Govender, "Acetal containing polymers as pH-responsive nano-drug delivery systems", *Journal of Controlled Release*, Vol. 328, pp. 736–761, 2020.

222. Gillies, E. R., A. P. Goodwin ad J. M. J. Frechet, "Acetals as pH-Sensitive Linkages for Drug Delivery", *Bioconjugate Chemistry*, Vol. 15, No. 6, pp. 1254–1263, 2004.

223. Basak, D., R. Bej and S. Ghosh, "Amphiphilic poly(disulfide) micelles and a remarkable impact of the core hydrophobicity on redox responsive disassembly", *Polymer Chemistry*, Vol. 6, No. 36, pp. 6465–6474, 2015.

224. Altinbasak, I., R. Sanyal and A. Sanyal, "Best of both worlds: Diels–Alder chemistry towards fabrication of redox-responsive degradable hydrogels for protein release", *RSC Advances*, Vol 6, No. 78, pp. 74757–74764, 2016.

225. Altinbasak, I., M. Arslan, R. Sanyal and A. Sanyal, "Pyridyl disulfide-based thiol–disulfide exchange reaction: shaping the design of redox-responsive polymeric materials", *Polymer Chemistry*, Vol. 11, No. 48, pp. 7603–7624, 2020.

226. Saha, B., S. Bhattacharyya, S. Mete, A. Mukherjee and P. De, "Redox-Driven Disassembly of Polymer–Chlorambucil Polyprodrug: Delivery of Anticancer Nitrogen Mustard and DNA Alkylation", *ACS Applied Polymer Materials*, Vol. 1, No. 9, pp. 2503–2515, 2019.

227. Oh, J. K., D. J. Siegwart, H. -i. Lee, G. Sherwood, L. Peteanu, J. O. Hollinger, K. Kataoka and K. Matyjaszewski, "Biodegradable microgels prepared by atom transfer radical polymerization as potential drug delivery carriers: Synthesis, biodegradation, in vitro release, and bioconjugation", *Journal of American Chemical Society*, Vol. 129, No. 18, 5939−5945, 2007.

228. Wang, Y., J. Nie, B. Chang, Y. Sun and W. Yang, "Poly(vinylcaprolactam)-Based Biodegradable Multiresponsive Microgels for Drug Delivery", *Biomacromolecules*, Vol. 14, No. 9, pp. 3034–3046, 2013.

229. Davis, M. E. and M. E. Brewster, "Cyclodextrin-based pharmaceutics: past, present and future", *Nature Reviews Drug Discovery*, Vol. 3, pp. 1023–1035, 2004.

230. Wang, J. and M. Jiang, "Polymeric Self-Assembly into Micelles and Hollow Spheres with Multiscale Cavities Driven by Inclusion Complexation", *Journal of American Chemical Society*, Vol. 128, No. 11, pp. 3703–3708, 2006.

231. Ma, X. and Y. Zhao, "Biomedical Applications of Supramolecular Systems Based on Host–Guest Interactions", *Chemical Reviews*, Vol. 115, No. 15, pp. 7794–7839, 2015.

232. Yuvayapan, S. and A. Aydogan, "Counter Cation Dependent and Stimuli-Responsive Supramolecular Polymers Constructed by Calix[4]pyrrole Based Host–Guest Interactions", *European Journal of Organic Chemistry*, Vol. 2019, No. 4, pp. 633–639, 2019.

233. Ozkan, M., Y. Kumar, Y. Keser, S. E. Hadi and D. Tuncel, "Cucurbit[7]uril-Anchored Porphyrin-Based Multifunctional Molecular Platform for Photodynamic Antimicrobial and Cancer Therapy", *ACS Applied Bio Materials*, Vol. 2, No. 11, pp. 4693–4697, 2019.

234. Wu, X., Y. Li, C. Lin, X. -Y. Hu and L. Wang, "GSH- and pH-responsive drug delivery system constructed by water-soluble pillar[5]arene and lysine derivative for controllable drug release", *Chemical Communication*, Vol. 51, No. 31, pp. 6832–6835, 2015.

235. Tang, M., Y. -H. Liu, X. -M. Xu, Y. -M. Zhang and Y. Liu, "Dual-responsive drug release and fluorescence imaging based on disulfide-pillar[4]arene aggregate in cancer cells", *Bioorganic Medicinal Chemistry*, Vol. 57, p. 116649, 2022.

236. Nandi, M., B. Maiti, K. Srikanth and P. De, "Supramolecular Interaction-Assisted Fluorescence and Tunable Stimuli-Responsiveness of L-Phenylalanine-Based Polymers", *Langmuir*, Vol. 33, No. 40, pp. 10588–10597, 2017.

237. Zhang, J. and P. X. Ma, "Host–guest interactions mediated nano-assemblies using cyclodextrin-containing hydrophilic polymers and their biomedical applications", *Nano Today*, Vol. 5, pp. 337–350, 2010.

238. Patra, D., F. Ozdemir, O. R. Miranda, B. Samanta, A. Sanyal and V. M. Rotello, "Formation and Size Tuning of Colloidal Microcapsules via Host−Guest Molecular Recognition at the Liquid−Liquid Interface", *Langmuir*, Vol. 25, No. 24, pp. 13852–13854, 2009.

239. Oz, Y., Y. Abdouni, G. Yilmaz, R. C. Becer and A. Sanyal, "Magnetic Glyconanoparticles for Selective Lectin Separation and Purification", *Polymer Chemistry*, Vol. 10, No. 24, pp. 3351-3361, 2019.

240. Zhang, Y. -M., Y. -H. Liu, Y. Liu, "Cyclodextrin-Based Multistimuli-Responsive Supramolecular Assemblies and Their Biological Functions", *Advanced Materials*, Vol. 32, No. 3, p. 1806158, 2020.

241. Arslan, M., R. Sanyal and A. Sanyal, "Cyclodextrin embedded covalently crosslinked networks: synthesis and applications of hydrogels with nano-containers", *Polymer Chemistry*, Vol. 11, No. 3, pp. 615-629, 2020.

242. Zan, M., J. Li, S. Luo and Z. Ge, "Dual pH-triggered multistage drug delivery systems based on host–guest interaction-associated polymeric nanogels", *Chemical Communication*, Vol. 50, No. 58, pp. 7824–7827, 2014.

243. Carneiro, S. B., F. I. C. Duarte, L. Heimfarth, J. d. S. S. Quintans, L. J. Quintans-Junior, V. F. d. V. Junior and A. A. N. de Lima, "Cyclodextrin–Drug Inclusion Complexes: In Vivo and In Vitro Approaches", *International Journal of Molecular Sciences*, Vol. 20, No. 3, p. 642, 2019.

244. Zhang, L., S. Man, H. Qiu, Z. Liu, M. Zhang, L. Ma and W. Gao, "Curcumin-cyclodextrin complexes enhanced the anticancer effects of curcumin", *Environmental Toxicology and Pharmacology*, Vol. 48, pp. 31–38, 2016.

245. Yang, Y., X. Jia, Y. -M. Zhang, N. Li and Y. Liu, "Supramolecular nanoparticles based on β-CD modified hyaluronic acid for DNA encapsulation and controlled release", *Chemical Communication*, Vol. 54, No. 63, pp. 8713–8716, 2018.

246. Wintgens, V., T. T. Nielsen, K. L. Larsen, C. Amiel, Size-Controlled Nanoassemblies Based on Cyclodextrin-Modified Dextrans, *Macromolecular Bioscience*, Vol. 11, No. 9, pp. 1254–1263, 2011.

247. Zhang, Y. -H., Y. -M. Zhang, X. Sheng, J. Wang, Y. Liu, "Enzyme-responsive fluorescent camptothecin prodrug/polysaccharide supramolecular assembly for targeted cellular imaging and *in situ* controlled drug release", *Chemical Communication*, Vol. 56, No. 7, pp. 1042–1045, 2020.

248. Fu, H. -G., Y. Chen, Q. Yu and Y. Liu, "Polysaccharide-Based Nanoparticles for Two-Step Responsive Release of Antitumor Drug", *ACS Medicinal Chemistry Letters*, Vol. 11, No. 6, pp. 1191–1195, 2020.

249. Chen, X., L. Chen, X. Yao, Z. Zhang, C. He, J. Zhang and X. Chen, "Dual responsive supramolecular nanogels for intracellular drug delivery", *Chemical Communication*, Vol. 50, No. 29, pp. 3789-3791, 2014.

250. Zou, Y., J. Wei, Y. Xia, F. Meng, J. Yuan and Z. Zhong, "Targeted chemotherapy for subcutaneous and orthotopic non-small cell lung tumors with cyclic RGD-functionalized and disulfide-crosslinked polymersomal doxorubicin", *Signal Transduction and Targeted Therapy*, Vol. 3, p. 32, 2018.

251. Miura, Y., T. Takenaka, K. Toh, S. Wu, H. Nishihara, M. R. Kano, Y. Ino, T. Nomoto, Y. Matsumoto, H. Koyama, H. Cabral, N. Nishiyama and K. Kataoka, "Cyclic RGD-Linked Polymeric Micelles for Targeted Delivery of Platinum Anticancer Drugs to Glioblastoma through the Blood–Brain Tumor Barrier", *ACS Nano*, Vol. 7, No. 10, pp. 8583–8592, 2013.

252. Tungala, K., P. Adhikary and S. Krishnamoorthi, "Trimerization of β-cyclodextrin through the click reaction", *Carbohydrate Polymers*, Vol. 95, No. 1, pp. 295–298, 2013.

253. Mulder, A., S. Onclin, M. Peter, J. P. Hoogenboom, H. Beijleveld, J. ter Maat, M. F. Garcia-Parajo, B. J. Ravoo, J. Huskens, N. F. van Hulst and D. N. Reinhoudt, "Molecular Printboards on Silicon Oxide: Lithographic Patterning of Cyclodextrin Monolayers with Multivalent, Fluorescent Guest Molecules", *Small*, Vol. 1, pp. 242–253, 2005.

254. Ipek, H., *Fabrication of Biopolymeric Nanogels Using Supramolecular Interactions*, M.S. Thesis, Boğaziçi University, 2015.

255. Nielsen, T. T., V. Wintgens, C. Amiel, R. Wimmer and K. L. Larsen, "Facile Synthesis of β-Cyclodextrin-Dextran Polymers by "Click" Chemistry", *Biomacromolecules*, Vol. 11, No. 7, pp. 1710–1715, 2010.

256. Swiech, O., A. Mieczkowska, K. Chmurski and R. Bilewicz, “Intermolecular Interactions between Doxorubicin and β-Cyclodextrin 4-Methoxyphenol Conjugates”, *The Journal of Physical Chemistry B*, Vol. 116, No. 6, pp. 1765–1771, 2012.

257. Xue, S. -S., C. -P. Tan, M. -H. Chen, J. -J. Cao, D. -Y. Zhang, R. -R. Ye, L. -N. Ji and Z. -W. Mao, “Tumor-targeted supramolecular nanoparticles self-assembled from a ruthenium-β-cyclodextrin complex and adamantane-functionalized peptide”, *Chemical Communication*, Vol. 53, No. 5, pp. 842–845, 2017.

258. Schibilla, F., J. Voskuhl, N. A. Fokina, J. E. P. Dahl, P. R. Schreiner and B. J. Ravoo, “Host-Guest Complexes of Cyclodextrins and Nanodiamonds as a Strong Non-Covalent Binding Motif for Self-Assembled Nanomaterials”, *Chemistry A European Journal*, Vol. 23, No. 63, pp. 16059–16065, 2017.

259. Chan, N., B. Khorsand, S. Aleksanian and J. K. Oh, “A dual location stimuli-responsive degradation strategy of block copolymer nanocarriers for accelerated release”, *Chemical Communication*, Vol. 49, No. 68, pp. 7534–7536, 2013.

260. Jazani, A. M., N. Arezi, C. Shetty, S. H. Hong, H. Li, X. Wang and J. K. Oh, “Tumor-targeting intracellular drug delivery based on dual-acid/reduction-degradable nanoassemblies with ketal interface and disulfide core locations”, *Polymer Chemistry*, Vol. 10, No. 22, pp. 2840–2853, 2019.

261. Hong, R., G. Han, J. M. Fernandez, B. -j. Kim, N. S. Forbes and V. M. Rotello, “Glutathione-Mediated Delivery and Release Using Monolayer Protected Nanoparticle Carriers”, *Journal of American Chemical Society*, Vol. 128, No. 4, pp. 1078–1079, 2006.

262. Garg, D., I. Matai and A. Sachdev, “Toward Designing of Anti-Infective Hydrogels for Orthopedic Implants: From Lab to Clinic”, *ACS Biomaterials Science & Engineering*, Vol. 7, No. 6, pp. 1933–1961, 2021.

263. Calo, E. and V. V. Khutoryanskiy, “Biomedical Applications of Hydrogels: A Review of Patents and Commercial Products”, *European Polymer Journal*, Vol. 65, pp. 252–267, 2015.

264. Wolinsky, J. B., Y. L. Colson and M. W. Grinstaff, “Local Drug Delivery Strategies for Cancer Treatment: Gels, Nanoparticles, Polymeric Films, Rods, And Wafers”, *Journal of Controlled Release*, Vol. 159, No. 1, pp. 14–26, 2012.

265. Aydin, D., M. Arslan, A. Sanyal and R. Sanyal, “Hooked on Cryogels: A Carbamate Linker Based Depot for Slow Drug Release”, *Bioconjugate Chemistry*, Vol. 28, No. 5, pp. 1443–1451, 2017.

266. Wang, J., H. He, R. C. Cooper, Q. Gui and H. Yang, “Drug-Conjugated Dendrimer Hydrogel Enables Sustained Drug Release via A Self-Cleaving Mechanism”, *Molecular Pharmaceutics*, Vol. 16, No. 5, pp. 1874–1880, 2019.

267. Gao, L., Y. Chen, Q. Luo, Y. Wang, X. Li, Z. Shen and W. Zhu, “Injectable Camptothecin Conjugated Hydrogels with Simultaneous Drug Release and Degradation”, *RSC Advances*, Vol. 6, No. 97, pp. 94661–94668, 2016.

268. Ono, R. J., A. L. Z. Lee, Z. X. Voo, S. Venkataraman, B. W. Koh, Y. Y. Yang and J. L. Hedrick, “Biodegradable Strain-Promoted Click Hydrogels for Encapsulation of Drug-Loaded Nanoparticles and Sustained Release of Therapeutics”, *Biomacromolecules*, Vol. 18, No. 8, pp. 2277–2285, 2017.

269. Fu, S., H. Dong, X. Deng, R. Zhuo and Z. Zhong, “Injectable Hyaluronic Acid/Poly(Ethylene Glycol) Hydrogels Crosslinked via Strain-Promoted Azide-Alkyne Cycloaddition Click Reaction”, *Carbohydrate Polymers*, Vol. 169, pp. 332–340, 2017.

270. Desai, R. M., S. T. Koshy, S. A. Hilderbrand, D. J. Mooney and N. S. Joshi, “Versatile Click Alginate Hydrogels Crosslinked via Tetrazine–Norbornene Chemistry”, *Biomaterials*, Vol. 50, pp. 30–37, 2015.

271. Alge, D. L., M. A. Azagarsamy, D. F. Donohue and K. S. Anseth, “Synthetically Tractable Click Hydrogels for Three-Dimensional Cell Culture Formed Using Tetrazine–Norbornene Chemistry”, *Biomacromolecules*, Vol. 14, No. 4, pp. 949–953, 2013.

272. Yu, F., X. Cao, J. Du, G. Wang and X. Chen, "Multifunctional Hydrogel with Good Structure Integrity, Self-Healing, and Tissue-Adhesive Property Formed by Combining Diels–Alder Click Reaction and Acylhydrazone Bond", *ACS Applied Materials & Interfaces*, Vol. 7, No. 43, pp. 24023–24031, 2015.

273. Oh, J., K. I. Jung, H. W. Jung and A. Khan, "A Modular and Practical Synthesis of Zwitterionic Hydrogels Through Sequential Amine-Epoxy 'Click' Chemistry and N-Alkylation Reaction", *Polymers*, Vol. 11, No. 9, p. 1491, 2019.

274. Pupkaite, J., J. Rosenquist, J. Hilborn, and A. Samanta, "Injectable Shape-Holding Collagen Hydrogel for Cell Encapsulation and Delivery Cross-Linked Using Thiol-Michael Addition Click Reaction", *Biomacromolecules*, Vol. 20, No. 9, pp. 3475–3484, 2019.

275. Ding, H., B. Li, Y. Jiang, G. Liu, S. Pu, Y. Feng, D. Jia and Y. Zhou, "pH-Responsive UV Crosslinkable Chitosan Hydrogel via 'Thiol-Ene' Click Chemistry for Active Modulating Opposite Drug Release Behaviors", *Carbohydrate Polymers*, Vol. 251, p. 117101, 2021.

276. Aimetti, A. A., A. J. Machen and K. S. Anseth, "Poly(Ethylene Glycol) Hydrogels Formed by Thiol-Ene Photopolymerization for Enzyme-Responsive Protein Delivery", *Biomaterials*, Vol. 30, No. 30, pp. 6048–6054, 2009.

277. Truong, V. X., M. P. Ablett, H. T. J. Gilbert, J. Bowen, S. M. Richardson, J. A. Hoyland and A. P. Dove, "In Situ-Forming Robust Chitosan-Poly(Ethylene Glycol) Hydrogels Prepared by Copper-Free Azide–Alkyne Click Reaction for Tissue Engineering", *Biomaterials Science*, Vol. 2, pp. 167–175, 2014.

278. Mulay, P., G. Shrikhande and J. E. Puskas, "Synthesis of Mono- and Dithiols of Tetraethylene Glycol and Poly(Ethylene Glycol)s via Enzyme Catalysis", *Catalysts*, Vol. 9, No. 3, p. 228, 2019.

279. Degirmenci, A., G. Y. Bas, R. Sanyal and A. Sanyal, "Clickable Polymer Brush Interfaces: Tailoring Monovalent to Multivalent Ligand Display for Protein Immobilization and Sensing", *Bioconjugate Chemistry*, Vol. 33, No. 9, pp. 1672-1684, 2022.

280. Wei, Q. and R. Haag, “Universal Polymer Coatings and Their Representative Biomedical Applications”, *Materials Horizons*, Vol. 2, pp. 567–577, 2015.

281. Seemann, A., S. Akbaba, J. Buchholz, S. Türkkan, A. Tezcaner, S.K. Woche, G. Guggenberger, A. Kirschning and G. Drager, “RGD-Modified Titanium as an Improved Osteoinductive Biomaterial for Use in Dental And Orthopedic Implants”, *Bioconjugate Chemistry*, Vol. 33, No. 2, pp. 294–300, 2022.

282. Dhingra, S., S. Sharma and S. Saha, “Infection Resistant Surface Coatings by Polymer Brushes: Strategies to Construct and Applications”, *ACS Applied Bio Materials*, Vol. 5, No. 4, pp. 1364–1390, 2022.

283. Maddahfar, M., S. Wen, S. M. Hosseinpour Mashkani, L. Zhang, O. Shimoni, M. Stenzel, J. Zhou, B. Fazekas de St Groth and D. Jin, “Stable And Highly Efficient Antibody–Nanoparticles Conjugation”, *Bioconjugate Chemistry*, Vol. 32, No. 6, pp. 1146–1155, 2021.

284. Asha, A. B., Y. -Y. Peng, Q. Cheng, K. Ishihara, Y. Liu and R. Narain, “Dopamine Assisted Self-Cleaning, Antifouling, and Antibacterial Coating via Dynamic Covalent Interactions”, *ACS Applied Materials & Interfaces*, Vol. 14, No. 7, pp. 9557–9569, 2022.

285. Azzaroni, O. “Polymer Brushes Here, There, and Everywhere: Recent Advances in Their Practical Applications and Emerging Opportunities in Multiple Research Fields”, *Journal of Polymer Science Part A: Polymer Chemistry*, Vol. 50, No. 16, pp. 3225–3258, 2012.

286. Fan, X., C. Xia, T. Fulghum, M. -K. Park, J. Locklin and R. C. Advincula, “Polymer Brushes Grafted From Clay Nanoparticles Adsorbed on A Planar Substrate by Free Radical Surface-Initiated Polymerization”, *Langmuir*, Vol. 19, No. 3, pp. 916–923, 2003.

287. Becer, C. R., R. Hoogenboom and U. S. Schubert, “Click Chemistry beyond Metal-Catalyzed Cycloaddition”, *Angewandte Chemie International Edition*, Vol. 48, No. 27, pp. 4900–4908, 2009.

288. Geng, Z., J. J. Shin, Y. Xi and C. J. Hawker, "Click Chemistry Strategies for The Accelerated Synthesis of Functional Macromolecules", *Journal of Polymer Science*, Vol. 59, No. 11, pp. 963–1042, 2021.

289. Cedrati, V., A. Pacini, A. Nitti, A. Martínez de Ilarduya, S. Munoz-Guerra, A. Sanyal and D. Pasini, "'Clickable' Bacterial Poly(γ-Glutamic Acid)", *Polymer Chemistry*, Vol. 11, pp. 5582–5589, 2020.

290. Zaccaria, C. L., V. Cedrati, A. Nitti, E. Chiesa, A. Martinez de Ilarduya, M. Garcia-Alvarez, M. Meli, G. Colombo, and D. Pasini, "Biocompatible Graft Copolymers from Bacterial Poly(γ-Glutamic Acid) And Poly(Lactic Acid)", *Polymer Chemistry*, Vol. 12, pp. 3784–3793, 2021.

291. Beria, L., T. N. Gevrek, A. Erdog, R. Sanyal, D. Pasini and A. Sanyal, "'Clickable' Hydrogels for All: Facile Fabrication and Functionalization", *Biomaterial Sciences*, Vol. 2, pp. 67–75, 2014.

292. Saha, S., M. L. Bruening and G. L. Baker, "Surface-Initiated Polymerization of Azidopropyl Methacrylate and Its Film Elaboration via Click Chemistry", *Macromolecules*, Vol. 45, No. 22, pp. 9063–9069, 2012.

293. Orski, S. V., G. R. Sheppard, S. Arumugam, R. M. Arnold, V. V. Popik and J. Locklin, "Rate Determination of Azide Click Reactions onto Alkyne Polymer Brush Scaffolds: A Comparison of Conventional and Catalyst-Free Cycloadditions for Tunable Surface Modification", *Langmuir*, Vol. 28, No. 41, pp. 14693–14702, 2012.

294. Tan, K. Y., M. Ramstedt, B. Colak, W. T. S. Huck and J. E. Gautrot, "Study of Thiol–Ene Chemistry on Polymer Brushes and Application to Surface Patterning and Protein Adsorption", *Polymer Chemistry*, Vol. 7, No. 4, pp. 979–990, 2016.

295. Hensarling, R. M., V. A. Doughty, J. W. Chan and D. L. Patton, "'Clicking' Polymer Brushes with Thiol-Yne Chemistry: Indoors and Out", *Journal of the American Chemical Society*, Vol. 131, No. 41, pp. 14673–14675, 2009.

296. Rahane, S. B., R. M. Hensarling, B. J. Sparks, C. M. Stafford and D. L. Patton, "Synthesis Of Multifunctional Polymer Brush Surfaces via Sequential and Orthogonal Thiol-Click Reactions", *Journal of Materials Chemistry*, Vol. 22, pp. 932–943, 2012.

297. Dübner, M., Gevrek, T. N., A. Sanyal, N. D. Spencer and C. Padeste, " Fabrication of Thiol-ene Clickable Copolymer Brush Nanostructures on Polymeric Substrates via Extreme Ultraviolet Interference Lithography", *ACS Applied Materials & Interfaces*, Vol. 7, No. 21, pp. 11337–11345, 2015.

298. Yuksekdag, Y. N., T. N. Gevrek and A. Sanyal, "Diels-Alder 'Clickable' Polymer Brushes: A Versatile Catalyst-Free Conjugation Platform", *ACS Macro Letters*, Vol. 6, No. 4, pp. 415–420, 2017.

299. Husemann, M., M. Morrison, D. Benoit, J. Frommer, C. M. Mate, W. D. Hinsberg, J. L. Hedrick and C. J. Hawker, "Manipulation of Surface Properties by Patterning of Covalently Bound Polymer Brushes", *Journal of the American Chemical Society*, Vol. 122, No. 8, pp. 1844–1845, 2000.

300. Meyer, U., F. Svec, J. M. J. Frechet, C. J. Hawker and K. Irgum, "Use of Stable Free Radicals for the Sequential Preparation and Surface Grafting of Functionalized Macroporous Monoliths", *Macromolecules*, Vol. 33, No. 21, pp. 7769–7775, 2000.

301. Li, J., X. Chen, and Y. -C. Chang, "Preparation of End-Grafted Polymer Brushes by Nitroxide-Mediated Free Radical Polymerization of Vaporized Vinyl Monomers", *Langmuir*, Vol. 21, No. 21, pp. 9562–9567, 2005.

302. Ma, H., M. Wells, T. P. Beebe and A. Chilkoti, "Surface-Initiated Atom Transfer Radical Polymerization of Oligo(Ethylene Glycol) Methyl Methacrylate from A Mixed Self-Assembled Monolayer on Gold", *Advanced Functional Materials*, Vol. 16, No. 5, pp. 640–648, 2006.

303. Siegwart, D. J., J. K. Oh and K. Matyjaszewski, "ATRP in the Design of Functional Materials for Biomedical Applications", *Progress in Polymer Science*, Vol. 37, No. 1, pp. 18–37, 2012.

304. Riachi, C., N. Schüwer and H. -A. Klok, “Degradable Polymer Brushes Prepared via Surface-Initiated Controlled Radical Polymerization”, *Macromolecules*, Vol. 42, No. 21, pp. 8076–8081, 2009.

305. Yamamoto, S. -I., J. Pietrasik, and K. Matyjaszewski, “The Effect of Structure on The Thermoresponsive Nature of Well-Defined Poly(Oligo(Ethylene Oxide) Methacrylates) Synthesized by ATRP”, *Journal of Polymer Science Part A: Polymer Chemistry*, Vol. 46, No. 1, pp. 194–202, 2008.

306. Zengin, A., E. Yildirim and T. Caykara, “RAFT-mediated Synthesis and Temperature-induced Responsive Properties of Poly(2-(2-methoxyethoxy)Ethyl Methacrylate) Brushes”, *Journal of Polymer Science Part A: Polymer Chemistry*, Vol. 51, No. 4, pp. 954–962, 2013.

307. Ranjan, R. and W. J. Brittain, “Synthesis of High Density Polymer Brushes on Nanoparticles by Combined RAFT Polymerization and Click Chemistry”, *Macromolecular Rapid Communications*, Vol. 29, No. 12-13, pp. 1104–1110, 2008.

308. Willcock, H. and R. K. O’Reilly, “End Group Removal and Modification of RAFT Polymers”, *Polymer Chemistry*, Vol. 1, No. 2, pp. 149–157, 2010.

309. Patton, D. L., M. Mullings, T. Fulghum and R. C. Advincula, “A Facile Synthesis Route To Thiol-Functionalized α,ω-Telechelic Polymers Via Reversible Addition Fragmentation Chain Transfer Polymerization”, *Macromolecules*, Vol. 38, No. 20, pp. 8597–8602, 2005.

310. Xu, J., J. He, D. Fan, X. Wang and Y. Yang, “Aminolysis of Polymers with Thiocarbonylthio Termini Prepared by RAFT Polymerization: The Difference Between Polystyrene and Polymethacrylates”, *Macromolecules*, Vol. 39, No. 25, pp. 8616–8624, 2006.

311. Nitti, A., A. Martinelli, F. Batteux, S. Protti, M. Fagnoni and D. Pasini, “Blue Light Driven Free-Radical Polymerization Using Arylazo Sulfones As Initiators”, *Polymer Chemistry*, Vol. 12, No. 40, pp. 5747–5751, 2021.

312. Mutlu, H., C. M. Geiselhart and C. Barner-Kowollik, “Untapped Potential for Debonding on Demand: The Wonderful World of Azo-Compounds”, *Materials Horizons*, Vol. 5, No. 2, pp. 162–183, 2018.

313. Tao, L., C. S. Kaddis, R. R. Ogorzalek Loo, G. N. Grover, J. A. Loo and H. D. Maynard, “Synthetic Approach To Homodimeric Protein–Polymer Conjugates”, *Chemical Communications*, pp. 2148–2150, 2009.

314. Heredia, K. L., G. N. Grover, L. Tao, and H. D. Maynard, “Synthesis of Heterotelechelic Polymers for Conjugation of Two Different Proteins”, *Macromolecules*, Vol. 42, No. 7, pp. 2360–2367, 2009.

315. Wu, P., M. Malkoch, J. N. Hunt, R. Vestberg, E. Kaltgrad, M. G. Finn, V. V. Fokin, K. B. Sharpless and C. J. Hawker, “Multivalent, Bifunctional Dendrimers Prepared by Click Chemistry”, *Chemical Communications*, No. 46, pp. 5775–5777, 2005.

316. Revell, D. J., J. R. Knight, D. J. Blyth, A. H. Haines and D. A. Russell, “Self-Assembled Carbohydrate Monolayers: Formation and Surface Selective Molecular Recognition”, *Langmuir*, Vol. 14, No. 16, pp. 4517–4524, 1998.

317. Mahajan, S. S. and S. S. Iyer, “ELISA and SPR Studies of Ricin Binding to β-Galactoside Analogs”, *Journal of Carbohydrate Chemistry*, Vol. 31, No. 4-6, pp. 447–465, 2012.

318. Tugulu, S., M. Harms, M. Fricke, D. Volkmer and H. -A. Klok, “Polymer Brushes as Ionotropic Matrices for The Directed Fabrication of Microstructured Calcite Thin Films”, *Angewandte Chemie International Edition*, Vol. 45, No. 44, pp. 7458–7461, 2006.

319. Luzinov, I., D. Julthongpiput, H. Malz, J. Pionteck and V. V. Tsukruk, “Polystyrene Layers Grafted to Epoxy-Modified Silicon Surfaces”, *Macromolecules*, Vol. 33, No. 3, pp.1043–1048, 2000.

320. Cengiz, B., N. Ejderyan and A. Sanyal, “Functional Polymeric Coatings: Thiol-Maleimide ‘Click’ Chemistry as a Powerful Surface Functionalization Tool”, *Journal*

of Macromolecular Science, Part A Pure and Applied Chemistry, Vol. 59, No. 7, pp. 443–455, 2022.

321. Xu, D. and S. V. Wegner, "Multifunctional Streptavidin–Biotin Conjugates with Precise Stoichiometries", *Chemical Science*, Vol. 11, pp. 4422–4429, 2020.

322. Coulibaly, F. S. and B. -B. C. Youan, "Concanavalin A–Polysaccharides Binding Affinity Analysis Using A Quartz Crystal Microbalance", *Biosensors and Bioelectronics*, Vol. 59, pp. 404–411, 2014.

323. Fan, F., C. Cai, L. Gao, J. Li, P. Zhang, G. Li, C. Li and G. Yu, "Microwave-Assisted Synthesis of Glycopolymers by Ring-Opening Metathesis Polymerization (ROMP) in an Emulsion System", *Polymer Chemistry*, Vol. 8, No. 44, pp. 6709–6719, 2017.

324. Rühe, J., "Polymer Brushes: On the Way to Tailor-Made Surfaces", *Polymer Brushes*, pp. 1–31, 2005.

325. Ayres, N., "Polymer Brushes: Applications in Biomaterials and Nanotechnology", *Polymer Chemistry*, Vol. 1, No. 6, pp. 769–777, 2010.

326. Jiang, L., H. Bagan, T. Kamra, T. Zhou and L. Ye, "Nanohybrid Polymer Brushes on Silica for Bioseparation", *Journal of Materials Chemistry B*, Vol. 4, No. 19, pp. 3247–3256, 2016.

327. Zdyrko, B., V. Klep, X. Li, Q. Kang, S. Minko, X. Wen and I. Luzinov, "Polymer Brushes as Active Nanolayers For Tunable Bacteria Adhesion", *Materials Science and Engineering: C*, Vol. 29, No. 3, pp. 680–684, 2009.

328. Poreba, R., A. los Santos Pereira, R. Pola, S. Jiang, O. Pop-Georgievski, Z. Sedlakova and H. Schönherr, "'Clickable' and Antifouling Block Copolymer Brushes as A Versatile Platform for Peptide-Specific Cell Attachment", *Macromolecular Bioscience*, Vol. 20, No. 4, p. 1900354, 2020.

329. Colak, B., S. Di Cio and J. E. Gautrot, "Biofunctionalized Patterned Polymer Brushes via Thiol–Ene Coupling for the Control of Cell Adhesion and the Formation of Cell Arrays", *Biomacromolecules*, Vol. 19, No. 5, pp. 1445–1455, 2018.

330. Edmondson, S. and W. T. S. Huck, "Controlled Growth and Subsequent Chemical Modification of Poly(Glycidyl Methacrylate) Brushes on Silicon Wafers.", *Journal of Materials Chemistry,* Vol. 14, No. 4, pp. 730–734, 2004.

331. Xuan, J., D. Han, H. Xia and Y. Zhao, "Dual-Stimuli-Responsive Micelle of an ABC Triblock Copolymer Bearing A Redox-Cleavable Unit and A Photocleavable Unit at Two Block Junctions", *Langmuir,* Vol. 30, No. 1, pp. 410–417, 2014.

332. Boz, R. K., D. Aydin, S. Kocak, B. Golba, R. Sanyal and A. Sanyal, "Redox-Responsive Hydrogels for Tunable and 'On-Demand' Release of Biomacromolecules", *Bioconjugate Chemistry,* Vol. 33, No. 5, pp. 839–847, 2022.

333. Gevrek, T. N., M. Cosar, D. Aydin, E. Kaga, M. Arslan, R. Sanyal and A. Sanyal, "Facile Fabrication of a Modular 'Catch and Release' Hydrogel Interface: Harnessing Thiol-Disulfide Exchange for Reversible Protein Capture and Cell Attachment", *ACS Applied Materials and Interfaces*, Vol. 10, No. 17, pp. 14399–14409, 2018.

334. Iwasaki, Y., Y. Omichi and R. Iwata, "Site-Specific Dense Immobilization of Antibody Fragments on Polymer Brushes Supported by Silicone Nanofilaments", *Langmuir,* Vol. 24, No. 16, pp. 8427–8430, 2008.

335. Shepherd, J. L., A. Kell, E. Chung, C. W. Sinclar, M. S. Workentin and D. Bizzotto, "Selective Reductive Desorption of A SAM-Coated Gold Electrode Revealed Using Fluorescence Microscopy", *Journal of the American Chemical Society*, Vol. 126, No. 26, pp. 8329–8335, 2004.

336. Darwish, S., N. Sadeghiani, S. Fong, S. Mozaffari, P. Hamidi, T. Withana, S. Yang, R. K. Tiwari and K. Parang, "Synthesis and Antiproliferative Activities of Doxorubicin Thiol Conjugates and Doxorubicin-SS-cyclic peptide", *European Journal of Medicinal Chemistry*, Vol. 161, pp. 594–606, 2019.

337. Degirmenci, A., R. Sanyal, M. Arslan and A. Sanyal, "Benzothiazole-Disulfide Based Redox-Responsive Polymers: Facile Access to Reversible Functionalizable Polymeric Coatings", *Polymer Chemistry*, Vol. 13, No. 18, pp. 2595-2607, 2022.

338. Wei, M., Y. Gao, X. Li and M. J. Serpe, "Stimuli-Responsive Polymers and Their Applications", *Polymer Chemistry*, Vol. 8, No. 1, pp. 127–143, 2017.

339. Moad, G., "RAFT Polymerization to form Stimuli-Responsive Polymers", *Polymer Chemistry*, Vol. 8, No. 1, pp. 177–219, 2017.

340. Cobo, I., M. Li, B. S. Sumerlin and S. Perrier, "Smart Hybrid Materials by Conjugation of Responsive Polymers to Biomacromolecules", *Nature Materials*, Vol. 14, pp. 143–159, 2014.

341. Jingcheng, L., V. S. Reddy, W. A. D. M. Jayathilaka, A. Chinnappan, S. Ramakrishna and R. Ghosh, "Intelligent Polymers, Fibers and Applications", *Polymers*, Vol. 13, No. 9, p. 1427, 2021.

342. Kocak, G., C. Tuncer and V. Bütün, "pH-Responsive Polymers", *Polymer Chemistry*, Vol. 8, No. 1, pp. 144–176, 2017.

343. Hoogenboom, R. and H. Schlaad, "Thermoresponsive Poly(2-Oxazoline)s, Polypeptoids, and Polypeptides", *Polymer Chemistry*, Vol. 8, No. 1, pp. 24–40, 2017.

344. Bertrand, O. and J. -F. Gohy, "Photo-Responsive Polymers: Synthesis and Applications", *Polymer Chemistry*, Vol. 8, No. 1, pp. 52–73, 2017.

345. Arslan, M., D. Aydin, A. Degirmenci, A. Sanyal and R. Sanyal, "Embedding Well-Defined Responsive Hydrogels with Nanocontainers: Tunable Materials from Telechelic Polymers and Cyclodextrins", *ACS Omega*, Vol. 2, No. 10, pp. 6658–6667, 2017.

346. Manouras, T. and M. Vamvakaki, "Field Responsive Materials: Photo-, Electro-, Magnetic- And Ultrasound-Sensitive Polymers", *Polymer Chemistry*, Vol. 8, No. 1, pp. 74–96, 2017.

347. Zhai, L., "Stimuli-Responsive Polymer Films", *Chemical Society Reviews*, Vol. 42, No. 17, pp. 7148–7160, 2013.

348. Arslan, M., R. Sanyal and A. Sanyal, "Thiol-Reactive Thiosulfonate Group Containing Copolymers: Facile Entry to Disulfide-Mediated Polymer Conjugation

and Redox-Responsive Functionalizable Networks", *Polymer Chemistry*, Vol. 11, No. 10, pp. 1763–1773, 2020.

349. Yang, Y. and M. W. Urban, "Self-Healing of Glucose-Modified Polyurethane Networks Facilitated by Damage-Induced Primary Amines", *Polymer Chemistry*, Vol. 8, No. 1, pp. 303–309, 2017.

350. Kilic, R. and A. Sanyal, "Self-Healing Hydrogels Based on Reversible Covalent Linkages: A Survey of Dynamic Chemical Bonds in Network Formation", *Advances in Polymer Science*, Vol. 285, pp. 243–294, 2020.

351. Hunter, A. C. and S. M. Moghimi, "Smart Polymers in Drug Delivery: A Biological Perspective", *Polymer Chemistry*, Vol. 8, No. 1, pp. 41–51, 2017.

352. Li, J., C. Tian, Y. Yuan, Z. Yang, C. Yin, R. Jiang, W. Song, X. Li, X. Lu, L. Zhang, Q. Fan and W. Huang, "A Water-Soluble Conjugated Polymer with Pendant Disulfide Linkages to PEG Chains: A Highly Efficient Ratiometric Probe with Solubility-Induced Fluorescence Conversion for Thiol Detection", *Macromolecules*, Vol. 48, No. 4, pp. 1017–1025, 2015.

353. Hu, L., Y. Wan, Q. Zhang and M. J. Serpe, "Harnessing the Power of Stimuli-Responsive Polymers for Actuation", *Advanced Functional Materials*, Vol. 30, No. 2, p. 1903471, 2020.

354. Huo, M., J. Yuan, L. Tao and Y. Wei, "Redox-Responsive Polymers for Drug Delivery: from Molecular Design to Applications", *Polymer Chemistry*, Vol. 5, No. 5, pp. 1519–1528, 2014.

355. Trivedi, M., J. Laurence and T. Siahaan, "The Role of Thiols and Disulfides on Protein Stability", *Current Protein & Peptide Science*, Vol. 10, No. 6, pp. 614–625, 2009.

356. Quinn, J. F., M. R. Whittaker and T. P. Davis, "Glutathione Responsive Polymers and Their Application in Drug Delivery Systems", *Polymer Chemistry*, Vol. 8, No. 1, pp. 97–126, 2017.

357. Fuoco, T., A. Finne-Wistrand and D. Pappalardo, “A Route to Aliphatic Poly(Ester)s with Thiol Pendant Groups: From Monomer Design to Editable Porous Scaffolds”, *Biomacromolecules*, Vol. 17, No. 4, pp. 1383–1394, 2016.

358. Gok, O., P. Erturk, B. S. Bolu, T. N. Gevrek, R. Sanyal and A. Sanyal, “Dendrons and Multiarm Polymers with Thiol-Exchangeable Cores: A Reversible Conjugation Platform for Delivery”, *Biomacromolecules*, Vol. 18, No. 8, pp. 2463–2477, 2017.

359. Matsumoto, N. M., G. W. Buchman, L. H. Rome and H. D. Maynard, “Dual pH- and Temperature-Responsive Protein Nanoparticles”, *European Polymer Journal*, Vol. 69, pp. 532–539, 2015.

360. Zhuang, J., B. Zhao and S. Thayumanavan, “Cascaded Step-Growth Polymerization for Functional Polyamides with Diverse Architectures and Stimuli Responsive Characteristics”, *ACS Macro Letters*, Vol. 8, No. 3, pp. 245–249, 2019.

361. Liu, J., V. Bulmus, C. Barner-Kowollik, M. H. Stenzel and T. P. Davis, “Direct Synthesis of Pyridyl Disulfide-Terminated Polymers by RAFT Polymerization”, *Macromolecular Rapid Communications*, Vol. 28, No. 3, pp. 305–314, 2007.

362. Boyer, C., J. Liu, V. Bulmus, T. P. Davis, C. Barner-Kowollik and M. H. Stenzel, “Direct Synthesis of Well-Defined Heterotelechelic Polymers for Bioconjugations”, *Macromolecules*, Vol. 41, No. 15, pp. 5641–5650, 2008.

363. Boehnke, N., J. K. Kammeyer, R. Damoiseaux and H. D. Maynard, “Stabilization of Glucagon by Trehalose Glycopolymer Nanogels”, *Advanced Functional Materials*, Vol. 28, No. 10, p. 1705475, 2018.

364. Perera, M. M. and N. Ayres, “Gelatin Based Dynamic Hydrogels via Thiol–Norbornene Reactions”, *Polymer Chemistry*, Vol. 8, No. 44, pp. 6741–6749, 2017.

365. Basak, D., R. Bej and S. Ghosh, “Amphiphilic Poly(Disulfide) Micelles and A Remarkable Impact of the Core Hydrophobicity on Redox Responsive Disassembly”, *Polymer Chemistry*, Vol. 6, No. 36, pp. 6465–6474, 2015.

366. Zhu, S., Z. -W. Li and H. Zhao, “Patchy Micelles Based on Coassembly of Block Copolymer Chains and Block Copolymer Brushes on Silica Particles”, *Langmuir*, Vol. 31, No. 14, pp. 4129–4136, 2015.

367. Han, H. S., T. Thambi, K. Y. Choi, S. Son, H. Ko, M. C. Lee, D. -G. Jo, Y. S. Chae, Y. M. Kang, J. Y. Lee and J. H. Park, “Bioreducible Shell-Cross-Linked Hyaluronic Acid Nanoparticles for Tumor-Targeted Drug Delivery”, *Biomacromolecules*, Vol. 16, No. 2, pp. 447–456, 2015.

368. Koda, Y., T. Terashima, M. Sawamoto and H. D. Maynard, “Amphiphilic/Fluorous Random Copolymers as A New Class of Non-Cytotoxic Polymeric Materials for Protein Conjugation”, *Polymer Chemistry*, Vol. 6, No. 2, pp. 240–247, 2015.

369. Lin, E. -W. and H. D. Maynard, “Grafting From Small Interfering Ribonucleic Acid (SiRNA) as an Alternative Synthesis Route to SiRNA–Polymer Conjugates”, *Macromolecules*, Vol. 48, No. 16, pp. 5640–5647, 2015.

370. Guo, F. and Z. Guo, “Inspired Smart Materials with External Stimuli Responsive Wettability: A Review”, *RSC Advances*, Vol. 6, No. 43, pp. 36623–36641, 2016.

371. Lou, X., Y. Huang, X. Yang, H. Zhu, L. Heng and F. Xia, “External Stimuli Responsive Liquid-Infused Surfaces Switching Between Slippery and Nonslippery States: Fabrications and Applications”, *Advanced Functional Materials*, Vol. 30, No. 10, p. 1901130, 2020.

372. Das, A., A. Shome and U. Manna, “Porous and Reactive Polymeric Interfaces: An Emerging Avenue for Achieving Durable and Functional Bio-Inspired Wettability”, *Journal of Materials Chemistry A*, Vol. 9, No. 2, pp. 824–856, 2021.

373. Escorihuela, J., A. T. M. Marcelis and H. Zuilhof, “Metal-Free Click Chemistry Reactions on Surfaces”, *Advanced Materials Interfaces*, Vol. 2, No. 13, p. 1500135, 2015.

374. Brzezinska, E. and A. L. Ternay, “Disulfides. 1. Syntheses Using 2,2’-Dithiobis(Benzothiazole)”, *The Journal of Organic Chemistry*, Vol. 59, No. 26, pp. 8239–8244, 1994.

375. Tsarevsky, N. V., J. Huang and K. Matyjaszewski, “Synthesis of Hyperbranched Degradable Polymers by Atom Transfer Radical (Co)Polymerization of Inimers with Ester or Disulfide Groups”, *Journal of Polymer Science Part A: Polymer Chemistry*, Vol. 47, No. 24, pp. 6839–6851, 2009.

376. Gevrek, T. N., R. N. Ozdeslik, G. S. Sahin, G. Yesilbag, S. Mutlu and A. Sanyal, “Functionalization of Reactive Polymeric Coatings via Diels-Alder Reaction Using Microcontact Printing”, *Macromolecular Chemistry and Physics*, Vol. 213, No. 2, pp. 166–172, 2012.

377. Tugulu, S., P. Silacci, N. Stergiopulos and H. -A. Klok, “RGD—Functionalized Polymer Brushes as Substrates for The Integrin Specific Adhesion of Human Umbilical Vein Endothelial Cells”, *Biomaterials*, Vol. 28, No. 16, pp. 2536–2546, 2007.

378. Möller, M., C. Hentschel, L. Chi and A. Studer, “Aggregation Behaviour of Peptide–Polymer Conjugates Containing Linear Peptide Backbones and Multiple Polymer Side Chains Prepared by Nitroxide-Mediated Radical Polymerization”, *Organic & Biomolecular Chemistry*, Vol. 9, No. 7, pp. 2403–2412, 2011.

379. Uhlig, K., H. Boerner, E. Wischerhoff, J. -F. Lutz, M. Jaeger, A. Laschewsky and C. Duschl, “On the Interaction of Adherent Cells with Thermoresponsive Polymer Coatings”, *Polymers*, Vol. 6, No. 4, pp. 1164–1177, 2014.

380. Schottelius, M., B. Laufer, H. Kessler and H. -J. Wester, “Ligands for Mapping α V β 3 -Integrin Expression in Vivo”, *Accounts of Chemical Research*, Vol. 42, No. 7, pp. 969–980, 2009.

381. Wischerhoff, E., N. Badi, J. -F. Lutz and A. Laschewsky, “Smart Bioactive Surfaces”, *Soft Matter*, Vol. 6, No. 4, pp. 705–713, 2010.

382. Lutz, J. -F., H. G. Börner and K. Weichenhan, “Combining ATRP and ‘Click’ Chemistry: A Promising Platform Toward Functional Biocompatible Polymers and Polymer Bioconjugates”, *Macromolecules*, Vol. 39, No 19, pp. 6376–6383, 2006.

383. Ferreira, P., P. Alves, P. Coimbra and M. H. Gil, “Improving Polymeric Surfaces for Biomedical Applications: A Review”, *Journal of Coatings Technology and Research*, Vol. 12, No. 3, pp. 463–475, 2015.

384. Lou, X., Y. Huang, X. Yang, H. Zhu, L. Heng and F. Xia, “External Stimuli Responsive Liquid-Infused Surfaces Switching between Slippery and Nonslippery States: Fabrications and Applications”, *Advanced Functional Materials*, Vol. 30, No. 10, p. 1901130, 2020.

385. Mertgen, A. -S., V. T. Trossmann, A. G. Guex, K. Maniura-Weber, T. Scheibel and M. Rottma, “Multifunctional Biomaterials: Combining Material Modification Strategies for Engineering of Cell-Contacting Surfaces”, *ACS Applied. Materials & Interfaces*, Vol. 12, No. 19, pp**.** 21342–21367, 2020.

386. Zhang, H., X. Zheng, W. Ahmed, Y. Yao, J. Bai, Y. Chen and C. Gao, “Design and Applications of Cell-Selective Surfaces and Interfaces”, *Biomacromolecules*, Vol. 19, No. 6, pp. 1746–1763, 2018.

387. Banerjee, I., R. C. Pangule and R. S. Kane, “Antifouling Coatings: Recent Developments in the Design of Surfaces That Prevent Fouling by Proteins, Bacteria, and Marine Organisms”, *Advance Materials* Vol. 23, No. 6, pp. 690–718, 2011.

388. Shi, Z. -Q., Y. -T. Cai, J. Deng, W. -F. Zhao and C. -S. Zhao, “Host–Guest Self-Assembly Toward Reversible Thermoresponsive Switching for Bacteria Killing and Detachment”, *ACS Applied Materials & Interfaces* Vol. 8, No. 15, pp. 23523–23532, 2016.

389. You, K., B. Gao, M. Wang, X. Wang, K. C. Okoro, A. Rakhimbekzoda and Y. Feng, “Versatile polymer-based strategies for antibacterial drug delivery systems and antibacterial coatings”, *Journal of Material Chemistry B*, Vol. 10, No. 7, pp. 1005-1018, 2022.

390. Shi, X., Y. Ye, H. Wang, F. Liu and Z. Wang, “Designing pH-Responsive Biodegradable Polymer Coatings for Controlled Drug Release via Vapor-Based Route”, *ACS Applied Materials &. Interfaces*, Vol. 10, No. 44, pp. 38449–38458, 2018.

391. Escorihuela, J., A. T. M. Marcelis, H. Zuilhof, “Metal-Free Click Chemistry Reactions on Surfaces”, *Advanced. Materials. Interfaces* Vol. 2, p.1500135, 2015.

392. Shi, X., G. Chen, L. Yuan, Z. Tang, W. Liu, Q. Zhang, D. M. Haddleton and H. Chen, “Integrating a Thermoresponsive Copolymer with Host–Guest Interactions for Fabricating Molecular Recognition Surfaces”, *Materials Horizons*, Vol. 1, No. 5, pp. 540–545, 2014.

393. Liu, K., Y. Kang, Z. Wang and X. Zhang, “25th Anniversary Article: Reversible and Adaptive Functional Supramolecular Materials: “Noncovalent Interaction” Matters”, *Advanced Materials*, Vol. 25, No. 39, pp. 5530–5548, 2013.

394. Loh, X. J., “Supramolecular Host–Guest Polymeric Materials for Biomedical Applications”, *Materials Horizons*, Vol. 1, No. 2, pp. 185–195, 2014.

395. Liao, X., G. Chen, M. Jiang, “Hydrogels Locked by Molecular Recognition Aiming at Responsiveness and Functionality”, *Polymer Chemistry*, Vol. 4, No. 6, pp. 1733–1745, 2013.

396. Yang, H., B. Yuan, X. Zhang and O. A. Scherman, “Supramolecular Chemistry at Interfaces: Host-Guest Interactions for Fabricating Multifunctional Biointerfaces”, *Accounts of Chemical Research*, Vol. 47, No. 7, pp. 2106–2115, 2014.

397. Zhang, Y., L. Ren, Q. Tu, X. Wang, R. Liu, L. Li, J. C. Wang, W. Liu, J. Xu and J. Wang, “Fabrication of reversible poly(dimethylsiloxane) Surfaces via Host-Guest Chemistry and Their Repeated Utilization in Cardiac Biomarker Analysis”, *Analytical Chemistry*, Vol. 83, No. 24, pp. 9651–9659, 2011.

398. Gokel, G. W., W. M. Leevy and M. E. Weber, “Crown ethers: Sensors for ions and molecular scaffolds for materials and biological models”, *Chemical Reviews*, Vol. 104, No. 5, pp. 2723–2750, 2004.

399. Ikeda, A. and S. Shinkai, “Novel Cavity Design using Calix[n]arene Skeletons: Toward Molecular Recognition and Metal Binding”, *Chemical Reviews*, Vol. 97, No. 5, pp. 1713–1734, 1997.

400. Roy, I., S. Bobbala, R. M. Young, Y. Beldjoudi, M. T. Nguyen, M. M. Cetin, J. A. Cooper, S. Allen, O. Anamimoghadam, E. A. Scott, M. R. Wasielewski and J. F. Stoddart, "A Supramolecular Approach for Modulated Photoprotection, Lysosomal Delivery, and Photodynamic Activity of a Photosensitizer", *Journal of the American Chemical Society*, Vol. 141, No. 31, pp. 12296–12304, 2019.

401. Cao, D., Y. Kou, J. Liang, Z. Chen, L. Wang, L. and H. Meier, "A Facile and Efficient Preparation of Pillararenes and a Pillarquinone", *Angewandte Chemie International Edition*, Vol. 48, No. 51, pp. 9721–9723, 2009.

402. Pirondini, L. and E. Dalcanale, "Molecular Recognition at The Gas–Solid Interface: a Powerful Tool for Chemical Sensing", *Chemical Society Reviews*, Vol. 36, No. 5, pp. 695–706, 2007.

403. Jiang, B., H. Guo, L. Zhao, B. Xu, C. Wang, C. Liu and H. Fan, "Fabrication of a β-Cyclodextrin-based Self-Assembly Containing a Redox-Responsive Ferrocene", *Soft Matter*, Vol. 16, No. 1, pp. 125–131, 2019.

404. Guo, H., J. Yang, J. Zhou, L. Zeng, L. Zhao and B. Xu, "Photoresponsive Self-Assembly of a β-Cyclodextrin Derivative with an Azobenzene Terminal Group in Water", *Dyes and Pigments*, Vol. 149, pp. 626–632, 2018.

405. Wankar, J., N. G. Kotla, S. Gera, S. Rasala, A. Pandit and Y. A. Rochev, "Recent Advances in Host–Guest Self-Assembled Cyclodextrin Carriers: Implications for Responsive Drug Delivery and Biomedical Engineering", *Advanced Functional Materials*, Vol. 30, No. 44, p. 1909049, 2020.

406. Zhang, L., S. Man, H. Qiu, Z. Liu, M. Zhang, L. Ma, L. and W. Gao, "Curcumin-Cyclodextrin Complexes Enhanced the Anti-Cancer Effects of Curcumin", *Environmental Toxicology and Pharmacology*, Vol. 48, pp. 31–38, 2016.

407. Ang, C. Y., S. Y. Tan, X. Wang, Q. Zhang, M. Khan, L. Bai, S. S. Tamil, X. Ma, L. Zhu, K. T. Nguyen, N. S. Tan and Y. Zhao, "Supramolecular Nanoparticle Carriers Self-Assembled from Cyclodextrin- and Adamantane-functionalized Polyacrylates for Tumor-Targeted Drug Delivery", *Journal of Materials Chemistry B*, Vol. 2, No. 13, pp. 1879–1890, 2014.

408. Hu, C., J. Wu, T. Wei, W. Zhan, Y. Qu, Y. Pan, Q. Yu and H. Chen, "A Supramolecular Approach for Versatile Biofunctionalization of Magnetic Nanoparticles", *Journal of Materials Chemistry B*, Vol. 6, No. 15, pp. 2198–2203, 2018.

409. Lee, H. J., P. T. Le, H. J. Kwon and K. D. Park, "Supramolecular Assembly of Tetronic–Adamantane and Poly(β-cyclodextrin) as Injectable Shear-Thinning Hydrogels", *Journal of Materials Chemistry B*, Vol. 7, No. 21, pp. 3374–3382, 2019.

410. Luong, T. D., M. Zoughaib, R. Garifullin, S. Kuznetsova, M. O. Guler and T. I. Abdullin, "In Situ functionalization of Poly(hydroxyethyl methacrylate) Cryogels with Oligopeptides via β-Cyclodextrin-Adamantane Complexation for Studying Cell-Instructive Peptide Environment", *ACS Applied Bio Materials*, Vol. 3, No. 2, pp. 1116–1128, 2020.

411. Sadhu, V. B., A. Perl, X. Duan, D. N. Reinhoudt and J. Huskens, "Supramolecular Microcontact Printing with Receptor-Functionalized PDMS Stamps", *Soft Matter*, Vol. 5, No. 6, pp. 1198–1204, 2009.

412. Guerrouache, M., C. Karakasyan, C. Gaillet, M. Canva and M. C. Millot, "Immobilization of a Functionalized Poly(ethylene glycol) onto β-Cyclodextrin-Coated Surfaces by Formation of Inclusion Complexes: Application to the Coupling of Proteins", *Journal of Applied Polymer Science*, Vol. 100, No. 3, pp. 2362–2370, 2006.

413. Cao, L., Y. Qu, C. Hu, T. Wei, W. Zhan, Q. Yu and H. Chen, "A Universal and Versatile Approach for Surface Biofunctionalization: Layer-by-Layer Assembly Meets Host–Guest Chemistry", *Advanced Materials Interfaces*, Vol. 3, No. 18, p. 1600600, 2016.

414. Ortiz, M., A. Fragoso and C. K. O'Sullivan, "Amperometric Detection of Antibodies in Serum: Performance of Self-Assembled Cyclodextrin/Cellulose Polymer Interfaces as Antigen Carriers", *Organic & Biomolecular Chemistry*, Vol. 9, No. 14, pp. 4770-4773, 2011.

415. Park, I. -K., H. A. von Recum, S. Jiang, and S. H. Pun, “Supramolecular Assembly of Cyclodextrin-Based Nanoparticles on Solid Surfaces for Gene Delivery”, *Langmuir*, Vol. 22, No. 20, pp. 8478–8484, 2006.

416. Kumar, A., H. A. Biebuyck and G. M. Whitesides, “Patterning Self-Assembled Monolayers: Applications in Materials Science”, *Langmuir*, Vol. 10, No. 5, pp. 1498–1511, 1994.

417. Huang, L., X. -H. Liu, X. -H. Zhang, L. Tan and C. -J. Liu, “A Highly Efficient Bactericidal Surface based on the Co-capture Function and Photodynamic Sterilization”, *Journal of Materials Chemistry B*, Vol. 6, No. 42, pp. 6831–6841, 2018.

418. Zhao, X., N. Qiu, Y. Ma, J. Liu, L. An, T. Zhang, Z. Li, X. Han and L. Chen, “Preparation, Characterization and Biological Evaluation of β-cyclodextrin-biotin Conjugate based Podophyllotoxin Complex”, *European Journal of Pharmaceutical Sciences*, Vol. 160, p. 105745, 2021.

419. Neirynck, P., J. Brinkmann, Q. An, D. W. J. van der Schaft, L. -G. Milroy, P. Jonkheijm and L. Brunsveld, “Supramolecular Control of Cell Adhesion via Ferrocene–Cucurbit[7]uril Host–Guest Binding on Gold Surfaces”, *Chemical Communications*, Vol. 49, No. 35, pp. 3679–3681, 2013.

420. Zhang, Q., Y. Cai, X. J. Wang, J. L. Xu, Z. Ye, S. Wang, P. H. Seeberger and J. Yin, “Targeted Photodynamic Killing of Breast Cancer Cells Employing Heptamannosylated β-Cyclodextrin-Mediated Nanoparticle Formation of an Adamantane-Functionalized BODIPY photosensitizer”, *ACS Applied Materials and Interfaces*, Vol. 8, No. 49, pp. 33405–33411, 2016.

APPENDIX A: ADDITIONAL SPECTRA

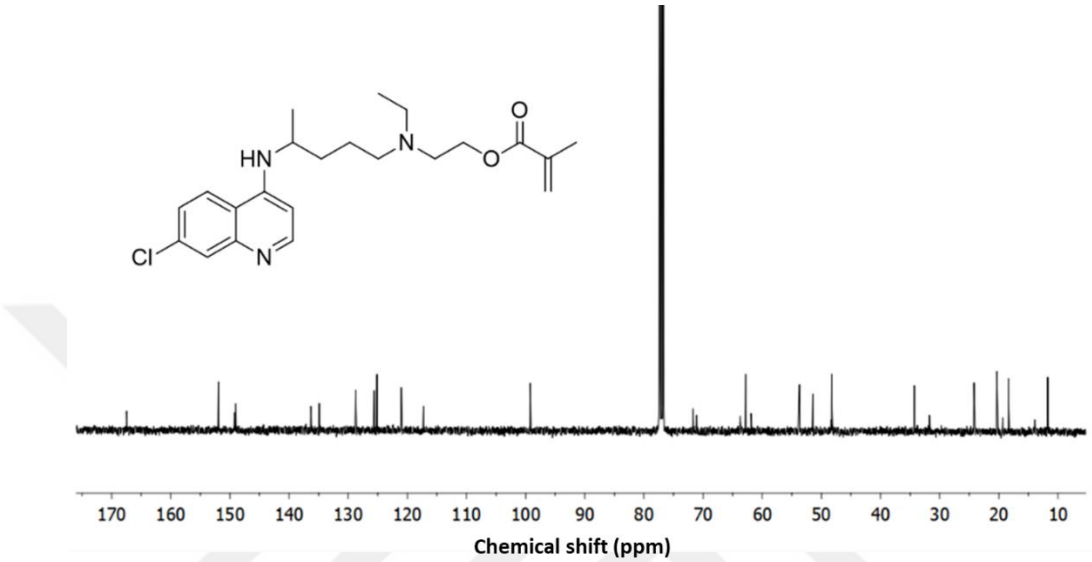

Figure A.1. ^{13}C NMR spectrum of HCQ-E-MA monomer ($CDCl_3$).

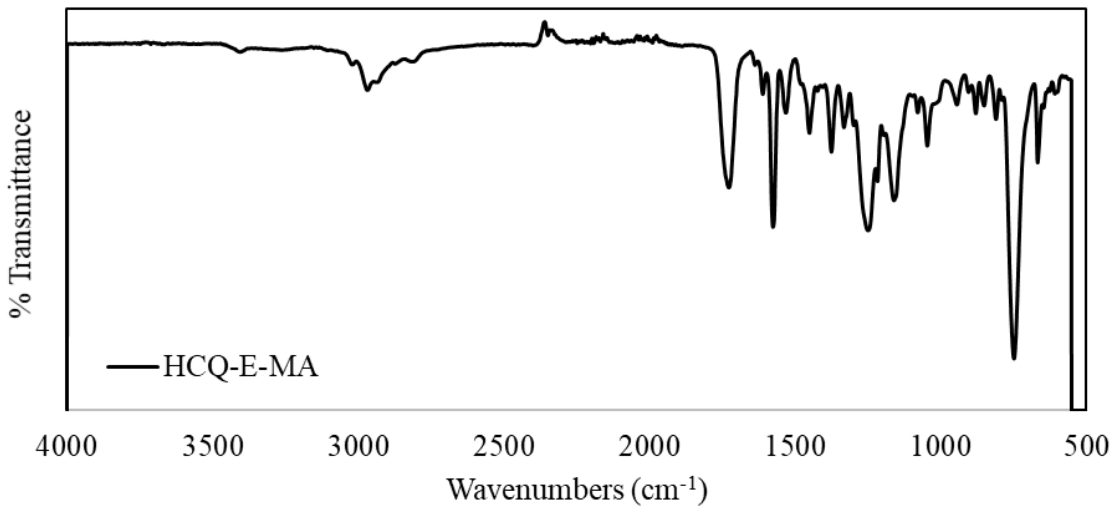

Figure A.2. FTIR spectrum of HCQ-E-MA monomer.

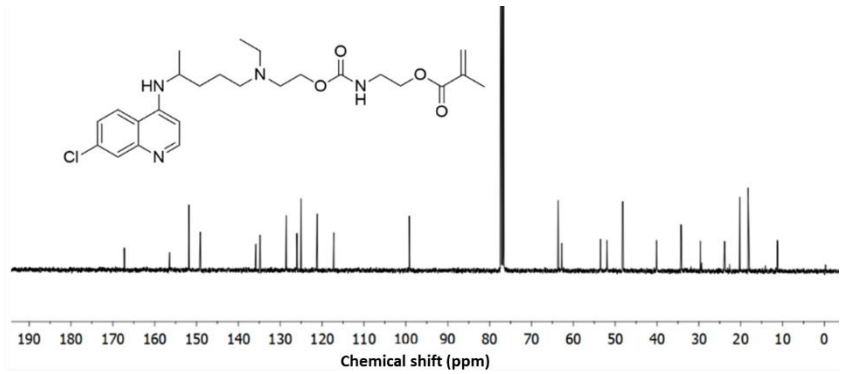

Figure A.3. ^{13}C NMR spectrum of HCQ-C-MA monomer ($CDCl_3$).

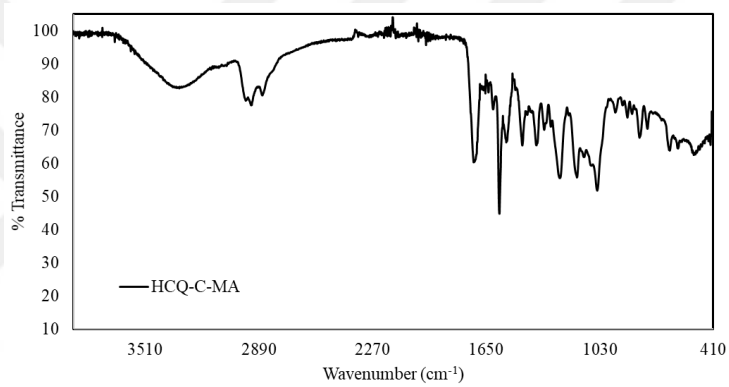

Figure A.4. FTIR spectrum of HCQ-C-MA monomer.

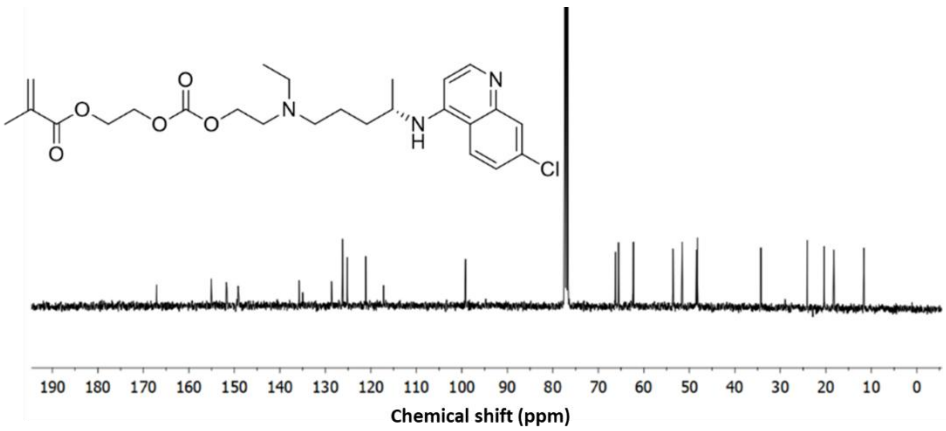

Figure A.5. ^{13}C NMR spectrum of HCQ-CB-MA monomer ($CDCl_3$).

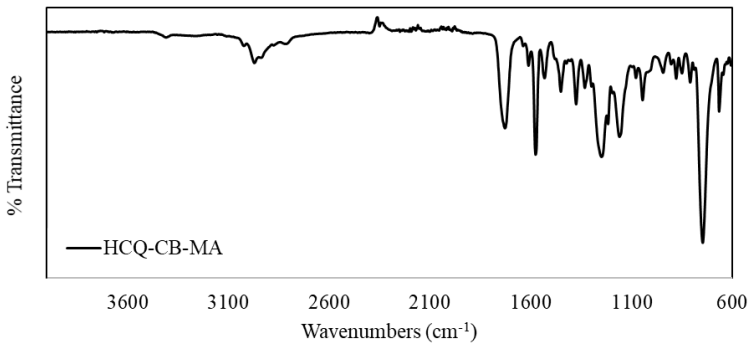

Figure A.6. FTIR spectrum of HCQ-CB-MA monomer.

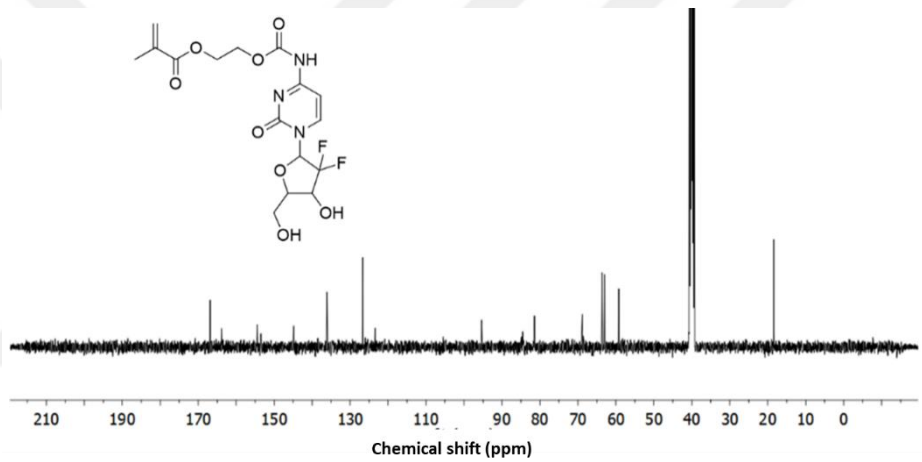

Figure A.7. ^{13}C NMR spectrum of GEM-C-MA monomer (DMSO d6).

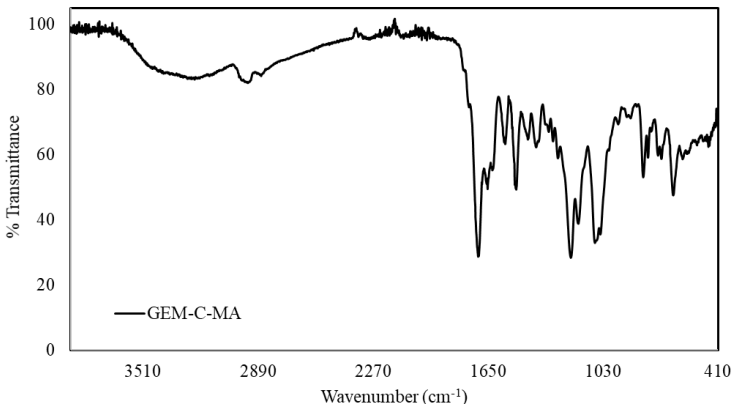

Figure A.8. FTIR spectrum of GEM-C-MA monomer.

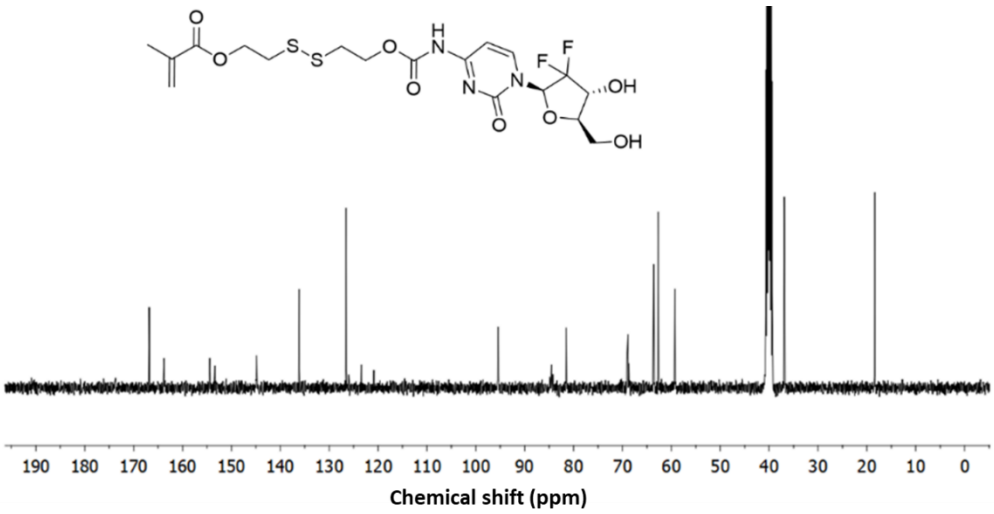

Figure A.9. ^{13}C NMR of GEM-SSC-MA monomer (DMSO d6).

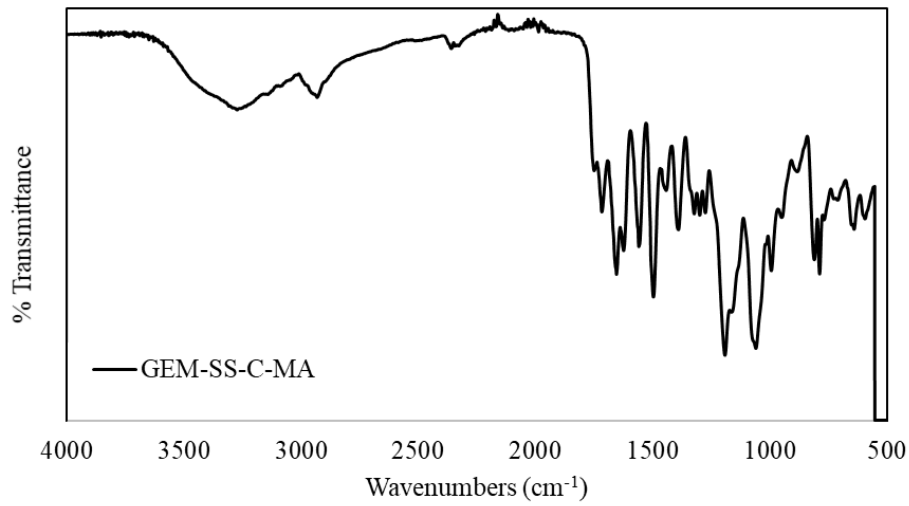

Figure A.10. FTIR spectrum of GEM-SSC-MA monomer.

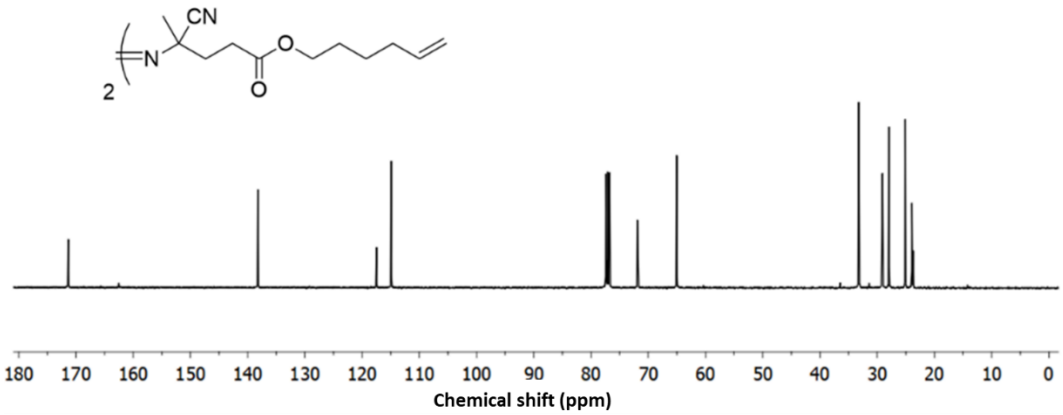

Figure A.11. ^{13}C NMR spectrum of azobis-ene ($CDCl_3$).

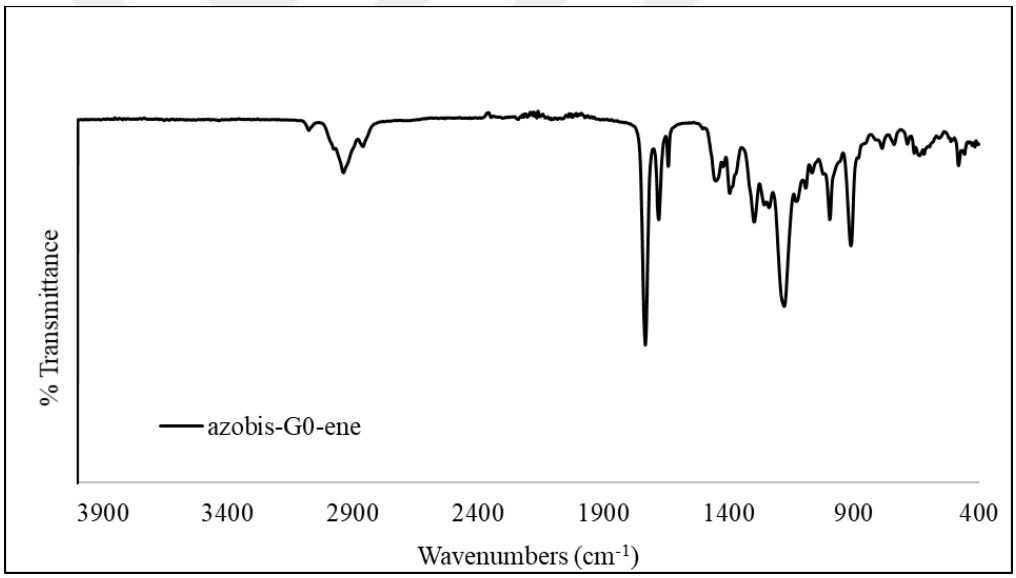

Figure A.12. FTIR spectrum of azobis-ene.

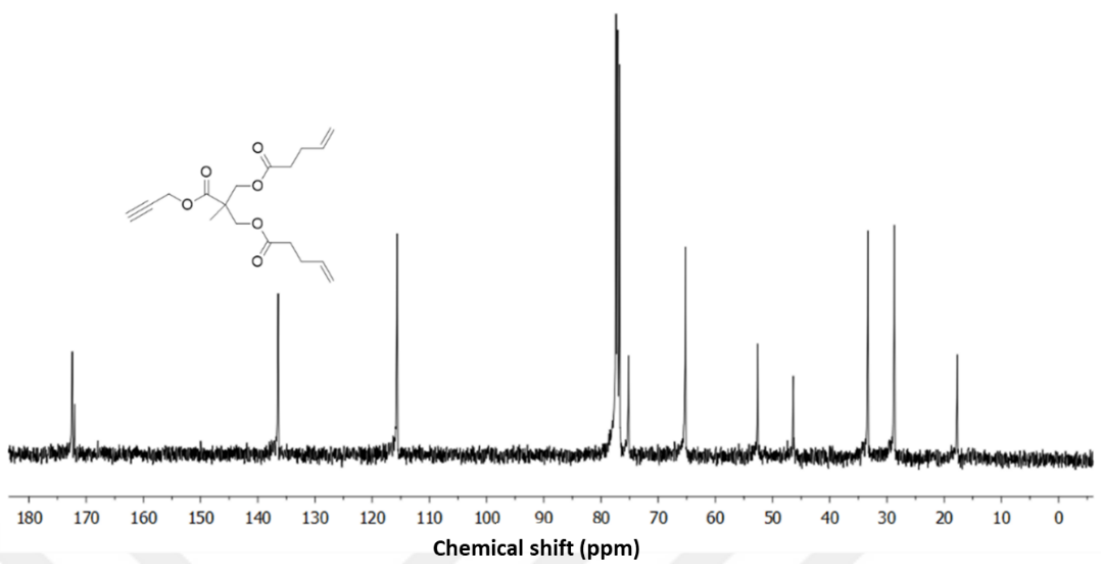

Figure A.13. ^{13}C NMR spectrum of G1-diene-alkyne ($CDCl_3$).

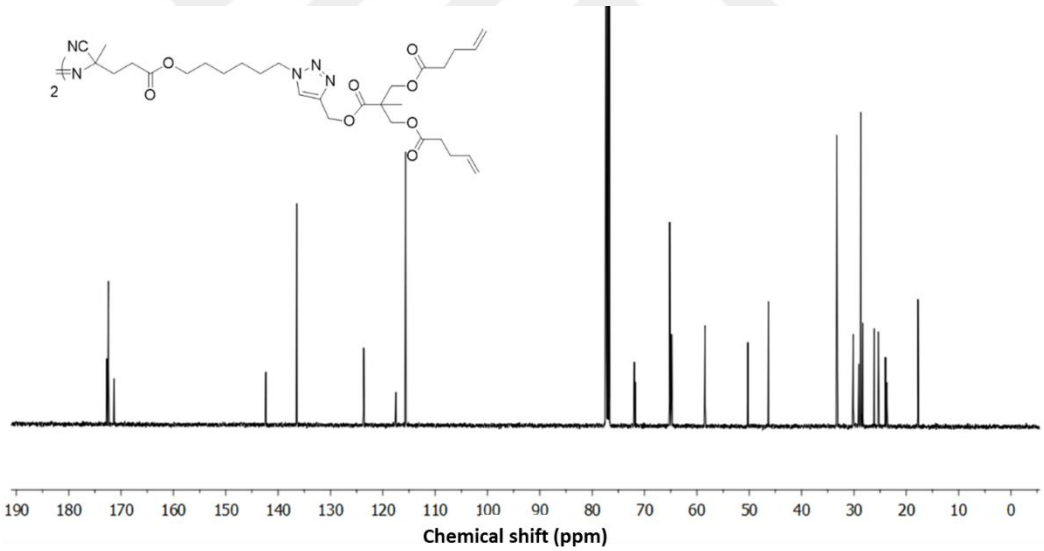

Figure A.14. ^{13}C NMR spectrum of Azobis-G1-diene ($CDCl_3$).

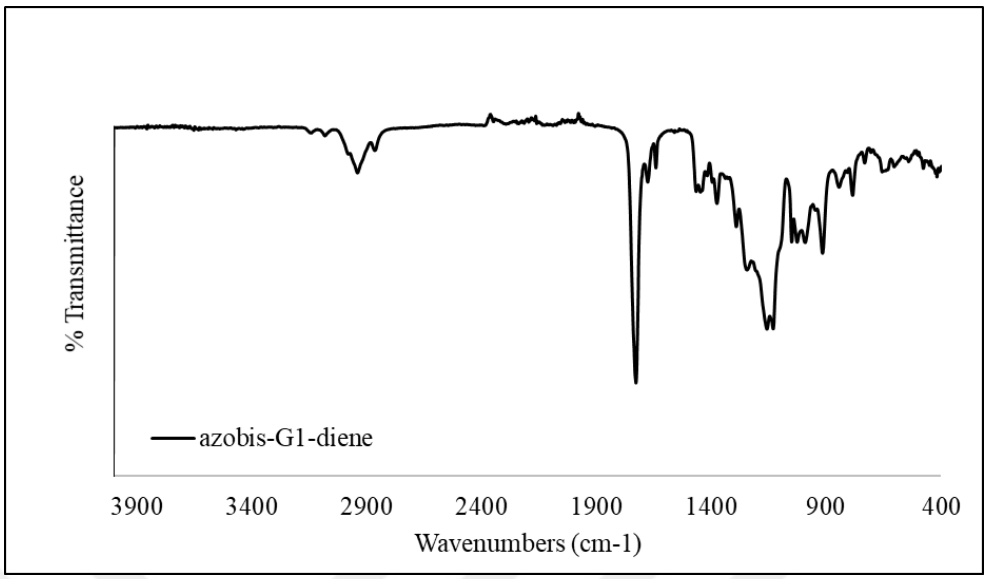

Figure A.15. FTIR spectrum of azobis-G1-diene.

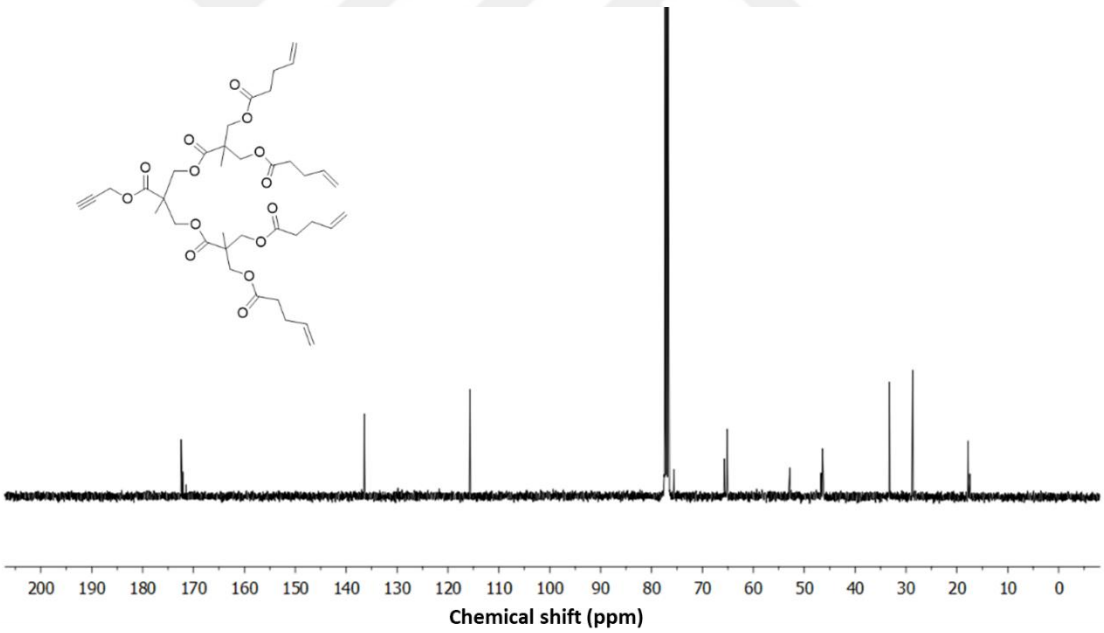

Figure A.16. ^{13}C NMR spectrum of alkyne bearing G2-tetraene ($CDCl_3$).

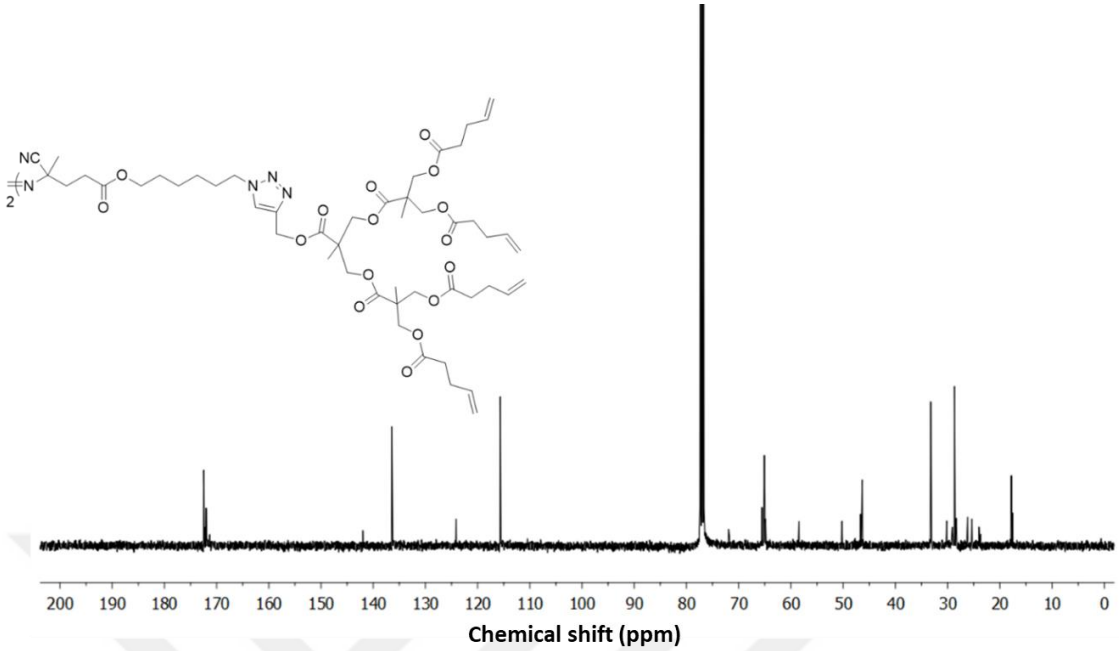

Figure A.17. ^{13}C NMR spectrum of Azobis-G2-tetraene ($CDCl_3$).

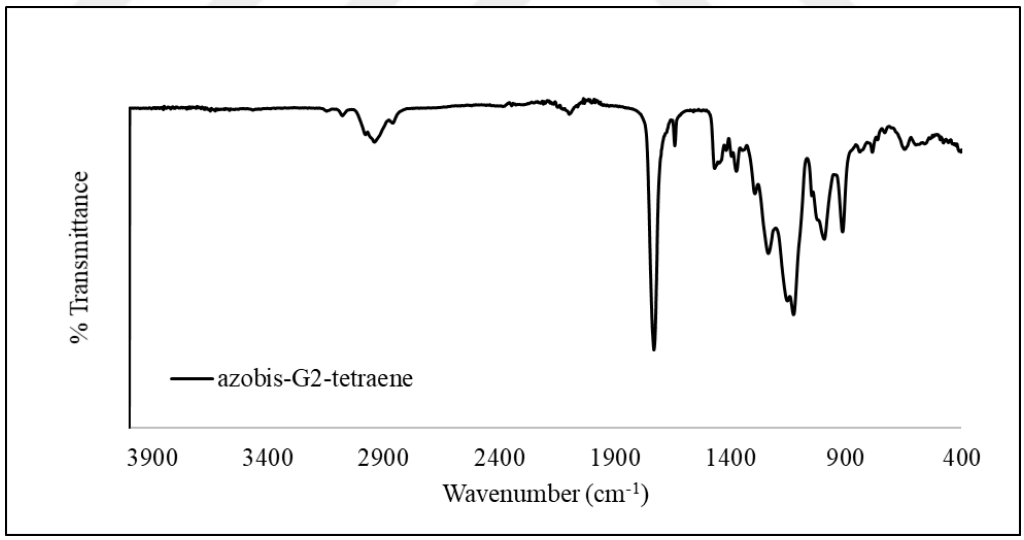

Figure A.18. FTIR spectrum of azobis-G1-diene.

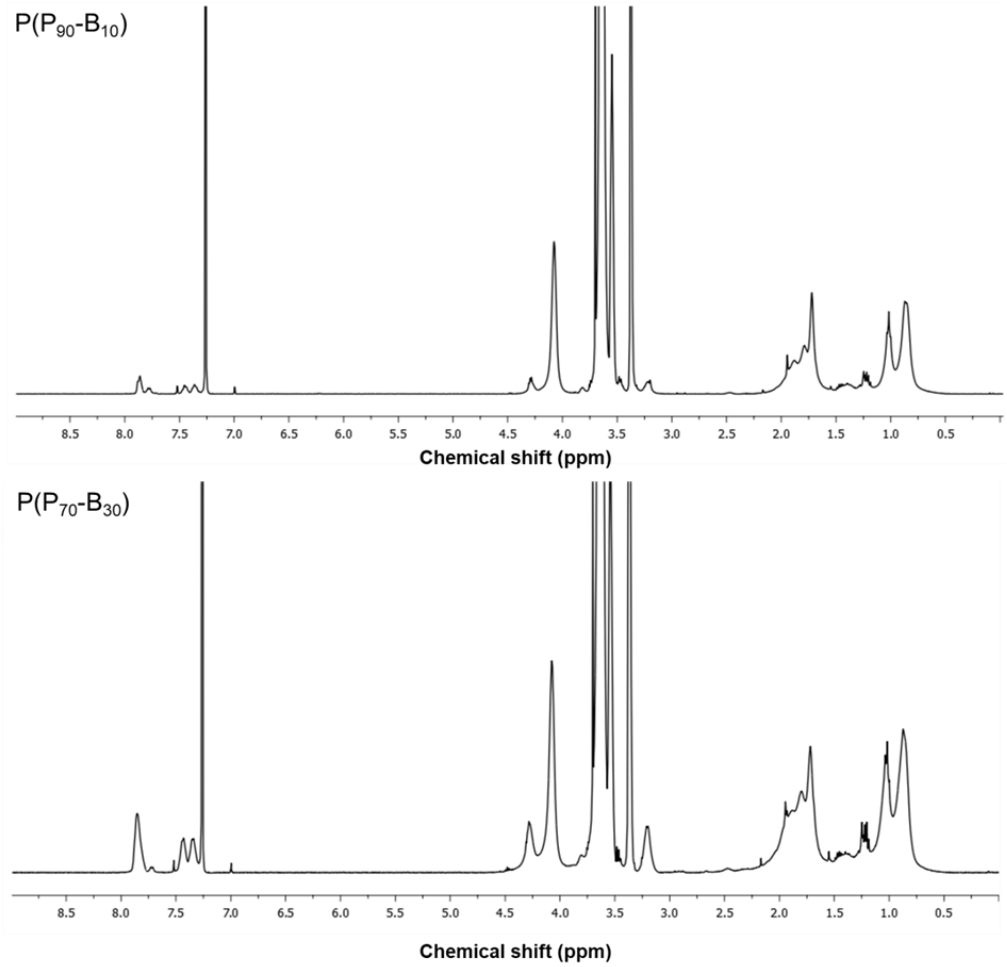

Figure A.19. ^{1}H NMR spectra of copolymer P(P_{90}-B_{10}) and P(P_{70}-B_{30}) in $CDCl_3$.

APPENDIX B: COPYRIGHT NOTICES

Oncol Rep. 2017 Aug; 38(2): 611–624.
Published online 2017 Jun 14. doi: 10.3892/or.2017.5718

PMCID: PMC5562049
PMID: 28627697

Cancer drug delivery in the nano era: An overview and perspectives

Zhen Li,[1,2] Shirui Tan,[3] Shuan Li,[1] Qiang Shen,[4] and Kunhua Wang[1,2]

Author information ▶ Article notes ▶ Copyright and License information ▼ Disclaimer

Copyright : © Li et al.

This is an open access article distributed under the terms of the Creative Commons Attribution-NonCommercial-NoDerivs License, which permits use and distribution in any medium, provided the original work is properly cited, the use is non-commercial and no modifications or adaptations are made.

Figure B.1. Copyright license of [22].

17.12.2022 19:12 Rightslink® by Copyright Clearance Center

CCC RightsLink

Home | Help | Email Support | Aysun Değirmenci

Multi-Functional Nanogels as Theranostic Platforms: Exploiting Reversible and Nonreversible Linkages for Targeting, Imaging, and Drug Delivery

ACS Publications Most Trusted. Most Cited. Most Read.

Author: Laura Chambre, Aysun Degirmenci, Rana Sanyal, et al
Publication: Bioconjugate Chemistry
Publisher: American Chemical Society
Date: Jun 1, 2018

Copyright © 2018, American Chemical Society

PERMISSION/LICENSE IS GRANTED FOR YOUR ORDER AT NO CHARGE

This type of permission/license, instead of the standard Terms and Conditions, is sent to you because no fee is being charged for your order. Please note the following:

- Permission is granted for your request in both print and electronic formats, and translations.
- If figures and/or tables were requested, they may be adapted or used in part.
- Please print this page for your records and send a copy of it to your publisher/graduate school.
- Appropriate credit for the requested material should be given as follows: "Reprinted (adapted) with permission from {COMPLETE REFERENCE CITATION}. Copyright {YEAR} American Chemical Society." Insert appropriate information in place of the capitalized words.
- One-time permission is granted only for the use specified in your RightsLink request. No additional uses are granted (such as derivative works or other editions). For any uses, please submit a new request.

If credit is given to another source for the material you requested from RightsLink, permission must be obtained from that source.

BACK CLOSE WINDOW

© 2022 Copyright - All Rights Reserved | Copyright Clearance Center, Inc. | Privacy statement | Data Security and Privacy | For California Residents | Terms and ConditionsComments? We would like to hear from you. E-mail us at customercare@copyright.com

Figure B.2. Copyright license of [58].

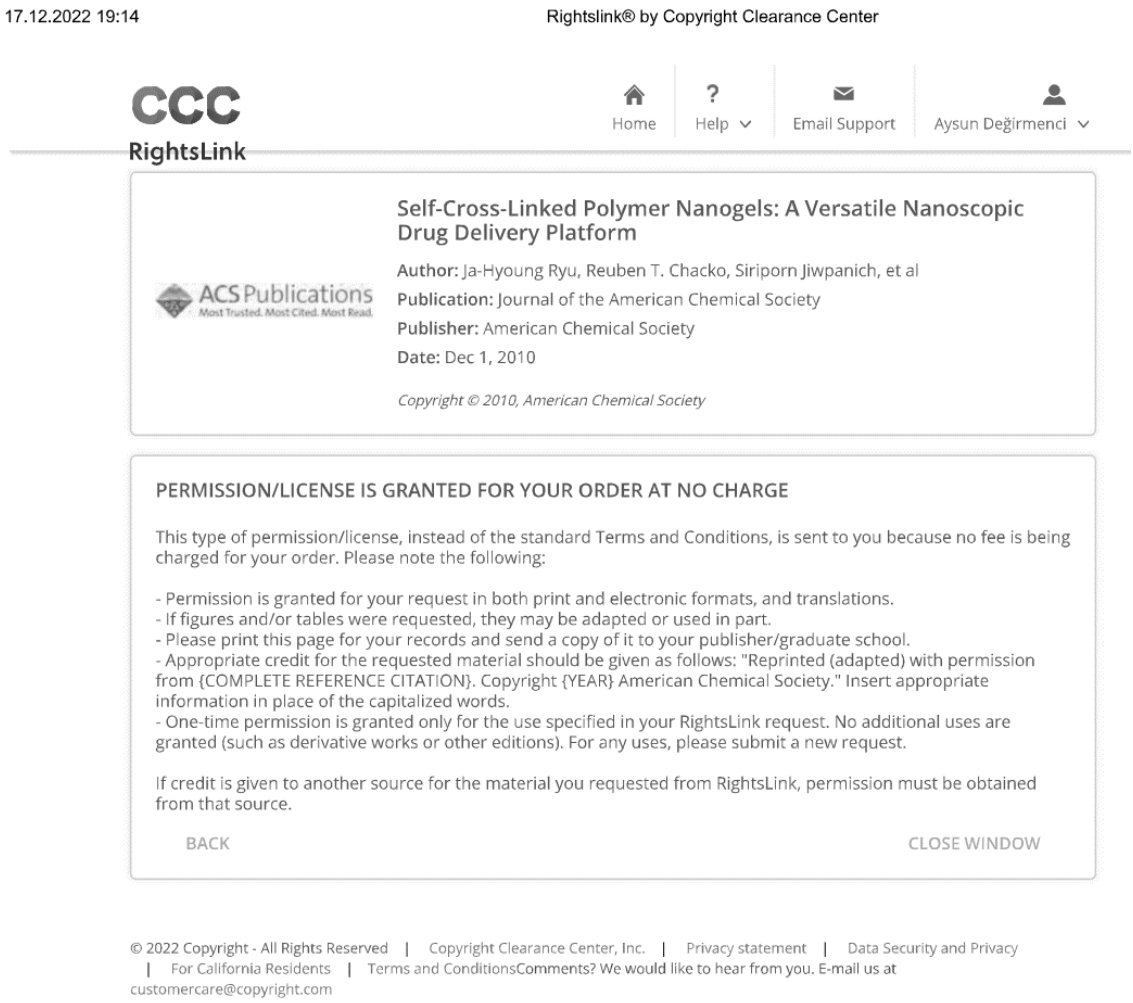

Figure B.3. Copyright license of [59].



Figure B.4. Copyright license of [160].



Figure B.5. Copyright license of [162].

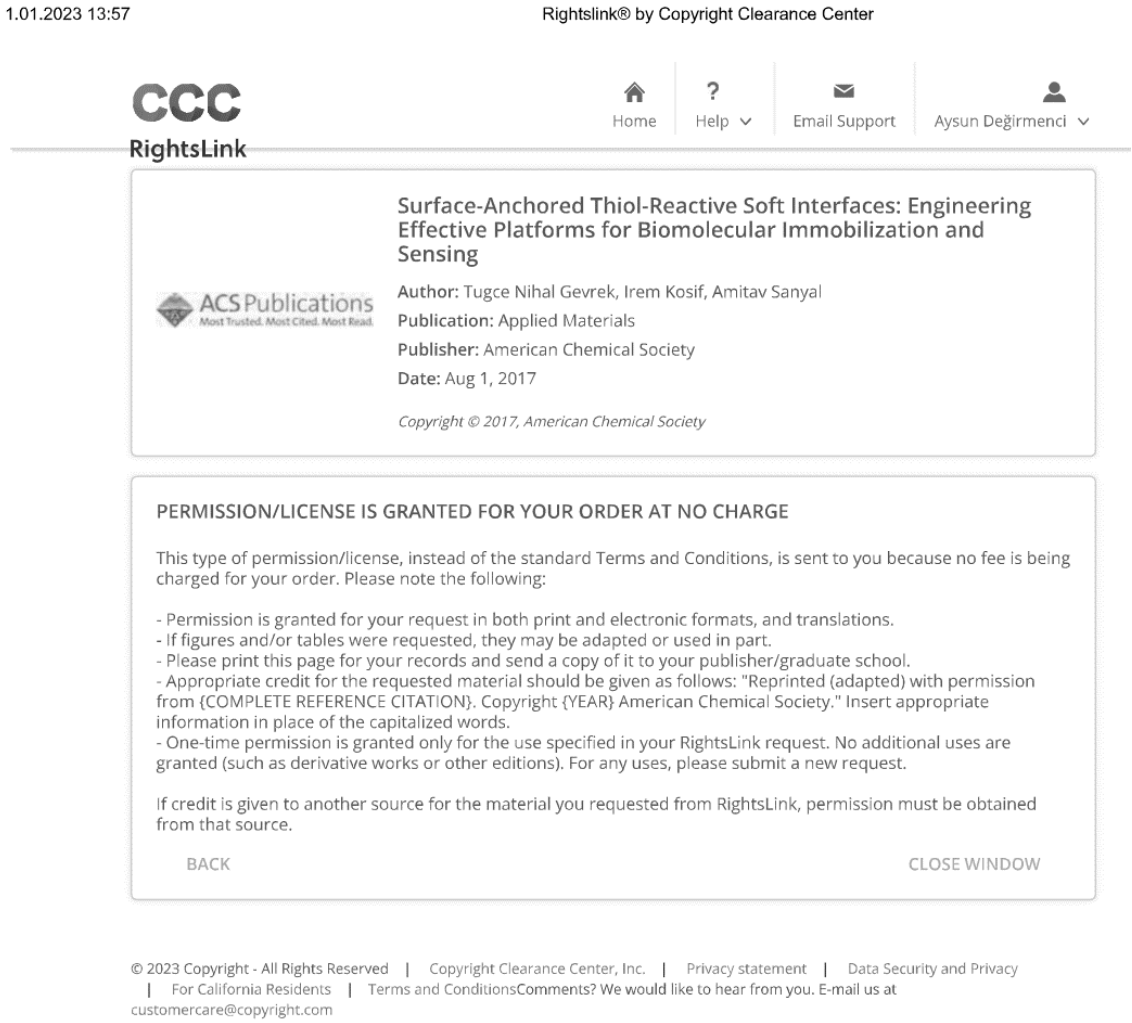

Figure B.6. Copyright license of [166].



Figure B.7. Copyright license of [201].

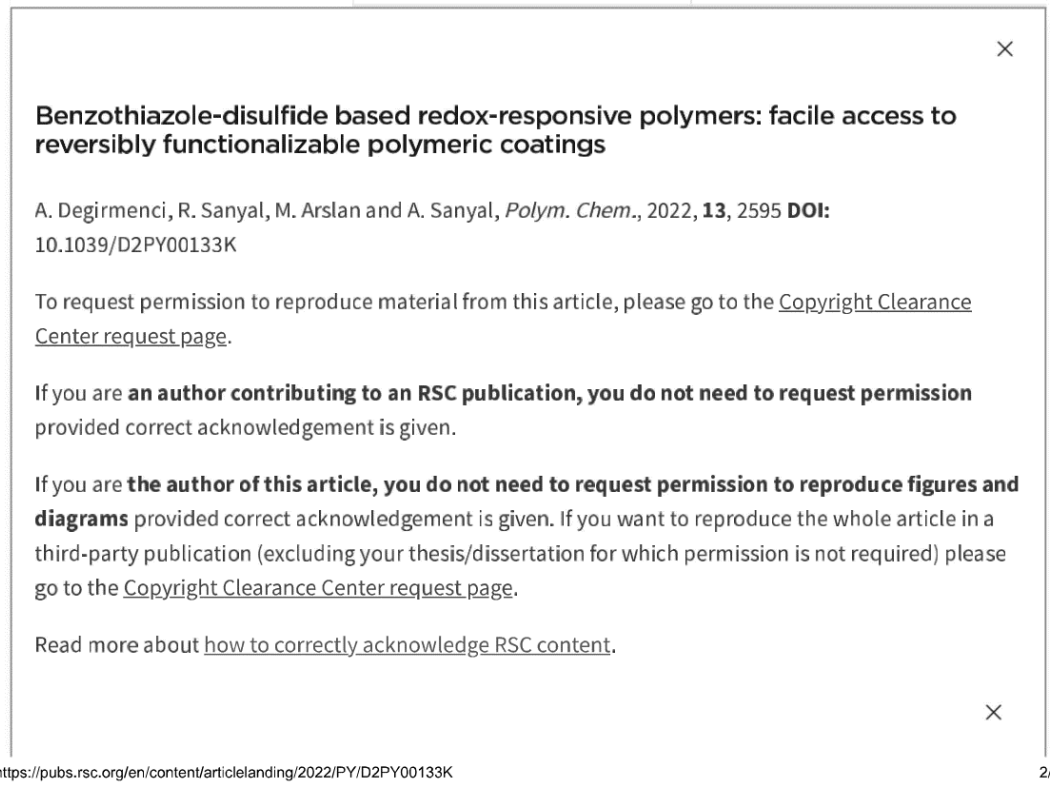

Figure B.8. Copyright license of [337].